JOURNAL OF THE ELECTROCHEMICAL SOCIETY

ELECTROCHEMICAL SCIENCE AND TECHNOLOGY

SOLID-STATE SCIENCE AND TECHNOLOGY

REVIEWS AND NEWS

VOL. 125, NO. 5 MAY 1978

JESOAN 125 (5) 683-832, 211C-236C

FUTURE MEETINGS

SEATTLE, WASHINGTON—MAY 21, 22, 23, 24, 25, & 26, 1978

Headquarters at The Olympic

Final program published in March 1978 issue of **This Journal.** If you would like a copy of the advance program booklet and other information pertaining to this meeting, please write: Seattle Meeting, The Electrochemical Society, Inc., P.O. Box 2071, Princeton, N.J. 08540.

PITTSBURGH, PENNSYLVANIA—OCTOBER 15, 16, 17, 18, 19, & 20, 1978

Headquarters at the Pittsburgh Hilton

The detailed Call for Papers published in December 1977-April 1978 issues of **This Journal.** Final program published in August 1978 issue of **This Journal.**

Planned symposia for the Pittsburgh Meeting include the following Divisions, Groups, and subjects:

Battery—Battery Design and Optimization, Organic and Inorganic Separators, General Session; **Battery and Energy Technology Group**—Batteries Systems for Vehicle Propulsion; **Corrosion**—Atmospheric Corrosion, Fundamental Aspects of Cathodic Protection, General Session; **Dielectrics and Insulation**—Double Dielectric Interfaces; **Dielectrics and Insulation and Electronics**—Fiber Optics: Materials and Devices; **Electrodeposition**—Engineering Topics in Electrodeposition, General Session; **Electronics**—Very Large Scale Integration (VLSI), Semiconductors General Sessions, General Materials and Processes General Session; **Electronics, Corrosion, and Dielectrics and Insulation**—Corrosion of Electronic Materials; **Electronics, Dielectrics and Insulation, and Electrothermics and Metallurgy**—Growth and Evaluation of Materials Prepared by Low Pressure CVD; **Electrothermics and Metallurgy**—Fine Particles; **Electrothermics and Metallurgy and Energy Technology Group**—Materials for High Temperature Gas-Cooled Nuclear Energy Conversion (Fission and Fusion Reactors); **Energy Technology Group**—General Session; **Energy Technology Group and Corrosion**—Electrochemical Phenomena in Solar Heating and Cooling, Photothermal, and Ocean Thermal Energy Conversion Systems; **Energy Technology Group and Battery**—Phosphoric Acid Fuel Cell Technology; **Industrial Electrolytic**—Electrochemical Methods in Extractive Metallurgy; and **Physical Electrochemistry**—Second International Symposium on Molten Salts.

BOSTON, MASSACHUSETTS—MAY 6, 7, 8, 9, 10, & 11, 1979

Headquarters at the Sheraton Boston Hotel

The detailed Call for Papers published in July-November 1978 issues of **This Journal.** Final program published in March 1979 issue of **This Journal.**

Planned symposia for the Boston Meeting include the following Divisions, Group, Subcommittee, and subjects:

Battery, Corrosion, Electrothermics and Metallurgy, and Energy Technology Group—High Temperature Fuel Cell Materials; **Corrosion**—General Session; **Dielectrics and Insulation**—Thin Film Ferroelectric Materials; **Dielectrics and Insulation and Electronics**—Display Technology, Low Temperature Processing, Materials Interactions in Packaging Technology; **Dielectrics and Insulation, Electronics, and Electrothermics and Metallurgy**—Laser Process Technology; **Dielectrics and Insulation, Electrothermics and Metallurgy, and Energy Technology Group**—Photovoltaic, Photothermal, and Hybrid Energy Systems and Devices; **Electronics**—Ion Implantation, Molecular Beam Epitaxy, Process Device Modeling, Semiconductors General Sessions, Phosphor Efficiency and Saturation, X-Ray Phosphors and Radiography, Luminescence General Session, General Materials and Processes General Session; **Electrothermics and Metallurgy**—Refractory Composites; **Electrothermics and Metallurgy and Energy Technology Group**—Characterization of Coal Combustion Products; **Energy Technology Group**—Future Energy Sources, General Session; **Energy Technology Group and Industrial Electrolytic**—Conservation of Electricity; **Energy Technology Group and Organic and Biological Electrochemistry**—Energy Conversion and Storage in Biological Systems; **Industrial Electrolytic**—Engineering Analysis, Fused Salt Technology, General Session; **Physical Electrochemistry**—Ion Exchange, Recent Advances in Electrode Kinetics; **New Technology Subcommittee and Corrosion**—Electrochemical Aspects of Ocean Resource Utilization; **New Technology Subcommittee, Corrosion, Dielectrics and Insulation, and Electronics**—Sensors in Biological Systems; and **New Technology Subcommittee and Electrothermics and Metallurgy**—Superconductor Materials.

LOS ANGELES, CALIFORNIA—OCTOBER 14, 15, 16, 17, 18, & 19, 1979

Headquarters at the Los Angeles Bonaventure

The detailed Call for Papers published in December 1978-April 1979 issues of **This Journal.** Final program published in August 1979 issue of **This Journal.**

Planned symposia for the Los Angeles Meeting include the following Divisions, Group, Subcommittee, and subjects:

Battery—Ambient Temperature Lithium Batteries, Lead Acid-New Developments, Power Sources for Biomedical Implantable Applications, General Session; **Battery, Electrothermics and Metallurgy, and Energy Technology Group**—Hybrid Electrochemical Propulsion Systems; **Corrosion**—Corrosion of Amorphous Metal Surfaces, Electrochemistry of Hot Corrosion; **Dielectrics and Insulation, Electrodeposition, and Electronics**—Patterning Technology; **Dielectrics and Insulation and Electronics**—Applications of Glasses in IC Technology, Degradation Mechanisms in Electronic Devices, New Processing Techniques, Silicon on Sapphire and Dielectric Isolation, Thin Films of Tunneling Dimensions; **Dielectrics and Insulation, Electronics, and Electrothermics and Metallurgy**—Seventh International Conference on Chemical Vapor Deposition; **Electrodeposition**—General Session; **Electronics**—Business Trends in the Electronics Industry, Gettering, Magneto-Optical Materials, Processing of Optical Imaging Devices, Semiconductors General Sessions, General Materials and Processes General Session; **Electronics and Electrothermics and Metallurgy**—Contact Materials and High Conductivity Interconnects; **Electronics, Electrothermics and Metallurgy, and Energy Technology Group**—Silicon Crystal Growth; **Electrothermics and Metallurgy**—Halide Lamp Science and Technology, High Temperature Chemistry; **Electrothermics and Metallurgy and Energy Technology Group**—Photothermal and Geothermal Energy Systems; and **New Technology Subcommittee and Corrosion**—Amorphous Metals, Marine Electrochemistry.

ELECTROCHEMICAL PREPARATIVE AND ANALYTICAL EQUIPMENT

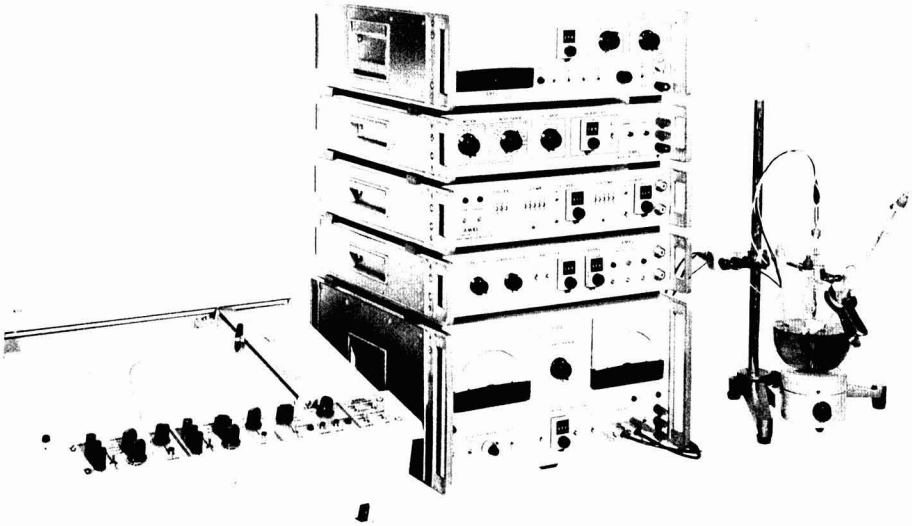

These are . . . THE ADVANCED ALTERNATIVES

And we challenge you to compare the features, performance and value of these fine new instruments.

- **Cells for preparative organic chemistry**
- Electrometers/Ammeters
- Corrosion Testing Equipment
- Analog/Digital Integrators
- Multi-channel Scanners
- Signal Function Generators
- Polarographs
- **Potentiostats/Galvanostats**

For a copy of the current catalog describing these and other instruments, please write, or call Dr. Dennis Crouse at 617-661-8080.

ECO

ECO Incorporated

FIFTY-SIX ROGERS STREET
CAMBRIDGE, MA 02142
Tel. 617-661-8080
TWX 710-320-6937

EXTENDED ABSTRACTS

Extended Abstracts of the Society's Spring Meeting in Seattle, Washington (Volume 78-1) are available from Society Headquarters at $10 per copy.

Extended Abstracts of other Society Meetings (Spring and Fall) are also available in limited numbers at $10 per copy.

To order the Extended Abstracts, please specify which volume and forward with full payment to The Electrochemical Society, Inc., P.O. Box 2071, Princeton, N.J. 08540.

NEW SOCIETY PROCEEDINGS VOLUMES

New proceedings volumes containing papers from several symposia/conferences will be published in 1978.

Proceedings of the Symposium on High Temperature Metal Halide Chemistry		
A 1977 symposium	Available April 1978	$17.00
Proceedings of the Symposium on Thin Film Phenomena: Interfaces and Interactions		
A 1977 symposium	Available April 1978	$14.00
Proceedings of the Symposium on Industrial Water Electrolysis		
A 1978 symposium	Available summer 1978	$12.00
Proceedings of the Topical Conference on Characterization Techniques for Semiconductor Materials and Science		
A 1978 symposium	Available summer 1978	$16.00
Proceedings of the Eighth International Conference on Electron and Ion Beam Science and Technology		
A 1978 symposium	Available fall 1978	$20.00
Proceedings of the Fourth International Symposium on Passivity		
A 1977 symposium (Hardbound)	Available late 1978	$45.00
Proceedings of the 28th Power Sources Symposium		
A 1978 symposium (Hardbound)	Available late 1978	$25.00

To order, forward full payment to The Electrochemical Society, Inc., P.O. Box 2071, Princeton, N.J. 08540

What's a "Corrodaputer"?

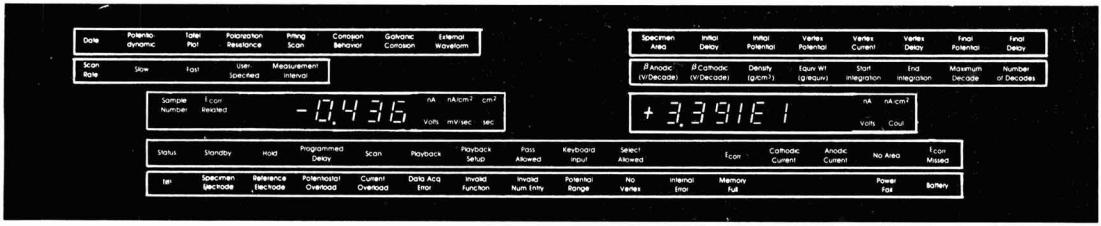

A system that uncomplicates your most complex corrosion measurements!

- Potentiodynamic polarizations
- Corrosion behavior diagrams
- Tafel plots
- Polarization resistance measurements
- Galvanic corrosion

The Model 350 Corrosion Measurement System has a built-in microcomputer that does it all for you!

MICROCOMPUTER POWER . . .
. . . GETS YOU STARTED

The microcomputer guides you through the instrument set up and tells you if you've made any invalid choices. It then runs the experiment and monitors and stores the incoming data.

. . . PLAYS IT BACK FOR YOU

Next it plays the properly scaled curve back for you on the built-in recorder and calculates things like current density, Tafel constants, corrosion rates and even current integrals. If that weren't enough the microcomputer also symbolizes the chart paper with the necessary information so you get a permanently labeled record of the experiment.

. . . EXPANDS YOUR CAPABILITY

If you like, you can then re-examine selected portions of the stored scan to get a scale-expanded replay of the stored data. Replay the data as many times as you wish, examining different portions of the curve each time.

The implications of all this are that now, in *one* experiment, you can get potentiodynamic polarization information for passivation tendencies, as well as Tafel and polarization resistance plots for corrosion rates, using a *single* specimen. Think of the savings in time and effort that can be made!

A commitment to better corrosion measurements

EG&G Princeton Applied Research is committed to providing the necessary instrumentation and support to help you make better electrochemical corrosion measurements. We have pioneered the use of incorporated microprocessors in to instruments and the Model 350 builds on this extensive background. Our staff of application chemists and field support specialists are always available for telephone consultation. In addition, our corrosion short courses and corrosion application notes can get you started in this field quickly, easily and painlessly. For more information on the Model 350 Corrosion Measurement System, write or call Princeton Applied Research Corporation, P. O. Box 2565, Princeton, New Jersey 08540; phone: 609/452-2111.

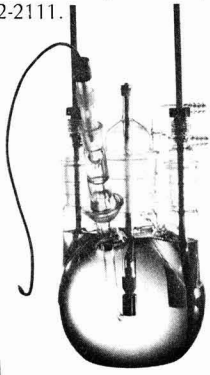

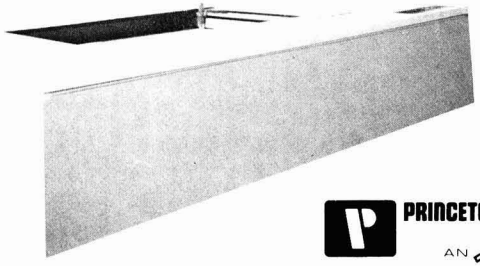

PRINCETON APPLIED RESEARCH
AN EG&G COMPANY

414

May 1978

ELECTROCHEMICAL SCIENCE AND TECHNOLOGY

TECHNICAL PAPERS

TECHNICAL NOTES

ELECTROCHEMICAL SOCIETY

Vol. 125 • No. 5

SOLID-STATE SCIENCE AND TECHNOLOGY

TECHNICAL PAPERS

Manuscripts submitted to the Journal should be sent in triplicate, to the Editorial Office at P.O. Box 2071, Princeton, N.J. 08540. They should conform to the revised "Instructions to Authors" available from Society Headquarters. Manuscripts so submitted, as well as papers presented before a Society technical meeting, become the property of the Society and may not be published elsewhere in whole or in part without written permission of the Society. Address such requests to the Editor.

The Electrochemical Society does not maintain a supply of reprints of papers appearing in its Journal. A photoprint copy of any particular paper may be obtained from University Microfilms, Inc., 300 N. Zeeb St., Ann Arbor, Mich. 48106.

Inquiries regarding positive microfilm copies of volumes should be addressed to University Microfilms, Inc., 300 N. Zeeb St., Ann Arbor, Mich. 48106.

Walter J. Johnson, Inc., 355 Chestnut St., Norwood, N.J. 07648, have reprint rights to out-of-print volumes of the Journal, and also have available for sale back volumes and single issues, with the exception of the current calendar year. Anyone interested in securing back copies should correspond directly with them.

Published monthly by The Electrochemical Society, Inc., at 215 Canal St., Manchester, N.H.; **Executive Offices, Editorial Office and Circulation Dept.**, and **Advertising Office** at P.O. Box 2071, Princeton, N.J. 08540, combining the JOURNAL and TRANSACTIONS OF THE ELECTROCHEMICAL SOCIETY. Statements and Opinions given in articles and papers in the JOURNAL OF THE ELECTROCHEMICAL SOCIETY are those of the contributors, and The Electrochemical Society assumes no responsibility for them.

Claims for missing numbers will not be allowed if received more than 60 days from date of mailing plus time normally required for postal delivery of JOURNAL and claim. No claims allowed because of failure to notify the Circulation Dept., The Electrochemical Society, P.O. Box 2071, Princeton, N.J. 08540, of a change of address, or because copy is "missing from files." Subscription to members as part of membership service; subscription to nonmembers $60.00 plus $5.00 for postage outside U.S. and Canada. Single copies $3.25 to members, $5.00 to nonmembers. Second Class Postage Paid at Princeton, New Jersey, and at additional mailing offices. Printed in U.S.A.

SOLID-STATE SCIENCE (Cont.)

TECHNICAL NOTES

ACCELERATED BRIEF COMMUNICATIONS

REVIEWS AND NEWS

NEWS

JOURNAL OF THE ELECTROCHEMICAL SOCIETY

ELECTROCHEMICAL SCIENCE AND TECHNOLOGY

MAY 1978

The Electrical Conductivity of β-PbF_2

Wei-Chou Fang*,[1] and Robert A. Rapp**

Department of Metallurgical Engineering, The Ohio State University, Columbus, Ohio 43210

ABSTRACT

The electrolytic properties of pure β-PbF_2 were studied by a-c conductivity measurements and Hebb-Wagner d-c polarization experiments as a function of fluorine pressure and temperature. The partial ionic and electronic conductivities of β-PbF_2 were determined over a range of fluorine pressure and temperature. Because of the introduction of p-type electronic conduction, the electrolytic domain of β-PbF_2 is truncated at high values of P_{F_2}, with $P_{F_2} = 10^{-21}$ atm at 492°C. At low P_{F_2}, predominant ionic conduction extends to P_{F_2} for the coexistence of Pb and PbF_2.

The electrolytic properties of nominally pure and doped β-PbF_2 and α-PbF_2 have been extensively investigated recently (1-16). Bonne and Schoonman (13) calculated the temperature dependences of the concentrations and mobilities of the interstitial fluoride ions and anion vacancies based on their a-c conductivity measurements of pure and doped β-PbF_2 and existing literature data. Their results indicated that interstitial fluoride ions are the principal mobile species in pure β-PbF_2 for temperatures greater than 300°C. Hebb-Wagner polarization experiments have also been conducted by many authors to elucidate the electronic conductivity in PbF_2. Kennedy *et al.* (4) reported that the electronic conductivity of pure β-PbF_2 at 150°C was p-type. At 25°C Kennedy and Miles (12) could not specify whether the electronic current in β-PbF_2 was carried by electrons or holes. Benz (10) found that pure β-PbF_2 was essentially an n-type conductor from 400° to 600°C. Schoonman *et al.* (8) also found an n-type conductor for pure β-PbF_2 single crystal from 52° to 137°C. Joshi and Liang (9) reported that α-PbF_2 is a p-type conductor.

Both α-PbF_2 and β-PbF_2 are known to be predominant ionic conductors. To elucidate the ionic domain (17, 18) of PbF_2, the determination of the range of log P_{F_2} beyond which electronic conduction becomes appreciable is studied here. Previous studies did not include several well-defined fluorine activities in conductivity studies on PbF_2. The present study consists of measurements of the total a-c conductivity, together with the measurements of the partial conductivity for electrons and electron holes as a function of fluorine activity. These results define the limits for the electrolytic domain for PbF_2. Hebb-Wagner polarization studies of β-PbF_2 also clarify the controversial results regarding n-type conduction as the predominant electronic conduction mode.

D-C Polarization Study

The Hebb-Wagner d-c polarization experiment (19) was adopted for the present study of β-PbF_2. Consider the d-c polarization cell

inert electrode	PbF_2	reversible (Me/MeF_2) electrode

[I]

A reversible electrode consisting of a more noble metal (Me) coexisting with its fluoride (MeF_2) provides a fixed and known P_{F_2} on one side of the cell. On the other side, a pure noble metal with low solubility for fluorine serves as an inert blocking electrode. The cell is subjected to various d-c potentials below the decomposition potential of PbF_2. If the right-hand reversible electrode is made negative, under the steady-state condition the ionic current is blocked and the steady-state polarization current i_∞ is then carried exclusively by electrons and electron holes according to the equation

$$i_\infty = i_\oplus + i_\ominus = \frac{RT}{FL}\{\sigma_\oplus^\circ\,[\exp(u) - 1] + \sigma_\ominus^\circ\,[1 - \exp(-u)]\} \quad [1]$$

where L is the cell constant (thickness/area), $\sigma_\oplus^\circ$ and $\sigma_\ominus^\circ$ are, respectively, the partial electron hole and electronic conductivities at the equilibrium fluorine activity of the reversible electrode and $u = EF/RT$, where E is the applied voltage, F is Faraday's constant, and R and T have their usual meaning. The details of the theory have been given elsewhere (19-21).

If the polarity of the applied voltage for cell (I) is reversed (positive reversible electrode), an equation similar to Eq. [1] can also be derived. The usual approach in polarization experiments by all the authors, except Patterson *et al.* (21), has been to assume the validity of Eq. [1] and then evaluate either $\sigma_\oplus^\circ$ or $\sigma_\ominus^\circ$ according to limiting cases given by Wagner (19, 20).

If the electrolyte is a predominant p-type electronic conductor, and $\exp(u) >> 1$, the equation for the current reduces to

$$i_\infty = i_\oplus = \frac{RT}{FL}\sigma_\oplus^\circ \exp(u) \quad [2]$$

An exponentially increasing current will be observed with increasing potential in a plot of i_∞ *vs.* E, while a linear relationship will be observed in a plot of log $(FL/RT)i_\infty$ *vs.* E. The value for the electron hole conductivity $\sigma_\oplus$ can then be calculated from the intercept of the latter plot.

If the electrolyte exhibits predominant n-type electronic conduction, Eq. [1] reduces to

$$i_\infty = i_\ominus = \frac{RT}{FL}\sigma_\ominus^\circ\,[1 - \exp(-u)] \quad [3]$$

* Electrochemical Society Student Member.
** Electrochemical Society Active Member.
[1] Present address: General Electric Research and Development Center, Schenectady, New York 12391.
Key words: solid electrolytes, conduction, electrolytic domain.

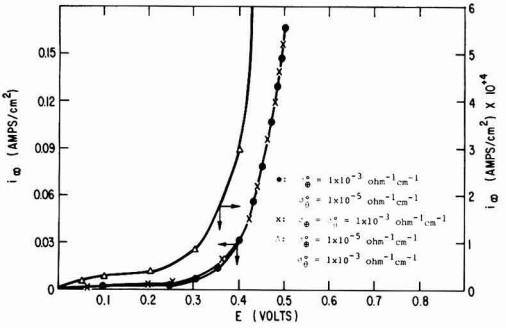

Fig. 1. Calculated i-E curves according to Eq. [1]. L = 0.2 cm^{-1}, T = 400°C.

In plots of i_∞ *vs.* E, with increasing voltage, the current increases and tends to the saturation value. From the plot of log $(FL/RT)i_\infty$ *vs.* E, the electronic conductivity can be calculated from the plateau current value which is $\sigma_\Theta°$.

Under certain conditions, the analysis of limiting cases can result in an erroneous conclusion. Figure 1 illustrates i-E plots for the complete Eq. [1] for three limiting cases. Each plot exhibits an apparent exponential curve when the applied voltage is above some value. Obviously, the decision between p- or n-type behavior based on the shape of the experimental plot is not reliable. An improved technique for analyzing polarization data was presented by Patterson *et al.* (21). Both sides of Eq. [1] may be divided by $[1 - \exp(-u)]$ or by $[\exp(u) - 1]$ to obtain

$$i_\infty/[1 - \exp(-u)] = \frac{RT}{FL}[\sigma_\oplus° \exp(u) + \sigma_\Theta°] \quad [4]$$

or

$$i_\infty/[\exp(u) - 1] = \frac{RT}{FL}[\sigma_\oplus° + \sigma_\Theta° \exp(-u)] \quad [5]$$

According to Eq. [5], a plot of $i_\infty/[\exp(u) - 1]$ *vs.* $\exp(-u)$ should give a straight line of slope $\frac{RT}{FL}\sigma_\Theta°$ and intercept $\frac{RT}{FL}\sigma_\oplus°$. Analogous equations can be obtained for a positive reversible electrode. Thus the values of both $\sigma_\oplus°$ and $\sigma_\Theta°$ can be simultaneously obtained from a single experimental run. The d-c polarization data in the present study were treated according to this method.

Experimental materials and procedures.—Cubic β-PbF_2 was made by heating the orthorhombic α-PbF_2 (99.99% pure) to over 500°C prior to each experimental run.

A-c conductivity measurements.—The various fluorine activities for a-c conductivity measurements were established through the double cell electrochemical arrangement shown in Fig. 2. The cell was comprised of two symmetrical cells with perforated platinum foils as fluorine gas electrodes contacting PbF_2. Reference electrodes were prepared from nickel-nickel fluoride-calcium fluoride mixtures in a volume ratio of approximately 6:2.5:2 and pressed in a 1.3 cm diam steel die. The calcium fluoride was added to eliminate electrode polarization. The electrolyte CaF_2 was prepared from pressed ultrapure calcium fluoride powder. The fluorine activity P_{F_2} at the platinum foils was fixed by the applied voltage E according to the relation

$$P_{F_2} = P_{F_2}° \text{ (Ni/NiF}_2\text{)} \exp\frac{2EF}{RT} \quad [6]$$

where $P_{F_2}°$ is the equilibrium fluorine pressure of the

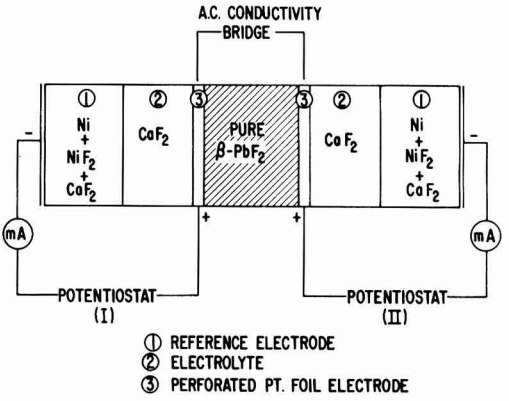

Fig. 2. Experimental cell to study the electrical conductivity of PbF_2.

reference electrode. Preliminary experiments showed that the actual P_{F_2} at the platinum electrodes was a linear function of the current through the cells which was monitored by a Keithley 153 microammeter. The current indicated the existence of a small steady-state fluorine ion discharge at the Pt/CaF_2 interface. This discharge resulted from fluorine escape through the bond between the CaF_2 electrolyte and the platinum foil. Because of the linear relation between the actual P_{F_2} and the cell current, a knowledge of the actual P_{F_2} at the platinum foils was possible. The applied voltages were provided from two potentiostats which were separately supplied with power to avoid an electrical ground loop between the two instruments. Measurements of the a-c conductivity at a frequency of 1592 Hz were made by the Wayne-Kerr Low Universal Bridge B211 which balances the sample conductance and capacitance against standards. When the conductance of a specimen was higher than 0.1 Ω^{-1} cm^{-1} a Wayne-Kerr Low Impedance Adaptor Q211 was used in conjunction with the bridge.

Hebb-Wagner d-c polarization measurements.—Figure 3 shows the cell arrangement for d-c polarization measurements. The reversible electrodes used for this cell were prepared from two-phase equilibrium mixtures of Cu/CuF_2 and Ni/NiF_2. Again, some CaF_2 was added to these mixtures to prevent polarization of the reversible electrode. The blocking electrode consisted of a Pt foil about 0.003 cm thick pressed against a vapor-deposited Au layer.

When Cu/CuF_2 mixtures were used as reversible electrodes at positive polarity, the applied voltages were kept below 640 mV (the difference in the standard Gibbs energies of formation for β-PbF_2 and CuF_2) to avoid the decomposition of PbF_2. On the other hand, for positive polarity at the blocking electrode, the applied voltage could be any value which would avoid excessive F_2 vapor generation (about 2.0V).

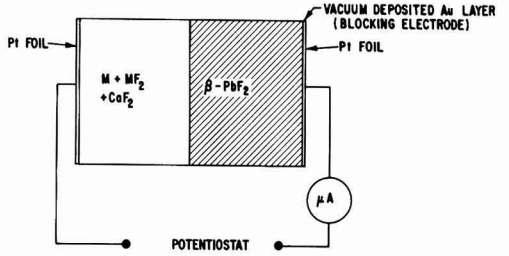

Fig. 3. Cell arrangement for d-c polarization studies of β-PbF_2

If Ni/NiF_2 electrodes are used at positive polarity, the permissible experimental voltage range is too small. Therefore, negative Ni/NiF_2 electrodes are preferred to allow a large applied voltage range (about 2.4V). The steady-state polarization currents were independent of the argon flow rate in the system and were stable over long periods of time.

Results and Discussion

A-c conductivity measurements.—The results of a-c total conductivity measurements are plotted in Fig. 4 as a function of fluorine pressure at various temperatures. By careful examination, there is a very small positive slope for each line. But essentially, the a-c conductivity of β-PbF_2 is independent of fluorine pressure, indicating that β-PbF_2 is a predominant ionic conductor over a wide range of fluorine activity.

D-c polarization measurements.—The converted plot of data for the cell

$$\ominus Ni/NiF_2 \mid PbF_2 \mid Au\oplus \qquad [II]$$

according to Eq. [5] is shown in Fig. 5. The values for $\sigma_\ominus^\circ$ and $\sigma_\oplus^\circ$ were obtained from the slope and intercept of the plot, respectively, as already discussed.

The curve shown in Fig. 5 is not a perfectly straight line as was expected, but exhibits an increasing slope with the increasing voltage. Taking the maximum and the minimum values of slope gives

$$\sigma_\ominus^\circ = 3.12\text{-}4.15 \times 10^{-6}\ \Omega^{-1}\,cm^{-1}$$

correspondingly

$$\sigma_\oplus^\circ = 2.14\text{-}1.04 \times 10^{-8}\ \Omega^{-1}\,cm^{-1}$$

for $P_{F_2}^\circ$ for coexistence of Ni and NiF_2. This result indicates that $\sigma_\ominus^\circ >> \sigma_\oplus^\circ$; in other words, pure β-PbF_2 is an n-type conductor at the equilibrium fluorine activity for Ni/NiF_2.

To obtain the polarization data for β-PbF_2 at the equilibrium fluorine activity of Cu/CuF_2, cell [III] was used. Positive polarity was applied at the blocking electrode

$$\ominus Cu/CuF_2 \mid PbF_2 \mid Au\oplus \qquad [III]$$

Unfortunately, some difficulties arose with this cell. Nonreproducible currents of the order of 1 μA were observed at applied voltages below 0.4V. Further, this cell required 1-1.5 days to reach a steady-state current. As a result, cell [III] with reverse polarity was used. As mentioned earlier, the maximum voltage for cell [III] with opposite polarity is only 640 mV, since higher voltages threaten the decomposition of the lead fluoride. On the other hand, potentials below 0.4V result in very small nonreproducible currents. Because of these two limitations, the voltage range between 0.4 and 0.6V was investigated. A converted plot of data for two such runs is shown in Fig. 6. The analysis yields for run No. 1

$$\sigma_\ominus^\circ = 1.89\text{-}3.81 \times 10^{-9}\ \Omega^{-1}\,cm^{-1}$$

$$\sigma_\oplus^\circ = 4.33\text{-}3.72 \times 10^{-5}\ \Omega^{-1}\,cm^{-1}$$

and for run No. 2

$$\sigma_\ominus^\circ = 6.39\text{-}6.61 \times 10^{-9}\ \Omega^{-1}\,cm^{-1}$$

$$\sigma_\oplus^\circ = 6.93\text{-}6.84 \times 10^{-5}\ \Omega^{-1}\,cm^{-1}$$

The values of $\sigma_\ominus^\circ$ and $\sigma_\oplus^\circ$ show that β-PbF_2 is a p-type conductor in equilibrium with Cu/CuF_2. Therefore, the fluorine activity at which the transition of p-type to n-type takes place falls between $P_{F_2}^\circ$ (Ni/NiF_2) and $P_{F_2}^\circ$ (Cu/CuF_2).

Figure 7 is a plot of log σ *vs.* log P_{F_2} for pure β-PbF_2; the slopes of log $\sigma_\oplus^\circ$ and log $\sigma_\ominus^\circ$ *vs.* log P_{F_2} approach, respectively, 0.5 and −0.5 at 492°C. These are the slopes expected from a Kroger-Vink diagram for F_i' and $V_F^\cdot$ defects in absolutely pure PbF_2, as well as in a doped crystal where an impurity fixes the defect concentration. Since $\sigma_\oplus^\circ$ and $\sigma_\ominus^\circ$ are negligible compared to σ_{ionic}, the total a-c conductivity is essentially equal to σ_{ionic}. Combining the results for $\sigma_\oplus^\circ$, $\sigma_\ominus^\circ$, and σ_{ionic} allows an estimation of the fluorine partial pressure $P_\oplus$ and $P_\ominus$ at which $\sigma_\oplus = \sigma_{ionic}$ and $\sigma_\ominus = \sigma_{ionic}$ at the temperature 492°C. For the condition $\sigma_\oplus = \sigma_{ionic}$, $P_\oplus$ equals 1.0×10^{-21} atm. The P_{F_2} for the condition where $\sigma_\ominus = \sigma_{ionic}$ is far below the P_{F_2} for PbF_2 decomposition and is therefore of no physical significance.

Only two different reference electrodes with differing values of P_{F_2} were used to determine the slopes in

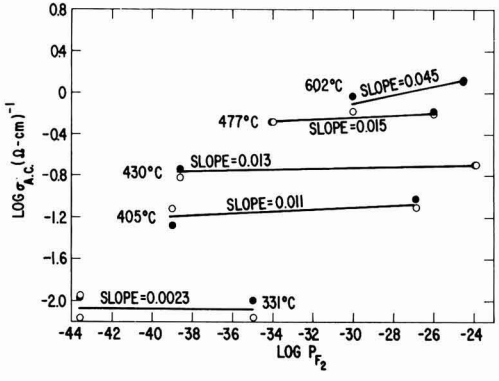

Fig. 4. Fluorine pressure dependence of total conductivity for β-PbF_2 at 330°-600°C. Open and closed circles represent duplicated runs.

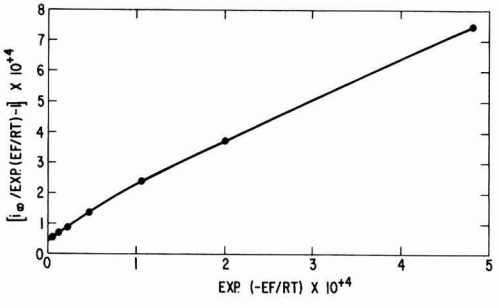

Fig. 5. Converted data plot for d-c polarization measurements with the cell $\ominus$ Ni/NiF_2 | β-PbF_2 | $Au\oplus$ at 492°C.

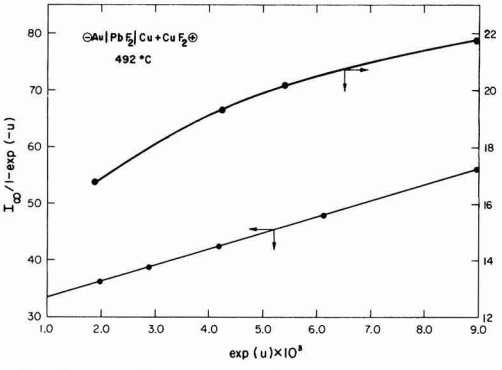

Fig. 6. Converted data for d-c polarization measurements with the cell $\ominus$ Au | PbF_2 | Cu/CuF_2 $\oplus$ at 492°C.

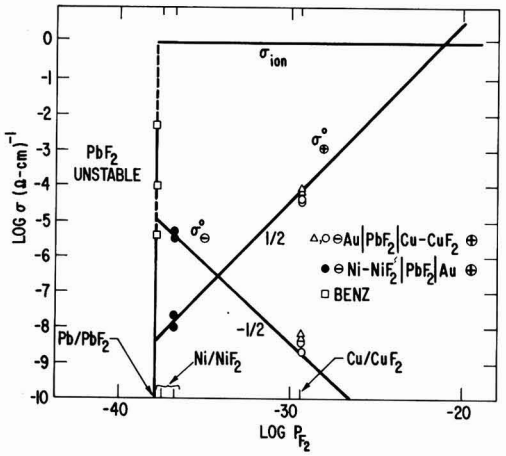

Fig. 7. Plot of log $\sigma_{a\text{-}c}$, log $\sigma_\oplus$, and log $\sigma_\ominus$ for the polarization and a-c conductivity study of β-PbF_2 at 492°C.

the plot of log σ *vs.* log P_{F_2}. These two seem to be the only available fluorides which are as solid, have low vapor pressures at relatively high temperature, but yet are less stable than PbF_2.

As mentioned earlier, controversial results of d-c polarization of PbF_2 exist between various authors (4, 8-10, 12). Recalculation of the experimental data of previous studies according to Eq. [4] and [5] becomes necessary and interesting. Data for $\sigma_\oplus^\circ$ and $\sigma_\ominus^\circ$ and β-PbF_2 in equilibrium with Pb from these recalculations (4, 8, 10, 12) are plotted as a function of temperature in Fig. 8, extrapolation of the present experimental results for $\sigma_\oplus^\circ$ and $\sigma_\ominus^\circ$ from Fig. 7 are also shown on the same plot. Figure 8 shows reasonable agreement among different authors and the present study. Data for $\sigma_\oplus^\circ$ and $\sigma_\ominus^\circ$ from Joshi and Liang (9) are not included in Fig. 8 because their results were for α-PbF_2. Figure 8 shows that β-PbF_2 is an n-type conductor in equilibrium with Pb over the temperature range 25°-600°C. This conclusion incorporates the controversial results on polarization experiments from various authors. The improved method for interpreting converted d-c polarization data of Patterson *et al.* was useful in determining both $\sigma_\oplus^\circ$ and $\sigma_\ominus^\circ$ in this study. Comparison of electronic conductivities is shown in Table I. The set of values with an asterisk represents the values of $\sigma_\ominus^\circ$ and $\sigma_\oplus^\circ$ that fit best in Eq. [4] or [5].

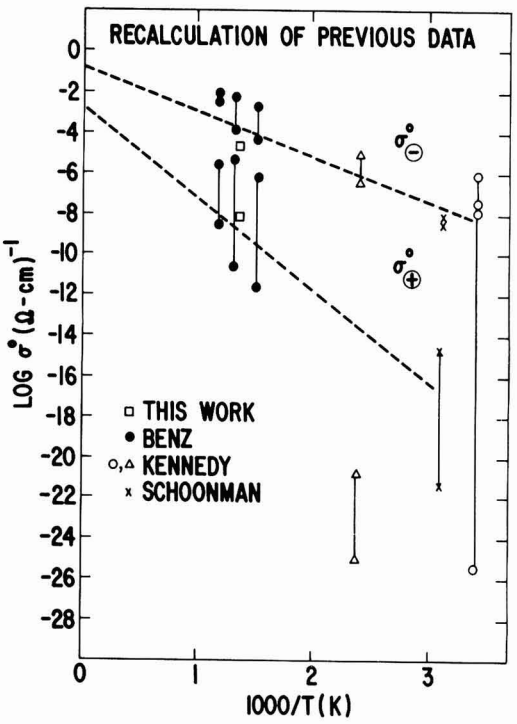

Fig. 8. Plot of log $\sigma_\oplus^\circ$ and log $\sigma_\ominus^\circ$ in equilibrium with lead as a function of temperature for β-PbF_2.

Obviously, opposite conclusions are then sometimes obtained from the simple limiting graphical interpretation and from the improved, converted interpretation of Patterson *et al.*

Conclusions

The a-c conductivity of pure β-PbF_2 has been found to be essentially independent of P_{F_2}. This pressure independence indicates that β-PbF_2 is an ionic conductor over the experimental ranges of P_{F_2} and temperature.

The measurements of electronic conduction of pure β-PbF_2 in the d-c polarization experiment indicates a $P_{F_2}^{-1/2}$ dependence for $\sigma_\oplus$, and a $P_{F_2}^{-1/2}$ dependence for $\sigma_\ominus$, in accordance with a simple Kroger-Vink diagram for β-PbF_2. Recalculation of data from previous

Table I. Review of the literature data and present results for Pb halide conductivity in equilibrium with Pb

Material	(C) Temperature	Proposed by orig. authors	$\sigma^*_\oplus$ $(\Omega\text{-}1\ cm)^{-1}$	$\sigma^*_\ominus$ $(\Omega\text{-}cm)^{-1}$	Present calculation	$\sigma^\circ_\oplus$ $(\Omega\text{-}cm)^{-1}$	$\sigma^\circ_\ominus$ $(\Omega\text{-}cm)^{-1}$	Ref.
β-PbF_2	25	—	—	—	n-type	2.05×10^{-16}* $\sim 3.76 \times 10^{-28}$	3.75×10^{-10}* $\sim 1 \times 10^{-8}$	12
β-PbF_2	150	p-type	3.3×10^{-11}	—	n-type	1.85×10^{-21}* $\sim 1.39 \times 10^{-25}$*	4.89×10^{-7}* $\sim 9.96 \times 10^{-6}$*	4
β-PbF_2	400	n-type	—	2.1×10^{-3}	n-type	7.37×10^{-7} $\sim 2.15 \times 10^{-12}$*	3.84×10^{-5} $\sim 1.93 \times 10^{-3}$*	10
	500	n-type	—	5.5×10^{-3}	n-type	4.8×10^{-6} $\sim 2.0 \times 10^{-11}$*	1.19×10^{-4} $\sim 4.97 \times 10^{-3}$*	10
	600	n-type	—	7.7×10^{-3}	n-type	1.7×10^{-5} $\sim 2.62 \times 10^{-9}$*	4.70×10^{-4} $\sim 7.92 \times 10^{-3}$*	10
α-PbF_2	127	p-type	1.72×10^{-20}	—	n-type	1.43×10^{-20} $\sim 1.4 \times 10^{-22}$*	5.5×10^{-10} $\sim 1.5 \times 10^{-8}$*	9
	259	p-type	1.82×10^{-11}	—	n-type	4.06×10^{-12} $\sim 1.71 \times 10^{-13}$*	1.22×10^{-8} $\sim 5.2 \times 10^{-8}$*	9
	287	p-type	8.60×10^{-11}	—	n-type	1.76×10^{-10} $\sim 8.12 \times 10^{-12}$*	1.13×10^{-9} $\sim 4.43 \times 10^{-8}$*	9
Pure β-PbF_2	492	(present estimates)			n-type	$\sim 2.5 \times 10^{-9}$*	2.86×10^{-5}*	
Pure β-PbF_2	52	n-type	—	4.7×10^{-3}	n-type	3.6×10^{-9} $\sim 4.7 \times 10^{-9}$*	2.2×10^{-15} $\sim 6.1 \times 10^{-22}$*	8

* Values of $\sigma^*_\oplus$ and $\sigma^*_\ominus$ best fitted to Eq. [4] and [5].

d-c polarization measurements for α-PbF_2 and β-PbF_2 from various authors, along with the $\sigma_\oplus$ and $\sigma_\ominus$ from the present study, gives the following conclusion: α-PbF_2 and β-PbF_2 are n-type conductors in equilibrium with Pb. P-type electronic conduction becomes important at high P_{F_2}, with $P_\oplus \approx 1.0 \times 10^{-21}$ atm at 492°C. The Patterson method was also applied to recalculate d-c polarization data existing in the literature for $PbBr_2$ and $PbCl_2$. The results indicate that both $PbCl_2$ and $PbBr_2$ are n-type conductors in equilibrium with Pb.

Acknowledgments

This work was supported by the Materials Science Program, Division of Physical Research, U.S. Energy Research and Development Administration, under contract E(11-1)-2671.

Manuscript submitted June 1, 1977; revised manuscript received Dec. 22, 1977.

Any discussion of this paper will appear in a Discussion Section to be published in the December 1978 JOURNAL. All discussions for the December 1978 Discussion Section should be submitted by Aug. 1, 1978.

Publication costs of this article were assisted by The Ohio State University.

REFERENCES

1. R. W. Bonne and J. Schoonman, *Solid State Commun.*, **18**, 1005 (1976).
2. J. Schoonman, G. J. Dirksen, and G. Blasse, *J. Solid State Chem.*, **7**, 245 (1973).
3. C. E. Derrington and M. O'Keeffe, *Nature (London), Phys. Sci.*, **246**, 44 (1973).
4. J. H. Kennedy, R. C. Miles, and J. Hunter, *This Journal*, **120**, 1441 (1973).
5. J. C. Gianduzzo and J. Pistre, *Electrocomp. Sci. Techn.*, **2**, 55 (1977).
6. J. M. Reau, J. Claverie, G. Campet, C. Deportes, D. Ravaine, J. L. Souquet, and A. Hammou, *C. R. Acad. Sci., Ser. C*, **280**, 225 (1975).
7. J. Schoonman, L. B. Ebert, C. H. Hsieh, and R. A. Huggins, *J. Appl. Phys.*, **46**, 2873 (1975).
8. J. Schoonman, G. A. Korteweg, and R. W. Bonne, *Solid State Commun.*, **16**, 9 (1975).
9. A. V. Joshi and C. C. Liang, *J. Phys. Chem. Solids*, **36**, 927 (1975).
10. R. Benz, *Z. Phys. Chem. N.F.*, **95**, 25 (1975).
11. C. C. Liang and A. V. Joshi, *This Journal*, **122**, 466 (1975).
12. J. H. Kennedy and R. C. Miles, *ibid.*, **123**, 47 (1976).
13. R. W. Bonne and J. Schoonman *ibid.*, **124**, 28 (1977).
14. J. Schoonman, *ibid.*, **123**, 1772 (1976).
15. J. H. Kennedy and J. C. Hunter, *ibid.*, **123**, 11 (1976).
16. A. V. Joshi and C. C. Liang, *ibid.*, **124**, 1253 (1977).
17. J. W. Patterson, *ibid.*, **118**, 1033 (1971).
18. J. W. Patterson, in "The Physics of Electronic Ceramics," L. L. Hench and D. B. Dove, Editors, p. 131, Marcel Dekker Inc., New York (1971).
19. C. Wagner, "International Committee of Electrochemical Thermodynamics and Kinetics," Proceedings 7th meeting, Butterworth Publications, London (1957).
20. C. Wagner, *Z. Elektrochem.*, **60**, 4 (1956).
21. J. W. Patterson, E. C. Bogren, and R. A. Rapp, *This Journal*, **114**, 752 (1967).

Lithium Dimethyl Sulfite Graphite Cell

Sanjay L. Deshpande*,[1] and Douglas N. Bennion*

Chemical, Nuclear, and Thermal Engineering Department, University of California, Los Angeles, California 90024

ABSTRACT

Reactions occurring at the positive and negative electrodes and in the solution phase of cells of the type Li/$LiClO_4$, DMSU/graphite have been studied. Discharge capability of 36 hr at a current density of 2 mA/cm^2 has been achieved. Discharge potential was about 3.00V measured *vs.* a lithium wire reference electrode. Coulombic efficiency was 100% at 2 mA/cm^2 but dropped rapidly at higher current densities. Charging potentials increased and discharge potentials decreased at higher current densities. Performance of the cell was poor when propylene carbonate was substituted for dimethylsulfite (DMSU) and $LiBF_4$. Changes in the positive electrode materials did not alter performance very much as long as graphite was present.

Lithium is attractive as a possible negative battery electrode because of its strong reducing potential and low equivalent weight. As a secondary or rechargeable electrode, lithium must operate in an aprotic solution. A major problem in developing room temperature, lithium storage batteries has been finding a suitable positive electrode which is compatible with the lithium negative electrode and the aprotic, electrolytic solution. A summary of various lithium battery systems has been presented elsewhere (1).

A possible battery system using a lithium negative electrode, $LiClO_4$-dimethylsulfite (DMSU) electrolytic solution, and a graphite positive electrode has been reported on previously (2-4). It was proposed (2) that a lamellar compound of graphite formed at the positive electrode as a product of the charge storage mechanism

$$nC + LiClO_4 = Li^+ + C_n ClO_4 + e^-$$

Some later results (4) suggested that the above reaction is not the dominant reaction and that the solvent, DMSU, is involved more directly in the electrochemical reaction. This paper is intended to determine more clearly the positive electrode reaction and the limits of operating capability when used in a Li/$LiClO_4$, DMSU/C secondary battery system.

Experimental

The electrolytic solutions were prepared by vacuum distilling the solvents and vacuum drying the salts. Further drying was achieved by stirring solvents and solutions with lithium chips followed by filtering. Lithium chips were covered with a white deposit as a result of the drying. The stir-and-filter operation

* Electrochemical Society Active Member.
[1] Present address: Honeywell Power Sources Center, Horsham, Pennsylvania 19044.
Key words: nonaqueous solvents, dimethyl sulfite, lithium perchlorate, intercalation, radical cations.

was repeated to expose fresh lithium to the water in the solvent and the solution. Water content was determined using the Karl Fischer technique. Only solutions containing an upper limit of 50 ppm water were used. Graphite powder (99.95% pure, 0.8 μm in size) was used to fabricate the positive electrode. It is a natural graphite originating from Madagascar. Teflon molding powder and Union Carbide National C-34 glue were used as binders. Carbon cloth and titanium foil were used as current collector backing plates.

All experiments were performed in an argon atmosphere dry box. The test cells were glass H-cells as shown in Fig. 1. The two compartments were separated by a fine-size glass frit. Polyethylene stoppers were used to minimize solvent losses by evaporation. Electrode leads came out the top between the polyethylene stopper and the glass wall. The two electrodes, one graphite the other lithium, were held flat to the bottom of their respective compartments by glass sleeves 2 cm inside diam and 1.25 cm high. The sleeves were short enough so they did not block the connecting limb. The liquid level was just above the connecting limb. Each compartment contained about 10 cm^3 of solution. The electrical circuit is shown in Fig. 2. A Perkin Elmer chromatograph, Model 880, with a hot wire detector was used to

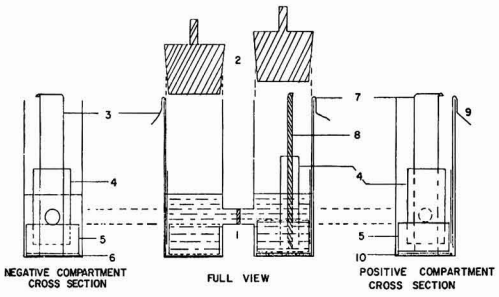

Fig. 1. The H-cell used in all experiments. 1. Glass frit; 2. polyethylene stoppers; 3. negative lead; 4. polypropylene masks for the three electrodes; 5. glass sleeve; 6. negative electrode; 7. positive lead; 8. reference electrode; 9. reference lead; 10. positive electrode.

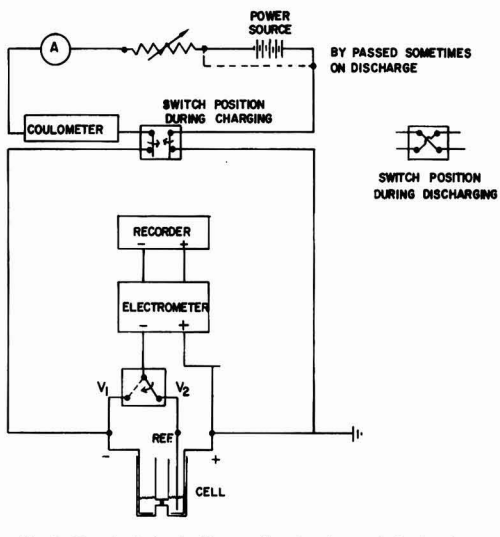

Fig. 2. Electrical circuit diagram for charging and discharging

analyze the electrolytic solution before and after cell operation. Further details of the experimental procedure, sources of material and equipment, and purification techniques can be obtained elsewhere (1).

Both pyrolized and cloth positive electrodes were used. In one case a plain platinum sheet was used. The pyrolized electrodes were made by mixing graphite glue with twice its weight of graphite powder. In one case just the glue was used. The paste was spread on carbon cloth and pressed between two steel plates to form a disk 1.00 mm or less thick. The disk was fired in an argon atmosphere at 800°C for about 6 hr. The result was a brittle, porous disk which adhered well to the cloth. The disk separated easily from the steel plates. The resistance across the cloth disks was about 5Ω. Cloth electrodes were the carbon cloth alone. Prior to use, the carbon electrodes were dried at 50 μm of Hg and 120°C for 6 hr.

In assembling the cells, gas bubbles trapped under the electrodes were shaken free. A thin strip of lithium was placed in the positive compartment as a reference electrode. Strips of polypropylene were placed over electrode leads and the reference electrode wire to prevent a direct current path to them.

The potential between the positive electrode and the lithium wire reference electrode was measured as a function of time while the cell operated at constant charging or discharging current. During one set of measurements, propylene carbonate was used in place of DMSU and $LiBF_4$ in place of $LiClO_4$.

The variables measured were: V_o, the open-ciruit potential right after assembly or a 30 sec interruption in current of the positive electrode *vs.* the reference electrode; V_o', the open-circuit potential after an interruption of a few hours in current of the positive electrode *vs.* the reference electrode; V_1 the operating potential of the complete cell, the positive *vs.* the negative electrode; V_2, the operating potential of the positive electrode *vs.* the reference electrode; V_f, cut-off potential, V_2, when discharging was stopped; Q_{in}, the charge put into the cell during charging; Q_{4V} the charge recovered from the cell with V_2 above 4.0V; Q_{Vf} the charge recovered from the cell with V_2 above V_f.

Potential measurements were made with the positive electrode grounded. Measured values were multiplied by -1 and then reported so that the reported values would conform to the usual sign convention.

Results

Demonstration of reversible electrical storage capacity.—The electrode weighed 0.7245g of which 0.3735g was carbon cloth, 0.2318g graphite powder, and the rest pyrolized graphite glue. Initial thickness was 1 mm and diam 2.0 cm. The electrolytic solution was 1.04 moles $LiClO_4$ per 1000 cm^3 of solution. The initial open-circuit potential, V_o, right after filling was 2.70V. The cell was cycled four times with progressively larger charge in (Q_{in}). Results are shown in Fig. 3, 4, 5, and 6. Charging and discharging was at 3.2 mA (1.0 mA/cm^2) on the first cycle and 6.3 mA (2.0 mA/cm^2) on cycles 2, 3, and 4. On cycle 2, current was increased to 10 mA for short intervals. The curves in Fig. 3, 4, 5, and 6 are typical of many tens of runs.

On the first cycle, two discharge plateaus were observed, one with $V_2 > 4.0$V and the other with V_2 between 3.0 and 2.8V. Typically, the higher plateau was not observed after the first one or two cycles and following a prolonged (several hours) stand after charging but before discharging. The cutoff voltage, V_f, was 2.5V. The coulombic efficiency on the first cycle exceeded 100%. The excess charge is attributed to reactive impurities initially present in the positive electrode.

On both charging and discharging the potential on prolonged open circuit drifted to $V_o' = 3.75$V. The charge and discharge curves were not significantly affected by long interruptions at open circuit. The sustained discharge for 36 hr at 2 mA/cm^2 demon-

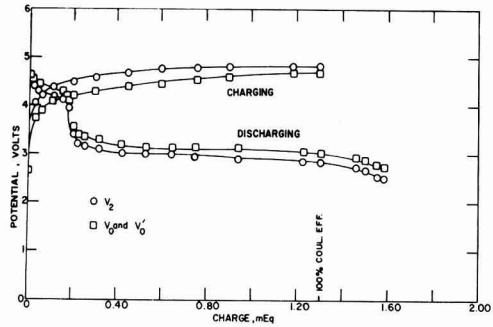

Fig. 3. Galvanostatic charge-discharge curves for the cell Li/$LiClO_4$, DMSU (1.0M)/graphite + graphite glue on carbon cloth. Cycle No. 1. $I = 3.20$ mA; $Q_{in} = 1.30$ mequiv.; coulombic eff. = 121.5% above $V_f = 2.50$V; discharge begun after 0 hr of wet stand on charge; positive electrode weight = 0.7245g; graphite = 0.2318g; carbon cloth = 0.3735g; initial thickness of carbon disk = 0.1 cm; top surface area = 3.14 cm^2; resistance = 1.0Ω.

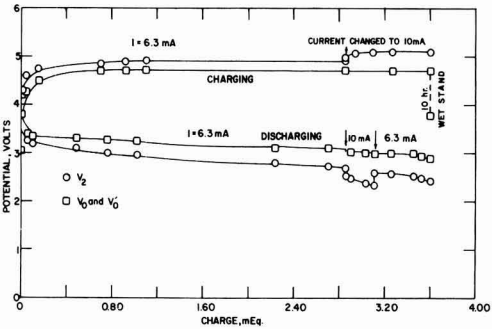

Fig. 4. Galvanostatic charge-discharge curves for the cell Li/$LiClO_4$, DMSU (1.0M)/graphite + graphite glue on carbon cloth. Cycle No. 2. $I = 6.30$ mA; $Q_{in} = 3.60$ mequiv.; coulombic eff. = 100.0% above $V_f = 2.50$V; discharge begun after 10 hr of wet stand on charge; positive electrode weight = 0.7245g; graphite = 0.2318g; carbon cloth = 0.3735g; initial thickness of carbon disk = 0.1 cm; top surface area = 3.14 cm^2; resistance = 1.0Ω.

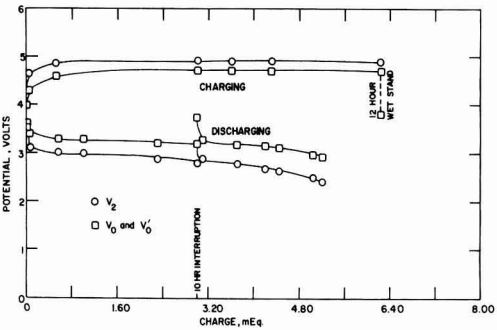

Fig. 5. Galvanostatic charge-discharge curves for the cell Li/$LiClO_4$, DMSU (1.0M)/graphite glue on carbon cloth. Cycle No. 3. $I = 6.3$ mA; $Q_{in} = 6.23$ mequiv.; coulombic eff. = 83.4% above $V_f = 2.50$V; discharge begun after 12 hr of wet stand on charge; positive electrode weight = 0.7245g; graphite = 0.2318g; carbon cloth = 0.3735g; initial thickness of carbon disk = 0.1 cm; top surface area = 3.14 cm^2; resistance = 1.0Ω.

strates a much larger energy storage than the capacity of 1 hr at 2 mA/cm^2 reported by Dunning *et al.* (2). However, Dunning *et al.* looked primarily at the higher, 4.2V plateau; while in this work the lower 2.9V plateau was examined.

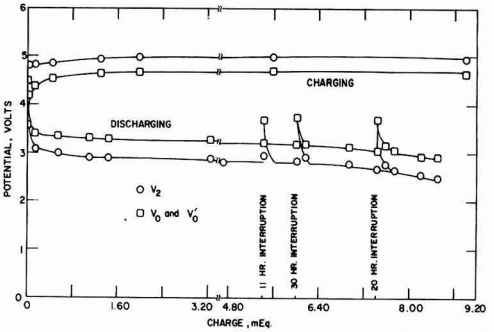

Fig. 6. Galvanostatic charge-discharge curves for the cell Li/$LiClO_4$, DMSU (1.0M)/graphite + graphite glue on carbon cloth. Cycle No. 4. $I = 6.3$ mA; $Q_{in} = 8.92$ mequiv.; coulombic eff. = 95.3% above $V_f = 2.50$V; discharge begun after 0 hr of wet stand on charge; positive electrode weight = 0.7245g; graphite = 0.2318g; carbon cloth = 0.3735g; initial thickness of carbon disk = 0.1 cm; top surface area = 3.14 cm^2; resistance = 1.0Ω.

This comparison is intended to highlight the importance of the lower discharge plateau. Dunning *et al.* used a positive electrode made out of reinforced pyrolytic graphite that weighed 1.4535g and had a cross-sectional area of 8.5 cm^2 (active area was 17 cm^2). About 4 cm^3 of electrolyte solution was used in that test. In comparison, the positive electrode (total weight 0.7245g) reported herein consisted of graphite powder (0.2318g) and graphite glue (0.1192g) and had a cross-sectional area of 3.14 cm^2. About 10 cm^3 of electrolytic solution were present in each half-cell. Table I compares the energy available at the two plateaus. By any criterion, energy available at the lower plateau is higher.

The positive electrode disk swelled from 1 mm thick initially to 5 mm thick after the fourth cycle. The swelling was rapid in the first two cycles, but it swelled little on the last two cycles. The disk remained rigid and adhered to the carbon cloth backing. Final disk resistance was about 3Ω. The surface of the electrode was covered with a thin white deposit. During the charging run of the first cycle, the solution in the positive half-cell gradually turned dark brown. When Anderson Physics Lab ultrapure $LiClO_4$ was used in place of K and K Labs $LiClO_4$, the brown substance did not appear.

The deposit on the negative electrode was dendritic and adhered weakly to the lithium substrate. A white, gelatinous floc appeared at the surface of the lithium. On long cycles a small but steady bubbling appeared on the lithium electrode. The appearance of a white floc agrees with observations of Selim and Bro (5).

Bubbles appeared on the lithium wire reference electrode occasionally during long charging periods, and twice during the 36 hr discharging run it corroded badly enough so that replacement was necessary.

To study the effect of operating current on cell performance, cells of the type just described were operated at varying currents. The results are shown in Fig. 7. Above 2 mA/cm^2 the coulombic efficiency drops rapidly. The current voltage curves are shown in Fig. 8 for charging and discharging. The potentials are average values of the plateau regions. After the high current operation, a cycle was carried out at

Table I. Comparison of upper and lower voltage discharge plateaus

	Upper plus lower plateaus (This paper)	Upper plateau only [Dunning *et al.* (2)]
Energy Stored-W-hr	0.6560	0.1428
W-hr/g electrode	0.9054	0.0982
W-hr/cm^2	0.2088	0.0084
W-hr/cc solution	0.0656	0.0357

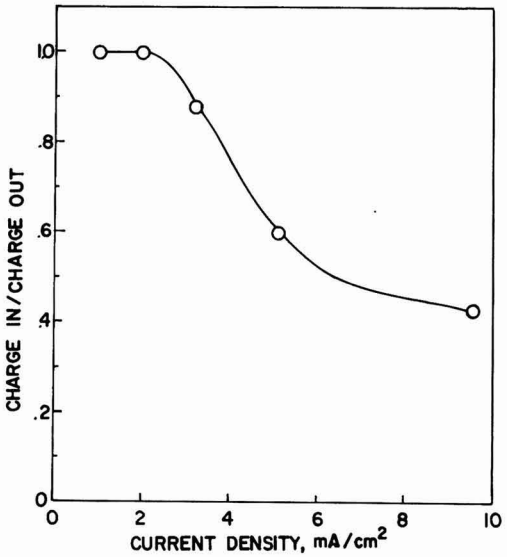

Fig. 7. Effect of operating current density on coulombic efficiency (based on a cutoff potential of $V_f = 2.0V$).

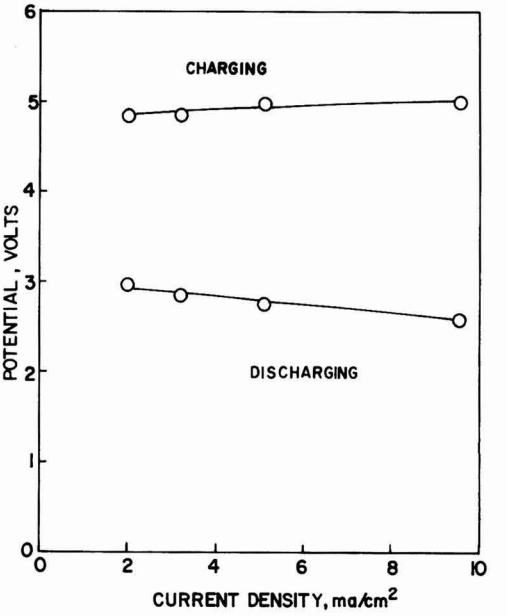

Fig. 8. Effect of operating current density on the potential of the positive electrode vs. the lithium wire reference electrode, V_2, during the charging and discharging runs.

6.3 mA (2 mA/cm²) and coulombic efficiency returned to 100%.

In order to check for involvement of electrolytic solution species in the electrode reactions, propylene carbonate (PC) was substituted for DMSU and $LiBF_4$ for $LiClO_4$. The results are shown in Fig. 9, 10, and 11. A comparison of results is shown in Table II. The results imply that DMSU is a necessary part of the positive electrode reaction process and that $LiClO_4$ gives better performance than $LiBF_4$.

The effect of different materials in the positive electrode on cell performance was examined. Results

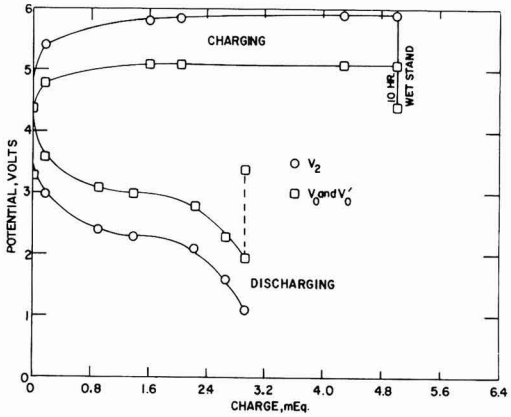

Fig. 9. Galvanostatic charge-discharge curves for the cell Li/$LiClO_4$, PC (0.89M)/graphite + graphite glue on carbon cloth. Cycle No. 5. $I = 6.3$ mA; $Q_{in} = 5.0$ mequiv.; coulombic eff. = 45.6% above $V_f = 2.0V$; positive electrode weight = 0.6260g; graphite = 0.1980g; carbon cloth = 0.3262g; initial thickness of carbon disk = 0.10 cm; top surface area = 3.14 cm²; resistance = 1.0Ω.

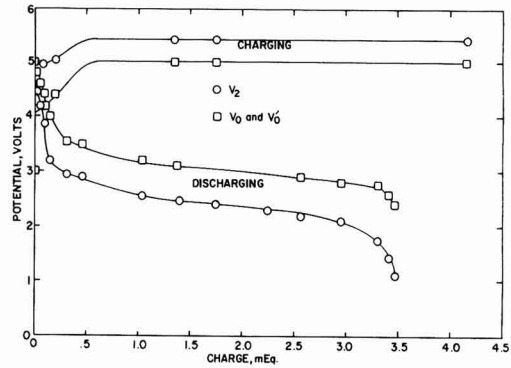

Fig. 10. Galvanostatic charge-discharge curves for the cell Li/$LiBF_4$, DMSU (1.03M)/graphite + graphite glue on carbon cloth. Cycle No. 3. $I = 6.3$ mA; $Q_{in} = 4.16$ mequiv.; coulombic eff. = 72.3% above $V_f = 2.0V$; positive electrode weight = 0.2218g; graphite = 0.0448g; carbon cloth = 0.1540g; initial thickness of carbon disk = 0.04 cm; top surface area = 3.14 cm²; resistance = 3.0Ω.

with bare platinum as the positive showed a fairly flat charging plateau at 5.6V, but no discharge plateau was observed. Pyrolized glue on carbon cloth (no graphite powder) gave typically observed results as shown in Fig. 12. Results using only carbon cloth are shown in Fig. 13. The charging runs were flat at 5.2V and not shown. The coulombic efficiency increased with increased cycling. During run 4, 41% of the 8.52 Mequiv. had been recovered when discharging was stopped because the reference electrode had dissolved away and cell resistance had increased from 1.0 to 2.8 kΩ. However, V_0 was steady at 3.2V. There was bubbling at the lithium counterelectrode and the reference electrode. Although all the carbon

Table II. Comparison of performance for four electrolytic solutions

	$LiClO_4$-DMSU	$LiClO_4$-PC	$LiBF_4$-DMSU	$LiBF_4$-PC
Charge recovered, m equiv.	8.50	2.26	3.00	1.10
Coulombic efficiency	95.3	42.2	72.3	50.0
Cutoff potential, V_f	2.5	2.0	2.0	1.25

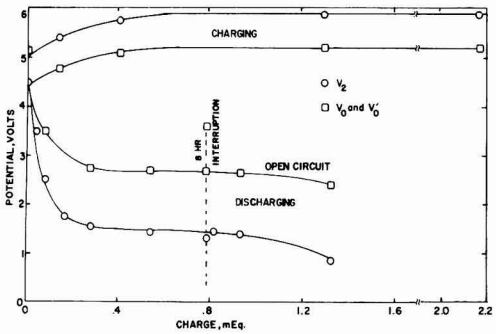

Fig. 11. Galvanostatic charge-discharge curves for the cell Li/$LiBF_4$, PC (1.55M)/graphite + graphite glue + carbon cloth. Cycle No. 3. I = 6.3 mA; Q_{in} = 2.17 mequiv.; coulombic eff. = 50.0% above V_f = 1.25V; positive electrode weight = 0.1709g; graphite = 0.0300g; carbon cloth = 0.1200g; initial thickness of carbon disk = 0.04 cm; top surface area = 3.14 cm^2; resistance = 3.0Ω.

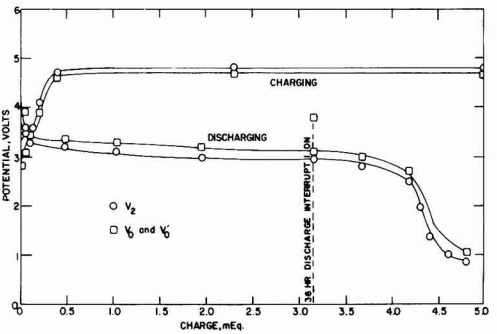

Fig. 12. Typical galvanostatic charge-discharge curves for the cell Li/$LiClO_4$, DMSU (1.53M)/graphite glue on carbon cloth. Cycle No. 2. I = 6.3 mA; Q_{in} = 5.0 mequiv.; coulombic eff. = 64.0% above V_f = 2.50V; positive electrode weight = 0.7258g; carbon cloth = 0.5053g; initial thickness of carbon disk = 0.07 cm; top surface area = 3.14 cm^2; resistance = 4.0Ω.

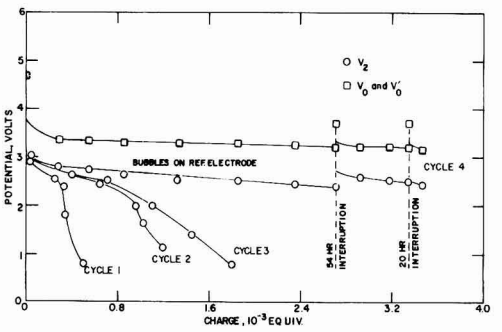

Fig. 13. Galvanostatic discharge curves for the cell Li/$LiClO_4$, (2.13M) DMSU/carbon cloth. V_2 (charging) = 5.15V. I = 6.30 mA; weight of carbon cloth electrode = 0.1273g; thickness = 0.02 cm; exposed area = 3.14 cm^2; V_0 (charging) = 4.70V.

	Cycle 1	Cycle 2	Cycle 3	Cycle 4
Charge in, 10^{-3} equiv.	1.25	2.28	3.13	8.52
Coulombic eff. above V_f = 2.50V	20.32	27.81	22.36	40.63

electrodes gave appreciable charge storage, the high surface area electrodes gave the greatest charge retention.

Gas chromatographic analysis was carried out on the electrolytic solution of the positive half-cell at various stages of charge and discharge. A new peak was observed at the end of charging which was not present at the end of discharging. This implies that the oxidizing agent formed on charging is at least partially soluble, and it is consumed on discharging.

X-ray powder diffraction data ($Cu_{K\alpha}$ radiation) on cycled positive electrodes in cells containing DMSU showed a number of diffraction lines that could not be assigned to a known compound. The most intense of these lines had a d value of 4.42Å followed in intensity by the line with d = 7.76Å. Thus, there is evidence for some intercalation of graphite. On samples of positive electrodes from cells using PC as solvent, however, there were only two unassigned peaks with d values of 2.39 and 1.80Å, the latter being more intense. Thus, intercalation of graphite (characteristic d = 3.38Å) in PC solutions is not significant.

Discussion

The need for carbon as natural graphite, carbonized graphite glue, or carbon cloth for charge storage in the positive electrode has been demonstrated by substantial charge storage in the carbon positive electrodes and the inability of a bare platinum electrode to demonstrate charge storage. Graphite or carbon appears to be a suitable catalyst and possibly a participant in the charge storage reactions at the positive electrode. The high storage of the graphite powder-graphite glue compared to carbon cloth alone is attributed to better adsorption properties of the powder plus glue.

The initial swelling of the pyrolized graphite-glue electrodes is attributed to formation of intercalation compounds, possibly intercalation of perchlorate anions and/or the solvent molecules. However, substantial charge storage was achieved with carbon cloth alone, which did not swell. This implies that the intercalation reactions are side reactions which do not contribute significantly to charge storage but help to increase the carbon surface area available for storage of the oxidizing agent produced during charging.

The attack on the lithium wire reference electrode and the new peak observed by gas chromatography of samples taken after charging imply that the oxidizing agent formed during charging is at least partially soluble. It is not expected that intercalation compounds would be soluble. Since the perchlorate ion is already highly oxidized and no chlorine or oxygen gas evolution was observed, it appears that DMSU is the principal reactant. This conclusion is further strengthened by the observations that, when DMSU was replaced by PC, the charge storage capability of the positive electrode, the coulombic efficiency, and the value of the discharge potential all dropped substantially (Table I).

DMSU molecules contain sulfur in the valence state 4. Valence states 5 and 6 are known for sulfur. Thus it is reasonable to expect DMSU to be oxidized during charging

$$(CH_3O)_2SO \rightarrow [(CH_3O)_2SO]^+ + e^-$$

or

$$(CH_3O)_2SO \rightarrow [(CH_3O)_2SO]^{+2} + 2e^-$$

During charging, it appears possible that the initial reaction product, presumably a radical cation, may rearrange or react further. The radical cation is expected to be reduced back to DMSU which would complete the reversible cycle. However, charged species resulting from subsequent rearrangement may form final products other than DMSU during discharge. Since there was a large excess of DMSU in all of the experiments run in this investigation, it has not been established whether or not subsequent cycles complete a reversible cycle or whether fresh DMSU

is oxidized each charge cycle implying that a storage battery type cycle does not exist for this system.

At the negative electrode dendritic lithium deposits were observed to change during discharging into a white floc which could be $LiClO_4$. If that is the case, it is implied that during discharging a local supersaturation of $LiClO_4$ occurs near the negative electrode. This behavior would be expected if the ClO_4^- mobility is much larger than the Li^+ mobility. Since the Li^+ is probably highly solvated, it is reasonable to expect the ClO_4^- ion to have a higher mobility. Preliminary x-ray analysis indicated the white precipitate was $LiClO_4$, but the results were not conclusive.

Acknowledgments

Financial support for this work has been provided by the U.S. Navy, Office of Naval Research.

Manuscript submitted April 13, 1977; revised manuscript received Dec. 19, 1977.

Any discussion of this paper will appear in a Discussion Section to be published in the December 1978 JOURNAL. All discussions for the December 1978 Discussion Section should be submitted by Aug. 1, 1978.

Publication costs of this article were assisted by the University of California.

REFERENCES

1. S. L. Deshpande, M.S. Thesis, School of Engineering and Applied Science, University of California, Los Angeles, California (1976).
2. J. S. Dunning, W. H. Tiedemann, L. Hsueh, and D. N. Bennion, *This Journal*, **118**, 1886 (1971).
3. Z. I. Mirza, M.S. Thesis, School of Engineering and Applied Science, University of California, Los Angeles, California (1971).
4. R. K. Hebbar, M.S. Thesis, School of Engineering and Applied Science, University of California, Los Angeles, California (1974).
5. R. Selim and P. Bro, *This Journal*, **121**, 1457 (1974).

Activities and Surface Tension of Liquid AgCl-KCl Solutions

Z. Moser,* M. Kucharski, and K. Rzyman

Institute for Metal Research, Polish Academy of Sciences, Kraków, Reymonta 25, Poland

ABSTRACT

Thermodynamic properties of liquid AgCl-KCl solutions were investigated at concentrations of $X_{AgCl} = 0.43$-1.00 at temperatures of 860°-1000°K by the method of formation cells with chlorine electrode. The partial thermodynamic data of AgCl were interpreted by Krupkowski's method and the relations of activity coefficients of both AgCl and KCl were obtained. Simultaneously, the surface tension measurements of pure AgCl, KCl, and AgCl-KCl liquid solutions were carried out using the maximum bubble pressure method at temperatures of 734°-1220°K dependent on the composition of investigated solutions and the melting points of pure salts. Using the thermodynamic data of bulk AgCl-KCl solutions, results of surface tension, and the calculations of the composition of the surface phase of the thickness 4.29×10^{-8} cm, the activity coefficients of AgCl in this phase were obtained.

Experimental methods dealing with the determination of thermodynamic properties of liquid solutions do not take into account the surface phenomenon, *i.e.*, the adsorption of the surface. On the other hand, the case of equilibrium between the surface phase and the bulk may be considered in order to explain surface properties. In this case, however, it is possible to determine the thermodynamic properties of both phases mentioned above despite the fact that the surface phase is not a separate one. To investigate these problems, thermodynamic properties of the bulk phase were determined by the emf method for the AgCl-KCl liquid solutions, while surface tension measurements of pure AgCl, KCl, and AgCl-KCl solutions made it possible to follow the change of activities in the solution in the surface layer.

Thermodynamic Properties of Liquid AgCl-KCl Solutions

Experimental investigations on AgCl-KCl liquid solutions form part of the studies on ternary salt solutions including AgCl-LiCl-KCl. The aim of these studies is to show the possibility of applying Krupkowski's formalism (1) to salt systems with single charge ions and to verify the similarities between liquid salt and metallic systems. It was shown by Moser and Fitzner (2) when analyzing available experimental data from the literature for the AgCl-LiCl-KCl system on plot $(\ln \gamma_{AgCl})_{X_{AgCl}=0}$ *vs.* X_{LiCl} that, as in the case of liquid metal solutions (3), the deviation from linear dependence forms the term connected with the binary system KCl-LiCl.

Applying the method of formation cells with a chlorine electrode of the following type

$$Ag(s)/AgCl\text{-}KCl(l)/Cl_2(g), \text{graphite} \qquad [1]$$

the thermodynamic properties of liquid AgCl-KCl solutions were investigated at concentrations of $X_{AgCl} = 0.43$-1.00 and at temperatures of 860°-1000°K. The scheme of the cell is shown in Fig. 1. A crucible, 2, made of silica and containing liquid salts, 6, was placed in an alumina crucible, 1. The following were immersed in liquid salts:

A. A high melting glass tube, 13, closed at one end with the orifice enabling contact with liquid salts, in the bottom of which was placed a silver electrode, 3. A silver electrode in the form of a sheet was connected with an alumina tube, 14, by alundum cement. The upper part of the silver sheet was connected with Pt wire, 4, passing through a rubber stopper, 5.

B. Pt-PtRh10 thermocouple, 11, was inserted into a silica tube enabling temperature measurements to ±2°C.

C. An asbestos diaphragm, 7, sealed in a silica tube, 8, separates the two electrode compartments and forms the bottom part of the chlorine electrode. The

* Electrochemical Society Active Member.

Key words: activity coefficient, fused salts, thermodynamics, solvents.

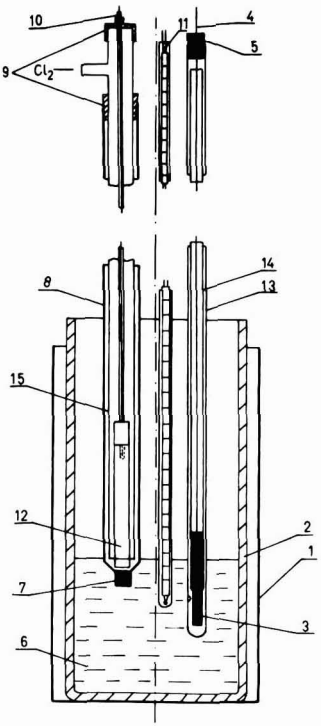

Fig. 1. Scheme of the experimental cell

chlorine electrode consists of a graphite rode, 12, connected with a high melting glass tube, 15, and a Pt wire. Seals, 9, were made of Teflon.

The results of emf measurements obtained for increasing temperatures (open circles) and decreasing (solid circles) are shown in Fig. 2. As these plots show the linear dependence of emf *vs.* temperature, the least squares method was used for averaging the data.

From the resulting linear equations presented in Table I. the emf values at the chosen temperatures of 873°-973°K were calculated each 20°. These emf data were used for calculations of silver chloride activities employing the Nernst equation with $P_{Cl_2} = 1$ atm and with the activity of silver taken as unity. The activity coefficients of silver chloride are calculated from the following relation

$$E_{AgCl} - E^{\circ}_{AgCl} = -\frac{RT}{n\mathbf{F}} \ln \gamma_{AgCl} - \frac{RT}{n\mathbf{F}} \ln X_{AgCl} \quad [2]$$

where E°_{AgCl} is the standard cell potential obtained with pure AgCl (bottom line in Fig. 2) and E_{AgCl} is the emf value of the formation cell.

The obtained experimental values of $\ln \gamma_{AgCl}$ were described by Krupkowski's relation

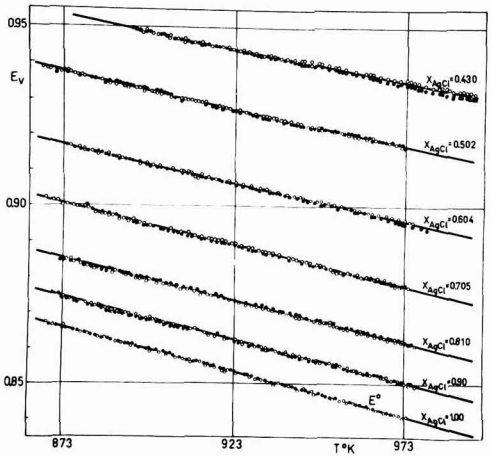

Fig. 2. EMF_{volts} *vs.* temperature in the system AgCl-KCl

$$\ln \gamma_{AgCl} = \omega(T)\,(1 - X_{AgCl})^m \quad [3]$$

The value of m ($m = 1.72$) was obtained from the plot $\log|\ln \gamma_{AgCl}|$ *vs.* $\log\,(1 - X_{AgCl})$ as the slope, and $\omega(T)$ as intercept. Next, the relation of $\omega(T)$ *vs.* temperature [$\omega(T) = -863/T + 0.1468$] were calculated. In this manner the following relations for $\ln \gamma_{AgCl}$ and $\ln \gamma_{KCl}$ were obtained in the form

$$\ln \gamma_{AgCl} = \left(-\frac{863}{T} + 0.1468\right)(1 - X_{AgCl})^{1.72} \quad [4]$$

$$\ln \gamma_{KCl} = \left(-\frac{863}{T} + 0.1468\right)[(1 - X_{AgCl})^{1.72} - 2.389\,(1 - X_{AgCl})^{0.72} + 1.389] \quad [5]$$

The form of $\omega(T)$ with $\alpha = -863$ and $\beta = 0.1468$ results in equations for partial ($\Delta\overline{H}_{AgCl}$) and integral enthalpy ($\Delta H'$) of the following form

$$\Delta\overline{H}_{AgCl} = -RT^2\left(\frac{\partial \ln \gamma_{AgCl}}{\partial T}\right) = R\alpha(1 - X_{AgCl})^{1.72} = -1714\,(1 - X_{AgCl})^{1.72} \quad [6]$$

$$\Delta H' = R\alpha\frac{1}{m-1}[1 - (1 - X_{AgCl})^{0.72}]X_{KCl} = -2381[1 - (1 - X_{AgCl})^{0.72}]X_{KCl} \quad [7]$$

The experimental data and those calculated from Eq. [4]-[7] as well as thermodynamic data at 973°K presented by Pelton and Flengas (4) are compared in Table I. Besides the partial thermodynamic properties of AgCl there also exists a good agreement of integral enthalpy when compared with Hersh and Kleppa's (5) calorimetric data (at $X_{AgCl} = 0.5$; $\Delta H' = -550$ cal/mole).

In addition it should be mentioned that similar parameters of $\omega(T)$ and m in Eq. [4] and [5] were

Table I. Experimental and calculated data in AgCl-KCl liquid solutions at 973°K

Experimental data			Calculated from Eq. [4]-[7]				Experimental data of Pelton and Flengas	
X_{AgCl}	$E_{volts} = a - b\,T°K$	γ_{AgCl}	γ_{AgCl}	γ_{KCl}	$-\Delta\overline{H}_{AgCl}$ (cal/mole)	$-\Delta H'$ (cal/mole)	X_{AgCl}	γ_{AgCl}
0.430	$E = 1.11102 - 1.8061 \cdot 10^{-4}T$	0.752	0.755	0.878	651	452	0.3497	0.699
0.502	$E = 1.11245 - 2.0075 \cdot 10^{-4}T$	0.800	0.800	0.835	517	468	0.4994	0.800
0.604	$E = 1.10670 - 2.1697 \cdot 10^{-4}T$	0.860	0.860	0.763	348	459	0.6992	0.907
0.705	$E = 1.10124 - 2.2999 \cdot 10^{-4}T$	0.914	0.913	0.681	210	411	0.8505	0.976
0.810	$E = 1.08831 - 2.3307 \cdot 10^{-4}T$	0.963	0.958	0.585	99	315		
0.900	$E = 1.08326 - 2.3937 \cdot 10^{-4}T$	0.990	0.986	0.530	33	193		
1.000	$E = 1.0_{\wedge}025 - 2.5648 \cdot 10^{-4}T$	1.000						

obtained when Krupkowski's method was applied to the data of Pelton and Flengas (4): $\omega(T) = -863/T + 0.054$; $m = 1.80$ as shown previously by Moser and Fitzner (2). The same method was also used by Ptak and Szczygiel (6) for interpretation of emf data of concentration cells applied to AgCl-KCl liquid solutions. The obtained values of $\omega(T) = -917/T$ and $m = 1.87$ also lead to data similar to those presented in Table I.

Surface Tension Measurements of Liquid AgCl, KCl, and AgCl-KCl Solutions

Measurements of surface tension have been carried out by the maximum bubble pressure method. Experimental arrangements were similar to those for liquid metals (7), but some modifications were introduced to limit the vapor transport effect. This limitation is an important factor as it was shown that measurements of surface tension of liquids with significant vapor pressure may result in erroneous data, in the case when the equilibrium of the gaseous with the liquid phase is not attained (8, 9). This phenomenon has been proved in the present investigations as liquid KCl and solutions AgCl-KCl rich in KCl have, in experimental conditions, sufficiently high pressure to influence the surface tension measurements, especially those carried out with free evaporation.

To limit this evaporation a crucible with tested salt was placed in special graphite vessel, 4, with a screwed cover in which an orifice for capillary introduction had been made. The other parts of experimental arrangements are presented in Fig. 3. They consist of a manometer filled with dibutylphalate, 1, a gas train for the purification of argon, 2, a quartz capillary, 3, a crucible vessel with the salt sample, 4, Pt-PtRh10 thermocouple, 5, a resistance furnace, 6, an arrangement to move the crucible with the salt up and down, 7, and a micrometer screw, 8. A quartz capillary with a diameter of 0.7-1 m/m was used. It was initially wetted in liquid salt which improves the reproducibility of results. First, a sample of the investigated salt was placed in the furnace which was then closed. In the meantime the gas train system was open and argon passed through this closed system for a minimum of 24 hr. Next, the furnace was switched on until the first desired temperature was attained. Then, the surface tension measurements were initiated after immersing the capillary at one or two chosen depths. The maximum pressure required for forming and detaching several bubbles was measured. The average value of this measurement was taken for the first approach of surface tension calculations using the relation

$$P = \frac{1}{2} r P_{max} \quad [8]$$

where P is the surface tension in dynes per centimeter, r the capillary radius, and P_{max} the maximum pressure required for forming and detaching bubble.

The real values of surface tension were obtained using Sudgen's correction method (10). For measurements, AgCl and KCl of high purity were used. Salts were stored in the heater at a temperature of 150°C for about 24 hr and, next, after transferring to the furnace, melted in a stream of gaseous dry HCl. HCl passed through the melt for about 0.5 hr. To obtain a homogeneous mixture of AgCl + KCl the weighed amounts of purified salts were also melted together in a stream of purified HCl and next cast in a quartz form, quickly cooled, and stored in a dessicator. The preparations of the salts for formation cells in the first part was analogical.

The results of surface tension measurements of pure AgCl *vs.* temperature are plottted in Fig. 4. The surface tension decreases linearly with the increase of temperature, also the obtained results are in good agreement with data from monograph (11) and are slightly different in comparison with Ref. (12). It should be added that the results for the different runs from this paper were averaged together by the least squares method as shown by the thick continuous line. The results for pure KCl shown in Fig. 5 were averaged in a similar way and the surface tension also changes linearly *vs.* temperature. Figure 5 presents the results obtained in this investigation for both limited evaporation (solid line) and free evaporation (dashed line). Differences appear between both sets, as at the investigated temperatures KCl has clearly noticeable pressure and the apparatus used enabled measurements in conditions approaching equilibrium between the liquid and gaseous phases. Our results for free evaporation are in good agreement with Ref. (13-15) as shown in Fig. 6.

As in the case of surface tension measurements of pure liquid KCl, our results with limited transport effect for AgCl-KCl mixtures show divergences in

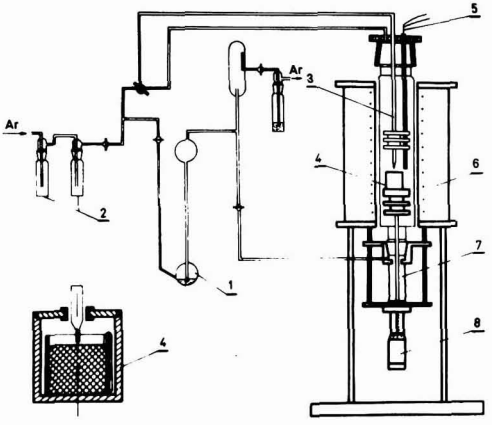

Fig. 3. Scheme of the experimental arrangements for the surface tension measurements.

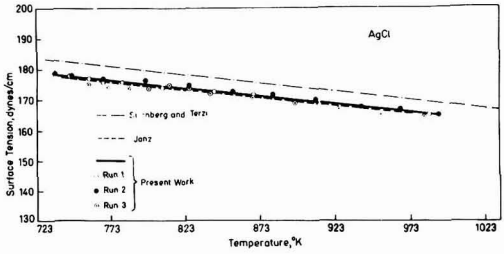

Fig. 4. The surface tension of AgCl *vs.* T°K

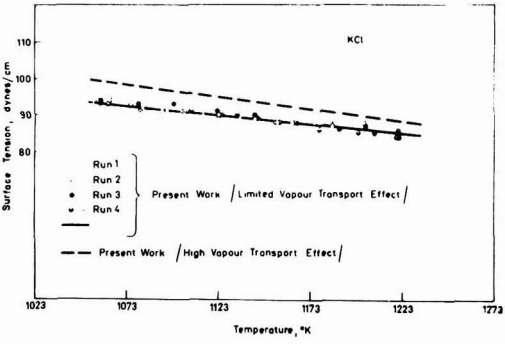

Fig. 5. The surface tension of KCl *vs.* T°K for limited and free evaporation.

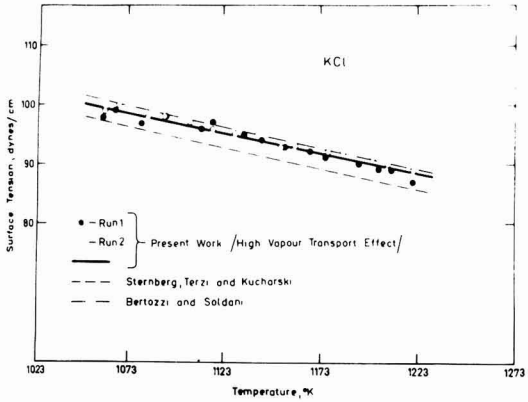

Fig. 6. The surface tension of KCl *vs.* T°K for free evaporation compared with the data from different sources.

comparison with literature data (13) for AgCl-KCl. Our data also decrease linearly with the increase of temperature. For both pure salts and AgCl-KCl solutions the relations of surface tension *vs.* temperature were described by linear dependences $\sigma = a - bt$°C, where a is the intercept and b the slope of the line. The values of both parameters for pure salts and mixtures, respectively, are summarized in Table II with the standard error of estimate and the temperature range of measurements.

On analyzing the maximum bubble pressure method it appears that it is less precise in comparison, for instance, with the pin method and, taking into account the standard error of estimate, errors in surface tension measurements are of the order of ±2-3 dynes. These errors, however, and the different influence of limitation of evaporation in respect to the composition of investigated salt compositions were sufficient to introduce in linear equations of surface tension *vs.* temperature (Table II) the lack of fluid change in slopes from pure AgCl to KCl.

Using the linear equation from Table II, surface tension was calculated at 973°K and a relation of σ *vs.* X_{AgCl} was plotted in Fig. 7 as shown by circles. The continuous line on this plot refers to Eberhart's relation (16). Eberhart has presented an equation for the surface tension of binary liquid mixtures based on the assumption that the surface tension is a linear function of the surface layer mole fraction. The condition for equilibrium between the surface layer and the bulk liquid phase gives a relationship between the surface and the bulk compositions and results in the following equation

$$\sigma = \frac{X_{AgCl}\sigma_{AgCl} + SX_{KCl}\sigma_{KCl}}{X_{AgCl} + SX_{KCl}} \qquad [9]$$

where σ_{AgCl} and σ_{KCl} are the surface tensions of the pure salts, and S is the coefficient dependent on temperature which gives the extent of surface layer enrichment of the component of lower surface tension. For results of surface tension at 973°K the value of the coefficient $S = 6.21$ was determined according to the procedure presented in Ref. (16).

Table II. Experimental data of surface tension for AgCl, KCl, and AgCl-KCl liquid solutions

X_{AgCl}	$\sigma = a - bt$°C	Standard error of estimate $s(\sigma)$	$\sigma_{700°C}$	Range of temperature (°C)
1.0	$\sigma = 202.54 - 0.0527t$	1.07	165.65	461-720
0.9	$\sigma = 167.50 - 0.0457t$	1.36	135.51	458-722
0.7	$\sigma = 173.40 - 0.0838t$	0.69	114.74	360-718
0.5	$\sigma = 149.70 - 0.0578t$	1.11	109.24	518-725
0.3	$\sigma = 161.30 - 0.0843t$	0.66	102.29	650-751
0.1	$\sigma = 138.40 - 0.0546t$	0.38	100.18	745-846
0.0	$\sigma = 133.10 - 0.0506t$	0.82	97.68	785-947
0.0	$\sigma = 151.70 - 0.0665t$	0.93	105.15	785-947*

* Data for pure KCl obtained with free evaporation.

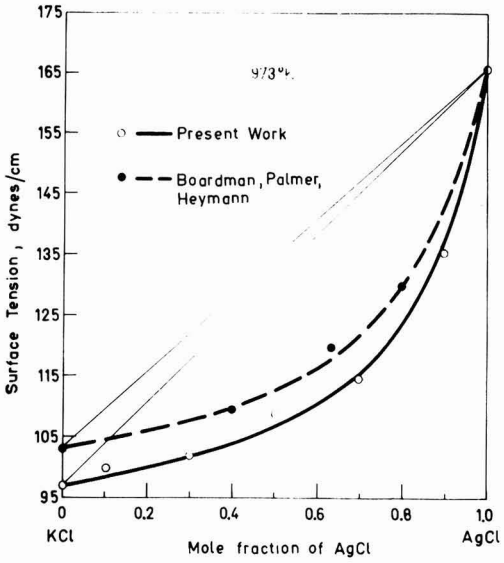

Fig. 7. The surface tension of the AgCl-KCl liquid solutions *vs.* X_{AgCl} at 973°K.

Composition of the Surface and the Relation Between the Thermodynamic Properties of the Bulk and Surface Phase

The basic relation which combines the surface tension with the activities of components in the surface layer and in the bulk phase according to (17) takes the form

$$RT \ln a_{AgCl^{\bar{\omega}}} = RT \ln a_{AgCl} + \frac{\overline{V}_{AgCl^{\bar{\omega}}}}{\tau}(\sigma - \sigma_{AgCl}) \qquad [10]$$

where $a_{AgCl^{\bar{\omega}}}$ and a_{AgCl} are the activities in the surface layer and in the bulk phase, respectively, τ is the assumed thickness of the surface layer, $\overline{V}_{AgCl^{\bar{\omega}}}$ is the partial molar volume of AgCl in the surface phase assumed to be equal molar volume V_{AgCl}, σ_{AgCl} is the surface tension of pure AgCl, and σ is the surface tension of AgCl-KCl solutions.

To obtain results of $\gamma_{AgCl^{\bar{\omega}}}$ in the surface phase a knowledge of the composition of the surface phase is necessary for interpretation by Krupkowski's method as in the case of the bulk. Various procedures for the computation of concentrations of both AgCl and KCl in the surface phase are presented below. On the basis of the assumption of the existence of the surface phase (18) it is possible to calculate the relative adsorption $\Gamma_{AgCl(KCl)}$ by the following relation

$$\Gamma_{AgCl(KCl)} = \Gamma_{AgCl} - \frac{X_{AgCl}}{X_{KCl}}\Gamma_{KCl} = -\frac{d\sigma}{d\mu_{AgCl}} \qquad [11]$$

where Γ_{AgCl} and Γ_{KCl} are the number of moles of AgCl and KCl, respectively, in the surface phase per unit area, μ_{AgCl} is the chemical potential of AgCl in the bulk phase, σ is the surface tension, and X_{AgCl} and X_{KCl} are the mole fractions of AgCl and KCl in the bulk phase.

The value of $\Gamma_{AgCl(KCl)}$ is independent of the arbitrarily assumed areas which separate from the solu-

tion the surface area to which we ascribe the properties of the phase. The only limitation is that the adsorption area must be contained between these two areas. The values of Γ_{AgCl} and Γ_{KCl} may be calculated if certain additional assumptions are made concerning the structure of the surface layer. One such assumption (9) may be represented by the equation

$$\Gamma_{AgCl}\overline{V}_{AgCl}^{\bar{\omega}} + \Gamma_{KCl}\overline{V}_{KCl}^{\bar{\omega}} = \tau \qquad [12]$$

where $\overline{V}_{AgCl}^{\bar{\omega}}$ and $\overline{V}_{KCl}^{\bar{\omega}}$ are the partial molar volumes of AgCl and KCl in the surface phase and τ is the thickness of the surface layer.

Basing on Eq. [10] and [12] values of adsorption Γ_{AgCl}, Γ_{KCl} may be calculated as follows

$$\Gamma_{AgCl} = \frac{X_{AgCl}\tau - X_{KCl}\overline{V}_{KCl}^{\bar{\omega}}\dfrac{d\sigma}{d\mu_{AgCl}}}{X_{KCl}\overline{V}_{KCl}^{\bar{\omega}} + X_{AgCl}\overline{V}_{AgCl}^{\bar{\omega}}} \qquad [13]$$

and

$$\Gamma_{KCl} = \frac{X_{KCl}\left(\tau + \overline{V}_{AgCl}^{\bar{\omega}}\dfrac{d\sigma}{d\mu_{AgCl}}\right)}{X_{KCl}\overline{V}_{KCl}^{\bar{\omega}} + X_{AgCl}\overline{V}_{AgCl}^{\bar{\omega}}} \qquad [14]$$

Considering Eq. [11], [12], [13], and [14], thermodynamic properties of AgCl-KCl solutions (Eq. [4]), and the results of surface tension measurements, the relative adsorption as well as adsorption of respective components were calculated assuming that $\overline{V}_{AgCl}^{\bar{\omega}} = V_{AgCl}$ and $\overline{V}_{KCl}^{\bar{\omega}} = V_{KCl}$. The molar volumes of AgCl and KCl were computed from densities of these salts, taken from monograph (11). Calculations were carried out for thicknesses of the surface phase, namely $\tau = 4.29 \times 10^{-8}$ cm and $\tau = 8.58 \times 10^{-8}$ cm. They are equal to a single and double diameter of a KCl molecule. Then the concentrations of AgCl and KCl in the surface phase were calculated from the relations

$$X_{AgCl}^{\bar{\omega}} = \frac{\Gamma_{AgCl}}{\Gamma_{AgCl} + \Gamma_{KCl}}$$

and

$$X_{KCl}^{\bar{\omega}} = \frac{\Gamma_{KCl}}{\Gamma_{AgCl} + \Gamma_{KCl}} \qquad [15]$$

When analyzing the results of the calculations, adding to the calculated number of moles of the respective components in the first layer of molecules of the thickness $\tau = 4.29 \times 10^{-8}$ cm the number of moles of the second layer of the same thickness but of bulk composition, the values of the AgCl concentration obtained were identical to those in calculations when it was assumed that $\tau = 8.58 \times 10^{-8}$ cm. This proves that the adsorption refers only to the first layer of molecules. The results of the calculations for the monomolecular layer are shown in Fig. 8.

The composition of the surface phase in the case of weak adsorption may also be calculated by the procedure assuming that the differences between the composition of surface and bulk phase take place only in the first layer of atoms. In such a case (18) the following relation is valid

$$\Gamma_{AgCl}A_{AgCl} + \Gamma_{KCl}A_{KCl} = 1 \qquad [16]$$

where A_{AgCl} and A_{KCl} are the partial molar areas of AgCl and KCl in the surface monomolecular layer, respectively. Using Eq. [16] and [11] the composition of AgCl in the surface layer was calculated and is also presented in Fig. 8.

In addition, the composition of the surface phase may be calculated as proposed by Eberhart (16) given the coefficient S and considering relations

$$S = \frac{X_{AgCl}^{\bar{\omega}}}{X_{KCl}^{\bar{\omega}}} \cdot \frac{X_{KCl}}{X_{AgCl}} \qquad [17]$$

and

$$X_{AgCl}^{\bar{\omega}} + X_{KCl}^{\bar{\omega}} = 1 \qquad [18]$$

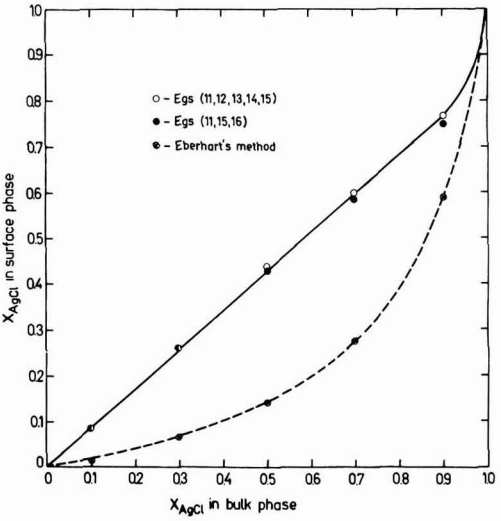

Fig. 8. Computed concentrations of AgCl in the surface phase vs. X_{AgCl} in the bulk phase.

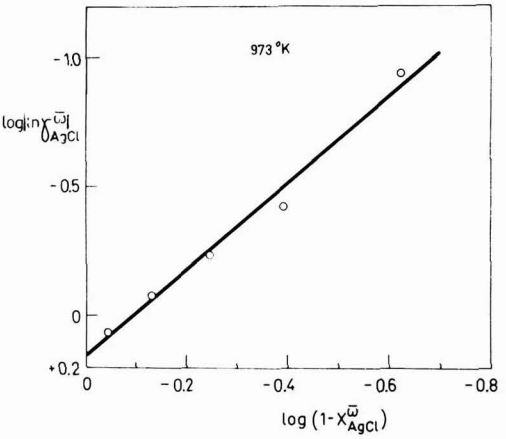

Fig. 9. The relation of log (ln $\gamma_{AgCl}^{\bar{\omega}}$) vs. log (1 − $X_{AgCl}^{\bar{\omega}}$) for the surface phase of the AgCl-KCl liquid solutions at 973°K.

Using Eq. [10] with the activities of the bulk calculated by Eq. [3] assuming that $\overline{V}_{AgCl}^{\omega} = V_{AgCl}$ and $\tau = 4.29 \times 10^{-8}$ and taking into account $X_{AgCl}^{\bar{\omega}}$ (Eq. [15]), activity coefficients of the surface monomolecular layer were computed. The obtained results were described as for the bulk by Eq. [3]. Figure 9 shows a fit of calculated values of activity coefficients ln $\gamma_{AgCl}^{\bar{\omega}}$ to Eq. [3] as log (ln $\gamma_{AgCl}^{\bar{\omega}}$) *vs.* log (1 − $X_{AgCl}^{\bar{\omega}}$).

In this procedure at 973°K, the following values were obtained: $m = 1.67$ and $\bar{\omega}(T) = -1.44$. By comparison with similar values of the bulk phase, $m = 1.72$ and $\omega(T) = -0.74$ it is concluded that the asymmetry of thermodynamic properties connected with parameter m is almost similar, and the main significant difference in the thermodynamic properties of the surface and bulk phase appear in the values of function $\omega(T)$.

The same conclusion may be reached using different values for surface tension obtained experimentally by Sternberg and Terzi (12). The calculated parameters m and $\omega(T)$ for the surface phase are equal to 1.87 and −1.32 at 973°K, respectively.

Conclusions

The results of surface tension measurements obtained with limited evaporation giving conditions approaching equilibrium between the liquid and gaseous phase are lower for KCl and liquid AgCl-KCl solutions in comparison with Ref. (12) and (19). The main reason for these differences lies in the fact that the experiments in Ref. (12) and (19) were not carried out in equilibrium between the liquid and gaseous phases. This is confirmed by the fact that the results of our measurements performed in conditions of free evaporation are close to literature data.

A similar influence of experimental conditions has been observed in surface tension measurements for liquid metals with high vapor pressures (8, 9).

In view of these facts it is desirable to conduct further research in order to elaborate the experimental method for surface tension measurements ensuring full equilibrium between liquid and vapor. Calculated values of the logarithm of the activity coefficients of AgCl in the surface phase interpreted by Krupkowski's method show that the thermodynamic asymmetry of this phase and the bulk phase of AgCl-KCl solutions is the same within the range of experimental errors, but the differences in the values of the $\omega(T)$ function of both phases suggest in the case of the surface phase much higher deviations from ideality than in the bulk phase. Differences in partial enthalpy and excess entropies of components in both phases may also be suggested.

Manuscript submitted Aug. 17, 1977; revised manuscript received Jan. 3, 1978.

Any discussion of this paper will appear in a Discussion Section to be published in the December 1978 JOURNAL. All discussions for the December 1978 Discussion Section should be submitted by Aug. 1, 1978.

REFERENCES

1. A. Krupkowski, *Bull. Acad. Pol. Sci., Ser. A*, **1**, 15 (1950); *This Journal*, **122**, 132 (1975); *ibid.*, **122**, 691 (1975); *Met. Trans.*, **6B**, 457 (1975); *ibid.*, **6B**, 653 (1975).
2. Z. Moser and K. Fitzner, *Rev. Roumaine Chim.*, **19**, 1573 (1974).
3. Z. Moser, *Metall. Trans.*, **6B**, 103 (1975).
4. A. D. Pelton and S. N. Flengas, *This Journal*, **118**, 1307 (1971).
5. L. S. Hersh and O. J. Kleppa, *J. Chem. Phys.*, **42**, 1309 (1965).
6. W. Ptak and Z. Szczygiel, *Arch. Hutn.*, **12**, 265 (1967).
7. W. Ptak and M. Kucharski, *ibid.*, **19**, 301 (1974).
8. D. W. G. White, *Trans. Metall. Soc. AIME*, **236**, 796 (1966).
9. M. Kucharski, *Zeszyty Naukowe AGH*, **3**, 329 (1977).
10. S. Sugden, *J. Chem. Soc.*, **121**, 858 (1922).
11. G. J. Janz, "Molten Salts Handbook," Academic Press, New York (1967).
12. S. Sternberg and M. Terzi, *Rev. Roumaine Chim.*, **15**, 527 (1970).
13. G. Bertozzi and G. Soldani, *J. Phys. Chem.*, **70**, 1536 (1966).
14. R. B. Ellis and A. C. Freeman, *ibid.*, **69**, 1943 (1965).
15. S. Sternberg, M. Terzi, and M. Kucharski, *Arch. Hutn.*, **22**, 169 (1977).
16. J. G. Eberhart, *J. Phys. Chem.*, **70**, 1183 (1966).
17. J. E. B. Randles and B. Behr, *J. Electroanal. Chem.*, **35**, 389 (1972).
18. E. A. Guggenheim, "Mixtures," Clarendon Press, Oxford (1952).
19. N. K. Boardman, A. R. Palmer, and E. Heymann, *Trans. Faraday Soc.*, **15**, 277 (1955).

Design of an Electrocoating Cell for Constant Current Density Operation

A Fourier-Transform Method of Solution of the Laplace Equation

Rodney L. LeRoy*

Noranda Research Centre, Pointe Claire, Quebec H9R 1G5, Canada

ABSTRACT

Continuous electrocoating is normally carried out by passage of a foil, strip, or wire substrate between parallel electrodes in a coating cell. It has been shown that improved unformity of deposition in such a cell, and thus improved dielectric properties of the product, can be achieved using a converging electrode geometry. A method is described for deriving the optimal electrode geometry based on solution of the Laplace equation in the electrolyte region. A semianalytical solution is used, with boundary conditions on the converging cathode being applied by a novel Fourier-transform method. For the electrocoating cell the resulting optimal geometry is well approximated by a simple result which assumes that current flow is perpendicular to the moving substrate.

Commercial application of electrodeposition of organic coatings has expanded rapidly over the last 15 years, first in the automotive industry and more recently in applying coatings to the products of the electrical, heating and cooling, furniture, aluminum extrusion, and other industries (1). The electrocoating process is particularly suited to application of thin, nonporous organic coatings to continuous foil, strip, or wire (2-4). In some applications, production speeds of 300-500 cm/sec have been achieved with uniform coating thicknesses of 2.5-5 μm.

The electrodeposition process is characterized by simultaneous occurrence of electrophoresis, electrolysis, and electroendosmosis (5, 6). All practical resin systems developed to date have been anaphoretic, involving deposition of the organic coating on a stationary or moving anode. The basic resin types used have thus been acidic and include carboxylated drying oils, alkyds and epoxy esters of high acid value, carboxyl-bearing acrylic copolymers, phenolics and triazine condensates. Typical coating baths consist of approximately 80-85% deionized water, 2-3% co-solvent, and 1% solubilizing base, with the balance being the anionic

* Electrochemical Society Active Member.

polymer. The potential applied to the electrocoating cell is typically 100-250V.

When potential is applied to the electrodes of the coating cell, the negatively charged polymer ions migrate toward the anode under the influence of the electrical field by the processes of ionic migration and electrophoresis. In the immediate vicinity of the anode several reactions can occur. For polycarboxylic acid polymers as were used in this work, direct decarboxylation can occur by the Kolbe reaction

$$2RCOO^- \rightarrow R—R + 2CO_2 + 2e \quad [1]$$

This reaction, however, is believed to be relatively unimportant, with the majority of the applied current being consumed by anodic dissolution of the anode substrate

$$M \rightarrow M^{z+} + ze \quad [2]$$

and by the anodic decomposition of water to give hydrogen ions and oxygen gas

$$2H_2O \rightarrow O_2 + 4H^+ + 4e \quad [3]$$

Some polymeric carboxylate ions are precipitated or coagulated in the vicinity of the anode by reaction with the ions of the substrate metal which are produced by reaction [2]. However, the principal anodic process is believed to be reaction [3], with polymer coagulation occurring by reaction with hydrogen ions in the low pH region in the immediate vicinity of the electrode. The local pH near the anode can drop to about 2, while most resins used for electrocoating will coagulate at pH values between 4 and 5 (7).

Thus anodic resin deposition occurs concurrently with vigorous evolution of oxygen gas. When an anode substrate is moved continuously through a coating cell between parallel cathode plates, a highly nonuniform current density distribution is established along the substrate in the coating cell. Deposition is rapid when the uninsulated substrate first enters the cell, but falls off as electrical insulation of the substrate by the deposited resin increases the resistance to the flow of current. These effects result in less than optimal coating properties. Resin deposition occurs at a very high rate at the entrance to the cell with simultaneous evolution of oxygen, resulting in a less homogeneous coating on the final product than would be achievable under more controlled conditions.

The final process occurring in the coating cell is electroendosmosis. This is the phenomenon by which much of the water in the film deposited on the anode substrate migrates in the direction of the cathode under the influence of the applied potential, resulting in water contents as low as 5-15%. On emergence from the cell, the electrocoated film is normally baked at between 150° and 200°C to promote further drying and, in many cases, oxidative cross-linking.

It has been found that use of a converging electrode geometry in an electrocoating cell can result in improved deposit properties by enabling a relatively constant current density on the anode substrate throughout the cell. The purpose of this paper is to describe a method of designing an electrode to achieve this constant current density objective. The method is based on solution of the Laplace equation within the electrolyte.

Basis of the Method

No calculations to derive optimal cathode geometries are possible until the boundary conditions in the electrocoating cell are defined. The cathode presents no problem in this regard, as the reaction here is simply hydrogen evolution. For typical substrates (*e.g.*, stainless steel) the overvoltage for this reaction will always be less than 1V in the range of current densities which are used. This is small compared with the potential applied to the cell, which is normally greater than 100V. Thus the cathode-electrolyte interface can be treated as being at the same potential as the cathode itself. The oxygen overvoltage on the anode and the reversible potential for the water decomposition reaction (totaling less than 1.6V) can be similarly neglected.

However, the potential on the anode-electrolyte interface varies strongly with position in the cell due to the deposition of the insulating polymer. In a parallel-electrode electrocoating cell, it would be difficult to deduce this anode interface potential as a function of position in the cell. For the converging electrode geometry, if it is assumed that a constant anode current density can be achieved, the problem becomes more amenable to solution. In this case, the constant electrocoating current density is under the control of the operator, so the variation of the anode film-electrolyte interface potential with time can be determined in a static experiment for the resin which is being used.

A typical result is illustrated in Fig. 1 for an aluminum substrate. The resin used was BASF Lewipal No. E-33, a mixed acrylate ester/acrylic acid resin solubilized with polyamines. The operating current density was 9.3 mA/cm^2. The film voltages measured in the static cell were obtained as a function of deposition time, but this result is readily translated into film voltage as a function of position in the continuous electrocoating cell as has been done in Fig. 1. This method is valid if the mass-transfer limiting current density is appreciably larger than the value selected. Provided this condition is satisfied, such static experiments allow translation of a desired constant current density of operation into a film voltage profile as a function of position in the electrocoating cell.

The conductivity of the resin-containing electrolyte must also be determined for use in the calculations described below. The conductivity of the BASF E-33 resin solution was 0.00056 Ω^{-1} cm^{-1}.

Derivation of the Cathode Geometry

A first approximation.—If it is assumed that current flows directly across the cell, perpendicular to the anode, the electrode geometry can be approximated using the equation

$$\text{total resistance } (R_t) = \text{solution resistance } (R_s) + \text{film resistance } (R_f) \quad [4]$$

Consider a small segment of the anode substrate, the length of which is $1/N$th of the total cell length L. Assuming that the current density is constant along the anode, the total resistance between this segment of the substrate and the corresponding segment of the cathode (on one side) is

$$R_t = U/(I/2N) \quad [5]$$

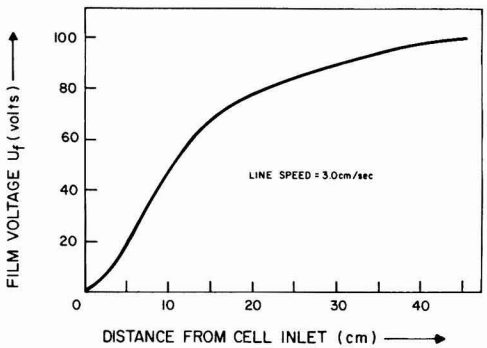

Fig. 1. Film voltage as a function of distance from the inlet of the continuous electrocoating cell. Data is translated from a static experiment assuming a constant current density in the cell of 9.3 mA/cm^2. The resin used was BASF E-33 of conductivity 0.00056 Ω^{-1} cm^{-1}.

where U is the total voltage applied to the cell, and I is the total current. By a similar argument, the film resistance on the segment of the anode being considered is

$$R_f = U_f/(I/2N) \quad [6]$$

where U_f (cf. Fig. 1) is the film voltage determined from static measurements. By definition the solution resistance is

$$R_s = \frac{d}{\kappa\left[\frac{W_a + W_c}{2}\right]\frac{L}{N}} \quad [7]$$

where d is the desired anode-cathode separation, κ is the solution conductivity, and W_a and W_c are, respectively, the widths of the anode and the cathode.

Substitution of the resistance factors from Eq. [5] to [7] into Eq. [4] gives the desired result for the anode-cathode separation as a function of position in the cell

$$d = \frac{\kappa L(W_a + W_c)}{I}(U - U_f) \quad [8]$$

The electrode configuration calculated from the film-voltage data of Fig. 1 using Eq. [8] is sketched as a broken curve in Fig. 2. Cell dimensions were $L = 45.7$ cm, $W_c = 10.2$ cm, and $W_a = 3.2$ cm, and the total current for a constant current density of 9.3 mA/cm^2 was set at $I = 2.7$A. An applied cell voltage of $U = 135$V was assumed. However, polarization effects and the reversible potential for the over-all cell reaction have been ignored, so in practice it would be necessary to adjust the applied potential until the required current density was achieved.

Solution of the Laplace equation.—Introduction.— The electrode geometry calculated using Eq. [8] is an approximation, because current does not flow directly across the cell perpendicular to the anode substrate. The current flowing at any point in the electrolyte is sensitive to the potentials at all points on the enclosing electrodes.

This problem is solved as follows. Assuming that the current is not significantly limited by mass-transfer effects, the potential $\phi(x, y)$ can be accurately represented by the Laplace equation in the region between the anode and the cathode (8, 9). This is

$$\frac{\partial^2\phi(x,y)}{\partial x^2} + \frac{\partial^2\phi(x,y)}{\partial y^2} = 0 \quad [9]$$

Rectangular coordinates are used for the cell geometry being considered here, with the x and y directions defined in Fig. 3 for an arbitrary, converging electrode geometry.

Laplacian problems are commonly encountered in aerodynamics, hydrodynamics, heat transfer, electrostatics, and many other physical problems as well as in electrochemical applications, so considerable effort has been devoted to their solution. One approach is to use experimentally based analogical or graphical methods (10, 11). However, such methods are time consuming to use and are not well adapted to iterative determination of an optimal electrode design. Also, with the availability of high-speed digital computers, numerical solutions of Eq. [9] can be obtained. Such brute force solutions depend on a process of iteration (12) and for a complex geometry, such as that of Fig. 3, solution can require several minutes of computer time and thus a substantial cost.

Analytical solutions are, therefore, to be preferred in many instances, even if they entail major approximations. Examples of such solutions abound (9, 13-15).

Once the potential distribution has been established, the current density J normal to the anode can be calculated directly from the gradient of the potential perpendicular to the substrate, from the Ohm's law expression

$$J = -\kappa\left.\frac{\partial\phi(x,y)}{\partial x}\right|_{x\to 0} \quad [10]$$

The process of determination of an optimal cathode geometry is as follows. A particular geometry is selected, Eq. [9] is solved for the potential in the electrocoating solution, and current density values along the anode substrate are calculated from Eq. [10]. If these values differ significantly from constancy, appropriate modifications are made in the electrode geometry and the process is repeated until relatively constant current density is achieved.

A suitable general form of the solution to Eq. [9] is

$$\phi(x,y) = \sum_{m=0}^{\infty}(A'_{1m}e^{ax} + A'_{2m}e^{-ax})(B_{1m}\sin(ay) + B_{2m}\cos(ay)) \quad [11]$$

where the infinite set of constants A'_{1m}, A'_{2m}, B_{1m}, B_{2m} and a must be determined from the boundary conditions. Thus, on the cathode, whatever its geometry, $\phi(x, y)$ must reduce to the value of the applied potential U, while on the anode substrate at $x = 0$ it must reduce to the film voltage U_f (cf. Fig. 1). In the method of solution which has been selected here, these boundary conditions are applied by identifying Eq.

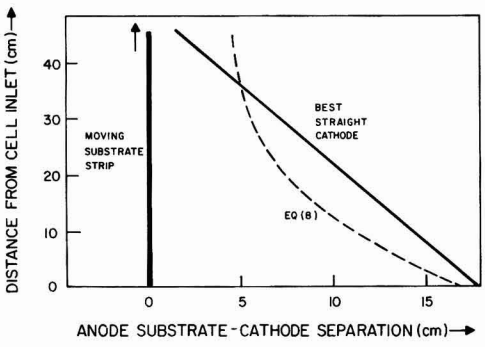

Fig. 2. Representative converging electrode geometries in the electrocoating cell. The broken curve is the cathode whose geometry is calculated from Eq. [8], based on the variation of film voltage with position in the cell which is given in Fig. 1. For the same film-voltage variation, the solid line is the linear electrode giving closest to constant current density.

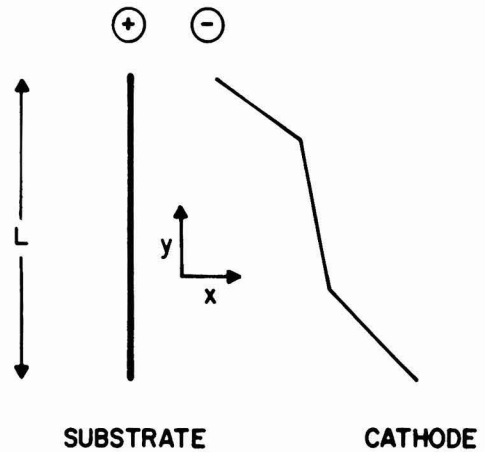

Fig. 3. A typical converging electrode geometry, with the cathode consisting of 3 straight-line segments.

[11] with Fourier expansions of the known potential on each of the two electrodes.

A third boundary condition applies at $y = 0$ and $y = L$. These are the insulating walls of the cell, and the lines of equipotential must be perpendicular to them. This condition may be expressed as (12, 15)

$$\left.\frac{\partial\phi(x,y)}{\partial y}\right|_{y=0,L} = 0 \qquad [12]$$

Examination of Eq. [11] reveals that Eq. [12] would be satisfied if all of the constants B_{1m} were 0, and the period of the function were L, i.e., if $a = m\pi/L$. In this case, $\phi(x, y)$ would reduce to

$$\phi(x,y) = \sum_{m=0}^{\infty}\left[A_{1m}e^{\frac{m\pi x}{L}} + A_{2m}e^{-\frac{m\pi x}{L}}\right]\cos\frac{m\pi y}{L} \qquad [13]$$

The two series of constants A_{1m} and A_{2m} would then be determined by application of the boundary conditions on the electrodes.

It was found that Eq. [13] would not converge to a sufficient degree of accuracy with a reasonable number of terms in the series. This was because the identification of the boundary conditions using Fourier series resulted in sharp discontinuities at $y = 0$ and $y = L$.

An approximate solution was, therefore, used. Boundary conditions were applied for a cell which was twice as long as the actual cell (Fig. 4). The anode potential outside the "true" cell was taken to be a constant at each end, equal to the value just inside the cell. The cathode potential was set equal to its constant value U over its entire length. In this way the potential lines were forced to be approximately perpendicular to the insulating walls at $y = L/2$ and $y = 3L/2$, even

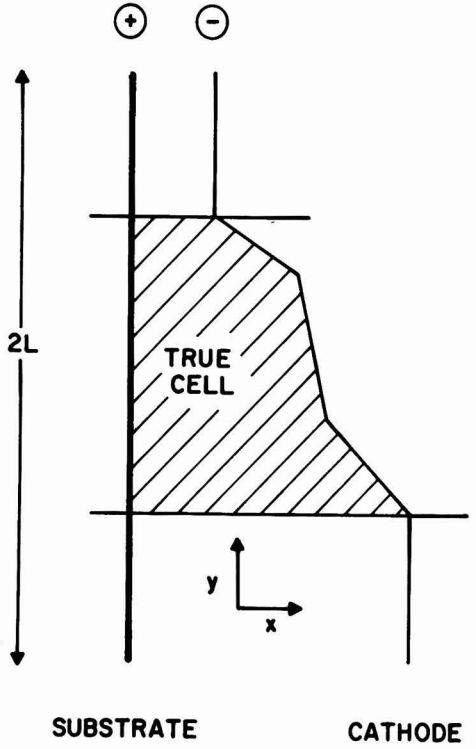

Fig. 4. Schematic representation of the geometry assumed in applying the boundary conditions to Eq. [14].

though $\partial\phi/\partial y$ was not analytically equal to zero at these points.

With this expanded cell geometry, the sine series of Eq. [11] was used as an approximation to the potential $\phi(x, y)$

$$\phi(x,y) = \sum_{m=1}^{\infty}\left[A_{1m}e^{\frac{m\pi x}{2L}} + A_{2m}e^{-\frac{m\pi x}{2L}}\right]\sin\frac{m\pi y}{2L} \qquad [14]$$

Boundary condition on the anode substrate.—The variation of film voltage U_f with position in the cell, exemplified by the result in Fig. 1, can be accurately approximated by a quadratic equation of the general form

$$U_f(y) = c_1y + c_2y^2 + c_3y^3 \qquad [15]$$

The parameters c_i are determined for the particular resin composition being used by least squares fitting of the data from the static experiment by Eq. [15]. For the data of Fig. 1, these constants are $c_1 = 5.799$ V cm^{-1}, $c_2 = 0.1180$ V cm^{-2}, and $c_3 = 0.000847$ V cm^{-3}.

The general expression for the potential (Eq. [14]) reduces on the anode substrate to

$$\phi(x=0,y) = \sum_{m=1}^{\infty}(A_{1m} + A_{2m})\sin\frac{m\pi y}{2L} \qquad [16]$$

The potential on the anode is already known to be

$$\begin{aligned} U_f(y) &= 0, && 0 < y < L/2 \\ &= c_1\left(y - \frac{L}{2}\right) + c_2\left(y - \frac{L}{2}\right)^2 + c_3\left(y - \frac{L}{2}\right)^3 && L/2 < y < 3L/2 \\ &= c_1L + c_2L^2 + c_3L^3 && 3L/2 < y < 2L \end{aligned} \qquad [17]$$

Equations [16] and [17] are equated by expanding Eq. [17] as a Fourier series in $\sin(m\pi y/2L)$. The result, when identified with the series of Eq. [16], gives a general expression for $T_{1m} = A_{1m} + A_{2m}$

$$T_{1m} = \frac{1}{L}\int_0^{2L} U_f(y)\sin\frac{m\pi y}{2L}\,dy \qquad [18]$$

The integral of Eq. [18] is recorded in Eq. [A-1] of Appendix A. Although somewhat formidable in appearance, the result depends only on the parameters c_1, c_2, and c_3 of the film voltage U_f. The expression is readily evaluated by computer and has a single value for each term of the Fourier series.

Boundary condition on the cathode.—Although the cathode geometry is not assumed at this time to be known, it can be defined in general terms by writing the anode-cathode distance d as a function of y, $d = T(y)$. Thus, the Laplace solution on the cathode may be written as

$$\phi(x=T(y),y) = \sum_{m=1}^{\infty}\left[T_{1m}e^{\frac{m\pi T(y)}{2L}} - A_{2m}\left[e^{\frac{m\pi T(y)}{2L}} - e^{-\frac{m\pi T(y)}{2L}}\right]\right]\sin\frac{m\pi y}{2L} \qquad [19]$$

where A_{1m} has been eliminated by writing it in terms of A_{2m} and the known parameter (Eq. [A-1]) T_{1m}.

The infinite series of constants A_{2m} are the only remaining unknowns in Eq. [19]. These constants are evaluated by equating Eq. [19] to the known value of the potential on the cathode, U. This constant potential is readily expanded in a Fourier sine series

$$U = \sum_{n=1}^{\infty} T_{2n} \sin \frac{n\pi y}{2L} \quad [20]$$

where

$$T_{2n} = \frac{1}{L} \int_0^{2L} U \sin \frac{n\pi y}{2L} dy$$

$$= \frac{2U}{n\pi} (1 - \cos n\pi) \quad [21]$$

At first glance it would appear that the parameters A_{2m} could be immediately calculated by identifying the coefficients of the sine terms in Eq. [19] and [20]. In the general case where $T(y)$ is not a constant this is not possible because the coefficient in Eq. [19] is itself a function of y. This difficulty is circumvented by expanding the summation of Eq. [19] itself as a sine series. Although the result appears cumbersome, it can be efficiently used in a digital machine for solution of the boundary condition and, thus, for calculation of the current density distribution from Eq. [10].

The general term of the Fourier expansion of the right-hand side of Eq. [19] may be written as follows, and equated to T_{2n}

$$\frac{1}{L} \int_0^{2L} \left\{ \sum_{m=1}^{\infty} \left[T_{1m} e^{\frac{m\pi T(y)}{2L}} - A_{2m} \left(e^{\frac{m\pi T(y)}{2L}} - e^{-\frac{m\pi T(y)}{2L}} \right) \right] \sin \frac{m\pi y}{2L} \right\} \sin \frac{n\pi y}{2L} dy = T_{2n} \quad [22]$$

This result can be rewritten as an infinite set of linear equations in the parameters A_{2m}

$$\sum_{m=1}^{\infty} K_{1m} A_{2m} = K_{2n} - L T_{2n} \quad [23]$$

where

$$K_{1m} = \int_0^{2L} \left\{ e^{\frac{m\pi T(y)}{2L}} - e^{-\frac{m\pi T(y)}{2L}} \right\} \sin \frac{m\pi y}{2L} \sin \frac{n\pi y}{2L} dy \quad [24]$$

and

$$K_{2n} = \int_0^{2L} \left\{ \sum_{m=1}^{\infty} T_{1m} e^{\frac{m\pi T(y)}{2L}} \sin \frac{m\pi y}{2L} \right\} \sin \frac{n\pi y}{2L} dy \quad [25]$$

The procedure used for solution of Eq. [23] is to truncate the summations (Eq. [23] and [25]) at a finite number of terms, for example 20. The parameters K_{1m} and K_{2m} are then evaluated for values of m from 1 to the cut-off value of m. Using these values, and the known values of T_{2n} (Eq. [21]), the linear Eq. [23] are solved for the parameters A_{2m}.

The Laplace solution.—Using the results of the preceding sections for T_{1m} and A_{2m}, the potential may be calculated at any point in the electrocoating solution

$$\phi(x, y) = \sum_{m=1}^{m'} \left[T_{1m} e^{\frac{m\pi x}{2L}} - A_{2m} \left(e^{\frac{m\pi x}{2L}} - e^{-\frac{m\pi x}{2L}} \right) \right] \sin \frac{m\pi y}{2L} \quad [26]$$

where m' is the cut-off value selected for truncating the series.

The current density perpendicular to the anode, at a distance x from it, can be written directly from this result and Eq. [10]

$$J = -\kappa \sum_{m=1}^{m'} \left(\frac{m\pi}{2L} \right) \left[T_{1m} e^{\frac{m\pi x}{2L}} - A_{2m} \left(e^{\frac{m\pi x}{2L}} + e^{-\frac{m\pi x}{2L}} \right) \right] \sin \frac{m\pi y}{2L} \quad [27]$$

It would theoretically be possible to evaluate the current density on the anode substrate by setting $x = 0$ in Eq. [27]. However, it has been found that better accuracy is achieved for reasonable values of the truncation parameter m' when J is evaluated for a small positive value of x, for example, between 0.2 and 0.5 cm. A similar effect has been noted by Waber for a related problem (16).

Definition of the cathode geometry.—The method of solution of the Laplace equation which has been developed here is most efficiently carried out if the parameters K_{1m} and K_{2m} can be expressed in analytical form. This is possible if the arbitrary cathode geometry being considered, $d = T(y)$, is expressed as a series of straight lines.

The cathode geometry is defined as follows in the computer program written to carry out this analysis. The number of straight line segments to be used, l, is entered first followed by the defining parameters of each segment as they are given in Fig. 5. The two parameters for each junction point are f_i, the fraction of the substrate length from the cell entrance, and d_i, the anode-cathode separation at this point. With the cathode defined in this way, Eq. [24] and [25] can be written in analytical form, the parameters A_{2m} and T_{1m} can be evaluated, and the current density distribution calculated from Eq. [27]. The analytical results for K_{1m} and K_{2n} are recorded in Appendix B.

Results and Discussion

Parallel electrodes.—The Laplace solution is simplified substantially when the anode-cathode separation is a constant, d. In this case the coefficients of sin $(m\pi y/2L)$ in Eq. [19] and [20] can be equated giving the following result for A_{2m}

$$A_{2m} = \frac{T_{1m} e^{\frac{m\pi d}{2L}} - T_{2m}}{e^{\frac{m\pi d}{2L}} - e^{-\frac{m\pi d}{2L}}} \quad [28]$$

Figure 6 records a typical potential distribution obtained for a cell having a parallel electrode configuration. In this case, the applied potential was $U = 100$V, and the film voltage U_f was assumed to increase linearly from 0 at the cell inlet ($y = L/2$) to 50V at the outlet ($y = 3L/2$).

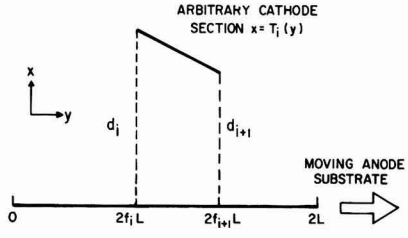

Fig. 5. Definition of the parameters used in representing a cathode of arbitrary geometry as a series of straight-line segments.

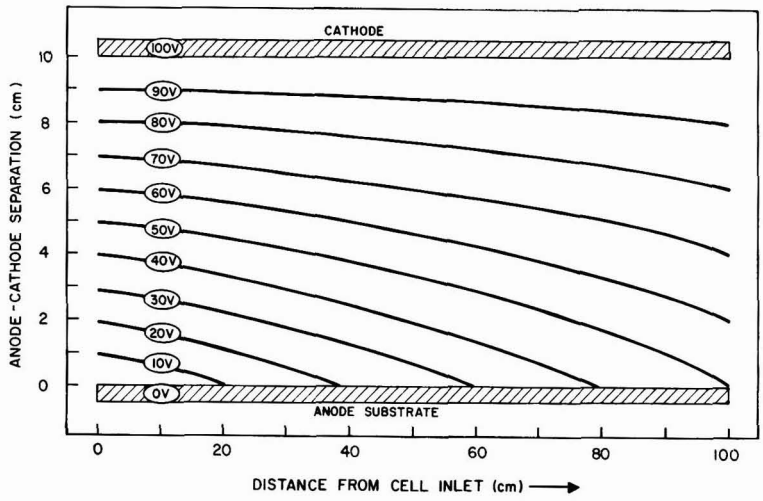

Fig. 6. Equipotential lines in an electrocoating cell between parallel electrodes, for an applied potential of 100V. The film voltage is assumed to rise linearly from zero volt at the cell inlet to 50V at the outlet. Anode-cathode separation is 10 cm, while the cell length is 100 cm.

Solution of the boundary condition on the substrate is simplified for such a linear film-voltage variation. In general, if the film voltage rises from 0 at the inlet to a fraction F of the total applied potential U at the outlet, Eq. [A-1] reduces to ($c_1 = FU/L$; $c_2 = c_3 = 0$)

$$T_{1m} = \frac{2FU}{m\pi}\left\{\frac{2}{m\pi}\left(\sin\frac{3m\pi}{4} - \sin\frac{m\pi}{4}\right) - \cos m\pi\right\} \quad [29]$$

For the example of Fig. 6, $FU = 50$V.

The potential distribution of Fig. 6 indicates that the current flow is strongly concentrated on the end of the anode at the cell entrance for the parallel electrode configuration. In fact, the current density at the entrance in this example is twice as great as it is at the exit.

Converging, straight electrodes.—An obvious "first guess" at a cathode geometry which would give more constant current density on the anode than a parallel configuration is a single straight converging element. This is illustrated, for example, by the solid lines of Fig. 2.

Several examples were worked out to delineate the qualitative effects of such a converging structure on the current density distribution. Results are summarized in Fig. 7. A total cell voltage of 100V was assumed, with the film voltage increasing linearly from zero at the cell entrance to 50V at the cell exit. Because of this assumed linearity in the film voltage, the result of Eq. [29] could be used, but the nonparallel structure of the electrodes necessitated the use of the full solution of Eq. [23] for A_{2m}. Current densities were calculated from Eq. [27] for $x = 0.5$ cm. Initial calculations were carried out with the potential (Eq. [14] and subsequent results) truncated at $m' = 20$ and 40 terms. Essentially identical results were obtained for both series lengths, so $m' = 20$ terms were used in all subsequent calculations.

The assumed cell length was 100 cm. The calculated current densities are expressed divided by the conductivity, so as not to introduce an extraneous arbitrary factor to these illustrative results.

In Fig. 7a the anode-cathode separation at the cell exit was set equal to 10 cm, and the current-density variation was calculated for electrode separations at the entrance of 10, 15, 20, and 40 cm. The parallel configuration ($d_1 = 10$ cm) gave a strong variation of current density with position in the cell, as was anticipated from Fig. 6. Increasing the entrance separation to 20 cm improved the constancy of the current density, while increasing it to 40 cm resulted in a relatively high current density at the cell exit. Similar results are recorded in Fig. 7b for an anode-cathode separation of 20 cm at the cell exit. Solution for each configuration required approximately 1.4 sec (core) on the McGill University IBM 360 computer.

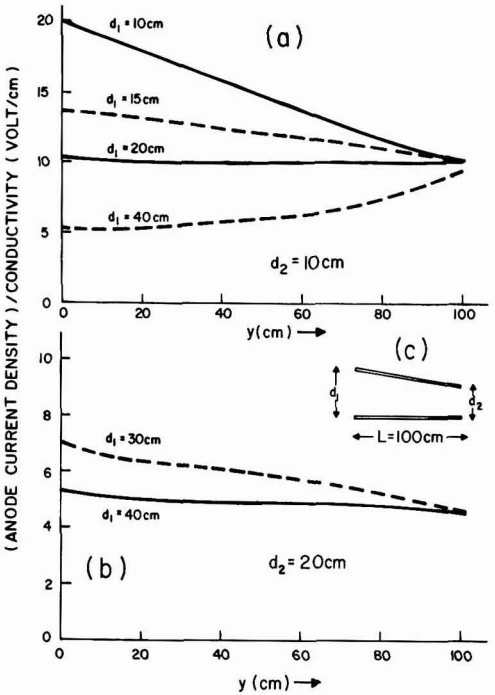

Fig. 7. Variation of anode current density with position in an electrocoating cell having converging, straight electrodes. An applied potential of $U = 100$V is assumed. Cell length is 100 cm, with the anode-cathode separation as defined in Fig. 7c. Results in Fig. 7a were computed for an electrode separation of 10 cm at the cell exit, while those in Fig. 7b assumed an electrode separation at the exit of 20 cm.

Further calculations were carried out using the experimental film voltage data of Fig. 1. This necessitated use of the full results of Eq. [A-1] for application of the boundary condition on the anode substrate. The nonlinearity of the film voltage variation resulted in

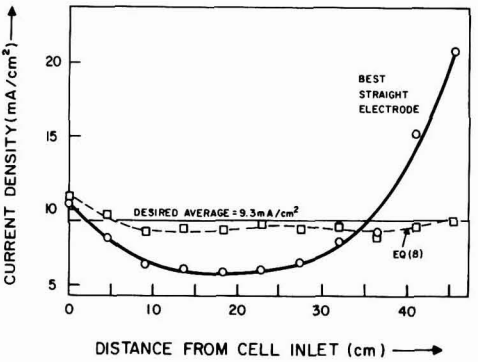

Fig. 8. Variation of current density with position in the electrocoating cell, for the variation of film voltage with position in the cell which is recorded in Fig. 1, and the electrode geometries drawn in Fig. 2. Both curves correspond to an applied potential of 135V. The broken curve is derived for the electrode geometry of Eq. [8], while the solid curve is for the "best" converging, straight electrodes (solid lines, Fig. 2).

relatively higher current densities near the cell entrance, and relatively lower current densities near its exit. The converging solid electrode drawn in Fig. 2 was derived in an iterative program which minimized the sum of the squares of the deviations of the current density from the desired average value. The corresponding current-density variation is plotted as a solid curve in Fig. 8. Clearly a single straight electrode can only very approximately compensate for the film voltage variation as it occurs in the practical cell.

In spite of the imperfect establishment of constant current density within the cell, use of the converging configuration of Fig. 2 resulted in substantially improved properties of electrocoated strip. Table I records a comparison of the properties of strips prepared in a continuous electrocoating cell with conventional, parallel electrodes (substrate-cathode separation 3.3 cm) and with the converging straight-line electrodes of Fig. 2. The continuous strip was 3.2 cm wide × 0.005 cm thick aluminum, run at a line speed of 3.3 cm/sec with the BASF E-33 resin. Both sets of electrodes were 10.2 cm wide, and the cell length was 45.7 cm. The current to each cell was kept constant at 2.7A, or 9.3 mA/cm² of substrate area.

The average build was 12% greater for the converging electrodes compared to the parallel electrodes, for the same average applied voltage. More important, the electrocoated deposits on the strips treated in the converging cell were of superior quality, containing fewer gas bubbles.

Table I. Comparison of parallel and converging electrode electrocoating cells

Electrode configuration	Run number	Applied voltage (V)	Coating thickness* (10^{-3} cm)
Converging**	1	131	3.81
	2	121	4.06
	3	125	3.81
	4	120	4.19
	Average	124	3.97
Parallel†	1	128	3.56
	2	126	3.56
	3	122	3.56
	4	121	3.56
	Average	124	3.56

* Measured after drying and curing.
** Linear cathode. Anode-cathode separation 17.8 cm at the entrance and 1.5 cm at the exit (Fig. 2).
† Anode-cathode separation was 3.3 cm.

Curvilinear cathode geometry.—No experiments were performed using a curvilinear cathode geometry. However, a calculation was made to test how closely a cathode designed according to the approximate Eq. [8] gives a constant current density through the cell.

Using the parameters for the BASF E-33 resin, Eq. [27] was solved by the method of this paper for the electrode defined by Eq. [8]. This electrode (the broken curve of Fig. 2) was approximated by 10 straight-line segments when applying the boundary condition on the cathode as described in Appendix B.

The resulting current-density variation in the cell for an applied potential of $U = 135$V is plotted as a broken curve in Fig. 8. The corresponding potential distribution in the electrocoating solution is sketched in Fig. 9. It is apparent that the calculation of Eq. [8] gives a good approximation to the desired electrode geometry. It is likely that converging cathode geometries derived using this equation could give further improvements in the properties of continuously electrocoated products.

Acknowledgments

I am indebted to Dr. M. A. Dudley for suggesting that improved electrocoating quality could be achievable using a converging electrode geometry. Mr. G. Bersolami carried out the experiments reported in Table I and Fig. 1. This work was supported by Canada Wire and Cable Limited. The work described in this paper is the subject of U.S. Patent No. 3,933,611 and equivalent patents granted or pending in other countries.

Manuscript submitted July 12, 1977; revised manuscript received Jan. 9, 1978.

Any discussion of this paper will appear in a Discussion Section to be published in the December 1978

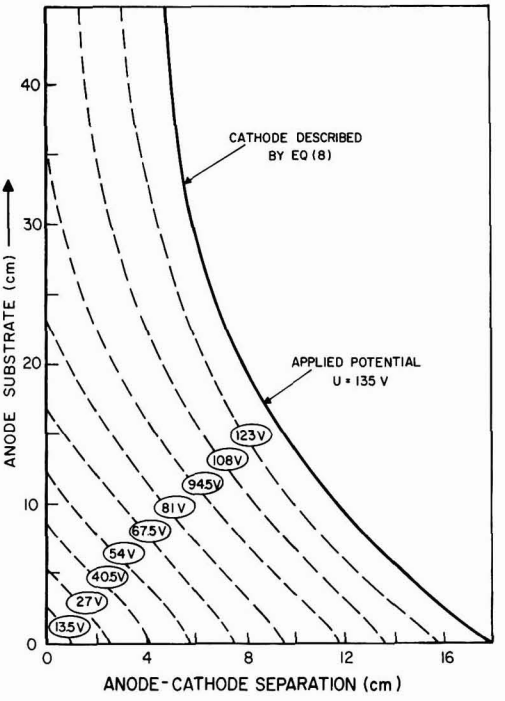

Fig. 9. Equipotential lines in the electrocoating solution for the cathode geometry defined by Eq. [8]. The film-voltage variation with position on the anode substrate is taken from Fig. 1.

JOURNAL. All discussions for the December 1978 Discussion Section should be submitted by Aug. 1, 1978.

APPENDIX A

Evaluation of the General Term in the Fourier Expansion of the Potential on the Substrate

The general term (Eq. [18]) is

$$T_{1m} = \frac{1}{L}\int_0^{2L} U_f(y)\,\sin\frac{m\pi y}{2L}\,dy \qquad [18]$$

Substituting for the substrate potential $U_f(y)$ from Eq. [17] and integrating yields the result

$$\begin{aligned}T_{1m} = {} & \frac{2}{m\pi}(c_1L + c_2L^2 + c_3L^3)\left(\cos\frac{3m\pi}{4} - \cos m\pi\right) \\ & + \frac{2}{m\pi}\left(-\frac{c_1L}{2} + \frac{c_2L^2}{4} - \frac{c_3L^3}{8}\right)\left(\cos\frac{m\pi}{4} - \cos\frac{3m\pi}{4}\right) \\ & + \frac{2}{m\pi}\left(\frac{2L}{m\pi}\right)\left(c_1 - c_2L + \frac{3c_3L^2}{4}\right)\left(\sin\frac{3m\pi}{4}\right. \\ & \left. - \sin\frac{m\pi}{4} - \frac{3m\pi}{4}\cos\frac{3m\pi}{4} + \frac{m\pi}{4}\cos\frac{m\pi}{4}\right) \\ & + \frac{2}{m\pi}\left(\frac{2L}{m\pi}\right)^2\left(c_2 - \frac{3c_3L}{2}\right)\left(\frac{3m\pi}{2}\sin\frac{3m\pi}{4}\right. \\ & - \frac{m\pi}{2}\sin\frac{m\pi}{4} - \left[\left\{\frac{3m\pi}{4}\right\}^2 - 2\right]\cos\frac{3m\pi}{4} \\ & \left. + \left[\left\{\frac{m\pi}{4}\right\}^2 - 2\right]\cos\frac{m\pi}{4}\right) + \frac{2}{m\pi}c_3\left(\frac{2L}{m\pi}\right)^3 \\ & \left(\left[3\left\{\frac{3m\pi}{4}\right\}^2 - 6\right]\sin\frac{3m\pi}{4} - \left[3\left\{\frac{m\pi}{4}\right\}^2 - 6\right]\right. \\ & \sin\frac{m\pi}{4} - \left[\left\{\frac{3m\pi}{4}\right\}^3 - 6\left\{\frac{3m\pi}{4}\right\}\right]\cos\frac{3m\pi}{4} \\ & \left. + \left[\left\{\frac{m\pi}{4}\right\}^3 - 6\left\{\frac{m\pi}{4}\right\}\right]\cos\frac{m\pi}{4}\right) \qquad [A\text{-}1]\end{aligned}$$

APPENDIX B

Evaluation of the Cathode Boundary Condition for an Arbitrary Cathode

The equation of the straight line segment of Fig. 5 is

$$T_i(y) = a_i - b_i y \qquad [B\text{-}1]$$

where

$$a_i = d_i + \frac{d_i - d_{i+1}}{f_{i+1} - f_i}f_i \qquad [B\text{-}2]$$

and

$$b_i = \frac{1}{2L}\frac{d_i - d_{i+1}}{f_{i+1} - f_i} \qquad [B\text{-}3]$$

Substituting this expression for $T_i(y)$ in Eq. [24] gives the general result for K_{1m}

$$\begin{aligned}K_{1m} = {} & \sum_{k=1}^{l}\left\{e^{\frac{m\pi a_k}{2L}}\int_{2f_kL}^{2f_{k+1}L} e^{-\frac{m\pi b_k y}{2L}}\sin\frac{m\pi y}{2L}\sin\frac{n\pi y}{2L}\,dy\right. \\ & \left. + e^{-\frac{m\pi a_k}{2L}}\int_{2f_kL}^{2f_{k+1}L} e^{\frac{m\pi b_k y}{2L}}\sin\frac{m\pi y}{2L}\sin\frac{n\pi y}{2L}\,dy\right\} \\ = {} & \sum_{k=1}^{l}\left\{e^{\frac{m\pi a_k}{2L}}I_1(k,m,n) - e^{-\frac{m\pi a_k}{2L}}I_2(k,m,n)\right\}\end{aligned} \qquad [B\text{-}4]$$

where the two integrals $I_z (z = 1, 2)$ are defined by the second equality. A similar result can be written for K_{2n}

$$\begin{aligned}K_{2n} = {} & \sum_{m=1}^{m'} T_{1m}\left\{\sum_{k=1}^{l} e^{\frac{m\pi a_k}{2L}}\int_{2f_kL}^{2f_{k+1}L} e^{-\frac{m\pi b_k y}{2L}}\right. \\ & \left.\sin\frac{m\pi y}{2L}\sin\frac{n\pi y}{2L}\,dy\right\} = \sum_{m=1}^{m'} T_{1m} \\ & \left\{\sum_{k=1}^{l} e^{\frac{m\pi a_k}{2L}} I_1(k,m,n)\right\}\end{aligned} \qquad [B\text{-}5]$$

where $I_1(k, m, n)$ has the same value as in Eq. [B-4].

Evaluation of K_{1m} and K_{2n} in this general case is completed by recording the value of the integral $I_z(k, m, n)$

$$I_z(k,m,n) = \xi(2f_{k+1}L) - \xi(2f_kL) \qquad [B\text{-}6]$$

where

$$\xi(y) = \frac{e^{\alpha y}}{2}\left\{\frac{\beta\sin\beta y + \alpha\cos\beta y}{\alpha^2 + \beta^2} - \frac{\gamma\sin\gamma y + \alpha\cos\gamma y}{\alpha^2 + \gamma^2}\right\} \qquad [B\text{-}7]$$

α, β, and γ are defined by

$$\alpha = (-1)^z\frac{m\pi b_k}{2L} \qquad [B\text{-}8]$$

$$\beta = \frac{(m-n)\pi}{2L} \qquad [B\text{-}9]$$

$$\gamma = \frac{(m+n)\pi}{2L} \qquad [B\text{-}10]$$

REFERENCES

1. C. O. Hutchinson, Paper presented at Electrocoat 71, (The National Paint, Varnish, and Lacquer Association), Chicago, Illinois, April 27-28, 1971.
2. Anon, "Coil Coating by Electrodeposition," *Can. Paint Finishing*, 30 (February 1971).
3. M. A. Dudley and R. L. LeRoy, Paper presented at The Electrochemical Society Meeting, Ontario-Quebec Section, Toronto, February 1973.
4. M. A. Dudley and P. L. Claessens, *Can Pat.* 984,331 (1976).
5. L. R. LeBras, *J. Paint Technol.*, **38**, 85 (1966).
6. A. R. H. Tawn, *Paint, Oil Colour J.*, 821 (Nov. 21, 1969).
7. F. Beck, *Farbe Lack*, **72**, 218 (1966).
8. J. Newman, in "Advances in Electrochemistry and Electrochemical Engineering," Vol. 5, C. W. Tobias, Editor, p. 87, Interscience, New York (1967).
9. E. McCafferty, Naval Research Laboratories Report 7835 (Jan. 31, 1975).
10. R. H. Rousselot, *Metal Finishing*, 56 (October 1959).
11. R. H. Rousselot, "Repartition du Potential et du Courant dans les Electrolytes," Dunod, Paris (1959).
12. J. A. Klingert, S. Lynn, and C. W. Tobias, *Electrochim. Acta*, **9**, 297 (1964).
13. H. E. Haring and W. Blum, *Trans. Electrochem. Soc.*, **44**, 313 (1923).
14. C. Kasper, *ibid.*, **77**, 353, 365 (1940); *ibid.*, **78**, 131, 147 (1940); *ibid.*, **82**, 153 (1942).
15. C. Wagner, *This Journal*, **98**, 116 (1951).
16. J. T. Waber, *ibid.*, **101**, 271 (1954).

The Influence of Carbon Matrix Characteristics on the Performance of Sulfur Electrodes for Sodium-Sulfur Cells

M. P. J. Brennan

Chloride Silent Power Limited, Astmoor, Runcorn, England

ABSTRACT

Sodium-sulfur cells of the central sulfur configuration, though free from the problems of case corrosion, can still exhibit capacity losses of up to 50% over 100 cycles of operation. This is mainly due to a failure to recharge fully in the two-phase regime of the operating cycle. This paper describes an investigation of the relationship between rechargeability and the surface properties of the carbon matrix employed as the current-collecting member in the sulfur electrode. The influence of cell constructional variants is also considered.

The earliest sodium-sulfur cells tested by Chloride Silent Power were of the tubular central sodium type, incorporating a beta-alumina tube of 13 mm diam. With these cells, sulfur utilization was found to diminish with time and cycling, typical values being 56% utilization after 300 cycles (100% being defined as conversion of the sulfur charge to Na_2S_3). At the time, a major contributory factor to the decline in utilization was recognized to be corrosion of the cell case by the molten sulfur and sodium polysulfide reactant contained within it. This could affect utilization both by tying up sulfur in the form of metal sulfides, and by breaking the electronic contact between the case and the carbon felt matrix dispersed within the sulfur electrode, leading to premature polarization on both charge and discharge. With the development of larger electrolyte shapes, it was possible to change the cell configuration, locating the sulfur electrode reactant within the beta-alumina tube, so that the cell case came into contact only with sodium. Current collection from the sulfur electrode was achieved by a carbon or graphite pole, located co-axially within the ceramic electrolyte.

With these central sulfur cells, it was found that despite the elimination of case corrosion, the utilization of sulfur still showed a declining trend with cycling, with effective capacity losses of up to 50% over 100 cycles being not uncommon. This was found to be mainly due to failure of the cells to recharge fully in the two-phase region of the operating cycle.

One theory advanced to explain the poor rechargeabilities linked this phenomenon to the relative wetting propensities of sulfur and sodium polysulfides on carbon surfaces. It was suggested that sulfur wets carbon more effectively than does molten sodium polysulfide, so that sulfur formed during recharging has a tendency to spread out over the carbon fibers as a continuous insulating film. As the proportion of occluded surface will be expected to increase as charging proceeds, this phenomenon should manifest itself as a rising cell resistance, which could lead to the cell failing to fully recharge either within a time limit (constant voltage charging) or voltage limit (constant current charging).

Chemical modification of the wettability of carbon fibers is a process well known in the fiber-reinforced composites industry (1, 2). It is generally found that the wetting of carbon fibers by epoxy resins is enhanced by subjecting the fibers to a preoxidation procedure. This can be either a wet oxidation, using nitric acid, permanganates, dichromates, etc. (2-4), or a dry oxidation in air, oxygen, or ozone (2, 5).

Were such treatments to preferentially enhance the wetting of carbon fibers by the predominantly ionic component of a two-phase sulfur/sodium polysulfide melt, then the performance of cells with modified matrices should be significantly improved. Conversely, if the pretreatment promoted wetting by the sulfur-rich phase, then a deterioration in cell performance could be expected.

It is an unresolved question as to whether the improvement in wetting observed with epoxy resins is due principally to changes in surface chemistry, or whether the roughening of the fiber surfaces which accompanies the oxidation process is the major factor. For this reason two pretreatments were employed in this section of the work. One, (oxidation with $Na_2Cr_2O_7/H_2SO_4$) is known to oxidatively etch carbon, whereas the other (neutralization with aqueous NaOH) was expected to change only the surface chemistry.

Another pretreatment investigated in this work involved subjecting carbon felt for cells to exposure to reagents known to intercalate in well-ordered graphite. There are many such reagents, falling into two broad groups, the electron donors, such as the alkali metals, and the electron acceptors. The latter group is more numerous, and includes some of the halogens, interhalogens, and transition metal chlorides. The formation of an intercalation compound is accompanied by a change in the electronic band structure of the graphite to produce a more metallic material (6) as evidenced by changes in electrical conductivity (7), and Hall effect coefficient (8). Surface properties are also altered (9). Full conversion of a graphite sample to an intercalation compound is possible only with highly ordered graphites, containing a minimum of lattice defects. Carbon fibers do not fall in this category, however lattice resolution studies with the electron microscope have shown the surfaces of the fibers to be more ordered than the interior (10), and lattice parameters close to those of pure graphite have been obtained by electron diffraction studies of fiber edges (11). Since the aim was to produce changes in the surface wetting characteristics of the fibers, restriction of the intercalation reaction to the surface layers was acceptable.

For a permanent effect on cell performance it was necessary that the intercalated felt be stable in the cell environment. This requirement at once ruled out the use of n-type lamellar compounds, based on alkali metal insertion, because in these the inserted species can usually be totally desorbed by the application of heat. Complete desorption of the inserted material in p-type compounds is usually impossible, and a certain amount remains forming the so-called residue compound. In particular chromyl chloride is capable of extensive fixation to form a permanent lamellar compound (12) and this reagent was chosen for this work. Also selected was antimony pentachloride, for its ease

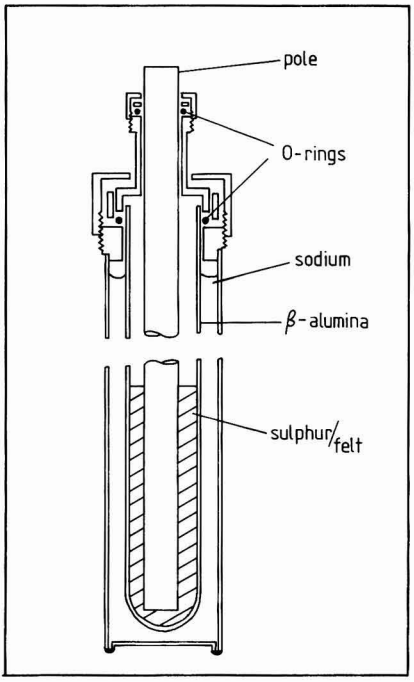

Fig. 1. Schematic diagram of the sodium-sulfur cell design used in this work.

of handling (like chromyl chloride it is a liquid), for its reported high reactivity (13), and because the intercalation reaction of $SbCl_5$ has been extensively studied (14).

Experimental

The cell design used in this work is shown in Fig. 1. It is a central sulfur cell based on an electrolyte tube of diameter 26 mm. The felt in the sulfur electrode was introduced in the form of rings surrounding the central graphite rod pole. RVC 4000 (Le Carbone) was the felt material, and the rings were held under an axial compression of 2:1. The cell operated in a temperature gradient, so that the electrodes could be sealed with silicon rubber O-rings; however, the 10 cm working length of the electrolyte was held at a temperature of 340° ± 15°C throughout. For the cells incorporating intercalated felt the graphite pole was drilled and tapped at the top end to accept a stainless steel (316) insert, upon which the upper O-ring seal was made. This produced a hermetic seal. In the other cells, the upper seal was made to the graphite rod and was not as leak-tight.

The felt variants were prepared as follows. (*i*) Oxidation: The felt rings were refluxed in an aqueous solution of sodium dichromate (0.3M) and sulfuric acid (2.0M) for 24 hr. They were then thoroughly washed with deionized water until the washings had a pH of 7. (*ii*) Neutralization: The felt rings were refluxed for 24 hr in an aqueous solution of sodium hydroxide (0.4M), then washed with deionized water as above. (*iii*) $SbCl_5$: The felt was predried for 2 days at 110°C and then refluxed with antimony pentachloride at 80°C for 12 hr. The felt was then washed with constant boiling point hydrochloric acid in a soxhlet extractor for 2 days, followed by extraction with deionized water until the washings had a pH of 7. (*iv*) CrO_2Cl_2: The felt was predried as above, then refluxed with chromyl chloride at 100°C for 2 hr. The washing procedure was the same as for antimony pentachloride. (*v*) Control: Because the cell design differed slightly for the two groups of pretreatments, control cells were made up to each design. In both cases the felt was refluxed with deionized water for 12 hr, then extracted with deionized water as above.

Samples of the oxidized felt were analyzed to obtain a quantitative estimate of the degree of surface oxidation induced. The method employed was that recommended by Ludtke (15) for the determination of carboxylate functions in oxycelluloses and adapted by Donnet *et al.* (16) for the determination of the same functions on carbon blacks. The method consists of refluxing the carbon material with an aqueous solution of calcium acetate, which effects an ion-exchange reaction liberating acetic acid, which is then estimated by titration. It was found that as-received felt did not liberate sufficient acetic acid for estimation by this technique, however the oxidized material was found to have an acidity of 0.45 mequiv. g^{-1}, slightly less than the figures reported by Donnet *et al* (16) for oxidized carbon blacks (0.62-1.2 mequiv. g^{-1}).

Two cells of each variant were constructed and cycled to the following regime at a temperature of 340° ± 15°C. (*i*) Discharge—via a fixed resistor arranged to give a discharge rate of approximately 0.3-0.2C (current density 40-60 mA-cm^2) and (*ii*) Recharge—via a series resistor for the remainder of the 24 hr cycle, with a cell voltage limit of 2.6V. Recharge was essentialy complete in 11 hr at an average current density of 20 mA-cm^{-2}.

For some cycles the cells were controlled by a computer, the discharge being terminated when the instantaneous open-circuit voltage fell to 1.76V. When not under computer control discharge was terminated at a load voltage of 1.35V.

Two cell characteristics were recorded for analysis; first the discharge capacity to 1.76V, and second the cell resistance at an open-circuit voltage of 2.00V on the discharge half-cycle. It was found that the resistance of a cell did not vary much from this value except at extremes of charge and discharge.

Cell Performances

Oxidized and neutralized felt.—The sulfur utilization for these cells was measured over a period of approximately 3000 hr ≡ 100 cycles. The data was analyzed for the following periods: 0-1000 hr, 1000-2000 hr, 2000-3000 hr. Table I lists the mean values recorded for each cell during each period, as a percentage of theoretical capacity. These figures suggest that the cells can be ranked in order of merit with respect to sulfur utilization as follows: control>neutralized>oxidized. The significance of this trend was determined by subjecting the data to variance analysis. Table II lists the values of the *F*-statistic and corresponding

Table I. Mean sulfur utilization

		0-1000 hr		1000-2000 hr		2000-3000 hr	
Cell	Type	Mean	SD	Mean	SD	Mean	SD
395	Control	76.9	4.3	72.2	4.4	62.8	9.0
398*	Control	77.3	2.9	76.1	1.3	See note*	
394	Neutralized	72.2	4.5	58.2	4.8	42.1	4.7
397	Neutralized	71.3	3.0	66.1	4.4	57.8	2.6
393	Oxidized	69.1	6.5	54.0	4.2	46.9	5.2
396	Oxidized	63.2	8.6	58.7	3.9	49.4	5.1

* This cell failed after 1944 hr on test.

Table II. Variance analysis

Time period (hr)	*F*	Significance level (%)
0-1000	10.05	95.3
1000-2000	9.92	95.2
2000-3000	1.22	55.0

significance level for each time period. Table III lists two-tailed probabilities derived from the *t*-test for the comparison of mean performance and shows that the ranking of felt treatments is significant in the early cycles, but the distinction becomes less clear at longer times.

The cell resistances were treated in the same way. Table IV lists the summary data. The resistances are quoted in the Ω-cm^2 form, derived by multiplying the total cell resistance by the area of beta-alumina carrying the current.

Although the trend is apparent in the early period that the cells can be ranked control<neutralized<oxidized in terms of resistance, variance analysis of the data indicated a significance of not greater than 82% at any time. A correlation between utilization and resistance is indicated, particularly in the first period, and this was evaluated by a least squares fit analysis of data. Table V gives the parameters in the linear regression equation $U = aR + b$, where U = utilization, R = resistance. "r" is the correlation coefficient for the regression which is seen to diminish with increasing time. The data is also shown graphically in Fig. 2.

Intercalated felt.—These cells were tested over a similar time period, but owing to experimental difficulties a limited amount of information was gathered during the period 1000-2000 hr. For this reason the data for these cells is grouped into only two periods for analysis, 0-1000 hr and 1000-3000 hr. Table VI lists the summary data for mean utilization, as a percentage of theoretical capacity. Only one cell of the $SbCl_5$ variant is quoted, the other having been recorded as an early failure. The data do not appear to indicate any correlation between cell type and performance, a conclusion borne out by the analysis of variance, which indicated less than 50% significance for either period. The resistance data also lacked any discernable trend,

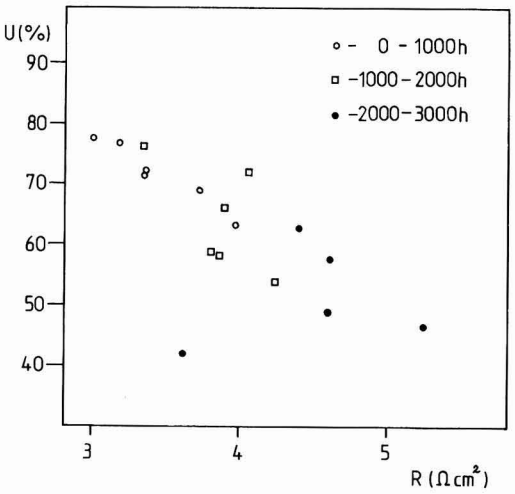

Fig. 2. A plot of mean percentage utilization (*U*) vs. mean resistance (*R*) for cells containing felt subjected to oxidative and neutralizing pretreatments. Control cell data is also included.

as shown in Table VII. Significant correlation with utilization was absent, the regression coefficients for a least squares fit being 0.2 and 0.4 for 0-1000 hr and 1000-3000 hr, respectively.

Discussion

For the first group of cells, the control cells gave consistently better performances than either of the pretreated variants. The differences between the groups were significant up to 2000 hr, but thereafter the confidence level diminished considerably. Considering these results in terms of the differential wetting hypothesis, one would conclude that the pretreatments enhance the preferential wetting of felt by sulfur, a result not unexpected. However there is an alternative interpretation which does not involve wetting effects. Sulfur is known to react with carbon surfaces at temperatures as low as 350°C (17, 18), giving rise to carbon-sulfur complexes of high stability, and accompanied by the evolution of small quantities of hydrogen sulfide and carbon disulfide. This chemical fixation of sulfur is hindered by the presence of oxygen (18, 19), suggesting some degree of competition for similar sites. It is highly likely, therefore, that a carbon surface saturated with oxygen functions will experience partial displacement of the oxygen on immersion in sulfur at 350°C, and the oxygen displaced therefrom will most likely be converted to sulfur dioxide. Mechanisms exist therefore whereby a sulfur electrode may contain vapor species which under the conditions of liquid flow set up during charging and discharging may combine to form macroscopic bubbles, as shown in Fig. 3. The presence of such bubbles will have a deleterious effect on sulfur utilization, by isolating reactive materials in pockets, as shown. Substantive evidence for this hypothesis may exist in the cell resistance data, for clearly any bubble large enough to isolate reactive material will also, by virtue of the "shadow" cast on the

Table III. Comparison between treatments

Hypothesis	0-1000 hr	1000-2000 hr	2000-3000 hr
Control = Neutr.	1%	11%	N/A
Control = Oxid.	7%	3%	N/A
Neutr. = Oxid.	20%	33%	84%

Table IV. Mean resistances

		0-1000 hr		1000-2000 hr		2000-3000 hr	
Cell	Type	Mean	SD	Mean	SD	Mean	SD
395	Control	3.18	0.35	4.06	0.12	4.40	0.08
398	Control	3.00	0.08	3.32	0.15	See note*	
394	Neutralized	3.66	0.40	3.86	0.37	3.62	0 26
397	Neutralized	3.35	0 41	3.90	0 48	4.61	0.14
393	Oxidized	3.73	0.13	4.25	0.17	5.25	0.51
396	Oxidized	3.97	0.51	3.31	0.74	4.60	0.15

* This cell failed after 1944 hr on test.

Table V. Utilization-resistance correlation

Period	*a*	*b*	*r*
0-1000 hr	−14.2	120.3	0.96
0-2000 hr	−16.1	126.6	0.80
0-3000 hr	−12.7	112.9	0.69

Table VI. Mean sulfur utilization

		0-1000 hr		1000-3000 hr	
Cell	Type	Mean	SD	Mean	SD
574	Control	84.5	1.43	85.1	0.59
575	Control	81.6	1.44	81.2	0.55
576	$SbCl_5$	82.6	5.44	83.4	1.33
577	CrO_2Cl_2	97.8	24.3	81.3	2.10
581	CrO_2Cl_2	77.9	4.58	77.4	3.18

Table VII. Mean resistances

		0-1000 hr		1000-3000 hr	
Cell	Type	Mean	SD	Mean	SD
574	Control	2.39	0.05	2.43	0.04
575	Control	5.01	0.36	4.81	0.32
576	$SbCl_5$	3.23	0.23	3.02	0.12
577	CrO_2Cl_2	3.57	0.19	5.35	0.83
581	CrO_2Cl_2	2.85	0.12	3.57	0.63

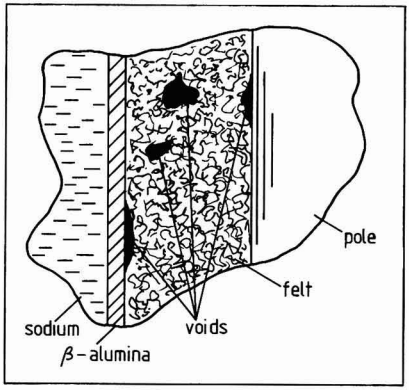

Fig. 3. Representation of the disposition of voids within the sulfur electrode.

electrolyte and pole, reduce the over-all conductance of the sulfur electrode. It is interesting, therefore, to note the correlation between utilization and resistance shown in Fig. 2 and tabulated in Table V. At short times the correlation is good, but becomes less clear over a longer period of test, as does the distinction between cell types, which indicates a common deterioration mechanism.

The cells which incorporated felts treated with intercalating agents did not appear to be distinguishable on the basis of utilization over 3000 hr. Neither did there appear to be the same relationship between utilization and resistance. The conclusion is drawn, therefore, that the variation in resistances for this group of cells must arise from a different cause to that proposed above. A likely cause of the variation is the contact resistance between the carbon pole and steel insert used in these cells, an enlarged detail of which is shown in Fig. 4. Carbon thread was compressed between the pole and the shoulder of the insert. The effectiveness of this arrangement in producing a reproducibly good contact between the two components was doubtful, and while it is not possible to state definitely that here was the cause of the variation in resistances, nevertheless it is a strong possibility.

One clear picture which emerged when the data for the oxidized/neutralized cells were compared with that for the intercalated cells was that superimposed on the performance variations within the two groups was a significant difference between them. In order to analyze this difference the data for the oxidized/neutralized cells were rearranged to cover the same time

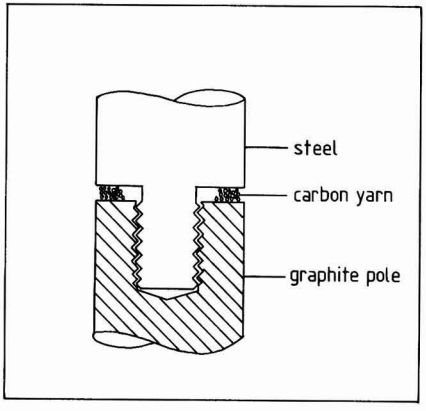

Fig. 4. The steel-to-carbon joint used on the current collectors of the later cells.

Table VIII. Mean utilization

Cell	Type	0-1000 hr Mean	0-1000 hr SD	1000-3000 hr Mean	1000-3000 hr SD
395	Control	76.9	4.3	67.8	8.31
398	Control	77.3	2.9	76.1	1.30
394	Neutralized	72.2	4.5	51.8	9.40
397	Neutralized	71.3	3.0	62.9	5.60
393	Oxidized	69.1	6.5	51.2	5.73
396	Oxidized	63.2	8.6	54.7	6.40
574	Control	84.5	1.43	85.1	0.59
575	Control	81.6	1.44	81.2	0.55
576	$SbCl_5$	82.6	5.44	83.4	1.33
577	CrO_2Cl_2	97.8	24.3	81.8	2.10
581	CrO_2Cl_2	77.9	4.58	77.4	3.18

periods as the intercalated cells, viz., 0-1000 hr and 1000-3000 hr. Mean utilization data are summarized in Table VIII.

Comparison of the two groups by the Student's *t*-test revealed that the differences between groups were significant at the 99.3% level for the period 0-1000 hr, and at the 99.9% level for the period 1000-3000 hr. The superiority of the latter group at longer periods is shown also in Fig. 5, where utilization data for this group are given over 5000 hr of cycling. The same conclusion is reached if only the control cells in each group are compared, indicating that the differentiating factor is unrelated to the felt characteristics. It is most likely that the cause of the improved capacity retention in the second group of cells is the much better quality of the sulfur electrode seal which resulted from compressing the sealing O-ring against a smooth steel member in these cells, rather than against a graphite rod as in the first group. It is clear, therefore, that efforts directed at improving sulfur electrode performance should not be undertaken in poorly sealed cells even when the experimental period is limited to 1000 hr of cycling.

Insofar as utilization is concerned, none of the felt pretreatments resulted in an improvement in this parameter, and two of them were found to have an adverse effect. However in the case of the second group of cells, it is hardly surprising that the control cells were not surpassed in view of the remarkably good performances they exhibited. When one bears in mind the fact that the cells were cycled to an instantaneous open-circuit voltage value of 1.76V, the 20% utilization loss which most of these cells incurred is not an unreasonable amount to ascribe simply to polarization at the 5 hr rate. We believe that the sustained high utili-

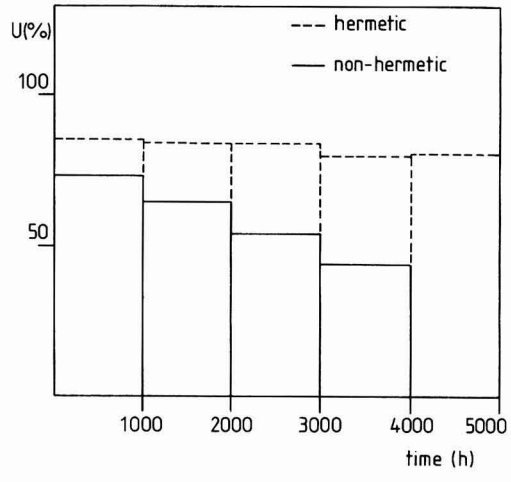

Fig. 5. A bar chart showing the mean percentage utilization (*U*) as a function of cell life for the hermetically sealed and non-hermetically sealed cells.

zation rates which these cells have operated at for more than a year now is a significant advance on the sulfur electrode position of 12 months ago, and gives tremendous encouragement for the further development of the sodium-sulfur battery to a commercially viable product.

Acknowledgment

I am indebted to my colleague Graham Robinson who initiated most of the early work leading up to this study and who contributed by helpful discussions throughout.

Manuscript submitted July 22, 1977; revised manuscript received Dec. 5, 1977. This was Paper 398 presented at the Philadelphia, Pennsylvania, Meeting of the Society, May 8-13, 1977.

Any discussion of this paper will appear in a Discussion Section to be published in the December 1978 JOURNAL. All discussions for the December 1978 Discussion Section should be submitted by Aug. 1, 1978.

Publication costs of this article were assisted by Chloride Silent Power Limited.

REFERENCES

1. R. J. Bobka and L. P. Lowell, AFML TR66-310, Part 1, U.S.A.F. Materials Laboratory (October 1966).
2. D. W. McKee and V. J. Mimeault, *Chem. Phys. Carbon*, **8**, 151 (1973).
3. M. Yamamoto, S. Yamada, Y. Sakatani, M. Taguchi, and Y. Yamaguchi, Paper 21, International Conference on Carbon Fibres—Their Composites and Applications, Plastic Institute, London (1971).
4. J. W. Herrick, 23rd Annual Technical Conference, S.P.I., Reinforced Plastics/Composites Division, Section 16A (February 1968).
5. J. C. Goan and S. P. Prosen, in "Interfaces in Composites," ASTM Special Tech. Pub. No. 452, pp. 3-26 (1969).
6. F. R. McDonnel, R. C. Pink, and A. R. Ubbelohde, *J. Chem. Soc.*, **1951**, 151.
7. G. R. Hennig, *J. Chem. Phys.*, **19**, 922 (1951).
8. G. R. Hennig, *ibid.*, **20**, 1443 (1952).
9. M. C. Robert, M. Oberlin, and J. Mering, *Chem. Phys. Carbon*, **10**, 141 (1973).
10. D. J. Johnson, D. Crawford, and B. F. Jones, *J. Mater. Sci.*, **8**, 286 (1973).
11. M. P. J. Brennan, Unpublished work.
12. J. G. Hooley, *Chem. Phys. Carbon*, **5**, 321 (1969).
13. R. C. Croft, *Aust. J. Chem.*, **9**, 184 (1956).
14. J. Melin and A. Herold, *C.R. Acad Sci. Paris, Ser. C.*, **269**, 877 (1969).
15. M. Ludtke, *Biochem. Z.*, **268**, 372 (1954).
16. J. B. Donnet, F. Hueber, C. Reitzer, J. Oddoux, and G. Riess, *Bull. Soc Chim. France*, **1962**, 1727.
17. R. Juza and W. Blanke, *Z. Anorg. Allgem. Chem.*, **210**, 81 (1933).
18. M. L. Studebaker and L. G. Nabors, *Rubber Age*, **80**, 661 (1957).
19. B. R. Puri, *Chem. Phys. Carbon*, **6**, 191 (1970).

Photooxidation of Water at α-Fe_2O_3 Electrodes

John H. Kennedy* and Karl W. Frese, Jr.

Department of Chemistry, University of California, Santa Barbara, California 93106

ABSTRACT

Photoelectrochemical properties of high purity α-Fe_2O_3 and TiO_2-doped α-Fe_2O_3 were investigated. Photocurrent efficiencies were measured in various electrolytes and found to depend on the electrolyte used. Direct measurement of spectrophotometric absorption coefficients showed them to be significantly higher than those deduced from i-V curves indicating that only a fraction of the light absorbed resulted in electrochemically reactive holes. When the lower absorption coefficients were employed the current-potential curves could be fit within $\pm 1\%$ to the depletion layer theory of Gärtner.

Recent interest in the photoelectrochemistry of semiconductor electrodes has led to the discovery of new materials capable of sustaining the photoelectrolysis of water (see for example Ref. (1-3) and references contained therein). Among these materials is α-Fe_2O_3 with a sufficiently low bandgap to be of practical interest and first reported on as CVD films by Hardee and Bard (3, 4). Later, Quinn *et al.* (5) reported on the properties of the flux-grown single crystal α-Fe_2O_3. However, a detailed study of the photoelectrochemical properties of polycrystalline ceramic α-Fe_2O_3 has been lacking, and therefore a study of ultrapure and TiO_2-doped α-Fe_2O_3 was undertaken.

We report here: (*i*) the effects of electrolyte on measured photocurrent efficiencies; (*ii*) quantitative comparison of absorption coefficients from spectral and photoelectrochemical methods; (*iii*) the effects of donor density on photocurrent efficiency; and (*iv*) a fit of the i-V characteristics to the depletion layer theory of Gärtner (6). Flatband potentials and donor densities for the polycrystalline α-Fe_2O_3 electrodes in this study have been previously reported (7). These polycrystalline electrodes appear to behave in a similar fashion to single crystal electrodes including photocurrent efficiencies and flatband potentials.

* Electrochemical Society Active Member.
Key words: absorption coefficient, α-Fe_2O_3, TiO_2-doped α-Fe_2O_3, photooxidation, water.

Experimental

Electrode preparation.—The details of the preparation of high purity (99.999%) and TiO_2-doped reagent α-Fe_2O_3 electrodes are given elsewhere (7).

Illumination.—The procedures used for monochromatic light intensity measurements are given elsewhere (2). Polychromatic light intensities, $300 \leq \lambda \leq 540$ nm $= E_g$, were determined with the Reinecke salt actinometer (8) for which the quantum yield ($\sim$0.30) is practically independent of wavelength. The equivalent photon current for the system including the 150W Xe lamp, infrared filter, and quartz lens was found to be 49.6 mA (300-540 nm) at the electrode surface. Lower light intensities were obtained using neutral density screens.

Electrical measurements.—The general cell arrangement, measurement of i-V curves, and calculation of photocurrent efficiencies were described previously (2).

Optical measurements.—The spectrophotometric absorption coefficient of polycrystalline α-Fe_2O_3 was measured using a KBr pellet technique (9-12). Pellets containing up to 500 ppm w/w α-Fe_2O_3 were made and had dimensions $\sim$0.03 cm thick $\times$ 1.29 cm diam. Absorbance measurements were made with a Beckman Model B spectrophotometer with a spectral slit width of $\leq$5 nm. Samples were run *vs.* a KBr blank

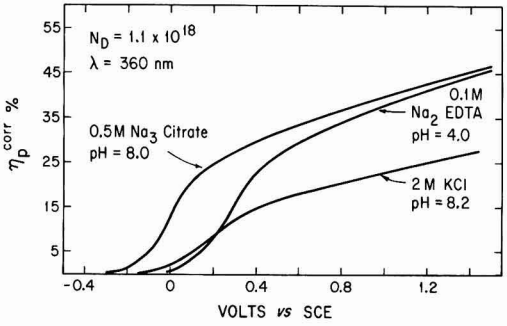

Fig. 1. Current-potential curves in various electrolytes. Polycrystalline α-Fe_2O_3; 23°C.

of comparable thickness utilizing a sample in-sample out technique. Suitable corrections for bulk scattering by α-Fe_2O_3 particles were applied and are discussed later.

Results

Photocurrent efficiency, η_p, curves obtained in 2*M* KCl, 0.1*M* Na_2 EDTA, and 0.5*M* Na_3 citrate are shown in Fig. 1. These efficiencies have been corrected for light reflection at the Fe_2O_3-solution interface according to well-known procedures (13). This correction amounted to 15-20%.

A significant enhancement of the efficiency was found for the chelating-type electrolytes. Comparison of the curves for citrate and EDTA solutions shows that the photocurrent efficiency is practically identical when compared at the same overvoltage. The rate of change of the potential at zero efficiency, V_o*, was −60 mV/pH. This potential (turn-on voltage) for the 2*M* KCl solution was 100 mV more anodic than the citrate solution at about the same pH (8.0 *vs.* 8.2), and the efficiencies at any given overvoltage in EDTA and citrate solutions were considerably higher than in KCl solution. Efficiencies comparable to those for KCl solutions were found in 0.5*M* Na_2SO_4 and 0.5*M* sodium acetate, and somewhat lower values in 0.5*M* KNO_3. The enhanced efficiency in the presence of citrate may be due to the interaction of these anions with the α-Fe_2O_3 electrodes and is discussed below.

The effect of the bulk citrate concentration on the increase in efficiency was investigated for three different electrodes resulting in qualitatively similar results as shown in Fig. 2. The effect had a threshold at 10^{-6}-10^{-5}M. The increase in efficiency was initially proportional to log[citrate]; with increasing concentration a saturation effect was observed. For all electrodes, both citrate and EDTA had no effect on the dark current at all concentrations studied. Finally, no effect was found with TiO_2 and $SrTiO_3$ polycrystalline electrodes, materials for which the valence bands are 0.7-0.8 eV below the valence band of α-Fe_2O_3.

Photocurrent efficiency curves at various wavelengths are shown in Fig. 3 for 0.5M citrate solution.

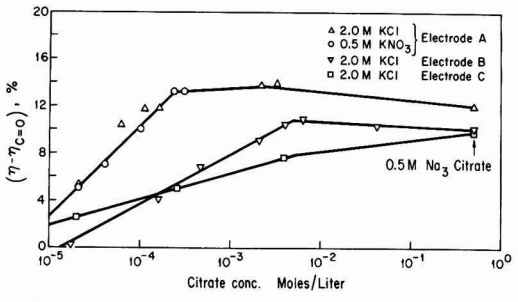

Fig. 2. Effect of bulk citrate concentration on photocurrent efficiency. 1.0V overvoltage; 23°C; 360 nm.

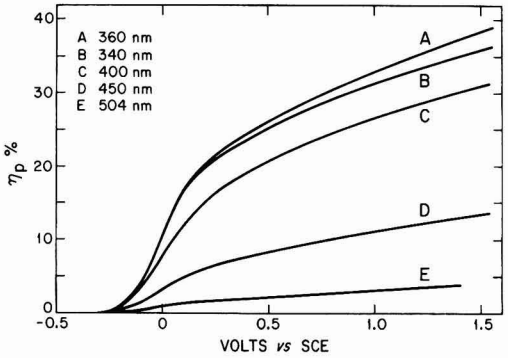

Fig. 3. Effect of wavelength on photocurrent efficiency. Polycrystalline α-Fe_2O_3; 0.5M Na_3 citrate; pH 8.0.

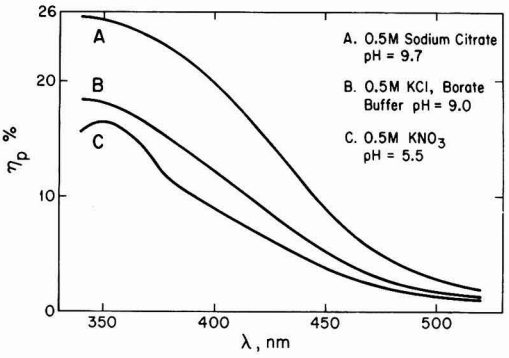

Fig. 4. Effect of electrolyte on photocurrent spectrum. 1.0V overvoltage; polycrystalline α-Fe_2O_3.

The photocurrent spectra in three different electrolytes are shown in Fig. 4. The relative efficiency in each electrolyte appears to follow the order of extent of surface adsorption (14) expected on the basis of chemical consideration. That is, the extent of complexing of the anions with Fe^{3+} should be in the order citrate > Cl^- > NO_3^-. A maximum in the photocurrent spectrum at ~350 nm is evident from Fig. 3 and 4. Light absorption by KNO_3 may be responsible for the more pronounced maximum for curve C in Fig. 4. Efficiencies observed in citrate and EDTA solutions agreed well with published (5) photocurrent efficiencies at single crystal α-Fe_2O_3 electrodes.

Photocurrent efficiencies for polychromatic light (300-540 nm) are shown in Fig. 5 at various pH

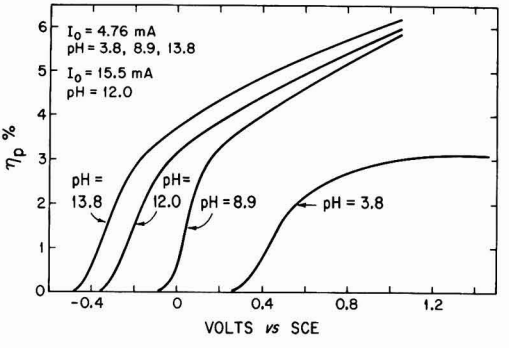

Fig. 5. Effect of pH on photocurrent efficiency for polychromatic light. Polycrystalline α-Fe_2O_3; 23°C.

values. In basic solutions the i-V characteristics were nearly identical showing a lack of saturation and comparable efficiencies at the same overvoltage. At pH 3.8, on the other hand, the efficiency was considerably lower and tended toward a saturation value. This could reflect a change in the rate-limiting step at high light intensities from solid-state process control (diffusion and/or conduction) to electron transfer control at the semiconductor-electrolyte interface. This change in mechanism could occur because of a reduced concentration of oxidizable species (*e.g.*, OH^-) either at the electrode surface or at the outer Helmholtz plane. It should be noted that the polychromatic light intensity of 4.76 mA in Fig. 5 was about 60 times the monochromatic intensity at 400 nm in Fig. 3 and 4.

Some experiments were carried out at higher light intensities utilizing the complete photosensitive range of α-Fe_2O_3. The variation of photocurrent with light intensity at 1.0V overvoltage is shown in Fig. 6. For both low intensity monochromatic light (lower line) and for high intensity polychromatic light (upper line) the photocurrent was proportional to the first power of light intensity within experimental error. This result shows that one photogenerated hole is involved in the rate-limiting step of the over-all electrode process.

Data for α-Fe_2O_3 highly doped with TiO_2 are shown in Fig 7 in which photocurrent efficiency at $(V - V_{fb}) = 1.25V$ is compared with doping level. The points for $N_d > 10^{19}$ cc^{-1} correspond to TiO_2 levels of 0.05-2.0% (Ti/Fe). The donor densities calculated from doping stoichiometry agreed well with N_d calculated from Mott-Schottky plots reported previously (7). The i-V curves for these samples were characterized by a sudden onset of a large dark current similar to those observed by Hardee and Bard (4). It was observed that lower doped samples exhibited less dark current under similar conditions. After subtraction of the dark current, normal-shaped i-V curves were obtained except that the turn-on voltage was shifted several tenths of a volt anodic, the shift increasing with TiO_2 concentration. This effect was probably due to the narrow-space charge layer at low overvoltages, resulting in photocurrents too small to be measured until sufficient space charge depth was established. However, an anodic shift of the flatband potential with the high level doping cannot be ruled out.

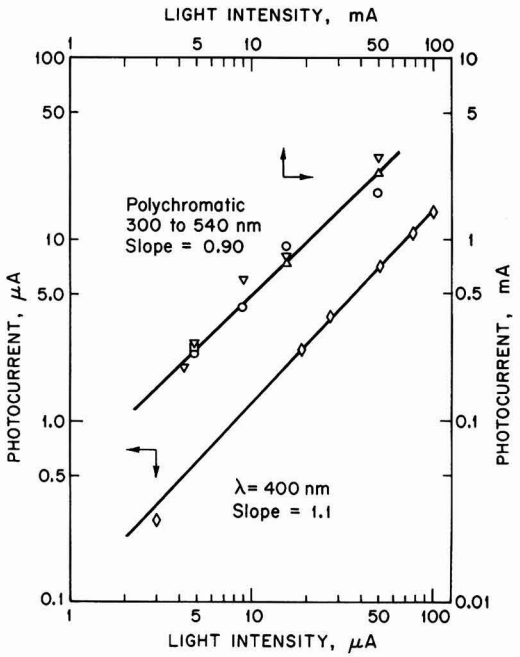

Fig. 6. Effect of light intensity on photocurrent. 1.0V overvoltage

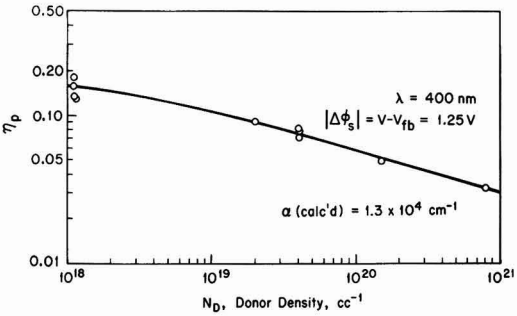

Fig. 7. Effect of donor density on photocurrent efficiency. Polycrystalline α-Fe_2O_3.

Absorption coefficients obtained directly from spectrophotometric data are shown in Fig. 8 (curve A) and compared with apparent absorption coefficients (Fig. 8, curve B) obtained by fitting the current-potential curves to the depletion layer theory of Gärtner (6). The spectrophotometric data are in good agreement with published data (15, 16) for polycrystalline α-Fe_2O_3 films. Correction for bulk scattering was made by assuming the validity of the equation

$$I = I_o \exp - (St_1 + \alpha t_2) \qquad [1]$$

where I and I_o are the transmitted and incident light intensities, S is the coefficient of scattering, α is the absorption coefficient, t_1 is the KBr pellet thickness, and t_2 is the apparent thickness of the α-Fe_2O_3 (volume of Fe_2O_3 in pellet/pellet area).

The scattering coefficient is related to scattering particle properties through the relation (17)

$$S = \pi a^2 N Q_S \qquad [2]$$

where a is the particle radius (assumed spherical), N is the particle density, cc^{-1}, and Q_S is the dimensionless efficiency factor for scattering. The efficiency factor represents the ratio of the effective surface area of a sphere which is available for light scattering to the cross-sectional area (18). In the limit of geometrical optics $Q_S \rightarrow 2$. Calculation of Q_S from the Mie scattering theory (17) is an involved but straightforward procedure. However, La Mer *et al.* (19) dis-

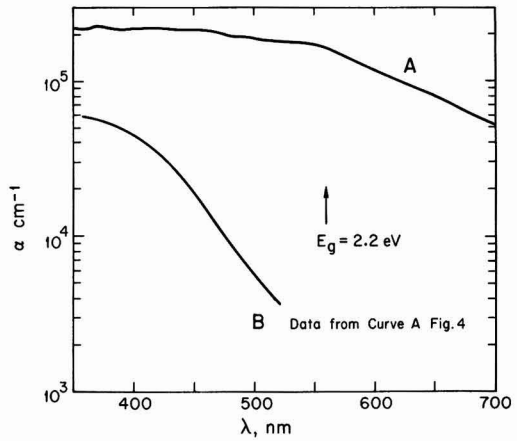

Fig. 8. Comparison of absorption coefficients calculated from spectral data and current-potential curves. Polycrystalline α-Fe_2O_3; 23°C. (A) Absorption coefficient from direct measurement. (B) Absorption coefficient calculated from photocurrent.

covered that both Mie calculations and their experimental values of Q_S could be plotted on one curve forming a universal scattering curve. The curve (18, 19) shows Q_S (K_S their notation) plotted *vs.* the dimensionless parameter, $[n_1\, d/\lambda\, (m^2 - 1)/(m^2 + 2)]$, where m is the relative refractive index, n_2/n_1; n_1 is the refractive index of the medium; n_2 is the refractive index of the scattering particle; and d/λ is the ratio of scattering particle diameter to the wavelength of light. The iron oxide particles were found by microscopic examination to have a diameter of 2.0 $\pm$ 0.5 μm. With $m = 3.0/1.56 = 1.9$, Q_S becomes a constant value of 2.0 for the wavelengths studied.

It is seen from Fig. 8 that in the case of α-Fe_2O_3 the absorption coefficient from optical measurements does not correspond to the absorption coefficient for the excitation process giving rise to the photocurrent. Further discussion of this point is given later.

Discussion

The mechanism by which complexing ions such as citrate and EDTA enhance the photocurrent at α-Fe_2O_3 electrodes is not known. However, the effect of citrate concentration on the increase in photocurrent followed a Temkin isotherm relationship. For intermediate coverage, $0.2 < \theta < 0.8$, the isotherm is usually written as (20)

$$r\theta = -q\Delta\phi + kT \ln K + kT \ln c \qquad [3]$$

where r is an interaction energy parameter, θ is the surface coverage, $\Delta\phi$ is the potential difference between the electrode surface and the solution, K is the equilibrium constant for adsorption in the absence of interaction between the adsorbing particles, and c is the bulk concentration of adsorbate. If it may be assumed that the increase in photocurrent efficiency is proportional to surface coverage, then η-$\eta_{c=0} \propto \ln$ [citrate] and Eq. [3] accounts for the linear portions of the curves in Fig. 2. The saturation effect is of course a property of the Langmuir isotherm which applies as $\theta \to 1$. The results did vary for different electrodes as can be seen in Fig. 2 even when compared in the same electrolyte, and they probably reflect the different surface conditions present. Consideration of these observations makes specific adsorption of citrate and EDTA on α-Fe_2O_3 a reasonable conclusion especially in view of the very high stability constants for these ions with Fe^{3+} in aqueous solution.

It would be expected that specific adsorption of strong complexing anions might shift the turn-on voltage and thereby cause an increase in photoefficiency. In actual fact, the flatband potentials and turn-on voltages did not shift sufficiently (<100 mV) to cause the observed change in efficiency. In addition, the efficiencies were measured at a given overvoltage so that any change in turn-on voltage would not be included. However, because the higher energy level of the valence bandedge of α-Fe_2O_3 compared to TiO_2 or $SrTiO_3$ may result in better energy overlap, photooxidation of citrate and EDTA by photogenerated holes at the α-Fe_2O_3 surface cannot be ruled out without evidence of the reaction products distribution in the various electrolytes. The additional possibility of "current doubling" also exists. In this mechanism (21, 22) photooxidation by a hole in the valence band leads to a radical species which then injects an electron into the conduction band in a chemical step. Thus two current carriers are produced for a single photon leading to the term "current doubling." This reaction is well known on other semiconductors with reactants containing the carboxylate group. This mechanism would lead to decomposition of the citrate or EDTA solute and probably not enhance the oxidation of water. Again, detection of decomposition products is needed and will be investigated in the future.

The η_p-V curves (*e.g.*, Fig. 1 and 3) were fit to the depletion layer theory of Gärtner (6) which leads to the following equation for the photocurrent efficiency

$$\eta_p = 1 - \exp(-\alpha L)/(1 + \alpha L p) \qquad [4]$$

In a previous (2) the application of this equation to i-V-λ data for polycrystalline $BaTiO_3$ electrodes was discussed and it was shown how Lp and N_d could be calculated using the following equation

$$\ln(1 - \eta_p^{corr}) = -\alpha \left(\frac{2\epsilon\epsilon_0}{qN_d}\right)^{1/2} (V\text{-}V_o^*)^{1/2} - \ln(1 + \alpha L p) \qquad [5]$$

A similar approach was taken with α-Fe_2O_3 data except that V_o^* has now been taken as a best fit parameter for the plots of $\ln(1 - \eta_p^{corr})$ *vs.* $(V\text{-}V_o^*)^{1/2}$, and values of N_d from Mott-Schottky plots (7) were used to calculate α, the absorption coefficient for the process giving rise to active holes. Equation [5] was applied for $(V\text{-}V_o^*) \gtrsim 250$ mV.

In order to obtain a good fit at low overvoltages (<250 mV) Eq. [4] was used with the value of L calculated from the parallel plate capacitor Eq. [23]

$$L = \frac{\epsilon\epsilon_0}{C} \qquad [6]$$

where C is given by the more general equation of Dewald (24)

$$C = \left(\frac{q^2 N_d \epsilon\epsilon_0}{2kT}\right)^{1/2} \frac{|e^y - 1|}{(e^y - y - 1)^{1/2}} \qquad [7]$$

The term y measures the space charge overvoltage, *i.e.*, $y = q\Delta\phi_S/kT$ and is negative for anodic bias. It was assumed that

$$V\text{-}V_o^* = |\Delta\phi_S| \qquad [8]$$

Equations [6] and [7] give the more familiar $|\Delta\phi_S|^{1/2}$ dependence for L under sufficient anodic bias corresponding to the Mott-Schottky regime. Typical calculated curves are compared with experimental points in Fig. 9. The experimental data correspond to those in Fig. 3 and have been corrected for reflection. The fit is seen to be usually $\pm$1% even at low overvoltages. The values for the various quantities determined from the data are summarized in Table I. An important point not yet fully understood is that V_o^* from best fit did not correspond to the flatband potential or the turn-on voltage for the photocurrent but was several tenths of a volt more anodic. This may be due in part to the fact that the Gärtner model implies an irreversible photocurrent. That is, no account is taken of possible cathodic current either in the valence band or conduction band. These effects would become more important at electrode potentials near the point of zero photocurrent.

It was also found that the theory could be fit to data with polychromatic light even though the theory was derived for monochromatic light. From this fit the calculated absorption coefficient was 1×10^4 cm^{-1} as would be expected if α represented some sort of

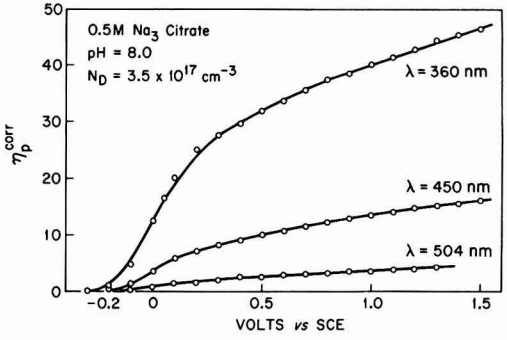

Fig. 9. Comparison of observed and calculated photocurrent efficiency. Polycrystalline α-Fe_2O_3; electrode no. 2.

Table I. Summary of values obtained from current-potential curves (99.999% α-Fe_2O_3)

Electrolyte	pH	V_o* (SCE)	α(calc.), cm^{-1}	Lp, cm
0.1M Na_2 EDTA	4.0	+0.20	5.9×10^4 (360 nm)	3×10^{-7}
0.5M Na_3 citrate	8.0	−0.10	3.1×10^4 (360 nm)	2×10^{-7}
0.5M Na_3 citrate	8.0	−0.10	9.3×10^3 (450 nm)	—
0.5M Na_3 citrate	8.0	−0.10	2.6×10^3 (504 (nm)	—
0.5M KCl	8.9	+0.17	2.3×10^4 (400 nm)	10×10^{-7}
2.0M NaOH	13.8	−0.48	$1.0 \times 10^{4*}$	4×10^{-7}

* Polychromatic light (300-540 nm), intensity 4.76 mA.

average value over the 300-540 nm spectral range. The diffusion lengths found for α-Fe_2O_3 were 2-4 $\times$ 10^{-7} cm and were considerably lower than values found for TiO_2 (1×10^{-5} cm) and the barium and strontium titrates (3-6 $\times$ 10^{-6} cm) (25). Possible reasons for these differences will be discussed in a future publication.

The absorption coefficients calculated from the data in Fig. 8 curve A using Eq. [5] and Lp data from Table I and Mott-Schottky values for N_d are compared with spectrophotometric α in Fig. 8. It is seen that the absorption coefficient from optical measurements did not correspond to the absorption coefficient for the excitation process giving rise to the photocurrent. It is reasonable to presume that the absorption coefficient derived from i-V characteristics corresponds to the ligand to metal-charge transfer ($O^{2-} \rightarrow Fe^{3+}$), yielding reactive holes on the oxygen sites (valence band). The spectrophotometric measurements show that another process with comparable absorption is occurring, *i.e.*, there is an overlap of at least two absorption bands. The large absorption coefficient indicated for this overlapping process may mean that another type of charge transfer is occurring—possibly metal to metal, which can be envisaged as

$$2Fe^{3+} \xrightarrow{h\nu} Fe^{2+}(Fe^{3+} - e^-) + Fe^{4+}(Fe^{3+} - h^+) \quad [9]$$

This process would give rise to a second type of hole, now on an iron site with a different energy level than the hole in the oxygen valence band. Indeed it has been suggested (27, 28) that this process is responsible for the intrinsic conductivity in α-Fe_2O_3 with $E_g \sim 1.7$-2.0 eV. The Fe^{4+} hole may no longer be capable of evolving oxygen from water while at the same time the electron trapped on iron (Fe^{2+}) may not be free to conduct and therefore would yield no photocurrent.

The validity of using absorption coefficients determined from i-V curves is supported by the plot shown in Fig. 10 calculated from data in curve B, Fig. 8. It is well known that for semiconductors the dependence of α on energy near the absorption edge usually follows the form (28)

$$\alpha h\nu = A(h\nu - E_g)^{n/2} \quad [10]$$

where A is a constant and n depends on the nature of the transition ($n = 1$ for a direct transition and $n = 4$ for an indirect transition). The slope in Fig. 10 is 2.07 giving $n = 4.1$, indicating an indirect transition requiring phonon support.

A further test of the plausibility of the absorption coefficient found for α-Fe_2O_3 was made by plotting the data in Fig. 7 in the form

$$\ln(1 - \eta_p^{corr}) = -\alpha\left(\frac{2\epsilon\epsilon_o\Delta\phi_S}{q}\right)^{1/2} \Big/ N_d^{1/2} - \ln(1 + \alpha Lp) \quad [11]$$

For $\lambda = 400$ nm, α was found to be 1.3×10^4 cm^{-1} in reasonable agreement with the value of 4.4×10^4 cm^{-1} from Fig. 8. This result supports the conclusion stated earlier that α for the charge transfer process leading to photocurrent is considerably smaller than the spectrophotometric value.

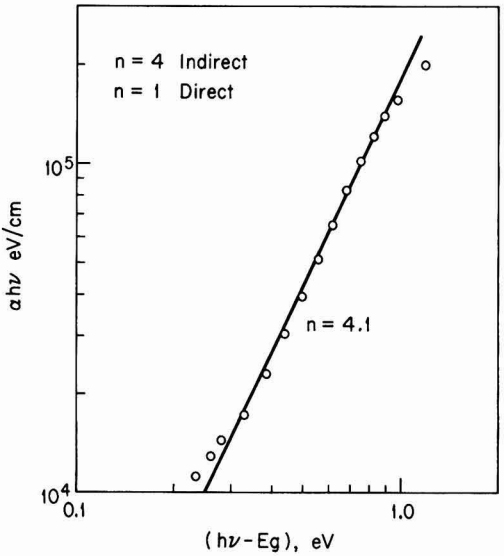

Fig. 10. Test for nature of electronic transition on absorption edge. Polycrystalline α-Fe_2O_3.

Acknowledgments

The authors acknowledge partial financial support of this project by the National Science Foundation, Grant No. DMR 73-07507 AO2 and by the Committee on Research, University of California.

Manuscript submitted Oct. 11, 1977; revised manuscript received Dec. 12, 1977. This was Paper 328 presented at the Philadelphia, Pennsylvania, Meeting of the Society, May 8-13, 1977.

Any discussion of this paper will appear in a Discussion Section to be published in the December 1978 JOURNAL. All discussions for the December 1978 Discussion Section should be submitted by Aug. 1, 1978.

Publication costs of this article were assisted by the University of California.

REFERENCES

1. J. M. Bolts and M. S. Wrighton, *J. Phys. Chem.*, **80**, 2641 (1976).
2. J. H. Kennedy and K. W. Frese, Jr., *This Journal*, **123**, 1683 (1976).
3. K. L. Hardee and A. J. Bard, *ibid.*, **124**, 215 (1977).
4. K. L. Hardee and A. J. Bard, *ibid.*, **123**, 1024 (1976).
5. R. K. Quinn, R. D. Nasby, and R. J. Baugham, *Mater. Res. Bull.*, **11**, 1011 (1976).
6. W. W. Gärtner, *Phys. Rev.*, **116**, 84 (1959).
7. J. H. Kennedy and K. W. Frese, Jr., *This Journal*, **125**, 723 (1978).
8. E. Wegner and A. Adamson, *J. Am. Chem. Soc.*, **88**, 394 (1966).
9. M. M. Stimson and M. J. O'Donnell, *ibid.*, **74**, 1805 (1952).
10. G. M. Wyman, *J. Opt. Soc. Ann.*, **45**, 965 (1955).
11. M. J. S. Dewar and A. R. Lepley, *J. Am. Chem. Soc.*, **83**, 4560 (1961).
12. B. L. Van Duren and C. E. Bardi, *Anal. Chem.*, **35**, 2198 (1963).
13. F. A. Jenkins and H. E. White "Fundamentals of Optics," 3rd ed., Chap. 25, McGraw-Hill, New York (1957).
14. S. M. Ahmed and D. Maksimov, *Can. J. Chem.*, **46**, 3841 (1968).
15. R. F. G. Gardner, F. Swett, and D. W. Tanner, *J. Phys. Chem. Solids*, **24**, 1183 (1963).
16. D. Lewis and W. Westwood, *Can. J. Phys.*, **42**, 2367 (1964).
17. H. C. Van de Hulst, "Light Scattering by Small

Particles," p. 415, John Wiley & Sons, New York (1957).
18. R. H. Harding, B. Golding, and R. A. Morgen, *J. Opt. Soc. Am.*, **50**, 446 (1960).
19. V. K. LaMer, OSRD Rept. 4904, PB 32208, U.S. Dept. of Commerce (1944).
20. J. O'M. Bockris and S. Srinivasan, "Fuel Cells," pp. 97-102, McGraw Hill, New York (1969).
21. W. P. Gomes, T. Freund, and S. R. Morrison, *This Journal*, **115**, 818 (1968).
22. T. Freund and W. P. Gomes, *Catal. Rev.*, **3**, 1 (1969).
23. F. Möllers, H. J. Tolle, and R. Memming, *This Journal*, **121**, 1160 (1974).
24. J. F. Dewald, *Bell Syst. Tech. J.*, **39**, 615 (1960).
25. K. W. Frese, Jr., Ph.D. Thesis, University of California, Santa Barbara (1977).
26. F. J. Morin, *Phys. Rev.*, **93**, 1195 (1954).
27. J. B. Goodenough, in "Advances in Solid State Chemistry," H. Reiss, Editor, Chap. 4, McMillan, New York (1964).
28. E. J. Johnson, in "Semiconductors and Semimetals," Vol. 3, R. K. Willardson and A. C. Beer, Editors, Chap. 6, Academic Press, New York (1967).

Coulometric Study of the Reduction of Dinitroaniline Compounds

Csaba P. Keszthelyi,*,[1] Barbara A. Kenney, and Paul J. Buras

Department of Chemistry, Louisiana State University, Baton Rouge, Louisiana 70803

and Lloyd M. Southwick and Guye H. Willis

United States Department of Agriculture, Agricultural Research Service, Baton Rouge, Louisiana 70893

ABSTRACT

The authors' d.c.-polarographic study [*Anal. Chim. Acta.* **82**, 29 (1976)] has been extended to include a coulometric investigation of the cathodic reduction of six substituted dinitroanilines: 4-(trifluoromethyl)-2,6-dinitro-*N*,*N*-dipropylaniline (I) was measured in 40% aqueous ethanol buffered at four *p*H values (1.5, 5.1, 7.4, 9.2), and *N*-butyl-*N*-ethyl-4-(trifluoromethyl)-2,6-dinitroaniline (II), 2,6-dinitro-4-isopropyl-*N*,*N*-dipropylaniline (III), N^1,N^1-diethyl-4-(trifluoromethyl)-2,6-dinitro-*m*-phenylenediamine (IV), 4-(methylsulfonyl)-2,6-dinitro-*N*,*N*-dipropylaniline (V), and 3,5-dinitro-N^4,N^4-dipropylsulfanilamide (VI) were measured in 40% aqueous ethanol buffered at one *p*H value (1.5). Preparative scale runs and product analyses indicate that the electroreduction mechanism is *p*H dependent, as evidenced by substantial benzimidazole formation at 1.5 *p*H and little production of this compound at 7.4 *p*H.

Controlled potential coulometry (1-4) utilizes the modern instrumental capabilities of potentiostats and is a powerful electroanalytical technique that makes possible the elucidation of certain chemical reaction paths by allowing direct measurement of the number of Faradays taken up by a given amount of a compound (5-7). Similar information has been obtained on occasion from d-c polarograms (8-10); whereas in favorable circumstances, it is possible to arrive at the correct number of electrons involved (n), examination of the Ilkovic equation

$$i_d = knCD^{1/2}m^{2/3}t^{1/6}$$

reveals that n can be expressed only in terms of several constants or parameters whose cumulative uncertainty affects n. Indeed, it is customary to use the Ilkovic equation to find the diffusion coefficient D—a procedure which in turn assumes that n is known. An alternative procedure that uses the slope of a polarogram to find n is not applicable to quasireversible systems, and hence to many systems, including the substituted dinitroanilines of our study.

Coulometry in nonaqueous media often employs electrodes fabricated from the platinum metal family (5), but in aqueous solvents the problem of hydrogen discharge curtails their utility and mercury becomes the common choice, as was discussed in the report of our previous polarographic study (11). It should be mentioned that there are specific problems associated with controlled potential coulometry and large mercury pool cathodes; these are discussed later on in the paper.

* Electrochemical Society Active Member.
[1] Present address: Visiting Exchange Scientist, U.S. National Academy of Sciences—Hungarian Academy of Sciences, Szeged, Hungary.

Key words: cathodic reduction, controlled potential coulometry, mercury pool, substituted dinitroaniline.

Experimental

The general instrumental link-up in the coulometric experiments is presented in a simplified manner in Fig. 1. A buffered ethanol:water solution (40%:60% by vol.) similar to the polarographic solutions discussed previously (11), containing 50.0 μmoles of solute in the 150 ml total volume used in the "working" compartment of the coulometry cell (Fig. 2), was thoroughly

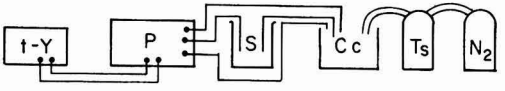

Fig. 1. Simplified block diagram of instrumental layout. Legend: *t-Y*: time-base X-Y recorder; P: potentiostat; S: silver coulometer; Cc: coulometry cell; Ts: bubbler-tower containing ethanol:water; N_2: purging gas tank.

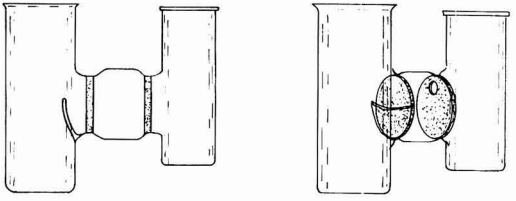

Fig. 2. Coulometry cell

purged with nitrogen, followed by applying a potential selected as appropriate from known $E_{1/2}$ values (11) in the three-electron mode. The actual mercury pool cathode (working electrode)-platinum coil anode (auxiliary electrode) voltage, reflecting *IR* losses due to the two medium porosity frits as well as solution resistance, was intermittently monitored with a Hewlett-Packard[2] 34703A/34740A DCV/DCA/Ω measurement system (the maximum voltage recorded was ~20V, far short for causing troublesome voltage-limiting conditions with the GBE Wenking 61-R potentiostat). In a number of experiments, the current output of the potentiostat was recorded on a Hewlett-Packard 7044-A X-Y recorder equipped with a time-base accessory. Because of the full-current output feature of the Wenking 61-R, measuring resistors and multipole switches were selected with special care. Product analysis for compound (I) at *p*H 1.5 and 7.4 was performed using a Perkin-Elmer 621 spectrophotometer and Varian HA-100 NMR spectrometer.

The coulometry cell (Fig. 2) containing the alcohol: water mixtures was preceded by a saturation tower containing a similar alcohol: water mixture, so that the purging nitrogen gas would not significantly alter the composition of the mixed solvent. A special feature of the coulometry cell was the glass lip protruding from the frit toward the center of the cathodic compartment; its purpose was to reduce the voltage drop along the surface of the mercury pool as a function of distance from the frit.

In a typical experiment, the 100 ml solution (60 ml aq. buffer + 40 ml ethanol) to be used in the auxiliary compartment and the 145 ml solution (90 ml aq. buffer + 55 ml ethanol) to be used in the working compartment were deaerated for 1 hr in separatory funnels placed above the coulometry cell; simultaneously, the coulometry cell itself was purged with N_2. After deaeration, the solutions were introduced and the background current was measured under the chosen conditions of stirring rate and applied potential; values ranged between 40 and 70 μA, with an observable slight decrease with time. Addition of 5 ml of alcohol containing the 50.0 μmoles of solute produced initial currents of less than 20 mA; electrolysis was continued past the 99% completion stage to background. Total time for an experiment was 12-15 hr, with the exception of silver coulometry and preparative scale (100 mg solute) runs which required up to 24 hr.

Silver coulometry was done using a 250 ml beaker containing 150 ml solution, 1*M* in $AgNO_3$ and 5*M* in $NaNO_3$ (alternately, 1*M* $AgNO_3$ and 2*M* KCN). The outside of the beaker was taped with black PVC tape to prevent photochemical decomposition and the top was also shielded from direct light. The electrodes (Ag wire or Ag foil) were suspended from a ⅛ in. diam glass rod that had an elongated W shape, and fit reasonably snugly on the spout and beaker rim. (Ideally the least number of sharp surfaces should produce best results, and the foil is preferable to the coiled wire.)

[2] Mention of tradenames is for the convenience of the reader and does not constitute any preferential endorsement by the U.S. Department of Agriculture over similar products available.

Only about 2/3 of the electrode was immersed in the solution to protect the contacts; voltage drop across the system, connected in series onto the auxiliary electrode, was about 2V. In silver coulometry weight is measured before the experiment, and after the experiment the electrodes are removed with Teflon-tipped forceps, washed thoroughly and gently in a stream of distilled water followed by acetone, then dried for 15 min at 50°C before weighing again. For reuse the electrodes were soaked in 1*M* KCN for over an hour, and the gaining electrode was polished with a piece of fine sandpaper (00) to remove loosely adhering silver. The losing electrode will eventually need replacement—for best results the two electrodes should never be interchanged. By measuring both the loss and gain values of the electrodes, a precision better than 0.5 mg was routinely observed, and with special care 0.1 mg can be expected according to our results. In case of higher discrepancy the loss figure was regarded as the more accurate because the gaining electrode often acquires crystalline deposition which may not adhere.

The present report is based on 56 coulometric determinations, with 36 runs on 4-(trifluoromethyl)-2,6-dinitro-*N*,*N*-dipropylaniline (I). Nine out of the 36 runs were preparative scale, including isolation and identification of product. Additional information concerning experiments is given in Table I and the following section.

Results and Discussion

Appropriate voltages for use in controlled potential coulometry can be selected from polarographic or sweep voltammetric information. Our polarographic study (11) gave the following $E_{1/2}$ values (−mV *vs.* SCE) at *p*H 1.5, 5.1, 7.4, and 9.2, respectively: (I) 190, 430, 700, 810; (II) 190, 430, 700, 810; (III) 170, 360, 720, 810; (IV) 230, 510, 720, 1010; (V) 160, 480, 710, 790; (VI) 160, 530, 680, 810. These values correspond to the second polarographic wave when it was distinguishable; at *p*H = 1.5 all compounds displayed a single wave whose height closely corresponded to the sum of the two wave heights for the compound observed at the higher *p*H's. A salient feature of the polarograms was the similarity in which *p*H affected all six compounds; for this reason, we felt that the essential coulometric information could be obtained by investigating all compounds at one *p*H and, in addition, one compound at all four *p*H's. The results are given in Table I.

The difference between our combined average value of ne^- ($7.53 \pm 0.16_6$) and the $8e^-$ required ideally to reach the dihydroxylamine stage was large enough that we interpret the difference as an indication of some kinetic perturbation rather than as an instrumental artifact. The assignment of two $4e^-$ reduction steps (11) on the basis of simple d-c polarography is, therefore, seen in the perspective of coulometry as a close approximation rather than an ultimate conclusion.

The chemistry of nitroaromatics is known to be complex. Peltier and his co-workers (12-14) have extensively studied the controlled potential electroreduction of a large number of substituted mono- and dinitro

Table I. Summary of coulometric experiments

Compound	*E* (V *vs.* SCE)	*p*H	*ne*⁻
4-(trifluoromethyl)-2,6-dinitro-*N*,*N*-dipropylaniline (I)*	−0.600	1.5	7.45
	−0.700	5.1	7.74
	−0.900	7.4	7.46
	−1.00	9.2	7.95
N-butyl-*N*-ethyl-4-(trifluoromethyl)-2,6-dinitroaniline (II)	−0.600	1.5	6.69
2,6-dinitro-4-isopropyl-*N*,*N*-dipropylaniline (III)	−0.600	1.5	6.93
N^1,N^1-diethyl-4-(trifluoromethyl)-2,6-dinitro-*m*-phenylenediamine (IV)	−0.600	1.5	8.75
4-(methylsulfonyl)-2,6-dinitro-*N*,*N*-dipropylaniline (V)	−0.600	1.5	7.80
3,5-dinitro-N^4,N^4-dipropylsulfanilamide (VI)	−0.600	1.5	7.23
All samples	—	—	$7.53 \pm 0.16_6$**

* Preparative scale runs gave *ne*⁻ value estimates that compare favorably: *p*H 1.5: 7.43 (5 runs); *p*H 7.4: 7.68 (3 runs).
** Standard deviation of the mean.

compounds. Their investigations, which included product identification, give evidence of the stepwise reduction of nitroaromatics. Their work also reveals complicating factors; n-values less than the theoretical seem to be characteristic of the nitroanilines.

Further insight into the electrochemistry of nitroaromatics is provided by the classical example of the reduction of picric acid in HCl; Lingane (2) found that 34 electrons are involved in the production of the primary product bis-(3,5-diamino-4-hydroxyphenyl) hydrazine, but subsequently Bergman and James (15), as well as Meites and Meites (16), demonstrated that ne^- is a function of both the initial picric acid concentration and the hydrochloric acid concentration.

In order to analyze the products of the pH 1.5 reduction, the pH of the reaction solution was adjusted to 7, the ethanol removed with a nitrogen stream, and the aqueous residue extracted with ether. Drying the extract with sodium sulfate and evaporation to dryness with nitrogen yielded an oily-solid red-brown residue. Thin layer chromatography (silica gel GF-254, benzene: ethyl acetate, 2:1) of the residue showed several u.v.-absorbing (254 nm) spots along the length of the plate and a single major spot (R_f = 0.14) which exhibited bright blue fluorescence under u.v. light. The residue gave the following spectroscopic data: infrared (film) 1620 cm^{-1}; NMR ($CDCl_3$) δ 7.50 (*s*, 1, ArH), 6.72 (*s*, 1, ArH), 4.20 (*t*, 2, CH_2), 3.75 (broad, 2, NH_2), 2.85 (quadruplet, 2, CH_2), 1.87 (*m*, 2, CH_2), 1.44 (*t*, 3, CH_3), and 0.99 ppm (*t*, 3, CH_3). These peaks in the NMR spectrum were observed almost to the exclusion of other absorptions and are similar to those reported for 2-ethyl-7-nitro-1-propyl-5-trifluoromethylbenzimidazole by Leitis and Crosby (17), who identified the benzimidazole as a product of the photochemical degradation of compound I.

Preparative thin layer chromatography of the residue on silica gel by developing three times with benzene: ethyl acetate, 2:1, afforded a chromatogram with the blue fluorescent spot at R_f 0.31-0.44. From this area a pale yellow solid was isolated which gave the following mass spectrum, *m/e* (%); 272 (15), 271 (100, M+), 256 (22), 252 (11), 243 (14), 242 (92), 229 (74), 228 (44), 227 (18), 214 (31), (212 (12), 159 (10).

We conclude from these spectroscopic data that the major product of the pH 1.5 reduction is 7-amino-2-ethyl-1-propyl-5-trifluoromethylbenzimidazole, compound VII

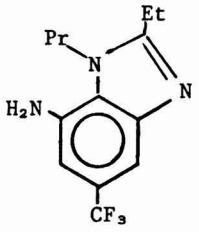

VII

Identification of a benzimidazole in our work at low pH is consistent with the studies of Feltier and co-workers (12c, 14), who observed benzimidazole formation in the electrochemical reduction of N,N-disubstituted-o-nitroanilines in 1*N* sulfuric acid: ethanol, 1:1.

The pH 7.4 reaction was worked up in a similar manner except without adjustment of the pH before ether extraction. Thin layer chromatography of the residue showed several u.v.-absorbing spots and a small fluorescent blue spot at R_f = 0.14. In addition to benzimidazole peaks, which were usually minor, the NMR spectrum ($CDCl_3$) of the resulting residue showed the following singlets in the aromatic region: δ7.68, 7.45, 7.14, 6.99, 6.73, 6.68, and 6.56 ppm. From one reaction to another the relative sizes of these peaks varied. We are continuing our study of the products of the pH 7.4 reduction. With regard to our NMR work, we plan to look into temperature-δ relationships for additional analytical capability.

Although the compounds of the present study are amenable to photodecomposition (17, 18), we found no evidence that exclusion of roomlight altered the polarographic or coulometric results at any of the four pH values. To our knowledge a converse study, involving the electrochemical investigation of photolysis products of these compounds (I-VI), has not been reported.

Conclusion

The present coulometric study of the number of electrons involved in the cathodic reduction of the substituted dinitroanilines, 4-(trifluoromethyl)-2,6-dinitro-*N*,*N*-dipropylaniline; *N*-butyl-*N*-ethyl-4-(trifluoromethyl)-2,6-dinitroaniline; 2,6-dinitro-4-isopropyl-*N*,*N*-dipropylaniline; N^1,N^1-diethyl-4-(trifluoromethyl)-2,6-dinitro-*m*-phenylenediamine; 4-(methylsulfonyl)-2,6-dinitro-*N*,*N*-dipropylaniline; and 3,5-dinitro-N^4 N^4-dipropylsulfanilamide in aqueous ethanol gave n values in close agreement with those previously estimated from polarographic measurements. The slight deviation of the experimentally obtained n value ($[7.53 \pm 0.16_6]$ e^-) from the number of electrons ideally required to reach the dihydroxylamine form ($8e^-$) is considered to be of chemical rather than artifactual origin and is not unexpected in view of the known complex chemistry of the species involved. The coulometric results necessitate a refinement of the previous mechanistic interpretation (11) based on d.c. polarography. Although there is only a relatively slight change in n values as a function of pH, preparative scale runs and product analyses reveal that the apparent merging of the two polarographic waves at low pH in effect involves a change in the reduction mechanism. Results of a separate study planned to provide information on this detail with the aid of additional electroanalytical techniques (5) will be presented subsequently.

Acknowledgment

We thank S. Swinney, P. Dasgupta, L. McGee, C. Lee, and M. Bertucci for contributions to this project.

Manuscript submitted Nov. 12, 1976; revised manuscript received Dec. 16, 1977.

Any discussion of this paper will appear in a Discussion Section to be published in the December 1978 JOURNAL. All discussions for the December 1978 Discussion Section should be submitted by Aug. 1, 1978.

Publication costs of this article were assisted by the U.S. Department of Agriculture.

REFERENCES

1. A. Hickling, *Trans. Faraday Soc.*, **38**, 27 (1942).
2. J. J. Lingane, *J. Am. Chem. Soc.*, **67**, 1916 (1945).
3. J. J. Lingane, *Anal. Chim. Acta*, **2**, 584 (1948).
4. A. J. Bard and K. S. V. Santhanam, *Electroanal. Chem.*, **4**, 215 (1970).
5. W. V. Childs, J. T. Maloy, C. P. Keszthelyi, and A. J. Bard, *This Journal*, **118**, 874 (1971).
6. E. J. Rudd, M. Finkelstein, and S. D. Ross, *J. Org. Chem.*, **37**, 1763 (1972).
7. H. Satonaka, Z. Saito, and T. Shimura, *Kanagawaken Kogyo Shikensho Kenkyu Hokoku*, **40**, 29 (1974).
8. O. H. Müller, *J. Biol. Chem.*, **145**, 425 (1942).
9. E. Friedheim and L. Michaelis, *ibid.*, **91**, 355 (1931).
10. R. Elema, *Rec. Trav. Chim.*, **50**, 807 (1931).
11. L. M. Southwick, G. H. Willis, P. K. Dasgupta, and C. P. Keszthelyi, *Anal. Chim. Acta*, **82**, 29 (1976).
12. M. Le Guyader, (a) *Bull. Soc. Chim. (France)*, **1966**, 1848; (b) *ibid.*, **1966**, 1858; (c) *ibid.*, **1966**, 1867.
13. A. Tallec, (a) *Ann. Chim.*, **3**, 155 (1968); (b) *ibid.*, **3**, 347 (1968); (c) *ibid.*, **4**, 67 (1969).
14. (a) M. Le Guyader and D. Peltier, *Bull. Soc. Chim. (France)*, **1966**, 2695; (b) A. Darchen and D. Pel-

tier, *ibid.*, **1974**, 673.
15. I. Bergman and J. C. James, *Trans. Faraday Soc.*, **50**, 60 (1954).
16. L. Meites and T. Meites, *Anal. Chem.*, **28**, 103 (1956).
17. E. Leites and D. G. Crosby, *J. Agr. Food Chem.*, **22**, 842 (1974).
18. C. S. Helling, *J. Environ. Qual.*, **5**, 1 (1976).

Kinetics of the Electrochemical Reduction of Dicyanoaurate

E. T. Eisenmann

Bell Laboratories, Columbus, Ohio 43213

ABSTRACT

The mechanism of the electrochemical reduction of dicyanoaurate was studied by means of steady-state and relaxation methods in combination with a rotating disk electrode. The deposition of soft gold, lead-doped soft gold and cobalt-hardened gold was found to proceed via one common mechanism that involves adsorption equilibria preceding and following the electron transfer step. Special effects, such as epitaxy and preferred orientation of soft gold, the small-grained texture of hard gold, and the lead-induced depolarization of soft gold plating are explained in terms of the energetic states of the adsorbed, oxidized, and reduced gold species. The effect of lead is to lower the activation energy of the electron transfer, which results in the accelerated establishment of a preferred orientation. Cobalt increases the activation energy of the electron transfer and gives rise to a high nucleation rate. The proposed mechanism is shown to explain equally well the anodic behavior of gold in alkaline cyanide electrolyte.

The importance of gold plating in electronic device technology has led to greatly diversified, usually proprietary plating formulations. Yet apart from the description of particular bath features, there is a definite scarcity of the documentation of fundamental processes involved in the electrodeposition of gold. Cheh and Sard (1) used galvanostatic techniques to study the morphology of gold deposits on a rotating-disk electrode from various electrolytes. Harrison and Thompson (2) employed voltammetric techniques and postulate a reaction mechanism that involves AuCN as reacting species. Recently, McIntyre and Peck (3) reported with considerable detail on the depolarization of the deposition of soft gold through heavy metal ions. Numerous publications are available on the effects of codeposited impurities on the physical properties of gold plates (4-6). The review of the literature indicates that kinetic studies have been practically limited to soft gold systems. Although soft gold as well as hard gold is almost universally deposited from electrolytes containing dicyanoaurate, there is no indication that a unifying kinetic study of the two types of gold baths was ever attempted. Recent work on the deposition of gold on the reeds of sealed contacts (7) suggested such a unifying study. Using predominantly potentiostatic, steady-state, and relaxation techniques in combination with a rotating-disk electrode various aspects of the electrode kinetics were investigated.

Experimental

The following solutions were used in the present study: (*i*) Commercial hard gold baths (Selrex CI and Technic Orosene 999), operated at pH = 4 and 30°C; (*ii*) Soft gold bath, containing 0.1M $KAu(CN)_2$, 0.3M potassium phosphate, and no or 2 ppm Pb, operated at pH = 7 and 30°C or 65°C. Polarization measurements were carried out in these electrolytes either with Pt rods of 0.5 cm^2 area (under constant convection) or with a rotating Pt disk of 0.32 cm^2.

It was assumed that the gold deposition would usually proceed with less than 100% current efficiency. The gold partial currents were, therefore, determined by means of a coulometric analysis of the gold deposit. This approach was, evidently, quite time consuming and precluded current or voltage scanning techniques. It is believed, however, that superior accuracy of the data was achieved in this manner.

Key words: electrocrystallization, electrode adsorption processes, epitaxy, lead-induced depolarization.

Potentiostatic Polarization

A Pt disk electrode was polarized under constant potential conditions for various lengths of time in the electrolytes described above. The gold partial currents were evaluated from plots of the (coulometrically determined) electrical equivalents of the gold deposits *vs.* the plating time. For the hard gold baths, these plots were found to yield straight lines, indicating that the gold partial current at constant potential is independent of the plating time. In contrast to this behavior, the same kind of plots for soft gold deposition were curved, corresponding to an acceleration of the rate of deposition with time.

The slopes of the straight lines obtained for one of the hard gold baths and the limiting slopes of the curves at short plating times obtained for the soft gold baths were plotted semilogarithmically *vs.* the deposition potential, Fig. 1. The straight portions of these curves have slopes of $-4.4V^{-1}$ at 30°C and $-3.6V^{-1}$ at 65°C, the difference being accountable by the thermal energy difference. The shift in the deposition potential at equal current density for soft gold at 65° and 30°C is explained by the increased solubility of HCN at the lower temperature, which results in a decrease of the equilibrium potential. The similar shift observed for hard gold *vs.* soft gold at 30°C may be due to any of several differences in the makeup of the baths. However, because of the very striking difference in the grain size of the two types of gold deposits, it is postulated that the cobalt content in the hard gold bath increases the activation energy of the electron transfer, and consequently the nucleation rate of the gold deposition.

Time Dependence of the Deposition Rate

The observed increase of the deposition rate of soft gold with time at constant potential corresponds to the "depolarization effect" studied by various authors (8, 9) under galvanostatic conditions. Since it was unknown to what extent the soft gold bath was contaminated with heavy metal ions, which are capable of inducing the depolarization, an addition of 2 ppm lead

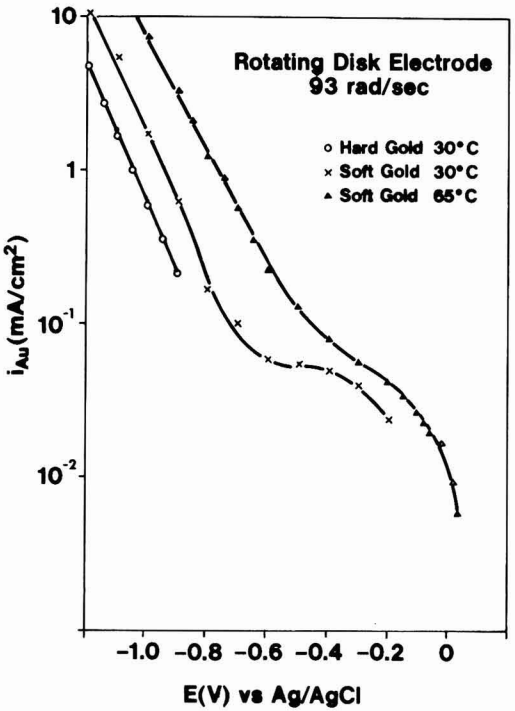

Fig. 1. Current density-potential curves at short polarization times.

was made to the plating solution. With this modified bath, gold was deposited potentiostatically for various lengths of time. Figure 2 shows the coulometric equivalents of the gold deposits in dependence of the deposition time. It is seen that at all potentials the gold deposit grows initially in proportion to t^2 and later in proportion to t, where t is the deposition time. Basically, the same behavior is also obtained for a soft gold bath without the intentional lead addition. However, the deposits grow for an extended period proportional to t^x, where $1 < x < 2$. Figure 2 indicates that in the case of lead-doped gold the time required for the current density to stabilize is practically independent of the deposition potential. Also, the steady-state condition is achieved at increasingly thicker deposits as the deposition potential assumes more negative values.

Generation of Polarization Curves under Steady-State Conditions

According to Fig. 2, steady-state conditions of the deposition of lead-doped gold are attained within about 5 min. Polarization curves were, therefore, derived from the slope of current density-time product *vs.* t curves for various potentials, at $t = 1000$ sec. A similar procedure was employed for the deposition of lead-free gold, measuring the slope between the plating times $t = 3$ and $t = 5$ hr. The results are given in Fig. 3. A considerable difference in the deposition potential between the two curves is noted at the center of the graph, which decreases, however, at very high and very low values of the deposition potential.

Both curves seem to approach the slope of the curves in Fig. 1 at extreme negative potentials, suggesting that the same mechanism is operative. The steep sections at the center of the graph are tentatively identified as the result of the proximity to the equilibrium potential, which is controlled by the concentration of cyanide at the electrode surface. In order to confirm this assumption it is necessary to explain the plateau which is evident at the right of the steep portions.

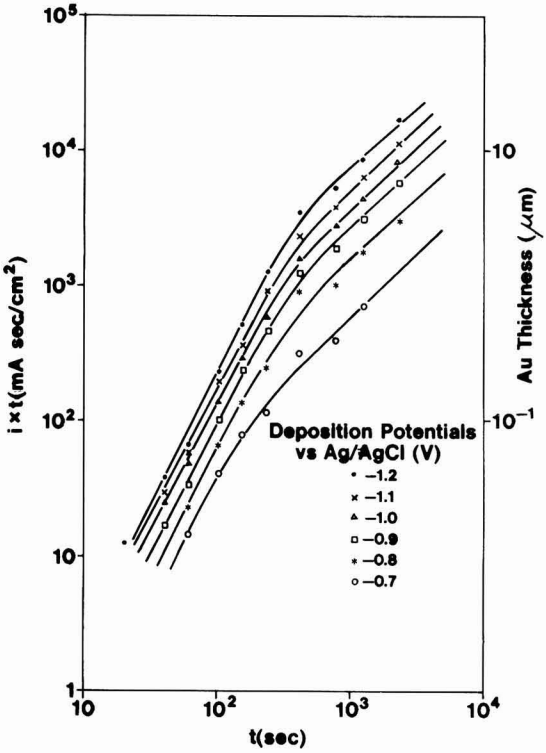

Fig. 2. The growth of Pb-doped soft gold

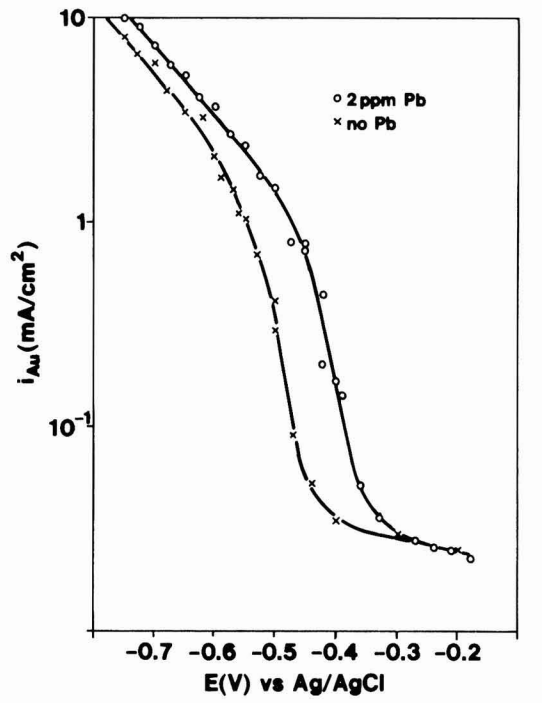

Fig. 3. Current density-potential curves for soft gold at long polarization times.

Evidence of Mixed Potential and Electroless Deposition at the Au/Au(CN)$_2^-$ Electrode

Rotating-disk experiments were designed to explain the plateau section in Fig. 1 and 3. In order to minimize the effect that may result from the accumulation of cyanide during plating, a large volume of electrolyte (2.5 liters) was circulated through the plating cell.

Under open-circuit conditions, a Pt disk electrode assumed a potential of +0.043V *vs.* Ag/AgCl at 65°C at a rotation velocity of 94 rad/sec. The potential increased with increasing rotation velocity. After prolonged exposure, the Pt disk was coated with gold. The rate of gold deposition appeared to be strongly dependent on the history of the bath (*e.g.*, previous use), but was constant within a given test series over many hours. This result proves that the open-circuit potential of the gold electrode corresponds to a mixed potential.

Discussion and Additional Results

Electroless deposition of gold.—The electron donor that causes the reduction of the Au(CN)$_2^-$ ions is hypothesized to be the cyanide ion, according to

$$CN^- \rightleftarrows 1/2(CN)_2 + e \qquad [1]$$

$$Au(CN)_2^- + e \rightleftarrows Au + 2CN^- \qquad [2]$$

or after adding Eq. [1] and [2]

$$Au(CN)_2^- \rightleftarrows Au + 1/2(CN)_2 + CN^- \qquad [3]$$

It is seen that the cyanide ion has the dual role of promoting reaction [1] and retarding reaction [2]. The kinetics of the over-all reaction [3] is, therefore, strongly dependent on the cyanide concentration. The oxidation potentials of reactions [1] and [2] can be expressed by the Nernst equation (brackets indicate activities or, approximately, concentrations)

$$E_{(CN)_2} = E^\circ_{(CN)_2} - \frac{RT}{F} \ln [CN^-] + \frac{RT}{2F} \ln [(CN)_2] \qquad [4]$$

$$E_{Au} = E^\circ_{Au} - 2\frac{RT}{F} \ln [CN^-] + \frac{RT}{F} \ln [Au(CN)_2^-] \qquad [5]$$

where

$$E^\circ_{Au} = -0.84V \text{ } vs. \text{ Ag/AgCl}^{10}$$

$$E^\circ_{(CN)_2} = -0.46V \text{ } vs. \text{ Ag/AgCl}^{10}$$

Reaction [3] is at equilibrium if

$$E_{Au} = E_{(CN)_2} \qquad [6]$$

From Eq. [4] and [5] it follows that equilibrium is achieved in a soft gold bath at room temperature if

$$\ln [CN^-][(CN)_2]^{1/2} = -16.8$$

i.e., if the cyanide and cyanogen concentrations are about 10^{-5} moles/liter.

Under equilibrium conditions, the mass balance of reaction [3] is shifted to the right as the concentration of cyanide decreases. Continuous removal of CN^- and $(CN)_2$ species from the reaction surface, *e.g.*, under the conditions of a rotating-disk electrode, allows continued deposition of gold. Favorable conditions for the reaction were generated in the experiments by continued degassing of the electrolyte. At *p*H = 7, the cyanide ion is protonated to form HCN, which along with cyanogen tends to escape into the gas phase. A large surface to volume ratio and agitation of the solution were used to promote this transition.

For the system under consideration, the deposition rate of gold i_{Au}, is equal to the mass fluxes of Au(CN)$_2^-$, CN^-, and $(CN)_2$

$$i_{Au} = \frac{k_1}{\delta} \Delta[Au(CN)_2^-] = -\frac{k_2}{\delta} \Delta[CN^-] = -\frac{k_3}{\delta} \Delta[(CN)_2] \qquad [7]$$

The Δ's indicate the difference between bulk and surface concentrations; k_1, k_2, and k_3 are constants and δ represents the diffusion layer thickness. At a rotating-disk electrode, the velocity of rotation, w, influences the diffusion layer thickness δ in the inverse proportion to $\sqrt{w}$ (11)

$$\delta = 1.61 \frac{D^{1/3}}{\nu} \frac{\nu}{w} \qquad [8]$$

(D = diffusion coefficient, ν = kinematic viscosity).

Concerning the concentration differences, $\Delta[CN^-]$ and $\Delta[(CN)_2]$, the following inequalities may be both true, both false, or either of them true.

$$[CN^-] \text{ (bulk)} << [CN^-] \text{ (surface)} \qquad [9]$$

$$[(CN)_2] \text{ (bulk)} <<](CN)_2[\text{ (surface)} \qquad [10]$$

If both are true then

$$\Delta[CN^-] = [CN^-] \text{ (surface)} \qquad [11]$$

$$\Delta[(CN)_2] = [(CN)_2] \text{ (surface)} \qquad [12]$$

From Eq. [7] together with Eq. [8], [11], and [12] (dropping the specific reference to the surface in Eq. [11] and [12]) it follows that

$$\frac{d \log i_{Au}}{d \log w} = \frac{d \log[CN^-]}{d \log w} + \frac{1}{2} \qquad [13]$$

$$\frac{d \log i_{Au}}{d \log w} = \frac{d \log[(CN)_2]}{d \log w} + \frac{1}{2} \qquad [14]$$

The concentration terms in Eq. [13] and [14] are expected to deviate from zero for the conditions of the electroless gold deposition.

In a carefully executed experiment at two velocities of the rotating-disk electrode, the rate of gold deposition was found to vary proportionally to $w^{1/4}$. This result indicates that the concentration terms in Eq. [13] and [14] are $-1/4$. Correlated with the variation of the deposition rate, the electrode potential was measured to increase by 0.032V per decade increase in rotation velocity. The combination of this information with the derivatives of Eq. [4] and [5] yields for 65°C (assuming that Eq. [9] and [10] are both true)

$$\frac{d E_{Au}}{d \log w} = -0.134 \frac{d \log[CN^-]}{d \log w} = 0.033V \qquad [15]$$

$$\frac{d E_{(CN)_2}}{d \log w} = -0.067 \frac{d \log[CN^-]}{d \log w} + 0.033 \frac{d \log[(CN)_2]}{d \log w} = 0.0084V \qquad [16]$$

Comparing Eq. [15] and [16] with the observed value of 0.032V per decade increase in rotation velocity it is evident that only Eq. [15] and, therefore, Eq. [9] and [13] are consistent with the experimental results. Hence E_{Au} is the controlling potential and reaction [2] is closer to its equilibrium than the electron donor reaction [1]. At potentials corresponding to the plateau section of Fig. 3 the deposition rate of gold was also found to follow the $w^{1/4}$ dependence as demonstrated in Fig. 4. It is noted that Eq. [7]-[9] may be insufficient to account for the observed transport process because the rate of cyanide removal from the reaction surface is most certainly enhanced by the protonation reaction

$$H^+ + CN^- \rightleftarrows HCN \quad (pK_A = 9) \qquad [17]$$

Assuming either extreme or minimal deviation from the equilibrium of reaction [17], the concentration of free cyanide at the surface of the rotating-disk electrode was calculated by means of Eq. [7] and [8]. Inserting the results into Eq. [5] yields the equilibrium potential for each polarization condition.

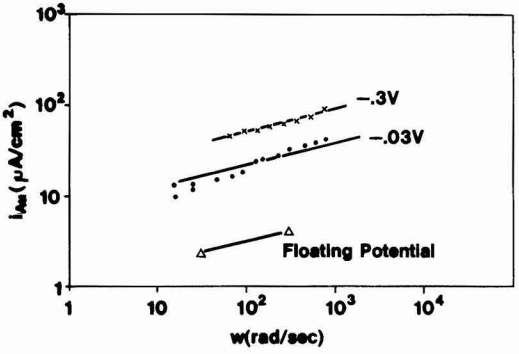

Fig. 4. Dependence of the Au deposition rate in the plateau range on convection.

The following is concluded from the comparison of the calculated with the applied electrode potentials. Under electroless and mildly polarized conditions at 65°C between 0.043 and −0.02V *vs.* Ag/AgCl, reaction [17] and electrode reaction [2] are practically at equilibrium. At current densities within the linear portion of the polarization curve, between −0.5 and −0.9V *vs.* Ag/AgCl, reaction [17] is far from its equilibrium and the difference between the calculated and the applied potential exceeds 0.1V, *i.e.*, the deposition of gold is activation controlled. The plateau section of the polarization curve is identified, therefore, as the result of the influence of the cyanide protonation on the equilibrium electrode potential.

Deposition of gold under activation control.—The equation describing the rate of a cathodic electrode process that proceeds under activation control at potentials far from the equilibrium potential in the absence of the double layer effect has the general form (12)

$$i = i_o \exp\left[-\alpha n \frac{\mathbf{F}}{RT} (E - E^e) \right] \qquad [18]$$

with

$$i_o = n\mathbf{F}k^\circ \; a_{ox}^{(1-\alpha)} \; a_R^{\alpha} \qquad [19]$$

where α = transfer coefficient; n = number of electrons exchanged; E = electrode potential; E^e = equilibrium electrode potential; a_{ox} = activity of the oxidized species; a_R = activity of the reduced species; and k° = apparent standard rate constant.

This equation may be used to correlate the slope of the polarization curves in Fig. 1 and 3 with specific reactions involved in the electrode process. From Eq. [18] and [19] it follows

$$\frac{d \ln i}{d E} = \frac{d \ln i_o}{d E} - \alpha n \frac{\mathbf{F}}{RT} + \alpha n \frac{\mathbf{F}}{RT} \frac{d E^e}{d E} \qquad [20]$$

$$\frac{d \ln i_o}{d E} = (1 - \alpha) \frac{d \ln a_{ox}}{d E} + \alpha \frac{d \ln a_R}{d E} \qquad [21]$$

In the present application, E^e is identical with E_{Au} of Eq. [5]. For constant hydrodynamic conditions the cyanide concentration at the electrode surface is proportional to the gold partial current, i_{Au}. Therefore, with Eq. [5], at constant convection

$$d E_{Au} = -2 \frac{RT}{\mathbf{F}} d \ln [CN^-] = -2 \frac{RT}{\mathbf{F}} d \ln i_{Au} \qquad [22]$$

Combining Eq. [20]-[22] yields for the deposition of gold (converting to the common logarithm)

$$\frac{d \log i_{Au}}{d E} = \frac{0.434}{1 + 2\alpha} (1 - \alpha) \frac{d \log a_{ox}}{d E} + \alpha \frac{d \log a_R}{d E} - \alpha \frac{\mathbf{F}}{RT} \qquad [23]$$

In many metal deposition reactions, α is found to be approximately 0.5. Accordingly, the slopes of log i *vs.* E curves usually show a slope that is equal to a simple fraction of $S = 0.434\mathbf{F}/2RT$. This is also observed in Fig. 1 and 3 for strong cathodic polarization, where the slopes amount to $-4.4V^{-1}$ at 30°C and $-3.6V^{-1}$ at 65°C. Considering the precision of the measurements, these slopes agree well with the assumption of $\alpha = 0.5$ and with

$$\frac{d \log i_{Au}}{d E} = -\frac{0.434\mathbf{F}}{4RT} \qquad [24]$$

By comparison with Eq. [23] it is concluded that

$$\frac{d \log a_{ox}}{d E} = -\frac{d \log a_R}{d E} \qquad [25]$$

Two distinct reaction paths can be visualized, which both conform with Eq. [25]:

The electron transfer proceeds without prechemical adsorption of the oxidized species ($Au(CN)_2^-$), to form Au atoms whose energetic state is not significantly different from that of their final lattice site. In this case

$$d \log a_{ox} = -d \log a_R = 0 \qquad [26]$$

The electron transfer is preceded by the chemisorption of the oxidized species and followed by the dissociation of the reduced species in the adsorption layer, according to the following sequence:

Prechemical adsorption equilibrium

$$Au(CN)_2^- \rightleftarrows (AuCN)ad + CN^- \qquad [27]$$

Electron transfer step (rate limiting)

$$(AuCN)ad + e \rightleftarrows (Au^\circ CN)^- ad \qquad [28]$$

Postchemical desorption and crystallization

$$(Au^\circ CN)^- ad \rightleftarrows Au(lattice) + CN^- \qquad [29]$$

Equilibria [27] and [29] may be dependent on the crystal orientation of the substrate as well as on various solution properties, *e.g.*, the presence of cobalt or lead. All modifications of equilibria [27] and [29] may result in a modification of the electron transfer probability. For each energetic condition, however, Eq. [25] is applicable. If the electrode is saturated with the adsorbates, then a_{ox} and a_R are independent of concentration variations in the aqueous phase and

$$d \log a_{ox} = -d \log a_R = 0 \qquad [26a]$$

Observations relating to effects of adsorption.—The effect of adsorption on the crystal size and preferred orientation of electrodeposits is, qualitatively, well known, as evidenced by the commercial use of addition agents and brighteners. Certain features of the gold-plating system are also indicative of adsorption processes and are discussed here.

The structure of soft gold is commonly referred to as "columnar," because etched cross sections show longish crystallites whose length axes coincide with the growth direction of the deposit. The nucleation rate is, evidently, small, and the tendency toward preferred growth orientation is large. If soft gold is deposited on the polished surface of a polycrystalline, annealed fcc metal, a strong epitaxial effect is observed. Substrate grains with the "right" orientation produce well-formed gold crystals at a substantially higher rate than adjoining grains, which do not have the "right" orientation, as shown in Fig. 5. Hard gold deposits, in contrast, have a grain size in the submicron range and exhibit, intrinsically, featureless surfaces. The nucleation rate during hard gold deposition is many orders of magnitude higher than during soft gold deposition.

It is noted that the principal difference between soft gold and hard gold lies in the crystallization behavior, while the electron transfer step is activation controlled in both cases. The role of adsorbed species is, therefore, that of either increasing or decreasing the activation

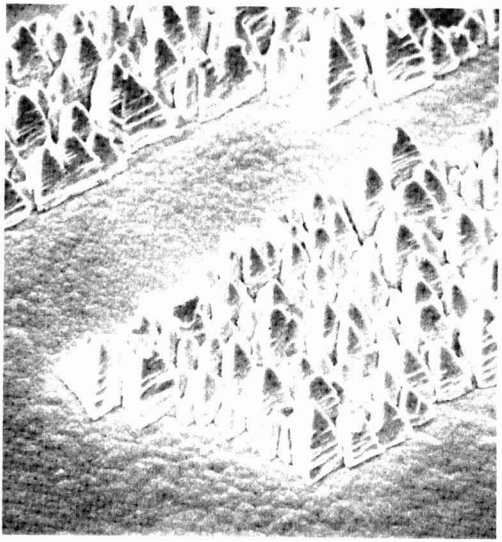

Fig. 5. Epitaxial growth of Au crystals on the surface of an annealed fcc metal.

energy of the electron transfer step. In terms of electrode processes, each crystal orientation has, at constant potential, a typical crystallization current density $i\{a, b, c\}$ (13), where for example

$$i\{100\} \neq i\{110\} \neq i\{111\} \quad [30]$$

Dependent on the relative magnitude of the crystallization current densities, more or less pronounced preferential orientation of the gold deposit results. The experimental current density, i_{Au}, is equal to the average of the various crystallization current densities. If the crystallization process is initiated on randomly oriented nuclei, preferential deposition tends to generate more surface area of equivalent orientation and an increase in i_{Au} results. This is observed during the deposition of regular and lead-doped soft gold. If the differentiation between the crystallization current densities is enhanced, *e.g.*, under the condition that coadsorbed lead lowers the activation energy of the electron transfer, Eq. [28], then one crystallization current density may become dominant. With negligible growth in all but one orientation, the increase in reactive surface area, and as a result the increase of i_{Au}, is proportional to the deposition time. This condition of extreme differentiation between the crystallization current densities is observed in Fig. 2 ($it \propto t^2$).

The deposition of hard gold proceeds without noticeable variation in i_{Au}. This result is consistent with the size of the crystallites formed, whose growth period is limited to a few seconds. In terms of Eq. [28], and in contrast to the effect of lead, the coadsorption of cobalt provides for an increase in the activation energy of the electron transfer. Under this condition, the differentiation between the crystallization current densities may be minimized, but more importantly, the nucleation rate is increased, thus explaining the texture of hard gold deposits.

Perturbation of the adsorption layer.—The transient behavior of the gold-cyanoaurate electrode has, to some extent, been described earlier (7). Additional experiments were deemed necessary to clarify the common and contrasting features of the deposition of soft gold, lead-doped soft gold, and hard gold. The potential transients of a rotating-disk electrode, after prepolarization at constant potential, were recorded, therefore, for a variety of conditions.

Regardless of the specific experimental conditions the potential transients were always found to follow the same pattern. After the interruption of the cathodic (*i.e.*, negative) polarization, the potential was found to increase in at least three distinctly different modes. The initial, fastest variation of the potential has been identified with double layer charging effects. The subsequent, slower variation was recognized to depend on the potential and the duration of the prepolarization period, as well as on the rotation velocity of the electrode. The third mode of potential variation proceeded at constant rate, dependent only on the temperature; however, the range over which the variation occurred was also dependent on other variables. Figure 6 shows the transients for hard gold, prepolarized for 3 min at potentials ranging from -1.1 to -0.4V *vs.* SCE in 0.1V steps. On the time scale used, the double layer charging effect is not discernible (regime 1).

The potential transients are strong indication that the electrochemical reduction of $Au(CN)_2^-$ proceeds via chemisorbed species (14, 15). Details of the curves

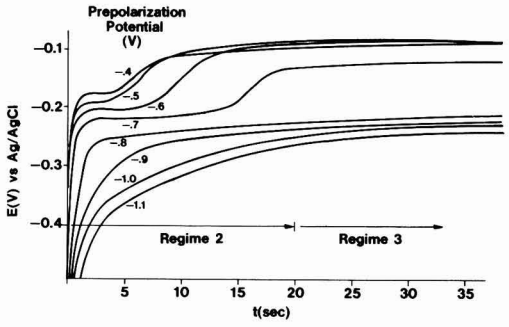

Fig. 6. Potential transients of the Au/Au(CN)$_2$-system (hard gold) after prepolarization.

shown in Fig. 6 are interpreted in terms of the sequence of reactions [27]-[29] as follows:

During the prepolarization period, reactions [27] and [29] are at equilibrium, while reaction [28] is not. At the instant of the current interruption, reaction [28] starts to approach equilibrium at a rate limited only by the recharging of the double layer. Once equilibrium is achieved, reactions [27] and [29], which were previously independent, are now coupled through reaction [28] in correspondence with Eq. [2]. Thermodynamic equilibrium with respect to the bulk of the electrolyte is, however, not achieved yet, mostly because the surface concentrations of CN^-, $(AuCN)ad$, and $(Au°CN)ad^-$ are higher than when in equilibrium with the bulk. Removal of CN^- tends to shift both equilibria, reactions [27] and [29], to the right. $(AuCN)ad$ remains constant, therefore, while $(Au°CN)ad^-$ decomposes. This occurs within the range of regime 2 of Fig. 5. The process appears to be diffusion controlled, as evidenced by the strong dependence of the potential decay upon the rotation velocity of the disk electrode. At all times, the potential is controlled by the ratio of $(AuCN)ad$: $(Au°CN)ad^-$. Predictably, $(Au°CN)ad^-$ as source of cyanide will be depleted after some time. Due to the lack of CN^-, the excess amount of $(AuCN)ad$ cannot revert to its origin, $Au(CN)_2^-$. The removal of $(AuCN)ad$ has to proceed via the electron transfer reaction [28], which seems impossible without a source of electrons. An electron source is available, however, as evidenced by the electroless deposition of gold. In preference to reaction [3] the process may be formulated as

$$(AuCN)ad \rightarrow Au(lattice) + \tfrac{1}{2}(CN)_2 \qquad [31]$$

It has been discussed earlier that the electron donor reaction [1] is not at equilibrium. Reaction [31] is, therefore, not at equilibrium either and the removal of $(AuCN)ad$ from the surface should be a first-order reaction. This is confirmed by the observation that the potential decay in regime 3 shows a close to linear dependence on time.

Addressing the potential variation in regime 3 of Fig. 6, it is noted that for prepolarization potentials <-0.8V the curves nearly coincide, while for potentials >-0.8V substantially deviating curves are obtained. This dispersion signifies the change of the surface concentration of the adsorbate from a saturated to a less-than-saturated state. The corresponding behavior, obtained with the other electrolytes, leads to the conclusion that the electrodeposition of gold proceeds, in practice, under surface saturation with $(AuCN)$. It is assumed that surface saturation means a nearly complete monolayer of the adsorbate, regardless of the type of electrolyte. From the potential level, at which the desorption of $(AuCN)ad$ starts in the three different electrolytes, it follows with equilibrium [28] that the surface concentration of $(Au°CN)ad^-$ is greatest for regular soft gold and about equal for lead-doped soft gold and hard gold. It should be mentioned that these results were obtained under prepolarization conditions where the deposition of lead-doped soft gold was far better equilibrated ("depolarized") than that of regular soft gold. In view of the crystallization phenomena discussed earlier, it is concluded that the establishment of a preferred crystal orientation is accompanied by a shift of equilibrium [29] from left to right. Concerning the behavior of the hard gold system, it is concluded that equilibrium [28] is shifted to the left relative to the conditions of soft gold deposition.

Reversibility of the electrode processes.—The electrochemical oxidation of gold in cyanide solution should, doubtlessly, follow the sequence of reactions [27]-[29] in reverse. An experiment was carried out accordingly in which a gold disk electrode was polarized anodically in 0.5M KCN solution at 55°C and two rotation velocities. Figure 7 shows the results which are interpreted as follows. Near the equilibrium potential at about -0.9V *vs.* Ag/AgCl the anodic current

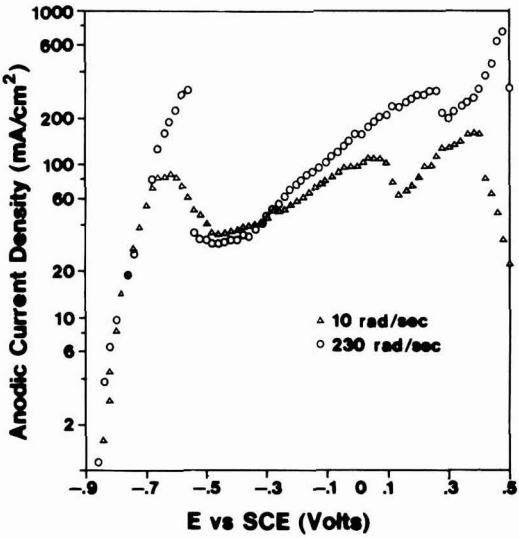

Fig. 7. Anodic dissolution of gold in 0.5M KCN at 55°C

density rises, as expected, very steeply. With increasing potential three maxima and minima are passed. The maxima at -0.6V and 0-0.2V are caused by diffusion limitation of the cyanide ions. As the surface concentration of CN^- approaches zero, the concentration of $(Au°CN)ad^-$ also approaches zero, which results in a rapid drop of the current density. Thereafter, even though the surface concentration of CN^- is not zero anymore, the dissolution rate at -0.5V is controlled by the formation of $(Au°CN)ad^-$. Over the potential range, where in previous experiments the surface concentration of $(AuCN)ad$ was found to deviate from saturation, the current density rises again. The decrease in coverage with AuCN promotes, necessarily, the reaction of gold in lattice sites with cyanide, and hence the rate of dissolution. At the point where once again the concentration of CN^- at the electrode surface drops to zero a change in mechanism occurs. At 0.1-0.2V it appears that trivalent gold is formed, as the current density at 225 rad/sec reaches 1.5 times the value observed at the other maxima. The minimum at 0.5V was positively identified with the onset of passivation since at still higher potentials no dissolution of gold was observed.

The features of the anodic dissolution of gold in cyanide solution are evidently compatible with the existence and the controlling nature of chemisorbed layers postulated for the cathodic reduction of dicyanoaurate.

Summary and Conclusions

The mechanism of the electrochemical reduction of dicyanoaurate was studied by means of steady-state and relaxation methods combined with rotating-disk electrode techniques. The experimental results permit the following statements:

1. The deposition of soft gold, lead-doped soft gold, and cobalt-hardened gold proceeds via one common mechanism that involves adsorption equilibria preceding and following the electron transfer step.

2. Special effects such as the epitaxy and preferred orientation of soft gold deposits, the small grained texture of hard gold, and the lead-induced depolarization effect during soft gold deposition can be explained in terms of the energetic states of the adsorbed, oxidized, and reduced gold species. These are influenced by the crystal orientation of the deposition site and by the coadsorption of cobalt and lead ions, respectively.

3. The proposed mechanism explains readily the features of the anodic dissolution of gold in alkaline cyanide electrolyte.

Acknowledgments

Thanks are due to P. C. Milner and P. W. Renaut for stimulating discussions, and to N. H. Winquist for preparing the electron micrographs.

Manuscript submitted May 19, 1977; revised manuscript received Nov. 14, 1977.

Any discussion of this paper will appear in a Discussion Section to be published in the December 1978 JOURNAL. All discussions for the December 1978 Discussion Section should be submitted by Aug. 1, 1978.

Publication costs of this article were assisted by Bell Laboratories.

REFERENCES

1. H. Y. Cheh and R. Sard, *This Journal*, **118**, 1737 (1971).
2. J. A. Harrison and J. Thompson, *J. Electroanal. Chem.*, **40**, 113 (1972).
3. J. D. E. McIntyre and W. F. Peck, Jr., *This Journal*, **123**, 1800 (1976).
4. R. L. Cohen, K. W. West, and M. Antler, *ibid.*, **124**, 342 (1977).
5. G. B. Munier, *Plating (East Orange, N.J.)*, **56**, 1151 (1969).
6. Ch. J. Raub, A. Knoedler, and J. Lendvay, *ibid.*, **64**, 35 (1976).
7. E. T. Eisenmann, "The Effect of Current Modulation on the Porosity of Gold-Cobalt Electrodeposits," to be published.
8. H. A. Reinheimer, U.S. Pat. 3,833,487 (1974).
9. J. D. E. McIntyre and W. F. Peck, Jr., *This Journal*, **123**, 1800 (1976).
10. NBS Technical Note 270-3, 4, U.S. Department of Commerce (1968).
11. V. G. Levich, "Physical Hydrodynamics," p. 69, Prentice-Hall, Inc., Englewood Cliffs, N.J. (1962).
12. P. Delahay, "Double Layer and Electrode Kinetics," p. 153, John Wiley & Sons Inc., New York (1965).
13. W. E. Tragert and W. D. Robertson, *This Journal*, **182**, 86 (1955).
14. M. Maja, *Atti Accad. Sci. Torino Cl. Sci. Fis. Mat. Nat.*, **99**, 1111 (1965).
15. D. M. MacArthur, *This Journal*, **119**, 672 (1972).

Flatband Potentials and Donor Densities of Polycrystalline α -Fe_2O_3 Determined from Mott-Schottky Plots

John H. Kennedy* and Karl W. Frese, Jr.**

Department of Chemistry, University of California, Santa Barbara, California 93106

ABSTRACT

Capacitance and conductivity measurements were made on high purity α-Fe_2O_3 and TiO_2-doped α-Fe_2O_3 in liquid junction cells. Flatband potentials and donor densities were determined from Mott-Schottky plots and evidence for deep and shallow donors is presented. Potentials of zero photocurrent were determined using chopped light and were in excellent agreement in basic solution with flatband potentials calculated from 1 kHz capacitance measurements.

Detailed studies of flatband potentials and their correlation with photoeffects have been carried out to date largely on single crystal samples. Also, it is not clear that space charge layer capacitance theories would apply to polycrystalline electrodes in electrochemical cells and that photoeffects could be obtained from polycrystalline samples comparable to single crystal samples. To help answer these questions we report here on capacitance data for the α-Fe_2O_3-electrolyte junction. Current-potential characteristics of these polycrystalline samples will be published separately. In a previous paper (1) we reported on the flatband potential (and photocurrents of) polycrystalline sintered $BaTiO_3$ electrodes with results which agreed well with published data for single crystal samples (2). The techniques used for the studies of $BaTiO_3$ have now been extended to the studies of other metal oxides, in particular, α-Fe_2O_3.

Experimental

Electrode preparation.—Alpha-iron(III) oxide n-type semiconductor electrodes were prepared from either high purity, 99.999% (Apache Chemical Company) or analytical reagent-grade (Mallinckrodt) material. The ultrapure material was pressed and sintered in air at various temperatures from 1050° to 1320°C for 4 hr and then quenched in room temperature air. This treatment resulted in electrodes with apparent densities of 75-85% of theoretical and conductivities ranging from 8×10^{-6} to 2×10^{-4} Ω^{-1} cm^{-1}. Attempts to make semiconducting electrodes from the reagent-grade material by air quenching always resulted in nonconductive material even for sintering temperatures of up to 1300°C. This was probably due to the presence of Cu^{2+}, Zn^{2+}, and Mg^{2+} impurities which would tend to compensate the n-type conductivity. However, the reagent-grade material could be made highly conductive ($\sigma \sim 1$ Ω^{-1} cm^{-1}) by heating in a stream of N_2 for temperatures $\gtrsim$1100°C. The conductivities were difficult to control, and therefore TiO_2 doping was used to obtain highly doped samples. Also, the N_2 reduced samples showed virtually no photoeffect, probably due to the very thin space charge layer. The reagent-grade material doped with TiO_2 was sintered at 1150°-1200°C in air for 14 hr and quenched in room temperature air. Densities were 95-99% of theoretical. The TiO_2 doping level was varied from 0.05% to 2% (Ti/Fe). No further treatment was given the electrodes after sintering.

A copper wire electrode lead was attached to the semiconductor electrodes by applying Ag epoxy (Epoxy Technology). The electrode and wire were then sealed in a glass tube with epoxy resin.

Capacitance measurements.—Capacitance measurements of the cell, α-Fe_2O_3/electrolyte/Pt, were made

* Electrochemical Society Active Member.
** Electrochemical Society Student Member.
Key words: semiconductor, photo conductivity, capacitance.

using a General Radio 1650-A impedance bridge operated at 1 kHz. Electrode potential measurements were made (*vs.* SCE) with a Keithley 610-C electrometer.

Dielectric constant measurements.—Dielectric constant measurements of high density, insulating α-Fe_2O_3 were made at various frequencies in the range 1-50 kHz. The dielectric cell was a parallel plate type with the area of one plate much larger (~150X) than the other. The cell was connected to the GR 1650-A impedance bridge and the capacitance measured with and without the α-Fe_2O_3 disk. Electrodes of conducting Ag epoxy were applied to each face of the α-Fe_2O_3 disks. A sine wave a-c voltage (10 mV amplitude) was applied to the bridge using a Hewlett-Packard Function Generator, Model 3311A.

Pulsed photocurrent.—Pulsed photocurrent measurements were made by using polychromatic light from a 300W tungsten source and a rotating-disk chopper. The chopping frequency was 40-60 Hz. The photocurrent was measured as the voltage drop across a precision 5 kΩ resistor with a Tektronix Model 564B storage oscilloscope with a Type 3A6 dual trace amplifier and Type 3B3 time base. The α-Fe_2O_3 electrode was biased cathodically until the voltage amplitude decreased to zero. The minimum photocurrent pulse which could be detected was $\lesssim 0.1$ μA.

Resistance measurements.—The resistance of the cell α-Fe_2O_3/electrolyte/Pt was measured under zero applied voltage with the impedance bridge at 1 kHz. The resistance was predominantly due to the α-Fe_2O_3 electrode since the contributions to the cell resistance from the Pt electrode and the electrolyte were negligible.

Results

Flatband potentials.—Mott-Schottky plots (3) were constructed from capacitance *vs.* electrode potential measurements at 1 kHz and are shown in Fig. 1 and 2 for undoped α-Fe_2O_3. The flatband potentials were obtained from the intercepts of $1/C^2$ *vs.* V by subtracting $kT/q = 0.025$V from the intercept. The flatband potentials and donor densities calculated from these plots are given in Table I.

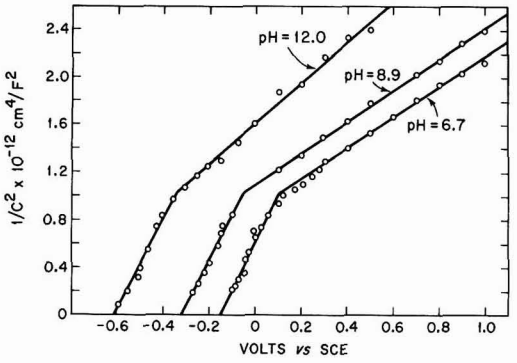

Fig. 1. Mott-Schottky plots for polycrystalline α-Fe_2O_3. Electrode No. 5. In dark, $t = 23$°C.

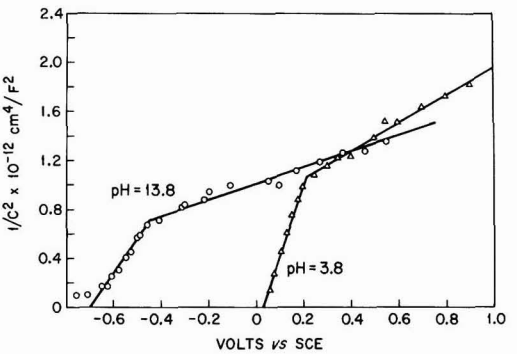

Fig. 2. Mott-Schottky plots for polycrystalline α-Fe_2O_3. Electrode No. 4. In dark, $t = 23$°C.

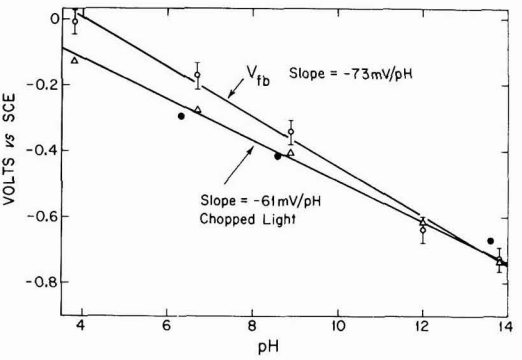

Fig. 3. Flatband potential and zero photocurrent potential of polycrystalline α-Fe_2O_3 *vs.* pH, $t = 23$°C. Solid circles from Ref. (4).

The flatband data are in remarkably good agreement with the data reported by Quinn *et al.* (4) for single crystal α-Fe_2O_3 differing by less than 0.1V. However, these authors did not correlate their data with pH. Flatband potentials for our polycrystalline samples at various pH values are shown in Fig. 3 together with the single crystal data (solid circles) given in Ref. (4). It is not clear whether or not the deviation of the pH dependence of the flatband potential from −59 mV/pH was significant. The deviation appears to increase in more acidic solutions indicating that electrode instability may be a factor. Another possible reason could be specific adsorption of chloride ions.

A striking feature of the Mott-Schottky plots is the sharp break at about +0.3V *vs.* flatband. Values

Table I. Shallow (N_1) and deep (N_2) donor densities obtained from Mott-Schottky plots (99.999% α-Fe_2O_3)

Electrolyte	pH	V_{fb} (SCE)	V_C (SCE)	$N_1 + N_2$, cm^{-3}	N_1, cm^{-3}	N_2, cm^{-3}
0.5M KCl*	3.8	0.00	0.21	1.5×10^{18}	3.1×10^{17}	12×10^{17}
0.5M KCl**	6.7	−0.17	0.10	1.3×10^{18}	4.1×10^{17}	9×10^{17}
0.5M KCl***	8.9	−0.34	−0.05	1.3×10^{18}	4.5×10^{17}	9×10^{17}
0.1M NaOH	12.2	−0.64	−0.35	1.0×10^{18}	4.6×10^{17}	5×10^{17}
2.0M NaOH	13.8	−0.73	−0.45	2.6×10^{18}	6.3×10^{17}	20×10^{17}

* Phthalate buffer.
** Phosphate buffer.
*** Borate buffer.

of the critical potential (V_C) for the break are given in Table I. The break was observed for three different samples at pH values from 3.8 to 13.8 in both KCl and NaOH solutions. This interesting feature can be explained by assuming the existence of two kinds of donors, one very close to the conduction band and the other at about 0.6V below the conduction band, and will be discussed in detail.

The potential of zero photocurrent was measured with pulsed illumination (nearly full output of 300W tungsten lamp) for the samples used in the capacitance measurements and the points shown in Fig. 3 represent averages at each pH. These potentials varied regularly with pH at a rate of −61 mV/pH. In the more basic solutions (pH = 12.2-13.8) the net current at zero photocurrent was cathodic whereas in more acidic solutions (pH 3.8-8.9) the net current was anodic.

Typical Mott-Schottky plots for TiO_2-doped α-Fe_2O_3 are shown in Fig. 4, and Table II summarizes the data for the total donor densities, N, TiO_2 stoichiometry, the bulk ionized donor densities, N^+, calculated from conductivity data, and the apparent fraction of ionized donors.

Dielectric constant.—The dielectric constant, ϵ, was calculated from capacitance data according to the following equation

$$\epsilon = 9.0 \times 10^{11} \frac{4\pi t}{A} \Delta C \qquad [1]$$

where t and A are the disk thickness and area and ΔC is the difference in the capacitance with and without the sample. A dielectric constant value of 80 was obtained. Quinn *et al.* (4) reported a value of 120 for the dielectric contact for α-Fe_2O_3 for an unspecified single crystal face.

Discussion

The two slopes for each of the plots in Fig. 1 and 2 suggest that the Mott-Schottky slope may be written (5) as

$$s_1 = \frac{2}{\epsilon\epsilon_0 q N_1} \quad \text{for} \quad V < V_C \qquad [2]$$

and

$$s_2 = \frac{2}{\epsilon\epsilon_{0q}(N_1 + N_2)} \quad \text{for} \quad V > V_C \qquad [3]$$

where N_1 and N_2 are the densities of the shallow and deep donors, respectively, and V_C is a critical voltage for ionization of the deep donors in the space-charge layer. The existence of a critical voltage can be traced to the nature of the Fermi-Dirac distribution function governing the number of ionized donors. The relation (3)

$$N^+(x) = N_2\left[\frac{1}{1 + g_e\,(E_F - E_D + e\Delta\phi(x)/kT)}\right] \qquad [4]$$

gives the number of ionized donors as a function of position, total deep donor density, donor energy level, and the space-charge potential drop. The degeneracy factor, g, is usually assumed to be two, however, for transition metal ion donors it could be larger due to spin-orbit coupling. It is characteristic of the Fermi-Dirac distribution function that a large change in occupancy is realized over a narrow voltage range, in fact according to Eq. [4] the fraction ionized changes from 0.1 to 0.9 within a ~100 mV change in $\Delta\phi(x)$. If V_C is arbitrarily identified with $N^+/N_2 = 0.5$ then

$$e(V_C - V_{fb}) \cong E_F - E_{D_2} \qquad [5]$$

within ~50 mV. The data show that the deep donor is located about 0.3V below E_F. Flatband data can give the position of the Fermi level relative to the bottom of the conduction band (E_C) provided the density of states in the conduction band, N_C, is known (5)

$$E_C - E_F = kT \ln \frac{N_C}{N_1} \qquad [6]$$

assuming each shallow donor donates one electron to the conduction band. For iron oxide N_C has been assumed to be 4×10^{22} cm^{-3} (6), the number of cations in the lattice. This is consistent with the model of phonon-assisted hopping for the conductivity mode in narrow d-band semiconductors. The Fermi level is calculated to be 0.3V (for $N_1 = 4 \times 10^{17}$ from Table I) below the conduction band. The position of the deep donor level is then 0.6V below the conduction band.

The conductivity and spectroscopic studies of Morin (7) were consistent with a deep donor at 0.6-0.8 eV below the conduction band. Gardner *et al.* (8) also found their low temperature conductivity data gave an activation energy of 0.7 eV that could be associated with the energy for carrier formation. A summary of the energy level data is shown in Fig. 5. It should be noted that since the chemical or physical identity

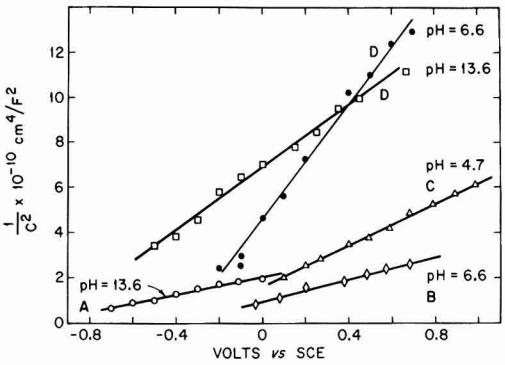

Fig. 4. Mott-Schottky plots for polycrystalline α-Fe_2O_3 at various TiO_2 doping levels and pH values. A, B, C, D refer to different TiO_2 doping levels as shown in Table II.

Table II. Total donor density (N) and ionized donor density (N^+) for TiO_2-doped α-Fe_2O_3

Electrolyte	V_{fb}	pH	N^+, cm^{-3}	N (Mott-Schottky), cm^{-3}	TiO_2, a/o	N^+/N
				Sample A $\sigma = 1.1 \times 10^{-3}$ (Ω-cm)$^{-1}$		
0.5M Acetate/HOAc	−0.23	4.7	3.2×10^{17}	8.8×10^{19}	1.0	4×10^{-3}
0.5M KCl	−0.43	6.6	3.2×10^{17}	8.3×10^{19}	1.0	4×10^{-3}
1M NaOH	−1.06	13.6	3.2×10^{17}	7.3×10^{19}	1.0	4×10^{-3}
				Sample B $\sigma = 4.5 \times 10^{-4}$ (Ω-cm^{-1})		
0.5M KCl	−0.42	6.6	1.3×10^{17}	7.0×10^{19}	0.5	2×10^{-3}
				Sample C $\sigma = 1.9 \times 10^{-3}$ (Ω-cm)$^{-1}$		
0.5M Acetate/HOAc	−0.38	4.7	5.6×10^{17}	3.8×10^{19}	0.25	2×10^{-2}
				Sample D $\sigma = 4.4 \times 10^{-4}$ (Ω-cm)$^{-1}$		
0.5M KCl	−0.39	6.6	1.3×10^{17}	1.2×10^{19}	0.1	1×10^{-2}
0.5M KCl	−0.74	9.0	1.3×10^{17}	2.5×10^{19}	0.1	5×10^{-3}
1M NaOH	−1.00	13.6	1.3×10^{17}	1.4×10^{19}	0.1	9×10^{-3}

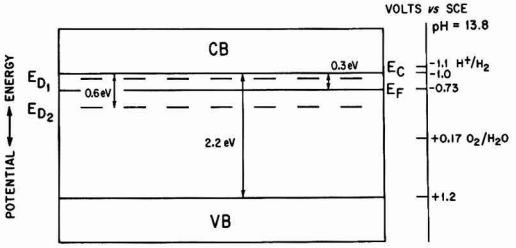

Fig. 5. Energy level diagram. Polycrystalline α-Fe_2O_3

of the donor level at E_2 is not known at present, it may not be an intrinsic property of α-Fe_2O_3 reduced to the level, $N_D \approx 10^{18}$ cm^{-1}. The indirect evidence presented, however, supports the assignment of the deep donor level as being Fe^{2+}.

Evidence for incompletely ionized donors and thus a deep donor level was also found for the TiO_2-doped α-Fe_2O_3 samples. The evidence was gained by comparing ionized donor densities calculated from conductivity and mobility data with donor densities calculated from Mott-Schottky slopes.

Advantage was taken of the fact that the bulk-ionized donor density, N^+, can be calculated from the standard conductivity equation

$$\sigma = N^+ q \mu_n \qquad [7]$$

and that electron mobility (μ_n) remains relatively constant with the doping level (9).

The value of electron mobility to be used in Eq. [7] was calculated by measuring the conductivity of three samples of thermally doped n-type α-Fe_2O_3 (99.999%) at room temperature. The values were 2.35×10^{-4}, 2.95×10^{-4}, and 5.62×10^{-5} $(\Omega\text{-cm})^{-1}$. These three samples showed two distinct Mott-Schottky slopes and the higher slope together with an assumed roughness factor of 2 were used to calculate N^+ for the thermally doped samples. From these values the mobility was calculated. The results for μ_n were 0.012, 0.017, and 0.034 cm^2/V sec for $t = 23°C$ and ionized donor densities of 4×10^{16} to 2×10^{17} cc^{-1}. The average value of 0.021 cm^2/V sec was adopted.

Measurement of the conductivity activation energy for these polycrystalline samples gave values of 0.05-0.10 eV (23°-100°C). Both the mobility and activation energies are in good agreement with the electron mobility equation suggested by Gardner *et al.* (10)

$$\mu_n = \frac{232}{T} e^{-0.1(eV)/kT} \qquad [8]$$

This equation gives a room temperature mobility of 0.016 cm^2/V sec for TiO_2-doped samples.

The value of μ_n could now be used along with conductivity measurements on TiO_2-doped samples (Table II) to calculate N^+, the concentration of ionized donors from Eq. [7]. The values are given in Table II.

The total donor density, N, was calculated from the Mott-Schottky slope according to

$$S = \frac{2}{\epsilon\epsilon_0 q N} \qquad [9]$$

using slopes shown in Fig. 4. As can be seen from Table II the fraction of ionized donors, $N^+/N \sim 5 \times 10^{-3}$. We take this value as strong evidence for a deep donor in TiO_2-doped α-Fe_2O_3. The deep donor level was estimated to be 0.4 eV below the conduction band by using an equilibrium constant approach and the concentrations of ionized and total donors given in Table II.

The flatband potentials extrapolated from the plots in Fig. 4 are about 0.2V more cathodic than those shown in Table I. Two factors could account for this difference. One is that the flatband potential is known (11) to depend on donor density increasing more cathodic by 60 mV per order of magnitude of donor density. This effect amounts to ~0.1V from comparison of the donor densities in Tables I and II. The second effect, pointed out by De Gryse *et al.* (12) is that the extrapolation of $1/c^2$ *vs.* V plots leads to a voltage, V_o, given by

$$V_o = V_{fb} + \frac{kT}{q} - \frac{\epsilon\epsilon_0 q N_D}{2C_H^2} \qquad [10]$$

where C_H is the Helmholtz layer capacitance $\sim 10^{-5}$ F/cm^2. This effect is magnified by high donor densities such as in our TiO_2-doped samples. The estimated shift in V_{fb} for the samples shown in Fig. 3 is 0.1V. Thus, the observed shift of ~0.2V is adequately accounted for by the theory.

We conclude that flatband potential data can be obtained from sintered polycrystalline α-Fe_2O_3 which are consistent with single crystal results, and that donor densities accurate to within a factor of four or less may be obtained without surface roughness corrections.

Acknowledgments

The authors acknowledge partial financial support of this project by the National Science Foundation, Grant No. DMR73-07507 AO2, and by the Committee on Research, University of California.

Manuscript submitted June 30, 1977; revised manuscript received Dec. 12, 1977.

Any discussion of this paper will appear in a Discussion Section to be published in the December 1978 JOURNAL. All discussions for the December 1978 Discussion Section should be submitted by Aug. 1, 1978.

Publication costs of this article were assisted by the University of California.

REFERENCES

1. J. H. Kennedy and K. W. Frese, Jr., *This Journal*, **123**, 1683 (1976).
2. R. D. Nasby and R. K. Quinn, *Mater. Res. Bull.*, **11**, 985 (1976).
3. H. Gerisher, in "Physical Chemistry," Vol. IXA, H. Eyring, D. Henderson, and W. Jost, Editors, chap. 5, Academic Press, New York (1970).
4. R. K. Quinn, R. D. Nasby, and R. J. Baugham, *Mater. Res. Bull.*, **11**, 1011 (1976).
5. V. A. Myamlin and Y. V. Pleskov, "Electrochemistry of Semiconductors," chap. 3, Plenum Press, New York (1967).
6. F. J. Morin, *Phys. Rev.*, **93**, 1195 (1954).
7. F. J. Morin, *ibid.*, **83**, 1005 (1951).
8. R. F. G. Gardner, F. Swett, and D. W. Tanner, *J. Phys. Chem. Solids*, **24**, 1183 (1963).
9. A. J. Bosman and J. H. Van Daal, *Adv. Phys.*, **19**, 1 (1970).
10. R. F. G. Gardner, F. Swett, and D. W. Tanner, *J. Phys. Chem. Solids*, **24**, 1175 (1963).
11. J. F. Dewald, *Bell Syst. Tech. J.*, **39**, 615 (1960).
12. R. De Gryse, W. P. Gomes, F. Cardon, and J. Vennik, *This Journal*, **122**, 711 (1975).

Structure and Cyclic Discharge Behavior of LiAl Electrodes

C. A. Melendres* and C. C. Sy

Argonne National Laboratory, Chemical Engineering Division, Argonne, Illinois 60439

Considerable interest exists in the use of lithium-aluminum alloys as negative electrodes in molten salt secondary batteries (1). A number of recent investigations have dealt with the electrochemical characterization of this binary alloy system. Equilibrium potentials as a function of alloy composition were measured by Yao *et al.* (2) and by Selman and co-workers (3). L'vov *et al.* (4) determined the diffusion coefficient of Li in LiAl at 450°C to be $\sim 10^{-6}$ cm²/sec from measurements of transition times during discharge. Similarly, James (5) has obtained a value of 5×10^{-5} cm²/sec at 450°C from discharge curves. In a study of the kinetics of the electrochemical incorporation of lithium into aluminum (6), we obtained a value for the Li diffusivity in LiAl on the order of 10^{-8} cm²/sec from galvanostatic charging curves. Values obtained on discharging the electrochemically formed LiAl electrodes were one to two orders of magnitude higher than on charging and were poorly reproducible. Realizing that this discrepancy may be due to changes in electrode morphology which accompany the incorporation or extraction of Li, we have conducted the present investigation on the structure of LiAl electrodes. We also hoped to obtain information on the role of electrode structure in determining the cycle life of LiAl electrodes in engineering prototype cells.

Experimental

The electrochemical measurements were carried out inside a glovebox under high purity helium atmosphere. The cell consisted of a 5.5 cm diam alumina crucible with three electrodes (Fig. 1): an Al or LiAl wire working electrode, a LiAl coil counterelectrode, and a reference electrode consisting of a cast Li-Al alloy [40 atomic percent (a/o) Li] that is 0.5 cm diam $\times$ 1.2 cm long. The composition of the latter is in the $\alpha + \beta$ region of the phase diagram (7); its potential at 450°C is about 290 mV anodic of Li/Li^+. The counterelectrode was prepared by electrochemically charging a 0.318 cm diam Al rod (previously formed into a coil) with Li to the $\alpha + \beta$ composition range. The Al working electrode was a 1.6 mm diam wire of 99.99% purity (Marz grade material purchased from Materials Research Corporation, Orangeburg, New York). The LiCl-KCl eutectic electrolyte was polarographic grade and was obtained from Anderson Physics Laboratories (Champaign, Illinois). The electrochemical and associated instruments that were used consisted of a Princeton Applied Research (PAR) Model 173 Potentiostat/Galvanostat, a PAR Model 179 Digital Coulometer, a Hewlett-Packard Model 7040A X-Y Recorder, and an R5103N Oscilloscope. Charged and discharged electrodes were mounted on plastic and examined using standard metallographic techniques. The mounted samples were ground successively through silicon carbide paper of grit sizes 120-C, 180-C, 240-A, 400-A, and 600-A, respectively. Polishing was done with alumina powder of 0.3 and 0.05 μm particle size. The last two operations were both done under oil using a Dow Corning 200 fluid (a dimethylpolysiloxane). Samples for electron microprobe analysis were ground with silicon carbide paper using HYPRES OS lubricant (Engis Equipment Company, Morton Grove, Illinois), polished with dia-

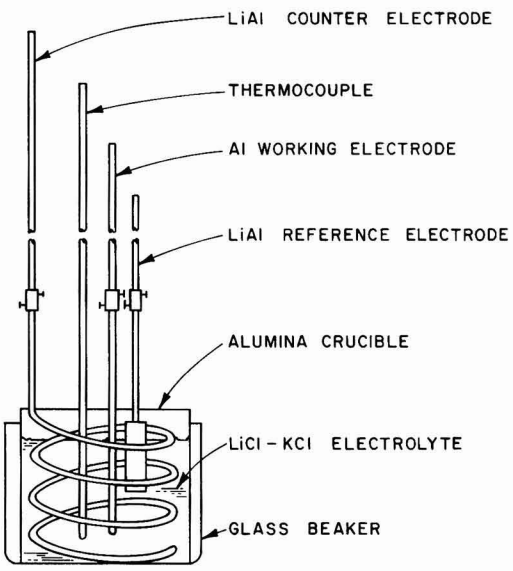

Fig. 1. Experimental apparatus

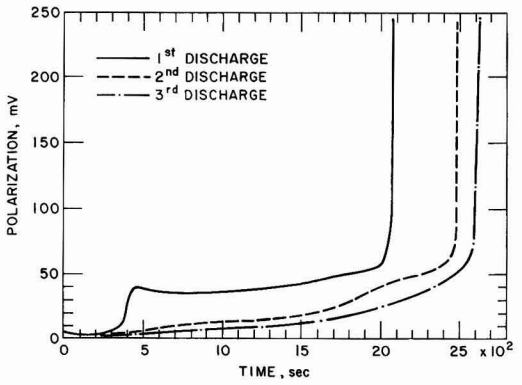

Fig. 2. Anodic polarization curves for successive discharge of LiAl wire electrodes (current density = 107 mA/cm² based on wetted area of original wire, $T = 450$°C).

* Electrochemical Society Active Member.

Key words: LiAl electrode, molten salt electrolyte, LiAl structure and morphology, anodic discharge behavior.

mond paste, and then ultrasonically washed with Freon-113 (Matheson Gas Products).

Results and Discussion

Cyclic discharge behavior of LiAl wire electrodes.— Figure 2 shows typical polarization behavior on cyclic discharge of LiAl wire electrodes that have been initially charged to the β-phase (48 a/o Li). As can be seen from this figure the anodic overpotential remains flat for some time and then increases rapidly. On subsequent discharges (following replacement of the Li removed by recharging at the same current density as initially used), a decrease in anodic polarization and an increase in transition time is observed. Coulometric determination of the charge passed at the transition point shows that the Li extracted anodically is 66, 78, and 81% of the initial loading for the first, second, and third cycles, respectively. The occurrence of a transi-

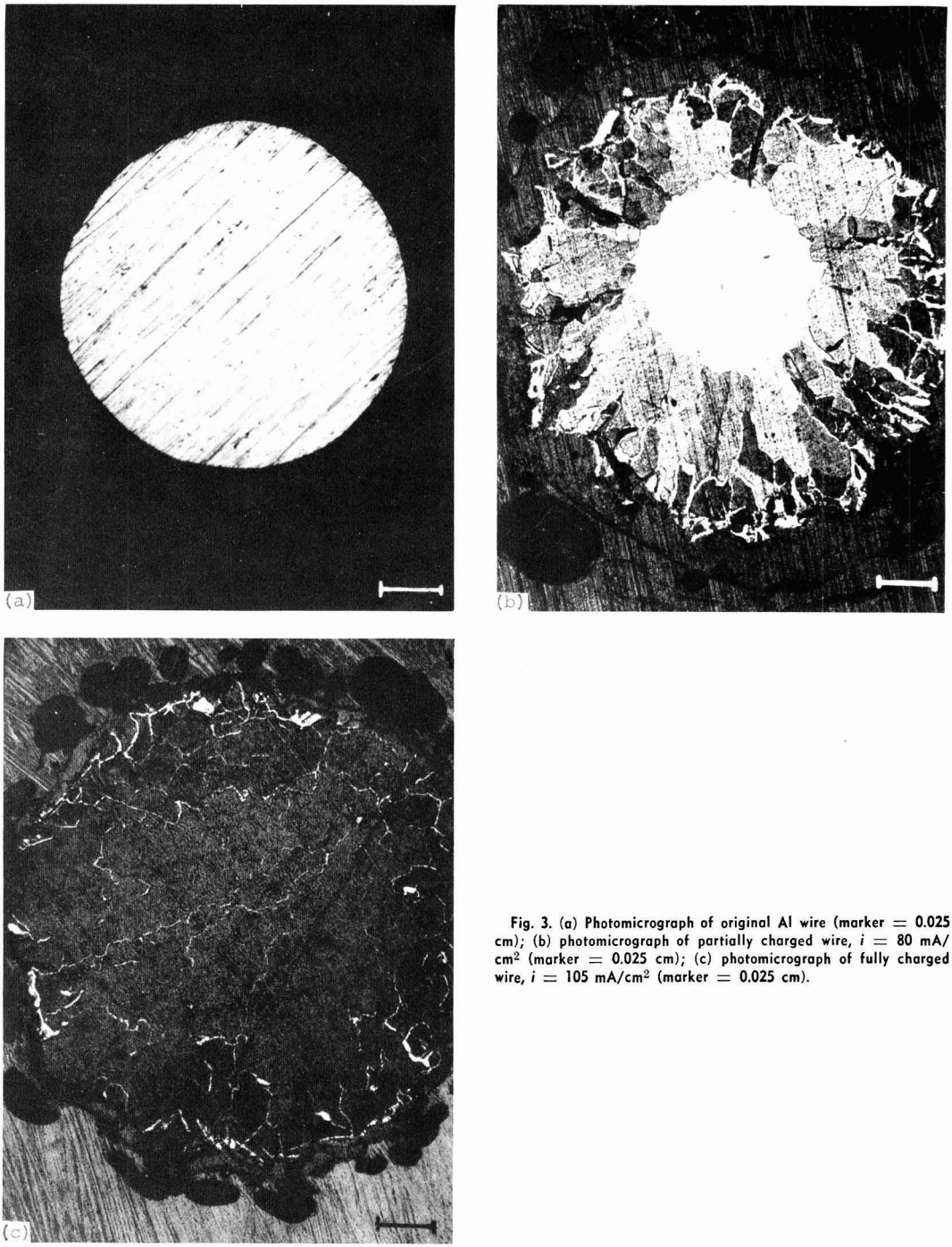

Fig. 3. (a) Photomicrograph of original Al wire (marker = 0.025 cm); (b) photomicrograph of partially charged wire, i = 80 mA/cm^2 (marker = 0.025 cm); (c) photomicrograph of fully charged wire, i = 105 mA/cm^2 (marker = 0.025 cm).

tion time in the discharge curves has been attributed by L'vov (4) and James (5) to diffusional limitation in the solid state. The increase in transition time with cycling indicates an apparent increase in Li diffusivity. Using Sand's equation (8) the values calculated for the curves shown correspond to 1.6×10^{-6}, 1.9×10^{-6}, and 2.02×10^{-6} cm^2/sec, respectively. This "development" of the electrode during cycling is presumably associated with structural changes in the electrode or the creation of defects. Difficulty in obtaining reproducible results was encountered in our attempts to carry out further cycling. In addition the electrode would not maintain its physical integrity. A slight decrease in the cathodic overpotential is also observed with cycling, but is not as pronounced as that on discharge.

Microstructure of charged electrodes.—Figure 3b shows a metallographically polished cross section of an aluminum wire partially charged with Li to 70% of capacity (based on conversion of the wire to β-LiAl, *i.e.*, 48 a/o Li). For comparison, a section of the original Al wire (0.145 cm diam) is shown in Fig. 3a. The light central core of Fig. 3b represents the unreacted portion of the wire (Al), whereas the annular region corresponds to that portion which converted to the β-phase (LiAl). A difference in optical reflectivity of some areas in the latter region is apparent. The presence of a "vein-like" structure emanating from the core is particularly striking. Such "veins" appear to persist even in the fully charged electrode (Fig. 3c). Electron microprobe analysis showed that areas of different optical reflectivity vary in aluminum content, *i.e.*, lighter areas are richer in Al (lower Li) than darker ones. This is illustrated by the Al K_α x-ray map (Fig. 4b) of area X in Fig. 4a. The intensity of white dots in the x-ray picture is proportional to the amount of Al present. Therefore, during charging, the incorporation of Li does not appear uniform throughout the electrode. Even in the fully charged state, Al-rich areas represented by the "veins" are present. Two other features worth pointing out here are: the presence of cracks on charged electrodes and the increase in diameter from 0.145 cm for the original Al wire to 0.213 cm for the fully charged LiAl electrode. This latter exemplifies the lattice expansion that accompanies the transition from pure Al or α-phase (lattice constant = 4.05Å) to β-LiAl (lattice parameter = 6.36Å). The cracks observed in the photomicrographs may be due to the mechanical stresses set up during the volumetric expansion.

Discharged electrodes.—Figures 5a and 5b show the structure of partially and nearly fully discharged electrodes, respectively. The breakdown of electrode structure is evident, and is obviously more prominent on discharge than on charge. The α-phase on the near surface layers of Fig. 5a (light areas) was confirmed by microprobe analysis. A β-LiAl core remains in the electrode of Fig. 5b as shown in the enlarged picture of Fig. 5c. It appears that, on anodic extraction of Li, the Al structure is not able to reform to the original and does so only in patches resulting in the broken-up appearance shown. The effect of depth of discharge on structural breakdown is also brought to light in these pictures. It appears in Fig. 5b that the β-phase holds the radial structure together. Presumably if the discharge can be carried to completion (*i.e.*, 100% Li recovery), the structure would fall into pieces. The progressive increase in electrode area on discharge probably counteracts the increasing anodic polarization with time giving rise to the relatively flat portion of the discharge curve.

Structure after cycling.—Figure 6 shows the microstructure of a LiAl electrode after three charge-discharge cycles. The anodic polarization curves for this electrode are the ones shown in Fig. 2. It is obvious that the observed decrease in electrode polarization with cycling must be due to comminution of the electrode. The presence of unutilized Li is shown by the β-core (center) in the picture.

Effect of current density and potential on structure.—In order to examine the effect of charging potential and current density on electrode structure, Al wires were charged completely to β-LiAl composition

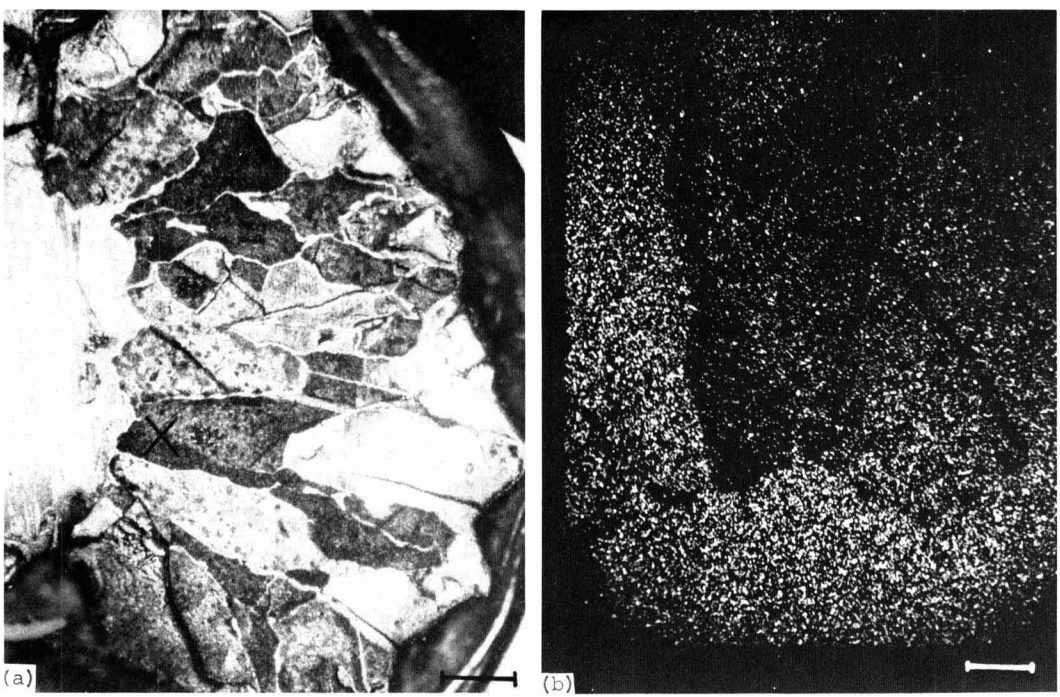

Fig. 4. (a) Enlarged area of portion of Fig. 3b (marker = 0.0125 cm); (b) aluminum K_α x-ray map of area "X" in 4a

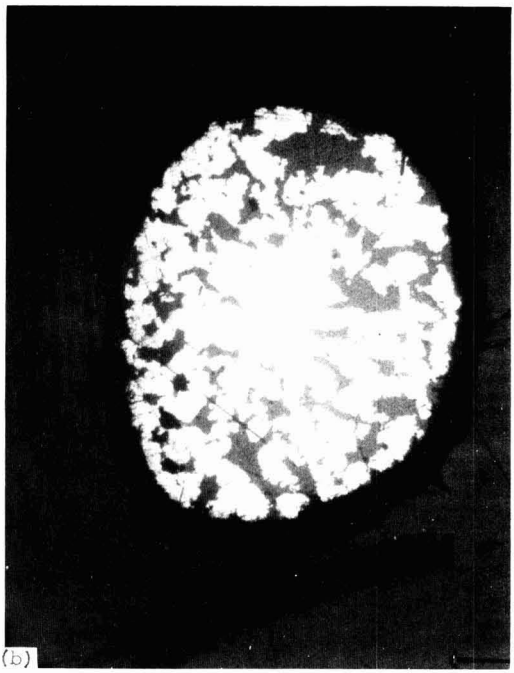

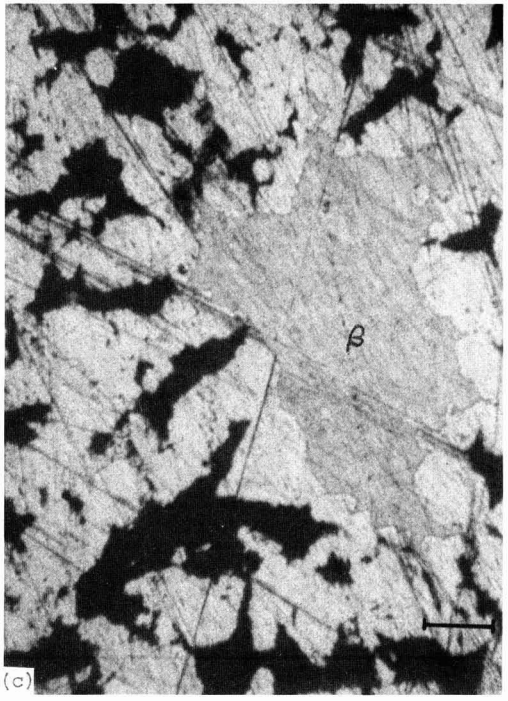

Fig. 5. (a) Photomicrograph of partially discharged LiAl electrode, $i = 380$ mA/cm^2 (marker = 0.025 cm); (b) photomicrograph of nearly fully discharged LiAl electrode, $i = 70$ mA/cm^2 (marker = 0.03125 cm); (c) photomicrograph of β-LiAl core portion of 5b (marker = 0.01 cm).

at constant potentials of −10, −20, −30, −40, −50, and −80 mV *vs.* LiAl and at current densities of 25, 50, 100, 150, 200, 300, and 500 mA/cm^2, respectively. The charged electrodes were mounted in plastic, then ground and polished metallographically. While a difference in structure among the electrodes is observed, we were unable to obtain any systematic correlation between the extent of structural breakdown and the charging potential or current density. Samples were also charged at a constant current density of 100 mA/cm^2, then discharged at current densities of 50, 100, 150, 200, and 300 mA/cm^2. A progressive decrease in the thickness of the outer α-phase layer (*cf.*, Fig. 5a) is observed with increasing current density due to the shorter transition times and progressively lower utilization. The effect on structure is roughly the same as that observed with varying the depth of discharge at constant current.

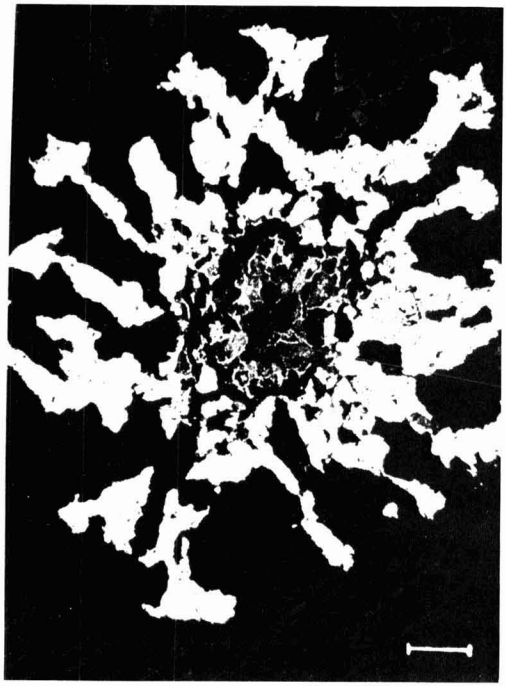

Fig. 6. Photomicrograph of discharged LiAl electrode after three cycles, $i = 107$ mA/cm^2 (marker = 0.025 cm).

Summary

A study of the anodic polarization behavior of LiAl wire electrodes shows a decrease in overpotential and an increase in transition time for Li extraction on successive discharge cycles. This appears to correlate with changes in the electrode structure as examined by metallographic techniques. The degree of electrode breakdown was found to be more pronounced on discharge than on charge and to depend mainly on the depth of discharge. Li distribution in wire electrodes during charging appears to be nonuniform. The results obtained show the need to consider structural changes in the interpretation of measurements of transport properties in solid alloy electrodes. Electrode comminution can lead to current collection problems and loss of active material in engineering-type cells; these can be important factors in determining the cycle life of such cells.

Acknowledgments

The authors are grateful to Dr. F. A. Cafasso for his continued interest and support of this work. We are indebted to Dr. A. Martin and F. Mrazek for assistance in metallography and to W. Shinn for the electron microprobe analysis. Valuable discussions were held with Dr. S. Siegel. This work was done under sponsorship of the U.S. Energy Research and Development Administration, Division of Physical Research.

Manuscript submitted Oct. 21, 1977, revised manuscript received Jan. 10, 1978.

Any discussion of this paper will appear in a Discussion Section to be published in the December 1978 JOURNAL. All discussions for the December 1978 Discussion Section should be submitted by Aug. 1, 1978.

Publication costs of this article were assisted by Argonne National Laboratory.

REFERENCES

1. W. J. Walsh, J. .W Allen, J. D. Arntzen, L. G. Bartholme, H. Shimotake, H. C. Tsai, and N. P. Yao in, "Proceedings of the 9th IECEC," San Francisco, Calif. p. 911 (1974).
2. N. P. Yao, L. A. Heredy, and R. C. Saunders, *This Journal*, **118**, 1039 (1971).
3. J. R. Selman, D. K. DeNuccio, C. C. Sy, and R. K. Steunenberg, *ibid.*, **124**, 1160 (1977).
4. A. L. L'vov, A. A. Gnilomedov, A. P. Selemenov, and E. N. Protasov, *Elektrokhim.*, **11**, 1322 (1975).
5. S. D. James, *Electrochim. Acta*, **21**, 157 (1976).
6. C. A. Melendres, *This Journal*, **124**, 650 (1976).
7. M. Hansen and K. Anderko, "Constitution of Binary Alloys," McGraw-Hill Book Co., New York (1969).
8. P. Delahay, "New Instrumental Methods in Electrochemistry," Interscience, New York (1954).

Propagation of Pitting on Aluminum Alloys

Steven Dallek*,[1] and R. T. Foley*

Department of Chemistry, The American University, Washington, D.C. 20016

Previous reports from this laboratory have dealt with the effect of anions on the pitting of aluminum (1, 2). The technique employed was based on a derived relationship between the pitting induction time, t_i, and the concentration of the halide ion and it yielded a stoichiometric number, n, the number of halide ions associated with an aluminum reaction site during the primary pitting process. This number for several aluminum alloys varied between one and four, dependent on the halide and the pH of the solution. The current-time curve obtained from the experiment also allows an observation with respect to the kinetics of the propagation of the pit which, with microscopic examination, produces some understanding of the influence of anions in promoting pitting. This is the subject of the present note.

* Electrochemical Society Active Member.

[1] Present address: Naval Surface Weapons Center, White Oak Laboratory, Silver Spring, Maryland 20910.

Key words: pitting corrosion, anion effects, halide effects, corrosion kinetics, pit geometry.

Experimental

The method of investigation (2) involves holding the metal sample potentiostatically in the passive anodic range in an appropriate electrolyte, rapidly injecting into the cell a specific concentration of halide solution, and then measuring the resulting current flowing at the electrode as a function of time. Following an induction period, t_i, which is a measure of the rate of pit initiation, the anodic current increases exponentially coinciding with the onset of visible pitting. The resulting current-time curve is a measure of the faradaic reactions associated with the growth of pits on the electrode surface. Furthermore, the shape of the curve can provide information on the morphology of the resulting pits, as discussed below. Experiments were conducted with aluminum alloys 1199 (99.997% Al) and 7075 (Zn, 5.1-6.1; Mg, 2.1-2.9; Cu, 1.2-2.0; Cr, 0.18-0.40; Fe, 0.7; Si, 0.5, Mn, 0.3; remainder Al) at pH's of about 1 and 6. The halides injected into the 1N H_2SO_4 solution were solutions of NaF, NaCl, NaBr,

and NaI. Experiments were conducted over the temperature range of 15°-60°C.

Results and Discussion

Microscopic observations of the pits formed on aluminum alloy 7075 in halide solutions, excluding fluoride solutions, showed that the pits were predominantly hemispherical. The rate of propagation expressed as current as a function of time took the form

$$i - i_p = a\,(t - t_i)^b$$

where i = the dissolution current; i_p = the passive current; t = time; t_i = induction time; a = a constant dependent on the halide; and b = a constant dependent on the geometry of the pit. In Fig. 1 the current-time curve for pitting initiation and propagation by Br^- ion in 1N H_2SO_4 is presented as a typical curve. A plot of log $(i - i_p)$ *vs.* log $(t - t_i)$ the slope of which is "b", is given in Fig. 2. An equation similar to the above was obtained experimentally and derived theoretically by Engell and Stolica (3) for the pitting of iron by chloride solution. In their derivation they assumed that the pitting sites are hemispherical, that the dissolution current density is much greater than the passive dissolution current density and is proportional to the sum of the pit cross sectional areas, and that the rate of development of new pits is linearly dependent on time. According to the derivation, when the number of pits is constant with time, b is 2; when the number of pits is proportional to time, b is 3. The data plotted for the aluminum alloy in Fig. 2 apparently meet or approximate these specifications, as the data fit the cubic equation quite well.

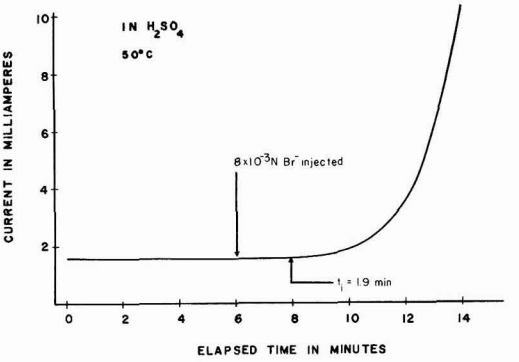

Fig. 1. A typical pitting initiation and propagation curve

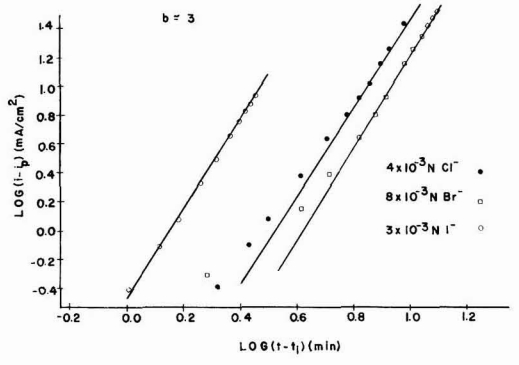

Fig. 2. Determination of "b" in pit growth equation. ●, Chloride solution, □, bromide solution, ○, iodide solution.

The data plotted in Fig. 2 follow the equations

for $3 \times 10^{-2}N$ I^-	$(i - i_p) = 0.073\ (t - t_i)^3$
for $4 \times 10^{-3}N$ Cl^-	$(i - i_p) = 0.0051\ (t - t_i)^3$
for $8 \times 10^{-3}N$ Br^-	$(i - i_p) = 0.00195\ (t - t_i)^3$

It is important to recognize that the behavior of aluminum alloys described here probably represents a special case insofar as the curves experimentally yield a $b = 3$ or exhibit cubic behavior. Tousek (4, 5) investigating the pitting corrosion of iron and nickel, developed equations for different current-time dependencies and then used the equations to describe the dimensions of the active pits. For iron, a value of $b = 3$ was obtained, but for a Cr-Ni-Fe alloy we obtained a value of $b = 2$. Stolica (6), investigating a number of Cr-Fe alloys, found that $b = 3$ for a 5.6% Cr-Fe alloy and a 14.9% Cr-Fe alloy, but for several others the current-time curves were too irregular to yield consistent exponents. The literature on the kinetics of pitting has been extensively reviewed by Szklarska-Smialowska (7, 8) and she has concluded that the Engell-Stolica treatment is oversimplified to apply in a general way to all cases of pitting. Rather, the pits should be placed in one of the three categories (8): (*i*) Case I: The pits are hemispherical and the radius of the pit approximates the pit depth; (*ii*) Case II: The pit is nonhemispherical, the radius is greater than the depth; (*iii*) Case III: The pit has a cylindrical shape with the radius less than the height of the cylinder. For this reason, experimentally, b values varying from 0.5 to greater than 5 have been obtained. Moreover, in the pitting of Ni in solutions containing various concentrations of $SO_4^=$ and Cl^- the b value changes with the ratio of the two ions (9). From the foregoing, it is concluded that a value of $b = 3$ conforms with hemispherical pits growing in cross section linearly with time with the number of pits also increasing linearly with time.

It is generally accepted that the morphology of the pits bears directly on the kinetics of pit growth. From the present study it is possible to record some qualitative trends from microscopic examination of the pitting specimens. The hemisphericity of pits propagated in chloride solution was always greater than those formed in bromide or iodide solution. In fluoride solution, pitting corrosion did not occur, but rather uniform surface corrosion resulting in the formation of an insoluble fluoride compound on the surface. Hemisphericity was also enhanced by going from near-neutral solution (pH = 5.8) to an acidic medium (pH = 0.3). The greatest deviations from hemisphericity were always observed in pits developed in bromide solution.

In addition to aluminum alloy Type 7075, experiments were performed with chloride and bromide on alloy Type 1199 to test the effect of alloy composition on pit morphology. The pits produced in chloride solution became almost perfectly hemispherical, although the most striking change occurred in bromide solution where the pit morphology also became hemispherical as compared with some irregularly shaped figures observed on alloy Type 7075.

There has been very little reported in the literature regarding the morphology of the pit as affected by the nature of the aggressive anion. Politycki and Fischer (10) described the different etching patterns formed on high purity aluminum by attack in HCl, HBr, HI, and HF. Cubic cavities were formed in HCl and HBr solutions, cubooctahedral cavities in HI, and no well-defined etch figures in HF solution. These patterns were explained in terms of steric relationships that derive from the direct contact between halide ions of a given radius with surface aluminum atoms separated by a given distance in the metallic lattice.

Tokuda and Ives (11) studied the pitting corrosion on nickel by chloride ion in sulfuric acid solution and analyzed the pit morphologies by simulation of dis-

solution, based on the assumption that a metal atom which has fewer nearest neighbors, and hence fewer bonds, is removed preferentially. However, this simple model failed to adequately account for the observed pit morphologies, and the authors thus incorporated into their model the concept of dissolution based on the accessibility of aggressive ions, a concept which correctly predicted the pit morphologies.

Conclusions

Pit propagation on aluminum alloys in chloride, bromide, and iodide solutions follows a cubic time expression due to the approximate hemisphericity of the pits. This is considered to be a special case in the general pitting of metals. The different pit morphologies obtained on aluminum depend on both the nature of the agressive anion in solution and on the composition of the metal sample.

Acknowledgment

The support of the Office of Naval Research under Contract N 00014-75-C-0799, NR 036-106 is gratefully acknowledged.

Manuscript submitted Sept. 22, 1977; revised manuscript received Jan. 19, 1978.

Any discussion of this paper will appear in a Discussion Section to be published in the December 1978 JOURNAL. All discussions for the December 1978 Discussion Section should be submitted by Aug. 1, 1978.

Publication costs of this article were assisted by The American University.

REFERENCES

1. F. D. Bogar and R. T. Foley, *This Journal*, **119**, 462 (1972).
2. S. Dallek and R. T. Foley, *ibid.*, **123**, 1775 (1976).
3. H. J. Engell and N. D. Stolica, *Z. Physik. Chem.*, **N.F. 20**, 113 (1959).
4. J. Tousek, *Corros. Sci.*, **12**, 1 (1972).
5. J. Tousek, *Collect. Czech. Chem. Commun.*, **33**, 1009 (1968).
6. N. Stolica, *Corros. Sci.*, **9**, 455 (1969).
7. Z. Szklarska-Smialowska, *Corrosion (Houston)*, **27**, 223 (1971).
8. Z. Szklarska-Smialowska, *Werkst. Korros.*, **22**, 780 (1971).
9. Z. Szklarska-Smialowska, *Corros. Sci.*, **12**, 527 (1972).
10. A. Politycki and H. Fischer, *Z. Elektrochem.*, **57**, 393 (1953).
11. T. Tokuda and M. B. Ives, *This Journal*, **118**, 1404 (1971).

JOURNAL OF THE ELECTROCHEMICAL SOCIETY

SOLID-STATE SCIENCE AND TECHNOLOGY

MAY 1978

An Instrumental Gravimetric Method for Indexing Materials, Contaminants, and Corrosion Products According to Their Hygroscopicity

J. D. Sinclair*

Bell Laboratories, Holmdel, New Jersey 07733

ABSTRACT

The moisture pickup characteristics of selected dusts, contaminants, corrosion products, and aged insulation and substrate materials have been determined in a dynamic humid environment by instrumental gravimetric analysis. These are compared with pure salts and other standard materials to categorize their relative hygroscopicities during the initial adsorption stage and subsequent stages of moisure pickup. In addition, the minimum relative humidities at which some pure salts and a variety of other substances will pick up moisture are reported.

Humidity has long been recognized as a dominant factor in the rate of deterioration of electronic devices. Degradation may occur as a result of inappropriate choice and design of materials, or because of in-service contamination or corrosion problems. In spite of the importance to the electronics industry of knowledge about the moisture pickup characteristics of components, contaminants, and corrosion products, the "hygroscopicity" of most substances is generally not known. This is due in part to the lack of a uniform concept of hygroscopicity. There are nearly as many definitions of the term as there are papers on the subject.

Since Vernon's (1) recognition nearly 50 years ago that significant corrosion of most materials will only occur above a "critical relative humidity" (CRH), attempts to predict the effects of humidity on devices have usually been based on knowledge or an estimate of this number. In many cases, Vernon's CRH relates to the thermodynamic CRH of the surface components. For composite materials, contaminants, and some corrosion products, it is generally not appropriate to apply the thermodynamic concept of the CRH because of the insoluble nature of the substances. In this work, the term will usually be used broadly to describe an effective relative humidity (RH) at which a surge in moisture pickup occurs.

Some information is available on the over-all moisture pickup at elevated humidity of substances often encountered in the electronics industry. In some early work, Mulder (2) found that $CaCl_2$ on exposure to water-saturated air at 16°-20°C increased its weight by 712% in an unspecified period. A 0.6% weight increase is documented by Mellor (3) for sodium chloride exposed to air, but the RH and exposure time were not specified.

Preston and Sanyal (4) reported that $CaCl_2$ and NaCl showed weight increases of 625 and 314%, respectively, during exposure to an atmosphere maintained at 97% RH (at room temperature) for 14 days. Lindsay (5) has studied the moisture content at intervals from 0 to 100% RH of fibrous materials used for electrical insulation, including manila paper, press board, leatheroid paper, silk, empire cloth, and asbestos paper. Excess water content ranged from 1 to 6% by weight at 30% RH and from 4 to 18% at 90% RH. Asbestos paper was the least hygroscopic material examined.

Alkali halides have been recently studied by Kanazawa *et al.* (6). The "hygroscopicity" of powdered NaCl, KBr, and KI, prepared by recrystallization from ethanol, was studied by comparing the surface conductivity of the salts with their water adsorption isotherms. Water molecules which were adsorbed to a thickness of less than two monolayers were stated to be physisorbed. Water films thicker than two monolayers were thought to dissolve salt and form mobile hydrated ions. The vapor pressures at which the adsorbed water molecules were said to form hydrated ions at 30°C were 33, 36, and 27%, respectively. Hara *et al.* (7) studied the effects of crystal structure and surface energy on the hygroscopicity of $NaClO_3$ and found that increasing strain within the crystal was coincident with an increase in hygroscopicity.

A number of workers have studied the moisture pickup of ammonium salt formulations used for fertilizers and explosives. Pawlikowski *et al.* (8) have studied the effect of grain size on "the velocity of water sorption" of ammonium nitrate fertilizers. Vakhrusev and Gradinar (9) have found that the "hygroscopic point" of ammonium nitrate fertilizers decreases from 63.3% RH for granulated material to 55.6% RH for fine grained material. Further, he finds the "hygroscopic point" decreases with increasing urea concentration by as much as 20% from 65% RH. On the other hand, Trzesniowski (10) found by gravimetric methods that granule size, mole ratio, and phosphoric acid content had no effect on the CRH of N-P fertilizers, though the CRH increased somewhat with increasing ammonium sulfate content. Shokin and Solov'eva (11) determined that coating ammonium bicarbonate ferti-

* Electrochemical Society Active Member.

Key words: moisture pickup, deliquescence, critical relative humidity, device deterioration.

lizers with petroleum products was very effective in reducing the rate of moisture "absorption." Runge (12) has developed equations based on percent weight changes for calculating the moisture pickup capacity of similar fertilizers based on the initial moisture and composition. Yee (13) has studied the CRH of water soluble fertilizers by measuring the RH over saturated salt solutions with an electric hygrometer.

Puri and Bhushan (14) have examined the moisture pickup capacity by percent weight gain of zinc, nickel, chromium, and cobalt oxides prepared in a variety of ways. At 50% RH, moisture pickup for zinc oxide ranged from 0.5 to 2.4%, for nickel oxide from 2.7 to 10.3%, for chromium trioxide from 0.9 to 4.8%, and for cobalt oxide from 0.2 to 2.5%. At 99% RH, the moisture pickup for zinc oxide ranged from 0.7 to 9.1%, for nickel oxide from 5.9 to 32.5%, for chromium trioxide from 3.8 to 15.2%, and for cobalt oxide from 3.2 to 30.0%. These wide variations indicate that the hygroscopicity of many substances cannot generally be estimated from a single physical measurement.

Kearsley and Birch (15) recently measured the hygroscopicity of glucose syrup fractions as percent weight gain at saturation (approximately 14 days at 75% RH) and found that the moisture content increased from 14 to 34% as the glucose fraction increased from 0.3 to 61.6%. The method of drying was found to affect the initial rate of moisture pickup but not the final moisture content of the sample. The presence of inorganic contaminants was determined to increase the rate of pickup and the capacity. Whittier and Gould (16) used vapor pressure meaurements for saturated solutions as the basis for comparing "hygroscopic tendencies" and determined the equilibrium humidities for sucrose, glucose, galactose, and lactose to be 77, 81, 81, and 93% RH, respectively.

Grebennikova *et al.* (17), Twomey (18), and Bakhanova and Ivanchenko (19) have investigated the growth of hygroscopic dust particles and droplets in moisturized air streams by *in situ* microscopic examination. Unkown dust particles were often identified by the relative humidity at which visible moisture collected on their surfaces.

Markowitz and Boryta (20) have determined "hygroscopicity potentials," for saturated salt solutions at various temperatures. These authors defined the hygroscopicity potential (HP) as being $RT \ln (p_{H_2O,\,pure}/p_{H_2O,\,system})$. By this procedure the thermodynamic imbalance in chemical potential between ambient water and system water is emphasized. Pawlikowski *et al.* (21) prefer a "hygroscopic value" $\Delta p = pn\text{-}pr$, where pn is the vapor pressure of the saturated salt solution and pr is the ambient water vapor pressure.

Modrzejewski and Pokora-Bartyzel (22) have defined the "hygroscopic point" of pulverized pharmaceutical substances as the RH at which the material takes on 1% moisture in 24 hr. They state that the value is somewhat lower than the CRH of saturated solutions but that it is constant and characteristic of each substance. Moisture pickup was monitored gravimetrically for samples stored in 10 chambers maintained at uniformly distributed RH's between 10 and 100%. The "hygroscopic point" was determined from a percent moisture *vs.* relative humidity plot.

Shen and Springer (23) presented expressions for moisture content as a function of time for homogeneous and composite materials exposed to humid air or water. Test data for graphite T-300 Fiberite 1034 composites supported the mathematical analysis. The method requires knowledge of the maximum moisture content and the moisture diffusivity and unfortunately is readily applicable only if the initial moisture concentration inside the material is uniform and the temperature and moisture content of the environment is constant. Balarev *et al.* (24) have recently tabulated 140 inorganic salts according to their increasing hygroscopicity. The rankings were based on the equilibrium vapor pressures of saturated salt solutions. Phipps and Rice (25) have described an extremely sensitive gravimetric method employing a quartz crystal oscillator to detect monolayers of water on thin metal films. Unfortunately, the technique is readily useful only under vacuum conditions and consequently is not directly applicable to the measurement of moisture pickup rates and capacities of contaminants, corrosion products, and many electronic materials. Very recently Foster and Arbach (26) used a recording microbalance to measure the moisture pickup characteristics of β''-sodium gallate as a function of particle size at 50% RH and found finely divided powder picked up approximately one mole of water for each gram-atom of sodium whereas monocrystals showed no measureable water pickup.

Mansfeld and Kenkel (27), Sereda (28), and Gutman (29) have developed atmospheric corrosion monitors which measure the "time-of-wetness" which local environmental contaminants produce under extended exposure to atmospheric humidity. The time-of-wetness is an experimental determination of the summation of time intervals during which the CRH of the surface contaminants is exceeded. Berukshtis and Klark (30) have attempted to correlate time-of-wetness and pollutant concentrations with corrosion rates of steel, aluminum, zinc, cadmium, and copper for several urban environments.

In ranking substances according to their experimental hygroscopicities, a number of factors should be considered, including the magnitude and rate of moisture pickup in a selected time interval and the temperature, RH, and flow characteristics of the test atmosphere. In this work the moisture pickup parameters for several pure salts were examined in a static moisture-saturated environment to gain further understanding of the factors which have, in the past, led to classifying pure substances as hygroscopic or nonhygroscopic. From this data and the work of the authors already described, gravimetric measures were recognized as being best suited to estimating moisture pickup characteristics. Subsequently, an instrumental gravimetric method was developed for rapidly measuring the CRH and moisture pickup rates for samples of electronic materials, corrosion products, dusts, and other contaminants. Through this information an indexing method evolved for ranking substances according to their hygroscopicities and, thereby, for assessing corrosion or device failure hazards.

Experimental

Static atmospheres.—Measurement of the moisture pickup of pure salts in a static environment was accomplished with small bell jars sealed through ground glass joints with Apiezon N. A beaker of distilled water and a beaker containing 1.0g of a reagent grade anhydrous salt were placed in each bell jar. The RH was presumed to equilibrate at 100% in a time frame which was negligibly small relative to the interval between measurements. The salts analyzed were $CaCl_2$, $ZnCl_2$, $CuCl_2$, $FeCl_2$, and NaCl. The bell jars were periodically opened and the water pickup by the salts was monitored gravimetrically. The time required for complete dissolution of each salt was noted.

Flowing atmospheres.—Rapid determination of the moisture pickup characteristics of pure salts, composite materials, contaminants, and corrosion products was accomplished with a du Pont 951 thermogravimetric analyzer coupled to a 990 thermal analyzer. Continuous moisture pickup rates for the various materials at nearly 100% RH at 23°C were determined by passing a stream of air, which had been moisturized by bubbling it through distilled water, through the microbalance sample tube (2.5 cm diam × 12 cm long). It was found that flow rate strongly affected the moisture pickup rate. Commercial "Arizona Road Dust" (AC

Fine prepared by the AC Spark Plug Division of General Motors Corporation) was analyzed at flow rates of 10, 100, and 1000 ml/min and was found to increase its weight by 1.0% after 570, 55, and 18 min, respectively. The substantial acceleration possible at rapid flow rates was offset by the reduced sensitivity and resolution caused, in part, by increased turbulence in the balance housing. A flow rate of 10 ml/min provided sufficient acceleration for the work anticipated for this study. Relative to flow rates found in buildings housing electronic equipment, a flow rate of 10 ml/min, when translated to linear dimensions, is about an order of magnitude lower than those typically encountered. The apparatus is capable of handling samples weighing from 0.1 to 110 mg and, if the atmosphere and sample are properly equilibrated prior to loading, the minimum detectable weight change is approximately 10 μg/hr.

Weight was recorded graphically as a function of time, and each run was allowed to proceed until the rate of weight gain approached zero or reached an extended steady state. It is impractical to provide weight *vs.* time profiles for every sample examined, but the general characteristics of each sample can usually be sufficiently described through knowledge of the initial, final, and average percent weight gain rates along with sample weight and total exposure time or total weight gain. Field samples were generally equilibrated for several days or weeks with the laboratory atmosphere (RH approximately 30%) before they were analyzed in the microbalance. Weight increase with time at 23°C was initially recorded for 19 pure chemicals whose hygroscopicities spanned a wide range. Sample weight for the laboratory samples varied from 25 to 107 mg with only two samples weighing less than 50 mg. The amount of water vapor passing through the sample chamber was in very large excess of the amount of water picked up by the samples. Therefore, the sample size effect is probably minimal except perhaps for the smaller samples. The texture and crystallinity of the samples were variable and probably contribute to the results.

CRH measurements were made using the same balance with a modified air stream apparatus. A minimum RH in the balance housing (maintained at 23°C) of 22% was achieved by passing a stream of dry air through a dispersion frit submerged in distilled water cooled to 0°C. By allowing the water to warm from 0°C to nearly 23°C under ambient control, the RH increased from 22% to nearly 100%.

The RH *vs.* time profile is shown in Fig. 1. Flow rates ranging from 10 to 5000 ml/min were examined. The lag time in establishing in the balance housing the specific RH created at the humidity source was substantial at the slower flow rates, but the faster flow rates caused severe turbulence. A flow rate of 1500 ml/min was found to be rapid enough to insure rapid response in the sample chamber to humidity variations without producing a severe loss of sensitivity or resolution because of turbulence. The unloaded apparatus including the sample pan registered a weight increase of 0.02 mg on increasing the RH from the minimum to the maximum level, which is a negligible correction for most of the samples encountered. A recording of weight *vs.* time was translated to weight (normalized to 20 mg) *vs.* RH using hand recorded data of water temperature *vs.* time. The relative humidity at which an onset in weight gain occurred was taken to be the CRH. For the pure salts examined, the moisture pickup process was reversible and the measured CRH remained constant.

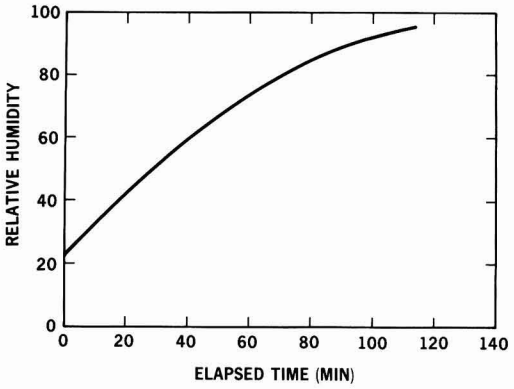

Fig. 1. Relative humidity program

Discussion

At least three different stages of moisture pickup, each of which should have a characteristic rate behavior, can be considered in evaluating the hygroscopicity of a pure dry salt which becomes exposed to a humid atmosphere. Initially, presuming the water vapor pressure in the atmosphere is greater than that of adsorbed water or water of hydration, water will be chemisorbed and physisorbed on the surface. The surface area and surface energetics of the salt will be dominating rate factors at this stage. Included in this phase will be the formation of possible hydrates. Secondly, as the hydration layers continue to physisorb, a thin continuous film of water will form on the surface. At this stage the thin continuous film will be a saturated salt solution and the water pickup rate will be a function of the difference between the vapor pressure of the saturated salt solution and the vapor pressure of the atmosphere. Eventually the salt will completely dissolve and the solution will begin to dilute. The rate of moisture pickup will then decrease as the solution dilutes and its vapor pressure increases. These stages are denoted phase one, phase two, and phase three in the following discussion.

Hygroscopicity of pure salts in a static environment. —The rate of moisture pickup of a substance will depend in part on its initial state, which will generally be either a phase one or phase two condition. It will also depend on the temperature, the humidity, and the moisture transport processes taking place at the surface. Moisture transfer in a static environment will be diffusion controlled but in an environment where convective transport processes occur, the air flow rate over the surface will be important.

The acquisition of moisture by 1.0g samples of 5 salts at 100% RH was monitored for 133 days. These results are shown in Fig. 2. The amount of moisture pickup registered for $CaCl_2$ or NaCl after 14 days is about one-third of that found by Preston and Sanyal (4). This discrepancy is probably caused by differences

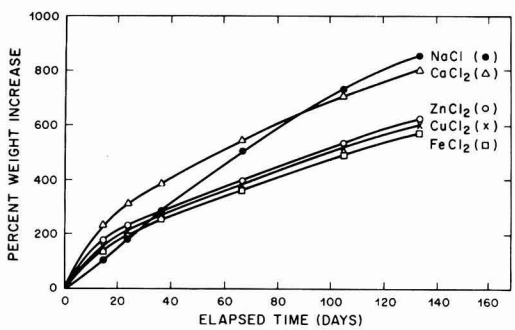

Fig. 2. Hygroscopicity of 1g samples of selected salts at 100% RH as measured by the percent weight increase.

in the experimental configurations. In both experiments $CaCl_2$ picked up twice as much moisture as NaCl in 14 days. $ZnCl_2$ and $CaCl_2$ picked up a sufficient amount of moisture to completely dissolve in 3 and 6 days, respectively, while $CuCl_2$, NaCl, and $FeCl_2$ dissolved in 20, 34, and 46 days, respectively. These observations are consistent with the usual expectation that $ZnCl_2$ and $CaCl_2$ are very hygroscopic materials while the other salts are moderately hygroscopic. Once a film of water has collected on the dry salt, a saturated salt solution will form. A saturated $ZnCl_2$ solution (CRH approximately 10% and vapor pressure approximately 2.4 mm Hg at 25°C) and a saturated $CaCl_2$ solution (CRH 31% and vapor pressure 7.3 mm Hg at 25°C) are expected to exhibit a stronger tendency to pick up water from a water-saturated atmosphere than a saturated NaCl solution (CRH 75.7% and vapor pressure 18.0 mm Hg at 25°C). The initial quantitative weight gains, as indicated by the percent weight increases, reflect this expectation but also indicate that the differences in solubility of these salts are partially responsible for the hygroscopicities commonly ascribed to them. The solubilities of $ZnCl_2$, $CaCl_2$, and NaCl are 4320, 819, and 350g solute/1000g water. If NaCl were as soluble as $ZnCl_2$ it can be very roughly estimated from the solubilities and the dissolution times that NaCl would have required about the same amount of time as $ZnCl_2$ to dissolve. Similarly, the dissolution time for NaCl, if it were as soluble as $CaCl_2$, would have been only two or three times that of $CaCl_2$. Dry NaCl, then, gains weight at a rate which is initially somewhat slower than $ZnCl_2$ and $CaCl_2$, but not nearly as slowly as the usual recognition of its hygroscopicity implies.

After dissolution of all the salt has occurred, the ionic molality of the solution is expected to determine the rate of moisture pickup more or less independently of the salt involved. If the magnitude of the water pickup is calculated in terms of the reciprocal of the ionic molality, which is a measure of the water pickup potential per ion present in solution, then the time required to attain a selected minimum value of this reciprocal may also be a useful method of expressing hygroscopicity. The reciprocal of the ionic molality is specified as a function of time in Fig. 3. The nonuniform behavior found for NaCl using pure percent weight gain information is no longer apparent. If the selected value for the reciprocal is arbitrarily chosen to be 0.20, the hygroscopicity is found to decrease in the order $CaCl_2 > ZnCl_2 > CuCl_2 > NaCl > FeCl_2$. For salts of only moderate solubility a higher minimum for the selected reciprocal value would be required to permit comparisons. The data suggest that selection of moderately higher values will lead to only minor variations in the relative order. For all the salt solutions the rate at which water vapor is condensed in the beakers decreases in a uniform manner consistent with a uniform increase in the vapor pressure of the solution as the salt concentration decreases.

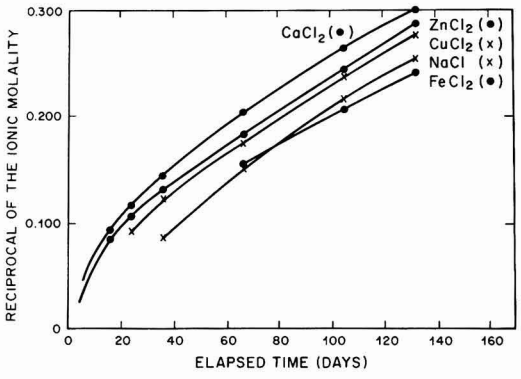

Fig. 3. Hygroscopicity of saturated solutions of selected salts at 100% RH as measured by the reciprocal of the ionic molality.

Interpretations based on solution concentrations are probably most useful and informative in analyzing laboratory data for pure salts, but the total capacity to pick up moisture in specific time intervals may be more useful in analyzing field samples, including dust, silt, and corrosion salts, since the amount of hygroscopic material in the sample may be very small. In this case, the extent to which the nonhygroscopic constituents can be dissolved and dispersed by the total amount of water present may be the dominant factor in terms of corrosion potential and other deleterious effects. It is apparent from the percent weight increase data given in Fig. 2 that once dissolution of the salts occurs, a beaker containing 1g of NaCl will pick up more water than a beaker containing 1g of $ZnCl_2$. This trend is expected to continue indefinitely. Similarly, a beaker containing 1g of NaCl will gain more weight than a beaker containing 1g of $CaCl_2$ for exposures to water-saturated air in a static environment of over 90 days. For some humid field environments, this suggests that contaminants and corrosion products containing NaCl in an otherwise nonhygroscopic matrix could be more hazardous than samples containing comparable amounts of $ZnCl_2$ or $CaCl_2$.

Table I summarizes some data for various procedures which could be used to estimate the hygroscopicity of pure salts. All the rankings, except those based on the CRH and solubility, were experimentally determined in this work.

The rank orders based on percent weight gain after 10, 40, and 100 day exposures are identical except for the position of NaCl, which ranges from the least to the most hygroscopic salt. It is surprising that $ZnCl_2$ appears somewhat less hygroscopic than $CaCl_2$ by either the percent-weight-gain or reciprocal-of-the-ionic-molality methods in that, because of its low CRH, dry $ZnCl_2$ becomes wet in all but the very driest of atmospheres, whereas $CaCl_2$ remains dry at RH's less than about 30%. Similarly, nonuniform characteristics are found for the set $FeCl_2$, $CuCl_2$, and NaCl. Their CRH's are 40, 69, and 75%, respectively, but the rank order of their hygroscopicities based on the reciprocal of the ionic molality is $CuCl_2 > NaCl > FeCl_2$. In a humid atmosphere, the CRH of a substance is apparently not always a satisfactory indicator of its hygroscopicity, but weight gain data by themselves, particularly if only one measurement period is examined, are not sufficient either. The length of the exposure affects the relative ranking and will be important in estimating moisture hazards with electronic devices. Whether a macroscopic method should be chosen or one which implicitly includes the effects of each ion in solution will depend on the circumstances and rather arbitrary preferences.

For most substances of interest to the electronic devices field, methods requiring measurements in solution will not be applicable. Modern instrumental gravimetric procedures readily provide a precise recording of weight change information which can be used

Table I. Relative hygroscopicities

Criteria for estimation	Rank order
1. Dissolution time	$ZnCl_2 > CaCl_2 > CuCl_2 > NaCl > FeCl_2$
2. Solubility (g solute/1000g water)	$ZnCl_2 > CaCl_2 > CuCl_2 > FeCl_2 > NaCl$
3. Percent weight gain after 10 days	$CaCl_2 > ZnCl_2 > CuCl_2 > FeCl_2 > NaCl$
4. Percent weight gain after 40 days	$CaCl_2 > NaCl > ZnCl_2 > CuCl_2 > FeCl_2$
5. Percent weight gain after 100 days	$NaCl > CaCl_2 > ZnCl_2 > CuCl_2 > FeCl_2$
6. Reciprocal of the ionic molality	$CaCl_2 > ZnCl_2 > CuCl_2 > NaCl > FeCl_2$
7. Critical RH	$ZnCl_2 > CaCl_2 > FeCl_2 > CuCl_2 > NaCl$

for ranking substances according to their hygroscopicity. The remainder of this paper describes such a procedure. By employing a flowing atmosphere, variable accelerations are feasible. Measurement of an effective CRH can be accomplished with RH programming of the flow system.

Critical relative humidities of pure salts and field samples.—Corrosion products and other contaminants contain varying amounts of hygroscopic materials, and consequently their moisture pickup characteristics are less predictable than those of pure salts. The surface area of the nonhygroscopic substances in the contaminant mixture, particularly if these substances are of low solubility, may be sufficient to chemisorb and physisorb most of the hygroscopic substances and all the moisture picked up by these substances, effectively stopping the moisture pickup process before a thin continuous film of water forms. For this and other reasons one of the most important moisture-related factors in considering corrosion and contamination problems with electronic devices is the rate at which a substance collects moisture in the first few hours of exposure to humidity levels above its CRH. Initial experimentation established that a significant weight change in a salt could be produced at the CRH starting with either a dry sample and increasing the RH or starting with a moist sample and decreasing the RH. For pure salts which were stable to moisture and did not react significantly with the aluminum sample pan, reproducible minima and maxima were recorded at the same RH for repetitive scans of the same sample. However, for corrosion products, dusts, and some materials the weight *vs.* RH plots were often complex and repetitive scans were not always reproducible. Generally, this behavior was caused by chemical or physical changes associated with the moisture pickup which were irreversible at reasonable conditions. For these reasons, the usual procedure for most samples was to equilibrate the sample at 22% RH and then to record a single run from low (22%) to high (nearly 100%) RH.

The results for four pure salts are shown in Fig. 4. The literature values for the CRH of KCNS and $NaNO_2$ (31) are 47 and 66%, respectively, at 20°C. The onset of weight gain for these salts in this work (23°C) occurred at 46 and 66%, respectively, establishing that the method is sufficiently sensitive and accurate to measure the CRH of many substances. The onset of weight gain for NaCl occurred at 84%, which is somewhat higher than the literature value of 76% (31), but NaCl was later found, as is discussed below, to pick up moisture at a slower rate during the initial adsorption phase than during the later stages controlled by the solution vapor pressure. It is anticipated that if the RH programming had proceeded at a slower rate the observed critical RH would be lower for this salt. This measurement requires development of more sophisticated humidity control equipment which is in progress. Moisture pickup for CrO_3 is initiated at 29% RH, which is somewhat below the literature value of 35% (31). This discrepancy may be due in part to the procedure used to determine the RH of the system. The vapor pressure of water in the air stream was assumed to be identical to the vapor pressure of the distilled water bath. The vapor pressure of the bath was estimated from its temperature. The temperature differential between the input air stream and the water bath for the low humidity readings was substantial and could lead to significant warming of the water at the surface of the air bubbles, thereby increasing the vapor pressure and the corresponding RH. The determined RH would be low consistent with the observation for CrO_3. An improved apparatus which will eliminate this uncertainty is under construction.

The results for several field samples are shown in Fig. 5-8. The electrolytic corrosion product samples No. 1 and 2, shown in Fig. 5, each exhibited two weight gain onsets but are otherwise very different. The electrolytic corrosion products from sample No. 2 were produced with relatively clean water and consisted primarily of copper and nickel oxides and carbonates with minor amounts of chloride salts. The weight onset at approximately 27% RH is probably associated with dust that was unavoidably collected with the corrosion products. The second onset at about 50% RH could be due to chloride salts. The concentration of such salts must be low, however, since the weight gain rapidly approaches saturation at approximately 65% RH. Corrosion product No. 1 was the result of water contamination from a water line serving an air conditioning system. The water contained chromate salts and possibly other additives for rust inhibition. The initial onset at 23% RH saturated at about 32%. The identity of this contaminant was not clear. The second onset is somewhat obscured but appears to occur at roughly 30% RH. This onset appears to be caused by a major hygroscopic component in the corrosion product as there is no indication that saturation is approached during the remainder of the run. The identity of this product was ascertained from chemical analysis

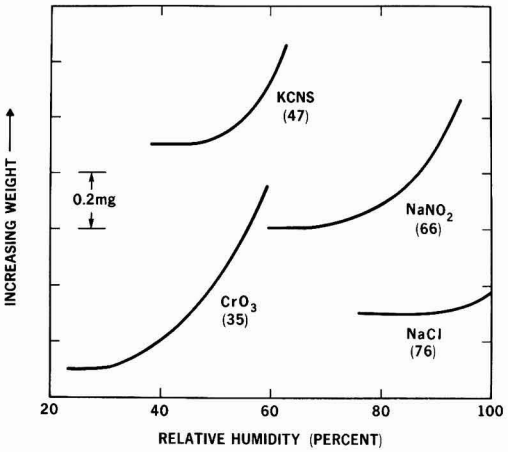

Fig. 4. Moisture pickup onset for selected salts on exposure to increasing RH.

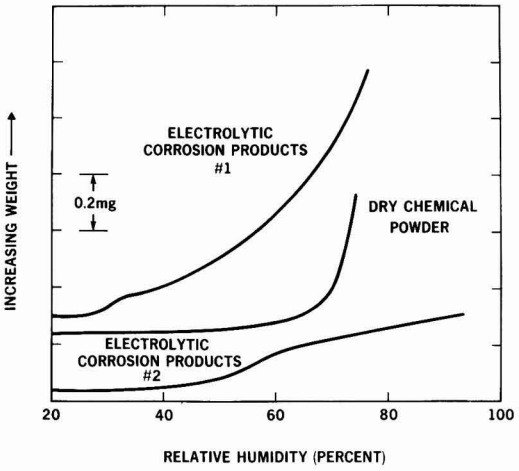

Fig. 5. Moisture pickup onset for corrosive contaminants on exposure to increasing RH.

to be a combination of copper, zinc, and calcium chromates.

The data for a contaminant found on an electromechanical switching device after a nearby battery fire had been extinguished with "dry chemical powder" are also shown in Fig. 5. Again, two onsets occur. The first onset at 27% RH is probably due to adsorption on dust present before the fire and on soot and dry chemical powder. The second onset at 55% RH can be attributed to the formation of a thin aqueous film on the dry chemical powder and the subsequent initiation of rapid moisture pickup. The dry chemical powder was primarily sodium bicarbonate.

The results for dust samples from Holmdel (No. 1) and two locations in New York City (No. 2 and 3) are shown in Fig. 6. The samples exhibited similar characteristics with initial moisture pickup occurring at about 26% RH. These dusts are not known to have caused significant moisture-induced problems on electromechanical switching equipment except at elevated humidity levels, suggesting that moisture pickup is primarily limited to an adsorption process. The large surface area and complex composition typical of dusts permit a significant weight increase to occur before appreciable thin films of aqueous salt solutions are created.

The information summarized in Fig. 7 and 8 demonstrates the utility of this method in ascertaining the quality of materials for electronic devices and assessing contamination or corrosion problems. Data for insulating materials used as substrates and for other purposes are shown in Fig. 7. A number of phenol fiber samples were examined and they exhibited widely variable behavior. The data for a typical sample are shown. An alumina ceramic material exhibited a moderate tendency to pick up moisture at very high RH. The epoxy glass sample was only slightly susceptible to moisture pickup at high RH. Aged textile insulation materials removed from copper wire from two locations in New York City are compared in Fig. 8 with recently manufactured product. Sample No. 1 is from a location which experienced contamination from hydrochloric acid. The onset point at 26% is substantially more pronounced than that of sample No. 2 (which was of similar vintage) or that of the new material. This difference is attributable to the presence of chloride salts in sample No. 1.

Hygroscopicity of substances in a dynamic environment.—Information on the moisture pickup characteristics of substances at high RH is useful for assessing contamination and corrosion hazards and for engineering equipment specifications and building environments. In this study these measurements were accomplished rapidly for a wide variety of substances using a 10 ml/min flow of air nearly saturated with water vapor to simulate typical indoor environments in an accelerated time frame. The substances are ordered on a time-averaged weight-percent basis in Tables II and III according to the increasing tendency of the various materials to gain weight through pickup of water from the nearly saturated air stream. The samples span a broad range of hygroscopicities and are arbitrarily categorized as strongly, moderately, or weakly hygroscopic according to whether their average weight gain rate is greater than 0.110, 0.011-0.110, or less than 0.011 %/min, respectively.

While ordering the samples on this basis seems generally most appropriate, examination of the data indicates this arrangement disguises some factors. For instance, $FeCl_3$ was determined to undergo an average percent weight gain of 0.421 %/min, but the rate decreased over the 94 min exposure period from 0.58 to 0.19 %/min. On the other hand, $CuCl_2 \cdot 2H_2O$ gained weight at an average rate of 0.087 %/min throughout a 324 min exposure period, and the weight gain rate for $FeCl_2 \cdot 4H_2O$ and NaCl actually increased slightly over the duration of the experiments. While it is pos-

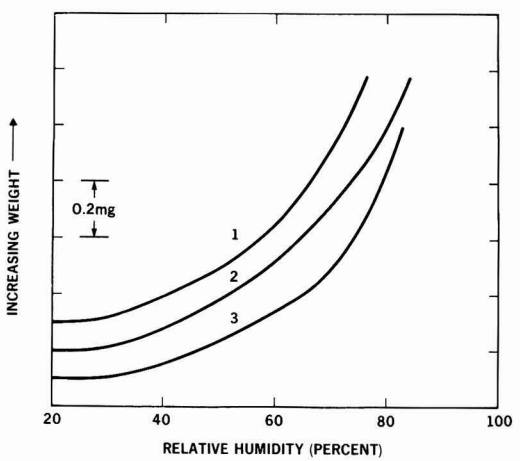

Fig. 6. Moisture pickup onset for dusts on exposure to increasing RH.

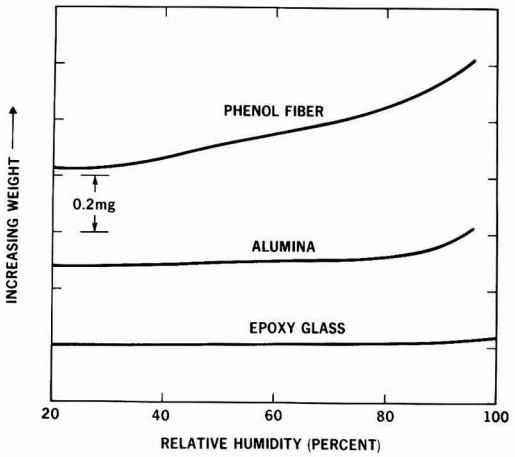

Fig. 7. Moisture pickup onset for insulation and substrate materials on exposure to increasing RH.

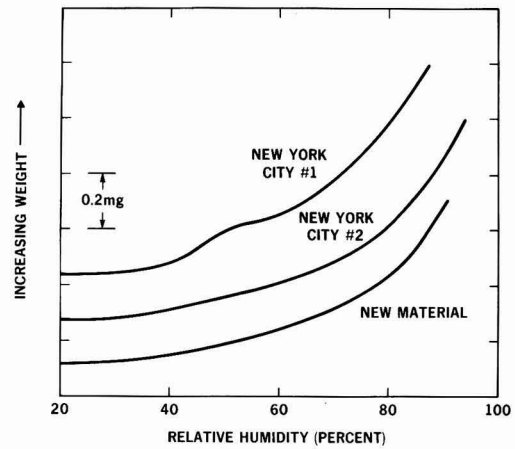

Fig. 8. Moisture pickup onset for textile insulation materials on exposure to increasing RH.

Table II. Hygroscopicity studies

Material	Initial rate of weight gain* (%/min)	Weight gain rate at termination† (%/min)	Total weight gain at termination (%)	Total exposure time (min)	Average weight gain rate throughout run (%/min)	Initial sample weight (mg)
A. Substances of very low hygroscopicity						
Phenol fiber insulation No. 3 (extended urban exposure)	<0.01	<0.01	0.27	1,350	0.0002	62
Epoxy glass (shredded)	<0.01	<<0.01	0.68	2,295	0.0003	67
Alumina ceramic (chips)	<0.01	0	0.18	600	0.0003	106
$PbCO_3$ (powder)	<0.01	0	0.03	68	0.0004	84
CuO (chopped wire)	<0.01	0.00	0.1	165	0.0006	58
Bakelite (chunks)	0.02	<<0.01	2.1	2,640	0.0008	66
Phenol fiber insulation No. 2 (freshly manufactured)	0.02	<<0.01	3.4	4,305	0.0008	57
Arizona Standard Dust	0.02	<<0.01	1.1	1,050	0.001	64
Phenol fiber insulation No. 4 (extended urban exposure)	0.02	<<0.01	2.7	1,380	0.002	35
Talc (hydrous magnesium silicate)	0.03	<<0.01	0.5	165	0.003	54
$NaHCO_3$ (powder)	0.01	<0.01	0.6	135	0.004	87
Textile insulation No. 1 (extended urban exposure)	0.08	0	4.1	825	0.005	58
Textile insulation No. 3 (freshly manufactured)	0.09	0	4.3	860	0.005	43
Textile insulation No. 2 (extended urban exposure)	0.09	0	6.0	1,200	0.005	45
Soot and fire extinguisher powder (White Plains)	0.05	<0.01	78.7	11,250	0.007	60
$CuSO_4 \cdot 5H_2O$ (crystalline)	0.06	<<0.01	0.8	107	0.007	69
$ZnCO_3$ (powder)	0.06	0.00	1.1	128	0.009	25
Phenol fiber insulation No. 1 (freshly manufactured)	0.03	0.01	1.1	113	0.010	73
B. Moderately hygroscopic substances						
Dust (New York, 30th Street)	0.10	0.01	36.0	3,000	0.012	20
Electrolytic corrosion (Philadelphia)	0.11	<0.01	16.2	1,350	0.012	13
Dirt (Red Bank)	0.06	0.00	1.1	84	0.013	69
$CuCO_3$ (powder)	0.05	<<0.01	2.1	167	0.013	102
Dust (New York, 36th Street)	0.06	0.01	21.6	1,545	0.014	31
Dust (New York, Second Ave.)	0.30	<0.01	12.9	860	0.015	21
Electrolytic corrosion (New York)	0.34	<0.01	33.4	1,760	0.019	19
KCl (crystalline)	0.02	0.02	2.2	90	0.024	50
Ag_2S (granules)	0.03	0.03	2.0	75	0.027	80
Electrolytic corrosion (Belle Harbour)	0.14	0.00	2.7	100	0.027	12
Cotton	0.36	0.00	1.7	60	0.028	22
Dust (Holmdel)	0.32	0.01	38.8	1,295	0.030	18
NaCl (crystalline)	0.03	0.04	3.8	110	0.035	87
$SnCl_2 \cdot 2H_2O$ (crystals)	0.05	0.03	6.9	145	0.048	57
$FeCl_2 \cdot 4H_2O$ (crystals)	0.05	0.06	8.9	175	0.051	80
$NiCO_3$ (powder)	0.13	0.03	8.8	143	0.062	45
$CuCl_2 \cdot 2H_2O$ (crystals)	0.09	0.09	28.2	324	0.087	66
C. Very hygroscopic substances						
Electrolytic corrosion (Albuquerque)	0.30	0.00	39.5	323	0.122	7
Drierite (calcium sulfate)	0.17	0.07	4.9	40	0.123	107
Silica gel	0.15	0.11	3.5	26	0.135	87
$ZnCl_2$	0.28	0.19	8.7	34	0.256	102
$CaCl_2$	0.34	0.34	8.1	24	0.338	53
$FeCl_3$	0.58	0.19	39.6	94	0.421	52

* Averaged for the first 2 min.
† Averaged for the last 2 min.

sible to measure or, in principal, calculate the percent weight increase of an initially dry sample maintained at a specific relative humidity until equilibrium is attained, the hazards of estimating corrosion rates of contaminated surfaces solely from such determinations are apparent. Thus, NaCl exposed to 95% RH has a theoretical potential to increase its weight to 1136% of its dry weight (see Table II), while $ZnCl_2$ will increase to only 610% of its dry weight. In a practical sense, however, a surface contaminated with NaCl gaining weight at the rate of 0.035 %/min at 100% RH would require about 48 hr to gain its own weight in water, while a similar amount of $ZnCl_2$ picking up moisture at the rate of 0.19 %/min (the experimental rate at termination of the experiment) would achieve the same weight gain in less than 6 hr. At these rates a 100 mg sample of $ZnCl_2$ (solubility 4320g/1000g H_2O) would completely dissolve in about 90 min, while a 100 mg sample of NaCl (solubility 350g/1000g H_2O) would require about 140 hr to completely dissolve.

A number of samples of corrosion products and contaminants, as well as materials used by the electronics industry, are ranked in Tables II and III with the pure chemicals. The manner in which the data can be used for assessing corrosion and contamination problems can be illustrated with a few examples.

Electrolytic corrosion products which contaminated equipment in an Albuquerque switching center that had been flooded are seen by this ranking procedure to be more hygroscopic than $CuCl_2 \cdot 2H_2O$ and of similar hygroscopicity to Drierite and silica gel. SEM/x-ray analysis of the contaminants indicated that a major component, in addition to sandy soil, was copper chloride or oxychloride. The data indicate the contamination on the Albuquerque equipment could produce serious consequences in the event a high humidity condition occurs. Caution must obviously be exercised, however, to avoid drawing unjustified conclusions based only on the average weight gain rates. For instance, the Albuquerque sample initially picks up moisture at a rate of 0.30 %/min but the rate decreases to essentially zero after 323 min. $CuCl_2 \cdot 2H_2O$ was found, though, to gain weight at a constant rate of 0.09 %/min throughout a 320 min run. Although the average weight gain rate is significantly higher for the Albuquerque sample, it would be inappropriate to predict, on this basis alone, that the Albuquerque sample would pose a greater hazard than contamination by pure $CuCl_2 \cdot 2H_2O$. In a humid environment the $CuCl_2 \cdot 2H_2O$ would eventually pick up moisture equivalent to several times its initial dry weight, while the Albuquerque sample would pick up a maximum of 39.5% of its initial weight. The sandy soil and other insoluble components present in the Albuquerque sample adsorb the cupric chloride and disperse the moisture picked up by the cupric chloride very effectively. Exposure to humidity levels above the calculated CRH for cupric chloride of 69% is rare for heated indoor environments in Albuquerque, so that the hazard posed by this contaminant was estimated to be minimal. Several years of successful operation of most of the equipment since the flood occurred indicates that this is indeed the case.

The electrolytic corrosion sample from the Belle Harbour (New York) equipment, in contrast to that from Albuquerque, contains only traces of chloride salts and is substantially less hygroscopic than the Albuquerque sample. On this basis, only minimal problems were anticipated if exposure to high humidity could be eliminated. The Belle Harbour switching

Table III. Hygroscopicity studies

Material	Average weight gain rate throughout run (%/min)	Solubility (g solute/ 1000g water)*	Maximum theoretical uptake of water at 95% relative humidity (percent of dry weight)*	Critical relative humidity: From this work	Critical relative humidity: Literature or calculated values
A. Substances of very low hygroscopicity					
Phenol fiber insulation No. 3 (extended urban exposure)	0.0002			<22	
Epoxy glass (shredded)	0.0003			Nondiscrete	
Alumina ceramic (chips)	0.0003			Nondiscrete	
$PbCO_3$ (powder)	0.0004	0.0014 (20°C)[L]			
CuO (chopped wire)	0.0006				
Bakelite (chunks)	0.0008			Nondiscrete	
Phenol fiber insulation No. 2 (freshly manufactured)	0.0008			27	
Arizona Standard Dust	0.001				
Phenol fiber insulation No. 4 (extended urban exposure)	0.002			25	
Talc (hydrous magnesium silicate)	0.003				
$NaHCO_3$ (powder)	0.004	69 (0°)[CRC]			
Textile insulation No. 1 (extended urban exposure)	0.005			26, 50	
Textile insulation No. 3 (freshly manufactured)	0.005			27, 55	
Textile insulation No. 2 (extended urban exposure)	0.005			23, 47, 69	
Soot and fire extinguisher powder (White Plains)	0.007			27, 50	
$CuSO_4 \cdot 5H_2O$ (crystalline)	0.007	255 (30°C)[ST]			98[CRC]
$ZnCO_3$ (powder)	0.009	0.206 (25°C)[L]			
Phenol fiber insulation No. 1 (freshly manufactured)	0.010				
B. Moderately hygroscopic substances					
Dust (New York, 30th Street)	0.10			27	
Electrolytic corrosion (Philadelphia)	0.012			23, 30	
Dirt (Red Bank)	0.012				
$CuCO_3$ (powder)	0.013	<0.03 (18°C)[L]			
Dust (New York, 36th Street)	0.06			26	
Dust (New York, Second Avenue)	0.015			25	
Electrolytic corrosion (New York)	0.019			27, 50	
KCl (crystalline)	0.024	373 (30°C)[ST]			
Ag_2S (granules)	0.027	9×10^{-15} (18°C)[CRC]			
Electrolytic corrosion (Belle Harbour)	0.027				
Cotton	0.028				
Dust (Holmdel)	0.030			26	
NaCl (crystalline)	0.035	350 (25°C)[ICT]	1136[PM]	84	75.7[CRC]
$SnCl_2 \cdot 2H_2O$ (crystals)	0.048	839 (0°C)[CRC]			
$FeCl_2 \cdot 4H_2O$ (crystals)	0.051	684 (25°C)[ICT]	855[PM]		40[PM]
$NiCO_3$ (powder)	0.062	0.8 (15°C)[L]			
$CuCl_2 \cdot 2H_2O$ (crystals)	0.087	770 (25°C)[ICT]	735[PM]		69[PM]
C. Very hygroscopic materials					
Electrolytic corrosion (Albuquerque)	0.122				
Drierite (calcium sulfate)	0.123	0.67 (20°C)[L]			
Silica gel	0.135	0.12 (25°C)[L]			
$ZnCl_2$	0.256	4320 (25°C)[ICT]	610[PM]		10[LG]
$CaCl_2$	0.338	819 (25°C)[ICT]	971[PM]		31[CRC]
$FeCl_3$	0.421	918 (20°C)[L]			

* L, W. F. Linke, Editor, "Solubility of Inorganic and Metal Organic Compounds," 4th ed (1965). CRC, "Handbook of Chemistry and Physics," 56th ed. (1975). ST, "Smithsonian Tables," 9th ed. ITC, "International Critical Tables," Vol. 4 (1929). PM, From calculations by P. C. Milner, LG, "Lange's Handbook of Chemistry and Theoretical Chemistry," 11th ed.

center is located in a very humid environment one block from the Atlantic Ocean, but, unfortunately, at the time this water damage occurred, the method described above for determining the CRH was not available and it was not feasible to estimate the CRH by other means. Consequently, specific recommendations concerning the maximum tolerable humidity were not possible.

Recently an electronic switching center in Philadelphia was contaminated with water containing a rust inhibitor. The equipment was powered and electrolytic corrosion occurred. The CRH of the primary contaminant was found to be about 30%, which suggests a serious problem could exist, since the local humidity would nearly always exceed that value. However, the over-all hygroscopicity based on average weight gain rate and total moisture pickup after 1350 hr (16%) was low. This information, coupled with the successful operation of most of the equipment for several weeks after the flood indicated that the restored equipment would continue to operate normally without the need for extensive modifications to the building humidity control.

The equipment installation in White Plains (New York), which suffered the small battery fire described earlier, was analyzed for moisture pickup by this procedure. The contaminant was found to be less hygroscopic than the Philadelphia sample in terms of the average weight gain rate, but this average was based on roughly 10 times the sampling period. The total pickup before an extended steady state was reached was 78.7%. This result, coupled with the dramatic increase in moisture pickup observed above 50% RH, shown in Fig. 5 and discussed above, indicated that cleaning or replacement of the equipment was necessary.

The dust samples from the New York City locations and from Holmdel behave similarly, though the dust from the rural Holmdel environment is, surprisingly, somewhat more hygroscopic. None of these dusts has caused particular problems with electronic equipment. The large surface area of the dusts permits relatively large amounts of moisture adsorption to occur without creating thin films of water. The texture of the Arizona Standard Dust sample was much finer and less fibrous than the dust found in New York City and Holmdel, suggesting the surface area per unit weight is probably greater. The hygroscopicity of the Arizona Dust is, however, about an order of magnitude lower than the other dusts. As more locations are sampled, it is anticipated that unusual dusts bearing localized hygroscopic components will be distinguishable from "ordinary" dusts.

All of the insulation and substrate materials examined fit into the category of substances of low hygroscopicity. Obviously, only nonhygroscopic substances are reasonable candidates for such uses. Within this category, however, a range of moisture pickup rates was found, even for similar materials. For instance, phenol fiber No. 3 picked up moisture at an average of 0.0002 %/min, while phenol fiber samples No. 2 and 4 exhibited rates of 0.0008 and 0.002 %/min, respectively. There appears to be no correlation between age and hygroscopicity, and apparently the dif-

ferences are manufacturing in origin for these samples. Except for one phenol fiber sample, the least hygroscopic substrate materials are the epoxy glass and the alumina ceramic. More data would be needed to draw firm conclusions about the relative hygroscopcity of these substrate materials, and these results should not be extrapolated to all epoxy glass, alumina, and phenol fiber substrates available. Wide variability is likely to exist for different manufacturers and in some cases for different lots. These data demonstrate, however, that instrumental gravimetric methods can be effectively employed in distinguishing the hygroscopic characteristics of a variety of substrate materials that might be considered for device applications.

The behavior of three textile material samples from insulated wire was very similar at the high humidity level at which these experiments were run. Samples 1 and 2 had been exposed approximately 35 years to an urban environment. Sample 2 is of particular interest, as mentioned earlier, because of its unique exposure to hydrochloric acid fumes. Textile insulation typically performs poorly at high humidity levels in terms of insulation resistance. Normally, these humidity levels are not encountered at indoor installations. Unfortunately, the present apparatus is not readily suited to monitoring weight gain characteristics at an intermediate RH, where the effects of contamination on sample 2 would be pronounced. It would also be interesting to know if the freshly manufactured sample would be distinguishable from sample 1 at an intermediate RH.

Conclusion

This work was carried out to determine whether instrumental gravimetric analysis is suited to readily measure the moisture pickup characteristics of materials and substances important to the electronics industry. It was found that many substances initiate moisture pickup processes that are detectable at discrete relative humidities. Furthermore, it was found that moisture pickup characteristics measured gravimetrically at high humidity levels can be used to rank substances in a manner which is useful for assessing hygroscopicity and corrosion hazards. Unknown mixtures of materials weighing only a few tenths of a milligram can be readily analyzed. Moderately to strongly hygroscopic materials can probably be analyzed with even smaller samples. The rate of hygroscopicity change was found, in some cases, to be a signature of the material analyzed, which may prove useful when analyzing samples of unknown composition. The information gathered here clearly demonstrates the need for and the usefulness of an expanded system capable of precise relative humidity programming. Such a system is now under development. Further experiments will include the effects of pollutant gases introduced into the air stream on the measured CRH and moisture pickup rates of substances.

Manuscript submitted Aug. 4, 1977; revised manuscript received Nov. 29, 1977. This was Paper 21 presented at the Philadelphia, Pennsylvania, Meeting of the Society, May 8-13, 1977.

Any discussion of this paper will appear in a Discussion Section to be published in the December 1978 JOURNAL. All discussions for the December 1978 Discussion Section should be submitted by Aug. 1, 1978.

Publication costs of this article were assisted by Bell Laboratories.

REFERENCES

1. W. H. J. Vernon, *Trans. Faraday Soc.*, **27**, 265 (1931); *ibid.*, **31**, 1668 (1935).
2. G. J. Mulder, in "A Comprehensive Treatise on Inorganic and Theoretical Chemistry," Vol. III, J. W. Mellor, Editor, p. 707 (1956).
3. J. W. Mellor, "A Comprehensive Treatise on Inorganic and Theoretical Chemistry," Vol. II, p. 552 (1956).
4. R. St. J. Preston and B. Sanyal, *J. Appl. Chem.*, **6**, 26 (1956).
5. D. C. Lindsay, "International Critical Tables," Vol. 2, pp. 321-325 (1927).
6. T. Kanazawa, M. Chikazawa, M. Kaiho, and T. Fujimaki, *Nippon Kagaku Kaishi*, **9**, 1669 (1973).
7. Y. Hara, S. Okimoto, and H. Osada, *Kogyo Kayaku Kyokai-sh*, **30**, 25 (1969).
8. S. Pawlikowski, S. Szymonik, and A. Chomiakow, *Chem. Stosowana*, **4**, 243 (1960).
9. Yu. A. Vakhrushev and Yu. B. Gradinar, *App. Chem. (USSR)*, **47**(3), 627 (1974).
10. W. Trzesniowski, *Przem. Chem.*, **53**, 225 (1974).
11. I. N. Shokin and A. S. Solov'eva, *Tr. Mosk. Khim.-Technol. Inst.*, **35**, 43 (1961).
12. P. Runge, *Chem. Tech. (Leipzig)*, **27**(6), 359 (1975).
13. J. Yee, *Ind. Eng. Chem.*, **16**, 367 (1944).
14. B. R. Puri and V. Bhushan, *J. Sci. Industr. Res.*, **11B**, 504 (1952).
15. M. W. Kearsely and G. G. Birch, *J. Fd. Technol.*, **10**, 625 (1975).
16. E. O. Whittier and S. P. Gould, *Ind. Eng. Chem.*, **22**, 77 (1930).
17. A. P. Grebennikova, O. M. Todes, and V. A. Fedoseev, *Colloid J.*, **24**, 352 (1962).
18. S. Twomey, *J. Appl. Phys.*, **24**, 1099 (1953).
19. R. A. Bakhanova and L. V. Ivanchenko, *Tr. Ukr. Nauchno-Issled. Gidrometeorol. Inst.*, **133**, 110 (1974).
20. M. M. Markowitz and D. A. Boryta, *J. Chem. Eng. Data*, **6**, 16 (1961).
21. S. Pawlikawski, S. Szymonik, and A. Chomiakow, *Przemysl Chemiczny*, **38**, 598 (1959).
22. F. Modrzejewski and O. Pokora-Bartyzel, *Acta Pol. Pharm.*, **5**, 480 (1966).
23. C-H. Shen and G. S. Springer, *J. Composite Mat.*, **10**, 2 (1976).
24. Kh. Balarev, Kh. Stoeva, and Kh. Stoev, *God. Vissh. Khim.-Tekhnol. Inst., Burgas, Bulg.*, **10**, (10), 623 (1973).
25. (a) P. B. P. Phipps, "The Role of Water in Atmospheric Corrosion," New York Chapter American Vacuum Society Symposium on Corrosion in Thin Films, Princeton, New Jersey, November 17, 1967.
(b) D. W. Rice, P. B. P. Phipps, and R. Tremoureux, "Atmospheric Corrosion of Nickel Thin Films and Foils," Symposium on Deterioration of Electronic Devices, Electrochemical Society Meeting, Philadelphia, May 8-13, 1977.
26. L. M. Foster and G. V. Arbach, *This Journal*, **124**, 164 (1977).
27. F. Mansfeld and J. V. Kenkel, *Corrosion*, **33**, 13, (1977); *Corros. Sci.*, **16**, 111 (1976).
28. P. J. Sereda, ASTM Bull. No. 246, 47 (1960).
29. H. Gutman, Metal Corrosion in the Atmosphere, ASTM STP 435, 223 (1968).
30. G. K. Berukshtis and G. B. Klark, "Corrosion of Metals and Alloys," Collection, NLL Boston Spa., 379 (1964).
31. "CRC Handbook of Chemistry and Physics," 52nd ed., R. C. Weast, Editor (1971-1972).

Kinetics of the Slow-Trapping Instability at the Si/SiO_2 Interface

A. K. Sinha* and T. E. Smith

Bell Laboratories, Murray Hill, New Jersey 07974

ABSTRACT

The slow-trapping instability can be a potentially major threat to reliability of p-channel enhancement-mode IGFET's. We have determined the kinetics of slow trapping for Al-gate MOS structures on (111) n-Si and evaluated the role of surface states, N_{SS}, for n- and p-type Si of (111) and (100) orientation. Slow trapping, as revealed by negative bias-temperature aging, generates a characteristic distribution of N_{SS} with a peak near the midgap. This effect is responsible for the fact that for n-Si, the threshold shift, $\Delta V_T >> \Delta V_{FB}$, the flatband shift, and for p-Si, $\Delta V_T < \Delta V_{FB}$. In the regime where ΔV_{FB} is less than the saturation value, our data on slow-trapping kinetics can be represented by the factorial relationship

$$\Delta V_{FB} \sim A|V_B|^n t^{0.2} \exp\left(-\frac{\epsilon_a}{kT}\right)$$

where V_B is the applied negative bias (10-40V), t is the time (10-10^3 min), T is the temperature (373°-573°K), k is the Boltzmann constant, $n = 4.76 - 5.3 \times 10^{-3}T$, $A \sim 1.6 \times 10^3$, and ϵ_a is the thermal activation energy (~0.64 eV). This equation emphasizes the strong field dependence of ΔV_{FB} at lower temperatures.

The so-called slow-trapping instability [instability No. VI of XVII compiled by Deal (1)] can be a potentially major threat to reliability of p-channel enhancement mode IGFET devices (1-4). This instability is revealed by a negative bias-temperature aging test which causes a negative shift in the flatband voltage and hence in the threshold voltage of the device. The exact mechanism of slow trapping has not been established. But it is known that slow trapping is more pronounced for MOS structures with a high fixed charge, Q_{SS} (4). Slow-trapping instability can be also aggravated by radiation damage (5) and by a low temperature post Al-metallization H_2 anneal (6).

Accelerated aging tests are commonly used to compare the slow-trapping characteristics of different MOS structures and also to evaluate the effectivity of various processing improvements [such as high temperature H_2 annealing (6)] aimed at reducing the slow trapping. However, a knowledge of kinetics is also obviously necessary in order to estimate the lifetime under device operating conditions and to stimulate work on understanding of slow-trapping phenomena.

The objective of the present work is twofold. First, the role of surface states, N_{SS}, was investigated in the slow-trapping phenomena. It is shown that a characteristic distribution of N_{SS} is generated as a result of slow trapping, and depending upon whether the Si is n- or p-type, the flatband shift ΔV_{FB} can be less than or greater than ΔV_T. Second, detailed kinetics measurements were made of slow trapping in Al/SiO_2/(111) n-Si capacitors. The effect of applied bias (for a given time and at lower temperatures) is found to be more severe than previously believed.

Experimental

Slow-trapping measurements were made on both n- and p-type Si wafers [(111 and 100) orientation, 2 in. diam, $N_{D,A} \sim 10^{15}$ cm^{-3}]. The wafers were cleaned and then oxidized to 1000Å thickness at 1100°C in a dry oxygen ambient in an HCl-cleaned quartz tube. The oxidized wafers received an *in situ* Ar-anneal at 1100 C for ½ hr. An array of MOS capacitors was fabricated by filament evaporating Al-field plates (20 mil diam) through a mechanical shadow mask. The SiO_2 was etched off from the back side and an Al back contact was formed also by filament evaporation. The samples were then H_2-baked at 450°C, ½ hr.

MOS measurements were made in a test facility consisting of an electroglas 910 prober equipped with a Temptronix TP 35 thermochuck and enclosed in a dry N_2 glove box (7). High frequency (1 MHz) C-V measurements were made at a sweep rate of 100 mV/sec. Quasistatic measurements were made at 20 mV/sec using the slow-ramp technique (8). The data were analyzed in the usual manner to give the Si-doping level (9), the flatband capacitance and voltage, the oxide fixed charge Q_{SS}, and the surface-state density as a function of the relative surface potential, ψ_S. The surface-state density was obtained from the high-low frequency capacitance technique (10) and ψ_S found as a function of bias using the Berglund techniques (11).

The extent of slow trapping was evaluated through measurements of negative shift in the flatband voltage, ΔV_{FB}, following bias-temperature aging at various temperatures in the range 100°-300°C, with applied negative bias of 10-40V, and for times of 10 min-16 hr.

Results and Discussion

Positive bias-temperature aging under conditions (10^5 V/cm, 200°C, 30 min) where slow trapping is very small caused little or no negative shift (<0.1V) in the C-V curves, signifying that the mobile charge contamination levels were below 2×10^{10} cm^{-2}.

Representative C-V curves.—Figure 1 shows typical C-V curves for a MOS structure on (111) n-Si in the as-received condition and after B-T aging at −23.5V, 250°C, for 15 min. The as-received sample had a Q_{ss} of 2×10^{11} cm^{-2} and a midgap N_{SS} of $\sim 5 \times 10^{10}$ cm^{-2} eV^{-1}. Upon negative B-T aging, the slow trapping is revealed in three ways: (*i*) the high frequency C-V curve is shifted to more negative values reflecting an increase in the apparent Q_{SS} and a ΔV_{FB} of −0.8V; (*ii*) the initially single minimum in the quasistatic C-V curve is split into two minima which now occur at significantly higher C/C_{ox}; this higher C/C_{ox} is the result of an order of magnitude increase in the N_{SS} which has a peak near the midgap, as shown in Fig. 2; (*iii*) there is an increase (by ~1.5V) in the negative threshold voltage from V_{T1} to V_{T2}, as indicated by the vertical

* Electrochemical Society Active Member.
Key words: MOS devices, reliability, surface states.

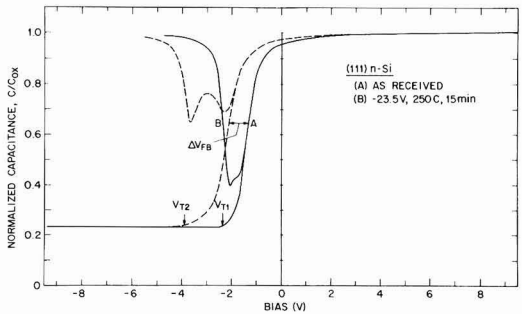

Fig. 1. C-V curves for Al/SiO_2/n(111)Si capacitors: (A) as-received; (B) after —23.5V, 250°C, 15 min bias-temperature aging.

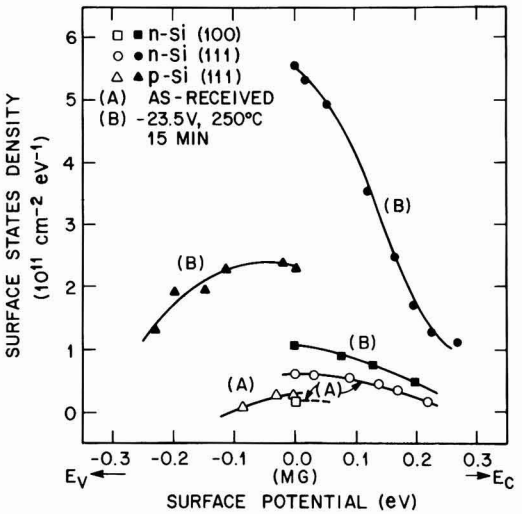

Fig. 2. Distribution of surface states in various Al/SiO_2/Si structures: (A) as-received; (B) after —23.5V, 250°C, 15 min B-T aging.

arrows in Fig. 1, with $\Delta V_T >> \Delta V_{FB}$. This is due to the fact that increases in both Q_{SS} and N_{SS} due to slow trapping with n-Si cause threshold shifts in the same direction, which are therefore additive. Moreover, for n-Si, there are fewer occupied surface states at V_T than at flatband voltage. For p-Si, there are more occupied states at T than at flatbands.

Figure 3 shows the effects of slow trapping in an Al-gate MOS structure on (111) p-Si. Here too there is a negative shift in the flatband voltage, ΔV_{FB}, which is nearly equal in magnitude to that observed with (111) n-Si. There is also a significant increase in N_{SS} and a tendency toward splitting of the minimum in the quasistatic C-V curve. However, in this case, ΔV_T is much smaller than ΔV_{FB}, since the apparent ΔV_T components due to additional Q_{SS} and N_{SS} now are in opposite directions. The distribution of $N_{SS}(\psi_S)$ for the (111) p-Si sample before and after B-T aging is shown in Fig. 2 and is similar to that for (111) n-Si.

Figure 4 shows C-V data for (100) n-Si before and after B-T aging. The magnitudes of both ΔV_{FB} and ΔV_T are smaller by a factor of four than those for (111) n-Si. It should be also noted that the initial Q_{SS} ($\lesssim 10^{10}$ cm^{-2}) and N_{SS} at midgap ($\sim 10^9$ cm^{-2} eV^{-1}, see Fig. 2) for this sample were lower by an order of magnitude when compared with (111) n-Si.

This and other recent work support the conclusion that the initial Q_{SS} may be a major factor controlling the slow-trapping instability—a small Q_{SS} correlates with reduced slow trapping. For (111) n-Si samples, the Q_{SS} can be decreased to $\lesssim 1 \times 10^{11}$ cm^{-2} by a high temperature H_2 anneal (800°-900°C, ½-1 hr). These samples show a very small ΔV_{FB} of ~0.2V after 250°C, —20V, 15 min aging. On the other hand, a low temperature H_2 anneal (450°C, ½ hr), which lowers the N_{SS}, tends to enhance the slow-trapping instability (6).

Kinetics data.—Kinetics measurements were made for (111) n-Si samples which had received the post-Al H_2-bake (450°C, ½ hr) but no high temperature H_2 anneal. The ΔV_{FB} was measured for various conditions of negative-bias temperature aging in which two of the three variables, namely, time, temperature, and bias, were kept constant and the third one was changed.

Figure 5 shows the effect of applied bias V_B on ΔV_{FB} induced by slow trapping. Results are shown for various temperatures (80°, 150°, 200°, 250°, and 300°C) for a fixed time of 15 min and for bias voltages ranging from —4 to —80V. [Although bias voltages are quoted in this paper, it should be understood that the field across the oxide and not the voltage is the parameter that determines ΔV_{FB} for various oxide thicknesses (4).] At a given temperature, ΔV_{FB} is a strong function of V_B, with

$$\frac{\partial \log (\Delta V_{FB})}{\partial \log |V_B|} \approx n \qquad [1]$$

where the exponent n ($1.5 < n < 3.2$) is an inverse function of the aging temperature T (°K), as shown in Fig. 6. According to this figure, n will approach unity around 400°C, at which temperature ΔV_{FB} will be a simple linear function of V_B. This is the form of ΔV_{FB} (V_B) relationship reported by Deal *et al.* (4) who plotted the maximum flatband shift measured at ~400°C. At this temperature, saturation in ΔV_{FB} is reached in a relatively short time of few minutes. For the temperatures used in the present work, 15 min was too short a time to reach saturation or steady-state

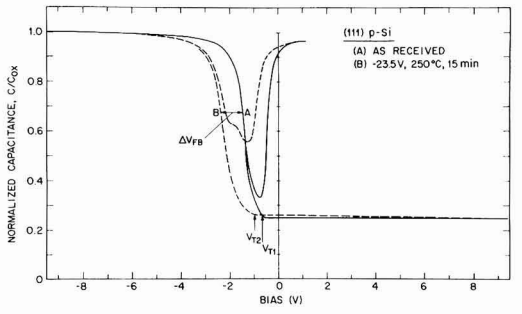

Fig. 3. C-V curves for Al/SiO_2/p(111)Si capacitors: (A) as-received; (B) after —23.5V, 250°C, 15 min B-T aging.

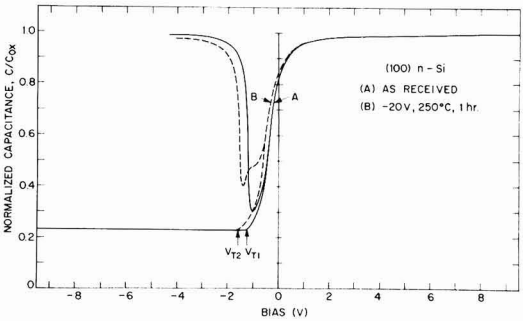

Fig. 4. C-V curves for Al/SiO_2/n(100)Si capacitors: (A) as-received; (B) after —23.5V, 250°C, 15 min B-T aging.

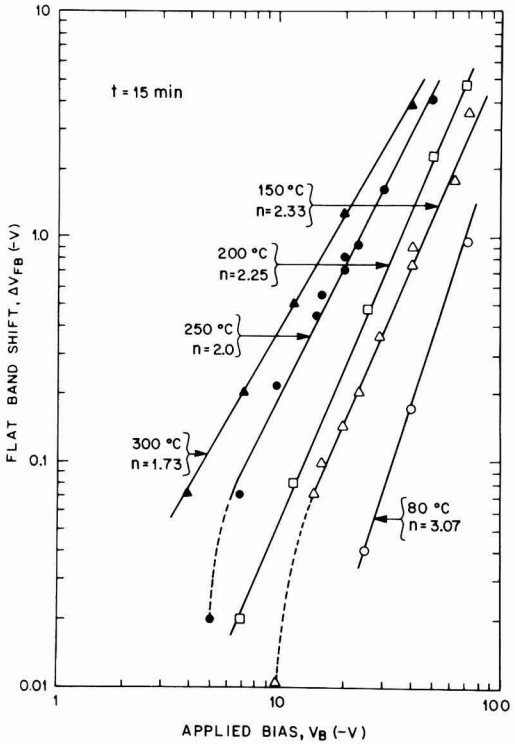

Fig. 5. Variation of slow-trapping induced flatband shift with applied bias at different temperatures, and for times of 15 min.

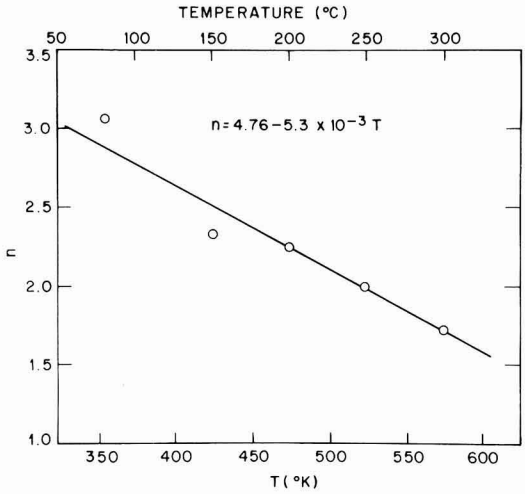

Fig. 6. Temperature dependence of exponent n in Fig. 5

conditions, yet it was adequate to reveal a ΔV_{FB} of 0.1-5V provided the bias fields were large enough.

The nonsteady-state conditions investigated in the present work were preferred because they were convenient and also because they correspond more closely to the device behavior during its operation. Thus, slow-trapping shifts usually cause the device threshold voltage to go out of specification long before the saturation value has been attained.

Figure 7 shows the variation with time of ΔV_{FB} at various temperatures, keeping V_B constant at -20V. It

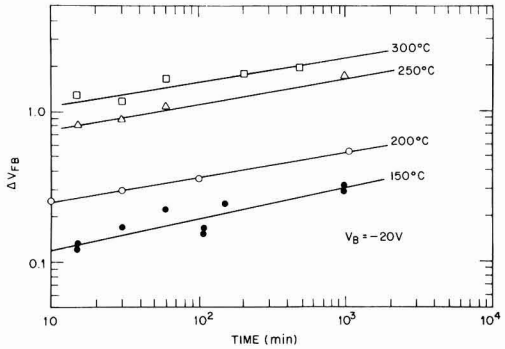

Fig. 7. Time dependence of flatband shift due to slow trapping at various temperatures and for an applied bias of -20V.

may be seen that a substantial portion of the slow trapping shift is revealed in 15 min; however, there continue to be additional shifts with increasing time. For the present samples, the time dependence ($t > 10$ min) was relatively weak, with

$$\frac{\partial \log \Delta V_{FB}}{\partial \log t} \approx 0.2 \qquad [2]$$

This form of time dependence again relates to ΔV_{FB} data below the saturation value.

Figure 8 shows an Arrhenius plot in which ΔV_{FB} has been normalized with $|V_B|^n$ and $t^{0.2}$. A remarkably good fit is obtained for the present set of samples, giving an apparent thermal activation energy of ~0.64 eV. Also shown in Fig. 8 are certain results taken from the work by Broydo and Waggener (12). The combined data show a relatively large degree of scatter, indicating that the slow-trapping kinetics are also a sensitive function of the starting material and that

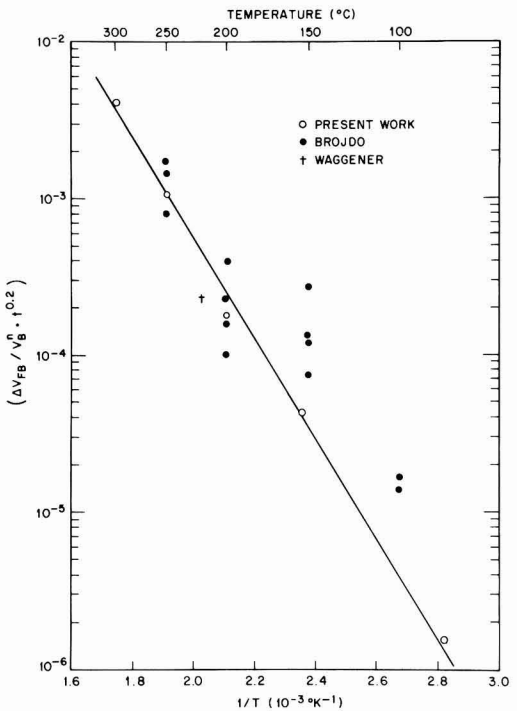

Fig. 8. Arrhenius plot of normalized ΔV_{FB} due to slow trapping

it may not yet be possible to provide a universal equation for ΔV_{FB}.

Results in Fig. 8 for the present samples (a single lot of six wafers) do indicate, however, that it is possible to rationalize over 30 measurements of ΔV_{FB} in terms of the following simple factorial relationship

$$\Delta V_{FB} = A|V_B|^{n(T)}t^{0.2}\exp\left(-\frac{\epsilon_a}{kT}\right) \quad [3]$$

where, $A = 1.576 \times 10^3$, $\epsilon_a = 0.64$ eV, $n = 4.76 - 5.3 \times 10^{-3}T$. Equation [3] contains only a single thermal activation energy term and it gives proper weight to the effects of applied bias and time. As noted earlier, the above functional dependence is valid only for ΔV_{FB} values prior to saturation.

The theoretical implications of Eq. [3] are not clear. We believe that the present results lend some support to the model of Deal (1), namely that slow trapping is caused by field-temperature induced structural rearrangements at the Si/SiO_2 interface. In Deal's model (1), a displaced oxygen atom which would otherwise bridge two Si atoms at the interface can simultaneously lead to a positive charge in the oxide and a surface state (dangling bond) in the Si. The ease of such a displacement would depend on the microstrain initially present in the Si-O bond at the interface. It is conceivable that the interfacial strain is related to the magnitude and screening distance of the fixed charge (excess Si atoms?) always present at the SiO_2/Si interface. It appears that this (compressive) strain also provides the driving force for slow trapping. The roles of temperature and applied field in causing dissociation of strained O-Si bonds appear to be complementary. Thus, as the temperature gets smaller, V_B tends to have a more pronounced effect on ΔV_{FB}.

Summary and Conclusions

The slow-trapping instability has been investigated for n- and p-type (111) Si and for n-type (100) Si.

1. For well-annealed MOS structures, negative bias-temperature aging causes a characteristic splitting of the quasistatic C-V curve; the resulting N_{SS} has a peak near the midgap. This N_{SS} effect is responsible for the fact that for n-Si, $\Delta V_T > \Delta V_{FB}$ whereas for p-Si, $\Delta V_T < \Delta V_{FB}$.

2. For a given time and temperature and ΔV_{FB} less than the saturation value, ΔV_{FB} increases with the applied field. The field dependence gets stronger at lower temperatures.

3. For a given field and temperature, and time greater than 10 min, there is a relatively slow variation ΔV_{FB} with time.

4. For a given set of identical samples, it is possible to normalize ΔV_{FB} with respect to the applied bias and time, the resulting temperature dependence yields a single-valued activation energy equal to 0.64 eV for the presently studied $Al/SiO_2/n(111)Si$ structures.

Acknowledgments

Thanks are due to J. V. Dalton and W. Sachs for their assistance with sample fabrication and to W. Bertram, H. J. Levinstein, and R. S. Wagner for helpful conversations.

Manuscript submitted June 23, 1977; revised manuscript received Nov. 7, 1977.

Any discussion of this paper will appear in a Discussion Section to be published in the December 1978 JOURNAL. All discussions for the December 1978 Discussion Section should be submitted by Aug. 1, 1978.

Publication costs of this article were assisted by Bell Laboratories.

REFERENCES

1. B. E. Deal, *This Journal*, **121**, 198C (1974).
2. E. H. Nicollian, "12th Annual IEEE Proceedings Rel. Phys.," p. 267 (1974).
3. S. R. Hofstein, *Solid-State Electron.*, **10**, 657 (1967).
4. B. E. Deal, M. Sklar, A. S. Grove, and E. H. Snow, *This Journal*, **114**, 266 (1967).
5. K. G. Aubuchon, E. Harari, and P. Chang, Ann. Rep. Contract No. N00014-72-C-0424, Dept. of Navy, Office of Naval Research, Arlington, Va., October 1974.
6. A. K. Sinha, H. J. Levinstein, L. P. Adda, E. N. Fuls, and E. I. Povilonis, To be published.
7. A. K. Sinha, *This Journal*, **123**, 65 (1976).
8. M. Kuhn, *Solid-State Electron.*, **13**, 873 (1970).
9. A. S. Grove, B. E. Deal, E. H. Snow, and C. T. Sah, *Solid State Electron.*, **8**, 145 (1965).
10. R. Castagne and A. Vapaille, *Surf. Sci.*, **28**, 157 (1971).
11. C. N. Berglund, *IEEE Trans. Electron. Devices*, **ed-13**, 701 (1966).
12. S. Broydo and T. Waggener, Private communication.

Two-Layer Model for Heat-Treated Anodic Tantalum Oxide

A. Climent, J. M. Martinez-Duarte and J. M. Albella[1]

Departamento de Física Aplicada e Instituto de Física del Estado Sólido (C.S.I.C.), Universidad Autónoma de Madrid, Cantoblanco, Madrid, Spain

ABSTRACT

The dielectric properties of Ta_2O_5 thin films, grown anodically in a phosphoric acid solution and subjected to heat-treatment, have been investigated as a function of frequency in the range 0.1-100 kHz and temperatures from $-100°$ to 300°C. The experimental evolution of tan δ and series capacitance with the frequency and temperature is reproduced theoretically assuming that the anodic oxide has two layers with a different exponential conductivity gradient. The imaginary part of the dielectric constant shows a relaxation process of the Maxwell-Wagner type, which is also explained by the above model for the oxide.

In the manufacture of tantalum capacitors the anodic oxide is normally subjected to temperatures above 200°C in the process of the pyrolytic deposition of the manganese oxide solid electrolyte. The dielectric properties of the resulting oxide have been thoroughly investigated by Smyth *et al.* (1), who reached the conclusion that a gradient in the electrical conductivity

[1] Permanent address: Instituto de Optica Daza de Valdés (C.S.I.C.), Serrano, 121, Madrid-6, Spain.
Key words: dielectric properties, Maxwell-Wagner model, tantalum capacitors, heat-treatment in anodic oxides.

across the oxide is formed due to the migration of oxygen atoms which are partially dissolved in the tantalum substrate. Furthermore, the incorporation of phosphorus in the outer part of the oxide during anodization in the standard phosphoric acid electrolyte has been well established by several techniques such as radiotracer measurements (2), Auger electron spectroscopy (3, 4), and infrared reflectance spectroscopy (5). For these samples, the heat-treatment results in two layers in the oxide with different electrical conductivity gradients (1). The outer layer presents a steeper gradient and lower conductivity than the inner layer as a consequence of a smaller diffusion of the oxygen atoms due to the phosphorus incorporation.

Based on the previous work of Smyth *et al.* (1), the two-layer exponential gradient model has been quantitatively applied in this paper to tantalum oxide anodized in a phosphoric solution. From the experimental results obtained in this work, all the parameters which characterize the dielectric properties of each layer have been evaluated. Then, according to the model, the curves of the dependence of capacitance and loss factor with frequency and temperature are computed and compared to the experimental values, resulting in a good agreement. In addition, it has been mathematically shown in detail how a relative maximum in the dependence of the loss factor with frequency arises in the two-layer exponential gradient model.

Experimental

Tantalum foil from Reframet Hoboken with a thickness of 0.1 mm and 99.96% purity was anodized in a 0.01% H_3PO_4 electrolyte at a current density of about 10A m^{-2}. Previous to anodization, the samples were thoroughly degreased and chemically etched in a 5:2:2 mixture of sulfuric, nitric, and fluorhydric acids. Samples of 1.5 × 0.5 cm were cut and three gold counterelectrodes with a diameter of about 2 mm were evaporated along each of the samples. A thin copper wire was attached to the gold spot by means of a gold paint. Finally, the samples were subjected to a 350°C heat-treatment for 20 min under high vacuum.

The series capacitance, C_s, and the loss factor, tan δ, $\pi/2 - \delta$ being the angle between the current and the voltage, were measured with a General Radio 1620-A capacitance bridge in which the oscillator was substituted by a Hewlett Packard 3310-A sinusoidal generator in order to increase the frequency range to 100 kHz. All the measurements were performed with the samples inside a cryostat connected to a vacuum pump. The temperature was controlled by means of a Chromel-Chromel Alumel thermocouple.

Results and Theoretical Model

Figures 1-4 show the dependence of the capacitance and tan δ with temperature and frequency. These results suggest the existence of a conductivity profile (1) with two different exponential gradients. They also imply the existence of a critical level of conductivity σ_c such that the portion of the dielectric film with $\sigma > \sigma_c$ is short-circuited acting as part of the electrode. σ_c is given by

$$\sigma_c = \omega \epsilon \epsilon_0 \qquad [1]$$

where ω is the angular frequency, ϵ the dielectric constant, and ϵ_0 the permittivity of vacuum. From Eq. [1] we can get an idea of the variation of the conductivity across the oxide by plotting the logarithm of frequency as a function of $1/C$, since $1/C$ is proportional to the effective thickness of the dielectric. Figure 5 shows such plots, obtained from Fig. 1, at different temperatures. It can be appreciated that for a temperature of 193°K and in the frequency range studied, σ_c should be above the value of σ at the $Ta\text{-}Ta_2O_5$ interface (conductivity profile at T_1 in Fig. 6a). As the temperature is raised to 303°K, the conductivity increases and the most conductive portion of the profile raises above σ_c (relative position as for the profile at T_2 in Fig. 6a). As the temperature is further increased to 383°K, the most resistive or outer layer of the film starts to appear and at 433°K

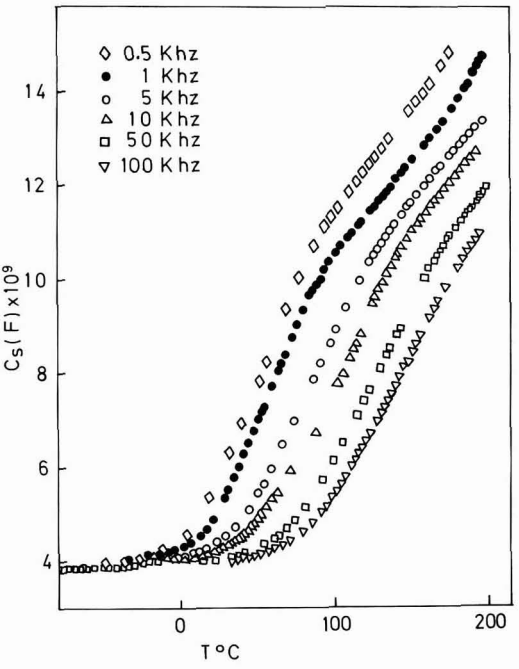

Fig. 1. Temperature dependence of capacitance at several frequencies. The sample was subjected to a heating of about 400°C during 20 min in vacuum. The formation voltage is 100V.

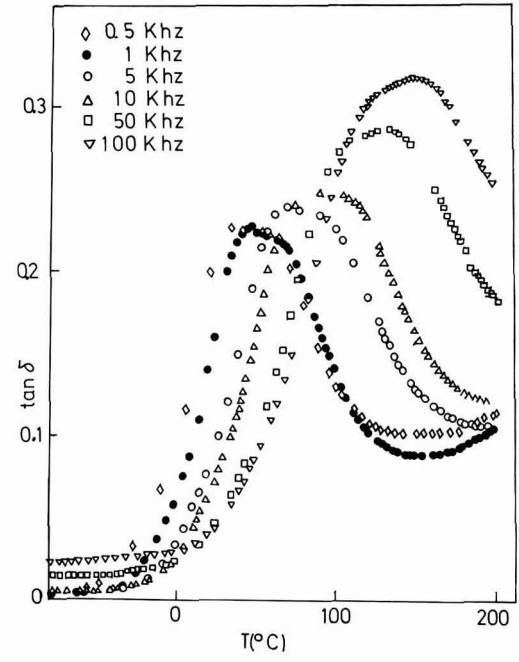

Fig. 2. Temperature dependence of tan δ for the sample of Fig. 1.

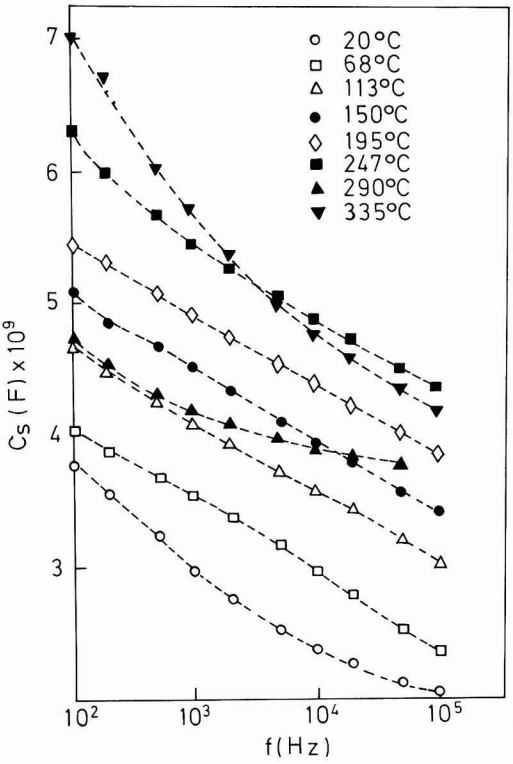

Fig. 3. Frequency dependence of capacitance at several temperatures. The sample was subjected to a heating of about 400°C during 20 min in air. The formation voltage is 120V.

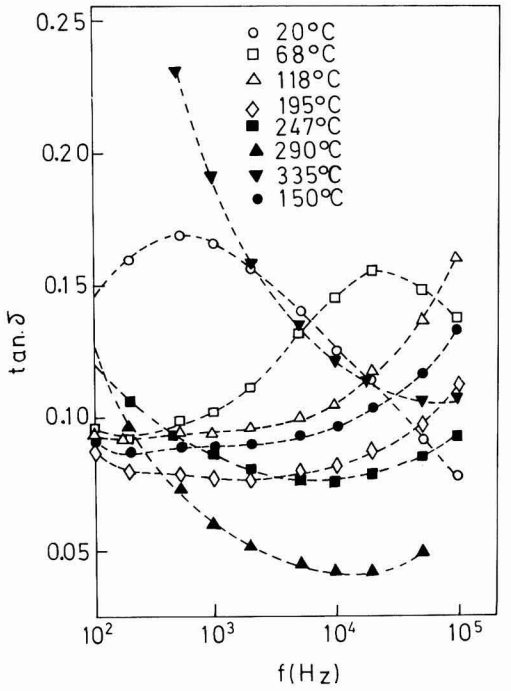

Fig. 4. Frequency dependence of tan δ at several temperatures for the sample of Fig. 3.

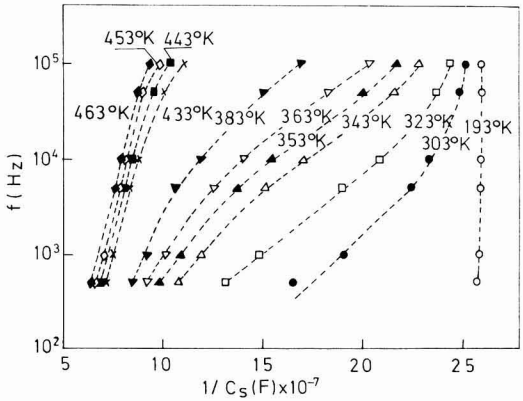

Fig. 5. log f vs. $1/C_s$ for the sample of Fig. 1

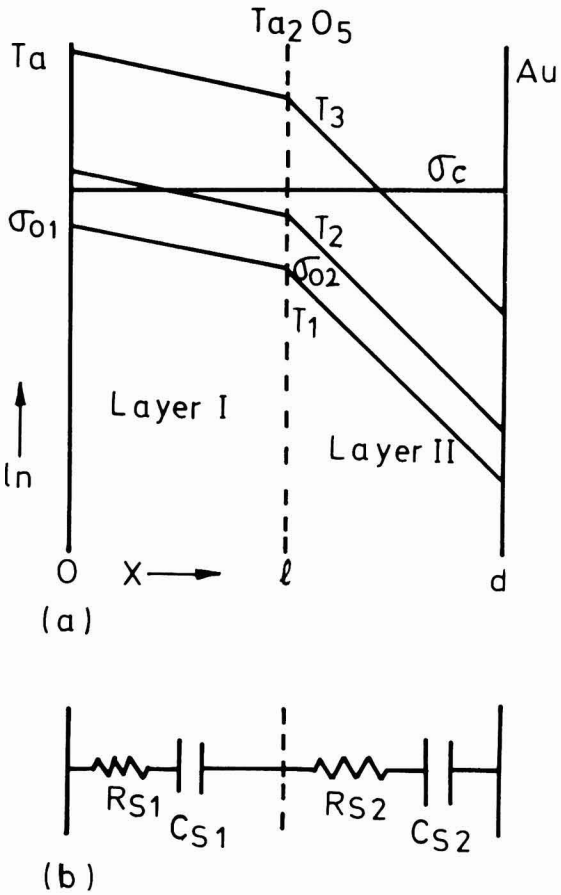

Fig. 6. (a) Double exponential gradient conductivity profile across the oxide for three temperatures $T_1 < T_2 < T_3$ and fixed frequency. (b) Equivalent circuit for the two-layer dielectric.

the conductivity of an important part of this layer is above σ_c (conductivity profile at T_3 in Fig. 6a).

The oxide's equivalent circuit chosen for our model is shown in Fig. 6b. It is formed by two capacitance-resistance series circuits, each representing one portion of the film, connected in series. Young (6) has obtained expressions for the series capacitance C_s and

the equivalent series resistance R_s of a dielectric with an exponential gradient conductivity profile of the form

$$\sigma = \sigma_0 \exp(-ax) \quad [2]$$

These expressions are

$$R_s = \frac{1}{aA\omega\epsilon\epsilon_0}\left(\tan^{-1}\frac{\omega\epsilon\epsilon_0}{\sigma_0 e^{-ad}} - \tan^{-1}\frac{\omega\epsilon\epsilon_0}{\sigma_0}\right) \quad [3]$$

$$\frac{1}{C_s} = \frac{1}{2aA\epsilon\epsilon_0}\log\left[\frac{1+\left(\frac{\omega\epsilon\epsilon_0}{\sigma_0 e^{-ad}}\right)^2}{1+\left(\frac{\omega\epsilon\epsilon_0}{\sigma_0}\right)^2}\right] \quad [4]$$

where A is the electrode's area and d is the thickness of the dielectric. In this derivation ϵ is supposed to be a constant, that is, the influence exerted on the capacity as a consequence of the variation of ϵ with frequency will be neglected in comparison to the influence due to a change in the effective dielectric thickness when $\sigma > \sigma_c$. We will apply next Eq. [3] and [4] to each of the layers in the dielectric.

At a distance x from the Ta-Ta_2O_5 interface and at a temperature T, the conductivity of the oxide can be expressed as

$$\sigma_{x,T} = B\exp\left(-\frac{E_x}{kT}\right) \quad [5]$$

where E_x, the activation energy of the conductivity (7), is given by

$$E_x = E_0 + bx \quad [6]$$

In this equation, E_0 is the activation energy at the Ta-Ta_2O_5 interface and the value of the coefficient b depends on the value of the slope of the exponential gradient. We will also take into account the variation of the dielectric constant with temperature according to

$$\epsilon = \epsilon_c + \alpha T \quad [7]$$

The values of ϵ_c and α can be deduced from the experimental values of Fig. 1 in the region of low temperatures where $\sigma_c > \sigma_{x=0}(T)$ and the decrease of the effective dielectric thickness has not occurred yet.

Taking into account the dependence of σ and ϵ with temperature by means of Eq. [5] and [7] and defining R_s and C_s for each layer of the dielectric by Eq. [3] and [4], we get

$$C_s(T,\omega) = \frac{C_{s1}(T,\omega)\cdot C_{s2}(T,\omega)}{C_{s1}(T,\omega)+C_{s2}(T,\omega)} \quad [8]$$

$$R_s(T,\omega) = R_{s1}(T,\omega) + R_{s2}(T,\omega) \quad [9]$$

$$\tan\delta(T,\omega) = R_s(T,\omega)C_s(T,\omega)\omega \quad [10]$$

The theoretical results predicted by the double layer conductivity profile model are obtained from Eq. [8] and [10] and later on compared to the experimental results. The parameters $\sigma_{x=0}(T)$, $\sigma_{x=1}(T)$, $a_1(T)$, and $a_2(T)$ in Eq. [8]-[10] are obtained from the experimental values. The dependence of a_1 and a_2 on temperature can be derived from Eq. [2], [5], and [6]

$$a_1 = \frac{b_1}{kT};\quad a_2 = \frac{b_2}{kT} \quad [11]$$

The values of the electrical parameters shown in Table I have been obtained by the procedure just indicated from the results of Fig. 1 and 2. The position l within the oxide (see bottom of Table I), where the exponential conductivity gradient changes, is first obtained from the break in slope of the lines in Fig. 5 and further adjusted by fitting the curves obtained from Eq. [8] and [10] to the experimental values.

The dependence of the capacitance and tan δ with temperature, at several frequencies, which is given by Eq. [8] and [10], has been calculated by means of a computer and are compared in Fig. 7 and 8 with the experimental results.

Table I. Values of some significant parameters for the sample described in Fig. 1

Formation voltage V_f = 100V
$b_1 = 1.554 \times 10^{-4}$ eV A^{-1} $b_2 = 1.164 \times 10^{-3}$ eV A^{-1}
a_1 (at 293°K) $= 6.15 \times 10^{-3}$Å^{-1} a_2 (at 293°K) $= 4.61 \times 10^{-2}$Å^{-1}
a_1 (at 520°K) $= 3.47 \times 10^{-3}$Å^{-1} a_2 (at 520°K) $= 2.60 \times 10^{-2}$Å^{-1}
At 293°K: $\sigma_0 = 8.62 \times 10^{-8}\Omega^{-1}$cm^{-1}; $\sigma_1 = 1.2 \times 10^{-10}\Omega^{-1}$cm^{-1}
σ_d(extrapolating) $= 5.3 \times 10^{-24}\Omega^{-1}$cm^{-1}
At 520°K: $\sigma_0 = 2.75 \times 10^{-3}\Omega^{-1}$cm^{-1}; $\sigma_1 = 6.8 \times 10^{-5}\Omega^{-1}$cm^{-1}
σ_d(extrapolating) $= 2.0 \times 10^{-12}\Omega^{-1}$cm^{-1}
Activation energy at interface Ta-Ta_2O_5: $E_0 = 0.60$ eV
Activation energy at interface between layers I and II: $E_1 = 0.76$ eV
$B = 1.79 \times 10^{3}\Omega^{-1}$cm^{-1}
$\epsilon = \epsilon_c + \alpha T$, where $\epsilon_c = 23.36$ and $\alpha = 3.44 \times 10^{-3}$ K^{-1}
Thickness d = 1730Å [assuming an anodization constant of k = 17.3 Å/V (11)]
l (distance between the Ta-Ta_2O_5 interface and the layer I-layer II interface): 1063Å

Discussion

The agreement between the values deduced from the two-layer conductivity profile model and the experimental values is quite good as it can be appreciated from Fig. 7 and 8. The maxima in the tan δ *vs.* T curves are usually higher and more pronounced for the computed curves. This is attributed to the hypothesis that the dielectric is only formed by two layers, the exponential conductivity gradient being constant in each layer. In practice, at the two metal-oxide junctions as well as at the junction between the two layers in the dielectric, the conductivity might have values quite different from the assumed ones. One refinement, therefore, could be to assume that the dielectric is divided into three zones, with one intermediate in which the exponential gradient has a slope with a value between a_1 and a_2.

The evolution with frequency of some of the parameters characterizing each of the two layers is represented in Fig. 9. From Eq. [8] and [9], tan δ can be written as

$$\tan\delta = \omega(R_{s1}+R_{s2})\frac{C_{s1}C_{s2}}{C_{s1}+C_{s2}} \quad [12a]$$

or

$$\tan\delta = \tan\delta_1\frac{C_{s2}}{C_{s1}+C_{s2}} + \tan\delta_2\frac{C_{s1}}{C_{s1}+C_{s2}} \quad [12b]$$

where $\tan\delta_i = \omega R_{si}C_{si}$, $(i = 1, 2)$.

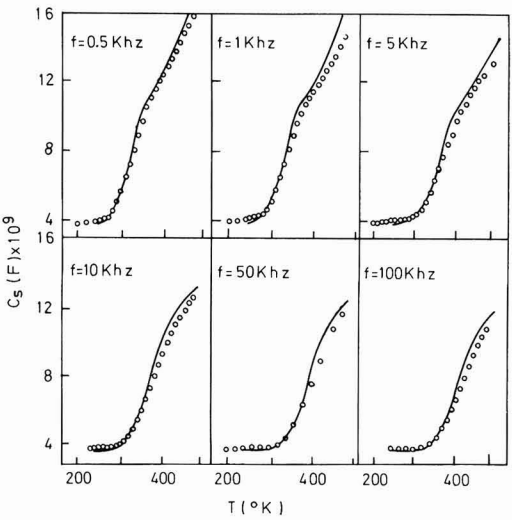

Fig. 7. Temperature dependence of capacitance for the sample of Fig. 1. The dots represent the experimental values and the lines represent the values computed from Eq. [8].

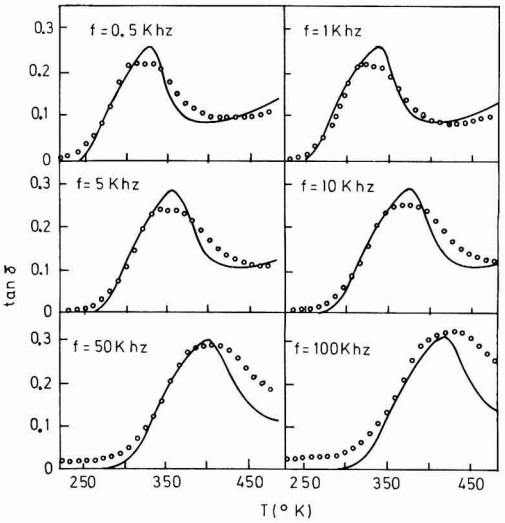

Fig. 8. Temperature dependence of tan δ for the sample of Fig. 1 (The symbols as in Fig. 7).

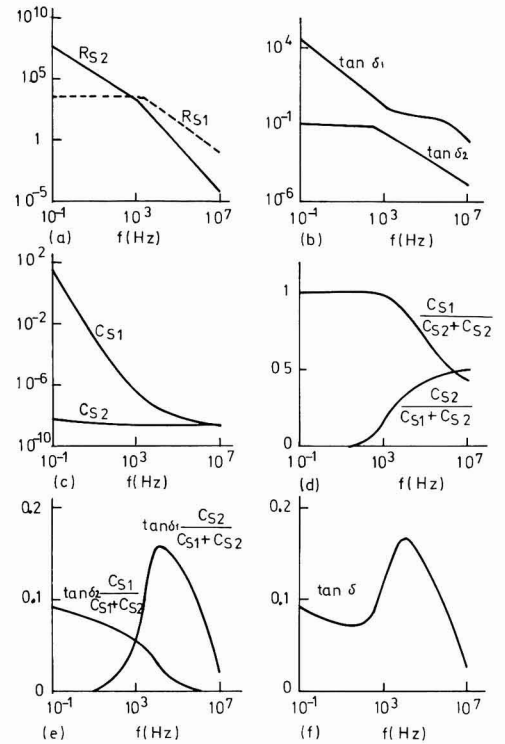

Fig. 9. Frequency dependence at $T = 68°C$ of several parameters computed from the double layer model for the dielectric (same sample as in Fig. 3).

At low frequencies (much lower than the frequency at which log σ changes its slope, about 1 kHz in this particular case), it can be observed in Fig. 9a that $R_{s2} >> R_{s1}$, and according to Eq. [12a]

$$\tan \delta \simeq \tan \delta_2 \frac{C_{s1}}{C_{s1} + C_{s2}} \qquad [13]$$

In addition, for these frequencies, $C_{s1} >> C_{s2}$ (Fig. 9c) and therefore

$$\tan \delta \simeq \tan \delta_2 \qquad [14]$$

For frequencies much higher than the frequency at which $R_{s1} = R_{s2}$ in Fig. 9b, we have $R_{s1} >> R_{s2}$ and

$$\tan \delta \simeq \tan \delta_1 \frac{C_{s2}}{C_{s1} + C_{s2}} \qquad [15]$$

In this case, as the frequency gets higher, $C_{s2}/(C_{s1} + C_{s2})$ increases much slower than tan δ_1 decreases and as a result of this tan δ given by Eq. [15] presents a maximum (Fig. 9f).

As the frequency increases, C_{s1} decreases and becomes comparable to C_{s2} (Fig. 9c), thus having a more important contribution to the total capacitance. All of this is in agreement with the existence of a critical level of conductivity σ_c as proposed by Smyth *et al.* (1). It is also interesting to notice that the graph of tan δ *vs.* log f is the specular image of the graph of tan δ *vs.* T as it should be expected from the conductivity profile model and has been experimentally checked (Fig. 4 and 8).

Figure 10 represents log f as a function of the value of $1/T$ for the occurrence of the maxima of tan δ in Fig. 8. From the slope of this line, an activation energy $E_\delta = 0.726$ eV can be gotten by assuming the following expression for the angular frequency

$$\omega = \omega_0 \exp\left(-\frac{E_\delta}{kT}\right) \qquad [16]$$

It can be easily shown that E_δ is the activation energy of the conductivity at the point in which the conductivity profile corresponding to the temperature for the occurrence of the maximum intersects the line $\sigma = \sigma_c = \omega\epsilon\epsilon_0$ and that the distance from this point to the Ta-Ta_2O_5 interface is the same for every temperature. Accordingly, it is not surprising that the value found for E_δ is of the same magnitude as the value reported for E_1 in Table I since the appearance of the maximum is related to the point where the exponential conductivity gradient changes its slope from a_1 to a_2. Similarly, a value for ω_0 equal to 8.6×10^{14} sec^{-1} is obtained from Eq. [16], which multiplied by $\epsilon\epsilon_0$ yields a value of the constant B which is very close to the one reported in Table I.

It can be concluded from this work that the two-layer exponential gradient conductivity profile model predicts, in the case of thermally treated Ta_2O_5 films anodized in phosphoric acid solutions, a dependence with frequency and temperature of the electrical parameters which is in satisfactory agreement with

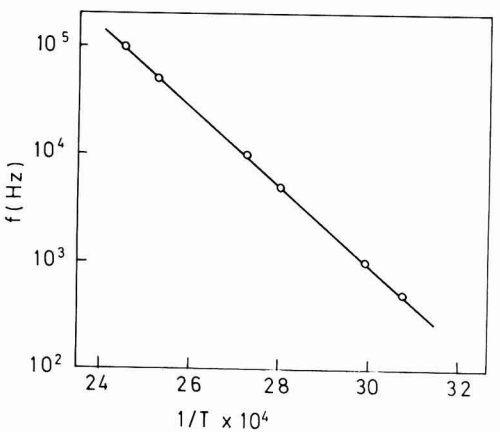

Fig. 10. Log f *vs.* $1/T$ for the occurrence of the maxima of tan δ in Fig. 8.

the experimental results. The agreement could still be improved by introducing some additional zones in the dielectric, the computations still being straightforward. The two-layer model can be assimilated to a generalized Maxwell-Wagner model (8) with a distribution of resistivity values and just one value for the dielectric constant. The behavior of tan δ with frequency found in this work is similar to the one predicted by the Maxwell-Wagner model.

As far as the value found for l in the present work (Table I), which implies that the boundary between the two layers in the oxide is closer to the oxide-counterelectrode interface, it is in qualitative agreement with the conclusions reached by Smyth *et al.* (1) for anodization in a low concentration phosphoric acid electrolyte. Applying the infrared reflectance spectroscopy technique, Kihara-Morishita (5) measured the relative thicknesses of the phosphorus-free and phosphorus-contaminated layers and found that, for Ta_2O_5 films of the thickness employed in this work, the boundary between the two layers is around the location computed in this paper. The conditions of anodization, *i.e.*, the concentration of the electrolyte and the current density, influence the amount of phosphorus incorporated, which in our case might be estimated as 0.03 moles of phosphorus per mole of Ta^{5+} (2).

Young (6) applied the one-layer exponential conductivity gradient to explain the behavior of R_s and C_s with frequency and obtained a straight line for the plot of $1/C_s$ as a function of log f. Winkel and Groot (9), advocating the multiple distribution of relaxation times model of Gevers and du Pré (10), emphasize that in some experimental results a curvature of the $1/C_s$ plots is observed at frequencies above 1 kHz, thus deviating from Young's simple model. In this context, it is interesting to observe that the curvature in the $1/C_s$ curves can also be explained by assuming a conductivity exponential gradient with two or more different slopes as proposed by Smyth *et al.* (1). In addition, it can be concluded from this work that the double-layer conductivity profile model can quantitatively account for the values of the dielectric properties of anodic tantalum oxide thermally treated. However, we do not believe that this model will substitute in every case the more general model of multiple relaxation times.

Manuscript submitted Sept. 21, 1977; revised manuscript received Dec. 5, 1977.

Any discussion of this paper will appear in a Discussion Section to be published in the December 1978 JOURNAL. All discussions for the December 1978 Discussion Section should be submitted by Aug. 1, 1978.

Publication costs of this article were assisted by the Universidad Autonoma de Madrid.

REFERENCES

1. D. M. Smyth, G. A. Shirn, and T. B. Tripp, *This Journal*, **110**, 1264 (1963); *ibid.*, **111**, 1331 (1964); *ibid.*, **113**, 100 (1966).
2. J. J. Randall, W. J. Bernard, and R. R. Wilkinson, *Electrochim. Acta*, **10**, 183 (1965).
3. M. Romand, G. Bouyssoux, J. S. Solomon, and W. L. Baun, *J. Electron Spectrosc.*, **9**, 41 (1976).
4. J. M. Martínez-Duart, C. Palacio, and J. M. Sanz, Paper presented at the Third International Conference on Solid Surfaces, Vienna, Sept. 12-16, 1977.
5. H. Kihara-Morishita, *Thin Solid Films*, **29**, 211 (1975).
6. L. Young, "Anodic Oxide Films," pp. 161-162, Academic Press, New York (1961).
7. D. M. Smyth, in, "Oxides and Oxide Films," Vol. II, J. W. Diggle, Editor, p. 95, Marcel Dekker, New York (1973).
8. J. Volger, in, "Progress in Semiconductors," Vol. IV, A. F. Gibson and R. E. Burgess, Editors, p. 206, Temple Press Books, Ltd. (1960).
9. P. Winkel and D. G. de Groot, *Philips Res. Rep.*, **13**, 489 (1958).
10. M. Gevers, *ibid.*, **1**, 298 (1946).
11. J. M. Albella, J. M. Martínez-Duart, and F. Rueda, *Opt. Acta*, **22**, 973 (1975).

Direct Determination of the Electrical Conductivity-Nonstoichiometry Relationship in Ionically Conducting Metallic Oxides

J. Fouletier and M. Kleitz*

E.N.S. d'Electrochimie et d'Electrométallurgie de Grenoble, Domaine Universitaire, 38401 St Martin d'Hères, France

ABSTRACT

The small quantities of oxygen driven off zirconia solid solutions by solid-state electrolysis were accurately measured and the relevant departure from stoichiometry determined by using oxygen gauges and pumps. The variations in the electronic conductivity and in the ionic transport number were determined as functions of temperature and deviation from stoichiometry. By measuring the rate of oxygen release during the first stage of the electrolysis of prereduced and homogenized samples, the ionic transport number was also determined according to another independent method. The two sets of results compared quite favorably. These methods of measurement offer the possibility of investigating nonstoichiometric oxides, especially in experiments involving small departures from stoichiometry and very reducing conditions.

In solid-state electrochemistry, an oxide is traditionally characterized by the variation of its conductivity as a function of equilibrium oxygen pressure and temperature $\sigma(p_{O_2}, T)$. Recently, Blumenthal and Hofmaier (1) proposed a technique of measuring the variation of conductivity with temperature at fixed values of the stoichiometric ratio.

A sound demonstration of a point defect model further requires another independent set of data, for

* Electrochemical Society Active Member.
Key words: electrical conductivity, ionic transport number, nonstoichiometry, zirconia.

example, the variation of the stoichiometric ratio as a function of the same parameters $x(p_{O_2}, T)$ (2). This can be determined by using a thermobalance when the corresponding weight changes are sufficiently large (3-5).

In this paper we propose a method of measurement which allows us to directly determine the variation of conductivity as a function of the stoichiometry ratio and temperature $\sigma(x, T)$. We also report on experimental observations which could lead to a second, complementary method of measurement of the ionic transport number employing the same parameters $t_i(x, T)$.

These methods, which are based on the utilization of solid-state oxygen pumps and gauges, can now be applied because of the recent improvements (6-7) in the performances and reliability of these devices. For example, a 10 ppm variation of the oxygen content in an inert gas stream can be measured within 5%. A straightforward calculation shows that such a variation occurring over a period of 5 min in a gas streaming at 5 liters·hr^{-1} flow rate corresponds to an extraction (or addition) of only 6 μg of oxygen. If this change results from oxygen pickup by a 100g sample, the measured variation corresponds to a relative change in its weight of 6×10^{-8}. This simple calculation indicates how attractive the use of these devices can be.

Experimental Setup

The experimental setup is essentially composed of a gas circuit (Fig. 1) involving a gas cylinder, an oxygen electrochemical pump, the experimental vessel, an oxygen gauge, and an accurate flowmeter connected in series. The oxygen content in the inert gas is established by the electrochemical pump and measured with the oxygen gauge on bypassing the experimental vessel. It is also measured by the gauge after the gas passes over the sample. Argon was used as the carrier gas. The flow rate ranged from 5 to 20 liters·hr^{-1} which corresponds to average linear velocities of 8-31 cm·sec^{-1}. All the details regarding the pump and gauge characteristics have been given in previous papers (6-11).

The oxygen gauge was composed of a laboratory-made closed-ended electrolyte tube of composition $(ZrO_2)_{0.91}(Y_2O_3)_{0.09}$. The electrodes were obtained by painting with platinum the outer and inner surfaces of its flat bottom. Air in contact with the outer electrode was used as a reference gas. The temperature of the cell was 650°C. The oxygen pressure in the working gas which circulates inside the tube was deduced from the voltage, E, measured between the electrodes by application of the Nernst law, the numerical expression of which was

$$E(\text{mV}) = 19.89 \times \ln \frac{p(\text{atm})}{0.201} \qquad [1]$$

The oxygen pump was formed of a simple tube of the same composition as the gauge. The electrodes coated on the inner and outer surfaces were also of porous platinum. Its operating temperature was 750°C. The working gas was circulated inside the tube. The amount of oxygen added or extracted from it per second was simply correlated to the current passing through the pump by the Faraday law

$$q(l_{NTP} \cdot \text{sec}^{-1}) = 5.803 \times 10^{-8} \times I(\text{mA}) \qquad [2]$$

The time lag of the gauge voltage after a rapid variation in oxygen concentration became significantly longer than 1 min with oxygen contents lower than 10 ppm. This could have greatly limited the methods we proposed. To avoid this difficulty, the experimental conditions were selected so that the oxygen content was either very low (purified argon) or higher than 10 ppm, apart from short transitions between these two states.

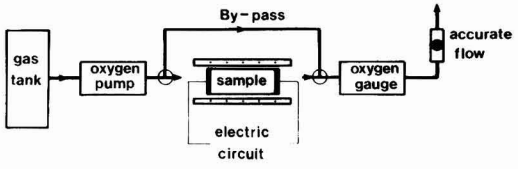

Fig. 1. Experimental setup

The sample was a small cylinder 2.2 cm long and 1.1 cm in diameter with porous platinum electrodes at both ends. These electrodes were connected either to an impedance meter for measuring the sample resistance or to a direct current source for electrolyzing the sample. Its composition was $(ZrO_2)_{0.87}(Y_2O_3)_{0.12}(CeO_2)_{0.01}$ or $(ZrYCe)O_{1.893}$. It was prepared by dry mixing of the oxide powders (ZrO_2, Merck, purity 99.9%; Y_2O_3, Pechiney; CeO_2, Pechiney), pressing at 1.5 tons·cm^{-2} and sintering at 2000°C for 2 hr.

For oxygen pressures higher than 10^{-7} atm, the electronic transport number of this material has been evaluated to a few percent (12). It was neglected in the following derivations.

Nonstoichiometry Measurement and Control

The intentional modifications of the stoichiometry and the corresponding measurements of the stoichiometric ratio variation were performed as follows.

The argon carrier gas flowing around the sample was purified by applying a suitable voltage of about −1.5V to the pump (13). Thus, all traces of free oxygen in the gas were eliminated and the traces of water vapor and carbon oxides partly reduced. The oxygen gauge exhibited a voltage around −0.9V. Then, a suitable constant current, I, was passed through the sample for a time, δ_e. The applied voltage (which included the ohmic drop in the sample and the decomposition voltage) greatly depended on the temperature. In the experiments reported below, it varied between a few volts and 200V. It was applied in such a way that oxygen evolved from the downstream side of the sample (positive electrode on this side). After a certain delay, which corresponded to the flow rate of the gas, the gauge indicated an enrichment in oxygen which lasted for a time, δ_e, and then sharply decreased (Fig. 2). From the plot of the gauge voltage *vs.* time, the determination of the amount of oxygen released by the sample during the electrolysis was calculated. The oxygen flux released at a given time was obtained by multiplying the gas flow rate, D ($l_{NTP} \cdot \text{hr}^{-1}$), by the ratio of the measured oxygen pressure p to the total pressure, p_{total}, in the gauge. The total amount of oxygen, Q, is simply determined by integration according to the equation

$$Q(\text{mole}) = \frac{D}{22.4} \cdot \int_0^{\delta_e} \frac{p}{p_{\text{total}}} \cdot dt \qquad [3]$$

It is straightforward to deduce from Q the induced deviation from stoichiometry x. Accordingly the formula of the reduced sample was written $(ZrYCe)_{1.893-x}$.

This technique constitutes an easy means to control the stoichiometric ratio by appropriately selecting the parameters I and δ_e. The sensitivity in the adjustment of these parameters is obviously far greater than the sensitivity in the stoichiometric ratio measurements and does not limit the performance of the method.

Initially we verified the validity of the method of measurement. The point to be checked concerned the possible errors due to measurement of oxygen pressure during transient periods. For that purpose we also measured the amount of oxygen picked up by the sample during its reoxidation. The sample was initially kept under pure argon. The experimental vessel was bypassed and the oxygen content in the gas fixed at a value in the range 10-100 ppm. Then the gas was passed through the experimental vessel and the gauge voltage recorded. The amount of oxygen absorbed by the sample was determined as for the reduction proc-

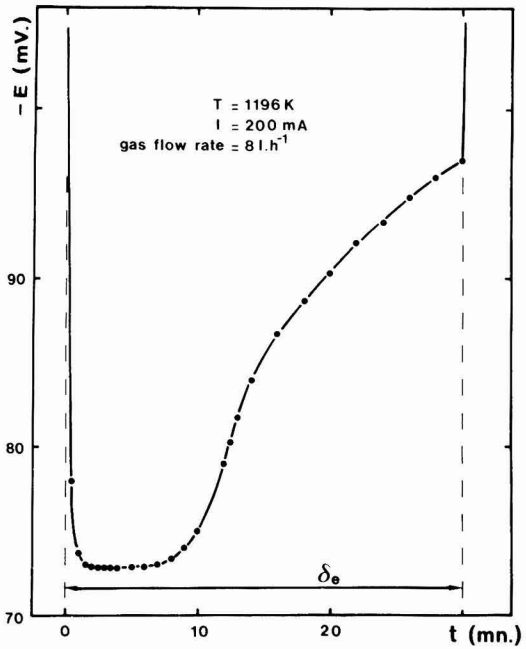

Fig. 2. Typical curve of the gauge voltage vs. time recorded during electrolysis of the sample.

ess. Some reoxidation runs were performed in several partial steps: purified argon, enriched argon, purified argon, enriched argon, etc., in order to increase the number of transient periods and to determine their effects as a possible source of error. Such experiments were carried out many times and have been reported in a previous paper dealing with an oxygen getter (10). For oxygen concentrations in the oxidizing gas higher than 10 ppm, the calculated amounts of oxygen lost during electrolysis and dissolved during reoxidation were always within 5%.

One of the assumptions of this measurement technique is that the sample exchanges no significant amount of oxygen when it is kept under pure argon, *i.e.*, its over-all stoichiometric ratio is fixed. This assumption which has also been made by Blumenthal and Hofmaier (1) was clearly confirmed by the fact that the equality mentioned above was also verified for delays of several days between the electrolysis and reoxidation runs.

Experimental Results: $\sigma(x,T)$ Relationship

After electrolysis, the sample resistance was measured in purified argon using the so-called impedance diagram method (14). In the experiments reported, several measurements were made after each electrolysis. The first measurements indicated a variation due to the homogenization of the sample. After a certain time (always less than a few hours in the runs reported), the results were stable. An example of the dependence of the resistance of the homogenized sample on the deviation from stoichiometry x is given in Fig. 3.

With the sample investigated, we could further derive the following. In all the experiments reported, the concentrations of the vacancies created by the reduction (less than 3×10^{20} cm^{-3}) remained small compared to the initial concentration (6.3×10^{21} cm^{-3}) which resulted from the cationic composition of the material. So, we could reasonably assume that the reduction process did not alter the ionic conductivity. If this assumption is correct, the variations of the measured resistance $R(x)$ concerned only the electronic

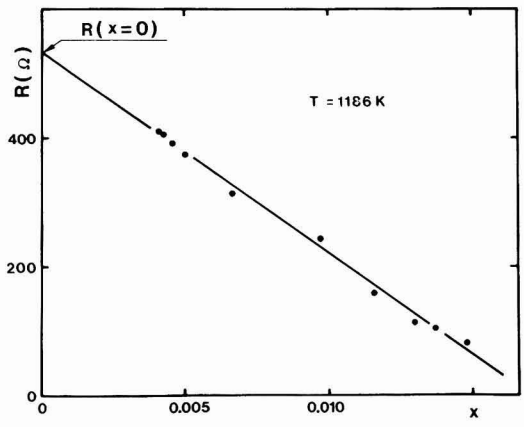

Fig. 3. Resistance variation as a function of the deviation from stoichiometry x.

conductivity. Consequently, the electronic resistance $R_e(x)$ of the sample at a given deviation from stoichiometry can be approximately calculated from

$$1/R(x) = 1/R_e(x) + 1/R_{ionic}(x) \qquad [4]$$

or with our assumption

$$1/R(x) = 1/R_e(x) + 1/R(x=0) \qquad [5]$$

The deduced variations of the electronic resistance as functions of temperature are shown in Fig. 4. A similar trend toward lower activation energies as the departure from stoichiometry increases has been observed by Casselton (15). Figure 5 shows the variations of the ionic transport number $t_i(x)$ calculated from the data in Fig. 3 using the equation

$$t_i = 1 - R(x)/R_e(x) \qquad [6]$$

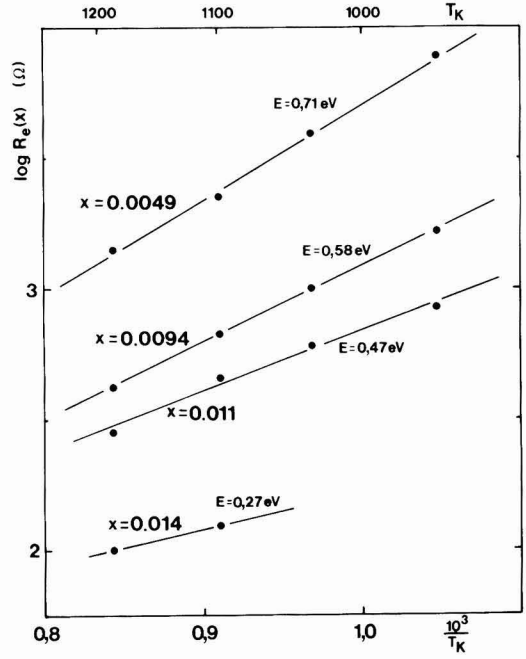

Fig. 4. Arrhenius plot of the electronic resistance of the sample for various deviations from stoichiometry x.

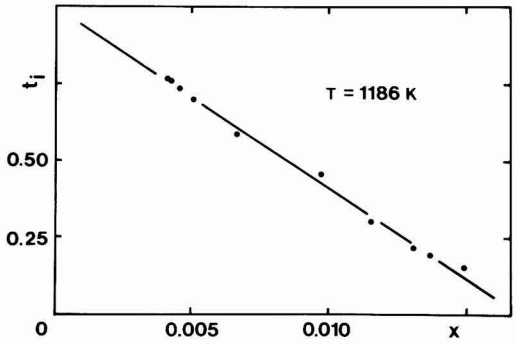

Fig. 5. Variation of the ionic transport number as a function of deviation from stoichiometry.

Direct Determination of $t_i(x,T)$ Relationship

This determination is based on a measurement of the rate that oxygen is driven off the reduced sample during its electrolysis.

When a solid oxide electrolyte is a pure anionic conductor, the quantity of oxygen carried by the ions and the relevant oxygen flow, J, released at the anode of the cell obeys Faraday's law

$$J = I/4\mathbf{F} \qquad [7]$$

where I is the current. This has been accurately checked with oxygen pumps (8).

The results reported above, on electrolysis experiments, also obeyed Faraday's law under appropriate conditions. This is consistent with the observations (16-18) that, during a certain lapse of time, no electrochemical coloration occurs on the anodic side. The ionic transport number remains locally equal to 1 (the small electronic transport number induced by the presence of 1% ceria in the zirconia solid solution is neglected). An example of the oxygen flow released from the sample, at a constant current, is given in Fig. 6 ($x = 0$). In a certain interval, the plot exhibits a plateau, the ordinate of which obeys formula [6]. After longer times the reduced zone had reached the anode, the local value of the ionic transference number markedly decreased

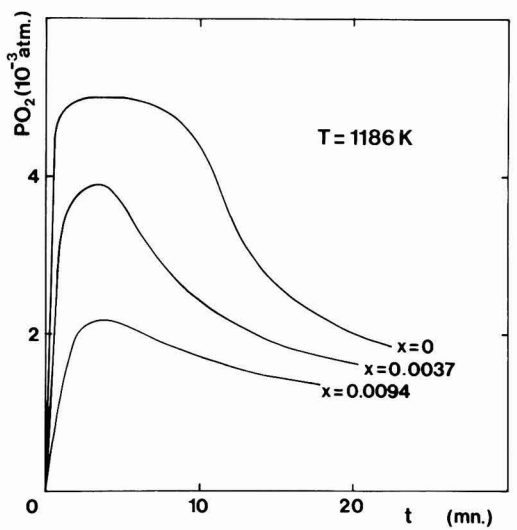

Fig. 6. Oxygen flow released from the sample during the electrolysis, for various initial deviations from stoichiometry.

Table I. Comparison of the ionic transport numbers deduced from Eq. [6] and [8] as functions of the deviation from stoichiometry x of the sample at 1186°K

x	t_i (resistance)	t_i (electrolysis)
0.0048	0.71	0.71
0.0094	0.44	0.42
0.014	0.16	0.13

and consequently so did the oxygen flow. This behavior also explains the shape of Fig. 2.

A simplistic approach to the general problem for a mixed conductor would allow us to conclude that the rate of oxygen evolution from the anode is given by

$$J = J_{th} \cdot t_i \qquad [8]$$

where t_i is the ionic transport number in the close vicinity of the anode and J_{th} the theoretical value corresponding to Faraday's law.

In order to see whether Eq. [8] was indeed obeyed, we carried out the following experiment. After the reduction of the sample to a certain degree (curve $x = 0$ in Fig. 6), the sample was maintained for a while in pure argon under open-circuit condition to let it homogenize. Then a new electrolysis experiment was performed, according to the same procedure, on this prereduced sample. Instead of a plateau, the oxygen flow *vs.* time plot exhibited a simple maximum located at lower oxygen pressure (Fig. 6). From the value of this maximum, which was assumed to represent the initial rate of oxygen evolution, we calculated an ionic transport number t_i (electrolysis) according to formula [8].

To verify the validity of Eq. [8], we compared such values of the ionic transport number to the values deduced from the resistance measurements reported above: t_i (resistance). Three results obtained for various degrees of prereduction are reported in Table I; there is good agreement. This suggests that the material was homogeneous up to the electrode surfaces before the electrolysis voltage was applied and the evolution of oxygen obeyed formula [8].

If this result is confirmed by further experimental results obtained under more appropriately defined conditions, such measurements could lead to a convenient estimation of ionic transport numbers. It would be especially appropriate for average ionic transport numbers for which the traditional emf method is frequently questionable (17, 19). It would also have the advantage of complementing the first type of measurement as the emf method complements conventional conductivity measurements.

It is emphasized that both types of measurement proposed can be performed however reducing the system may be. That is a great advantage over the gas-equilibration technique which is limited on the low oxygen pressure side, and over the use of metal-oxide electrodes which requires tedious manipulations. An obvious deficiency, however, is the lack of information they can provide about equilibrium oxygen pressures.

Manuscript submitted Nov. 1, 1977; revised manuscript received Jan. 3, 1978. This was Paper 78 presented, in part, at the Washington, D.C. Meeting of the Society, May 2-7, 1976.

Any discussion of this paper will appear in a Discussion Section to be published in the December 1978 JOURNAL. All discussions for the December 1978 Discussion Section should be submitted by Aug. 1, 1978.

Publication costs of this article were assisted by the Laboratoire d'Energétique Electrochimique (Institut Polytechnique de Grenoble).

REFERENCES

1. R. N. Blumenthal and R. L. Hofmaier, *This Journal*, **121**, 126 (1974).
2. R. N. Blumenthal and R. K. Sharma, *J. Solid State Chem.*, **13**, 360 (1975).
3. R. J. Panlener, R. N. Blumenthal, and J. E. Garnier, *J. Phys. Chem. Solids*, **36**, 1213 (1975).

4. J. E. Garnier, R. N. Blumenthal, R. J. Panlener, and R. K. Sharma, *ibid.*, **37**, 369 (1976).
5. O. Toft Sorensen, *J. Solid State Chem.*, **18**, 217 (1976).
6. J. Fouletier, H. Seinera, and M. Kleitz, *J. Appl. Electrochem.*, **5**, 177 (1975).
7. J. Fouletier, P. Fabry, and M. Kleitz, *This Journal*, **123**, 204 (1976).
8. J. Fouletier, G. Vitter, and M. Kleitz, *J. Appl. Electrochem.*, **5**, 111 (1975).
9. M. Kleitz and J. Fouletier, in "Measurement of Oxygen," H. Degn, I. Balslev, and R. Brook, Editors, Elsevier Scientific Publishing Co., Amsterdam (1976).
10. J. Fouletier and M. Kleitz, *Vacuum*, **25**, 307 (1975).
11. J. Fouletier, H. Seinera, and M. Kleitz, *J. Appl. Electrochem.*, **4**, 305 (1974).
12. C. Deportes, G. Robert, and M. Forestier, *Electrochim. Acta*, **16**, 1003 (1971).
13. M. Kleitz, Thesis, Grenoble, 1968.
14. E. Schouler, M. Kleitz, and C. Deportes, *J. Chim. Phys.*, **70**, 923 (1973).
15. R. E. W. Casselton, *J. Appl. Electrochem.*, **4**, 25 (1974).
16. P. Fabry, C. Deportes, and M. Kleitz, *J. Solid State Chem.*, **6**, 230 (1973).
17. P. Fabry, Thesis, Grenoble, 1976.
18. J. Fouletier, Thesis, Grenoble, 1976.
19. P. Fabry, C. Deportes, and M. Kleitz, *J. Solid State Chem.*, **5**, 1 (1972).

Electronic Conductivity in Solid CaF_2 at High Temperature

J. Delcet, R. J. Heus, and J. J. Egan

Brookhaven National Laboratory, Upton, New York 11973

ABSTRACT

Polarization measurements have been made on CaF_2 using cells of the type

$$\underset{x_{Ca}=0.9}{\text{Ca-Pb(l)} \mid \text{CaF}_2\text{(s)} \mid \text{Fe(s)}} \qquad \text{(I)}$$

and

$$\text{Fe(s)} \mid \text{CaF}_2\text{(s)} \mid \underset{x_{Ca}=0.25}{\text{Ca-Bi(l)}} \qquad \text{(II)}$$

Steady-state values of the currents at various applied voltages yielded the electronic conductivity in CaF_2 as a function of calcium activity. Results are presented between 800° and 950°C. The experimental arrangement is described and appropriate equations are presented. Values of the transference number of ions are given as a function of temperature and the activity of Ca in CaF_2.

Calcium fluoride has proven to be a useful solid electrolyte for high temperature emf studies (1-20). A review has been given by Tretyakov and Kaul (21). It remains an ionic conductor under very reducing conditions and is useful for measurements with electropositive metals such as U, Th, and Mg in contrast to solid oxide electrolytes.

The problem of electronic conduction in CaF_2 has previously been studied by Wagner (22) and by Hinze and Patterson (23). Using the measurements of Mollwo (24) on the number of color centers in CaF_2 and their mobility, Wagner has calculated the transference number of electrons as a function of calcium activity. Hinze and Patterson have measured the total electrical conductivity as a function of the partial pressure of fluorine. They have concluded that CaF_2 exhibits negligible electronic conductivity even when equilibrated with Ca metal. Baukal (25) has measured the electronic conduction in CaF_2 doped with NaF at temperatures between 490° and 550°C.

In this study the electronic conductivity of pure CaF_2 is measured directly using a polarization technique developed by Wagner (26, 27). This technique has previously been used to study copper halides (28-32), silver halides (33-36), thallium bromide (37), doped oxides of zirconium, thorium, and hafnium (38-41), and lead fluoride (42).

General Approach

The general ideas and detailed equations for the polarization technique to measure electronic conductivity in ionic crystals are discussed in detail in Ref. (27). Cells are employed having a reversible reference electrode and an inert electrode. Ionic conductivity is suppressed by operating at potentials below the onset of ionic currents.

To study CaF_2 the following cell was employed

$$\underset{x_{Ca}=0.90}{\text{Ca-Pb(l)} \mid \text{CaF}_2\text{(s)} \mid \text{Fe(s)}} \qquad \text{(I)}$$

where the reference electrode is the Ca-Pb alloy. The current at various applied voltages, where the Ca-Pb alloy is negative, is given by the expression

$$i = \frac{RT}{\mathbf{F}G}\left\{ \sigma_e' \left[1 - \exp\left(-\frac{E\mathbf{F}}{RT}\right)\right] + \sigma_h' \left[\exp\left(\frac{E\mathbf{F}}{RT}\right) - 1\right]\right\} \qquad [1]$$

Here G is the cell constant (thickness of CaF_2 crystal divided by the area of the electrodes), σ_e' and σ_h' are the electron and electron hole conductivities of CaF_2 equilibrated with the reference electrode and E is the potential applied to Cell (I). A Ca-Pb alloy was used instead of pure Ca metal for experimental reasons. Ca-Pb ($x_{Ca} = 0.90$) is liquid at 800° and could be contained in iron cups which fit closely onto the CaF_2 crystals. Electrodes of solid Ca formed a conducting film on the CaF_2 surface and interfered with the measurements. The activity of Ca in the Ca-Pb alloy was calculated from the heat of fusion of Ca and the Ca-Pb diagram.

If the electron hole conductivity is very small under highly reducing conditions and the voltage applied to Cell (I) is small compared to the potential at which FeF_2 forms, Eq. [1] reduces to

$$i = \frac{RT}{\mathbf{F}G}\sigma_e'\left[1 - \exp\left(-\frac{E\mathbf{F}}{RT}\right)\right] \qquad [2]$$

* Electrochemical Society Active Member.
Key words: electrical conductivity, transport properties, solid electrolyte, electrolyte, mass transport.

Results of current-potential curves on Cell (I) yield the value of σ_e'. To obtain the electronic conductivity at other activities of Ca one may use the equation

$$\sigma_e = \sigma_e' \left(\frac{a_{Ca}}{a_{Ca}'} \right)^{1/2} \quad [3]$$

Polarization experiments on cells of type (II) where the inert iron electrode is made negative also yield electronic conductivity

$$\begin{matrix} Fe(s)\,|CaF_2(s)\,|Ca\text{-}Bi(l) \\ \qquad\qquad x_{Ca} = 0.25 \end{matrix} \quad (II)$$

Under reducing conditions, the steady-state current of Cell (II) at various applied voltages is given by

$$i = \frac{RT}{FG} \sigma_e'' \left[\exp\left(\frac{EF}{RT} \right) - 1 \right] \quad [4]$$

where σ_e'' is the electronic conductivity of CaF_2 whose Ca activity is the same as that for Ca-Bi ($x_{Ca} = 0.25$). The activity of Ca in the Ca-Bi alloy is obtained from emf measurements on the auxiliary cell

$$\begin{matrix} Ca\text{-}Pb(l)\,|CaF_2(s)\,|Ca\text{-}Bi(l) \\ x_{Ca} = 0.90 \qquad\quad x_{Ca} = 0.25 \end{matrix} \quad (III)$$

The emf of Cell (III) is given by the expression (43)

$$E = \frac{1}{2F} \int_{\mu_{Ca}''}^{\mu_{Ca}'} t_{ion} d\mu_{Ca} \quad [5]$$

where

$$t_{ion} = \frac{\sigma_{ion}}{\sigma_e + \sigma_{ion}} = \frac{\sigma_{ion}}{\sigma_e^{\circ} a_{Ca}^{1/2} + \sigma_{ion}} \quad [6]$$

Here σ_e° is the electronic conductivity of CaF_2 with $a_{Ca} = 1$. Equation [5] may then be expressed as

$$E = \frac{RT}{2F} \int_{a_{Ca}''}^{a_{Ca}'} \frac{\sigma_{ion}}{a_{Ca}(\sigma_e^{\circ} a_{Ca}^{1/2} + \sigma_{ion})} da_{Ca} \quad [7]$$

$$E = \frac{RT}{2F} \ln \frac{a_{Ca}'}{a_{Ca}''} + \frac{RT}{F} \ln \frac{\sigma_e'' + \sigma_{ion}}{\sigma_e' + \sigma_{ion}} \quad [8]$$

where

$$\sigma_e' = \sigma_e'' \left(\frac{a_{Ca}'}{a_{Ca}''} \right)^{1/2} \quad [9]$$

This equation can be solved for a_{Ca}'' or the activity of Ca in the Ca-Bi alloy if one determines σ_e'' from steady-state measurements on Cell (II), knowing the activity a_{Ca}' from the phase diagram. The activity a_{Ca}'' is given by the expression

$$a_{Ca}''^{1/2} = \frac{\exp\left(-\frac{\eta F}{RT} \right) - \sigma_e'' a_{Ca}'^{1/2}}{\sigma_{ion}} \quad [10]$$

where

$$\eta = E - \frac{RT}{2F} \ln a_{Ca}' - \frac{RT}{2F} \ln (\sigma_{ion} + \sigma_e'') \quad [11]$$

Polarization cells of type (II) were found very useful for the measurements above 800°C. After determining a_{Ca}'' the electronic conductivity may be calculated at any activity by use of the equation

$$\sigma_e = \sigma_e'' \left(\frac{a_{Ca}}{a_{Ca}''} \right)^{1/2} \quad [12]$$

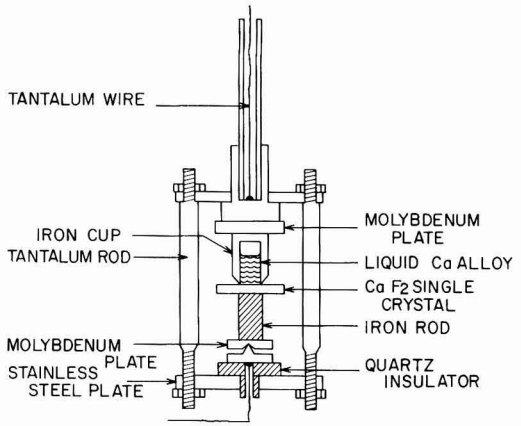

Fig. 1. Experimental arrangement for polarization cells

Experimental Details

The experimental setup for both Cell (I) and (II) is shown in Fig. 1. The iron cup is filled with either a Ca-Pb alloy or a Ca-Bi alloy. The open end of the cup is machined to a sharp edge so that it digs into the CaF_2 single crystal under pressure. CaF_2 softens somewhat around 600°C. The pressure arises from the cell arrangement, since the iron rod and cup expand more than the holder made of tantalum rods. The CaF_2 crystals were generally between 0.1 and 0.2 cm thick. The diameter of the inert iron electrode is 1.0 cm for Cell (I) and 1.6 cm for Cell (II). In order to minimize the edge effect caused by the CaF_2 diameter being larger than the iron electrode diameter, the ratio of the crystal thickness to the electrode area was kept small in accordance with Barrer, Barrie, and Rogers (44). Cell (III) used essentially the same arrangement as shown in Fig. 1 except that two iron cups were used and the cell operated in a horizontal position. The entire cell arrangement was contained in a vacuum-tight Vycor tube filled with purified argon.

Results and Discussion

Steady-state currents obtained at various applied voltages for Cell (I) operated at 800°C are shown in Table I. Steady values were obtained only after several days of cell operation at a given voltage. Values of σ_e' were calculated from Eq. [2] and values of σ_e° from Eq. [3] with $a_{Ca} = 1$. Only currents measured on the plateau of the current voltage curve yielded consistent values of t_{ion}.

Attempts to operate Cell (I) at voltages lower than 0.300V proved unsuccessful. It is believed that the

Table I. Results from cells of type (I)

E	i (μa)	G	σ_e'	σ_e°	t_{ion}°	α_{Ca}'
1.000	250	0.302	8.17×10^{-4}	8.6×10^{-4}	0.635	0.90
0.500	242	0.302	7.94×10^{-4}	8.4×10^{-4}	0.641	0.90
0.300	183	0 302				
1.000	344	3.222	8.27×10^{-4}	8.7×10^{-4}	0.633	0.90
0.500	330	0.222	7.95×10^{-4}	8.4×10^{-4}	0.641	0.90
0.300	283	0.222				

Table II. Results from experiments on cells of type (II) and (III)

T°C	E_{III} (volts)	σ_{ion}	σ_e''	a_{Ca}''	σ_e°	α_{Ca}'
800	0.7436	1.5×10^{-3}	1.72×10^{-7}	3.89×10^{-8}	8.72×10^{-4}	0.632
825	0.7391	2.45×10^{-3}	3.55×10^{-7}	5.95×10^{-8}	1.46×10^{-3}	0.627
850	0.7345	4.0×10^{-3}	7.1×10^{-7}	9.47×10^{-8}	2.31×10^{-3}	0.634
875	0.7300	6.1×10^{-3}	1.36×10^{-6}	1.42×10^{-7}	3.61×10^{-3}	0.628
900	0.7256	9.3×10^{-3}	2.5×10^{-6}	2.16×10^{-7}	5.38×10^{-3}	0.634
950	(0.7164)	2.1×10^{-2}	8.4×10^{-6}	4.59×10^{-7}	1.24×10^{-2}	0.629

greater solubility of Ca in the crystal at lower voltages caused a density change in CaF_2 which breaks the seal formed between the cup holding the alloy and the CaF_2 crystal.

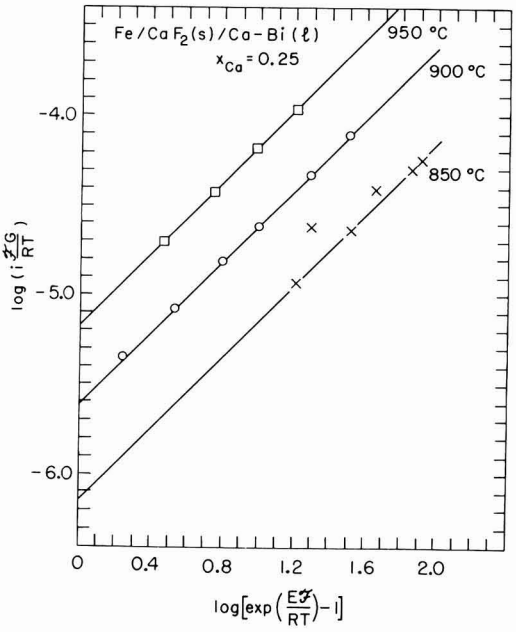

Fig. 2. Results of polarization measurements on Cell (II)

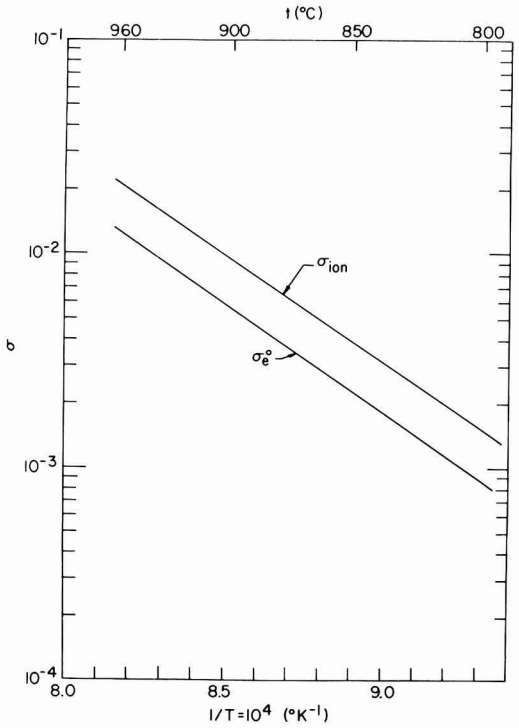

Fig. 3. Ionic and electronic ($a_{Ca} = 1$) conductivity of CaF_2 at various temperatures.

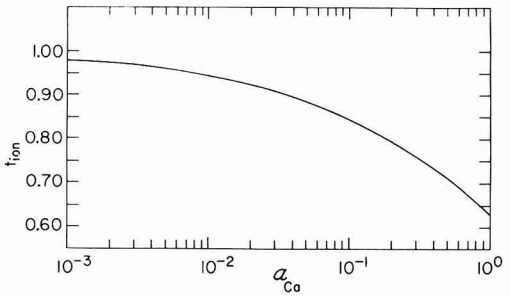

Fig. 4. The transference number of ions in CaF_2 at various Ca activities.

Results from Cells (II) and (III) are shown in Table II at temperatures between 800° and 950°C. Steady-state currents from Cell (II) are shown graphically in Fig. 2. One expects a slope of one for this plot and experiments showed this to be true. Cell (III) was operated between 800° and 900°C, the value of 950°C being an extrapolation.

Values of t_{ion}° were calculated in all cases with Eq. [6], using the results of Ure (45) for the ionic conductivity of CaF_2. The values of the electronic and ionic conductivity in CaF_2 are plotted in Fig. 3, the electronic conductivity being for CaF_2 equilibrated with Ca metal. Figure 4 shows the transference number of ions in CaF_2 at various activities of Ca.

Acknowledgment

The authors would like to thank Prof. Carl Wagner for many helpful comments during the course of this work.

Manuscript submitted Nov. 5, 1975; revised manuscript received Dec. 19, 1977. This was Paper 193 presented at the San Francisco, California, Meeting of the Society, May 12-17, 1974.

Any discussion of this paper will appear in a Discussion Section to be published in the December 1978 JOURNAL. All discussions for the December 1978 Discussion Section should be submitted by Aug. 1, 1978.

Publication costs of this article were assisted by Brookhaven National Laboratory.

REFERENCES

1. R. Benz and C. Wagner, *J. Phys. Chem.*, **65**, 1308 (1961).
2. J. J. Egan, *ibid.*, **68**, 978 (1964).
3. S. Aronson, "Compounds of Interest in Nuclear Reactor Technology," p. 247, AIME (1964).
4. S. Aronson and J. Sadofsky, *J. Inorg. Nucl. Chem.*, **27**, 1769 (1965).
5. S. Aronson and A. Auskern, in "Thermodynamics," Vol. 1, p. 165, IAEA, Vienna (1966).
6. K. Gingerich and S. Aronson, *J. Phys. Chem.*, **70**, 2517 (1966).
7. W. K. Behl and J. J. Egan, *This Journal*, **113**, 378 (1966).
8. R. J. Heus and J. J. Egan, *Z. Phys. Chem. (Frankfurt am Main)*, **49**, 38 (1966).
9. R. Bones, J. Markin, and V. Wheeler, *Proc. Brit. Ceram. Soc.*, **8**, 51 (1967).
10. F. Moattar and J. S. Anderson, *Trans. Faraday Soc.*, **67**, 2303 (1971).
11. R. J. Heus and J. J. Egan, *Z. Phys. Chem. (Frankfurt am Main)*, **74**, 108 (1971).
12. H. Kleykamp, *Ber. Bunsenges. Phys. Chem.*, **73**, 354 (1969).
13. T. N. Rezukhina and B. S. Pokarev, *J. Chem. Therm.*, **3**, 369 (1971).
14. W. H. Skelton, N. J. Magnani, and J. F. Smith, *Met. Trans.*, **2**, 473 (1971).
15. W. H. Skelton. N. J. Magnani, and J. F. Smith, *ibid.*, **1**, 1833 (1970).
16. H. Holleck and H. Kleykamp, *J. Nucl. Mater.*, **35**, 158 (1970).

17. W. H. Skelton and J. W. Patterson, *J. Less-Common Metals*, **31**, 47 (1973).
18. W. H. Skelton, N. J. Magnani, and J. F. Smith, *Met. Trans.*, **4**, 917 (1973).
19. M. Kanno, *J. Nucl. Mater.*, **51**, 24 (1974).
20. R. J. Heus and J. J. Egan, *ibid.*, **51**, 30 (1974).
21. Y. D. Tretyakov and A. R. Kaul, in "Physics of Electrolytes," Vol. 2, p. 623, Academic Press, New York (1972).
22. C. Wagner, *This Journal*, **115**, 933 (1968).
23. J. W. Hinze and J. W. Patterson, *ibid.*, **120**, 96 (1973).
24. E. Mollwo, *Nachr. Gesellsch. Wissenack. Gottingen Math. Physik. Kl. N.F.*, **6**, 79 (1934).
25. W. Baukal, *Ber. Bunsenges. Phys. Chem.*, **79**, 1148 (1975).
26. C. Wagner, *Z. Electrochem.*, **60**, 4 (1956).
27. C. Wagner, *Proc. CITCE*, **7**, 361 (1957).
28. J. B. Wagner and C. Wagner, *J. Chem. Phys.*, **26**, 1597 (1957).
29. A. V. Joshi and J. B. Wagner, Jr., *J. Phys. Chem. Solids*, **33**, 205 (1972).
30. A. V. Joshi, in "Fast Ion Transport in Solids," North Holland Publishing Co., Amsterdam (1973).
31. A. V. Joshi and J. B. Wagner, Jr., *This Journal*, **122**, 1071 (1975).
32. J. Goldman and J. B. Wagner, Jr., *ibid.*, **121**, 1318 (1974).
33. B. Ilschner, *J. Chem. Phys.*, **28**, 1109 (1958).
34. D. Raleigh, *J. Phys. Chem. Solids*, **26**, 329 (1965).
35. K. Weiss, *Electrochim. Acta*, **16**, 201 (1971).
36. Y. J. van der Meulen and F. A. Kröger, *This Journal*, **117**, 69 (1970).
37. A. Morkel and H. Schmalzried, *J. Chem. Phys.*, **36**, 3101 (1962).
38. J. Patterson, E. Bogren, and R. Rapp, *This Journal*, **114**, 752 (1967).
39. L. D. Burke, H. Rickert, and R. Steiner, *Z. Phys. Chem. (Frankfurt am Main)*, **74**, 146 (1971).
40. J. D. Schieltz, J. W. Patterson, and D. R. Wilder, *This Journal*, **118**, 1257 (1971).
41. R. Hartung, *Z. Phys. Chem. (Leipzig)*, **254**, 393 (1973).
42. R. Benz, *Z. Phys. Chem. (Frankfurt am Main)*, **95**, 25 (1975).
43. C. Wagner, *Z. Phys. Chem.*, **B21**, 25 (1933).
44. R. M. Barrer, J. A. Barrie, and M. G. Rogers, *Trans. Faraday Soc.*, **58**, 2473 (1962).
45. R. W. Ure, Jr., *J. Chem. Phys.*, **26**, 1363 (1957).

Some Studies on a Solid-State Sulfur Probe for Coal Gasification Systems

K. T. Jacob[1]

Department of Mechanical Engineering, University of California, Berkeley, California 94720

and D. Bhogeswara Rao[2] **and Howard G. Nelson**

Ames Research Center, NASA, Moffett Field, California 94035

ABSTRACT

Measurements on the solid electrolyte cell

$$(Ar + H_2 + H_2S/CaS + CaF_2 + (Pt)//CaF_2//(Pt) + CaF_2 + CaS/H_2S + H_2 + Ar)$$

show that the emf of the cell is directly related through the Nernst equation to the difference in sulfur potentials established at the two $Ar + H_2 + H_2S$/ electrode interfaces. The electrodes are designed to convert the sulfur potential gradient across the calcium fluoride electrolyte into an equivalent fluorine potential gradient with the aid of the reaction, $CaF_2(s) + \frac{1}{2} S_2(g) \rightarrow CaS(s) + F_2(g)$. The response time of the probe varies from approximately 9 hr at 990°K to 2.5 hr at 1225°K. The conversion of calcium sulfide and/or calcium fluoride into calcium oxide should not be a problem in anticipated commercial coal gasification systems. Suggestions are presented for improving the cell for such commercial applications.

The ability to continuously monitor the sulfur potential in coal gasification reactors is of crucial importance for efficient gasifier operation and for accurate life prediction of corroding construction materials. From an engineering point of view, *in situ* solid-state sensors that directly measure the sulfur potential are preferable to devices that employ liquid electrolytes or involve sampling of gases for low temperature analytical procedures. Despite the concerted efforts of many laboratories during the last decade to find suitable sulfide electrolytes, analogous to $CaO\text{-}ZrO_2$ or $Y_2O_3\text{-}ThO_2$ for oxygen potential measurements, no acceptable material has been identified in which the ionic transport number is higher than 0.99 over a large range of sulfur potentials and temperatures.

[1] Permanent address: Department of Metallurgy and Materials Science, University of Toronto, Canada, M5S 1A4.
[2] Also from: Materials and Molecular Research Division, Lawrence Berkeley Laboratory, Berkeley, California 94720.
Key words: sulfur probe, calcium fluoride sensor for sulfur, galvanic cell, solid electrolyte cell, coal gasification-sulfur control.

The prospect of designing a suitable sulfide electrolyte does not appear promising in the near future because the bandgaps in the sulfides are generally narrower than in the corresponding oxides (1). An alternate approach may be to use calcium fluoride (CaF_2) as the electrolyte in a solid-state cell, in which the electrodes are designed to convert the sulfur potential in the gas into an equivalent fluorine potential.

Calcium fluoride has been found to be a suitable electrolyte at high temperatures and over a large range of fluorine potentials (2-7). Colorless, pure CaF_2 contains virtually equal concentrations of interstitial anions and anion vacancies. The fluoride ions are the mobile species, and they migrate as interstitials and vacancies. At very low fluorine potentials or in the presence of calcium vapor, an excess of calcium dissolves in CaF_2 according to the reaction

$$Ca(g) + 2F_Fx \rightarrow CaF_2 + 2e_Fx \qquad [1]$$

where F_Fx is a fluoride ion on a regular anion site,

and $e_F x$ is an electron substituted for an anion, producing a color (F) center. Wagner (8) has given an analysis of the onset of electronic conduction in CaF_2 due to the dissolution of calcium metal. Patterson (9) has also discussed the electrolytic conduction domain for CaF_2 at high temperatures. Because of the extreme electronegativity difference between Ca^{2+} and F^- ions and the correspondingly large forbidden bandgap for CaF_2, positive hole conduction will not be significant until the fluorine pressure is increased to several atmospheres. The open-circuit emf (E) across the electrolyte is a direct measure of the chemical potential difference, provided the fluorine pressures at the electrodes and the temperatures of operation lie within the electrolytic conduction domain (that is, the transport number of electrons or holes is less than 0.01).

An advantage of the solid electrolyte sensors is that the output is an electric potential that can readily be used to actuate a control circuit. It was, therefore, decided to study the efficiency of the solid electrolyte cell

$$Ar + H_2 + H_2S/CaS + CaF_2 + (Pt)//CaF_2//(Pt) + CaF_2 + CaS/H_2S + H_2 + Ar \quad [2]$$

as a part of our program on the development of a sulfur probe. The experimental results, the limitations of this technique to coal gasification systems, as well as anticipated improvements are presented in this paper.

Experimental

Materials.—High purity Ar + H_2 + H_2S gas mixtures and their analyses were obtained from Matheson. A slight decrease in the H_2S concentration of the gases was observed over extended periods of storage, presumably due to the reaction of H_2S with the storage tank. Correction factors for gas ratios were obtained by periodically observing the ion intensity ratios of H_2S to H_2 in a mass spectrometer. For the electrolyte, optical grade single crystals of CaF_2, in the form of disks of 1.5 cm in diameter and 0.2 cm thick, were obtained from Harshaw Chemical Company. Ultra pure anhydrous CaF_2 (99.999%)[3] and CaS (99.99%) powders were supplied by Apache Chemical Company and Ventron Corporation. Fine platinum powder and porous platinum sheet with porosity of 29% were obtained from Johnson-Matthey Company. The electrode pellets were made by double end compression of an intimate mixture of −200 mesh size powders of CaF_2, CaS, and Pt in the molar ratio 1.5 : 1 : 0.2. The pellets were sintered in evacuated silica capsules at 1225°K for 12 hr.

Apparatus.—A schematic diagram of the apparatus is shown in Fig. 1. A disk of CaF_2 electrolyte was spring loaded against an alumina tube with a gold O-ring between them to obtain a gastight joint. The alumina tube was held firmly in a water-cooled brass head, to which the springs were attached. Since gold softens at the high temperatures used in these experiments, low tension springs were sufficient to produce a gastight joint. Thus, the ceramic components of the assembly were not subjected to high applied stresses. Electrode pellets containing CaF_2 + CaS + Pt were spring loaded on either side of the electrolyte, with a thin porous platinum sheet sandwiched between the pellet and the electrolyte. Platinum leads, flame sprayed with alumina, were spot-welded to the porous platinum sheets. At the low sulfur potentials used in the experiments, no chemical attack on the platinum was observed in the hot zone of the furnace. At the cooler end, however, there was some evidence of reaction between platinum and H_2S gas. Therefore, in this region, the platinum leads were protected by an alumina sheath closed on both ends by alumina cement.

[3] CaF_2 contained the following elements in parts per million level: 0.5 Pb, 0.5 Ni, 0.5 Cd, 0.5 Mn, 500 Sr, 100 Ba, 5 Li, 10 Sn, and 5 K.

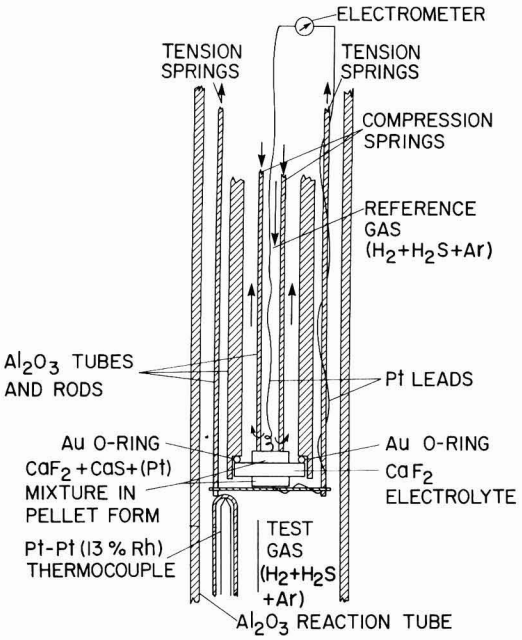

Fig. 1. Schematic diagram of the apparatus used for testing the CaF_2 electrolyte-based sulfur probe.

The cell was designed to provide two separate gastight compartments around the two electrode pellets. Separate gas streams with differing sulfur potentials were passed through these compartments. The test gas was admitted to the system at the lower end of the reaction tube and flowed past the outer electrode pellet at a rate of 250 ml min^{-1}. The reference gas was passed around the inner electrode at a flow rate of 100 ml min^{-1}. The two gas streams were isolated in the reaction tube and escaped through different ports in the brass head. The escaping gases were bubbled through two 25 cm high columns of NaOH solution to remove H_2S and HF. The exit gases were further scrubbed before being pumped through the fume exhaust system.

The entire cell assembly, attached to the brass head, was lowered into a vertical alumina reaction tube. The cell was electrically shielded by connecting a platinum foil, wrapped around the reaction tube, to ground. The reaction tube was heated by a Kanthal resistance furnace. Temperatures of the furnace and of the cell were measured by two separate Pt-Pt (13% Rh) thermocouples. The furnace temperature was controlled to ±1°K by use of a stepless current-compensating controller.

Procedure.—The test cell was assembled as shown in Fig. 1, and the reaction tube was evacuated by a mechanical pump to a pressure of 0.5 Nm^{-2} and then backfilled with purified argon. The argon purification train consisted of magnesium perchlorate (to absorb the residual moisture) and copper turnings at 700°K and titanium turnings at 1100°K (to remove residual oxygen). The cell was heated to 500°K, evacuated, and refilled with argon. The temperature of the cell was then raised to 1225°K. The reference gas was introduced into the inner gas compartment of the cell, while argon flow was maintained through the outer reaction tube. Gastightness of the O-ring seal was checked by analyzing the argon stream exiting from the reaction tube for traces of H_2S. After ensuring that the test cell was leaktight and the two gas streams were isolated, the test gas was introduced into the reaction tube. Cell voltage was monitored using a Keithley digital voltmeter with an internal impedance

of $10^{12}\Omega$. After the start of the experiment, approximately 5 hr were required to obtain a steady emf.

Two procedures were followed during the investigations: (*i*) During isothermal runs, cell temperature was kept constant at 1073° or 1173°K and the steady, reversible emf corresponding to different test gases was measured, and (*ii*) for two selected test gases, the temperature dependence of the steady, reversible emf was measured.

Results

Response time.—Composition of the test gases and the reference gas and the emf obtained at 1073° and 1173°K are shown in Table I. Generally, the response time of the cell at 1225°K, after a small change in temperature or gas composition, was 2.5 hr, while at a lower temperature of 990°K the response time was approximately 9 hr. The cell emf was insensitive to moderate increase in the flow rate of the test gas and/or the reference gas. However, when the flow rate of one of the streams was increased by factors greater than two, while keeping the flow rate of the other stream constant, significant changes in the emf were noted: about 20 mV during the transient period and about 15 mV during the steady-state period. The changes were, however, not always reproducible. When the flow rates of both streams were changed simultaneously by the same amount, the cell emf remained virtually constant. It is likely that a substantial increase in the flow of gas through one stream may have resulted in differential cooling, thus creating a thermal gradient across the electrolyte. Changes in emf resulting from the presence of a steady-state thermal gradient are quantitatively related to the partial entropy of fluorine in the gas phase, as discussed by Fitzner, Jacob, and Alcock (10).

Reversibility of the emf was checked by passing small currents (5 μA) through the cell in either direction for 2 min. It was found that the emf returned to the steady value before the titration in approximately 30 min. After several days of use, the electrode pellets became fragile and fractured easily.

Calculation of sulfur potentials.—Experimental emf's obtained at 1073° and 1173°K for different test gases are compared in Fig. 2 with known values calculated from the difference in sulfur potential between the test gas and the reference gas. The emf developed across a CaF_2 electrolyte can be related through the Nernst equation to the partial pressure of fluorine (fluorine potential) across the electrolyte, provided the ionic transport number is close to unity

$$E = \frac{\Delta\mu_{F_2}{}^{R} - \Delta\mu_{F_2}{}^{T}}{n\mathbf{F}} = \frac{RT}{n\mathbf{F}} \ln \frac{p_{F_2}{}^{R}}{p_{F_2}{}^{T}} \qquad [3]$$

where E is the emf, $\Delta\mu_{F_2}{}^{R}$ and $\Delta\mu_{F_2}{}^{T}$ are the fluorine potential at the reference and the test electrodes, $\mathbf{F}$ is the Faraday constant, n is the number of electrons ($= 2$) involved in the transfer of one molecule of F_2 gas between the two electrodes, R is the gas constant, T is the absolute temperature, and p_{F_2} is the fluorine partial pressure. The gas phase containing Ar + H_2 + H_2S establishes a partial pressure of sulfur (sulfur potential) over the electrode, depending on the ratio of H_2 to H_2S, by virtue of the reaction

Table I. Composition of the test gas mixtures and the corresponding cell emf's

Test gas	Composition (vol. %)			EMF (mV)	
Number	H_2	H_2S	Ar	1073°K	1173°K
1	40.6	8.3	51.1	−32	−34
2	50.4	2.05	47.55	43	47
3	54.0	0.79	45.21	87	96
4	55.1	0.18	44.72	160	174
5*	25.2	2.52	72.28	—	—

* Reference gas.

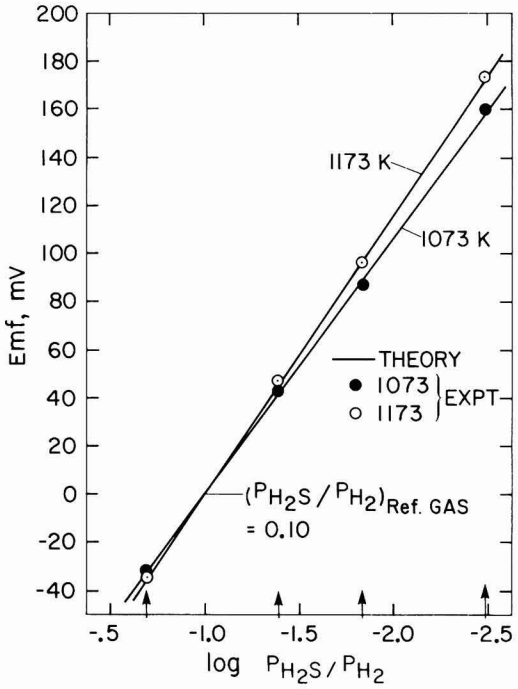

Fig. 2. Variations of the emf with H_2S/H_2 ratio of the test gas at 1073° and 1173°K; — theoretical values Eq. [9].

$$H_2(g) + \tfrac{1}{2}\,S_2(g) \rightarrow H_2S(g) \qquad [4]$$

$$\tfrac{1}{2}\,\Delta\mu_{S_2} = RT \ln p_{S_2}{}^{1/2} = \Delta G^{\circ}{}_4 + RT \ln (p_{H_2S}/p_{H_2}) \qquad [5]$$

where $\Delta G^{\circ}{}_4$ is the standard Gibbs' free energy change for reaction [4] (11). The sulfur potential established by the gas phase, when in contact with the electrode pellet consisting of CaS and CaF_2, fixes a fluorine potential through the reaction

$$CaF_2(s) + \tfrac{1}{2}\,S_2(g) \rightarrow CaS(s) + F_2(g) \qquad [6]$$

$$\Delta\mu_{F_2} = \tfrac{1}{2}\,\Delta\mu_{S_2} - \Delta G^{\circ}{}_6 \qquad [7]$$

where $\Delta G^{\circ}{}_6$ is the standard Gibbs' free energy change for reaction [6]. The platinum in the electrode pellet acts as a catalyst for the reaction. Since there is neither a ternary compound nor significant solid solubility in the CaF_2-CaS system, the condensed phases in the electrode pellets are present at unit activity. Combining Eq. [3] and [7], an expression is obtained relating the emf to the difference in the sulfur potential between the electrodes

$$E = \frac{\Delta\mu_{S_2}{}^{R} - \Delta\mu_{S_2}{}^{T}}{2n\mathbf{F}} = \frac{RT}{2n\mathbf{F}} \ln \frac{p_{S_2}{}^{R}}{p_{S_2}{}^{T}} \qquad [8]$$

Equation [8] may also be expressed in terms of the ratio of H_2S to H_2 in the gas phase over the two electrodes

$$E = \frac{RT}{n\mathbf{F}} \ln \frac{(p_{H_2S}/p_{H_2})^{R}}{(p_{H_2S}/p_{H_2})^{T}} \qquad [9]$$

The measured emf's as shown in Fig. 2, do not deviate by more than 2.5 mV from that calculated using Eq. [9]. Deviations from theoretical values have the same sign at different temperatures for each test gas. Thus, it is likely that these deviations arise from small errors in gas analysis.

The variation of the emf of the cell with temperature and with two test gases (3 and 4 in Table I) is shown

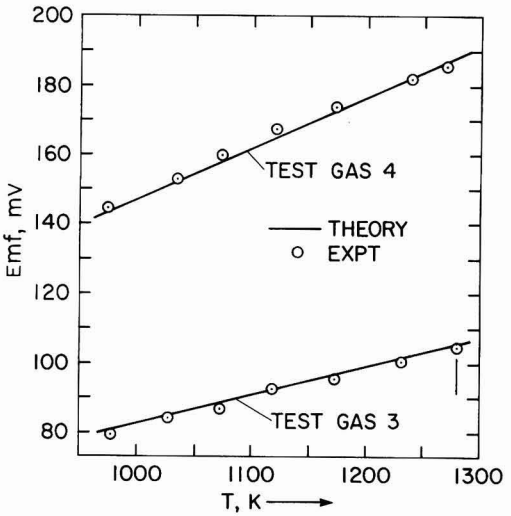

Fig. 3. The temperature dependence of the reversible emf with test gases 3 and 4 passing through the cell; — theoretical values Eq. [10].

in Fig. 3. Again, measured temperature dependence is in agreement with the theoretical value given by the derivative of Eq. [9] with respect to temperature

$$\frac{dE}{dT} = \frac{R}{n\mathbf{F}} \ln \frac{(p_{H_2S}/p_{H_2})^R}{(p_{H_2S}/p_{H_2})^T} \qquad [10]$$

Discussion

The activity of calcium at the electrodes, during the present investigation, can be evaluated by considering the reaction

$$CaS(s) + H_2(g) \rightarrow H_2S(g) + Ca(s) \qquad [11]$$

The activity of calcium, a_{Ca}, is given by

$$a_{Ca} = (p_{H_2}/p_{H_2S}) \exp(-\Delta G^\circ_{11}/RT) \qquad [12]$$

where ΔG°_{11} is the standard Gibbs' free energy change for reaction [11] (11). It can readily be shown from known thermodynamic data that the activity of calcium varies from 9.5×10^{-19} to 6.0×10^{-17} at 1113°K over the range of test gas composition (gases 1 and 4, respectively, Table I). Wagner (8) has suggested that the electronic transport number of CaF_2 is 10^{-2} when the activity of calcium is 6×10^{-6} at 1113°K. It is apparent, therefore, that the electronic transport number is much less than 10^{-2} and contributes very little to the results of the present study.

The exact factors affecting the slow response time of galvanic cells based on a CaF_2 electrolyte have not yet been determined. The length of the electrolyte may influence the response time. In the present investigation the dimensions of the electrolyte were unaltered and a further study is necessary to relate the response time with electrolyte length. The more important are that the kinetics of the electrode reaction [6] may be rate controlling, or the transport of ions in CaF_2 may be slow, such that the composition gradient across the electrolyte cannot readjust rapidly after a perturbation in the chemical potential at the electrode. Additionally, since the fluorine potentials are low ($p_{F_2} \simeq 10^{-24}$ to 10^{-28} Nm^{-2}), gas phase polarization at the electrolyte-electrode interface may be the rate-limiting step. This latter possibility seems rather improbable, however, because sufficient concentration of HF gas should be created by the reaction of H_2S with CaF_2 to transport the fluorine potential to the electrolyte surface.

Electrical current techniques, such as voltage recording after a galvanostatic pulse or impedance measurement at low frequencies, can be used to determine whether the kinetics of the electrode reaction is responsible for the slow response of the cell (13). Heyne and Engelson (14) have recently suggested that for oxygen probes containing calcia-stabilized zirconia as the electrolyte, the uptake or release of oxygen by the electrolyte, when the partial pressure of oxygen in the ambient atmosphere is altered, is the main reason for the sluggishness in response and variation with time of the emf developed. If a similar mechanism is valid for CaF_2, a reduction in the thickness of the electrolyte or doping, to increase the effective diffusion coefficient, may accelerate the response of the probe to changes in sulfur potential. Another alternative is to use β-alumina as the electrolyte (15). β-alumina has much higher conductivity than CaF_2, especially at lower temperatures. Further, the electrodes would be redesigned to convert the sulfur potential gradient into an equivalent sodium potential gradient.

Although systematic studies on the catalytic behavior of platinum or other materials have not been undertaken, it was found in preliminary experiments that approximately 0.2 moles of platinum per mole of CaS is the optimum amount of catalyst in the electrode pellets. To use the cell for sulfur potentials higher than those studied in this investigation, a more suitable catalyst than platinum is needed. Platinum readily forms sulfides at higher sulfur potentials (12). Transition metal sulfides that do not react with CaS and in which cations exist in multivalent states may prove to be good catalysts.

Typical compositions of the raw gases in some coal gasification processes are shown in Table II. It can readily be shown that under the conditions of coal gasification, the conversion of CaS to CaO, according to the scheme

$$CaS(s) + H_2O(g) \rightarrow CaO(s) + H_2S(g) \qquad [13]$$

is not thermodynamically favorable. However, the reaction of $H_2S(g)$ with CaF_2

$$CaF_2(s) + H_2S(g) \rightarrow CaS(s) + 2HF(g) \qquad [14]$$

will result in a partial pressure of HF in the immediate neighborhood of the electrode that can vary from 2.8×10^2 to 80 Nm^{-2}. Since all the gas passing through the probe is not saturated in HF, the average HF concentration in the exit gas is estimated to be approximately 200 ppm and, therefore, must be scrubbed for the removal of HF. Additionally, for commercial application, the probe must be designed in such a way as to prevent particulate material in the gas from depositing on the electrodes of the sensor.

Conclusion

The theory, design, and operation of a solid-state sulfur probe based on CaF_2 electrolyte has been demonstrated. The cell responds to changes in sulfur potential in a manner predicted by the Nernst equation. Further research is needed to determine the main reason for the slow response of the cell. The rate-limiting steps may be either the kinetics of electrode reactions or the

Table II. Composition of raw gases in various coal gasification processes (16)

	Battelle-Union Carbide agglomerate ash process	BCR-Bi-gas process	Bureau of Mines synthane process	IGT Hygas process
H_2	48.8	15	19	19
H_2O	14	52	36	20
CO	26	12	9	17
CO_2	5	13	21	16
H_2S	0.3	0.53	1.1	0.78
N_2	0.5	—	—	—
NH_3	0.002	0.25	0.6	0.4
CH_4	6	7	12	13

Compositions are given in volume percent.

rate of transport through the electrolyte. If the reaction kinetics is rate controlling, suitable catalysts may be developed to overcome the problem. If the slow transport of ions in the electrolyte is the reason for the sluggish response, a cell based on β-alumina electrolyte may be more suitable.

Acknowledgments

The authors thank Dr. Ian Finnie, University of California, Berkeley, and Mr. A. V. Levy, Lawrence Berkeley Laboratory, for their support and encouragement.

Manuscript submitted Sept. 28, 1977; revised manuscript received Dec. 15, 1977.

Any discussion of this paper will appear in a Discussion Section to be published in the December 1978 JOURNAL. All discussions for the December 1978 Discussion Section should be submitted by Aug. 1, 1978.

Publication costs of this article were assisted by the Ames Research Center.

REFERENCES

1. C. N. R. Rao and K. P. R. Pisharody, *Prog. Solid State Chem.*, **10**, 207 (1976).
2. R. Benz and C. Wagner, *J. Phys. Chem.*, **65**, 1308 (1961).
3. J. J. Egan, *ibid.*, **68**, 978 (1964).
4. W. K. Behl and J. J. Egan, *This Journal*, **113**, 378 (1966).
5. W. J. Heus and J. J. Egan, *Z. Phys. Chem. N.F.*, **49**, 38 (1966).
6. S. Aronson and A. Auskern, in "Thermodynamics," Proceedings of Symposium, Vienna, 1965, Vol. 1, p. 165, International Atomic Energy Agency, Vienna (1966).
7. N. L. Lofgren and E. H. McIver, "Thermodynamic Properties of Some Fluoride Systems," U.K.A.-E.A. Rep., 5169 (1966).
8. C. Wagner, *This Journal*, **115**, 933 (1968).
9. J. W. Patterson, *ibid.*, **118**, 1033 (1971).
10. K. Fitzner, K. T. Jacob, and C. B. Alcock, *J. Chem. Thermodyn.*, In press (1977).
11. D. R. Stull and H. Prophet *et al.*, JANAF Thermochemical Tables, pp. 760, 761, NSRDS-NBS 37, U.S. Department of Commerce, Washington, D.C. (1971).
12. W. Biltz and R. Juza, *Z. Anorg. Chem.*, **190**, 166 (1920).
13. J. E. Bauerle, *J. Phys. Chem., Solids*, **30**, 2657 (1969).
14. L. Heyne and D. den Engelson, *This Journal*, **124**, 727 (1977).
15. J. T. Kummer, *Prog. Solid State Chem.*, **7**, 141 (1972).
16. A. J. McNab, "Materials Problems and Research Opportunities in Coal Conversion," NSF-OCR Workshop Proceedings, Table II, Ohio State University, p. 33 (April 1974).

Reduction of Excess Phosphorus and Elimination of Defects in Phosphorus Emitter Diffusions

B. L. Morris and L. E. Katz*

Bell Laboratories, Allentown, Pennsylvania 18103

ABSTRACT

The successful production of LSI bipolar circuits requires that a high level of transistor junction yield be maintained. One of the chief causes of junction degradation is the defects induced by the high concentration of phosphorus normally used in the emitter diffusion of bipolar transistors. This diffusion results in a total phosphorus concentration that is greater than the electrically active phosphorus; precipitates and other defects result from this excess phosphorus. These defects can cause crystal damage which in turn can degrade junction integrity, and in the worst case lead to emitter-collector shorts. The purpose of this work was to find processing parameters which may be used to minimize the excess phosphorus in an emitter diffusion. We have studied the effect of bubble rate, the amount of preheat time, thickness of preformed barrier oxide, percent oxygen in the gas stream, and percent time that the bubbler is on for a 1000°C phosphorus diffusion using PBr_3. The diffusions were characterized by sheet resistance, junction depth, total surface concentration (as measured by an electron microprobe), and Sirtl etching. It is shown that the proper choice of diffusion processing parameters minimizes the excess phosphorus, eliminates etching defects, improves transistor junction yield, and results in only a small increase in final sheet resistance. This occurs when the total phosphorus concentration, averaged over 0.34 μm from the surface, is kept below 4.0 to 4.5 $\times$ 10^{20} cm^{-3}.

The most common n-type dopant used in silicon integrated circuit (SIC) processing is phosphorus, and the two most widely used phosphorus diffusion sources are $POCl_3$ and PBr_3. A considerable amount of work exists (1-4) on the relationship between the electrical properties of these diffusions and the process parameters. It is well known that for high concentrations of phosphorus ($C_{atomic} \geq 10^{20}/cm^3$) the amount of electrically active phosphorus is less than the total amount introduced during diffusion (5). The explanation given in the literature for this difference is that the excess phosphorus forms precipitates which are not electrically active (6-9). Although a large amount of work has been done on the relationship between the electrical properties of phosphorus diffusions and processing parameters, very little work has been reported on how to minimize this excess phosphorus (8).

The work presented here was undertaken to determine the processing parameters which would result in a minimum amount of excess phosphorus for the typical emitter diffusions used in bipolar digital SIC's. This is important since the excess phosphorus can cause crystal damage resulting in the creation of recombination-generation centers (9-11) in the region of the emitter-base junction, and/or emitter collector shorts. At the same time, the electrically active con-

* Electrochemical Society Active Member.
Key words: phosphorus diffusion, defects in silicon, bipolar transistors.

centration should be as high as possible since in many cases the emitter diffusion is used as a diffused cross-under and a sheet resistance as low as possible is desired to minimize parasitic voltage drops. For circuits operated at low current levels such as injection logic and low power transistor-transistor logic, an increase in the sheet resistance of approximately 50% or less should not have any effect on the noise immunity of the circuits.

All of the work described in this paper was done on 3 in. diam slices using standard bipolar processing. The goal was to determine processing which can reduce the electrically inactive phosphorus concentration without appreciably changing the sheet resistance (*i.e.*, the electrically active phosphorus concentration).

Experimental

The diffusion system used for PBr_3 predepositions is shown schematically in Fig. 1. The bubble rate is the amount of nitrogen that is bubbled through a flask of liquid PBr_3. The oxygen is needed to form a phosphorus-doped glass on the silicon surface. It is this glass which acts as the diffusion source. The main N_2 is adjusted if bubble rate or O_2 content is changed, so that the total gas flow is always 8.0 liters/min. This flow has been found sufficient to assure uniformity and eliminate backstreaming.

The processing variables which control the total amount of phosphorus are: diffusion temperature; total diffusion time; bubble rate (nitrogen flow: liters/min); percent oxygen in gas stream; percent time bubbler is on; temperature of PBr_3 source; preheat time (time elapsed before bubbler is turned on). In a typical bipolar process, the desired emitter junction depth is $\approx$1.2 μm. Typical total diffusion time and temperature to achieve this junction depth are 35-40 min at 1000°C. To first order, all of the other parameters listed above have a secondary effect on this junction depth, and hence on the active base width of the transistor. Although it has been shown that higher phosphorus diffusion temperatures can result in a smaller amount of excess phosphorus than lower temperatures (8), due to the higher phosphorus solubility at higher temperatures, use of higher temperatures is ruled out due to the very short, and hence poorly controllable, total diffusion times.

Two approaches were initially taken to reduce the electrically inactive phosphorus concentration. The first of these involved lowering the amount of phosphorus in the gas stream by varying the bubble rate, percent time that the bubbler is on, and percent of oxygen. The second approach was to grow a thin layer of thermal oxide on the silicon just prior to the phosphorus diffusion. This may be done in a separate oxidation furnace or *in situ* in the phosphorus diffusion furnace by using a relatively long preheat time and a high O_2 level.

All diffusions except those used in junction yield studies were into p-type bulk wafers with a <111> orientation and a resistivity in the range of 0.5-1.0 Ω-cm. The diffusions were performed at 1000°C for total times of 36 or 60 min which correspond to emitter junction depths of 1.2 and 1.6 μm, respectively. The nitrogen bubble rate was varied from 0.5 to 2.0 liters/min. The oxygen flow was varied from 0 to 20% of the total gas flow. Bubbler time was varied from 16 to 92% of the total diffusion time.

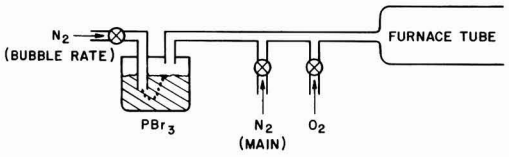

Fig. 1. Diffusion system used for PBr_3 predepositions

Three lots of 24 n-type epitaxial wafers each (0.5 Ω-cm, 5-6 μm thick, <111> oriented) were run to observe the effect of the emitter diffusion on transistor junction yield, which we define as the percent of transistors with $BV_{CEO} \geq 5V$ at 10 μa. The first lot was split four ways; two different low phosphorus methods, a "worst case" high phosphorus diffusion, and an intermediate phosphorus diffusion which is the standard currently used in production. The second and third lots were split two ways; standard diffusion and low phosphorus diffusion. Twenty large transistors, emitter area 270 mil^2, were measured on each wafer. The transistor junction yield, the base pinch sheet resistance (the sheet resistance of the base under the emitter), and final (*i.e.* reoxidized) emitter sheet resistance were also measured.

Results and Discussion

Sirtl etching of wafers following the phosphorus diffusions was used to reveal dislocation size and density for the different diffusion conditions. Since defect analysis is performed at high magnification (200×), the statistical variation from sample to sample for these wafers was considerable, hence large areas from each of the wafers within a particular run must be examined. Typical defects from such an examination using Normarski interference contrast microcopy are shown in Fig. 2 and 3. The diffusion conditions of the various samples will be discussed later. It is possible to prepare samples with no defects (Fig. 2a), with small defects (Fig. 2b and 2c), and with large defects (Fig. 2d and Fig. 3a-3d). These defects, as mentioned earlier, are dislocations arrays. Their sizes, as revealed by etching, range from ~3-5 μm for the small defects to 50-60 μm for the large ones. Because of the range in size and position of these defects, no quantitative estimate of their density has been attempted. All results are presented in a qualitative and comparative manner.

Table I shows the effect of the total phosphorus concentration on the defects produced by the emitter diffusion as observed by Sirtl etching. The phosphorus concentration was varied by varying the percent of time the bubbler is on, the bubble rate, and the percentage of oxygen in the gas flow.

This table indicates that a reduction of the phosphorus concentration below 4.0 to 4.5 × 10^{20}/cm^3 (averaged over the first 0.34 μm) by appropriate choice of diffusion parameters is sufficient to produce defect-free emitters.

The second approach used to reduce the phosphorus induced defects involves growing a thin oxide prior to the phosphorus diffusion. Table II shows the results for a separate oxidation, and once again it is found

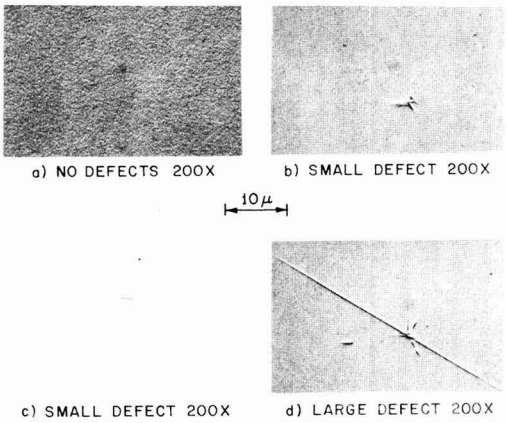

Fig. 2. Defects produced by phosphorus predeposition (1000°C)

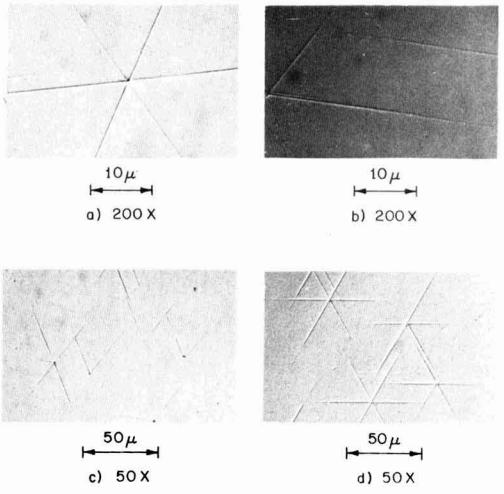

Fig. 3. Large defects produced by phosphorus predeposition (1000°C).

that reducing the phosphorus concentration below 4.0 to 4.5 $\times$ 10^{20}/cm^3 (averaged over 0.34 μm) results in the elimination of phosphorus-induced defects. Table III shows results for thin, $\lesssim$ 110Å, oxides grown *in situ* in the phosphorus diffusion furnace in dry O_2. In this case the number of defects decreases as the oxide thickness increases, but there is no apparent decrease in the total phosphorus concentration. This apparent contradiction of the previous correlations may be understood by recalling that: (*i*) the electron microprobe measurement gives an average concentration

Table I. Effect of total phosphorus concentration on defects

(Total diffusion time 60 min)

Sheet resistance R_S (Ω/□)	Total phos. conc.* per cm^3	Etching results (refer to Fig. 2 and 3)
5.6	3.3 $\times$ 10^{20}	No defects
4.4	4.5 $\times$ 10^{20}	Small defects at center, large defects at edge
4.2	5.4 $\times$ 10^{20}	Small and large defects at center, large defects at edge
4.2	6.1 $\times$ 10^{20}	Small and large defects at center, large defects at edge
4.0	7.5 $\times$ 10^{20}	Small and large defects at center, large defects at edge

* Averaged over 0.34 μm depth (electron microprobe results).

Table II. Diffusion through previously formed thin oxide

(Total diffusion time 60 min)

Barrier oxide thickness (Å)	Sheet resistance R_S (Ω/□)	Total phos. conc.*	Etching results (refer to Fig. 2 and 3)
0	3.9	5.9 $\times$ 10^{20}	Large defects throughout
165.0	4.2	5.4 $\times$ 10^{20}	Large defects but lower density than above
290.0	4.6	4.9 $\times$ 10^{20}	Small defects
450.0	5.4	4.3 $\times$ 10^{20}	None
700.0	8.3	2.9 $\times$ 10^{20}	None
1000.0	17.8	$<$1 $\times$ 10^{20}	None

* Averaged over 0.34 μm.

Table III. Diffusion through an *in situ* oxide

(Total diffusion time 60 min)

Oxide formed (Å)	Sheet resistance R_S (Ω/□)	Total phos. conc.* (cm^{-3})	Etching results (refer to Fig. 2 and 3)
50	4.5	4.8 $\times$ 10^{20}	Low density of small defects
66	4.5	4.4 $\times$ 10^{20}	Low density of small defects
110	4.2	4.7 $\times$ 10^{20}	Very few, small defects

* Averaged over 0.34 μm depth.

over $\approx$0.34 μm from the surface; and (*ii*) it is the maximum phosphorus concentration which occurs at the surface that is the cause of the SiP precipitates and dislocation networks. It appears, therefore, that even a thin oxide ($\lesssim$110Å) over the silicon acts to decrease the surface phosphorus concentration and "flatten out" the profile, with very little effect on the total amount of phosphorus that is diffused into the silicon.

The *in situ* oxidation method has a number of advantages over a preformed oxide layer; it eliminates the need for an additional process step, it eliminates the possibility of accidental removal of the thin oxide during a reclean, and it results in a reproducibly thin oxide ($\approx$100Å) which decreases the defect density while resulting in a minimal increase in the sheet resistance.

The results of combining these two approaches (lowering the amount of phosphorus in the ambient and growing an SiO_2 layer prior to diffusion) are shown in Table IV. In three "low phos" examples, the phosphorus glass thickness is not appreciably different from the "standard" condition for any of these cases. After the emitter reoxidation, 900°C for 60 min in steam, the final sheet resistance of low phos III is slightly greater than standard, while the other two cases have appreciably larger values. The amount of oxide grown over the emitter, which is known to depend on the phosphorus concentration, is also shown in the table.

Table IV. Some characteristics of "optimum" emitter diffusion

(Total diffusion time 36 min)

	Diffusion conditions		After predep			After reox			
Emitter diffusion	Oxygen (%)	Bubble rate (l/min)	Glass thickness (Å)	R_S (Ω/□)	Total phos conc.*	R_S (Ω/□)	Total phos conc.*	Oxide thickness (Å)	Etching results
Low phos I	10	0.5	670	11.4	2.4 $\times$ 10^{20}	16.5	1.7 $\times$ 10^{20}	3450	No defects
Low phos II	10	0.75	715	8.8	3.1 $\times$ 10^{20}	12.7	2.7 $\times$ 10^{20}	3700	No defects
Low phos III	10	1.0	720	7.7	3.4 $\times$ 10^{20}	11.0	3.5 $\times$ 10^{20}	3860	Some small defects
Standard	3	1.0	600	6.2	4.3 $\times$ 10^{20}	9.0	4.6 $\times$ 10^{20}	4020	Small defects at center, large defects near edges

* Averaged over 0.34 μm depth.

Table V. Effect of emitter diffusions on transistor junction yield

(Total diffusion time 36 min)

Diffusion emitter	Diffusion conditions: Bubble rate (l/min)	Diffusion conditions: Oxygen (%)	Junction yield (% BV_{CEO} > 5v at 10 μA)	Base pinch sheet res. (kΩ/□)	Final emitter sheet res. (Ω/□)	Total phosphorus concentration* (cm^{-3})
Lot No. 1						
Low phos I	0.5	10	90%	4.1	13	2.9×10^{20}
Low phos III	1.0	10	83%	5.0	10	4.1×10^{20}
Standard	1.0	3	52%	5.3	9.2	4.4×10^{20}
High phos	2.0	3	52%	5.0	7.0	1.1×10^{21}
Lot No. 2						
Low phos I	0.5	10	69%	5.7	14.0	2.6×10^{20}
Standard	1.0	3	43%	5.8	9.4	4.6×10^{20}
Lot No. 3						
Low phos III	1.0	10	83%	3.3	9.8	Not measured
Standard	1.0	3	67%	3.7	8.5	Not measured

* Averaged over 0.34 μm from surface.

The results of the transistor junction yield experiments previously described are shown in Table V. For Lot 1 the low phos I results may be too optimistic due to the wide basewidth of this part of the split lot (as indicated by the low base pinch sheet resistance). However the results of low phos III *vs.* standard clearly show a real improvement.

Conclusion

To increase transistor junction yield the amount of excess, electrically inactive, phosphorus in the emitter diffusion must be kept to a minimum. Two approaches to this are: (*i*) minimize the amount of phosphorus in the gas stream; and (*ii*) grow a thin layer of thermal oxide over the silicon prior to the diffusion. These two approaches have been combined into "optimum" diffusion schedules which produce total phosphorus concentrations (averaged over 0.34 μm from the surface as measured by electron microprobe) less than or equal to approximately 4.0 to 4.5 $\times 10^{20}$ cm^{-3}. As a result, defect-free surfaces are obtained and transistor junction yield is significantly increased (up to ~80%) as compared to higher concentration phosphorus diffusions.

Acknowledgments

The help of David Wonsidler in making the electron microprobe measurements is gratefully acknowledged.

Manuscript submitted Oct. 3, 1977; revised manuscript received Dec. 28. 1977.

Any discussion of this paper will appear in a Discussion Section to be published in the December 1978 JOURNAL. All discussions for the December 1978 Discussion Section should be submitted by Aug. 1, 1978.

Publication costs of this article were assisted by Bell Laboratories.

REFERENCES

1. J. C. C. Tsai, *Proc. IEEE*, **57**, 1499 (1969).
2. P. C. Parekh, *This Journal*, **119**, 173 (1972).
3. M. S. R. Heynes and P. G. G. van Loon, *ibid.*, **116**, 890 (1969).
4. J. S. Kesperis, *ibid.*, **117**, 554 (1970).
5. E. Tannenbaum, *Solid-State Electron*, **2**, 123 (1961).
6. R. J. Jaccodine, *J. Appl. Phys.*, **39**, 3105 (1968).
7. M. L. Joshi and S. Dash, *IBM J.*, **11**, 271 (1967).
8. P. Negrini, D. Nobili, and S. Solmi, *This Journal*, **122**, 1254 (1975).
9. C. Donolato, P. G. Merli, and I. Vecchi, *ibid.*, **124**, 473 (1977).
10. F. Barson, M. S. Hess, and M. M. Roy, *ibid.*, **116**, 304 (1969).
11. F. Barson, S. P. Klepner, and D. K. Seto, Paper 144 presented at the Toronto, Canada, Meeting of the Society, May 11-16, 1975.

Formation and Properties of Thin Tunnelable SiO_2 Films Using a Vaporized O_2 Source at Liquid N_2 Temperature

Masatada Horiuchi, Yoshiaki Kamigaki, and Takaaki Hagiwara

Hitachi, Limited, Central Research Laboratory, Kokubunji, Tokyo 185, Japan

ABSTRACT

A high temperature (700°-1100°C) oxidation process for the formation of thin tunnelable SiO_2 (20-70Å) is described. This oxidation process uses liquid O_2 at liquid N_2 temperature as a source of oxidant and oxygen is vaporized just before the furnace tube to supply a water-free oxidant ambient. The activation energy (20.2 kcal/mole) of oxidation rate differs from that previous (43.9 kcal/mole) which has been evaluated for thin oxide growth using the O_2/N_2 partial pressure method. By the use of this technique we can control thickness to ±0.5Å accuracy. The rate of oxidation has been found to be governed by the inverse-logarithmic growth law, *i.e.*, Mott-Cabrera's field-assisted diffusion law. Electrical characteristics, such as dynamic conductance, capacitance, and tunnel current, are measured and discussed. The increment of the oxidation temperature is found to result in the decrease of surface-state density at the Si-SiO_2 interface. The process described enables the way for wider application of thin oxide devices.

There has been a good deal of recent interest in thin oxide nonvolatile memory devices such as metal-nitride-oxide silicon (MNOS) devices. This is because of the proposed use of MNOS devices in electrically alterable read-only memories as well as for various other applications (1). In these devices, a thin tunnelable oxide plays a very important role in governing several properties of the memory actions, such as switching speed, retention characteristics, and degradation phenomena. Although there is a considerable amount of information available about the kinetics and electrical properties of relatively thick (0.02-1 μm) SiO_2 layers (2-4), there has been comparatively little published on thin (<200Å) SiO_2 films (5-7). Most importantly, there is little information on the reproducibility of the formation and quality control of thin tunnelable oxides.

This paper presents a study of the growth of thin tunnelable oxides (20-80Å) on freshly etched Si at 700°-1100°C in dry oxygen. It describes the successful development of a technique for reproducibly fabricating thin tunnelable SiO_2 films (on Si) and for improving the Si-SiO_2 interface properties.

Experimental Procedures

Sample preparation.—Most of the single crystal silicon wafers in this study were 8-12 Ω-cm p-type with a chemmechanically polished (100) face. Conductance measurements were carried out using sample wafers of 0.002 Ω-cm p^{++}-type or 0.009 Ω-cm n^{++}-type (111) face. The wafers were cleaned by a standard ammoniacal peroxide process as a preoxidation wafer treatment after the field oxide was etched off to expose the gate region. Wafers for studying the rate of formation of thin tunnelable SiO_2 films did not have a field oxide, so only the cleaning sequence was carried out.

All thickness measurements were made ellipsometrically. The films formed in air during 7-10 min measurement time on freshly etched Si wafers were measured to be about 6.0Å (assuming that the films were SiO_2 films). In this study, the refractive indexes of $n_{SiO_2} = 1.47$ and $n_{Si} = 4.08\text{-}0.028i$ were assumed.

The oxidation was carried out in a resistance-heated 3 zone oxidation furnace tube with a specially prepared oxygen source for the desired amount of oxidation time. The oxidation apparatus for formation of thin tunnelable SiO_2 is shown in Fig. 1. In this oxidation process, the oxygen source is liquid O_2 vaporized at the temperature of liquid N_2 and carried into a conventional oxidation furnace with purified N_2 gas. N_2 gas does not bubble through liquid O_2 but simply passes over liquid O_2 face. The oxygen vaporization just before the furnace tube inherently decreases impurity content in the oxidant ambient. Oxidation was carried out at 700°-1100°C.

After oxide growth samples to be used for measurement of the electrical properties were placed in a vacuum system. Aluminum was evaporated with a resistive heater and gate electrodes were formed by photoetching. Contact with the back side of the structure was accomplished by N^+ diffusion before formation of the thin SiO_2 films.

Measuring procedure.—Dynamic conductance and capacitance measurements are made by properly adjusting the phase shifter of the lock-in amplifier (8). A ramp voltage supply provides d-c voltage to the sample, thereby enabling data to be plotted automatically. Signal frequency is about 19.2 Hz and peak-to-peak voltage is about 5 mV. The absolute measurement of conductance or capacitance is made by a substitution technique in which the system is first calibrated to give a certain deflection for a known conductance or capacitance. After calibration the sample is switched into the circuit. This system can verify conductance values of more than 2×10^{-8} mho.

Results and Discussion

Thickness evaluation.—The vapor pressure of oxygen does not stabilize for about two days after liquefaction at liquid N_2 temperature. The fluctuation of the formed oxide thickness under these conditions is plotted

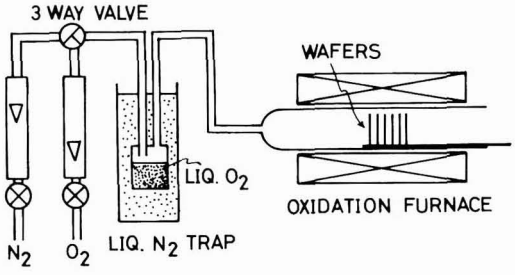

Fig. 1. Oxidation apparatus for formation of thin tunnelable SiO_2 with liquid O_2 source vaporized at liquid N_2 temperature.

Key words: high temperature oxidation, excellent accuracy, inverse-logarithmic growth law, surface-state density decrease.

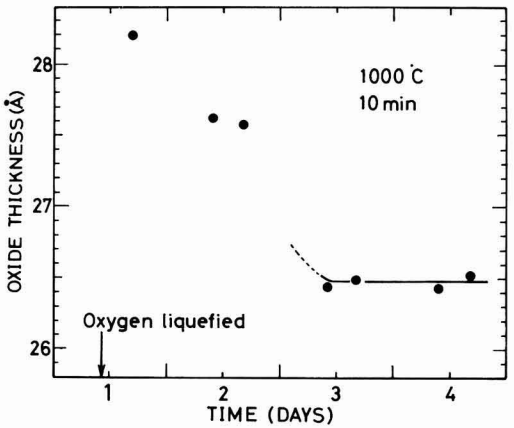

Fig. 2. Fluctuation of the oxide thickness under the same conditions (1000°C, 10 min). Oxide thickness is reproducible within ±0.5Å accuracy after three days from oxygen liquefaction.

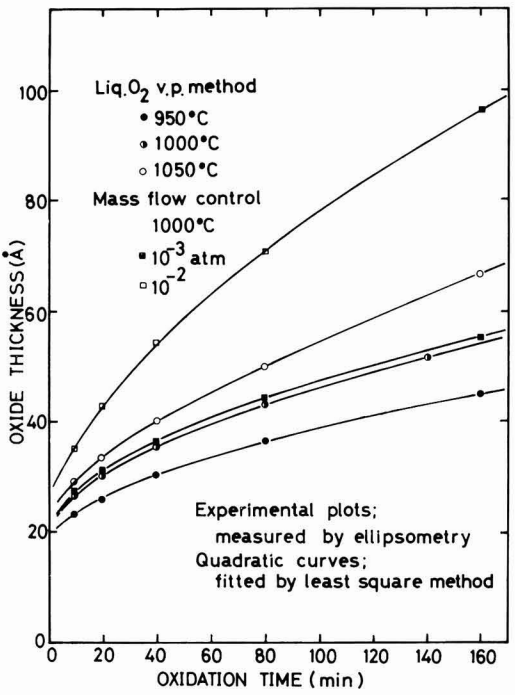

Fig. 3. Rate of formation of thin tunnelable SiO_2 films using a liquid O_2 source vaporized at liquid N_2 temperature. The results of the O_2-N_2 mixture method varying oxygen concentration at 1 atm total pressure by mass-flow controller are shown for comparison.

against time after liquefaction in Fig. 2. After three days, the oxygen vapor pressure reaches a steady-state condition and good reproducibility can be obtained within ±0.5Å accuracy.

The rate of formation of thin tunnelable SiO_2 films using liquid O_2 oxidant source is shown in Fig. 3. The results of the O_2-N_2 mixture method (varying oxygen concentration at 1 atm total pressure by mass flow controller) are shown in this figure for comparison. By comparison with the O_2-N_2 mixture method, partial pressure of O_2 is verified as being nearly equal to 10^{-3} atm for the liquid O_2 vapor pressure method.

In this figure, the Deal-Grove linear parabolic relationship, $X^2 + AX = B(t + \tau)$ is not applied as an analytical procedure, but the second-order regression curves $t = a_0 + a_1X + a_2X^2$ are fitted to the experimental data plots using the least squares method. This is because the Deal-Grove relationship cannot actually be applied in the case of thin oxide growth involving field and space charges within the oxide layer thinner than oxide-Debye length (9, 10).

It has been reported in the previous paper (10) that the thin oxide growth under low oxygen partial pressure is governed by the inverse-logarithmic growth law $dX/dt = u \exp(X_1/X)$, *i.e.*, one case ($X_1 >> X$) of the Mott-Cabrera's field-assisted diffusion law $dX/dt = 2u \sinh(X_1/X)$, where $u \propto \exp(-W/kT)$ and X_1 are the characteristic velocity and distance, respectively (11).

The results of the experimental and analytical data at 950° and 1000°C oxidation temperature are presented in detail in Table I. Average relative error $\overline{dX/X}$ is as small as 0.34%. Average thickness error $\overline{dX}$ is remarkably small, *i.e.*, 0.11Å. The Deal-Grove's rate constants can easily be calculated from Table I.

The resulting rate constant A has negative values in our experimental range. This means that the Deal-Grove linear parabolic relationship cannot be accepted in our experimental range. The relation between oxidation velocity and oxide thickness is also given in Table I. The log $(d\bar{X}/dt)$ *vs.* $1/X$ plots at 950°, 1000°, and 1050°C are shown in Fig. 4. It is clear that a strictly linear relation can be obtained in this figure. The values u and X_1 can be obtained from Fig. 4, *i.e.*, u by extrapolating the straight line back to $1/\bar{X} = 0$. The gradient of this line gives X_1. The good linear relationship, as is seen in Fig. 4, proves that the oxide growth using liquid O_2 vapor pressure method is also governed by the inverse-logarithmic law, *i.e.*, Mott-Cabrera's field-assisted diffusion growth law.

All values obtained for u can be plotted as a function of oxidation temperature. Activation energy (W) in the Arrhenius expression is about 20.2 kcal/mole.

This value is smaller than 43.9 kcal/mole, that of previous study (10) where O_2-N_2 partial pressure method was used as a thin oxide formation. However, it may be compared with 25.8 kcal/mole for the thicker oxide formation as referred to by Revesz and Evans (3). They obtained this value by rf heating oxidation with dry O_2 containing less than 0.1 ppm of water. According to them, the water and sodium content in the oxidizing ambient greatly affects the rate constant and its activation energy. The activation energy increases with the increment of sodium and water content. In their study or in the previous studies (2, 12), 43.3-44.0 kcal/mole were presented as the largest values of activation energy.

In our experiment liquid O_2 is vaporized just before the furnace tube, and water vapor in the oxidant

Table I. Data analysis for the oxidation of silicon with the liquid O_2 vapor pressure method

	950°C				1000°C			
t	X	$\bar{X}$	dX	dX/dt	X	$\bar{X}$	dX	dX/dt
10	23.03	22.98	0.05	0.3326	26.44	26.29	0.15	0.4507
20	25.74	25.85	−0.11	0 24 6	30.05	30.12	−0.07	0.3283
40	30.18	30.09	0 09	0.1824	35.51	35.65	−0.14	0.2358
80	36.19	36 22	−0 03	0.1313	43.66	43.54	0.12	0.1682
160	45.01	45.01	0.00	0.0937	52.26*	52.29	−0.03	0.1276
$\overline{dX}$		0.07Å				0.11Å		
$\overline{dX/X}$		0.26%				0.34%		
a_0		3.31 × 10				2.66 × 10		
a_1		−4.99				−3.46		
a_2		1.74 × 10^{-1}				1.08 × 10^{-1}		
u		2.55 × 10^{-2}				3.54 × 10^{-2}		
X_1		59.0Å				67.3Å		

t = min, X = Å, a_0 = min, a_1 = min/Å, a_2 = min/Å².
* Oxidation time is 140 min.

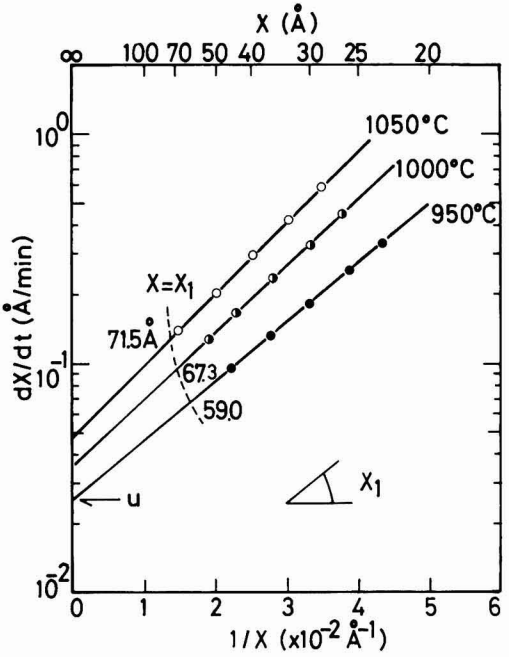

Fig. 4. Relation between $\log(d\bar{X}/dt)$ and $1/\bar{X}$ at 950°, 1000°, and 1050°C. This figure utilizes the values from Table I. The values of u and X_1 are given by extrapolating the straight line back to $1/X_1$ and by the slope of this line, respectively.

source at liquid N_2 temperature is less than 2×10^{-26} atm, *i.e.*, water-free oxidant source. According to this, the liquid O_2 vapor pressure method may apparently be distinguished from other thin oxide formation methods for impurity content in the formed oxide.

Electrical properties.—A typical capacitance *vs.* voltage characteristic measured by a lock-in amplifier with 100 kHz superposed frequency is shown in Fig. 5. Thickness of this film measured by ellipsometry is 57.2Å. Maserjian *et al.* (13) provided a method to evaluate the value of the density of states-effective

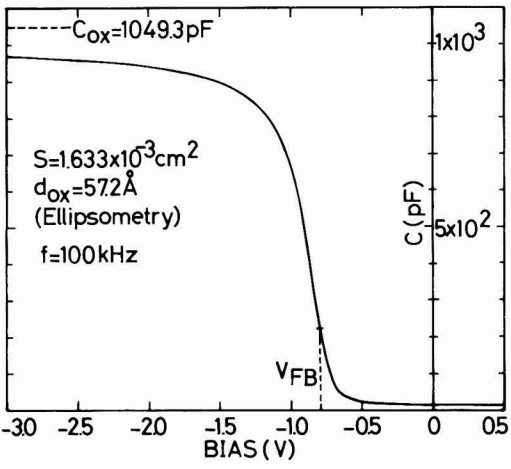

Fig. 5. A typical capacitance *vs.* voltage characteristic. Oxide thickness measured by ellipsometry is 57.2Å. Capacitance fails to saturate at the oxide capacitance C_{ox}. Thus, the C_{ox} value is estimated after Ref. (13) exactly.

mass m_D for the valence band. According to their method, m_D is evaluated as 0.296 m_o. The value of m_D obtained from this method differs considerably from the bulk density of states mass which is $m_D = 0.55\ m_o$ for the valence band. Maserjian *et al.* suggested that one possible reason for this is surface quantization effects. They calculated $m_D = 0.29\ m_o$ for the valence band of the (100) surface assuming the triangular potential approximation for a strongly accumulated semiconductor surface. Quite good agreement can be seen between the value found from surface quantization and our calculated value in spite of measurement at room temperature.

The flatband voltage value is nearly −0.8V and discrepancy from the Al-Si work function difference (14) is less than 0.05V. No hump caused by the interface state density distribution (15, 16) can be observed in this capacitance curve. These facts prove the quality of the thin oxide films described in this paper.

Tunnel current is measured in a "transistor structure" with a N^+-diffused region instead of the usual diode structure. The use of the transistor permits the estimation of the amount of charge transfer between the Si substrate and trap sites in thin oxide nonvolatile memory devices. A cross-sectional view of this transistor is shown in Fig. 6. In this figure, the current between the Si surface inversion layer and counter-electrode can be distinguished from the conventional MOS diode tunnel current.

Typical current density *vs.* voltage (J-V) curves for various oxide thicknesses are shown in Fig. 6 for two different current paths. The broken lines show the J-V characteristics between Al electrode and Si substrate (N^+-diffused region is electrically in floating condition). The dottted lines show the J-V characteristics between the Al electrode and N^+-

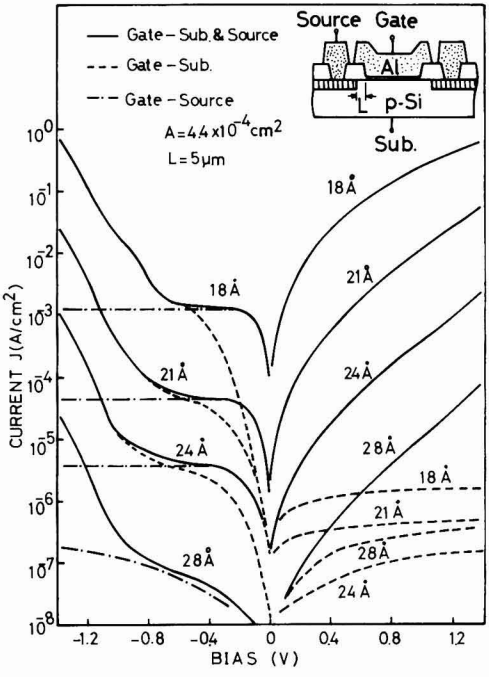

Fig. 6. Typical current density J *vs.* voltage V curves with various oxide thickness. Oxide films are formed at 1000°C. Broken lines show the J-V curves between Al and Si substrate. Dotted lines show the J-V curves between the Al and N^+ diffused region through the surface inversion layer. Solid curves indicate the J-V curves between Al and Si substrate by shorting the N^+-diffused region and substrate.

diffused region through the surface inversion layer (the substrate is electrically in floating condition). The solid lines indicate data summarizing the above two curves (current densities are measured between the Al electrode and substrate by shorting the N^+ region and substrate). The dotted lines in the positive voltage regime coincide exactly with the solid curves.

When the oxide is moderately thin (<40Å) and the electron supplement source is the only generation current in the depletion layer, electrons can more easily transit from the Si surface to the metal electrode than maintain the inversion layer at the Si surface (Si surface is strongly depleted). The broken lines in the positive direction show this generation-limited current. This current density is independent of the applied voltage and oxide thickness. Furthermore coincidence of the dotted curves with the solid one in the positive direction indicates that most electrons are supplied from the N^+-diffused regions. The current in the positive direction may be limited by the length L of the offset region and the conductance value at this regime or by the tunnel transition probability. These currents are functions of the oxide thickness and applied voltage. The solid curves correspond to the real behavior of tunnel transitions for the switching actions in thin oxide nonvolatile memory devices.

To improve switching speed, especially in the case of electron injection from the substrate to trap sites, it is desirable that devices adopt thinner tunnelable oxide, if possible, without any fatal demerit to other device properties. Another recommendation is decrementation of the offset length, L, *i.e.*, providing a large conductance value without leakage or degradation of thin oxide films over the N^+-diffused regions.

To evaluate another feature of thin tunnelable oxide prepared by the liquid O_2 vapor pressure method, a-c conductance of MOS diode is measured with 30-22Å thick oxide over p^{++}- or n^{++}-degenerate substrates. The electrode is a mask-evaporated 1 mm diam Al dot. A typical a-c conductance dI/dV *vs.* applied voltage V curves with 30Å thick oxide over p^{++}-degenerate substrates are shown in Fig. 7. As an experimental parameter, oxidation temperature is varied from 700° to 1100°C. Conductance values for the low temperature (700°C) oxidized sample increase rapidly with increment of applied voltage in the negative direction. For a sample oxidized at 900°C, a little hump in the conductance curve can be observed for the negative bias regime corresponding to the forbidden band. For the higher temperature (1100°C) oxidized sample, only an abrupt conductance increment corresponding to the electron injection from the metal electrode to the lower edge of the conduction band can be observed. The discrepancy for positive-biased conductance curves may be caused by the fact that the heavy degeneration effect and the valence bandedge become obscure in p^{++} substrates with over 10^{19} impurities/cm^3 (17).

The frequency dependence of a-c conductance for p^{++} substrates with 22Å thick tunnelable oxide is shown in Fig. 8. The tunnelable oxide is formed at 900°C. The significant properties of these humps in the conductance curves are that (*i*) the location of the humps along the voltage axis is independent of frequency over the range 19.2 Hz-19.2 kHz; and (*ii*) the magnitude of the hump increases a little with increasing frequency. Because of property (*i*), this hump cannot due to inversion layer coupling (18). It must be due either to tunneling to interface states or to charge exchange between the interface states and the majority carriers at the valence band.

In case of a MOS tunnel diode with p^{++} substrate and thin (20-40Å) oxide film, metal carriers tunnel through the oxide into interface states and then rapidly recombine with the majority carrier at the valence band for bias corresponding to the forbidden bandgap. Thus, the current through the interface states is tunneling controlled ($\tau_{tunnel} >> \tau_{recombine}$) (19). Then the humps in Fig. 8 may be due to tunneling to interface states.

Frequency response of a-c conductance characteristic depends on the transition probability of an elec-

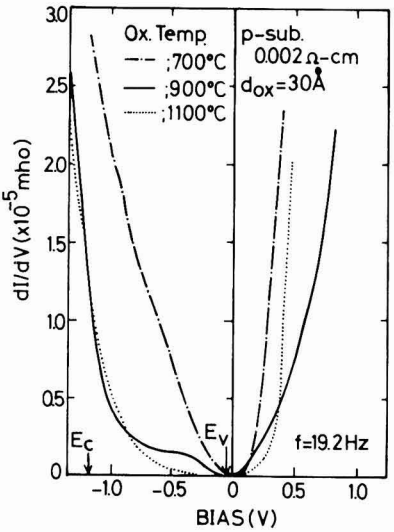

Fig. 7. A typical a-c conductance vs. applied voltage curves with 30Å thick oxide over p^{++} substrates.

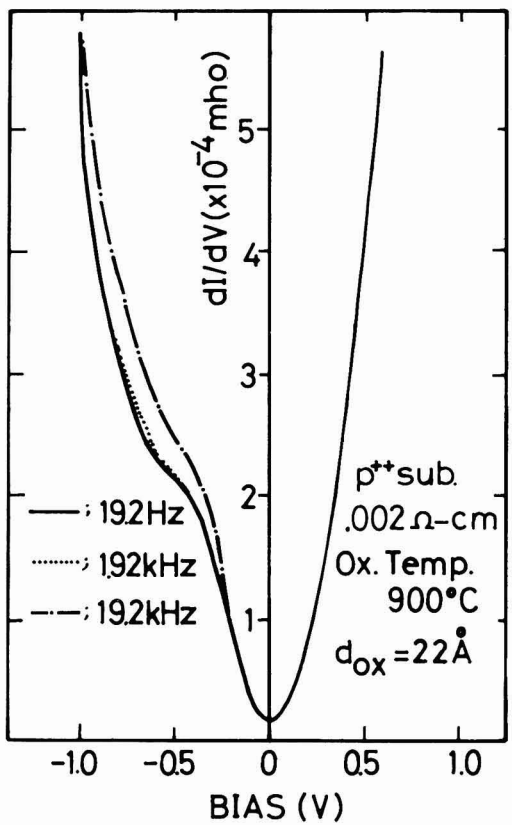

Fig. 8. Frequency dependence of a-c conductance for p^{++} substrates with 22Å thick oxide. The oxide is formed at 900°C.

tron from the metal into the interface states. The characteristic frequency depends linearly on the density of interface states (18). Thus, little frequency dependence indicates that there are few interface states in that sample.

D-c and a-c conductance distinctly reflect the effect of the semiconductor band structure and the density of interface states. Freeman and Dahlke provided a theoretical analysis (19) to evaluate the d-c and low frequency a-c conductance characteristics assuming various energy distributions of interface states. In the case of degenerate substrate, surface potential is usually a negligible correction and the variable range of surface potential at maximum is less than 3×10^{-3}V for p^{++} substrates with the applied voltage range in Fig. 7. According to this fact and Freeman's theoretical evaluation, tunneling conductance is approximately proportional to the density of interface states. This indicates that humps or increments in conductance curves shown in Fig. 7 correspond to the distribution map of interface state density. An energy band diagram and distribution map of interface state density derived from Fig. 7 is shown in Fig. 9. In this figure, the vertical axis is expressed in arbitrary units. This is because the magnitude of experimental results does not coincide with the calculated one. This discrepancy may be caused by the misestimation of values such as capture cross section of interface state or average attenuation constant at the interface.

The a-c conductance curves for a sample having an n^{++} degenerate (0.009 Ω-cm) substrate with a 22Å thick oxide is shown in Fig. 10.

The tunnelable oxide is formed at 900°C. The approximate voltages corresponding to bandedges are also shown in this figure as E_v and E_c. As can be seen in Fig. 10, conductance values increase simply as a result of increment in the positive and negative applied voltage.

For n^{++} substrate, the effective oxide barrier is expected to be smaller than for those of p^{++} sample (14). For a negative bias on the gate electrode, electrons tunnel from the gate to empty states of the semiconductor conduction band, resulting in a large, rapidly increasing current. A small positive bias on the gate produces increased electron tunneling from the semiconductor conduction band into the gate electrode. In addition to this current component, electron tunneling from the interface states into the metal gate is generated by a further increase in bias. This second component (19) is due to the decrease in effective oxide barrier.

For larger voltage additional tunneling from the valence band to the gate electrode occurs. However, this tunneling has a comparatively small influence on the total conductance characteristic on account of the high oxide barrier, *i.e.*, p^{++} sample. This is why

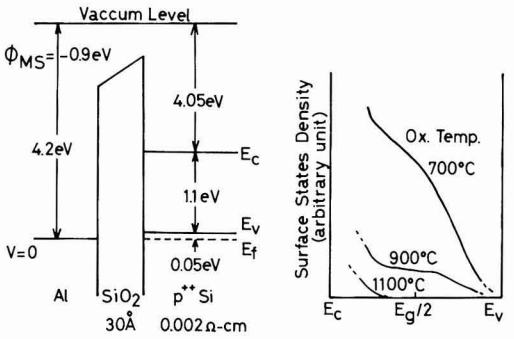

Fig. 9. Energy band diagram of MOS tunnel diode with 30Å thick oxide over p^{++} substrates and a distribution map of Si-SiO_2 surface state density evaluated from Fig. 7.

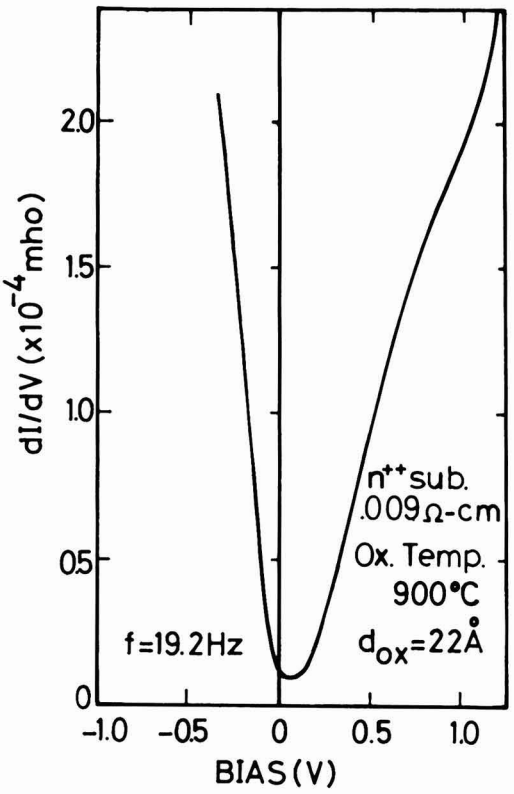

Fig. 10. Typical a-c conductance curve for a sample with an n^{++} substrate under 22Å thick oxide which is formed at 900°C. The band structure of Si has a much smaller influence on the conductance characteristics compared to p^{++} samples.

the Si band structure has a much smaller influence on the conductance characteristics of the n^{++} sample (Fig. 10) compared to the p^{++} one (Fig. 7 and 8).

Conclusion

Thin tunnelable oxides (20-80Å) are formed by a high temperature (up to 1100°C) oxidation method within ±0.5Å accuracy. This oxidation process uses liquid O_2 as an oxidant source at liquid N_2 temperature. The partial pressure of vaporized O_2 in steady-state conditions is verified as being nearly equal to 1×10^{-3} atm. The oxidation kinetics in our experimental range are governed by the inverse-logarithmic relation which is caused by the field-assisted diffusion law.

The activation energy of oxidation rate is evaluated as 20.2 kcal/mole and this value is smaller than previous data. The smaller value of the activation energy may suggest that the described process is distinguished from other formation methods of thin oxide films for impurity content in the oxide films.

Electrical properties such as effective mass in the valence band and Si-SiO_2 interface state density are evaluated and discussed by capacitance and a-c conductance measurements. Results obtained are; $m_D = 0.296\ m_o$ and interface state density decreases with increasing oxidation temperature. No hump can be observed in the capacitance curve for the sample oxidized at higher temperature. This indicates that less interface state is originated by the oxidation process described. Interface state density for p^{++} substrate increases as the energy level approaches the lower edge of the conduction band within the forbidden

band for samples oxidized at low temperature. However, for n^{++} substrate, interface state density cannot be estimated because interface states are filled with conduction electrons due to recombination.

To estimate the real behavior of charge transition in the thin oxide nonvolatile memory devices, tunnel currents are measured in an actual transistor structure. This permits the current between the Si surface inversion layer and the counterelectrode to be distinguished from the conventional MOS diode tunnel current. As a result, it is predicted that channel conductance near the source region may play an important role in governing the electron injection rate into the trap sites.

The thin tunnelable oxide layers described have been and are being used in FTMIS (floating silicon gate tunnel injection metal-insulator-silicon) memory devices. They are tunnel-mode type nonvolatile memory devices (20, 21). In the thin oxide memory devices, memory characteristics such as fatigue phenomena depend strongly on the properties of the thin oxide and most devices have degradated after 10^6-10^8 cycles of operation (1). However, FTMIS memory devices with thin tunnelable oxide described can operate without any fatigue phenomena after 2×10^{12} cycles endurance operation (21). Thus, this oxidation process is best fit for fabrication of various kinds of thin oxide devices.

Acknowledgment

The authors wish to express their appreciation to Dr. Ruji Kondo, Sigeru Nishimatsu, Hisao Katto, and Yokichi Itoh for their valuable advice and technical discussion throughout the course of this study.

Manuscript submitted April 19, 1977; revised manuscript received Nov. 15, 1977.

Any discussion of this paper will appear in a Discussion Section to be published in the December 1978 JOURNAL. All discussions for the December 1978 Discussion Section should be submitted by Aug. 1, 1978.

Publication costs of this article were assisted by Hitachi, Limited.

REFERENCES

1. J. J. Chung, *Proc. IEEE*, **64**, 1039 (1976).
2. B. E. Deal and A. S. Grove, *J. Appl. Phys.*, **36**, 3770 (1965).
3. A. G. Revesz and R. J. Evans, *J. Phys. Chem. Solids*, **30**, 551 (1969).
4. B. E. Deal, M. Shlar, A. S. Grove, and E. H. Snow, *This Journal*, **114**, 266 (1967).
5. J. A. Aboaf, *ibid.*, **118**, 1370 (1971).
6. Y. J. van der Meulen, *ibid.*, **119**, 530 (1972).
7. T. Smith and A. J. Carlen, *J. Appl. Phys.*, **43**, 2455 (1972).
8. J. Shewchun and A. Waxman, *Rev. Sci. Instr.*, **37**, 1195 (1966).
9. D. W. Hess and B. E. Deal, *This Journal*, **122**, 579 (1975).
10. Y. Kamigaki and Y. Itoh, *J. Appl. Phys.*, **48**, 2891 (1977).
11. N. Cabrera and N. F. Mott, *Rep. Prog. Phys.*, **12**, 163 (1948).
12. J. T. Law, *J. Phys. Chem.*, **61**, 1200 (1957).
13. J. Macerjian, G. Petersson, and C. Svensson, *Solid-State Electron.*, **17**, 335 (1974).
14. B. E. Deal, E. H. Snow, and C. A. Mead, *J. Phys. Chem. Solids*, **27**, 1873 (1956).
15. W. R. Hunter, D. H. Eaton, and C. T. Sah, *Appl. Phys. Lett.*, **17**, 211 (1970).
16. S. Karr and W. E. Dahlke, *ibid.*, **18**, 401 (1971).
17. P. V. Gray, *Phys. Rev.*, **140**, No. 1A, 179 (1965).
18. J. Shewchun, A. Waxman, and G. Warfield, *Solid-State Electron.*, **10**, 1165 (1967).
19. L. B. Freeman and W. E. Dahlke, *ibid.*, **13**, 1483 (1970).
20. M. Horiuchi, Paper presented at the IEEE International Electron Devices Meeting, Washington, D.C., 1972.
21. M. Horiuchi and Y. Itoh, *IEEE Trans. Electron Devices.*, **ed-24**, 587 (1977).

The Effect of Chloride Etching on GaAs Epitaxy Using TMG and AsH_3

Rajaram Bhat*,[1] and Sorab K. Ghandhi*

Electrical and Systems Engineering Department, Rensselaer Polytechnic Institute, Troy, New York 12181

ABSTRACT

A study has been made of the effect of *in situ* etching of (100) Cr-doped semi-insulating and Te-doped n^+-GaAs substrates on epitaxial layers, grown by the reaction of trimethylgallium and arsine. It is shown that *in situ* etching enables the growth rate to be increased by a factor of two while retaining a specular surface. In addition, the Hall mobility is higher in epitaxial layers grown on *in situ* etched substrates than on unetched ones. Epitaxial films on both $AsCl_3$ and HCl gas-etched substrates had a room temperature mobility that decreased from $\simeq$6100 cm^2/V-sec in 5.5 μm layers to $\simeq$5100 cm^2/V-sec in 1 μm layers. However, for layers grown on substrates which were not *in situ* etched, the mobility decreased from $\simeq$5800 to $\simeq$3800 cm^2/V-sec for layer thicknesses from 5.5 to 1 μm, respectively. Further it is shown that the carrier concentration profile is more abrupt near the epitaxial layer/Te-doped GaAs substrate interface when the substrates were *in situ* etched. Finally, experiments with chloride etching during growth were disappointing because it was not possible to obtain simultaneously good surface morphology, low carrier concentration, and high mobility for any given set of reactor conditions.

The growth of epitaxial layers of III-V semiconductors using organometallic compounds as sources of the group III element and hydrides as sources of the group V element was first reported by Manasevit (1). Since that time, the inherent simplicity of organometallic systems has been exploited in the growth of many other materials. One of their many advantages is that the

* Electrochemical Society Active Member.
[1] Present address: General Electric Company, Semiconductor Products Department, Syracuse, New York.

metal alkyl-hydride reaction is an irreversible one, so that etching and autodoping effects are notably absent. Unfortunately, however, this feature necessitates the use of an *in situ* etch step prior to epitaxial growth, which has been recognized by many workers as an essential step in the growth sequence to improve the quality of the epitaxial deposit (2, 3, 4). In GaAs epitaxial growth systems using trimethylgallium (5), this necessitates the use of etchants such as HCl gas or $AsCl_3$ vapor to incorporate this capability. The experimental conditions under which vapor-phase etching and polishing of GaAs substrates can be achieved have been established earlier (6, 7). In this paper, we report the effects of *in situ* etching on the properties of the subsequently deposited GaAs layer. It is demonstrated that *in situ* etching enables an increase in the growth rate while still retaining a specular surface. In addition, it is shown that this etching step results in an improvement in the electrical properties of the epitaxial layers, especially when they are thin (1-2 μm). Hall measurements, in conjunction with layer-by-layer stripping, were used to characterize epitaxial layers deposited on semiinsulating Cr-doped substrates. *C-V* and *dC/dV-V* measurements on Au-GaAs Schottky barrier diodes were used to obtain the free carrier concentration profiles in epitaxial layers grown on n^+ Te-doped GaAs.

Finally, we report on the results of GaAs epitaxy involving the reaction of TMG and AsH_3 in the presence of HCl gas or $AsCl_3$ vapor. The experimental results were disappointing, however, since we found that it was not possible to achieve simultaneously good morphology, low carrier concentration, and high mobility for any given set of reactor conditions.

Experimental Conditions

Apparatus.—*In situ* etching and epitaxial growth were carried out in a conventional rf heated, cold-wall reactor whose schematic is shown in Fig. 1. The reactants were introduced into a 50 mm ID, 37 cm long, horizontally positioned quartz reaction chamber containing a pyrolytic graphite-coated graphite susceptor. A baffle (not shown) was used to mix the reactants prior to their entry into the hot zone. The temperature was monitored using a Pt/Pt-13% Rh thermocouple enclosed in a quartz sheath and inserted into the susceptor, and verified by infrared pyrometric measurements. Gases were delivered to the reaction chamber through stainless steel tubing, except in the case of HCl gas and $AsCl_3$ vapor where Monel and Teflon, respectively, were used to minimize contamination.

Reactants.—Technical grade hydrogen (99.95% purity) was successively passed through an oxygen-removing catalyst,[2] a molecular sieve,[2] a palladium purifier,[2] and a cold trap at 77°K to obtain the carrier gas used in this investigation. This carrier gas was passed through a stainless steel bubbler containing electronic grade trimethylgallium[3] at 0°C. The arsine gas used was a 10% mixture of electronic grade arsine (99.998% purity) in six nines hydrogen.[4] The etchants used were either a 1% mixture of electronic grade HCl gas (99.995% purity) in six nines hydrogen[3] or vapors of $AsCl_3$[5] (99.9999% purity) produced by passing hydrogen through a Pyrex bubbler, containing the liquid at room temperature.

Substrates.—Experiments were carried out on chromium-doped semi-insulating and tellurium-doped n^+-GaAs substrates, with 2° off (100) towards (110) orientation. The wafers were obtained with one side chemimechanically polished by the vendors.[6] These were degreased in hot methanol, boiled in hydrochloric acid for 2 min, rinsed in methanol, and blown dry in filtered nitrogen. They were then etched in Caro's etch [$10H_2SO_4$ (97%):$1H_2O_2$ (30%):$1H_2O$] at 60°C for 30 sec, rinsed in DI water, rinsed in methanol, and blown dry in filtered nitrogen.

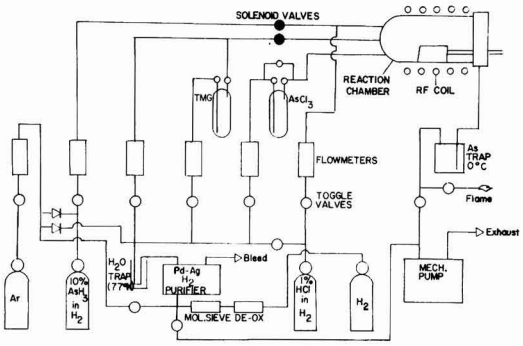

Fig. 1. Schematic of the epitaxial reactor

Procedure.—Substrates measuring 5 × 10 mm were placed on the susceptor such that they were nearly perpendicular to the direction of gas flow. The system was evacuated with a mechanical pump before establishing a flow of hydrogen (5 liters/min). The susceptor was then heated to 900°C (in those cases where an *in situ* etch was performed), after introducing the required amount[7] of arsine (30 ml/min) to prevent decomposition of the GaAs substrates. The etching was performed using either a flow of 4.2 ml/min of HCl gas or a hydrogen flow of 80 ml/min through the $AsCl_3$ bubbler. These processes removed a 4.5 μm thick layer from the substrate surface at a rate of 2.25 μm/min. The temperature was then stabilized at 700°C before commencing epitaxial growth. Subsequent GaAs epitaxial layers were deposited using a total hydrogen flow of 5 liters/min, an arsine flow of 15 ml/min, and a hydrogen flow through the TMG bubbler of up to 12 ml/min. The growth rate was determined by cleaving and staining.

In a second series of experiments GaAs layers were also grown on *in situ* etched substrates in the presence of HCl gas or $AsCl_3$ vapor. The introduction of HCl gas during deposition resulted in an increase in the free electron concentration by at least an order of magnitude. This was attributed to the impure nature of the gas, and all further experiments were restricted to the use of high purity $AsCl_3$ vapors during the growth. In these experiments, GaAs was deposited on (100) Cr-doped substrates at 700°C, using a hydrogen flow of 5 liters/min, a hydrogen flow through the TMG bubbler of 10 ml/min, and arsine flow of 15 ml/min. The hydrogen flow through the $AsCl_3$ bubbler was varied between zero and 80 ml/min.

Surface Morphology and Growth Rates

Effect of in situ etching on surface morphology.—Epitaxial layers were deposited on both *in situ* etched and unetched substrates. Layers on unetched substrates exhibited specular surfaces at low growth rates ($\leq$ 0.25 μm/min), corresponding to a H_2 flow through the TMG bubbler of $\leq$ 5 ml/min. With *in situ* etching, however, mirror-like surfaces could be achieved for growth rates as high as 0.5 μm/min. This is shown in the Nomarski interference micrographs of Fig. 2 for layers grown at 0.4 μm/min, both with and without *in situ* etching. Furthermore, differences in surface quality of layers deposited on HCl gas and $AsCl_3$ etched GaAs substrates were very slight, as shown in this figure.

[2] Matheson Gas Products, East Rutherford, New Jersey 07073.
[3] Alfa Products Division, Beverly, Massachusetts 01915.
[4] Precision Gas Products, Incorporated, Rahway, New Jersey 07065.
[5] Metal Specialties, Fairfield, Connecticut 06430.
[6] Laser Diode Laboratories, Incorporated, Metuchen, New Jersey.

[7] In this paper, flow rates for AsH_3 and HCl gas are all quoted in terms of the actual arsine and hydrogen chloride gas content of the diluted gas.

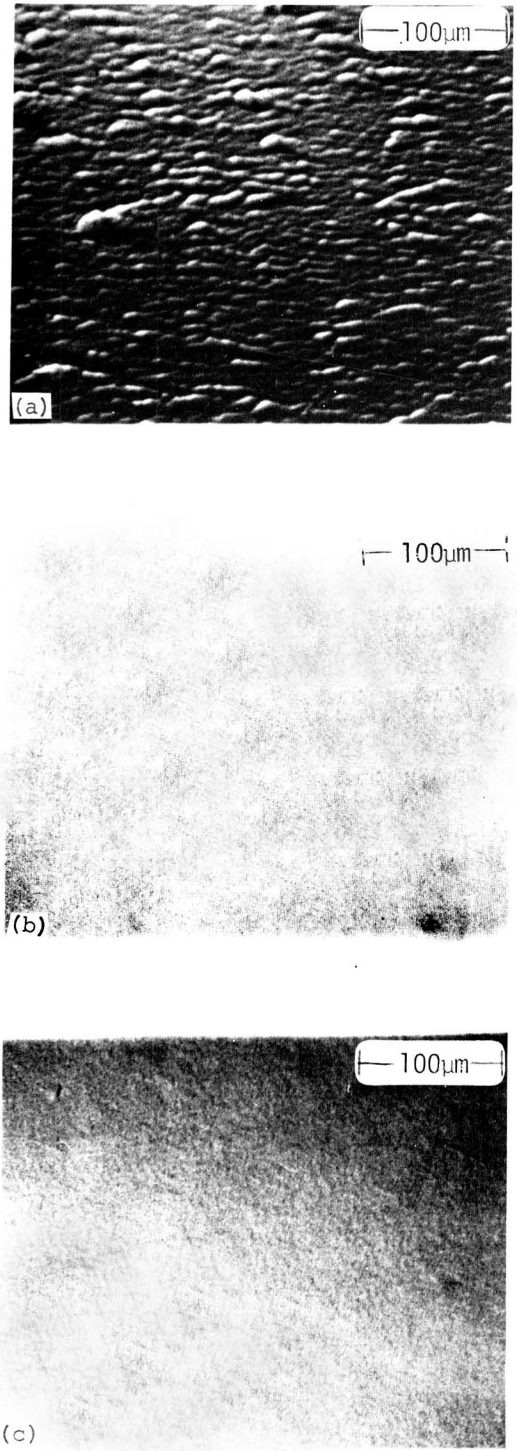

Fig. 2. Typical Nomarski interference photomicrographs showing the effect of *in situ* etching of GaAs substrates on the surface morphology of epitaxial layers (a) no *in situ* etch; (b) HCl gas etch; and (c) $AsCl_3$ etch (growth rate: 0.4 μm/min).

Effect of introducing $AsCl_3$ vapor during epitaxy.—The growth rate of layers deposited at 700°C in the presence of $AsCl_3$ fell linearly with increasing hydrogen flow through the $AsCl_3$ bubbler, varying from 0.4 μm/min for no $AsCl_3$ to 0.2 μm/min for a hydrogen flow of 80 ml/min. There was considerable scatter in the data, however, accompanied by a deterioration in surface morphology at low growth rates. Better surfaces were obtained for layers deposited at 900°C. However, this temperature is far from the optimum for growth using TMG and AsH_3, and resulted in layers with low mobility and high compensation.

Electrical Properties

Epitaxial layers on Cr-doped substrates.—Epitaxial layers were deposited at 700°C on unetched and on *in situ* etched (100) Cr-doped semi-insulating substrates. A total hydrogen flow of 5 liters/min, an arsine flow of 15 ml/min, and a hydrogen flow of 10 ml/min through the TMG bubbler were used to obtain a growth rate of 0.4 μm/min. Tables I and II list[8] the carrier concentration and mobility of epitaxial layers of varying thickness, as obtained by Hall measurements on successively etched layers. Room temperature values of mobility ranged from 6150 cm^2/V-sec for thick (5.5 μm) layers for substrate etching with $AsCl_3$, to 3800 cm^2/V-sec for thin (1 μm) layers with no substrate etching. Results at liquid nitrogen temperature showed a similar trend.

Hall measurements were also made on 5 μm thick GaAs layers, grown at 700°C in the presence of $AsCl_3$ vapor. As expected, the increase of hydrogen flow through the $AsCl_3$ resulted in a fall in carrier concentration, as shown in Fig. 3. However, this fall in elec-

[8] Error limits on this data are ±10% on thickness, ±5% on mobility, and ±15% on carrier concentration. Layer thickness variations over the surface of the Hall samples were undetectable.

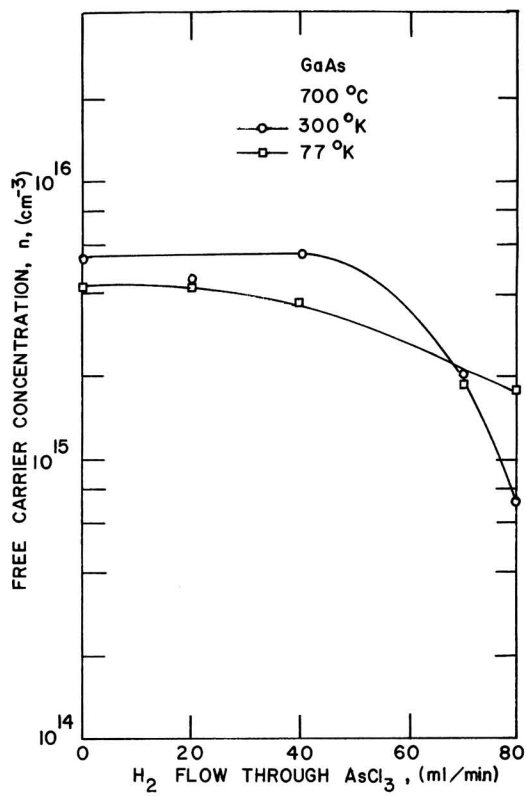

Fig. 3. Carrier concentration *vs.* hydrogen flow rate through the $AsCl_3$ bubbler during epitaxy.

Table I. Carrier concentration and mobility at room temperature for epitaxial layers of different thickness

Thickness, μm	No etch		HCl gas etch		$AsCl_3$ etch	
	Carrier concentration, per cm^3	Mobility, cm^2/V-sec	Carrier concentration, per cm^3	Mobility, cm^2/V-sec	Carrier concentration, per cm^3	Mobility, cm^2/V-sec
5.5	8.3×10^{15}	5780	8.4×10^{15}	6100	5.7×10^{15}	6150
4	8.6×10^{15}	5550	9.1×10^{15}	6020	5.7×10^{15}	6070
2	8.74×10^{15}	5240	1.13×10^{16}	5710	6.1×10^{15}	5770
1	1.6×10^{16}	3800	1.4×10^{16}	5010	3.4×10^{16}	5090

Table II. Carrier concentration and mobility at liquid nitrogen temperature for epitaxial layers of different thickness

Thickness, μm	No etch		HCl gas etch		$AsCl_3$ etch	
	Carrier concentration, per cm^3	Mobility, cm^2/V-sec	Carrier concentration, per cm^3	Mobility, cm^2/V-sec	Carrier concentration, per cm^3	Mobility, cm^2/V-sec
5.5	6.2×10^{15}	13,800	6.4×10^{15}	14,400	4.5×10^{15}	15,300
4	6.83×10^{15}	12,700	6.8×10^{15}	13,900	4.75×10^{15}	15,000
2	8.1×10^{15}	11,100	8.7×10^{15}	13,700	5.6×10^{15}	14,000
1	4.8×10^{15}	7,000	1.2×10^{16}	12,000	5.7×10^{15}	12,500

tron concentration was accompanied by increasing compensation in the films, as evidenced by the disparity in the 300° and 77°K data. Figure 4 shows that the compensation ratio (8) changed from below 0.5 for no $AsCl_3$ to as high as 0.95 for 80 ml/min hydrogen flow through the $AsCl_3$ bubbler.

Experiments with films grown at 900°C showed a similar trend. Consequently, the quest for making films of improved quality (lower carrier concentration, lower compensation ratio, and higher mobility) by epitaxy in the presence of $AsCl_3$ vapor was abandoned.

Epitaxial layers on Te-doped substrates.—GaAs epitaxial layers were deposited on unetched and *in situ* etched Te-doped (100) substrates, the deposition and *in situ* etching being performed simultaneously with those on Cr-doped substrates used for obtaining the Hall measurement data presented earlier. The layers were chemically thinned to approximately 1 μm to allow carrier concentration profiling of the epitaxial layer-substrate interface using Au-GaAs Schottky barriers. The free carrier concentration profiles were obtained from C-V and dC/dV-V data using the relation

$$n(x) = \frac{C^3}{q\epsilon_r\epsilon_o A^2 (dC/dV)}$$

where $n(x)$ is the free carrier concentration at a depth x below the surface, C is the capacitance of the Schottky barrier, of area A, ϵ_o, ϵ_r are the permittivity of free space and relative permittivity of GaAs, respectively, q is the electronic charge, and V is the reverse voltage applied across the Schottky barrier.

Figure 5 shows normalized plots of the free carrier concentration profiles obtained [any effect due to the presence of traps (9) has been ignored]. The carrier concentration in these layers was approximately 5×10^{15} per cm^3. Doping profiles obtained for *in situ* etched substrates are seen to be far more abrupt than for the case with no substrate etching.

Discussion

Epitaxial layers on Cr-doped substrates.—A number of observations can be made from a study of the data of Tables I and II. Thus:

(*i*) The mobility was higher in those layers deposited on substrates which were vapor etched than

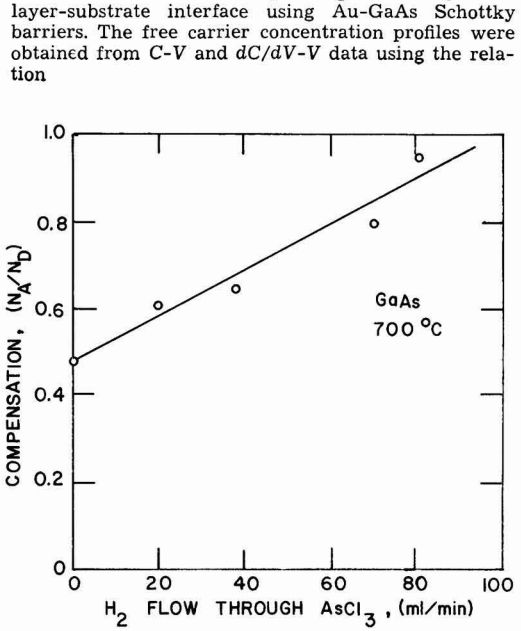

Fig. 4. Compensation ratio *vs.* hydrogen flow rate through the $AsCl_3$ bubbler during epitaxy.

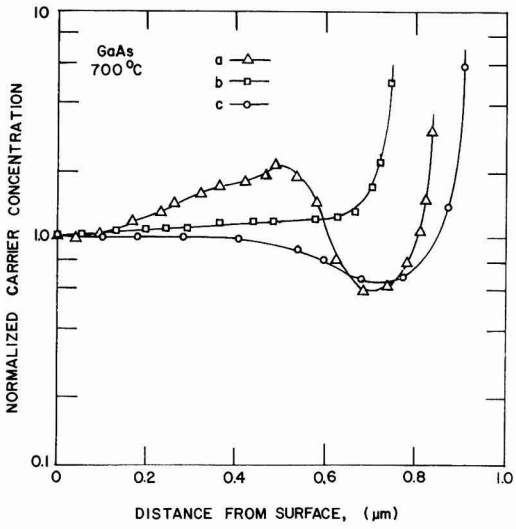

Fig. 5. Normalized carrier concentration profiles of epitaxial layers on (100)Te-doped GaAs substrates (a) unetched substrates; (b) HCl gas etched substrates; and (c) $AsCl_3$ etched substrates.

in those which were not vapor etched. *In situ* etching of substrates, therefore, enables the growth of epitaxial layers of superior crystalline quality. The room temperature mobility was comparable for epitaxial layers on $AsCl_3$ and HCl etched substrates. The slightly higher 77°K mobility obtained for layers on $AsCl_3$ etched substrates is due to the lower carrier concentration in these layers.

(*ii*) The mobility in all cases decreased with epitaxial layer thickness, the decrease being most rapid for layers grown on unetched substrates. A decrease in mobility with epitaxial layer thickness has also been observed by other investigators (10-12), and has been attributed to the increasingly important role of space-charge scattering effects at the epitaxial layer-substrate interface. The results obtained in this study indicate that *in situ* etching of substrates prior to growth results in a cleaner surface and thus reduces, but does not eliminate, the space charge centers due to defects created in the epitaxial layers. It should be noted that growth instabilities exist even when ideally clean and perfect GaAs substrate surfaces are used. These will set a lower limit to the density of space charge centers, and are inherent to the growth process. The decrease in mobility with epitaxial layer thickness can also be due to increasing compensation, and hence ionized impurity concentration, with decreasing thickness. However, the relative contributions of ionized impurity and space charge scattering in thin layers cannot be estimated from the available data.

(*iii*) The free carrier concentration is highest in layers grown on HCl etched substrates, particularly in thin layers. This is probably due to contamination of the substrate surface by n-type impurities present in the HCl gas. In contrast, the $AsCl_3$ used for this study was better than six nines purity, so contamination of the substrate surfaces by this etchant is not expected. This is borne out by the fact that the lowest carrier concentrations are observed in layers grown on $AsCl_3$ etched substrates (except for the 1 μm layers, where strong compensation effects are present, as described below).

(*iv*) The carrier concentration decreased with decreasing layer thickness for both unetched and $AsCl_3$ etched substrates. This effect was, however, significantly more rapid for layers grown on unetched substrates. Acceptor-type defects introduced in the early stages of growth are believed to be responsible for this behavior, since substantially more defects are expected to occur in epitaxial layers grown on unetched than on etched substrates. With HCl gas etching, contamination of the substrate surface masks the compensation due to these acceptor-type defects, and results in an increase in carrier concentration at the epitaxial layer-substrate interface.

Epitaxial layers on Te-doped substrates.—It is seen from Fig. 5 that the carrier concentration for layers on HCl gas etched substrates increased monotonically as the epitaxial layer-substrate interface was approached. However, a slight fall in carrier concentration was noted near the interface for epitaxial layers on $AsCl_3$ etched substrates. These observations can be explained by noting that instabilities during the early stages of growth cause acceptor-type defects to be created. The effect of these acceptor-type defects is not observed in the case of epitaxial layers on HCl gas etched substrates because of the n-type contaminants introduced by this etchant in the interface region. However, substrates etched with $AsCl_3$ were not contaminated since this etchant was ultrapure. As a result, epitaxial layers on these substrates showed a decrease in carrier concentration near the interface because of these acceptor-type defects. In contrast, the carrier concentration profile exhibited a pronounced undulation near the interface for layers grown on unetched substrates. A possible explanation for this behavior can be based on the fact that a large concentration of acceptorlike defects can be expected to occur for this case. In addition, the unetched surface of GaAs is highly reactive, and probably has a large concentration of adsorbed sulfur (an n-type impurity) on its surface because of the Caro's etch prior to growth (13). The competing decay of these impurities with distance may, in this situation, lead to the observed undulation in the impurity profile.

Epitaxial layers deposited in the presence of $AsCl_3$ vapor.—There are a number of possible explanations for the increase in the compensation of epitaxial layers from TMG and AsH_3 in the presence of $AsCl_3$ vapor. Of these, the most plausible is that the $AsCl_3$ removes donor impurities faster than acceptor impurities from the source materials. The major acceptor impurity in GaAs grown from TMG and AsH_3 is carbon, whereas the major donor impurity is silicon (14, 15). The change in Gibbs free energy for the reaction of these impurities with the etchant species (HCl) is negative for silicon, so that only silicon chlorides are stable at growth temperatures. Consequently, silicon is selectively removed during epitaxy in the presence of $AsCl_3$ vapor, resulting in an increase in the compensation ratio. In marked contrast, the principal impurities in the halide transport system are silicon and zinc, both of which have stable chlorides at deposition temperatures. Consequently, increasing the $AsCl_3$ concentration in halide transport systems is a highly successful technique for reducing the free electron concentration with no increase in the compensation ratio (16).

Conclusions

In summary, *in situ* etching of GaAs substrates prior to epitaxy enables the growth of epitaxial layers with specular surfaces at higher growth rates than are otherwise possible. The mobility, particularly in thin ($\simeq$ 1 μm) layers, was higher for layers on substrates which were *in situ* etched. The carrier concentration profiles for epitaxial layers on Te-doped substrates were more abrupt at the interface for layers on substrates which were vapor etched than on those which were not. Epitaxial layers on $AsCl_3$ and HCl gas-etched substrates had comparable mobility. Further, the carrier concentration, particularly in thin layers, was higher in epitaxial layers on HCl gas-etched substrates due to n-type contaminants introduced by this etchant. Finally, experiments with epitaxial growth in the presence of $AsCl_3$ showed that it was possible to obtain a reduction in the free electron concentration by this technique. However, this was accompanied by an increase in the compensation ratio and a general deterioration in the crystal quality. This result is in marked contrast to that obtained by workers with halide transport systems.

Acknowledgments

This work was partly supported by Grant No. DAAG29-76-G-0127 from the U.S. Army Research Office, Durham, North Carolina. One of the authors (R. Bhat) wishes to acknowledge Fellowship support from the IBM Research Foundation. The authors are also indebted to Ms. R. C. Rafun for assistance in manuscript preparation.

Manuscript submitted June 20, 1977; revised manuscript received Dec. 19, 1977.

Any discussion of this paper will appear in a Discussion Section to be published in the December 1978 JOURNAL. All discussions for the December 1978 Discussion Section should be submitted by Aug. 1, 1978.

Publication costs of this article were assisted by Rensselaer Polytechnic Institute.

REFERENCES

1. H. M. Manasevit, *Appl. Phys. Lett.*, **12**, 156 (1968).
2. C. M. Wolfe, A. G. Foyt, and W. T. Lindley, *Electrochem. Tech. J.*, **6**, 208 (1968).
3. R. D. Fairman and R. Solomon, *This Journal*, **120**, 541 (1973).

4. T. Nozaki and T. Saito, *Jpn. J. Appl. Phys.*, **11**, 110 (1972).
5. H. M. Manasevit and W. I. Simpson, *This Journal*, **116**, 1725 (1969).
6. R. Bhat, B. J. Baliga, and S. K. Ghandhi, *ibid.*, **122**, 1378 (1975).
7. R. Bhat and S. K. Ghandhi, *ibid.*, **124**, 1447 (1977).
8. C. M. Wolfe, G. E. Stillman, and W. T. Lindley, *J. Appl. Phys.*, **41**, 3088 (1970).
9. L. C. Kimerling, *ibid.*, **45**, 1839 (1974).
10. B. J. Baliga and S. K. Ghandhi, *This Journal*, **121**, 1646 (1974).
11. Y. Nakayama, S. Ohkawa, H. Hashimoto, and H. Ishikawa, *ibid.*, **123**, 1227 (1976).
12. A. Shibatomi, N. Yokoyama, H. Ishikawa, K. Dazai, and O. Ryuzan, *J. Cryst. Growth*, **31**, 240 (1975).
13. D. J. Stirland and B. W. Straughan, *Thin Solid Films*, **31**, 139 (1976).
14. S. J. Bass, *J. Cryst. Growth*, **31**, 172 (1975).
15. S. Ito, T. Shinokara, and Y. Seki, *This Journal*, **120**, 1419 (1973).
16. J. V. DiLorenzo, *J. Cryst. Growth*, **17**, 189 (1972).

Effect of Proton Damage on Optical Modulation Spectra of Gallium Arsenide

Moshe Oren,[1] A. R. Quinton, and Claude M. Penchina

Department of Physics and Astronomy, University of Massachusetts, Amherst, Massachusetts 01003

ABSTRACT

We studied the effect of proton bombardment on the electroreflectance (ER), electroabsorption (EA), and transmission (T) spectra of high resistivity Cr-doped single crystal GaAs. The high resolution of ER and EA and their sensitivity to crystalline order make it possible to study shift, broadening, and gradual distortion of the spectral peaks as disorder increases with successive irradiations. The sample is bombarded with 150 keV protons. We have measured ER and EA at the absorption edge E_0, ER at the E_1 critical point, and d-c optical absorption. All these measurements are sensitive to proton irradiation of the sample; the most sensitive one is ER at E_0. In the range of 3×10^{14} to 5×10^{15} protons/cm^2, optical absorption just below the energy gap increases sublinearly with proton dose; the peak-to-peak amplitudes of ER at E_0 and E_1 vary linearly with the logarithm of the dose and hence can be used to measure the degree of damage in the sample. The EA signal at E_0 develops a tail toward the low energy side of the spectrum. The ER at E_0 has a peak shift of $\approx$4 meV to higher energy while the peak of the ER signal at E_1 shifts by about 15 meV to lower energy. Broadening is evident in the ER signals at E_0 and E_1. Annealing at 300°C for up to 2 hr only partially recovers the unbombarded state. A model based on the gradual amorphization of the sample by an increasing number of proton damaged, amorphous islands with well-defined boundaries can partially explain the experimental results.

Lattice damage in single crystals plays a major role in device applications. Lattice damage caused by ion implantation received special attention in recent years following the introduction of ion implantation as a method for doping semiconductor materials. There are several experimental techniques that can be applied to study radiation damage in semiconductors, among others: optical (1), electrical (2), Rutherford back scattering (3), and electron paramagnetic resonance (4).

The optical absorption and reflection of GaAs were found to be sensitive to ion bombardment damage but the sensitivity of such measurements (reflectivity in particular) is low, and quantitative results are difficult to obtain.

In the present work we use electromodulation (EM) spectroscopy to study the effect of proton bombardment on single crystal, semi-insulating GaAs. In electromodulation one measures the change in reflectance (ΔR) or transmittance (ΔT) when an external electric field is applied to the sample (5). The EM response is spectrally concentrated around the critical points in the band structure. A phase sensitive detection system tuned to the frequency and phase of the external field greatly enhances the sensitivity of the measurement to critical points in the spectrum. These critical points are a manifestation of the long range order in the crystal; a change in the EM signal on successive bombardment would indicate, therefore, the gradual relaxation in this long range order. This relation allows a semi-quantitative measure of lattice damage to be made.

EM has been applied to date primarily to problems of intrinsic band-structure analysis (5), but as a powerful spectroscopic method it is now finding new areas of applications. Jonath *et al.*, (6) studied electroabsorption (EA) of oxygen impurities in GaAs. Bauer (7) used EA to study the symmetry properties of defect states in nitrogen-doped GaP and their interaction with the host band structure. Gavrilenko *et al.* studied the influence of low energy argon ion bombardment on the electroreflectance (ER) and photoluminescence spectra of n-type $Al_xGa_{1-x}As$ solid solution (8) and Si (9). Anderson *et al.* (10) used ER to detect shallow impurity levels in GaAs doped with Si, Te, Zn, or Cd impurities. A disadvantage of this method is that different types of lattice damage cannot be distinguished.

Experimental

High resistivity, n-type GaAs:Cr single crystal was used in this experiment. The sample had $\approx 10^8$ Ω-cm room temperature resistivity. For radiation damage experiments it is preferable to have the sample front surface free of any evaporated electrode or insulating layer. For that reason, the sample geometry used in the ER and the EA measurements is based on the transverse configuration (11). Slices were cut from the GaAs crystal, lapped, polished with 0.3μ alumina powder, and then etch polished with Monsanto Syton solution. For contacts, two Au films were evaporated on the

[1] Present address: Spire Corporation, Bedford, Massachusetts 01730.

Key words: electroreflectance, electroabsorption, GaAs-Cr, amorphous GaAs, ion implantation.

polished sample surface forming a gap 1 mm wide (see insert in Fig. 1). The current voltage characteristics up to 900V show good ohmic behavior. The light beam was incident in the [111] crystal direction. The magnitude of the ER signal is a function of surface potential. Therefore, it varies from sample to sample due to slight changes in surface preparation, which may alter considerably the surface potential. To avoid this complexity, only half of the gap between the field electrodes was bombarded and the other half was used as a reference for all successive measurements. The gap height is more than twice the height of the incident light beam in order that the light will not overlap the bombarded and nonbombarded regions.

The system used for the ER and EA measurement is shown in Fig. 1. It includes the following components: 250W tungsten halogen lamp, monochromator, optics, dewars, and detectors. All measurements were made at LN_2 temperature. Two photomultipliers (PM) were permanently mounted in the sample chamber, 1P28 PM to measure ER at E_1 critical point and 7102 PM for ER at the E_0 critical point. A removable front surface aluminum mirror directs the reflected beam into the PM in use. A PbS detector was used for the EA and transmission measurements. The two PM's were wired such that higher voltage was impressed between the last dynode and the anode than on the intermediate stage of the voltage divider. This allows greater linear swing of the anode voltage, which is desirable when a small a-c signal, superimposed on a large d-c signal, is to be measured. The voltage applied to the sample was 1 kHz, 2000V peak-to-peak sine wave superimposed on 1000V d-c. For the ER measurement a d-c photon flux was used, a lock-in amplifier measured the a-c signal ($I_0 \cdot \Delta R$) and an electrometer measured the d-c reflection ($I_0 \cdot R$). For the transmission (T) and EA measurements the incident light beam was chopped at 147 Hz; two lock-in amplifiers tuned at 1 kHz and 147 Hz measured the ΔT and T signal, respectively.

Sample bombardment was done with a 150 keV proton beam. The sample was mounted on a water-cooled holder. An in-line cold trap was used to remove oil vapor that may otherwise be carried along with the proton beam to contaminate the sample surface. In addition when a high dose was used ($\gtrsim 5 \times 10^{15}$ p/cm^2), a thin carbon film ($\approx$ 20 μm) was inserted in front of the sample, to further prevent possible oil contamination.

Isothermal annealing of the sample was done at 300°C in an oil-free vacuum system ($\approx 5 \times 10^{-7}$ Torr).

Results

Transmission.—The sample transmission in the range of the fundamental absorption edge was measured at LN_2 temperature for various bombardment doses. In order to determine more conveniently the effect of proton damage on the sample transmission, the ratio of the transmitted intensity from the bombarded (T_b) and nonbombarded (T_o) regions was determined at one wavelength. Such a graph is shown in Fig. 2 (insert). Taking into account reflection losses, R, from the sample front and back surfaces, one can write

$$T_o = (1 - R)^2 \exp(-\alpha_o d_o) \quad [1]$$

α_o and d_o are the sample absorption coefficient and thickness, respectively (multiple internal reflections are neglected). The transmission through the bombarded region is

$$T_b = (1 - R')(1 - R) \exp(-\alpha_o d_o - \alpha_b d_b) \quad [2]$$

where R' is the reflectivity coefficient from the front surface of the bombarded region, α_b is the average value of the change in absorption coefficient over the bombarded layer thickness d_b. Measurement of $I_o \cdot R$ (when R is the reflectivity and I_o is the incident intensity) in the vicinity of the absorption edge shows a change of less than 5% due to proton bombardment. Similarly, Kalma (12) found no change in reflectivity in the vicinity of the absorption edge of GaAs following a 1 MeV electron irradiation; Sell and MacRae (1b), found a change of $\sim 3\%$ in reflectivity at 2.5 eV in argon-implanted GaAs. We assume therefore $R \approx R'$. Then

$$\ln(T_o/T_b) = \alpha_b d_b \quad [3]$$

α_b can be related to the number, N, of the optically active defects produced in the bombarded layer (13)

$$\alpha_b = N\sigma_b \quad [4]$$

where σ_b is the cross section for optical absorption by these defects. The best straight line fit to the data in the log-log plot of Fig. 2 (insert) provides the relation

$$T_o/T_b = \gamma\phi^\beta \quad [3a]$$

with $\ln \gamma = -16.9$ and $\beta = 0.48$. Therefore, from Eq. [3], [3a], and [4]

$$d_b N\sigma_b = d_b\alpha_b = \ln\gamma + \beta \ln\phi \quad [5]$$

The production rate of defects is sublinear in dose. This is due to damaged regions overlapping and possible room temperature annealing (14, 15).

If we approximate the damaged layer thickness, d_b, by the projected range (16) ($\approx 1.5\mu$) of the proton beam, the wavelength dependence of the added absorption due to bombardment can be expressed using Eq. [3]. Such a graph is presented in Fig. 2. The featureless increase in absorption indicates that the bombardment generates a continuous distribution of energy levels right below the bandgap with no evidence of discrete levels in this range. Kalma (12) studied electron irradiated GaAs, Si, Ge, InSb, and PbTe and

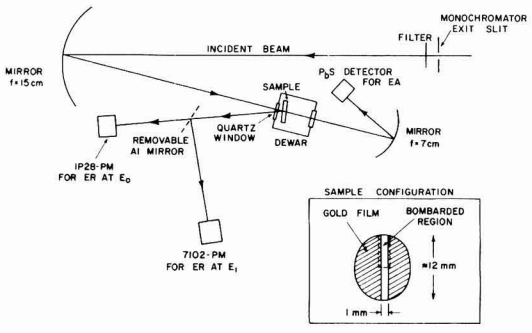

Fig. 1. Optical system used for the ER and EA measurements

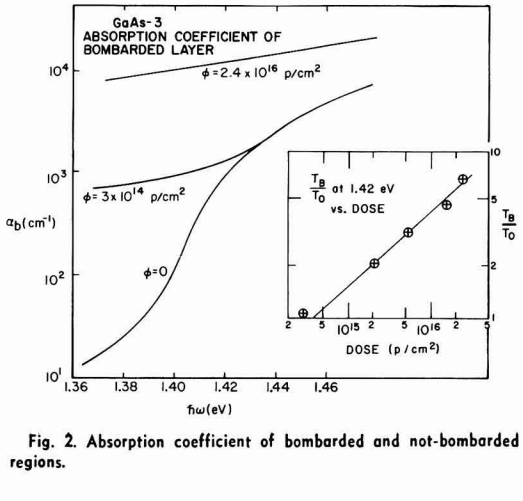

Fig. 2. Absorption coefficient of bombarded and not-bombarded regions.

suggested that increased absorption near the bandedge observed in GaAs can be attributed to tailing of the density of states into the bandgap. Note that the range of α_b ($\approx 10^4$ cm^{-1}) is about two orders of magnitude higher than the absorption coefficient observed in neutron damaged GaAs (17).

Theoretical Model

A simple picture of gradual amorphization of the sample by the incident radiation was used by a number of workers (3, 18) to describe the process in which long-range order in the bombarded layer is destroyed. In such a picture each incident proton produces a highly disordered region along its track in the sample. Assuming these regions have well-defined boundaries, at low dose they are separated from each other except for random overlapping. As the dose increases the overlapping increases until a completely amorphous layer is formed. The added absorption coefficient in this picture will be due to the introduction of amorphous islands with higher absorption

$$\alpha_b = \frac{A}{A_o}(\alpha_a - \alpha_c) \qquad [6]$$

where A is the area of the amorphous regions, A_o is the total sample area exposed to the beam, and subscripts a, b, and c correspond to amorphous, bombarded, and crystalline, respectively.

Based on this description we can define a quantity $\sigma(\phi)$ which is the cross section for added amorphization per proton which hits a previously undamaged area. The probability that an additional incident proton will not hit the amorphous region A is $1 - (A/A_o)$. In terms of this cross section, the change in A per incident proton, dA/dP will be therefore

$$\frac{dA}{dP} = \frac{A}{A_o}\frac{dA}{d\phi} = \left(1 - \frac{A}{A_o}\right)\sigma(\phi) \qquad [7]$$

and after integration

$$1 - \frac{A}{A_o} = \exp[-\int \sigma(\phi)\, d\phi] \qquad [7a]$$

Using Eq. [6] and [7a]

$$\exp[-\int \sigma(\phi)\, d\phi] = 1 - \frac{A}{A_o} = 1 - \frac{\alpha_b}{\alpha_a - \alpha_c} \qquad [8]$$

Using the experimental data for α_b as expressed in Eq. [5] and taking the logarithmic derivative of Eq. [8], we get

$$\sigma_{TR}(\phi) = \frac{1}{\phi(K_2 - \ln \phi)} \qquad [9]$$

with

$$K_2 = \frac{d(\alpha_a - \alpha_c)}{\beta} - \frac{1}{\beta}\ln\gamma \qquad [10]$$

For $h\nu = 1.42$ eV, $\alpha_a H >> \alpha_c$, thus α_a approximated by α_b at high dose (where $A \to A_o$)

$$\alpha_a(1.42 \text{ eV}) \cong \alpha_b(1.42 \text{ eV}, \phi = 2.4 \times 10^{16} \text{ p/cm}^2)$$
$$= 1.24 \times 10^4 \text{ cm}^{-1} \qquad [11]$$

this gives

$$K_2 = 38.9 \qquad [10a]$$

This same picture will be applied for the ER data, and the result compared with the results above.

ER at E_o and E_1 Critical Points

Figure 3 shows the ER at the absorption edge E_o and Fig. 4 shows the ER response at the E_1 critical point. The most obvious feature of the bombarded spectrum is the reduction in signal intensity in both cases compared to the unbombarded spectrum. To better evaluate this effect, the peak-to-peak amplitude (PPA), Δ_b, of the bombarded region, normalized to the

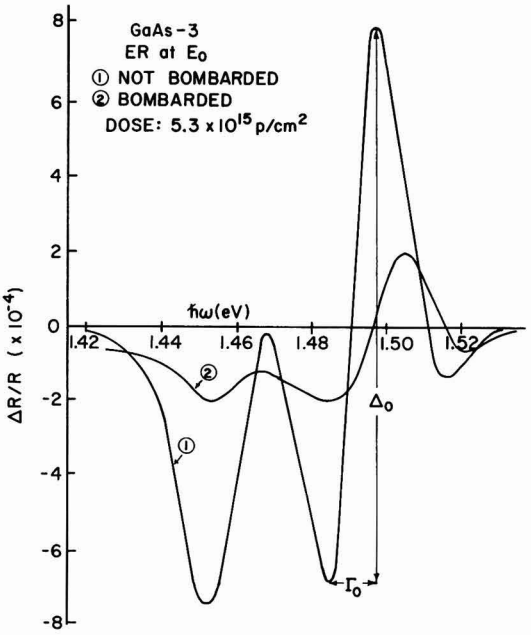

Fig. 3. ER at E_o from the bombarded and not-bombarded regions

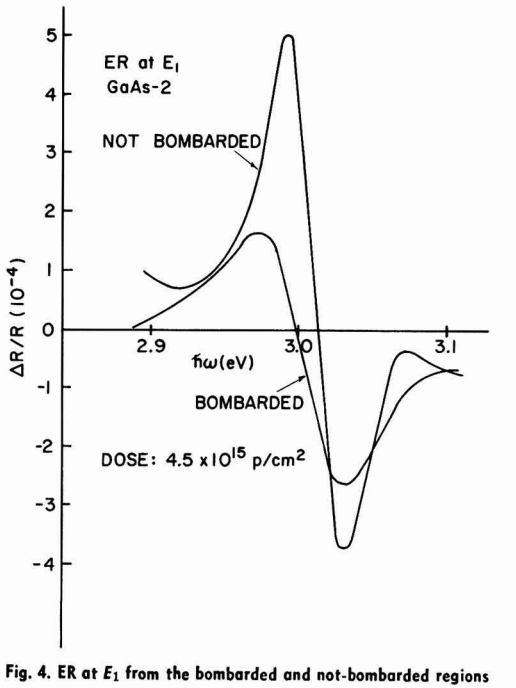

Fig. 4. ER at E_1 from the bombarded and not-bombarded regions

PPA from the nonbombarded region, Δ_o, is plotted *vs.* dose in Fig. 5 for both E_o and E_1 critical points.

It is apparent that the attenuation of Δ for a given dose is larger at E_o than at E_1. This can be explained qualitatively by the higher penetration depth of the light beam at E_o. At the bandgap transition, the penetration depth of the light is of the same order as that of the proton beam range, $\approx 1.5\mu$ (19), where the induced crystalline damage is mostly concentrated. At the E_1 transition the light penetration depth is only

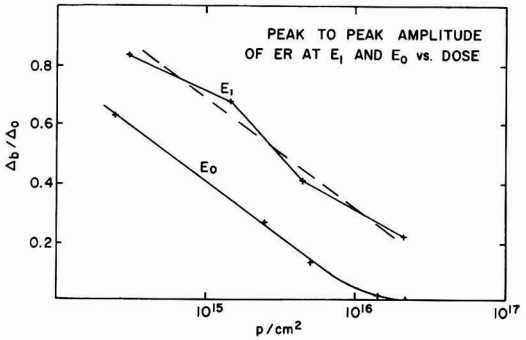

Fig. 5. Peak-to-peak amplitude (PPA) of the ER at E_1 and E_0 normalized to the PPA from the not-bombarded region.

0.017μ (19). The ER signal at E_0 is reduced to below the detection limit ($\approx 10^{-6}$) for dose $\gtrsim 2.4 \times 10^{16}$. This increased sensitivity of ER at E_0 to irradiation damage can be a useful tool for damage detection. The PPA will be used to give a semi-quantitative value for the amount of damage introduced into the sample, averaged over the damaged layer thickness. The ER will not distinguish, though, between the various types of damage in the sample. It is of interest to note that the linear fits of Eq. [3] to both E_0 and E_1 data are parallel, although the data at the E_1 critical point are more scattered. Between 2.5×10^{14} p/cm² and 5×10^{15} p/cm² the decrease in Δ_b/Δ_o for E_0 is linear in the logarithm of the dose ϕ

$$\Delta_b/\Delta_o = a \ln(\phi/\phi_o) \qquad [12]$$

with: $a = -0.16$ and $\ln \phi_o = 36.9$. For the E_1 critical point we get

$$\Delta_b/\Delta_o = a' \ln(\phi/\phi_o') \qquad [13]$$

with: $a = a' = -0.16$, $\ln \phi_o' = 38.0$.

Proton bombardment resulted in a small shift of about 15 meV toward the low energy in the ER peak at E_1, and 4 meV shift toward higher energy in the ER peak at E_0. A contribution to the shift at E_0 may come from the uneven attenuation of the ER peak due to strong variation in the penetration depth of the light beam near the absorption edge combined with the fact that the damaged layer peaks about 1.5μ below the surface.

Gavrilenko *et al.* (9) found that bombardment of Si with 1 keV He^+ ions causes a shift in the E_1 ER peak to higher energy; 1 keV Ar^+ bombardment of $Al_xGa_{1-x}As$ solution shifts the ER peak at E_1 to lower energy (8). Figure 6 shows the increased broadening in the E_1 and E_0 ER peaks *vs.* bombardment dose. Here too, note the higher values obtained for E_0 compared to E_1. Various sources can contribute to broadening of the ER signal, among others, temperature effect, local random electric field, and microstress due to defects. In our case a local electric field can be created by the proton doping of the damaged crystal.

The ER signal disappears at high dose. Based on the gradual amorphization model, the ER peak-to-peak amplitude, Δ_b, at a given dose, will be proportional to the area fraction which is still in the crystalline state

$$\Delta_b = \Delta_o\left(1 - \frac{A}{A_o}\right) \qquad [14]$$

Thus from Eq. [7a], [12], and [14]

$$\exp[-\int \sigma(\phi)\, d\phi] = 1 - \frac{A}{A_o} = \frac{\Delta_b}{\Delta_o} = a \ln(\phi/\phi_o) \qquad [15]$$

Taking the logarithmic derivative on both sides

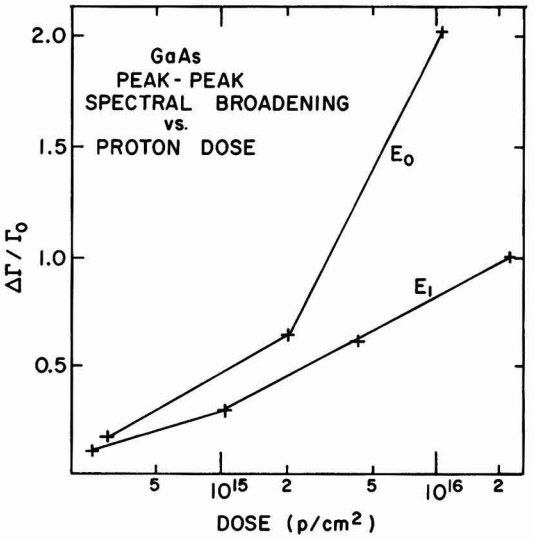

Fig. 6. Spectral broadening *vs.* proton dose of the ER signals at E_0 and E_1.

$$\sigma_{ER} = \frac{1}{\phi(K_o - \ln \phi)} \qquad [16]$$

where $K_o = \ln \phi_o$.

We previously found (Eq. [12]) that

$$K_o = \ln \phi_o = 36.9 \qquad [17]$$

Thus, from electroreflectance at E_o, at a dose of $\phi = 10^{15}$ p/cm² we get (Eq. [12], [16], and [17])

$$\sigma_{ER}\ (\phi = 10^{15}\ \text{p/cm}^2) = 4 \times 10^{-16}\ \text{cm}^2$$

Similarly, from transmission measurements, at this same dose we get (Eq. [9] and [10a]

$$\sigma_{TR}(\phi = 10^{15}\ \text{p/cm}^2 = 2 \times 10^{-16}\ \text{cm}^2$$

The relatively small discrepancy between the values obtained for σ_{ER} and σ_{TR} indicates that the simple picture used to describe the amorphization process is essentially correct in the first approximation. The result $\sigma_{ER} > \sigma_{TR}$ is to be expected because the ER is more sensitive to bombardment; partially damaged regions, neglected in the simple model, will affect the ER more than the transmission. It was suggested (20) that such partially damaged regions are caused by diffusion of defects from the outer portion of the ion track, into the undamaged bulk.

EA at the Absorption Edge E_o

The effect of proton bombardment on the band-to-band electroabsorption (EA), $\Delta T/T$, of the sample is shown in Fig. 7. Just below the bandgap, $\Delta T/T$ is negative, corresponding to a red shift of the absorption edge on application of the electric field as expected from the Franz Keldysh theory (5). Due to the high value of αd ($\sim 10^2$-10^3) the expected (5) oscillations in $\Delta T/T$ above the bandgap, have not been observed. Such oscillations have been seen previously by workers studying EA in thin films of GaAs (21).

The peak in the $\Delta T/T$ spectrum around 1.45 eV gradually disappears with increasing proton bombardment dose; ΔT also develops a tail toward the low energy side which is also seen in the $\Delta T/T$ spectrum below 1.45 eV. This newly created tail in the EA spectrum suggests the creation of a tail in the joint-density of states of the conduction and valence bands. This assumption is also in agreement with the results for α_b, the added absorption coefficient of the bombarded layer.

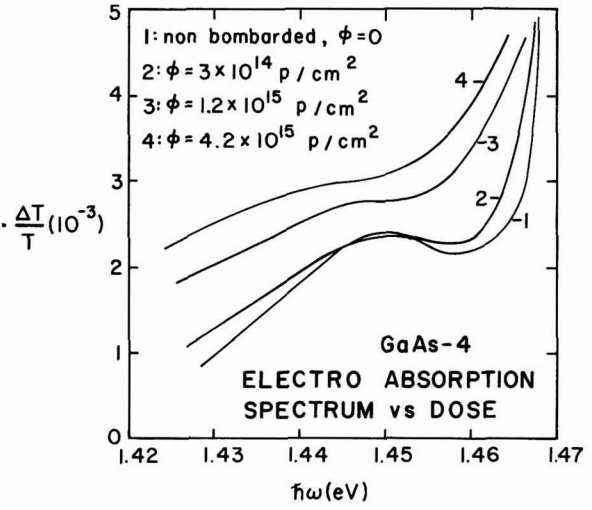

Fig. 7. EA *vs.* dose of bombarded and not-bombarded regions

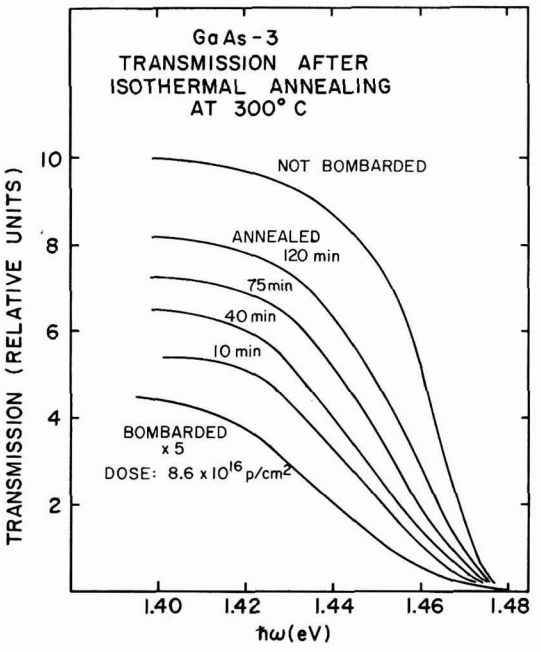

Fig. 8. Transmission from the bombarded region after isothermal annealing at 300°C.

Annealing

The effect of heat-treatment on the sample transmission in the vicinity of the E_0 critical point is shown in Fig. 8.

The sample was subjected to a bombardment dose of 8.6×10^{16} p/cm^2 (which completely eliminated its ER signals) and then isothermally annealed in vacuum at 300°C for up to 2 hr. The heat-treatment only partially recovers the transmission (Fig. 8) and ER signals before bombardment. For a given annealing time, the recovery of the ER signal is smaller than the recovery of the transmission; this is in agreement with our previous finding that the ER at E_0 is more sensitive to crystalline damage than the transmission and does not necessarily indicate that different types of defects are involved.

Dyment *et al.* (22) showed that the optical absorption of proton bombarded GaAs can be annealed more easily than the resistivity. They concluded that there must be at least two types of defects involved in the bombardment process.

Summary and Conclusions

All electromodulation signals decrease in intensity following proton bombardment of the sample. Due to better overlap of the incident light beam and the damaged region, the ER at E_0 is the most sensitive to proton bombardment. The added absorption just below the energy gap increases sublinearly with dose in the dose interval between 3×10^{14} and 5×10^{15} p/cm^2. In the same dose interval, the peak-to-peak spectral amplitude, Δ, of the ER at E_0 and E_1 critical points both vary linearly with the logarithm of the dose and thus can be used as a measure for the degree of the sample amorphicity.

The EA at E_0 develops a tail toward the low energy side of the spectrum. The ER at E_0 has a shift of ≈ 4 meV to higher energy while the peak of the ER signal at E_1 shifts by ≈ 15 meV to lower energy. The origins of these shifts are not yet clear.

Annealing at 300°C for up to 2 hr only partially recovers the unbombarded state. The recovery is not linear in time.

A model based on the gradual amphorization of the sample by an increasing number of proton-damaged amorphous islands with well-defined boundaries was considered. The change in absorption coefficient, α_b, or the change in the ER signal, in this model, depends on the volume fraction, A/A_0, made amorphous by the bombardment. Assuming a layer of average thickness d_b to be damaged, the number of unit cells made amorphous per incident proton will be

$$N = d_b \cdot \frac{dA}{dP}/a_0^3 = d_b\left(1 - \frac{A}{A_0}\right)\sigma(\phi)/a_0^3 \quad [18]$$

where a_0 is the lattice constant for GaAs (5.65Å).

Using Eq. [12] and [15]-[18], we find from the E_0 ER data

$$N = -\frac{ad_b}{\phi a_0^3} = \frac{1.3 \times 10^{17}/\text{cm}^2}{\phi}$$

which corresponds to 26 unit cells amorphized per incident proton for $\Phi = 5 \times 10^{15}$ p/cm^2. Wempe *et al.* (3) found that in a 300 keV proton bombardment of GaP a similar number of unit cells was made amorphous per incident proton: *i.e.*, 10 for a dose of 10^{15} or 10^{16} protons/cm^2. The ER signal at E_0 is reduced below the detection limit ($\Delta R/R \sim 10^{-6}$) at $\phi \sim 2.5 \times 10^{16}$ p/cm^2 while the ER at E_1 is reduced to that level only at $\phi \sim 10^{17}$ p/cm^2. According to our model this implies that a dose of about 10^{17} p/cm^2 amorphizes the sample throughout the damaged layer of thickness ~ 1.5 μm, whereas 2.5×10^{16} p/cm^2 amorphizes it only in the region near 1.5 μm away from the surface.

The electronic band structure of a tetrahedrally bonded amorphous material is expected to have tails in the density of states which extend from the valence and conduction bands into the bandgap (23, 24). The tail in the EA signal at E_0 is tentatively attributed to transitions between these tails of the density of states.

Acknowledgment

This work was supported in part by the Office of Naval Research under Contract N00014-76-C-0890.

Manuscript submitted June 23, 1977; revised manuscript received Oct. 20, 1977.

Any discussion of this paper will appear in a Discussion Section to be published in the December 1978 JOURNAL. All discussions for the December 1978 Discussion Section should be submitted by Aug. 1, 1978.

REFERENCES
1. (a) T. Pankey, Jr. and J. E. Davey, *J. Appl. Phys.*, **41**, 697 (1970). (b) D. D. Sell and A. V. MacRae, *ibid.*, **41**, 4929 (1970).
2. B. R. Prumax, J. C. North, and G. L. Miller in, "Second International Conference on Ion Implantation in Semiconductors," I. Ruge and J. Graul, Editors, p. 212. Springer-Verlag, New York (1971).
3. S. H. Wemple, J. C. North, and J. M. Dishman, *J. Appl. Phys.*, **45**, 1578 (1974).
4. B. L. Crowder, R. S. Title, H. H. Brodsky, and G. D. Pettit, *Appl. Phys. Lett.*, **16**, 205 (1970).
5. For general reference on modulation spectroscopy see: (a) M. Cardona, "Solid State Physics," Suppl. 11, Academic Press, New York (1969); (b) "Semiconductors and Semimetals," Vol. 9, R. K. Willardson and A. C. Beer, Editors, Academic Press, New York (1972).
6. A. D. Jonath, E. Voronkov, and R. H. Bube, *J. Appl. Phys.*, **46**, 1754 (1975).
7. R. S. Bauer, *J. Electron. Mater.*, **4**, 1067 (1975).
8. V. I. Gavrilenko, A. V. Drazhan, V. A. Zuev, D. V. Korbutyak, and V. G. Litovchenko, *Sov. Phys. Semicond.*, **10**, 185 (1976).
9. V. I. Gavrilenko, A. P. Dubchak, V. A. Zuev, V. G. Litovchenko, and V. S. Lysenko, *ibid.*, **9**, 460 (1975).
10. W. J. Anderson, C. A. Douglass III, and Y. S. Park, *J. Appl. Phys.*, **46**, 3875 (1975).
11. V. Rehn and D. S. Kysen, *Phys. Rev. Lett.*, **18**, 848 (1967).
12. A. H. Kalma, *IEEE Trans. Nucl. Sci.*, **ns-19**, 209 (1972); also see Ref. 1(a).
13. S. M. Spitzer and J. C. North, *J. Appl. Phys.*, **44**, 214 (1973).
14. B. L. Gregory and H. H. Sander, *Proc. IEEE*, **58**, 1328 (1970).
15. A. W. Tinsley, *Radiat. Eff.*, **23**, 165 (1974).
16. J. F. Gibbons, W. S. Johnson, and S. W. Myroie, "Projected Range Statistics," 2nd ed., Halsted Press, New York (1975).
17. A. A. Gutkin, D. N. Nasledov, and F. E. Faradzhev, *Sov. Phys. Semicond.*, **8**, 298 (1974).
18. B. O. Seraphin and H. G. Bennett, in "Semiconductors and Semimetals," Vol. 3, R. K. Willardson and A. C. Beer, Editors Academic Press, New York (1967).
19. F. F. Morhead and B. L. Crowder, *Radiat. Eff.*, **6**, 27 (1970).
20. J. C. Dyment, J. C. North, and L. A. D'Asaro, *J. Appl. Phys.*, **44**, 207 (1973).
21. L. W. Aukerman, P. W. Davis, R. D. Graft, and T. S. Shilliday, *This Journal*, **34**, 3590 (1963).
22. E. W. Mitchell and C. Norris, *J. Phys. Soc. Jpn.*, **21**, 656 (1967).
23. B. A. Bobylev, A. F. Kravchenko, and A. S. Terekhov, *Sov. Phys. Semicond.*, **7**, 1381 (1974).
24. W. J. Anderson and Y. S. Park., *J. Appl. Phys.*, **47**, 3094 (1976).

Surface Electrical Properties of the Wustite Phase

J. Nowotny and I. Sikora

Research Laboratories of Catalysis and Surface Chemistry, Polish Academy of Sciences, ul. Niezapominajek, 30-239 Kraków, Poland

ABSTRACT

The iron-oxygen system has been studied using work function measurements between 675° and 950°C, the stability range of the wustite phase. The work function of wustite *vs.* nonstoichiometry indicates a decrease of the Fermi energy below 850°C while for the temperatures between 900° and 950°C an initial decrease is followed by the final increase. The measured work function data depend only on the temperature and oxygen partial pressure. This indicates that the system is well equilibrated. The values of the partial pressures of oxygen corresponding to the wustite phase equilibria with iron and with magnetite determined in this work agree well with the reported literature data. A short equilibration time favors the work function method as a convenient one for investigating phase diagrams of oxide systems. The experimental data do not confirm the p- to n-type transition postulated for $Fe_{1-y}O$ on the basis of earlier measurements of the Seebeck coefficient.

Electrical properties of wustite have been the subject of several papers dealing mainly with the Seebeck coefficient and electrical conductivity measurements (1-11). Several essential questions, however, concerning electrical data as well as their correlation with structural properties of this phase have not been sufficiently explained. There are still essential contradictions concerning the conductivity mechanism within the wustite phase field and its defect structure *vs.* nonstoichiometry. Moreover, there is a general lack of thermodynamic data for temperatures below 900°C at which the system wustite-oxygen requires considerably longer times to achieve its equilibrium state. On the other hand, the rare experimental data available for the phase diagram of the iron-oxygen system below 900°C show many discrepancies.

One of the most extensively studied problems of the wustite phase concerns its defect structure. As is known, wustite exhibits a very large nonstoichiometry varying from 5 atom percent (a/o) at the iron-wustite boundary up to about 15 a/o at the wustite-magnetite phase boundary. This nonstoichiometry may simply be related to the concentration of cation vacancies. Taking into account, however, interactions between these simple defects leading to the formation of Roth's complexes ($V_{Fe}Fe_iV_{Fe}$) (12), clusters n ($V_{Fe}Fe_iV_{Fe}$) (13, 14), and even structural domains (15-19), the real concentration of defects involving both cation vacancies and interstitial cations may reach 30 a/o. This significant value implies a complex picture of the defect structure of wustite, especially at its higher nonstoichiometry.

Numerous works concerning the defect structure of the wustite phase are based mainly on either gravimetric investigations, leading directly to deviations from stoichiometry, or electrical conductivity, giving information about the concentration and mobility of

Key words: work function, ferrous oxide, surface potential, Fermi energy, nonstoichiometry.

electron carriers as well as about the degree of ionization of ionic defects.

Bransky and Tannhauser (7) have found that electrical conductivity of wustite above 1000°C, for lower nonstoichiometry is proportional to the sixth root of the oxygen partial pressure. Such dependence fits the simple model involving formation of doubly ionized cation vacancies when oxygen is incorporated into the wustite lattice

$$\tfrac{1}{2}\, O_{2/g/} \rightleftharpoons O_O^x + V_{Fe}^z + zh^{\cdot} \qquad [1]$$

where according to the Kroger-Vinck notation O_O^x denotes the oxygen in the anion sublattice, V_{Fe}^z the cation vacancy, z the degree of ionization, and $h^{\cdot}$ the electron hole.

Applying the mass action law and assuming that interactions among defects may be neglected as well as supposing appropriate electroneutrality conditions of the lattice, the deviation from stoichiometric composition may be expressed as the following function of temperature

$$y = V_{Fe}^z = \text{const}\; p_{O_2}^{1/n} \exp\left[-\frac{\frac{1}{z+1}\Delta H_f}{RT} \right] \qquad [2]$$

where $1/n$ is the parameter depending on the ionization degree of cation vacancies and ΔH_f is the enthalpy of formation of the vacancies. The parameter $1/n$ may thus be determined by measuring directly the changes of the deviation from stoichiometry, or any parameter that can be correlated with the concentration of cation vacancies (*e.g.*, electrical conductivity) as a function of oxygen partial pressure p_{O_2}

$$\frac{1}{n} = \frac{\partial \ln y}{\partial \ln p_{O_2}} = \frac{\partial \ln \sigma}{\partial \ln p_{O_2}} \qquad [3]$$

Equation [3] is valid only when the mobility of electron carriers is independent of their concentration.

The simple model illustrated by Eq. [1] has been supported by the gravimetric studies of Hauffe and Pfeiffer (20). Also Smyth (21) postulated doubly ionized cation vacancies as predominant defects. More detailed investigations of this phase, however, have shown that the parameter $1/n$, determined both gravimetrically and by electrical conductivity (22, 23), changes from 1/4, for the smallest deviation from stoichiometry, to 1/6, or even below, with increasing y, thus indicating that the effective charge of defects *vs.* y changes continuously. According to the present knowledge of the defect structure of wustite this phenomenon can be attributed to association (12) and clustering (13) of defects. Vallet and Raccah (15), Kleman (16), and Fender and Riley (17) postulate the existence of three separate "phases" or structural domains within the wustite phase field; however, they do not give a defect structure for these domains. Moreover, numerous investigations of several structure-sensitive properties of wustite (*e.g.*, electrical conductivity) *vs.* oxygen partial pressure do not indicate a drastic change of defect structure at compositions corresponding to the postulated domain boundaries (24). Thus the existence of the domains still remains an open question.

Bransky and Tannhauser (7) have found a change of sign of the Seebeck coefficient of wustite for the composition O/Fe = 1.09. The authors suggest that this effect, observed above 900°C, can be attributed to the transition of the conductivity from p-type at low stoichiometry to n-type at high oxygen content. The change of sign of the Seebeck coefficient above 900°C has been confirmed by Wagner and co-workers (5, 6) for both poly- and single-crystalline samples of wustite. This effect has also been observed by Meussner, Richards, and Fujii at 1000°C (4), but at much higher oxygen content than that observed by Bransky and Tannhauser or by Wagner and co-workers (5). Nevertheless the supposition concerning p- to n-type transition is in strong contradiction to electrical conductivity data which show no minimum in the whole range of the wustite homogeneity range *vs.* oxygen content. This would indicate that only one type of electron carriers (electrons or holes) predominate throughout the whole wustite field. Recently, the p-type conductivity of the wustite phase has been confirmed by Bowen, Adler, and Auker (11). Seltzer and Hed (9) have proposed an original interpretation of these apparently conflicting data. The authors involved a "negative term" describing the temperature dependence of the scattering mechanism in the transport of charge carriers through the crystal lattice. Their calculation based on this assumption gives good agreement with the literature data of the electrical conductivity and Seebeck coefficient reported for the wustite phase.

Statement of the Problem

The discussion of the literature data shows that the electronic properties of the wustite phase still remain the subject of dispute and require additional investigation for an explanation of the electronic phenomena as well as the correlation between structural and electronic data for this highly defect crystal. The purpose of the present work is to apply the work function technique which may supply direct information about the chemical potential of electrons (Fermi energy level) for the surface layer of investigated oxide sample.

The work function technique has been widely used for investigations of adsorption properties of oxides and metals. The measurements have generally been carried out in the range of low and moderate temperatures. However, under these conditions most of the oxides are in a "quenched" state. Thus the measured work function data gave information concerning the surface oxide layer, which because of kinetic reasons was not equilibrated with either the crystalline bulk or the gaseous phase. Under these conditions, the nonstoichiometry of the surface layer is in a continuous change as the oxide crystal tends toward an equilibrium state (25). Thus the measured work function values depend essentially on the experimental procedure applied and the sample history.

It should be emphasized that the absolute value of the work function of metal oxides, as well as of most of the binary compounds, has no physical meaning when measured at temperatures where the compounds are not equilibrated with the gas phase. In these cases the state of the surface depends on many uncontrolled factors, such as surface coverage by adsorbed impurities, surface topography, and nonstoichiometry of the layer near the surface. Each of these factors has a strong influence on the measured value of the work function. Relative work function changes may be used for monitoring some surface processes, *e.g.*, chemisorption of gases. Then the measured electronic effect accompanying chemisorption represents the chemical affinity between the investigated surface and the adsorbate. In this kind of study, the absolute value of the work function may be used as a monitor for adjusting the standardized procedure to a reproducible surface state, or for following the kinetics of any surface process accompanied by electronic transitions. As the temperature increases, however, the whole crystalline grain is being brought into thermodynamic equilibrium with the coexistent gas atmosphere. Under these, conditions the surface state, and thus the work function, are independent of the experimental procedure applied before the measurement and are determined by the parameters of the experiment, such as temperature and gas composition.

The work function measurements commonly reported for studies of the surface electrical properties of metal oxides are based on the dynamic condenser

method. This method, proposed by Kelvin (26) and improved by Zisman (27) and numerous other investigators (28-39), is the most convenient one for studying oxides under a controlled gaseous atmosphere. The dynamic condenser method described in the literature operates in a temperature range up to about 400°C; however, this range is too low for such transition metal oxides as NiO, CoO, MnO, or FeO. Thus the purpose of the present work was to perform the work function measurements at a sufficiently high temperature that the investigated crystal could be equilibrated with oxygen. The relatively well-known ferrous oxide (wustite) seemed to be a very interesting system for the present studies because this oxide phase shows the largest nonstoichiometry among the other transition metal oxides of the series exhibiting the NaCl-type structures as NiO, CoO, or MnO. It was also expected that the work function data of the wustite phase might supply interesting material for comparison with other available electrical data involving the electrical conductivity and the Seebeck coefficient. In the present studies the work functions of the iron-oxygen system were measured *vs.* the oxygen activity in the gaseous phase. Experimental conditions were adjusted in order to cross the wustite phase field from metallic iron to the magnetite phase.

Experimental

Apparatus.—The dynamic condenser method was used for the work function measurements (40, 41). It is illustrated schematically by the block diagram in Fig. 1. The method is based on the measurement of the constant potential difference (CPD) existing between the plates forming the condenser, 3, whose capacity varies with time. The vibration of the condenser generates an a-c voltage across the resistance, 4. The value of this voltage is proportional to CPD. The a-c voltage is then amplified, 5, and monitored, 6. When CPD is compensated by an external d-c voltage, $V_{d.c.}$, 2, from the compensator, 1, a minimum in the signal is observed on the monitor

$$V_{CPC} - V_{d.c.} = 0 \qquad [4]$$

Thus the CPD is equal to the value of $V_{d.c.}$ with the opposite sign. The plates of the dynamic condenser are the sample being investigated, 1, and the reference electrode, 2. The CPD is equal to the difference in the work function of the plates of the dynamic condenser

$$V_{CPD} = \frac{\Phi_1 - \Phi_2}{e} \qquad [5]$$

Hence an increase of the CPD corresponds to an increase in the work function of the oxide. The measurement of changes in the work function of the oxide sample *vs.* oxygen pressure are possible only when the surface potential of the reference electrode is known or is constant in the experimental conditions applied

$$\Delta\Phi_1 = e(\Delta V_{CPD}) + \Delta\Phi_2 \qquad [6]$$

A platinum plate was used as the reference electrode. Changes in the work function of the platinum plate for high temperatures may be calculated as for the oxygen electrode

$$\Delta V_{Pt} = \frac{\Delta\Phi_2}{e} = \frac{RT}{4F} \ln \frac{p_{O_2}^{(1)}}{p_{O_2}^{(2)}} \qquad [7]$$

where values $p_{O_2}^{(1)}$ and $p_{O_2}^{(2)}$ correspond to the extreme oxygen pressures of the experimental conditions.

The oxygen partial pressure in the reaction chamber is controlled by the ratio of the CO-CO_2 gas mixture at a total pressure of 1 atm. The experimental compositions of the CO_2-CO gas mixture are indicated in Fig. 2 by the dividing spots on the isothermal (dotted) lines. The lowest oxygen activity is determined here by pure carbon monoxide limiting investigations of the iron-oxygen system to the right side from line 1 in Fig. 1. Thus at temperatures below 750°C the experiments concern only the phase boundary wustite-magnetite.

Figure 3 shows the experimental setup including both the gas flow system for adjusting required composition of CO_2-CO mixture and the schematic of the dynamic condenser. The details of the construction

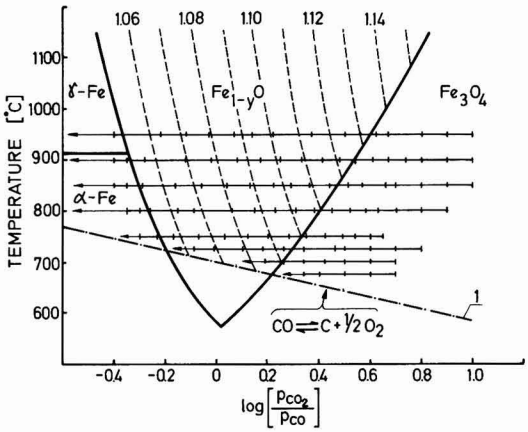

Fig. 2. Wustite phase field according to Darken and Gurry (29) in temperature *vs.* logarithm of the CO_2/CO ratio. Dashed curves indicate constant composition O/Fe. Curve 1 represents the decomposition line of CO. Spots on the isothermal lines correspond to the experimental conditions applied in this work.

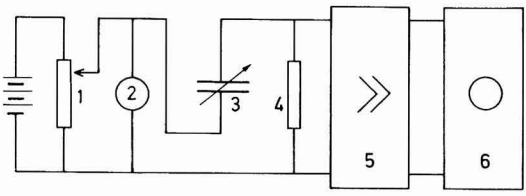

Fig. 1. Schematic drawing of the electrical circuit for the work function measurements: 1, compensator; 2, voltmeter; 3, dynamic condenser; 4, high impedance; 5, amplifier; 6, monitor.

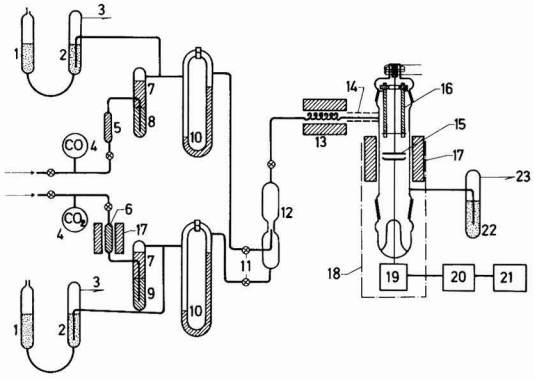

Fig. 3. Experimental setup: 1, chamber with dibuthyl-phtalate for fixing overbubbling pressure; 2, overbubbler of manostat; 3, overflow gas outlet; 4, gas chambers; 5, ascarite; 6, copper turnings; 7, silicagel; 8, molecular sieves Type 4A; 9, molecular sieves Type 3A; 10, flowmeter; 11, stopcock; 12, gas mixer; 13, preheater of the reaction gas mixture; 14, thermal isolation; 15, dynamic condenser; 16, vibrator of the dynamic condenser; 17, heating element; 18, electrical screening; 19, preamplifier; 20, amplifier and compensator; 21, monitor; 22, gas flow controller; 23, reaction gas outlet.

of the dynamic condenser were described previously (42). The powdered, spectroscopically pure iron sample (prepared by Johnson-Matthey) was spread over the lower stainless steel electrode. The sample formed a layer about 0.5 mm thick. The gas mixture entered the upper part of the chamber of the dynamic condenser, passed down over the sample, and was exhausted near the bottom. The gas flow velocity was about 0.9 cm/sec as recommended by Darken and Gurry (43) to prevent the formation of a concentration gradient in the experimental gas mixture. Oxygen partial pressures corresponding to the appropriate compositions of the CO_2-CO mixture were calculated using the data of Jacobi (44)

$$\frac{p_{CO}}{p_{CO_2}} = [p_{O_2} \exp(68{,}100T^{-1} - 20.9)]^{-0.5} \quad [8]$$

The reading accuracy of the CPD was about 0.05V.

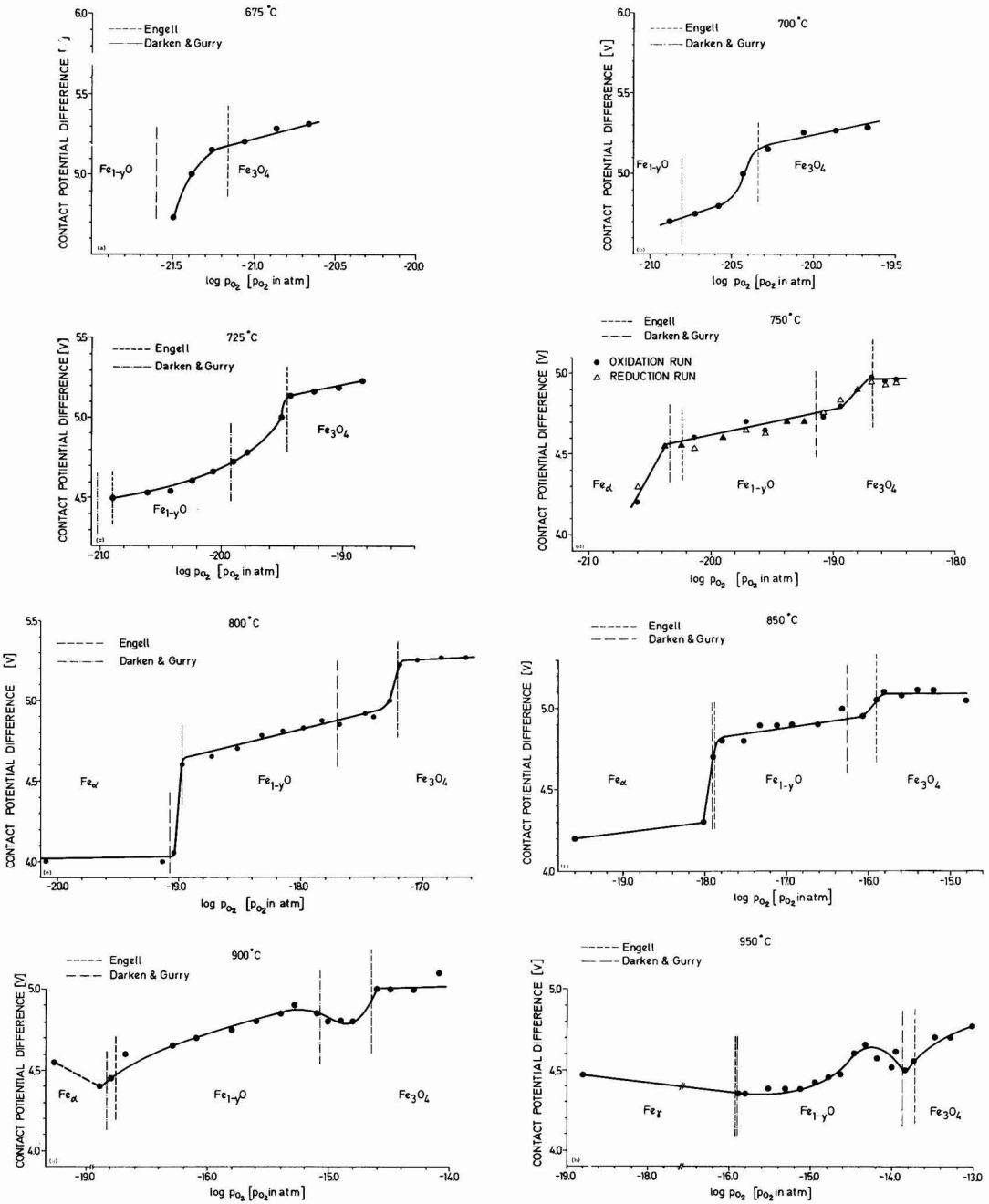

Fig. 4. Contact potential difference CPD for the iron-oxygen system measured at different temperatures vs. gas composition corresponding to the stability range of the wustite phase for temperatures: a, 675°C; b, 700°C; c, 725°C; d, 750°C; e, 800°C; f, 850°C; g, 900°C; h, 950°C. Oxygen partial pressures corresponding to equilibria at the phase boundaries Fe-$Fe_{1-y}O$ and FeO-Fe_3O_4 are indicated after Engell (3) and Darken and Gurry (29).

Procedure

The reaction system was heated to the required temperature in the gas mixture corresponding to the magnetite phase. Then the gas composition was gradually changed toward decreasing oxygen activity as illustrated by the dotted lines in Fig. 2. Experiments for which oxygen activity decreased or increased in successive readings were termed reduction or oxidation runs, respectively. The CPD was measured when a constant value was reached, *i.e.*, in 5-10 min after the new ratio of the CO_2-CO mixture was fixed on the new level. The experimental values of the CPD were taken from two to three independent readings. The data are reproducible within 0.1V.

Results and Discussion

Figures 4a-h illustrate the measured values of CPD as the function of oxygen partial pressure for a series of the temperatures between 675° and 950°C within the phase field of wustite as indicated in Fig. 2. The experimental data were found to be the same for both oxidation and reduction runs, as can be seen in Fig. 4d for 750°C. For other temperatures the CPD data for the oxidation runs are given. The dotted, vertical lines indicate the literature values of equilibrium oxygen partial pressures corresponding to the phase boundaries iron-wustite and wustite-magnetite, according to Engell (31) and Darken and Gurry (29). The observed sharp CPD changes fit the literature data well, thus indicating that the work function is a parameter very sensitive to the crystalline structure.

The change in the surface potential of the platinum reference electrode, calculated according to Eq. [7] for extreme oxygen pressures corresponding to Fe/FeO and FeO/Fe_3O_4 phase boundaries, was equal to about 0.05V. According to Eq. [7], these changes are linear in the coordinates used for plotting the experimental data in Fig. 4a-h. According to Eq. [6], the work function changes of the investigated sample are the sum of the measured CPD changes and $\Delta\Phi_2$. Because of the very small $\Delta\Phi_2$ values, however, the CPD changes are practically equal to $\Delta\Phi_1$.

As seen in Fig. 4c-f, the work function increases almost linearly within the wustite phase *vs.* oxygen partial pressure between 725° and 850°C. This is in accordance with the reported defect structure of wustite showing cation vacancies forming acceptor centers in the energetic model of wustite according to Eq. [1]. An increase in their concentration shifts the Fermi level downward. Since the energetic model of the wustite phase is not sufficiently developed it is difficult to indicate the form of the defects and their acceptor "activity." These may be both doubly and singly ionized cation vacancies as well as complexes. The observed increase of the work function indicates that the p-type conductivity should dominate within the whole wustite range if p-type is assumed at the lowest nonstoichiometry. This effect is in contradiction to the data of Bransky and Tannhauser (7) as well as of Wagner and co-workers (5) who reported a monotonous decrease of Seebeck coefficient (referring to the increase of the Fermi level) *vs.* increase of nonstoichiometry.

Figures 4g and 4h refer to 900° and 950°C, respectively. For 900°C and at low nonstoichiometry, the CPD changes linearly with oxygen pressure as was found for the experimental runs below 900°C. A slight decrease of the work function is observed at higher nonstoichiometry. This effect is even more pronounced at 950°C. In both cases, however, the final work function value is still higher than the initial one. Thus the postulated change of the conductivity type from p-type, at low nonstoichiometry, to n-type, at higher oxygen content (3-6) cannot be confirmed in the present investigations. The maxima of the work function observed at 900° and 950°C for higher nonstoichiometry may correspond to the change of sign of the Seebeck coefficient which was found by Bransky and Tannhauser (7) as well as Geiger, Levin, and Wagner (5). Both work function and Seebeck coefficient indicate an increase of the Fermi level *vs.* oxygen pressure at higher O/Fe ratios than those referring to the maxima. The discrepancy in the results of the Seebeck effect and the work function observed at lower nonstoichiometry, however, requires additional investigation involving the simultaneous measurement of the electrical parameters. It should be emphasized, however, that a good qualitative agreement between the work function and the electrical conductivity data was found for lower defect concentrations (both parameters indicating decrease of the Fermi energy *vs.* oxygen content), although the maxima of the work function *vs.* oxygen pressure was not confirmed.

Over the temperature range studied in this work, no effect was observed that could be ascribed to structural "regions" which have been postulated by Vallet and Raccah (15), Kleman (16), and Fender and Riley (17).

All of the experimental studies of CPD *vs.* log p_{O_2} show, more or less, sharp changes of the work function. These changes occur at values of oxygen partial pressures corresponding to the expected phase transformations of wustite into the metallic iron phase, on one hand, and into the magnetite phase, Fe_3O_4, on the other. The parameters of temperature and oxygen partial pressure determined in the present studies for the appropriate phase equilibria are plotted in Fig. 5 and compared with other literature data. The equilibrium data of oxygen partial pressure obtained from the work function measurements were recalculated after Engell (45) into corresponding values of nonstoichiometry y in order to compare the presently obtained results with the literature data reported in this measure (Fig. 6). As seen the data obtained from the work function agree very well with the data obtained by Engell (31), Marion (46), Vallet and Raccah (15), and other investigators (47). The results obtained here may be helpful in more precise determinations of the wustite phase boundary especially at lower temperatures (between 575° and 800°C) for which great discrepancies are observed among the available data.

Conclusions

1. The work function values of the iron-oxygen system measured at temperatures above 675°C were determined from the temperature and oxygen partial pressure and are independent of the experimental procedure applied. This indicates that the sample was equilibrated, and the work function data is characteristic of the studied materials.

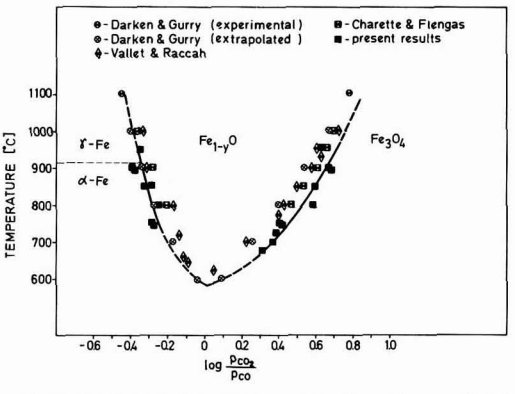

Fig. 5. Experimental data for the wustite phase diagram plotted in temperature *vs.* logarithm of the CO_2/CO ratio.

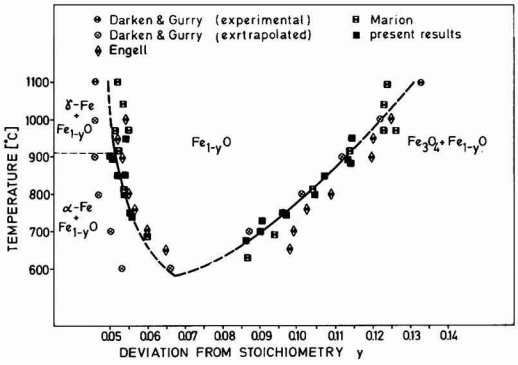

Fig. 6. Experimental data for the wustite phase diagram plotted in temperature vs. oxide composition.

2. The work function data do not confirm the earlier postulated p- to n-type transition for the wustite phase (3-6).

3. The work function is very sensitive to crystalline structure and thus may be used to determine the partial pressure of oxygen corresponding to the thermodynamic equilibrium state between the two phases. A surprising agreement between the presently obtained data from the work function measurements and the literature data concerning phase boundaries of the wustite phase indicates that this typical surface sensitive method is capable of giving information relevant to the bulk when the investigated system is well equilibrated.

4. The phase boundaries of the wustite phase determined from the work function measurements agree well with other literature data (31-33).

5. The hypothesis of Vallet and Raccah (15), Kleman (16), and Fender and Riley (17) concerning different structural domains in the wustite phase was not confirmed in the present investigations.

Acknowledgments

This work has been done with the financial support of the Metallurgical Institute, Academy of Mining and Metallurgy, Kraków, under contract MR-19-1.6.5. This support is gratefully acknowledged.

Manuscript submitted May 4, 1977; revised manuscript received *ca.* Dec. 19, 1977.

Any discussion of this paper will appear in a Discussion Section to be published in the December 1978 JOURNAL. All discussions for the December 1978 Discussion Section should be submitted by Aug. 1, 1978.

REFERENCES

1. C. Wagner and E. Koch, *Z. Phys. Chem., B*, **32**, 439 (1936).
2. F. Marion, Thesé d'Etat, Université de Nancy (1955).
3. D. S. Tannhauser, *J. Phys. Chem. Solids*, **23**, 25 (1962).
4. R. A. Meussner, L. E. Richards, and C. T. Fujii, Rep. NPL Progr., p. 26 (December 1965).
5. G. H. Geiger, R. L. Levin, and J. B. Wagner, Jr., *J. Phys. Solids*, **27**, 947 (1966).
6. W. J. Hillegas, Jr. and J. B. Wagner, Jr., *Phys. Lett.*, **25A**, 742 (1967).
7. I. Bransky and D. S. Tannhauser, *Trans. AIME*, **239**, 75 (1967).
8. W. J. Hillegas, Jr., Ph.D. Thesis, Northwestern University (1968).
9. M. S. Seltzer and A. Z. Hed, *This Journal*, **117**, 815 (1970).
10. D. Neuschutz and N. Towhidi, *Arch. Eisenhuttenwes.*, **41**, 303 (1970).
11. H. K. Bowen, D. Adler, and B. H. Auker, *J. Solid State Chem.*, **12**, 355 (1975).
12. W. L. Roth, *Acta Crystallogr.*, **13**, 140 (1960).
13. F. Koch and J. B. Cohen, *ibid., Sect. B*, **25**, 275 (1969).
14. Chyong Rkhi Khing, A. D. Romanov, Ya. L. Shaiovich, and R. A. Zvinchuk, *Vestn. Leningr. Gosudarstvennogo Univ.* (News of the Leningrad National University, in Russian), **4**, 144 (1973).
15. P. Vallet and P. Raccah, *Mem. Sci. Rev. Metall.*, **62**, 1 (1965).
16. M. Kleman, *ibid.*, **62**, 457 (1965).
17. B. E. F. Fender and F. D. Riley, *J. Phys. Chem. Solids*, **30**, 793 (1969).
18. J. S. Anderson, *Bull. Soc. Chim. Fr.*, No. 7, 2203 (1969).
19. J. S. Anderson, NBS Spec. Publ. 364, p. 295, Solid State Chemistry Proceedings, 5th Materials Research Symposium, July 1972.
20. K. Hauffe and H. Pfeiffer, *Z. Metallk.*, **44**, 27 (1953).
21. D. M. Smyth, *J. Phys. Chem. Solids*, **19**, 167 (1961).
22. I. Bransky and A. Z. Hed, *J. Am. Ceram. Soc.*, **51**, 231 (1968).
23. B. Swaroop and J. B. Wagner, Jr., *Trans. Metall. Soc. AIME*, **239**, 1215 (1967).
24. S. Bialas, J. Nowotny, and I. Sikora, In preparation.
25. J. Nowotny, *Bull. Acad. Pol. Sci., Ser. Sci. Chim.*, **21**, 413 (1973).
26. Lord Kelvin, *Phil. Mag.*, **46**, 82 (1898).
27. W. A. Zisman, *Rev. Sci. Instrum.*, **3**, 367 (1932).
28. R. Gunn, *Phys. Rev.*, **40**, 307 (1932).
29. W. E. Meyerhof and P. H. Miller, *Rev. Sci. Instrum.*, **17**, 15 (1946).
30. J. C. P. Mignolet, *Discuss. Faraday Soc.*, **8**, 326 (1950).
31. J. C. Devins and S. I. Reynolds, *Rev. Sci. Instrum.*, **28**, 11 (1957).
32. V. F. Bogoliubov, *Radiotekh. Elektron.*, **2**, 323 (1957).
33. P. H. Burshtein and L. A. Larin, *Zh. Fiz. Khim.*, **32**, 194 (1958).
34. J. F. Rybkin, N. F. Schevtschenko, and N. A Izmailov, *ibid.*, **35**, 220 (1961).
35. A. A. Zhukhovitski and A. A. Andreev, *Dokl. Akad. Nauk SSSR*, **142**, 1319 (1962).
36. S. M. Kotshergin and G. A. Golikov, *Zh. Fiz. Khim.*, **37**, 1116 (1963).
37. O. M. Artamonov and P. J. Berlaga, *Prib. Tekh. Eksp.*, **2**, 151 (1963).
38. T. Delchar, A. Eberhagen, and F. C. Tompkins, *J. Sci. Instrum.*, **40**, 179 (1963).
39. H. Pauly, H. W. Petmecky, and C. Schmidt, *Z. Angew. Phys.*, **91**, 207 (1965).
40. J. Nowotny and I. Sikora, *Bull. Acad. Pol. Sci., Ser. Sci. Chim.*, **23**, 1045 (1975).
41. R. Chruściel, J. Deren, and J. Nowotny, *Exp. Techn. Phys.*, **14**, 127 (1966).
42. J. Nowotny and I. Sikora, *Z. Phys. Chem. N. F.*, In print.
43. L. S. Darken and R. W. Gurry, *J. Am. Chem. Soc.*, **67**, 1398 (1945).
44. H. Jacobi, Ph. D. Thesis, Technische Universität Clausthal (1965).
45. H. J. Engell, *Arch. Eisenhuettenwes.*, **28**, 109 (1957).
46. F. Marion, *Doc. Metall.*, No. 24, 5 (1955).
47. G. G. Charette and S. N. Flengas, *This Journal*, **115**, 796 (1968).

Aluminum Oxidation in Water

C. C. Chang, D. B. Fraser, M. J. Grieco, T. T. Sheng, S. E. Haszko,
R. E. Kerwin, R. B. Marcus, and A. K. Sinha*

Bell Laboratories, Murray Hill, New Jersey 07974

ABSTRACT

Water rinse of aluminum metallized integrated circuits must be carefully monitored because the Al can oxidize rapidly under certain conditions. Al oxidation in 10 MΩ deionized water was therefore studied using Auger spectroscopy, and transmission and scanning electron microscopies, to investigate the oxide growth as a function of water temperature and rinse time, use of photolithography, and Cu-doping of the Al. Al oxide thicknesses were 20-30Å before any treatment and were 35, 70, and ≅3000Å after 5 min rinses in 40°, 60°, and 80°C water, respectively. Photolithography and Cu doping induced no large effects. In 40°C water, little oxidation occurred for 20 min and rapid oxidation began after 40 min, especially at nucleation sites with C and Si contamination. The oxide grown in water has a porous structure, is nearly amorphous, and contains gamma-alumina and hydrated oxides. Near 80°C, several thousand angstroms of oxide can grow in minutes.

Oxidation of Al metallization in integrated circuits (IC's) can significantly affect device yield by increasing the contact resistance. This is especially true with beam leaded (1) devices to which contacts are established without any physical means of breaking the oxide barrier over the Al. Even with wire bonded devices, excessive oxide growth is obviously undesirable. Because deionized (DI) water rinsing of Al is an integral part of IC processing, the growth of Al oxide in DI water was investigated in this work.

Experimental

Sample preparation.—The samples studied are listed in Table I together with the relevant final treatments. Abbreviated descriptions of the processing steps are given in Table II; the water rinse step, No. 4, is the critical operation of interest here. The Cu-doped Al films of Table I were 1.5 μm thick, with 0.5 atom percent (a/o) Cu deposited at either ≅40°C or at 300°C by e-gun evaporation, and the undoped films were similarly deposited at 40°C. The column labeled "EG-BHF" refers to a 30 sec dip in 1:1:1 ethyleneglycol: buffered-HF: H_2O etch, and "450°C anneal" refers to a 30 min anneal in 1 atm H_2. The EG-BHF treatment removes Al oxide as well as some Si-nitride and SiO_2, with only a minimal attack of the Al and therefore its value as a cleaning etch for the entire Al metallized IC wafer was examined. In Table I, all "Testers" are full-surface Al films (on oxidized Si) unless photolithography is indicated. The device samples 18 to 21 were pulled from device lots, after the processing steps indicated; these steps are listed in Table II. The DI water entering the overflow rinse bath had a resistivity over 10 MΩ and was heated in a stainless steel tube just prior to admission into the bath.

Analysis methods.—Instances of extensive Al oxidation could be detected under the optical microscope, by a halo type of feature along the edges of patterned Al. After 450°C anneal, the oxide layer sometimes developed cracks and the oxide could be removed with adhesive tape, as demonstrated in Fig. 1. A scanning electron microscope (SEM) was used in this work for rapidly evaluating the effect of a particular water rinse and to scan many different areas of a chip. Typical SEM micrographs are displayed in Fig. 2. Surface oxide films >100Å thick appeared to quickly degrade the SEM spatial resolution. Auger electron spectroscopy (AES) was used for chemical analysis and for measuring oxide thicknesses <100Å. Details of this technique, which utilizes the chemically shifted Auger peak of Al in the oxide, is described in Ref. (2); the technique requires no ion milling and has high rela-

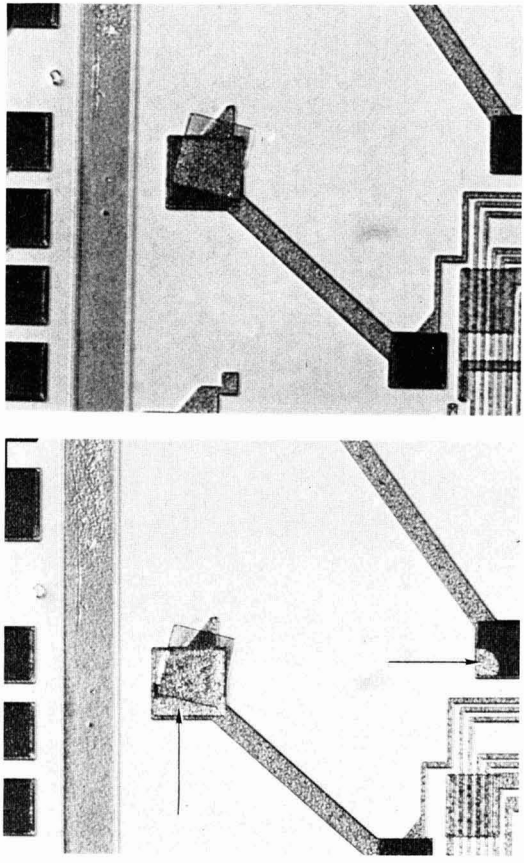

Fig. 1. Optical micrographs of films in contact windows to Al; after step 10 of Table II, sample 20. (Top) a wafer that was rinsed in 80°C DI water. (Bottom) after adhesive tape was applied to above sample and removed; the two arrows point to areas of missing Ti-Pt. The displaced square near center is a sheet of Al oxide which became detached and moved, probably just prior to Si-nitride deposition.

* Electrochemical Society Active Member.
Key words: integrated circuits, dielectric, oxidation, insulator.

Table I. Al oxide thickness vs. treatment

	Cu-doped	Photolithog.	DI water (°C)	EG-BHF	450°C anneal	Oxide thickness (Å)
Testers samples						
1	Yes	—	None			32
2	Yes	—	40			35
3	Yes	Yes	40			35
4	Yes	—	40, 10 min			33
5	Yes	—	40, 20 min			31.2 ± 0.4
6	—	Yes	40	—	—	38
7	Yes	Yes	40	Yes	—	42
8	Yes	Yes	40	Yes	Yes	65
9	Yes	Yes	50	—	—	62
10	Yes	—	60	—	—	61
11	—	Yes	60		—	70
12	Yes	—	80		—	3000
13	Yes	Yes	80		Yes	2900
14	—	Yes	80		—	3300
15	Yes	Yes	80		—	Thick
16A	Yes		None			29
16B	Yes		40, 20 min			29
16C	Yes		40, 40 min			33
16D	Yes		40, 60 min			46
17A			None			19
17B			40, 20 min			38
17C			40, 40 min			55
17D			40, 60 min			87
Devices						
18, step 7	Yes	Yes	80	Yes	Yes	>>100
19, step 4	Yes	Yes	80	—	—	>6000
20, step 10	Yes	Yes	80	Yes	Yes	1600
21, step 4	Yes	Yes	40	—	—	43

Notes: Unless otherwise specified, DI water rinse time is 1 min, then 5 min, at indicated temperature, then 5 min in 20°C water, utilizing a separate bath for each rinse; nonstandard times at temperature following the first 1 min are indicated.

Table II. Abbreviated summary of process sequence

1. Al deposition.
2. Photolithography (HR100*), Al etch (H_3PO_4-based etchant).
3. Photoresist strip (A30**, 110°C, 10 min).
4. Overflow DI water rinse.
5. EG-BHF clean, 30 sec.
6. 450°C, H_2 anneal, 1 atm, 30 min.
7. EG-BHF clean, 30 sec.
8. Si-nitride (passivation layer) deposition.
9. Contact window photolithography and etch.
10. Ti and Pt deposition in preparation for beam leads.

Notes: EG-BHF = 1:1:1 mixture of ethylene glycol, buffered HF, and water. Although water is not a necessary component, it enhances the cleaning ability by increasing the rate of Al attack; however, water also increases the residual oxide thickness by hydration.
* HR100: photoresist (Phillip Hunt).
** A30: photoresist stripping solution (Allied Chemical).

tive accuracy (several angstroms) and spatial resolution (<10 μm). Thicknesses >100Å were estimated approximately using the ion-mill Auger technique, assuming the ion milling rate for SiO_2. This estimate is obviously inaccurate and was used only to demonstrate that the oxide grown was very thick. Final detailed information was obtained using the transmission electron microscope (TEM) by examining thin cross sections of the regions of interest. This last technique has been described elsewhere (3).

Results

Preliminary identification of Al oxidation problem.—An optically visible film formed on Al by rinsing in 80°C water (device sample 18) was determined by AES to be essentially pure Al oxide. On this sample, a halo visible optically and by the SEM on SiO_2 areas more than 20 μm away from patterned Al was also found by AES to be Al oxide; evidently, this oxide spreads beyond Al areas. Optical examination after Al etch and before photoresist strip had revealed no Al on these SiO_2 areas so that this oxide is not formed from unetched Al residues. These initial results clearly established the importance of Al oxidation during device processing.

Auger studies.—Testers 1-17 of Table I were then prepared and AES experiments were performed to answer four questions:

1. What are typical Al-oxide thicknesses after various treatments?
2. What is the critical DI water temperature below which oxidation rate becomes negligible?
3. Does oxidation depend on Cu doping?
4. Does oxidation proceed in pure water, free of photoresist and/or A30 carry-over?

Results are as follows: Samples 1, 16A, and 17A established the typical air-formed oxide thickness (20-30Å) on as-deposited Al (Cu doped and undoped). We have not compared the initial oxide growth rates of Cu doped and undoped Al in detail. Typically, oxide thicknesses were about 20Å within 2 hr after deposition, about 30Å after several weeks, and about 35Å after several months of air exposure for both types of Al. Samples 1-15 were taken from many different deposition runs and received varying times of air exposure prior to experimental treatments and analyses. Therefore, their initial surface oxides varied somewhat and these variations may have masked the smaller effects; the experiments using these samples were intended to reveal only the stronger effects. This defect is rectified for samples 16A-17D, as explained below.

Samples 2, 4, and 5 showed that the surface oxide thickness does not increase appreciably up to 20 min at 40°C (35Å maximum). The statistical accuracy of the Auger data is demonstrated with sample 5, for which the average oxide thickness and standard deviation of one measurement each from five different areas within about 3 mm of each other were 31.2 ±0.4Å. Thus in principle, measured differences between samples of 3% (1Å at 30Å) could be significant; in practice, it has been demonstrated (2) that differences of 10% (3Å) are meaningful.

Samples 3 and 6 showed that photolithography does not affect the oxide thickness after 40°C rinse for Cu doped and undoped Al, respectively.

Sample 7 showed that the EG-BHF etch leaves a surface oxide of about 42Å.

Sample 8 revealed that the H_2 anneal, preceded by the EG-BHF treatment, increases the oxide thickness by about 30Å, to about 65Å. It might appear surprising at first that oxide growth occurs in a reducing (H_2) ambient. However, we have reproduced this result many times (not listed in Table I) and it is in fact consistent with the following two observations. (*i*) H_2 anneal has not been found to decrease the oxide thick-

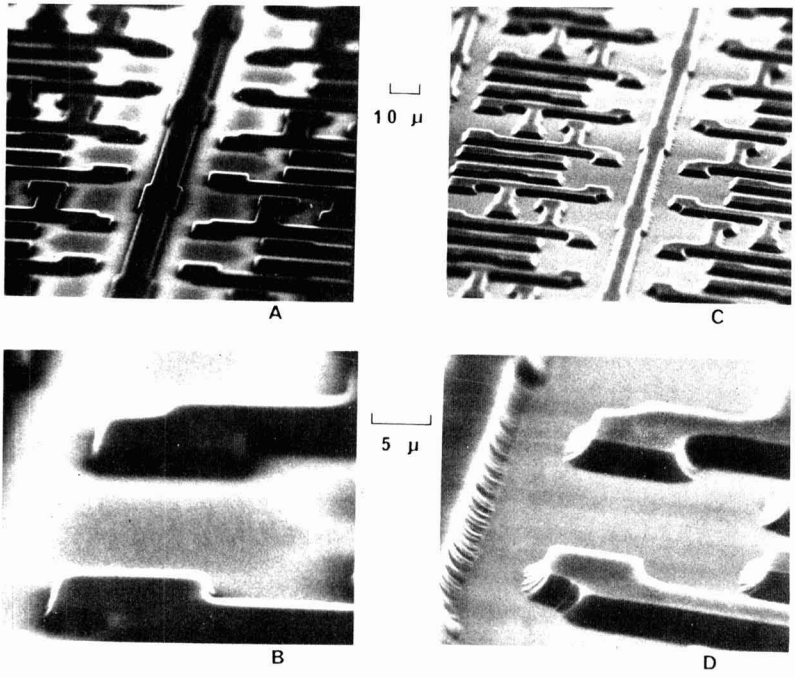

Fig. 2. SEM micrographs of the halo feature due to thick oxide growth. (A), (B) taken at two magnifications using sample 15 with thick surface film. The halo is the light contrast surrounding Al features; note the poor spatial resolution caused by the presence of an insulating film. (C), (D) from sample 3 with thin oxide (35Å); there is no halo, and spatial resolution is greatly improved.

ness in any of the present experiments, and (*ii*) it is obviously not possible to remove all contaminants during the anneal. We propose that small amounts of contaminants, either from the furnace or the wafers themselves, cause the Al to oxidize; once formed, the oxide is apparently stable in H_2 at 450°C.

Samples 9, 10, and 11 demonstrated that the oxide thickness begins to increase at 50°-60°C, to 60-70Å. Photolithography and Cu doping did not produce large effects.

Samples 12-15 showed the rapid oxide growth (to approximately 3000Å) at 80°C, which is fairly independent of photolithography and Cu doping. The 3000Å estimate does not take into account the porosity factor; for example, if the porosity factor (defined as the percentage of total film thickness occupied by pore space) is 75%, the actual oxide thickness could be 1.2 μm. The oxide thickness on sample 15 was estimated from SEM photographs of cleaved specimens to be at least several thousand angstroms.

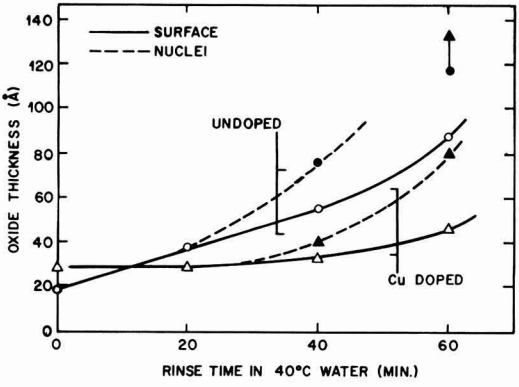

Fig. 3. Oxidation rate of Cu-doped (triangles) and undoped (circles) Al in 40°C water, samples 16 and 17. Filled points are data from the contaminated nucleation centers. The arrow on the filled circle at 116Å indicates that the oxide was thicker than 116Å.

For samples 1-15, wafers from several Al deposition runs were used, so that the initial oxide thickness before treatment probably varied from wafer to wafer. To ensure identical starting conditions, samples 16 and 17 (Cu doped and undoped, respectively) were cleaved into 4 quarters each. These were then treated in 40°C water for 0, 20, 40, and 60 min, and the resultant surface oxide thicknesses were measured and are shown in Fig. 3. When viewed in the SEM mode of the Auger apparatus, the untreated surfaces 16A and 17A appeared featureless, and the Auger spectra revealed only slight C and S contamination. The inability to detect Si indicated that the cleaving operation for separating each wafer into samples A-D resulted in no serious Si contamination. After 20 min rinse, a faint, uneven texture was visible on both samples 16B and 17B, when viewed in the SEM mode of the Auger apparatus. After 40 min treatment, these features appeared clearly as nucleation centers that were sufficiently large (>10 μm) for Auger analysis. They were found to be oxide nuclei which grew even larger after 60 min treatment; the Auger data from these areas are also included in Fig. 3. The arrow on the data point at 116Å indicates that the oxide was >116Å thick.

No Si was detectable (<0.1%) on 16A and 17A, but about 2% Si was found on all B, C, and D samples. Since similar amounts of Si were found on surfaces of unbroken wafers after 40°C rinse, this contaminant was not unique to these cleaved samples. Although the significance of this surface Si is not clear, the nucleation centers contained higher Si and C contamination, suggesting that the more rapid oxidation at these centers is related to the contaminants. Possible sources of these contaminants are the wafer itself for Si and the original C contamination on the Al surface. This result points out the importance of removing all photoresist residues during IC processing. The data of Fig. 3 lead to the following conclusions (applies to 40°C rinse):

1. Cu-doped Al oxidized more slowly than undoped Al. However, it is not known whether the slower oxi-

dation rate of the doped film was due to its thicker initial passivating oxide, or to a difference in some other property of films deposited in different machines.

2. Oxidation rate is slow for the first approximately 20 min and becomes rapid after about 40 min.

3. Oxidation is more rapid at nucleation sites. These sites were more contaminated with C and Si than the rest of the surface.

For sample 18, a device wafer after 80°C rinse, the total oxide thickness was not measured, but was determined by Auger analysis to be >>100Å, in agreement with the above.

For sample 19, the oxide growth caused by 80°C rinse was measured following the processing to step 4 of Table II. The oxide thickness was estimated from TEM micrographs to be 6000-9000Å.

Sample 20 was processed to step 10 and the oxide thickness was estimated using Auger analysis by ion milling through the Ti-Pt layer and into the Al at a contact window. The oxide thicknesses of $\gtrsim$ 6000 and 1600Å for samples 19 and 20, respectively, verify the rapid oxide growth for a device configuration, and comparison of samples 19 and 20 suggests that large amounts of oxide are removed by the brief EG-BHF etch.

Finally, sample 21 demonstrated that devices can be processed using 40°C water rinse with oxide growth limited to 43Å. This oxide thickness, which further increases upon H_2 anneal, is uncomfortably close to the limit of 55Å beyond which electrical contact problems after subsequent Ti deposition are expected, as established in a separate report (4); this point is further amplified in the Discussion.

AES indicated that after photolithography and 40°C water rinse, the amount of surface C was <0.5 atom layer (<1Å) and the Al surface is therefore sufficiently clean for the next processing step. The only other contaminants detected were about 0.05 atom layer of Si and S and much smaller quantities of Cl and F, and the dopant Cu in Cu-doped Al.

Attempts were made in this work to check the Auger measurements, d(Auger), of Al-oxide thickness by comparison with ellipsometric measurements, d(ellip.), for the full surface testers. Values of d(ellip.) were usually in reasonable agreement with d(Auger) but they sometimes differed by over a factor of 3, with d(ellip.) always larger. When the electrical breakdown voltages of these oxides were measured, the breakdown voltage was linear with d(Auger) but not related in any obvious manner to some of the d(ellip.) values (4). Therefore, we conclude that ellipsometric measurements may be sensitive to the contaminants and precise structure of the oxide and cannot be used except under certain controlled conditions. Values of d(Auger) have also been checked using a gravimetric method (in which the oxide film is weighed) and were in agreement with the resulting d(grav.) (4). Thus in addition to a fairly sound theoretical basis (2), there is experimental evidence that the Auger method of oxide thickness measurement gives probably the most reliable results available at present.

TEM analyses.—TEM of cleaved edges of sample 12 revealed the oxide to be about 5000Å thick and to have a porous, filamentary structure; typical micrographs are exhibited in Fig. 4. The oxide thickness estimates from TEM are often over a factor of two larger than from ion-mill Auger analysis. This disagreement is due at least in part to the film porosity. Cleaved samples were investigated in addition to sectioned samples (following paragraph) because of the avoidance of sectioning and ion-milling artifacts (sectioned samples are ion milled during the final stages of preparation). Avoidance of these artifacts is particularly important for obtaining reliable diffraction patterns (discussed below). Although the cleavage method is simple and fast, the cleavage geometry is not precisely known for the oxide, and details of the Al film are difficult to study because of the uneven cleavage geometry and because the Al probably deforms during breakage. Therefore, some samples were also sectioned and examined.

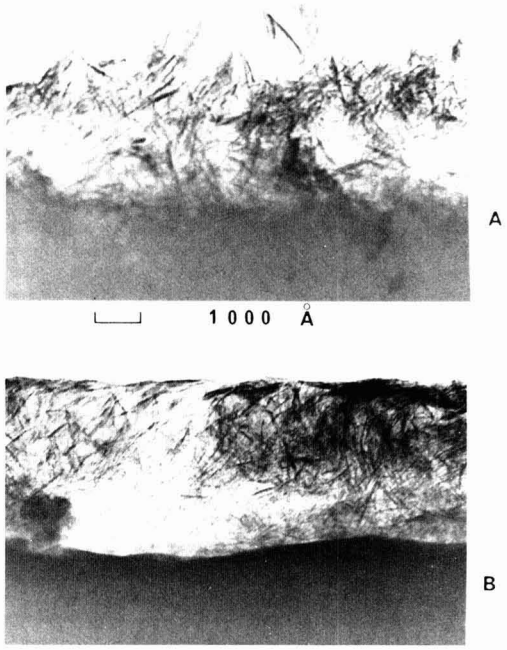

Fig. 4. TEM micrographs from a cleaved edge of sample 12, (80°C water rinse), taken from two areas. The filamentary material is Al oxide; the featureless region below the oxide is Al. The plane of the Al surface is tilted about 45°C from the electron beam axis.

TEM micrographs of cross sections of device wafer 19 are shown in Fig. 5 and 6. The appearance of the Al oxide is similar to that of sample 12 in Fig. 4, although the method of sample preparation for TEM was entirely different (simple cleaving *vs.* sectioning). In Fig. 5, a "hairline crack" can be seen running the entire width of the photograph from left to right just above the oxide-Al interface. This crack may be responsible for the lifting of the oxide as seen in Fig. 1. There is no preferential oxidation of the Al grain boundaries. Figure 6 was taken from an area tens of microns away from an Al runner that was found to the far right, out of the photograph. The horizontal line running across the photograph near center is the surface of the substrate Si, and the wavy features below this surface are mostly diffraction contrast from ion milling artifacts such as thickness variations. The cantilevered object entering from the left is a poly-Si gate (left edge) which ascends the (45°) tapered field oxide to a poly-Si runner (center). Material surrounding the poly-Si is SiO_2; close scrutiny reveals faint outlines of the various layers of thermal and deposited SiO_2. The Al oxide (filamentary material) is seen to migrate onto the SiO_2 surface and its thickness decreases toward the left, away from the Al source to the right (out of the picture).

Electron diffraction analysis of sample 12 indicated a nearly amorphous phase of gamma-alumina; the electron diffraction data are presented in Table III, under the "Measured" column, and compared to the expected values for gamma-alumina, boehmite, and bayerite. Relative intensities (x-ray) are also given in parentheses. The best match is with gamma-alumina; there is a possible presence of the monohydrate, boehmite, and no indication of the presence of the trihydrate, bayerite. This does not mean that bayerite is absent, as it may be in a more amorphous state

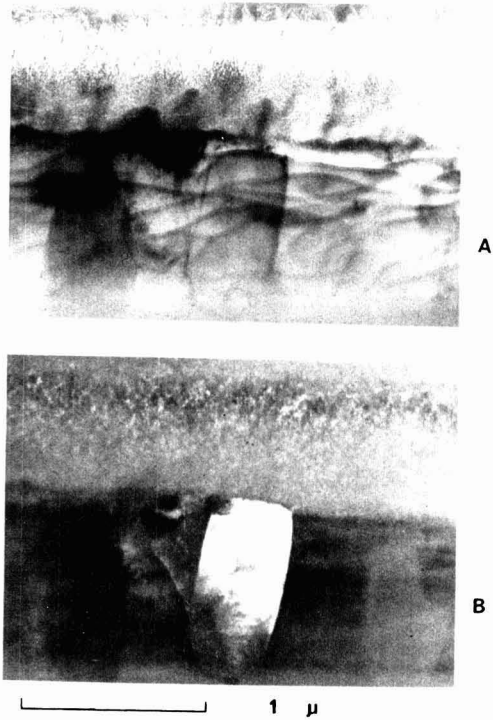

Fig. 5. TEM of thin cross sections of sample 19 taken perpendicular to the plane of the chip; the Al surface normal points up in the photograph. (A) Bright field picture showing the Al oxide (upper half) and the polycrystalline Al (lower half of photograph). (B) Dark field picture of the same area; revealing the precise location of the oxide-Al interface and the presence of small crystallites in the oxide.

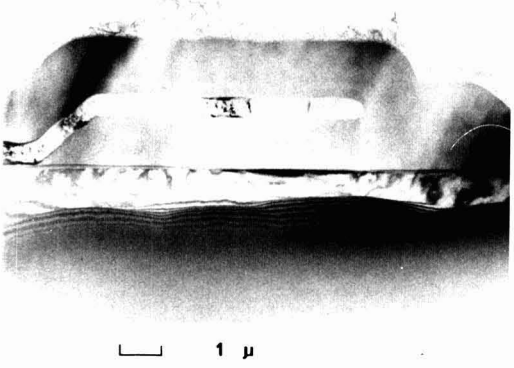

Fig. 6. SiO_2 area of sample 19, tens of microns away from an Al runner located to the far right (out of the picture). The identity of each feature is explained in the text. The filamentary material on the SiO_2 surface is Al oxide. The bubbles seen above the Al oxide are artifacts in the epoxy used to embed the specimen to facilitate handling. The Al oxide is thinner toward the left, away from the Al runner, suggesting that the runner is the source of the oxide.

than the others. All three compounds have been previously identified in diffraction patterns from Al oxidized in hot water (5, 6) (to a much greater extent than attempted here). The absence of the strong lines at d = 4.56, 2.80, 2.28, and 1.52Å for gamma-alumina and 6.11Å for boehmite in our diffraction data might

Table III. Crystallographic d-spacings (Å) of oxide on sample 12

Measured	Gamma-alumina	Boehmite	Bayerite
		6.11 (100)	
			4.71 (90)
	4.56 (40)		
			4.35 (70)
3.16 (weak)		3.16 (65)	3.20 (30)
	2.80 (20)		
2.41 (medium)	2.39 (80)	2.35 (55)	2.36 (4)
	2.28 (50)		
			2.22 (100)
1.96 (strong)	1.98 (100)	1.98 (6)	1.98 (4)
		1.86 (30)	
		1.85 (25)	
			1.72 (40)
		1.66 (14)	1.60 (10)
	1.52 (30)	1.53 (6)	1.55 (8)
		1.45 (16)	1.46 (12)
		1.43 (10)	1.45 (8)
1.39 (strong)	1.40 (100)	1.38 (6)	1.39 (6)
		1.31 (16)	1.33 (18)
1.13 (weak)	1.14 (20)	1.16 (4)	1.17 (6)
0.966 (v. weak)	0.989 (10)		
0.877 (v. weak)	0.886 (10)		
0.790 (v. weak)	0.806 (20)		

Note: From JCPDS Tables (formerly ASTM); x-ray intensities are given in parentheses and all lines with intensities totaling >(10) are listed. "Measured" results are electron diffraction data, 200 keV.

be due to the difference in atomic scattering factor between x-ray and electron diffraction, and to diffraction effects from extremely small crystallites with anisotropic growth habits.

The relatively thick oxide film on sample 12 (3000Å) could not be detected using x-ray diffraction and we attribute this result to its nearly amorphous nature. In agreement with this conclusion, no individual crystallites could be resolved with TEM. For the more extensively oxidized device wafer of Fig. 5 with an oxide 6000-9000Å thick, small particles, about 50Å in diameter, were visible in the dark field micrographs (Fig. 5B).

Discussion

The most significant new results of this work are the accurate quantitative measurements of the first <100Å of oxide growth in 10 MΩ DI water, under conditions actually experienced in IC processing. The fact that Al oxidizes in hot water is well documented (5-11). Our results are in qualitative agreement with literature; namely, that oxidation becomes rapid above 60°C and that the initial thin oxide is essentially amorphous. Although alloying of the Al and contaminants in the water certainly produce large effects (5, 9, 12) all the workers agree that the purest Al in the purest water available to them has resulted in oxidation (5-12).

The mechanism of Al oxidation in water has been described in some detail (6, 8). Oxidation proceeds in two major steps. In the first, Al and water react and release hydrogen, forming gamma-alumina. In the second, this oxide is hydrated and also redeposited. Thus the role played by any initial passivating oxide in delaying the onset of this oxidation is obviously important.

More generally, Al corrosion occurs in polar liquids, such as water and methanol (12). It is in polar liquids that nonneutral *p*H is readily attained, and the dependence on *p*H of the oxidation rate of Al in hot water has been clearly demonstrated (6, 8). This means, for example, that replacement of water with nonaqueous solutions will not necessarily eliminate the oxidation problem, since many nonaqueous solutions, such as methanol, are polar. Our finding that a low level of Cu doping retards oxidation slightly is of interest because, at high levels (≅4%), Cu has been reported to increase the corrosion activity (5, 9). However, our result is in qualitative agreement with the fact that anodization rate decreases with Cu doping (10). Investigation of Si-doped Al may also be interesting, because it has been reported (7) that Si doping retards Al oxidation in water. This last point is

interesting because Si is always present in Si IC processing and Si was one of the contaminants found on the Al in this work.

The usefulness of the above results to IC processing is obvious. Although DI water rinse is most effective at higher temperatures, we have established that above 50°C, oxide growth rate becomes too fast and the allowed thickness limit (4) of about 55Å can be exceeded in a matter of minutes. This limit is the sum of the amount of oxide that is effectively nullified by subsequent Ti deposition (45Å) and the electron tunneling distance (12Å), as determined by electrical breakdown measurements. The EG-BHF etch was shown here to be very effective for removing thick Al oxide. However, it leaves a relatively thick residual oxide (about 40Å) which further increases in thickness upon H_2 anneal (to about 65Å). A different etch based on a mixture of CrO_3 and H_3PO_4 has been shown (4) to leave a much thinner residual oxide (about 30Å) and may be preferable for reducing oxide thickness.

The rapid oxidation property of Al is not always undesirable and can be exploited to useful purpose. For example, even a mild treatment in hot water may be sufficient to passivate exposed Al areas of an IC chip. If an entire device is coated with Al, a passivating layer can be grown by completely oxidizing the Al. It should be kept in mind, however, that during oxidation, hydrated oxides will migrate and redeposit on adjacent areas that are tens of microns away from the Al. Since many materials are stable in hot water, they can be used as mask material for selective oxidation of thin Al films.

Conclusions

1. 40°C is a "safe" temperature for DI water rinse of Al (up to about 20 min); 50°-60°C is the "danger point" beyond which excessive oxidation will occur. The Al surface is quite clean (<1Å of C) after a 5 min, 40°C rinse following photolithography.

2. Al-oxide growth occurs in pure water; (HR100) photolithography, (H_3PO_4-based) Al etch, (A30) resist stripping, and Cu doping ($\cong$0.5 a/o), do not significantly affect the oxidation rate.

3. This oxide is porous and contains nearly amorphous gamma-alumina and probably some hydrated oxides.

4. The Al oxide is able to spread >20 μm from the Al to adjacent areas; this probably occurs by dissolution of gamma-alumina and redeposition of the hydrated oxides (6, 8).

5. This oxide is loosely adherent to Al, especially after 450°C H_2 anneal, and causes poor adhesion of subsequent metals deposited over the Al.

Acknowledgment

The authors are grateful to M. H. Read for x-ray diffraction analysis.

Manuscript submitted Sept. 29, 1977; revised manuscript received Jan. 3, 1978.

Any discussion of this paper will appear in a Discussion Section to be published in the December 1978 JOURNAL. All discussions for the December 1978 Discussion Section should be submitted by Aug. 1, 1978.

Publication costs of this article were assisted by Bell Laboratories.

REFERENCES

1. M. P. Lepselter, *Bell Syst. Tech. J.*, **45**, 233 (1966).
2. C. C. Chang and D. M. Boulin, *Surf. Sci.*, **69**, 385 (1977).
3. T. T. Sheng and C. C. Chang, *IEEE Trans. Electron Devices*, **ed-23**, 531 (1976).
4. T. A. Shankoff, C. C. Chang, and S. E. Haszko, *This Journal*, **125**, 467 (1978).
5. R. K. Hart, *Trans. Faraday Soc.*, **53**, 1020 (1957).
6. M. Pourbaix, in "Atlas of Electrochemical Equilibria in Aqueous Solutions," p. 168, Pergamon Press (1966).
7. J. M. Bryan, *J. Soc. Chem. Ind.*, **69**, 169 (1950).
8. W. Vedder and D. A. Vermilyea, *Trans. Faraday Soc.*, **65**, 561 (1969).
9. R. S. Alwitt and L. C. Archibald, *Corros. Sci.*, **13**, 687 (1973).
10. G. C. Schwartz, Abstract 80, Electrochemical Society Symposium, Toronto, Canada, May 11-16, 1975.
11. K. A. Phatak, S. S. Tamhankar, and K. Sathianandan, *Thin Solid Films*, **41**, 137 (1977).
12. P. A. Totta, Abstract A-3, American Vacuum Society Symposium, Philadelphia, October 1975.

Silicon-on-Sapphire Crystalline Perfection and MOS Transistor Mobility

C. E. Weitzel* and R. T. Smith

RCA Corporation, RCA Laboratories, Princeton, New Jesrey 08540

ABSTRACT

Experimental data show that there is a correlation between the crystalline perfection of a (100) silicon-on-sapphire epitaxial film and the magnitude and direction of misorientation of the sapphire substrate from the {1$\bar{1}$02} normal. The perfection is ascertained by measuring the half-width of Si {400} θ:2θ x-ray diffraction profiles. Data obtained from SOS/MOS transistors show a direct relationship between epitaxial perfection and FET mobility. Other factors which influence the perfection of the SOS film are growth temperature and film thickness.

For many years considerable effort has been expended in optimizing the quality of the epitaxial silicon films grown on sapphire substrates. In the earliest work (1-3), the optimization was achieved by selecting the appropriate Al_2O_3 planes which allow single crystal silicon growth and by using silane rather than silicon tetrachloride as the source gas. To achieve higher quality SOS films later workers (4-11) found it necessary to optimize other parameters: type of sapphire, substrate polishing and cleaning, predeposition firing, growth rate and temperature, and post-deposition annealing. Additional work (12-18) was directed toward understanding and optimizing changes in the SOS films which resulted from MOS transistor fabrication. More recently a vast array of sophisti-

* Electrochemical Society Active Member.
Key words: x-ray diffractometry, θ:2θ half-width, FET mobility, growth temperature, Czochralski sapphire.

cated analysis techniques have been used by numerous workers (19-35) whose goal is to understand and optimize the Si-Al_2O_3 system.

Despite all of this work on optimizing (100) SOS films, there is no mention of the possible dependence of SOS film quality on the sapphire substrate misorientation from the {1$\bar{1}$02} plane. Recently we presented data (36) that were obtained from wafers cut from EFG (edge defined film fed growth) sapphire ribbons that were polished using techniques that subsequently have been improved. These data indicate that small misorientations of the substrate away from the {1$\bar{1}$02} affect the SOS film perfection, and as a result the transistor mobility. More importantly the data show that the most perfect (100) SOS films are not obtained on the {1$\bar{1}$02} sapphire plane but rather off this plane. The data presented here are corroborating observations obtained using state-of-the-art Czochralski substrates. The relative crystalline perfection of SOS films is determined by x-ray diffraction profiles and is shown to correlate with SOS/MOS transistor mobility. The data from the Czochralski substrates also indicate that the most perfect SOS films are grown on substrates which are off the {1$\bar{1}$02} plane. Since the same results were obtained for both sources of sapphire and both polishing techniques we must conclude that the optimum substrate orientation is independent of these parameters. The transistor mobility and film perfection are also shown to be directly related for SOS films grown at different temperatures and of different thicknesses.

Experimental Techniques

The 1½ in. diam sapphire substrates used in this investigation were cut from Czochralski sapphire boules and polished by Union Carbide using state-of-the-art techniques. Since a systematic investigation of substrate misorientation was planned, the misorientation of a large number of substrates was measured using x-ray Laue and diffractometry techniques. Each wafer had a fiducial flat ground at 45° to an Al_2O_3 "a" axis lying in the plane of the wafer face. The projection of the Al_2O_3 "c" axis in the polished side of the wafer was determined relative to the ground fiducial flat by the back-reflection Laue method. Components of misorientation of the face of the wafers from the {1$\bar{1}$02} were thus measured in orthogonal directions perpendicular and parallel to the projection of the "c" axis. The orthogonal components of misorientation were measured on a Siemens diffractometer equipped with a Siemans single crystal orienter and using a Cu $K\alpha_1$ {1$\bar{1}$02} reflection. Components of misorientation were read directly to an accuracy of ±0.02°.

From this pool of substrates four groups of five substrates were selected to be processed together. In selecting the substrates for each group, care was taken to select substrates with widely varying misorientation so that any difference in transistor parameters would be obvious. Figure 1 shows the misorientation components of 20 of the substrates which were studied. A perfectly oriented wafer would be located at the origin of this graph. Figure 1 also shows how the wafers are divided into four processing lots and the processing lot number. At the time the wafers were purchased, the orientation specification was 2.0° in any direction from {1$\bar{1}$02}. Only three of the 20 wafers were outside of this specification.

After the components of misorientation of the substrates were measured, the substrates were fired in H_2 at 1200°C for 30 min. The epitaxial silicon films were grown on five substrates at a time in a five-sided barrel reactor by the pyrolysis of SiH_4 at 970°C pyrometer. The films were doped $1 \times 10^{15}/cm^3$ n-type during growth. Nominally 0.6 μm films were grown in 20 sec. Following epitaxial silicon growth, diffraction profiles were obtained from both the Al_2O_3 {2$\bar{2}$04} and Si {400} in the rocking curve (ω-scan) and θ:2θ

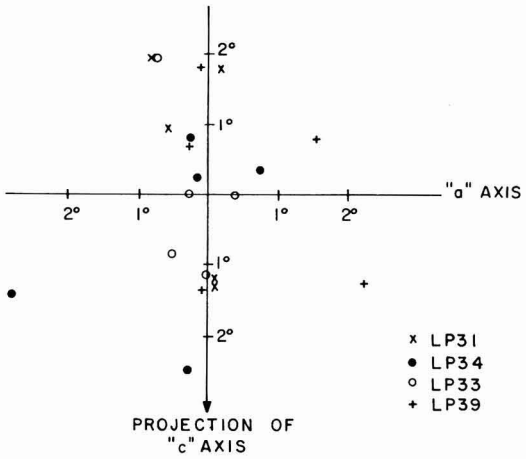

Fig. 1. Misorientation components of 20 Czochralski {1102} sapphire substrates.

modes. These diffraction profiles were obtained from a rectangular area about 1 cm × 1 mm near the center of each wafer. A Siemans ω-drive diffractometer with Cu Kα radiation was used to record the peak profiles. The smallest entrance and receiving slits (0.125 and 0.05 mm, respectively) were used to minimize the instrumental broadening. Scanning speeds were 1/8°/min in the θ:2θ mode and 1/4°/min in the ω-mode. The crystal scanning-chart speed coupling gave a strip chart recording sensitivity of 0.03125°/cm and 0.0625°/cm in the θ:2θ and ω-modes, respectively. In the θ:2θ mode, one samples only from a set of parallel planes, and the broadening over instrumental may be caused by a crystalline defect causing nonuniformity in the d-spacing of these planes or small crystallite size effects or both. In the ω-mode the detector is set at a fixed position centered within an angular range of 0.02° about the maximum diffracted intensity setting; hence any plane having a d-spacing characteristic of the angular setting of the detector may be sampled as the crystal alone is rotated through its diffracting range. Broadening in this mode may be caused by relative misorientation of crystallites or sample curvature or both Each sample was oriented such that its diffraction normal was in the plane of the diffractometer. This was accomplished by incrementally rotating the sample about its face normal and successively readjusting the crystal ω setting and detector 2θ setting to maximize the diffracted intensity. The correct setting is attained when ω reaches a maximum or minimum value.

Following characterization of the epitaxial silicon film, SOS/MOS transistors were fabricated using the P+ polysilicon gate deep depletion process (37). Briefly the processing steps are: silicon island definition and etching, growth of 1200Å of channel oxide, polysilicon deposition, doping and etching, channel oxide self-aligned etch, doping of sources and drains from doped oxides, contacts, metallization and overcoat. The process results in the fabrication of an n-channel deep depletion transistor and a p-channel enhancement mode transistor. The average FET mobility for a wafer is determined by averaging the mobilities measured at five points on each wafer, one point at the center of the wafer and four points equally spaced around the perimeter of the wafer within ¼ in. of the wafer edge. The mobility of each point is arrived at by plotting the drain current *vs.* gate voltage with $V_D = 0.1V$. The transconductance is determined from the linear part of this curve where the g_m is maximum. The FET mobility is then calculated using the physical dimensions of the transistor (38).

Experimental Results

Substrate misorientation and silicon epitaxial perfection.—Of the four diffraction profiles obtained from each sample, the Si $\theta:2\theta$ half-widths were found to have the greatest correlation to device performance. The Si ω-scan half-widths paralleled those of the $\theta:2\theta$ with some exceptions. It is thought that these exceptions are due to the dependence of the ω-scan half-width on the direction of scan. Since each crystal was oriented so that it was scanned in the direction of misorientation and the orientation of each was different, a common scanning direction did not exist. Since the $\theta:2\theta$ half-widths are a valid qualitative comparison of relative crystalline quality or perfection, we have chosen to compare device performance characteristics with the crystalline quality as obtained from $\theta:2\theta$ scan half-widths.

The half-widths obtained from $\{2\bar{2}04\}$ $\theta:2\theta$ scans of all the Al_2O_3 substrates were found to have a mean value of 0.0413° ± 0.0029°. Although the Al_2O_3 half-widths showed very little variation, the {400} $\theta:2\theta$ half-widths of Si deposited on these substrates ranged from 0.117° to 0.157° as shown in Table I. The half-width of a {400} Cu $K\alpha_1$ reflection of bulk Si obtained with the same instrumental conditions was found to be 0.0500°. Thus it appears that the method was insensitive to any variations in the quality of the Al_2O_3 substrate, if present; while, the $\theta:2\theta$ half-widths of the epi Si were from 2.3 to 3.1 times as large as those of bulk Si. Repeated half-width measurements of the same SOS sample indicated that the measured half-widths are reproducible to within ±3.0%. The diffraction profiles of the {400} Si reflection were similar to those reported earlier (36).

The half-widths obtained from each of the 20 wafers are shown in Table I. The wafers in each processing lot are listed in order of increasing $\theta:2\theta$ half-width. Therefore, the SOS film having the smallest half-width is listed first in each group of five wafers, and the one with the largest half-width is listed last. An examination of the components of misorientation of each wafer revealed a correlation between the component of misorientation parallel to the mirror plane and the $\theta:2\theta$ half-width as shown in Table I. The wafers, whose component of misorientation parallel to the mirror plane is positive, have the smallest half-widths; whereas, the wafers whose component of misorientation is negative have the largest. Therefore, wafers misoriented in the top half plane of Fig. 1 consistently have smaller half-widths than those in the bottom half plane. This correlation is obvious for all of the lots except LP33. Possible causes of this lack of correlation in lot LP33 are discussed later. No correlation was found between the components of misorientation parallel to the "a" axis and the $\theta:2\theta$ half-widths. This is not surprising since most of the wafers are only slightly displaced from the mirror plane, Fig. 1.

Table I. $\theta:2\theta$ X-ray half-widths of SOS films, sapphire substrate component of misorientation parallel to mirror plane and SOS/MOS transistor mobility

Processing lot	Sapphire substrate component of misorientation parallel to mirror plane (degrees)	Silicon $\theta:2\theta$ half-width (degrees)	SOS/MOS transistor mobility (cm²/V sec) n-channel Max	Avg	Min	p-channel Max	Avg	Min
LP31	+1.80	0.117	457	447	440	218	214	209
	+1.92	0.123	460	424	402	207	204	197
	+0.92	0.134	356	353	344	177	170	163
	−1.22	0.138	350	343	320	176	174	169
	−1.28	0.142	336	320	300	171	165	155
LP33	+1.94	0.125	453	447	445	161	159	158
	−0.03	0.126	491	483	477	186	182	180
	−1.13	0.129	506	483	431	168	164	153
	0.00	0.134	575	542	518	189	186	176
	−0.84	0.145	432	416	399	153	150	146
LP34	+0.82	0.118	458	432	415	164	162	159
	+0.35	0.122	451	426	409	169	161	154
	+0.25	0.128	347	337	330	143	141	139
	−1.41	0.133	320	314	305	136	131	128
	−2.50	0.141	295	268	236	130	114	109
LP39	+0.69	0.130	509	497	487	202	197	194
	+0.81	0.134	555	530	523	225	218	212
	+1.85	0.142	483	456	419	191	188	179
	−1.34	0.150	420	410	405	193	185	169
	−1.26	0.157	Wafer broke					

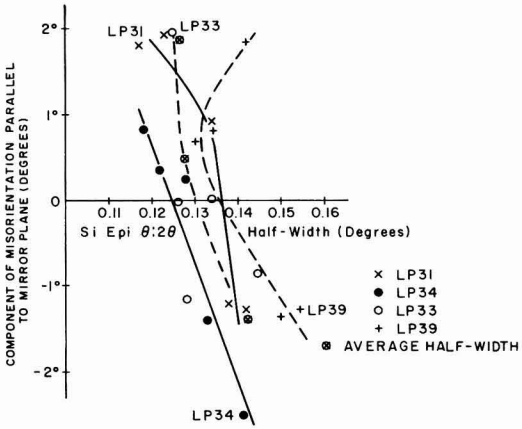

Fig. 2. Silicon {400} $\theta:2\theta$ half-widths vs. component of misorientation parallel to the mirror plane.

The data from the first two columns of Table I are shown graphically in Fig. 2. The ordinate in Fig. 2 is the component of misorientation parallel to the mirror plane and the abscissa is the $\theta:2\theta$ half-width. The lines are drawn to approximately fit the experimental data points. Three of the lines show a monotonic decrease in $\theta:2\theta$ half-width as the component of misorientation changes from negative to positive; whereas, the fourth line, for processing lot LP39, shows a decrease followed by an increase for the most positive component of misorientation. The 20 points plotted in Fig. 2 could be gathered together into three groups: those with components of misorientation parallel to the mirror plane of about −1°, those with components between 0° and +1°, and those with components around +2°. The average half-widths of these three groups are 0.140°, 0.128°, and 0.127°, respectively. These averages also reflect the correlation with substrate orientation. The average half-width and misorientation component of these three groups is plotted in Fig. 2 by the circled X.

Silicon $\theta:2\theta$ half-width and SOS/MOS transistor mobility.—Since the $\theta:2\theta$ diffraction profile is a measure of the quality of the epitaxial film, such a parameter should also correlate with the electrical properties of the film that are also affected by film quality. Since the mobility of charge carriers is limited by scattering events, the mobility of carriers in a more highly defected material would necessarily have to be smaller than in a more defect-free material. This correlation is shown by the transistor mobility data in Table I. The maximum, minimum, and average mobilities of both n-channel and p-channel transistors on each wafer are shown. With the exception of data for lot LP33, the average mobility decreases as the $\theta:2\theta$ half-width increases. The maximum and minimum mobilities for each wafer also show this trend. For most of the wafers the maximum and minimum mobilities differ from the average mobility by less than 5%. For a few wafers, however, the difference is as great as 10%.

This correlation between crystalline perfection and FET mobility is shown graphically in Fig. 3. The FET mobility for n-channel deep depletion transistors and p-channel enhancement transistors from lot LP34 is plotted *vs.* the $\theta:2\theta$ half-width of the silicon epitaxial film. The spread in mobility above and below

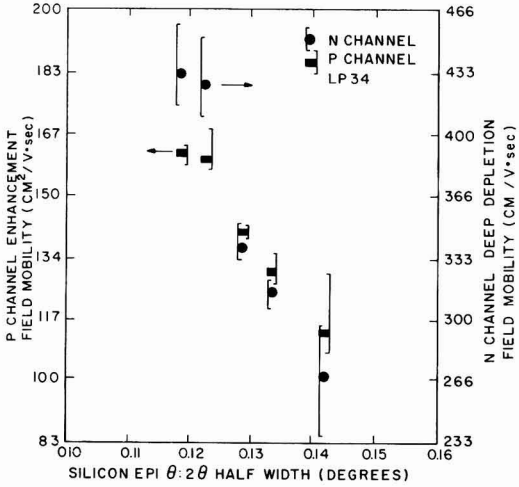

Fig. 3. FET mobility of n-channel deep depletion and p-channel enhancement transistors vs. θ:2θ half-width of silicon epitaxial film for wafers in lot LP34.

the average is shown by the vertical bar. The data show that the mobility in the accumulation layer of the n-channel device is reduced from 432 cm²/V sec for a half-width of 0.118° to 268 cm²/V sec for a half-width of 0.141°. The average mobility in the inversion layer of the p-channel device decreases from 162 to 114 cm²/V sec. For a 3.32° change in substrate orientation, the mobility is reduced to 70% of its maximum value. The average mobilities for the devices on wafers in the three groups previously discussed in reference to Fig. 2 also show the same effect. The average n-channel mobility for the three groups is 380, 450, and 443 cm²/V sec, respectively, and the average p-channel mobility for the groups is 164, 183, and 197 cm²/V sec, respectively.

Since the crystalline perfection correlates with misorientation direction and also with the FET mobility, the mobility must also correlate with misorientation direction. This correlation is shown in Fig. 4 for processing lot LP31. In Fig. 4 the misorientation components for each substrate are plotted on a graph similar to Fig. 1. Next to each point is given the average n-channel and p-channel FET mobility. Devices fabricated on substrates which are above the origin, which in Fig. 2 have been shown to have lower

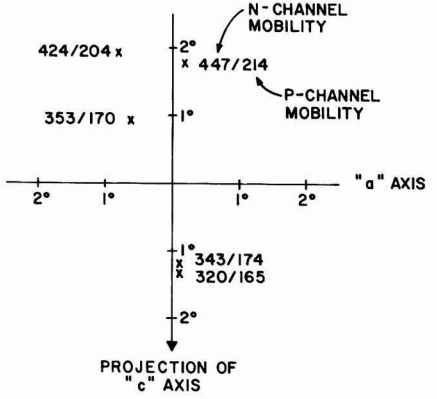

Fig. 4. FET mobility of n-channel deep depletion and p-channel enhancement transistors vs. components of substrate misorientation for wafers in lot LP31.

defect concentrations, have higher FET mobilities than devices fabricated on substrates which are located below the origin which have been shown to have higher defect concentrations.

Other parameters affecting SOS epitaxial perfection.—The correlation between substrate misorientation, silicon θ:2θ half-width, and SOS/MOS transistor mobility is quite obvious when the data from the five wafers which were processed together are compared. However, the correlation becomes less obvious when all 20 wafers are grouped together for analysis. In addition, the lack of correlation for the data from lot LP33 is unexpected in light of the data from the other lots. These facts indicate that, in addition to substrate misorientation, there are other factors which affect SOS epitaxial quality. If other parameters were not important, all of the lines connecting the data points in Fig. 2 would cross the zero degree axis at the same point. Instead, there is a 0.0115° variation in half-width on this axis. This variation exists in spite of the fact that the wafers were processed as identically as is presently possible.

The factors that are not totally controlled are probably those that affect the substrate polishing and cleaning and the silicon growth. Until recently no technique for quantitatively measuring the perfection of a polished sapphire surface has been available. The infrared work by Duffy and Zanzucchi (31) is a step in this direction. An important factor to control with regard to the silicon growth is the temperature. This is usually done with an optical pyrometer. Since the pyrometer measures the temperature through the wall of the growth reactor any deposit that accumulates on the inside wall of the reactor will cause an error in the temperature at which the film is grown. The sensitivity of the quality of the SOS film to growth temperature is shown by the data in Fig. 5. To eliminate the effect of the accumulating deposit the bell jar was thoroughly cleaned prior to growing the SOS films for this experiment. In addition after each deposition run the bell jar was cleaned again. These precautions were taken so that the susceptor temperature could be measured accurately. The FET mobility of n-channel deep depletion transistors is plotted on the ordinate and the growth temperature, as measured by an optical pyrometer, is plotted on the abscissa. The vertical bars indicate the spread in mobility across each 1½ in. diam wafer. The misorientation components of all of the wafers are the same to within 0.100°. As the deposition temperature is increased from 930° to 1000°C, the average FET mobility increases from 260 cm²/V sec to a high of 445 cm²/V sec and back down to 258 cm²/V sec. The spread in mobility across a wafer is smallest for films grown near the optimum temperature. The films grown at 930° and 1000°C had

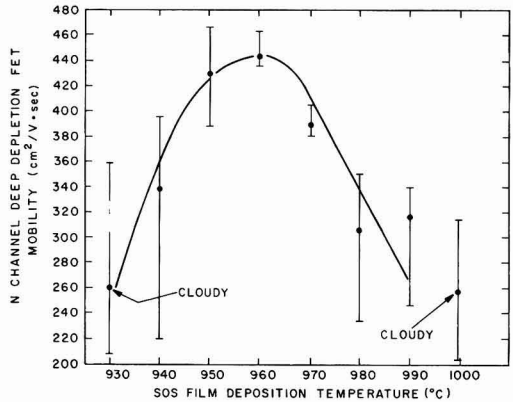

Fig. 5. N-channel FET mobility vs. SOS film growth temperature

a cloudy or milky appearance when viewed with intense low-angle lighting. In all probability there are degrees of cloudiness not discernible to the human eye for some of the other lower mobility wafers. The crystalline structure of the cloudy films is presently being studied. The $\theta:2\theta$ half-width of cloudy films is larger than that of noncloudy films for identically oriented wafers. The data indicate that temperature control to within $\pm 5.0°$ of the optimum temperature is desirable. However, it is still not that simple, because the temperature across the surface of the growth susceptor varies. In addition, the temperature variation across a warped wafer will be different from that across a flat wafer.

Talysurf measurements indicate that occasionally the films on one or more wafers in a deposition run are thicker or thinner than expected. Again as with temperature, this can have a measurable effect on FET mobility and $\theta:2\theta$ half-width, as shown in Fig. 6. The misorientation components of all of the wafers are the same within 0.100°. The mobility for n-channel deep depletion transistors is plotted on the left-hand ordinate, and $\theta:2\theta$ half-width is plotted on the right-hand ordinate. Again the vertical bar indicates the spread in mobility across the wafer. The preprocessed film thickness is plotted on the abscissa. Approximately 700Å of silicon is consumed during oxidation in the process. As the film thickness decreases the mobility first decreases slowly and then rapidly below 3000Å. This mobility decrease is mirrored by an increase in $\theta:2\theta$ half-widths. These mobility data are consistent with those of other workers (39-41). These data indicate that the defect density of an SOS film increases as the Si-Al_2O_3 interface is approached. Cross-section transmission electron micrographs also show this dependence of defect density on film thickness (24).

The high temperature processing steps that the film undergoes during the fabrication of MOS devices also have a significant effect on the defect density of the SOS epitaxial film, as shown by the data in Fig. 7. These data were taken by measuring the $\theta:2\theta$ half-width of as grown 0.6μ thick films. Then a thermal SiO_2 layer is grown in HCl steam on each of the films, as would be done in normal processing. A different oxidation temperature and time was used for the two films. Normally the SiO_2 is used as an etch mask for the silicon film. However, in this experiment the oxide is merely removed before the $\theta:2\theta$ half-widths are re-measured. The results are shown in Fig. 7. It is interesting to note that the film with the larger half-width that was oxidized at the higher temperature for the longer time had the smaller half-width following the oxidation. Next the films were oxidized as if the channel oxide were being grown. The oxide was removed, and the half-widths remeasured. This process was repeated after each of the anneals at 1050°C

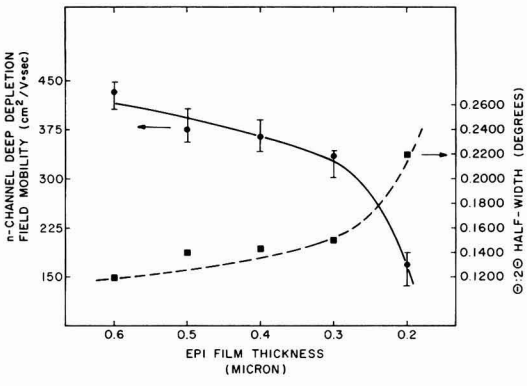

Fig. 6. N-channel FET mobility and $\theta:2\theta$ half-width vs. SOS film thickness.

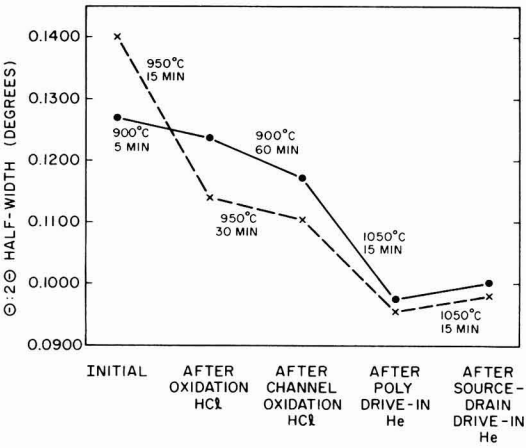

Fig. 7. Effect of high temperature processing steps on silicon {400} $\theta:2\theta$ half-widths.

in helium for 15 min. The data clearly show that the high temperature processing steps cause a decrease in the $\theta:2\theta$ half-width. This is indicative of an annealing out of some of the defects in the SOS film. That the more defective film had less defects at the end of the processing shows the importance of the time and temperature for improving the perfection of the film. Finally the data show that continued annealing does not reduce the SOS, $\theta:2\theta$ half-width to that observed for bulk silicon, 0.0500 degrees. Rather the half-width decrease saturates at a value between 0.0900 and 0.1000 degrees. These results were confirmed by other experiments in which SOS films were annealed in inert ambients for periods of hours or days. In all cases the half-widths decreased; and in many cases following saturation, the half-widths increased with further annealing, as did the data in Fig. 7. The smallest half-width measured for an annealed 0.6μ SOS film was 0.0844 degrees, and only one other film out of about 30 had a measured half-width of below 0.0900 degrees.

Discussion

The experimental data presented here is additional evidence for the correlation between sapphire substrate misorientation, silicon $\theta:2\theta$ half-width, and SOS/MOS transistor mobility. In the earlier work (36) this correlation was found using wafers cut from EFG sapphire ribbons that were polished using techniques that have subsequently been improved. As a result there was concern that the source of the sapphire and polishing techniques might have contributed to the effect. The present observations, however, were obtained using substrates cut from Czochralski boules. These wafers were fabricated using state-of-the-art techniques which included a final polish using colloidal-silica type polishing agents. Since the same behavior was found for both sources of sapphire and both polishing techniques, we must conclude that one factor that determines the qualtity of the SOS film is the substrate misorientation. In addition the data show that the highest quality SOS films are not grown on the $\{1\bar{1}02\}$ plane, as was formerly supposed, but rather off this plane by an, as yet, undetermined amount. This optimum orientation is presently being sought.

Although most of the experimental data clearly shows the correlation between substrate misorientation, SOS film perfection, and FET mobility, anomalous results are occasionally found. In this work the data from lot LP33 is clearly anomalous when compared with the data from the other lots. In addition the wafer with the component of misorientation parallel to the mirror plane of +1.85 degrees in lot LP39 is

also somewhat anomalous. One possible explanation of this behavior is that factors other than substrate misorientation are affecting the film quality. The data in Fig. 5 and 6 show that growth temperature and film thickness are two other factors which affect film perfection. The growth temperature could be different for wafers in the same deposition run if the faces of the susceptor are at different temperatures or if there is poor thermal contact between the wafer and susceptor which could be caused by wafer warpage. The data in Fig. 5 clearly show that a deviation of only 10°C from the optimum growth temperature can cause a signficant decrease in transistor mobility. A limited study of film thickness variation for wafers grown at identical conditions revealed that although the thickness of 90% of the films was within ±10% of the average thickness of all the SOS films, the thickness of the films on the other 10% of the wafers differed by as much as ±25%. This translates to a film thickness variation of ±1500Å. The data in Fig. 6 show that a variation in thickness of this magnitude would also have a significant effect on θ:2θ half-width and transistor mobility.

The data in Table I show that for the anomalous wafer in lot LP39 not only is the mobility lower than expected, but the half-width is also greater than would be expected for a wafer with this misorientation. Therefore, the correlation between mobility and half-width still holds; whereas the correlation with misorientation is violated. This type of behavior would be expected if the film were too thin or if the growth temperature were not optimum.

In light of the correlation between misorientation, half-width, and mobility for the data from the other three lots, the data for lot LP33 is most disconcerting. The data for lot LP33 in Table I show very little correlation between any of the measured parameters. If the half-width data correlated with the mobility data, but not the misorientation the arguments used for the wafer in lot LP39 with regard to growth temperature and film thickness could be applied here. However, the data for LP33 in Table I do not show this correlation. Therefore, the only explanation for the lack of correlation is that either the wafers became mixed up or that there are other factors which can affect the film mobility but not the half-width.

The data which show the decrease in half-width following various processing steps points out an important fact about SOS films. The fundamental properties of SOS films are not unaffected by the processing steps required for transistor fabrication. On the contrary SOS films are very sensitive to processing parameters. These x-ray diffraction techniques are merely another tool that can be used to acquire a better understanding of the dynamics of the Si-Al_2O_3 system. The ultimate goal of all this work is the optimization of SOS transistor performance.

Summary

Experimental data obtained from state-of-the-art Czochralski sapphire substrates were presented which show a correlation between substrate misorientation, SOS film perfection, as measured by x-ray diffraction techniques, and SOS/MOS transistor mobility. The correlation is identical to that obtained in earlier work (36) in which EFG ribbon wafers were used. The data indicate that the optimum substrate orientation is not the $\{1\bar{1}02\}$ plane but rather off this plane. Growth temperature and film thickness are also shown to have a large effect on film perfection and transistor performance.

Acknowledgments

The authors are indebted to D. Capewell and T. Pawlicki for their technical assistance.

Manuscript submitted June 8, 1977; revised manuscript received Nov. 9, 1977. This was Paper 177 presented at the Las Vegas, Nevada, Meeting of the Society, Oct. 17-22, 1976.

Any discussion of this paper will appear in a Discussion Section to be published in the December 1978 JOURNAL. All discussions for the December 1978 Discussion Section should be submitted by Aug. 1, 1978.

Publication costs of this article were assisted by the RCA Corporation.

REFERENCES

1. H. M. Manasevit and W. I. Simpson, *J. Appl. Phys.*, **35**, 1349 (1964).
2. H. M. Manasevit, A. Miller, F. L. Morritz, and R. Nolder, *Trans. Metall. Soc. AIME*, **233**, 540 (1965).
3. R. Nolder and I. Cadoff, *ibid.*, **233**, 549 (1965).
4. C. W. Mueller and P. H. Robinson, *Proc. IEEE.* **52**, 1487 (1964).
5. P. H. Robinson and C. W. Mueller, *Trans. Metall. Soc. AIME*, **236**, 268 (1966).
6. D. J. Dumin and P. H. Robinson, *This Journal*, **113**, 469 (1966).
7. D. J. Dumin, *J. Appl. Phys.*, **38**, 1909 (1967).
8. J. F. Allison, D. J. Dumin, F. P. Heiman, C. W Mueller, and P. H. Robinson, *Proc IEEE*, **57**, 1490 (1969).
9. D. J. Dumin and E. C. Ross, *J. Appl. Phys.*, **41**, 3139 (1970).
10. D. J. Dumin, *Solid-State Electron.*, **13**, 415 (1970).
11. D. J. Dumin, P. H. Robinson, G. W. Cullen, and G. E. Gottlieb, *RCA Rev.*, **31**, 620 (1970).
12. D. J. Dumin and P. H. Robinson, *J. Appl. Phys.*, **39**, 2759 (1968).
13. E. C. Ross and G. Warfield, *ibid.*, **40**, 2339 (1969).
14. G. W. Cullen, G. E. Gottlieb, and C. C. Wang, *RCA Rev.*, **31**, 355 (1970).
15. J. H. Scott and J. R. Burns, Abstract 138, p. 355, The Electrochemical Society Extended Abstracts, Spring Meeting, Los Angeles, Calif., May 10-15, 1970.
16. D. J. Dumin, *J. Vac. Sci. Technol.*, **8**, 235 (1971).
17. G. E. Gottlieb, J. F. Corboy, G. W. Cullen, and J. H. Scott, *Metall. Trans.*, **2**, 653 (1971).
18. G. W. Cullen, *J. Cryst. Growth*, **9**, 107 (1971).
19. C. C. Chang, *J. Vac. Sci. Technol.*, **8**, 500 (1971).
20. P. T. Picroux and G. J. Thomas, *J. Appl. Phys.*, **44**, 594 (1973).
21. M. Druminski, C. Kühl, E. Preuss, F. Schwidefsky, and J. Tihanyi, Abstract 139, p. 329, The Electrochemical Society Extended Abstracts, Vol. 74-2, Fall Meeting, New York, N.Y., Oct. 13-17, 1974.
22. P. Rai-Choudhury and D. K. Schroder, Abstract 143, p. 339, The Electrochemical Society Extended Abstracts, Vol. 74-2, Fall Meeting, New York, N.Y., Oct. 13-17, 1974.
23. C. Lee and K. Hu, Abstract 177, p. 417, The Electrochemical Society Extended Abstracts, Vol. 75-1, Spring Meeting, Toronto, Canada, May 11-16, 1975.
24. M. S. Abrahams and C. J. Buiocchi, *Appl. Phys. Lett.*, **27**, 325 (1975).
25. A. M. Goodman, *IEEE Trans. Electron Devices*, **ed-22**, 63 (1975).
26. G. W. Cullen, J. F. Corboy, and R. T. Smith, *J. Cryst. Growth*, **31**, 274 (1975).
27. C. Kühl, H. Schlötterer, and F. Schwidefsky, *This Journal*, **123**, 97 (1976).
28. M. S. Abrahams, C. J. Buiocchi, R. T. Smith, J. F. Corboy, J. Blanc, and G. W. Cullen, *J. Appl. Phys.*, **47**, 5139 (1976).
29. J. Blanc and M. S. Abrahams, *ibid.*, **47**, 5151 (1976).
30. M. S. Abrahams, C. J. Buiocchi, G. W. Cullen, and J. F. Coroby, *Appl. Phys. Lett.*, **28**, 275 (1976).
31. M. T. Duffy and P. J. Zanzucchi, Abstract 171, p. 460, The Electrochemical Society Extended Abstracts, Vol. 76-2, Fall Meeting, Las Vegas, Nevada, Oct. 17-22, 1976.
32. E. Preuss, Abstract 173, p. 465, The Electrochemical Society Extended Abstracts, Vol. 76-2, Fall Meeting, Las Vegas, Nevada, Oct. 17-22, 1976.
33. E. Preuss and H. Schlötterer, Abstract 178, p. 476, The Electrochemical Society Extended Abstracts, Vol. 76-2, Fall Meeting, Las Vegas, Nevada, Oct. 17-22, 1976.
34. M. Druminski, Abstract 183, p. 490, The Electrochemical Society Extended Abstracts, Vol. 76-2, Fall Meeting, Las Vegas, Nevada, Oct. 17-22, 1976.
35. A. M. Goodman and C. E. Weitzel, *IEEE Trans. Electron Devices*, **ed-24**, 215 (1977).

36. C. E. Weitzel and R. T. Smith, *This Journal*, **124**, 1080 (1977).
37. A. C. Ipri and J. C. Sarace, *IEEE J. Solid-State Circuits*, **sc-11**, 325 (1975).
38. A. S. Grove, "Physics and Technology of Semiconductor Devices," p. 326, J. Wiley and Sons Inc. New York (1967).
39. A. C. Ipri, *J. Appl. Phys.*, **43**, 2770 (1972).
40. S. T. Hsu and J. H. Scott, *RCA Rev.*, **36**, 240 (1975).
41. K. Lehovec and S. Lin, *J. Appl. Phys.*, **47**, 2088 (1976).

Optical Monitoring of the Etching of SiO_2 and Si_3N_4 on Si by the Use of Grating Test Patterns

H. P. Kleinknecht and H. Meier

Laboratories RCA Limited, CH-8048 Zurich, Switzerland

ABSTRACT

An optical technique is described which monitors both the etch depth and the amount of lateral underetching during the etching process. This technique applies to wet chemical etching as well as to plasma etching. For this purpose a test pattern containing one or more diffraction gratings is included on the mask, which is used to define the particular etching step. During the etching process a laser beam is aimed at this test pattern on the Si wafer and the reflected first-order diffraction intensities are monitored. As the etching progresses and the grating profile deepens, the diffracted intensity goes through oscillations which give an in-process indication of etch depth and etch rate. In the wet process the complete underetching underneath the photoresist bars of the grating is signaled by a drastic drop in the diffraction intensity. The simultaneous monitoring of a number of gratings with different bar widths permits one to follow the underetching in fine steps.

In silicon devices and integrated circuits fabrication many processing steps involve etching of SiO_2 and Si_3N_4 layers on Si through photoresist patterns. The lateral dimensions and the profiles of the patterns etched into the layers depend to some degree on the amount of underetching or undercutting in lateral direction underneath the photoresist mask. In many cases this undercutting is undesirable because it reduces the edge definition. In other cases a certain amount of undercutting is desirable for a sloped, rounded edge of the layer which is required in order to ensure continuity of the metallization stripes at the edge. In any case it is necessary to have control over the amount of underetching, and it is desirable to have in-process control over this parameter.

One technique, which reduces undercutting, is plasma etching (1). Unfortunately, in contrast to wet etching, the plasma-etching process does not stop completely when the SiO_2 has been removed, but it continues to etch into the silicon. This problem has been addressed by Heinecke (2), who has obtained a ratio of etch rates of 10:1 in favor of SiO_2. However, with etch rates being very much dependent on rf power, temperature, flow rate, and pressure (3, 4), one still would like to monitor the etch depth *in situ*.

Poulsen and Smith (5) have described an endpoint detection system which operates on the change of the spectral emission from the plasma during the plasma etching process. Konnerth and Dill (6) have used a computed-controlled spectrophotometer for measuring the thickness of glass and SiO_2 layers during etching and of photoresist during development. Van der Meulen and Hien (7) have constructed an automated ellipsometer for *in situ* measurement of dielectric layers at high temperature.

This paper describes a technique for in-process monitoring of the etching which is probably cheaper and more flexible than the systems quoted above and which has been shown to work for wet chemical etching as well as for plasma etching of SiO_2 and Si_3N_4 layers on Si wafers. In addition to the etch depth, this technique also monitors the amount of underetching which, to the knowledge of the authors, has not been done before. The new method uses test patterns in the form of diffraction gratings which can be arranged in a "knock-out" area on the normal photomask used for the delineation of the particular etching step to be controlled. Such gratings can be monitored during the etching process by reflection of a laser beam which results in a diffraction pattern. The intensities of the diffraction orders can give information about the profile of the grating, in particular on the etch depth, etch rate, and undercutting.

Key words: wet etching, plasma etching, etch depth, etch rate, underetching.

Figure 1 shows in a schematic way what can be expected to happen if, for instance, a SiO_2 layer is etched in HF through a fine photoresist grating pattern: As the etching progresses, the thickness, h, of the SiO_2 layer will decrease. This will cause the phase difference of the light reflected from the photoresist bars and from the SiO_2 to change. As a result the diffracted intensity will oscillate. This oscillation will stop when the etch has reached the SiO_2-Si interface. At the same time the etching will progress laterally. As soon as this lateral underetching has gone as far as half the width of the photoresist bars ($u \geq a/2$), the grating bars will start to shift and finally fall off. This will destroy the periodicity of the grating, and as a consequence the diffraction pattern, *e.g.*, the first order, will decrease in intensity.

Exploratory Tests with Wet Etching

In order to test this, a number of polished silicon wafers were covered with a SiO_2 layer of 0.94 μm thickness (as measured by ellipsometry), coated with photoresist and exposed through a mask containing 1.5×3 mm^2 areas with a grating-like parallel bar pattern of a periodicity of 10.2 μm and a width of the bars of $a = 3.0$ μm.

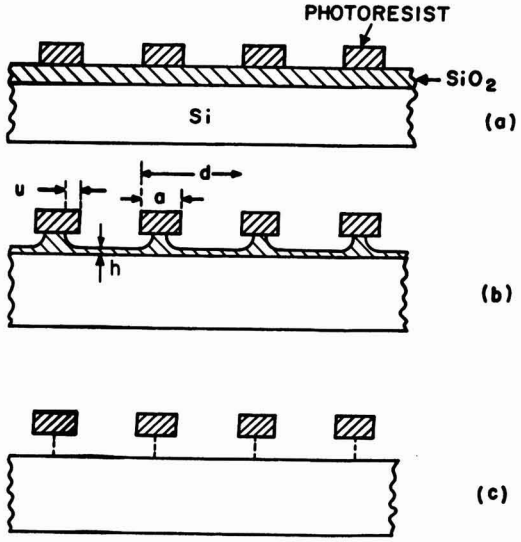

Fig. 1. Etching of a grating test pattern

Samples cleaved from these wafers were mounted on a Teflon holder which could be immersed into a Teflon etch container provided with a window of transparent acrylic sheet. The optical setup is described in Fig. 2. The beam of a He-Ne laser ($\lambda = 6328$Å) is chopped and aimed approximately perpendicular at the grating area of the sample. During the etching, which was done in buffered HF, the intensity, I_1, of the first-order diffraction beam was measured with a silicon PIN diode and a lock-in amplifier.

Figure 3 shows the recorder curves for three consecutive experiments. One observes the expected oscillations which stop after 5.5 min, indicating that the etching has reached the Si-SiO_2 interface. After about 7 min there is the sharp decrease which indicates an undercutting of $u = a/2 = 1.5$ μm. This interpretation was confirmed by microscopic inspection of the samples after the etching cycle.

Analysis of the Diffraction Intensity

For a quantitative interpretation of the oscillations of the diffracted intensity *vs.* time one has to use diffraction theory, which is relatively simple for the Fraunhofer regime only. The diffracted intensities of the 10 μm grating were measured for up to 12 orders with the incident beam polarized parallel and perpendicular to the grating lines. No significant difference was observed, which was taken as a justification to use the Fraunhofer integral (8). One can write the diffracted amplitude, U, for the case of a square aperture as

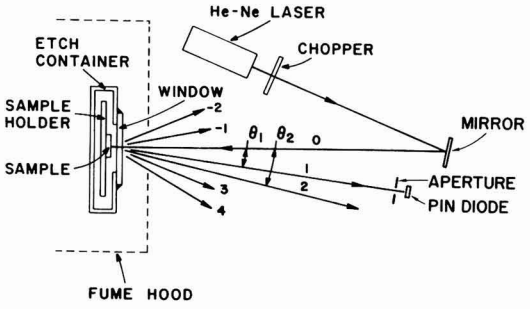

Fig. 2. First experimental set-up

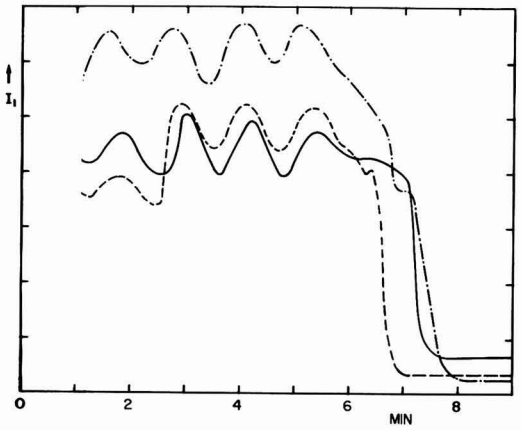

Fig. 3. First-order intensities *vs.* time of three samples with 10 μm gratings measured during wet etching.

$$U(\zeta) \propto \frac{e^{i\zeta N} - 1}{e^{i\zeta} - 1} \int_0^d r(x) e^{-i\zeta \frac{x}{d}} dx \qquad [1]$$

Here N is the total number of grating lines, d the grating constant, and

$$\zeta \equiv \frac{2\pi}{\lambda} d \sin\Theta \qquad [2]$$

Θ is the angle of diffraction (see Fig. 2). $r(x)$ is the complex reflectivity as a function of the coordinate x running perpendicular to the grating bars in the plane of the grating. The analysis will be restricted to a rectangular grating profile as shown in Fig. 4. Fortunately, as will be shown below, this will be good enough for our purpose. For this case the reflectivity, $r(x)$, can be taken to be constant across the grating bars ($= r_a$) and across the spaces in between ($= r_b$). If ϕ is the phase difference between the two reflectivities, one has

$$r(x) = \begin{cases} r_a \equiv |r_a| & i(o < x < a) \\ r_b \equiv |r_b| \exp(i\phi); & (a < x < d) \end{cases} \qquad [3]$$

where $|r_a|$, $|r_b|$ and ϕ are independent of x.

On inserting Eq. [3] into Eq. [1] the intensity $I(\zeta) = |U|^2$ can be calculated. $I(\zeta)$ is large for $\zeta = m \cdot 2\pi$ only, *i.e.*, for the directions of the diffraction orders (order number m), namely

$$I(m) \propto \frac{\sin^2\left(m\pi \frac{a}{d}\right)}{m^2} [|r_a|^2 + |r_b|^2 - 2|r_a||r_b| \cos\phi] \qquad [4]$$

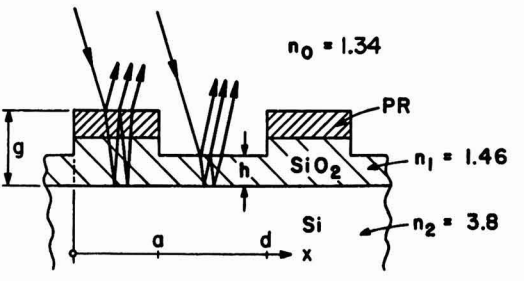

Fig. 4. Rectangular grating profile used for calculating diffraction intensities.

Note that the bracket does not contain the order number, m. In order to test the validity of the rectangular profile approximation, the intensities of the first 10 diffraction orders were measured quantitatively on several samples and plotted as a function of the order number, m. Figure 5 gives such a plot. The curve is a computer fit to the measured points according to Eq. [4]. As can be seen, the rectangular approximation is justified for the first three orders which is good enough for the present work since only the first-order intensities are used.

The reflectivities r_a and r_b in Eq. [4] depend on the refractive indexes and the thicknesses of the four media: etching solution, photoresist, SiO_2, and Si. For monitoring the SiO_2 thickness, h, in the region $a < x < d$ during etching, one only needs an expression for r as a function of h. Since in the practical case the photoresist is not etched, r_a can be considered to be constant. Using, for instance, Ref. (9) one gets for normal incidence

$$r_b = \frac{r_1 + r_2 \exp(i2\beta)}{1 + r_1 r_2 \exp(i2\beta)} \exp(i2\gamma) \qquad [5]$$

with

$$r_1 = \frac{n_0 - n_1}{n_0 + n_1}; \quad r_2 = \frac{n_1 - n_2}{n_1 + n_2} \qquad [6]$$

and

$$\beta = \frac{2\pi}{\lambda} n_1 h; \quad \gamma = \frac{2\pi}{\lambda} n_0 (g - h) \qquad [7]$$

n_0 is the refractive index of the etching solution (buffered HF), which we measured to be 1.34; $n_1 = 1.46$ for SiO_2; $n_2 = 3.8$ for Si at $\lambda = 6328$Å. The factor $\exp(i2\gamma)$ in Eq. [5] is due to profile depth, $g - h$ (see Fig. 4). From this one can calculate $|r_b|$, ϕ, and the bracket of Eq. [4], which is proportional to the intensity. The result is plotted in Fig. 6 for three photoresist thicknesses, *i.e.*, three different values of r_a. As can be seen, the main oscillations are the same for all three curves, having a period of about $\Delta h = 0.22$ μm.

Knowing this period, one can by comparison of Fig. 3 and 6 assign to each point in time an oxide thickness, h. We notice that within 5.5 min we go through a total of 4.5 periods of 0.22 μm each, which gives a layer thickness of 0.99 μm in good agreement with the ellipsometric value of 0.94 μm and an etch rate of 0.18 μm/min.

Plasma Etching of SiO_2 Layers

The technique of monitoring the etch depth and the etch rate described above was also tried out with plasma etching. The etching apparatus used was a commercial system: Model "PDE/PDS-301" built by the LFE Corporation. The etching chamber of this system has a plane front window which is suitable for the optical tests. The samples and the optical equipment were the same as described above.

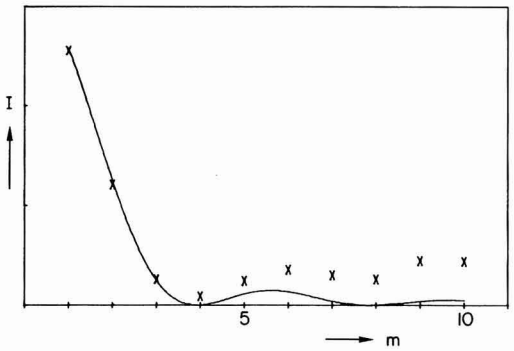

Fig. 5. Intensity vs. order number of a sample containing a 10 μm photoresist grating on Si + SiO_2. The curve is a fit to Eq. [4].

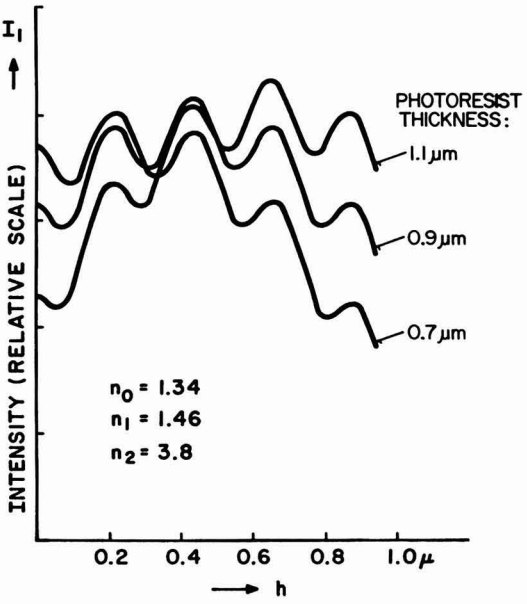

Fig. 6. Calculated first-order intensity as a function of the SiO_2 thickness, h, for three different photoresist thicknesses.

Figure 7 gives recordings of the first-order intensities for three runs with different flow rates of the reactive gas. Aside from the shoulders and small maxima in the top curve, which are very likely due to sputter abrasion of the photoresist, one can see that the spacing of the maxima decreases, *i.e.*, the etch rate increases, with increasing gas flow. In addition, the spacing of the maxima decreases, as the etching goes on; very likely an increase of etch rate due to heating (3).

It has to be pointed out that similar reflectivity oscillations can be obtained by interference in specular

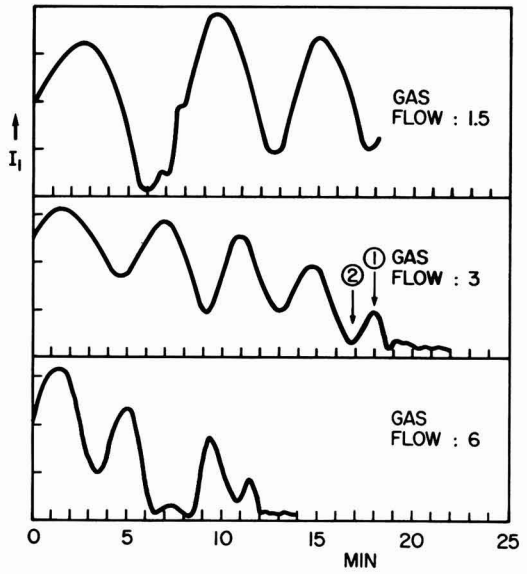

Fig. 7. First-order intensities vs. time of three samples measured during plasma etching.

reflection on uniform SiO_2 layers without gratings. However, the practical disadvantage of the specular reflection for monitoring IC processing is that it requires a uniform area on the sample which is as large as the laser beam. If a large part of the beam is reflected from other areas of the structure containing photoresist, other oxides, etc., this reflection will largely go in the same specular direction and distort or bury the wanted signal. The grating gives the possibility to use test areas on the wafer, which can be smaller than the laser beam. The detector properly positioned as in Fig. 2 will receive nearly no other signal but the one coming from the grating. All light reflected, diffracted, and scattered from other structures on the wafer will go mostly in other directions.

For a quantitative evaluation one again has to go through the analysis which was indicated above for wet etching with the only difference that now the refractive index of the surrounding medium is $n_0 = 1$ instead of 1.34. The results of these calculations are strong oscillations in I_1 with a period of 0.217 μm.

The middle and bottom curves in Fig. 7 show 5 maxima. The last maximum occurs after 4.4 periods giving a total oxide thickness of $4.4 \times 0.217 = 0.95$ μm in good agreement with the ellipsometric thickness measurement. After the 5th maximum the intensity drops to a low constant value. Microscopic inspection after that showed that the spaces not covered by photoresist were heavily pitted and showed a mat silvery gray color characteristic of bare Si.

In several etching experiments the process was interrupted at the top of the 5th maximum (arrow 1 in Fig. 7). The microscope then showed that the Si was bare and very little pitting was present. For other samples etching was stopped at the 4th minimum (arrow 2 in Fig. 7) leaving a residual SiO_2 layer of uniform blue color indicating a thickness of 700-800Å. These experiments prove that satisfactory control can be achieved by the monitoring process with the possibility to stop the etching at a given etch depth regardless of the etch rate, *i.e.*, independent of the particular conditions.

Nevertheless, this technique permits very rapid and simple measurement of the etch rates as the process goes on. As a demonstration of this we summarize in Fig. 8 these preliminary plasma etch data in terms of the etch rates in SiO_2 as a function of gas flow for two rf power levels. The etch rate at the beginning of the process (initial) is lower than the final value because of heating.

Plasma Etching of Si_3N_4 and SiO_2

The problem of defining patterns and etching windows into Si_3N_4-SiO_2 double layers is particularly suited for plasma etching. In this case wet chemical etching is rather complicated and troublesome. Therefore the optical monitoring technique was tried out for this case too, using samples with 1000Å of Si_3N_4 on top of 1 μm of SiO_2. Figure 9 gives one of the I_1 *vs* t curves taken during the process. In the first 5 min a

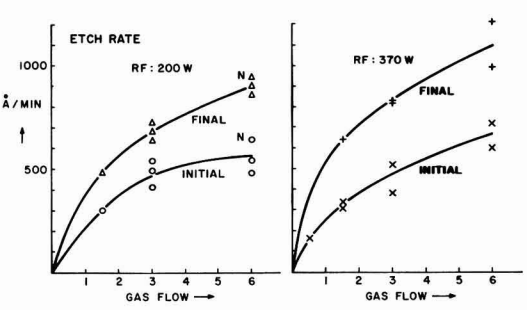

Fig. 8. Etch rates *vs.* gas flow in plasma etching

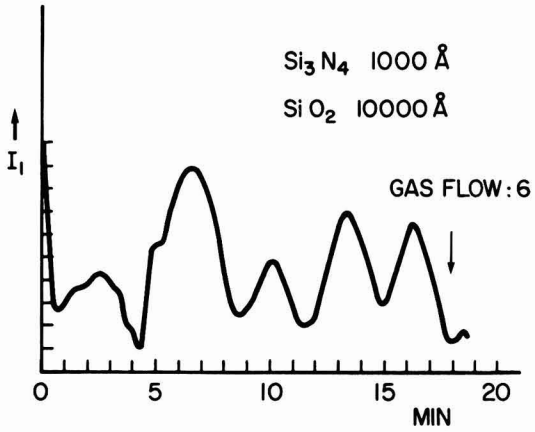

Fig. 9. First-order intensity *vs.* time during plasma etching of a Si_3N_4-SiO_2 double layer.

rather irregular pattern is seen which is interpreted as the etching through Si_3N_4 indicating an etch rate of 200 Å/min. After that the curve looks similar to the other SiO_2 etching curves. The etch rates obtained from the curve fit quite well with the other SiO_2 etch rate data. They are included in Fig. 8 with the points marked "N".

With the particular sample in Fig. 9 the etching was terminated after the 5th oxide maximum as shown. The microscope showed bare Si and pitting. In another run with a similar sample the etching was interrupted at the 4th minimum (arrow in Fig. 9). This left a blue, uniform 700Å thick SiO_2 layer. This thin SiO_2 layer can now easily be removed with dilute HF without the danger of undercutting.

Refinement of the Technique for Wet Etching

Encouraged by these exploratory experiments, we have proceeded to refine the technique to bring it closer to usefulness in the factory. In order to obtain a finer measure for the degree of underetching a test pattern containing 4 gratings with 4 different periodicities, $d = 10$, 6, 4, and 3 μm, and bar width $a \sim d/2$, was designed, which is sketched at the top of Fig. 10. The dimension, 1×1 mm, is small enough to fit into a "knock-out" area of the wafer. The four gratings are rotated by 45° with respect to one another. This results in 4 diffraction patterns which also are rotated by 45°, making the separation of the 4 signals easier. The bottom part of Fig. 10 shows the diffraction reflexes as they appear on a screen if the laser beam strikes the test pattern with normal incidence.

By positioning four Si detectors at the locations of the four first orders, one can simultaneously monitor the underetching of the 4 gratings. With $a = d/2$ one will expect the fall-off of the 4 signals for a lateral underetching, u, equal to 0.75, 1.0, 1.5, and 2.5 μm, respectively.

Figure 11 gives the traces of the signal from 3 of those 4 gratings recorded simultaneously during one etch run. One sees the oscillations, simultaneous in all 3 traces, and the fall-off successively for the 3, 4, and 6 μm gratings.

A large number of etching runs in buffered hydrofluoric acid were made. No special care was taken to keep the etch rate constant by temperature control or by always using fresh solutions, etc. This was not done, because the objective of the optical test is to obtain the right amount of etching in the presence of changing etch rates. In spite of these changes the characteristic behavior of the four first-order diffraction intensities of the 10, 6, 4, and 3 μm gratings as shown on the recorder were always the same. Another example of

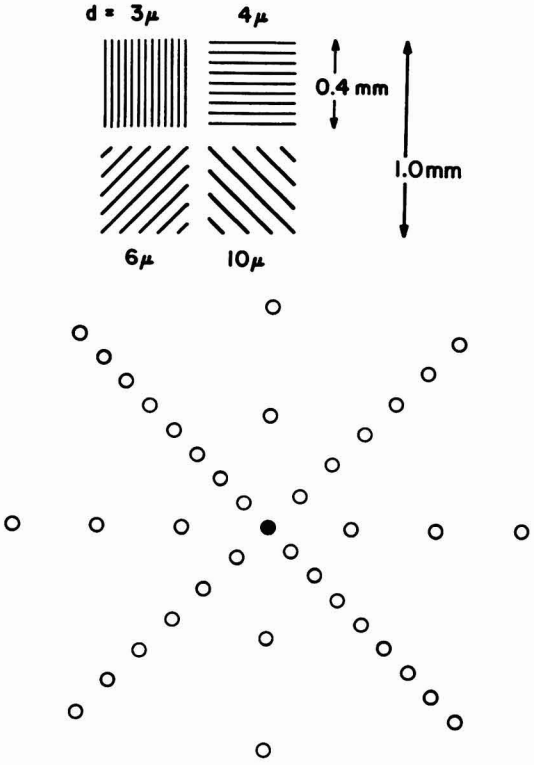

Fig. 10. Schematic drawing of the 4 grating test pattern (top) and the corresponding diffraction pattern.

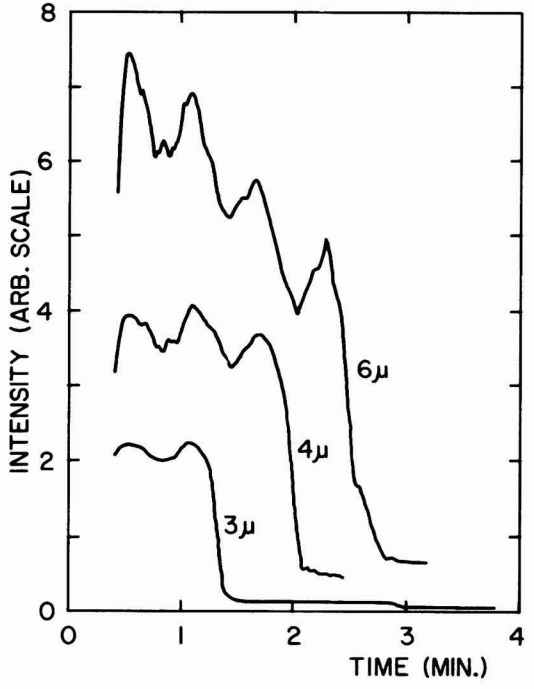

Fig. 11. Recorder trace of an etch run with first-order intensities for 3 gratings simultaneously.

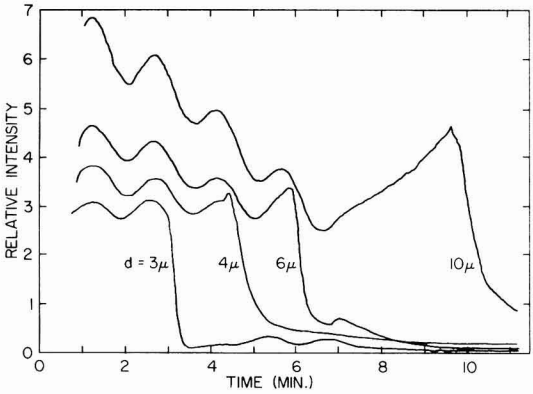

Fig. 12. Recorder trace of a typical etch run: first-order intensities of the four gratings (d = 3, 4, 6, and 10 μm) vs. time.

such a recorder trace for all 4 gratings is shown in Fig. 12. Again, all four signals oscillate in synchronism, each period corresponding to a decrease in h of about 0.22 μm. After about 2.2 periods, *i.e.*, after 0.48 μm of normal etching, the 3 μm grating starts to fall off. This indicates that in this case lateral undercutting has penetrated somewhat faster (0.75 μm) than the normal etching. After 3.3 periods (0.7 μm of normal etching) the 4 μm grating starts to fall off, indicating an undercutting of 1.0 μm, and after 4.1 periods (0.9 μm) the fall-off of the 6 μm grating starts, signaling an undercutting of 1.5 μm. The oscillations of the signal from the 10 μm grating stop after about 5 periods corresponding to the SiO_2 thickness of 1.1 μm. From then on the 10 μm signal rises smoothly until it shows a fall-off after 16 min, at which point the lateral etching has reached about 2.5 μm.

As can be seen from this plot, the normal etch rate is rather uniformly 0.16 μm/min and the lateral undercutting is about 1.5 times as fast as the normal etching for all four gratings. These figures may be different for other etch conditions. However, in any case a recording of the type of Fig. 12 gives the etch rate, and most important, signals the exact time at which the lateral underetching has reached a certain extent, namely, for the test pattern used here, 0.75, 1.0, 1.5, and 2.5 μm.

Finally Fig. 13 shows the equipment used for these last experiments. The test sample, T, is placed in a suitable etch container in the fume hood, H. This sample can be the end wafer of a whole lot of wafers being etched together. The beam of the laser, L, (λ = 0.6328 μm, 1 mW) goes through the chopper, C, and is di-

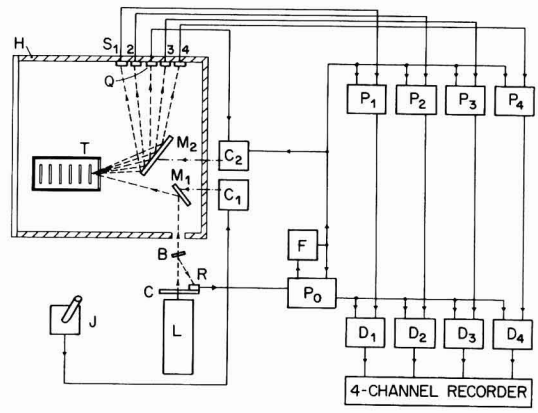

Fig. 13. Block diagram of the test set

rected by the mirror, M_1, at the test pattern on the sample. The mirror, M_2, directs the reflected diffraction pattern at the four silicon solar cells, S_1, S_2, S_3, and S_4, which are connected to the four phase-sensitive amplifiers P_1, P_2, P_3, and P_4. The signal coming from the reference detector, R, is amplified in P_0 and processed in F to be used as a frequency reference. The amplifiers P_1-P_4 are sample-and-hold type operational amplifiers, which make the system insensitive to room light. In order to be independent of any changes in the incident laser intensity, the reference signal is fed together with the signals from P_1 to P_4 into the divider circuits D_1, D_2, D_3, and D_4.

During the first experiments it was recognized that it was desirable to adjust the mirror, M_1, very quickly and conveniently in order to "find" the test pattern on the wafer during a few seconds after immersion into the etch bath. For this reason, the mirror, M_1, was equipped with servo motors for remote control of the two tilt angles, which are operated from the joy stick, J, via the servo circuit, C_1.

The mirror, M_2, is equipped with a similar servo system in order to make sure that, regardless of the orientation of M_1 and of the sample, the diffraction pattern always strikes the solar cells S_1-S_4. This servo system is controlled by the signal of a quadrant sensor, Q, which senses the position of zero-order diffracted beam.

Conclusion

Test patterns in the form of diffraction gratings offer a simple technique for the in-process control of the etching of patterns into SiO_2 through photoresist masks both for wet etching as well as for plasma etching. In the case of the wet etching the time at which the undercutting has reached a given amount can be determined by a pronounced drop of the diffraction signal. A test pattern containing several gratings of different line widths appears to be promising for the tailoring of a desired amount of undercutting. In plasma etching the grating technique gives reliable control of the etch depth even if the SiO_2 is covered with a Si_3N_4 layer.

The theory of this process as well as detailed information about the equipment has been given.

Acknowledgments

The authors would like to thank J. Gaylord of Somerville, New Jersey and N. Goldsmith and W. Schneider of Princeton, New Jersey for help and stimulation in the early part of the work, and A. Oberholzer for experimental assistance.

Manuscript submitted Nov. 14, 1977; revised manuscript received Dec. 28, 1977.

Any discussion of this paper will appear in a Discussion Section to be publisned in the December 1978 JOURNAL. All discussions for the December 1978 Discussion Section should be submitted by Aug. 1, 1978.

Publication costs of this article were assisted by Laboratories RCA Limited.

LIST OF SYMBOLS

a	width of grating lines
d	grating constant
ζ	see Eq. [2]
ϕ	phase of reflectivity r_b
g	see Fig. 4
h	thickness of SiO_2
I	intensity
I_1	intensity of first order
λ	laser wavelength
m	order number
$n_{0,1,2}$	refractive indexes
N	total number of grating lines
$r(x)$, $r_{a,b}$, r_1, r_2	reflectivities
Θ	diffraction angle
u	width of underetching
U	diffracted amplitude
x	coordinate in grating plane perpendicular to the grating lines

REFERENCES

1. R. G. Poulsen, *J. Vac. Sci. Technol.*, **14**, 266 (1977).
2. R. A. H. Heinecke, *Solid-State Electron.*, **19**, 1039 (1976).
3. R. G. Poulsen and M. Brochu, "Etching," H. G. Hughes and M. J. Rand, Editors, p. 111, The Electrochemical Society Softbound Symposium Series, Princeton, N.J. (1976).
4. R. Kumar, C. Ladas, and G. Hudson, *Solid State Technol.*, **19**, 54 (1976).
5. R. G. Poulsen and G. M. Smith in, "Semiconductor Silicon 1977," H. R. Huff and E. Sirtl, Editors, p. 1058, The Electrochemical Society Softbound Symposium Series, Princeton, N.J. (1977).
6. K. L. Konnerth and F. H. Dill, *IEEE Trans.*, **ed-22**, 452 (1975).
7. Y. J. van der Meulen and N. C. Hien, *J. Opt. Soc. Am.*, **64**, 804 (1974).
8. M. Born and E. Wolf "Principles of Optics," p. 401-403, Pergamon Press, Inc., Elmsford, N.Y. (1965).
9. M. Born and E. Wolf, *ibid.*, pp. 61 and 62 (1965).

Oxidation of Copper in CO_2 at 800°-1000°C

W. J. Tomlinson and J. Yates[1]

Department of Applied Sciences, Lanchester Polytechnic, Eastlands, Rugby, United Kingdom

ABSTRACT

The oxidation of spectrographically pure copper in carbon dioxide has been studied at 800°-1000°C. An initial linear oxidation rate changed gradually to a second, lower, linear oxidation rate. During the first linear stage the surface was covered with a feathery pattern of small dendrites of unknown structure which were replaced progressively with more massive crystallites of Cu_2O associated with the second linear stage. The thickness of the Cu_2O layer at 1000°C when the surface was fully covered was 14 μm. Surface finish, preannealing, and gas flow rate in the range 0.1-2.0 cm sec^{-1} had no effect on the reaction. It is reasoned that the rate-controlling process was the decomposition of CO_2 to form chemisorbed oxygen which was influenced by a change of catalytic activity on the surfaces of the structures associated with the two linear kinetic curves.

Oxidation is a multistep process. The early stages involve oxygen dissolution in the metal and nucleation and growth of the oxide. Once the surface is covered with a continuous layer of oxide, for oxidation to continue the following steps for the reactants must occur: (*i*) transport within the gas, (*ii*) reaction at the gas/

[1] Chester Education Department, Chester, United Kingdom.
Key words: linear kinetics, nucleation, Cu_2O.

oxide interface, (*iii*) transport within the oxide, and (*iv*) reaction at the metal/oxide interface. One step is usually rate controlling, and the reaction is reflected in the kinetics. Parabolic oxidation kinetics typically indicates that diffusion within the oxide layer is rate controlling. Linear kinetics are relatively uncommon and imply that the slow step is a phase boundary reaction; provided the reaction products form a uniform dense layer they frequently change to a parabolic form as the amount of oxidation increases.

Linear oxidation in CO_2 or CO_2-CO mixtures has been observed with Fe by Hauffe and Pfeiffer (1) and other workers (2-5), with Co (6), Mn (7), Ni (8), and with Cu (9, 10). Hauffe and Pfeiffer found that the linear oxidation rate of Fe in CO_2/CO mixtures is proportional to $(P_{CO_2}/P_{CO})^{2/3}$, and the rate depended solely on the decomposition of CO_2 to form chemisorbed oxygen. Smeltzer (2) interpreted his linear oxidation rates of Fe in CO_2 as incorporation of chemisorbed oxygen into FeO at temperatures below 910°C and both dissociation of CO_2 and incorporation into FeO above 910°C. C. Wagner (11) derived a formula which indicated that the linear oxidation rate should depend not only on the CO_2/CO ratio but also on the sum of the partial pressures of CO_2 and CO. This was confirmed by Pettit *et al.* (4). Swaroop and J. B. Wagner studied the oxidation of Cu in CO_2/CO mixtures at 1000°C (10). Two linear curves were observed with a distinct change occurring at an oxide thickness of 0.4-0.6 μm. From the pressure dependence of the first linear rate constant, it was inferred that the reaction mechanism did not involve chemisorption.

The present work investigates the oxidation of Cu in CO_2 at 800°-1000°C. The equilibrium pressures of oxygen with CO_2, Cu_2O, and CuO are shown in Table I. From these data CuO is not expected to form on Cu oxidized in CO_2, and it is seen that the P_{O_2} from dissociation of CO_2 is only slightly greater than that from dissociation of Cu_2O. However, these data are for bulk substances at equilibrium, and during oxidation the interfacial energies and dynamic flow conditions will alter the thermodynamic data and possibly the catalytic effects due to the electronic/atomic defect equilibria being altered. The early stages of oxidation are usually very sensitive to surface structure and cleanliness, and so the purity of the Cu and CO_2, and the surface finish are important. Transport in the gas may also have an influence because of the low pressure of oxygen in CO_2.

Experimental

The Cu was spectrographically pure with maximum impurities (ppm): Ag 10, Pb 2, Si 1, Ca < 1, Mg < 1, Fe < 1. It was supplied by Johnson Matthey and Company Limited as 0.25 mm thick cold-worked sheet and cut into coupons about 4 cm^2 surface area with a hole for a Pt suspension wire. Four surface finishes were used. In the as-received condition the specimen was simply degreased in acetone before exposure. Mechanical polishing consisted of polishing to 6/0 grade paper then washing in turn with distilled water and acetone. The bath used for chemical polishing (12) consisted of 55 v/o HNO_3 (density 1.75), 25 v/o glacial acetic acid, and 20 v/o H_3PO_4 (density 1.40), and the specimen was immersed for 1-2 min at 55°C and then washed as above. The bath for electrochemical polishing was 33 cm^3 HNO_3 and 67 cm^3 CH_3OH cooled to 0°C and operated at 3V and 1 A cm^{-2} for 30 sec. After polishing the specimen was washed as above.

The quartz-spring thermobalance was similar to one used previously (13). The main difference was a magnetic winch which allowed insertion and removal of a specimen to and from the hot zone while under vacuum or CO_2. Temperature control was within ± 2°C and the weight gain could be measured to within ± 0.03 mg cm^{-2}. The operating procedure was as used previously (13), but in addition the oxidized specimen could be quickly quenched in cool CO_2.

Special analytical grade CO_2 supplied by Distillers Company Limited was used. It had maximum impurities : residual gases (non-KOH soluble) < 25 ppm (by volume), water < 50 ppm (by weight), and other gases < 5 ppm (by volume). The water content was further reduced by passing through silica gel and then phosphorus pentoxide. Gas flow was measured by a rotameter. Gas pressure was 1 atm.

Standard x-ray diffraction techniques were used to examine the surface products.

Table I. Equilibrium pressures of oxygen at 1000°C [Ref. (10)]

Reaction	P_{O_2} (atm)
$CO_2 = CO + \frac{1}{2} O_2$	1.2×10^{-5}
$Cu_2O = 2Cu + \frac{1}{2} O_2$	5.6×10^{-7}
$2CuO = Cu_2O + \frac{1}{2} O_2$	1.4×10^{-1}

Results

Figure 1 shows the rate curves for the oxidation of chemically polished Cu in CO_2 flowing at 0.2 cm sec^{-1}. At 900° and 1000°C there were two linear curves with the gradient of the first curve greater than that of the second, and an intermediate region which is shown dashed. At 800°C there was only one linear curve. The amount of oxidation was small, and in such cases surface finish, gas speed, and preannealing might be particularly important so oxidation data were obtained under the following conditions: (*i*) Cu chemically, mechanically, and electrolytically polished, and in the as-received condition, was oxidized at 800°-1000° in CO_2 flowing at 0.2 cm sec^{-1}; (*ii*) chemically polished Cu was oxidized at 1000°C in CO_2 flowing at 0.1-2.0 cm sec^{-1}; and (*iii*) Cu was preannealed at 1000°C and 10^{-5} mm Hg, chemically or electrolytically polished, then oxidized at 1000°C in CO_2 flowing at 0.2 cm sec^{-1}. In all cases the results were of the same form as Fig. 1. All these data are summarized in Tables II, III, and IV.

In Fig. 1 the points in the dashed region could belong to either curve. This represents a gradual transition from the first linear curve to that of the second. The extrapolated intersection coordinates of the lines were used to characterize the change, and these are reported with the other kinetic data in Tables II, III, and IV. It is seen that at 900° and 1000°C the transition

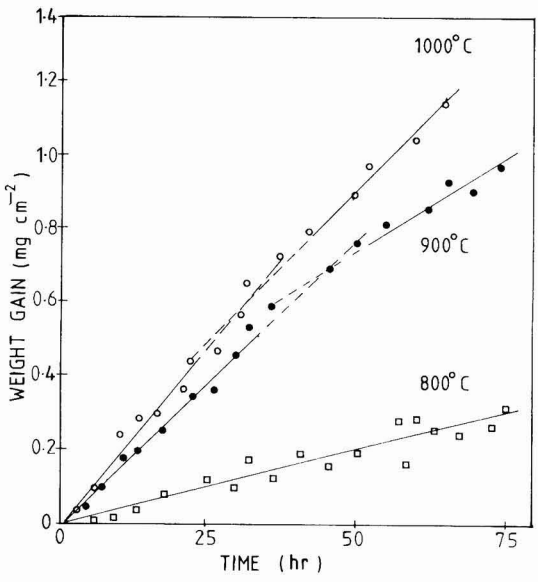

Fig. 1. The oxidation of chemically polished Cu in CO_2. Gas speed 0.2 cm sec.

Table II. Linear rate constants and transition coordinates for Cu with various surface finishes oxidized in CO_2 at various temperatures. Gas speed 0.2 cm sec^{-1}.

Surface finish	Temperature (°C)	Rate constants ($g\ cm^{-2}\ sec^{-1} \times 10^{-9}$) K_{L_1}	K_{L_2}	Transition coordinates Wt. gain ($mg\ cm^{-2}$)	Time (hr)
Chemical	1000	5.33	4.72	0.6	31
Chemical	1000	6.11	4.53	0.8	36
Chemical	900	4.32	2.89	0.7	45
Chemical	900	4.39	3.19	0.7	44
Chemical	800	1.11	—	—	—
Mechanical	1000	6.83	4.53	0.8	33
Mechanical	1000	6.28	4.67	0.7	31
Mechanical	900	4.00	3.31	0.6	42
Mechanical	900	4.31	3.33	0.6	39
Mechanical	800	0.94	—	—	—
Electrochemical	1000	5.31	4.03	0.6	31
Electrochemical	1000	5.28	4.06	0.7	37
Electrochemical	900	3.28	2.78	0.6	51
Electrochemical	900	3.61	2.94	0.6	46
Electrochemical	800	0.75	—	—	—
As-received	1000	6.33	4.03	0.70	31
As-received	1000	6.08	4.50	0.70	32
As-received	900	4.58	3.89	0.60	36
As-received	900	4.39	3.44	0.60	38
As-received	800	1.00	—	—	—

Table III. The effect of gas speed on chemically polished Cu oxidized in CO_2 at 1000°C

Gas speed ($cm\ sec^{-1}$)	Rate constants ($g\ cm^{-2}\ sec^{-1} \times 10^{-9}$) K_{L_1}	K_{L_2}	Transition coordinates Wt. gain ($mg\ cm^{-2}$)	Time (hr)
0.1	5.31	4.64	0.7	37
0.5	5.00	4.42	0.6	33
1.0	5.33	4.50	0.7	36
2.0	5.06	3.86	0.6	33

Table IV. The effect of preannealing 12 hr at 10^{-5} Torr before oxidation in CO_2 at 1000°C. Gas speed 0.2 cm sec^{-1}.

Surface finish	Rate constants ($g\ cm^{-2}\ sec^{-1} \times 10^{-9}$) K_{L_1}	K_{L_2}	Transition coordinates Wt. gain ($mg\ cm^{-2}$)	Time (hr)
Chemical	5.28	3.89	0.7	37
Electrochemical	5.83	3.33	0.6	38

Table V. Average linear rate constants for Cu oxidized in CO_2

Temperature (°C)	K_{L_1} ($g\ cm^{-2}\ sec^{-1} \times 10^{-9}$) Mean	Std. dev.	Coef. variation	K_{L_2} ($g\ cm^{-2}\ sec^{-1} \times 10^{-9}$) Mean	Std. dev.	Coef. variation
1000	5.67	0.57	10.05	4.19	0.44	10.50
900	4.11	0.45	10.55	3.22	0.36	11.18
800	0.95	0.15	15.79	—	—	—

occurs at a critical weight gain of 0.6-0.7 mg cm^{-2} but at 800°C the total amount of oxidation was only 0.3 mg cm^{-2} so the transition was absent. An unexpected feature of the kinetic data is its insensitivity to changes in surface finish, preannealing, and gas speed in the range 0.1-0.2 cm sec^{-1}. Because of this insensitivity, all the data have been analyzed together, and the results are reported in Table V. The Arrhenius function of the first linear curve is shown in Fig. 2.

Specimens oxidized 72 hr at 900° and 1000°C were examined by x-ray diffraction powder techniques, and in back reflection after 40 and 72 hr at 1000 C and 72 hr at 800° and 900°C. The amount of reaction product at 800°C was too small to be detected. Cu_2O was observed in all other cases but no CuO was detected.

The surface was examined after oxidation at various times at 800°, 900°, and 1000°C. Figure 3 shows typical oxidized surfaces. There were two types of surface structures, one small, feathery, and acicular, and the other much larger, thicker, and more rounded. For convenience in this paper they will be called dendrites and crystallites, respectively. The crystallites were identified as Cu_2O, but the structure of the dendrites is uncertain. The formation of the surface products always followed the sequence: dendrites were nucleated

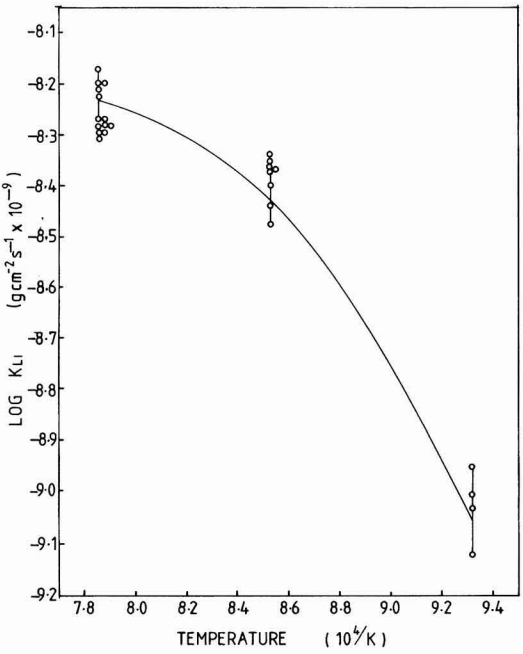

Fig. 2. The Arrhenius function of the first linear rate constant

(Fig. 3a) and spread rapidly over the whole surface (Fig. 3b), crystallites then nucleated on the dendrites, and further oxidation resulted in the growth of the crystallites (Fig. 3c) until the whole surface was covered (Fig. 3d). In Fig. 3 note that (a) is for oxidation at 800°C and the others for specimens oxidized at 1000°C. The reaction at 1000°C was so fast that it was not possible to record at 1000°C the stage shown in Fig. 3a for oxidation at 800°C. The times the structures appeared at each temperature are shown in Table VI where it is seen that the structures always appeared in the same sequence, but after longer times as the temperature was lowered. No detailed topographical studies were carried out but the crystal heights were estimated using the depth-of-focus of a microscope. Using a fine adjustment with a drum calibrated in micrometers, under oil immersion it was observed that for a given oxidation the crystallites were approximately the same height, and that at 1000°C their height was nearly the same for crystallites on specimens oxidized for 20 and 40 hr. The height of the dendrites was always very much less than the height of the crystallites. Figure 4 shows the cross section of the dendrites and crystallites formed on a specimen oxidized for 24 hr at 1000°C. The concave Cu surface clearly reflects the Cu used in the nucleation and growth of the oxide. The maximum thickness of the dendrites and crystallites shown are about 1-2 and 10 μm, respectively. Cu_2O has a density of 6.0 g cm^{-3} (14), so at 1000°C the Cu_2O film was about 14 μm thick when the surface was covered.

Discussion

The kinetic data summarized in Table V indicates good reproducibility for the rate constants in the two linear kinetic stages over the temperature range 800°-1000°C. Swaroop and Wagner (10) also observed at 1000°C two linear curves and the first one had rate constants in the range 6.1 to 8.93 $\times$ 10^{-9} g cm^{-2} sec^{-1}. This agrees well with the present, lower, values of 5.00-6.83 $\times$ 10^{-9} g cm^{-2} $sec.^{-1}$. However, the two linear curves of Swaroop and Wagner appear to make a sharp transition whereas in the present work the change was gradual over a large weight gain range.

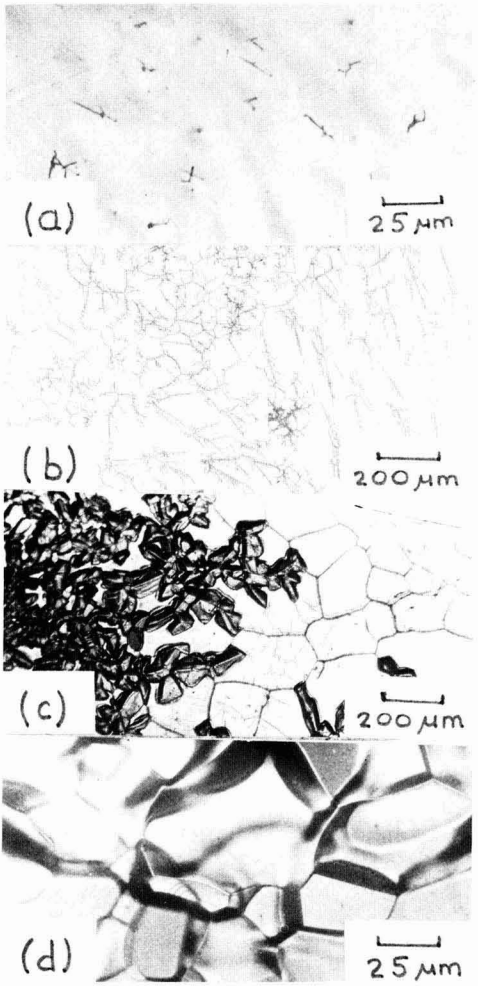

Fig. 3. Surface morphology of chemically polished Cu oxidized in CO_2. (a) 800°C, 72 hr; dendrites nucleated. (b) 1000°C, 10 min; dendrites cover the surface, a crystallite nucleating. (c) 1000°C, 20 hr; dendrites and crystallites. (d) 1000°C, 72 hr; surface covered with crystallites.

There is a direct relation between the kinetics and surface morphology. The kinetic transition co-ordinates are shown in Tables II, III, and IV, where it is seen that the change occurs at a critical amount of oxidation of 0.6-0.7 mg cm^{-2}, and in the time range 30-38 hr at 1000°C and 36-51 hr at 900°C. When compared with the surface morphologies, it is seen that the first linear kinetic curve occurs when mainly dendrites cover the surface, and the second linear curve is associated with the crystallites, and the gradual change in kinetics reflects the change in structure as the crystallites grow to cover the surface. Because the two gradients are so close, scatter in the data tends to mask the transition and so the change in kinetics cannot be defined precisely. A more appropriate equation describing the apparent dependence of the rate constant on surface features would be

$$\text{rate} = K_{L_1}(1 - f) + K_{L_2} f$$

where f is the fraction of the surface that is covered with crystallites.

Table VI. The surface morphology of chemically polished Cu oxidized in CO_2 flowing at 0.2 cm sec^{-1}

	Time oxidized (hr)			
°C	0.17	20	40	72
1000	D	DC	DC	C
900	D	DC	DC	DC
800	—	—	—	D

D = dendrites only.
DC = crystallites and dendrites present.
C = surface covered with crystallites.

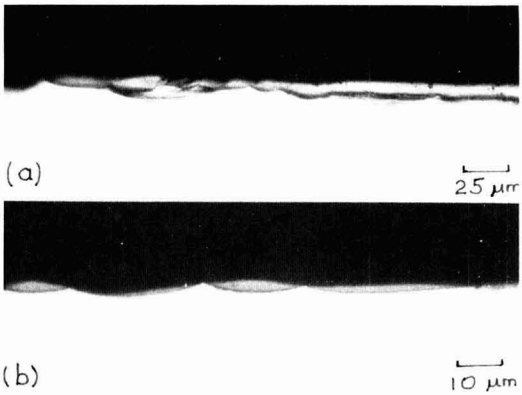

Fig. 4. Chemically polished Cu oxidized in CO_2 for 24 hr at 1000°C. Unetched. Cu at bottom. (a) Cross section of a crystallite about 10 μm thick. Note the concave Cu surface due to removal of Cu into the preexisting dendrites and separate crystallites before lateral growth formed the uniformly thick massive crystallite. (b) Cross section of dendrites in the intercrystalline regions. Note the concave Cu surface containing the oxide dendrites with a maximum thickness of 1-2 μm.

Linear oxidation kinetics reflect a phase boundary reaction, or a constant rate of supply of gas from the interior of the gas across a boundary layer of constant thickness. In the present case gas supply is not the rate-controlling process since the thickness of the boundary layer, and so the flux of gas reaching the surface, is a function of gas speed, and no effect of gas speed on the oxidation rate was detected. Moreover, if the gas supply was rate controlling, then there would be only one linear reaction rate corresponding to the gas supply, whereas two linear kinetic curves were observed. The insensitivity of the kinetics to surface finish and preannealing indicates that the rate-controlling process is also not at the metal/oxide interface. It appears from these considerations that reaction control is at the oxide/gas interface where the possible reactions are chemisorption and incorporation represented by the equations

$$CO_2(g) = CO(g) + O^-(\text{ads}) + h^{\cdot}$$

$$O^-(\text{ads}) = O_o^x + V_{Cu}'$$

with similar equations for O(ads) and O^{2-}(ads). Here the defect chemistry notation of Kröger and Vink (15) is used. The average activation energies of the first linear curve (Fig. 2) are of the order $E_{800\text{-}900} = 170$ kJ mol^{-1} and $E_{900\text{-}1000} = 50$ kJ mol^{-1} and while these have no detailed diagnostic value it is clear that they are within those typical of adsorption processes, and also they become less as the temperature is increased. Hauffe and Pfeiffer (1) have shown that the rate-controlling process during the oxidation of Fe in CO_2/CO mixtures is the decomposition of CO_2 on the surface to form chemisorbed O^-. Also Kobayashi and Wagner

have shown (16) that the catalytic activity of a surface depends not only on the composition of the gas phase, but also on the composition of the solid phase, in particular the concentration of electronic defects.

During the second linear stage the catalytic surface is clearly Cu_2O crystallites but during the first linear stage the surface structure is uncertain. While spread over the whole surface, the dendrites represent only a small fraction of the area. The Cu atoms in Cu_2O form a fcc lattice with oxygen atoms occupying one quarter of the tetrahedral sites (17). The linear misfit in the Cu_2O/Cu system is 18% (18), and it is probable that the dendrites are a distorted epitaxial form of Cu_2O. Considerable effort has been made in nucleation studies to identify the surface structures in between the nuclei but its nature is still largely conjectural. Rhead (19) assumed on the basis of known data that a thin layer exists which is intermediate between a chemisorbed layer and an oxide layer which is formed by place exchange, and the mixed character of such an adsorbed layer has been shown by recent emission microscopical research where molecules made up of a nucleus of three or four metal atoms around an oxygen atom have been identified (20).

With Cu_2O the equation of nonstoichiometry is

$$\tfrac{1}{2}\, O_2(g) = O_o^x + V_{Cu}'' + 2\, h^{\cdot}$$

and there is a relation between the concentrations of atomic and electronic defects. Since the energies of the intermediate layer/metastable Cu_2O and Cu_2O are different they will have different concentrations of atomic defects and so by the above, different concentrations of $h^{\cdot}$, *i.e.*, the two surfaces will have similar but slightly different catalytic activities. The two linear rate constants are similar in magnitude and so could reflect the different rates of catalytic decomposition of CO_2 to form adsorbed oxygen on the two similar surfaces. Moreover, the higher linear rate constant is associated with the intermediate surface structures which would be expected to have a higher catalytic activity. Also a nonlinear activation energy as observed for the first linear rate (Fig. 2) is not inconsistent with these ideas. Dissociation of defect complexes and/or ionization of defects may occur (21, 22) as the temperature is raised, and these would alter the concentrations of atomic and electronic defects and so affect the catalytic activity of the surface. A complication with oxidation in CO_2 is that there will be additional oxygen at higher temperatures owing to the greater degree of dissociation of CO_2. However, in the present case there is a lower than expected oxidation rate at higher temperatures and this would indicate that the rate of oxidation is less sensitive to the extra oxygen present than it is to the reduced catalytic activity of the surface. A possible cause of such a reduced catalytic activity as the temperature is raised is that the intermediate structure of the catalytic surface may move towards a lower energy and so less active structure. A similar mechanism to decomposition of CO_2 has been observed with the decomposition of N_2O on Cu_2O and the simultaneous oxidation of Cu, where the catalytic decomposition depended on the concentration of $h^{\cdot}$ (23).

Swaroop and Wagner (10) found that the first linear rate constant for Cu oxidized in CO_2/Ar mixtures obeyed an empirical equation of the form

$$K_{L1} = CP^{n}_{CO_2}$$

where C and n are constants, and found values of n = 1.3 and 1.5. For oxidation of Ni in CO_2/CO mixtures $n = 1$ and for Fe in CO_2/CO mixtures $n = 0.33$ while Fe in low pressure oxygen $n = 0.7$ (10). It is stated (10) that for $n > 1$ the oxidation mechanism is not due to chemisorption but the basis of this statement is not clear. Moreover, Swaroop and Wagner have taken their surface oxide in the first linear stage to be Cu_2O and have assumed it forms a uniform layer, whereas in the present work the first linear kinetics is associated with an intermediate surface structure whose area is changing, and it may be that the cause of the unusual (if indeed they are) n values for Cu is the changing areas during nucleation and growth available for a catalytic chemisorption reaction.

Conclusions

Copper oxidized in CO_2 at 800°-1000°C follows an initial linear kinetic law which changes gradually to a second, lower, linear law. At any temperature small feathery-patterned unstable dendrites formed. Later crystallites of Cu_2O formed on the dendrites and grew to cover the whole surface. The first linear curve was associated with a surface covered with dendrites and the second linear curve with the Cu_2O crystallites. Surface finish, preannealing, and gas flow rate in the range 0.1-2.0 cm sec^{-1} have no effect on the oxidation rate. It is considered that the rate-controlling process is the catalytic decomposition of CO_2 on the surface to form chemisorbed oxygen.

Manuscript submitted Oct. 27, 1976; revised manuscript received Nov. 18, 1977.

Any discussion of this paper will appear in a Discussion Section to be published in the December 1978 JOURNAL. All discussions for the December 1978 Discussion Section should be submitted by Aug. 1, 1978.

REFERENCES

1. K. Hauffe and H. Pfeiffer, *Z. Metallk.*, **44**, 27 (1953).
2. W. W. Smeltzer, *Acta Metall.*, **8**, 377 (1960).
3. W. W. Smeltzer, *Trans. Metall. Soc. AIME.*, **218**, 674 (1960).
4. F. Pettit, R. Yinger, and J. B. Wagner, Jr., *Acta Metall.*, **8**, 617 (1960).
5. F. Pettit and J. B. Wagner, Jr., *ibid.*, **12**, 35 (1964).
6. F. Pettit and J. B. Wagner, Jr., *ibid.*, **12**, 41 (1964).
7. K. Fueki and J. B. Wagner, Jr., *This Journal*, **112**, 970 (1965).
8. K. Fueki and J. B. Wagner, Jr., *ibid.*, **112**, 1079 (1965).
9. I. G. Murgulescu and D. Cismaru, *Acad. Repub. Pop. Rom. Stud. Cercet. Chim.*, **7**, 197 (1959).
10. B. Swaroop and J. B. Wagner, Jr., *This Journal*, **114**, 685 (1967).
11. C. Wagner, Mimeographed notes, Course 3.23, Kinetics in Metallurgy, Massachusetts Institute of Technology (Spring, 1955).
12. H. A. H. Pray, I. Igelstrud, and G. L. Simund, U.S. Pat. 2,446,060 (1948).
13. I. A. Menzies and W. J. Tomlinson, *J. Iron Steel Inst. (London)*, **204**, 1239 (1966).
14. L. H. Van Vlack, "Physical Ceramics for Engineers", Addison-Wesley, Reading, Massachusetts (1964).
15. F. A. Kröger and H. J. Vink, in "Solid State Physics" Vol. 3, F. Seitz and D. Turnbull, Editors, pp. 431-435, Academic Press, London (1955).
16. H. Kobayashi and C. Wagner, *J. Chem. Phys.*, **26**, 1609 (1957).
17. R. W. G. Wyckoff, "Crystal Structures," Vol. 1, p. 331, Wiley-Interscience, New York (1963).
18. D. A. Goulden, *Phil. Mag.*, **33**, 393 (1976).
19. G. E. Rhead, *Trans. Faraday Soc.*, **61**, 787 (1965).
20. J. Oudar, "Physics and Chemistry of Surfaces," p. 92, Blackie and Sons Ltd., Glasgow (1975).
21. J. Oudar, *ibid.*, p. 109.
22. P. Kofstad, "Nonstoichiometry, Diffusion and Electrical Conductivity in Binary Metal Oxides," p. 331, Wiley-Interscience, New York (1972).
23. R. M. Dell, F. S. Stone, and P. F. Tiley, *Trans. Faraday Soc.*, **49**, 201 (1953).

Thermodynamic Properties of Metal-Water Systems at Elevated Temperatures

Dale F. Taylor

General Electric Corporate Research and Development, Schenectady, New York 12301

ABSTRACT

The advent of commercial nuclear power generation has created an increased need for thermodynamic data on metal-water systems at temperatures up to 350°C. The entropy correspondence principle discovered by Criss and Cobble [*J. Am. Chem. Soc.*, **86**, 5385 and 5391 (1964)] provides an excellent means of estimating high-temperature partial molar ionic entropies and hence high-temperature heat capacities, from entropy values at 25°C. It is therefore often possible to calculate both equilibrium constants and standard electrode potentials with surprising accuracy for elevated temperatures. Unfortunately, different conventions have been used by several authors in publishing calculated numerical data. One purpose of the present paper is to clarify these differences. In addition, a means of simplifying the calculations is described. This new approach permits rapid modification or augmentation of existing values when more accurate data become available, or when information at other temperatures is required. Values of K_w, the ionization product of water, and $E°_{AgX/Ag}$, the standard electrode potentials of silver-silver halide electrodes, are calculated as examples for temperatures up to 300°C, and these values are compared with available experimental data.

The advent of commercial nuclear power generation has created an increased need for thermodynamic data on metal-water systems at temperatures up to 350°C. An understanding of the corrosion processes which can facilitate the transport of radioactive contaminants or cause cracking of structural materials is particularly important, and with faster reaction rates at higher temperatures, thermodynamic properties play an increasingly important role in controlling the chemistry of dissolved species.

Unfortunately the entropy, heat capacity, and volume data required for calculating the relevant values of $\Delta G°$, and hence the equilibrium constants and standard cell potentials, for conditions other than 25°C and 1 atm pressure are not presently available for many species of interest. However, the entropy correspondence principle discovered by Criss and Cobble (1) provides an excellent means of estimating high-temperature partial molar ionic entropies, and hence high-temperature heat capacities, from entropy values at 25°C. It is therefore often possible to calculate both equilibrium constants and standard electrode potentials with surprising accuracy for elevated temperatures. For example, at temperatures up to 250°C, most predicted values of K_w, the ionization product of water, and $E°_{AgX/Ag}$, the standard electrode potentials of silver-silver halide electrodes, agree with available measured values within the quoted experimental uncertainty. Beyond 250°C, the contribution of pressure to changes in free energy starts to become important, and systematic deviations occur. Calculations involving temperatures above 300°C are probably only semiquantitatively correct.

Robins *et al.* (2), Townsend (3), Cowan and Staehle (4), MacDonald *et al.* (5-7), and Cobble and Murray (8) among others, have used this approach to predict the thermodynamic behavior of several elements and their oxidation products in high-temperature aqueous systems. Some confusion may arise, however, because different conventions have been used in listing numerical data. One purpose of the present paper is to clarify these differences.

In addition, a means of simplifying the calculations is described. This new approach permits rapid modification or augmentation of existing values when more accurate data become available, or when information at other temperatures is required.

Key words: electrolyte, chemical potential, heat capacity, entropy, equilibrium constant, standard hydrogen electrode (SHE), electrode potential.

Free Energy Changes at Elevated Temperatures

For a reaction which goes to completion at temperature T and pressure P, the change in free energy is given by

$$\Delta G = \sum_p \alpha_p \mu_p - \sum_r \alpha_r \mu_r \qquad [1]$$

where α_p and α_r are the stoichiometric coefficients of the products and reactants, respectively, and $\mu(T, P)$ is the chemical potential: the molar free energy for pure substances and the partial molar free energy for species in solution.

Since the activity of system component i, a_i, is defined by

$$\mu_i(T, P) = \mu_i° + RT \ln a_i \qquad [2]$$

where $\mu_i°$ is the chemical potential of component i in some conveniently specified standard state at temperature T, the value of $\mu_i°$ depends on the units chosen to express a_i, and on the choice of standard state. The standard state for gases is the hypothetical pure ideal gas at unit pressure, usually 1 atm. The standard chemical potential $\mu°_{gas}$ thus depends only on temperature. The standard state for a liquid or solid element or compound is its stable state of aggregation as a pure substance at equilibrium, and therefore $\mu°_{solid}$ and $\mu°_{liquid}$ depend on both the temperature and pressure. This is the usual choice of standard state for the solvent in an electrolyte solution, but it is not convenient for the solute. The standard state for electrolyte solutions is that of a hypothetical ideal solution at unit concentration, most often unit molality to avoid complications from density changes, and $\mu°_{solute}$ is dependent on both temperature and pressure.

If the chemical potential of any component in its standard state is known at 25°C, 1 atm (298.15°K, 1.01325×10^5 Pa), integration of the relationships

$$\left(\frac{\partial \mu_i}{\partial T}\right)_P = -\overline{S}_i, \quad \left(\frac{\partial \mu_i}{\partial P}\right)_T = \overline{V}_i \qquad [3]$$

with the definition

$$\left(\frac{\partial \overline{S}_i}{\partial T}\right)_P \equiv \frac{\overline{C}_{Pi}}{T} \qquad [4]$$

yields the chemical potential of this component in its

standard state at any temperature (or pressure for condensed phases and electrolyte solutions)

$$\mu_i^\circ(T,P) = \mu_i^\circ(25^\circ\text{C, 1 atm}) + \int_{1\text{ atm}}^{P} \overline{V}_i^\circ dP' + \int_{298.15}^{T} \overline{C}_{P_i}^\circ dT' - T\int_{298.15}^{T} \overline{C}_{P_i}^\circ d\ln T' - (T - 298.15)\overline{S}_i^\circ(25^\circ\text{C, 1 atm}) \quad [5]$$

where the superscript ° denotes the standard state and unit activity, V, S, and C_P have their usual thermodynamic meanings, and the superscript $^-$ denotes $(\partial/\partial n_i)_{P,T,n_j}$: the molar value for pure substances and the partial molar value for components in solution.

$\Delta\mu_i^\circ$ is independent of the integration path, but since $\overline{V}_i^\circ$ and $\overline{C}_{P_i}^\circ$ are each functions of both T and P, the order of integration is important. $\overline{C}_{P_i}^\circ$ is generally available as a function of temperature for a pressure of 1 atm. $\overline{V}_i^\circ$ is then required as a function of P at temperature T.

$\mu_i^\circ(25^\circ\text{C, 1 atm})$ for ions in solution and pure compounds is defined as the molar Gibbs free energy of formation by Eq. [1] and the convention which assigns a chemical potential of zero to H^+_{aq} and the elements in their standard states at the arbitrary reference point of 25°C and 1 atm. Thus the values of $\mu_i^\circ(T, P)$ calculated from [5] are not correct on an absolute scale, but the value of $\Delta G^\circ(T, P)$ calculated from [1] for any reaction is correct because a change is being evaluated and the arbitrary zero cancels out. This approach to calculating $\Delta G^\circ(T, P)$ is particularly convenient when a number of reactions with several common reactants and products are being considered. MacDonald was the first to adopt the procedure, but added an unnecessary complication by extending the Gibbs energy of formation terminology to temperatures and pressures other than 25°C and 1 atm (5, 9, 10).[1]

Cobble anticipated minor effects from changes in partial molar volumes at temperatures up to 300°C, and suggested that the pressure term could be ignored, especially since very little is known about the partial molar volumes of ions (11). It will be shown that this approximation is a good one.

Accurate molar heat capacity data is available for many pure substances in a readily integrable power series of the form (12, 13)

$$\overline{C}_{P_i}^\circ(T) = A_i + B_iT + C_iT^{-2} \quad [6]$$

but ionic partial molar heat capacities are generally not available.

Criss and Cobble (1) developed a technique for evaluating $\overline{S}_i^\circ(T)$ for ions, and their results suggest a very simple new approach to calculating $\overline{C}_{P_i}^\circ$, one which is both more accurate at higher temperatures than the average value they proposed, and conveniently consistent with [6].

[1] Cobble and Murray (8) have chosen to list values of the free energy function (FEF) based on a reference temperature of 25°C

$$\text{FEF}_i(T) \equiv \frac{\mu_i^\circ(T) - \overline{H}_i^\circ(25^\circ\text{C})}{T} = \frac{\overline{H}_i^\circ(T) - \overline{H}_i^\circ(25^\circ\text{C})}{T} - \overline{S}_i^\circ(T)$$

Thus, since

$$\text{FEF}_i(T) = \frac{1}{T}\int_{298.15}^{T} \overline{C}_{P_i}^\circ(T')dT' - \int_{298.15}^{T} \overline{C}_{P_i}^\circ(T')d\ln T' - \overline{S}_i^\circ(25^\circ\text{C})$$

$$\mu_i^\circ(T) = \mu_i^\circ(25^\circ\text{C}) + T[\text{FEF}_i(T)] - 298.15[\text{FEF}_i(25^\circ\text{C})]$$

This modification of the direct approach requires separate specification of μ_i° (25°C) values and some additional computation. However, the value of $\overline{S}_i^\circ$ (25°C) is immediately available as—FEF$_i$ (25°C), and the slow variation of the free energy function with temperature permits interpolation between calculated values.

Criss and Cobble observed that "a standard state can be chosen at every temperature such that the partial molar entropies of one class of ions at that temperature are linearly related to the corresponding entropies at some reference temperature." The zero for ionic entropies at each temperature was defined by the value of $\overline{\overline{S}}^\circ_{H^+}(T)$, the partial molar ionic entropy of the hydrogen ion which resulted in the best linear fit of experimental data. The reference temperature was chosen to be 25°C. Thus for a given class of ion (simple cations, simple anions, oxy-anions, acid oxy-anions)

$$\overline{\overline{S}}_i^\circ(T) = a(T) + b(T)\overline{\overline{S}}_i^\circ(25^\circ\text{C}) \quad [7]$$

where $\overline{\overline{S}}$ denotes a partial molar entropy not referred to the conventional scale which sets $\overline{\overline{S}}^\circ_{H^+}(T) \equiv 0$.

In fact, the $\overline{\overline{S}}_i^\circ$ values defined in this manner appear to be absolute or "third law" entropies. $\overline{\overline{S}}^\circ_{H^+}$ (25°C) is −5.0 calories mole^{-1} degree^{-1}, in relatively good agreement with the value of −4.48 calories mole^{-1} degree^{-1} deduced by deBethune *et al.* for the standard ionic entropy of electrochemical transport of hydrogen ions at 25°C (14), and the value of −5.5 calories mole^{-1} degree^{-1} obtained by Laidler and Pegis for the standard entropy of hydration of hydrogen ions (15).

Entropies on the conventional scale are related to the absolute scale at any temperature by the equation

$$\overline{\overline{S}}_i^\circ(T) = \overline{S}_i^\circ(T) + z\overline{\overline{S}}^\circ_{H^+}(T) \quad [8]$$

where z is the charge on the ion (with sign). At 25°C, this becomes

$$\overline{\overline{S}}_i^\circ(25^\circ\text{C}) = \overline{S}_i^\circ(25^\circ\text{C}) - 5.0z \quad [9]$$

Criss and Cobble noted that up to 150°C the parameters $a(T)$ and $b(T)$ in Eq. [7] varied approximately linearly with temperature, with most of the deviation occurring near 60°C. On this basis they extrapolated their results to 300°C. Thus for a given class of ion, the tabulated values can be reproduced quite accurately by relationships of the form

$$a = a_1 + a_2T, \quad b = b_1 + b_2T \quad [10]$$

and by substituting from Eq. [7] and [10] into [4]

$$\overline{C}_{P_i}^\circ(T) = [a_2 + b_2\overline{\overline{S}}_i^\circ(25^\circ\text{C})]T \equiv B_iT \quad [11]$$

Equation [11] will be referred to as the linear ionic heat capacity approximation (LIHCA). This relationship makes computer or calculator programs based on Eq. [5] and [6] directly applicable to ionic species with $A_i = C_i = 0$, and μ_i° can be calculated in one step for any temperature in the range where the constant pressure approximation is valid. Note that the choice of $\overline{S}_i^\circ(25^\circ\text{C})$ or $\overline{\overline{S}}_i^\circ(25\text{C}^\circ)$ in Eq. [5] does not affect the value of ΔG° obtained from [3] provided that the same choice is made for calculations of all μ_i°. Since absolute values must be used in [11], there is less confusion if they are used throughout. In either case, the choice of convention must be clearly stated.

The apparent linearity of partial molar ionic heat capacities with temperature was noted first in studies of weak acids (16, 17), and the work of Criss and Cobble (1) seems to confirm its generality. Naumov *et al.* (18) also list partial molar ionic heat capacities in this form. A reasonable estimate of high-temperature partial molar ionic heat capacities can thus be obtained easily when the values at 25°C are available.

Electrode Potentials at Elevated Temperatures

The change in free energy for the generalized reduction in an aqueous system

$$aA + hH^+ + ne^- = bB + wH_2O \quad [12]$$

is not experimentally accessible, but the tendency for any such reduction to occur can be measured relative

to a standard reduction, usually chosen to be the standard hydrogen electrode (SHE) reaction

$$H^+(a_{H^+} = 1) + e^- = 1/2\ H_2(a_{H_2} = 1) \quad [13]$$

in aqueous systems. Thus for constant n, the values of $\Delta G^\circ_{A/B}$ at any temperature for the complete reactions represented by

$$aA + (h - n)H^+ + \frac{n}{2}H_2 = bB + wH_2O \quad [14]$$

are one basis for comparing the relative tendencies of the reductions represented by [12] to occur at that temperature.

Since

$$\Delta G = -n\mathbf{F}E \quad [15]$$

where E is a measurable cell potential and $\mathbf{F}$ is the Faraday, it is logical to define a "standard electrode potential" for [12]

$$E^\circ_{A/B} \equiv -\Delta G^\circ_{A/B}/n\mathbf{F} \quad [16]$$

The standard electrode potential for [12] at any temperature can therefore be obtained by determining $\Delta G^\circ_{A/B}$ through Eq. [1] and [5]. It follows as a natural consequence of [16] that

$$E^\circ_{H^+/H_2} = 0 \quad [17]$$

at all temperatures since $\Delta G^\circ_{A/B}$ is identically zero when Eq. [12] represents the SHE reaction.

The definition of the standard electrode potential can be generalized to include activities other than unity for the reactants and products in [12] through Eq. [1] and [2]. Since the activities of H_2 and H^+ contributed from [13] are unity by definition

$$E_{A/B} = E^\circ_{A/B} - \frac{RT}{n\mathbf{F}} \ln\left[\frac{a_B{}^b a_{H_2O}{}^w}{a_A{}^a a_{H^+}{}^h}\right] \quad [18]$$

The electrode potential, or "potential *vs.* SHE at the same temperature" provides a very convenient basis for comparison among all the reactions which are possible in the system at a given temperature.

The concept of the electrode potential is by definition independent of the convention which sets $\mu^\circ_{H_2}$ and $\mu^\circ_{H^+}$ equal to 0 at 25°C, and does not require, as suggested by Van Rysselberghe (19), that

$$\tfrac{1}{2}\mu^\circ_{H_2} = \mu^\circ_{H^+} \quad [19]$$

This relationship is true only at the temperature for which $\mu^\circ_{H_2}$ and $\mu^\circ_{H^+}$ are defined to be zero.

The variation of $E_{A/B}$ with temperature defines the "isothermal" temperature coefficient of the electrode potential since $E_{A/B}$ is referred to the SHE at the same temperature. Another alternative for describing the effect of temperature on reaction [12] is to measure the tendency for this reaction to occur at temperature T relative to the same reaction at a fixed reference temperature, normally 25°C. This is satisfying from an experimental point of view since any two identical electrodes at different temperatures in the same cell will develop a potential difference which is independent of metallic thermocouple effects and the thermal liquid junction potential (14).

For two hydrogen electrodes, this thermal cell reaction is

$$H^+(T) + \tfrac{1}{2}H_2(25°C) = \tfrac{1}{2}H_2(T) + H^+(25°C) \quad [20]$$

and

$$\Delta G^{\circ *}_{H^+/H_2}(T) = \tfrac{1}{2}\mu^\circ_{H_2}(T) - \mu^\circ_{H^+}(T) \quad [21]$$

where * denotes the 25°C "thermal" convention. In a manner analogous to that used in defining E°, a standard "thermal" electrode potential can be defined for the SHE

$$E^{\circ *}_{H^+/H_2}(T) = -\Delta G^{\circ *}_{H^+/H_2}(T)/\mathbf{F} \quad [22]$$

It is important to note that absolute ionic entropies must be used in Eq. [5] to obtain standard thermal electrode potentials. The use of absolute entropies for all calculations therefore seems advisable.

Comparison of the Linear Ionic Heat Capacity Approximation with Experimental Data

Very accurate values for the ionic dissociation constant of water, K_w (20), and the standard electrode potentials (*vs.* SHE at the same temperature) of the silver/silver halide electrodes (21-23) are available for comparison with predicted values over a wide temperature range. Both comparisons have been made previously on a limited or graphical basis using the multiparameter Criss-Cobble approximation (4, 6, 11). These studies provide an excellent source of calculated data. In addition, the measurements of Fales and Mudge (24) are available for verifying predictions of thermal hydrogen electrode potentials up to 60°C.

Table I contains the thermodynamic data used in all the calculations of μ_i° values. The parameters for water are not included since $\mu^\circ_{H_2O}$ values were taken directly from the data of Helgeson and Kirkham (25) and these are listed in Table II. $\mu^\circ_{OH^-}(25°C)$ was calculated by [1] using the value of $\Delta G^\circ_w(25°C)$ determined by Sweeton, Mesmer, and Baes (20)

$$H_2O = H^+ + OH^- \quad [23]$$

$$\Delta G^\circ_w = -RT \ln K_w = \mu^\circ_{H^+} + \mu^\circ_{OH^-} - \mu^\circ_{H_2O} \quad [24]$$

B_i values (for $\overline{C}_{P_i}^\circ$) were calculated from Eq. [4] for H^+ and Eq. [11] for the other ions. A linear fit of the Criss-Cobble entropy parameters to 300°C, excluding the values at 60°C, resulted in the following values for H^+, and simple anions

$$(\partial \overline{\overline{S}}^\circ_{H^+}/\partial T)_P = 9.35 \times 10^{-2}\ \text{cal mole}^{-1}\ \text{deg}^{-2}$$
$$a_2 = -1.77 \times 10^{-1}\ \text{cal mole}^{-1}\ \text{deg}^{-2}$$
$$b_2 = -1.12 \times 10^{-4}\ \text{deg}^{-1}$$

Table II summarizes the results from calculations of ΔG°_w and pK_w using the linear ionic heat capacity approximation (LIHCA). The number of significant figures is not warranted by the accuracy of the original

Table I. Thermodynamic data

	μ° (25°C) (26, 27) (calories mole^{-1})	$\overline{\overline{S}}^\circ$ (25° C) (26, 27) (calories mole^{-1} degree^{-1})	$\overline{C}_P^\circ = A + BT + CT^{-2}$ (12, 13) (calories mole^{-1} degree^{-1})		
			A	*B*	*C*
H^+	0	−5.0	0	9.35×10^{-2}†	0
OH^-	−37596	2.43*	0	-1.77×10^{-1}†	0
Cl^-	−31372	18.5	0	-1.79×10^{-1}†	0
Br^-	−24850	24.7	0	-1.80×10^{-1}†	0
I^-	−12330	31.6	0	-1.80×10^{-1}†	0
H_2	0	31.208	6.52	0.78×10^{-3}	0.12×10^{5}
Ag	0	10.17	5.09	2.04×10^{-3}	0.36×10^{5}
AgCl	−26244	23.0	14.88	1.00×10^{-3}	-2.70×10^{5}
AgBr	−23160	25.6	7.93	15.40×10^{-3}	0
AgI	−15820	27.6	5.82	24.10×10^{-3}	0

† Calculated using the linear ionic heat capacity approximation (LIHCA).
* Consistent with ΔS°_w (25°C) and $\overline{S}^\circ_{H_2O}$ (25°C) from (20) and (25).

Table II. Thermodynamic parameters for the ionic dissociation of water—comparison of experimental values with those calculated using the linear ionic heat capacity approximation (LIHCA)

Temp. (°C)	$\mu^\circ_{H_2O}$ (25) (cal mole^{-1})	$\mu^\circ_{H^+}$ (LIHCA) (cal mole^{-1})	$\mu^\circ_{OH^-}$ (LIHCA) (cal mole^{-1})	ΔG°_w (LIHCA) (calories)	ΔG°_w (20) (calories)	pK_w (LIHCA)	pK_w (20)
25	−56686	0	−37596	19090	19090 ± 9	13.994	13.993 ± 0.009
50	−57122	96	−37601	19617	19624 ± 12	13.268	13.272 ± 0.006
75	−57593	133	−37496	20230	20245 ± 12	12.700	12.709 ± 0.006
100	−58096	112	−37280	20928	20939 ± 12	12.258	12.264 ± 0.009
125	−58630	32	−36953	21709	21704 ± 18	11.917	11.914 ± 0.009
150	−59191	−106	−36516	22569	22541 ± 21	11.657	11.642 ± 0.012
175	−59779	−302	−35968	23509	23460 ± 24	11.465	11.441 ± 0.012
200	−60392	−557	−35309	24526	24468 ± 24	11.329	11.302 ± 0.012
225	−61029	−870	−34539	25620	25578 ± 27	11.241	11.222 ± 0.012
250	−61688	−1242	−33659	26787	26801 ± 36	11.191	11.196 ± 0.015
275	−62369	−1672	−32668	28029	28151 ± 69	11.176	11.224 ± 0.027
300	−63069	−2161	−31566	29342	29638 ± 117	11.189	11.301 ± 0.045

data, but all μ_i° and ΔG° values were calculated to the nearest calorie for direct comparison with the results published by other authors. Six of the calculated pK_w values are within ±0.1% of the experimental values, and all ten of the values up to 250°C deviate less than ±0.25%. The deviation at 275°C is −0.43%, and at 300°C, −1%.

This systematic error escalation above 250°C probably results from contributions to ΔG° by the rapidly increasing vapor pressure of water. Sweeton *et al.* indicated that the effects of density changes on the partial molar volumes of ions are not well understood in this temperature region (20). Extrapolation of the constant pressure approximation to temperatures above 300°C is a questionable procedure, especially since no experimental data are available for comparison.

The accuracy below 300°C is quite remarkable. MacDonald and Butler (6, 9) assumed all discrepancies in K_w were the result of inaccuracies in $\mu^\circ_{H^+}$ and recalculated "corrected" values of this parameter for application to other systems. However, since Criss and Cobble obtained $\bar{S}^\circ_{H^+}$ by fitting all available ionic entropy data (1), $\mu^\circ_{H^+}$ is probably more accurate than the other calculated values, and further comparison with experimental observations seems to bear this out.

Table III lists the results from calculations of μ_i° for components of the hydrogen and silver-silver halide electrodes, again using the linear ionic heat capacity approximation.

Corresponding standard potentials (*vs.* SHE at the same temperature) appear in Table IV, along with values calculated from MacDonald and Butler's results (6) and observed values (21-23). Equation [14] takes the form

$$AgX + \tfrac{1}{2} H_2 = Ag + H^+ + X^- \qquad [25]$$

and hence

$$E^\circ_{AgX/Ag} = (\mu^\circ_{AgX} + \tfrac{1}{2}\mu^\circ_{H_2} - \mu^\circ_{Ag} - \mu^\circ_{H^+} - \mu^\circ_{X^-})/\mathbf{F} \qquad [26]$$

A value of 23060.9 calories V^{-1} equivalent^{-1} was used for **F**.

Once again, the calculated results are quite accurate. The agreement for Ag/AgCl is almost perfect. The very systematic error of ~+4 mV for Ag/AgBr can be eliminated by a change of +90 cal in the $\mu^\circ_{Br^-}$(25°C) value. The Ag/AgI results do not agree nearly as well, and no simple adjustment of parameters can bring them more closely into line. However, the linear ionic heat capacity approximation with no special adjustment of parameters duplicates the MacDonald-Butler results at lower temperatures, and yields consistently better results at higher temperatures.

The excellent agreement with experimental results obtained for K_w and the silver-silver chloride and

Table III. Standard chemical potentials for components of the hydrogen and silver-silver halide electrodes calculated using the linear ionic heat capacity approximation (LIHCA)

Temperature (°C)	(calories mole^{-1})								
	H^+	H_2	Ag	AgCl	AgBr	AgI	Cl^-	Br^-	I^-
25	0	0	0	−26244	−23160	−15820	−31372	−24850	−12330
60	118	−1106	−368	−27073	−24081	−16812	−31910	−25604	−13325
90	127	−2074	−701	−27822	−24909	−17703	−32196	−26076	−14003
100	112	−2401	−816	−28079	−25193	−18009	−32256	−26197	−14193
125	32	−3225	−1109	−28736	−25917	−18789	−32327	−26422	−14588
150	−106	−4061	−1413	−29415	−26664	−19593	−32287	−26534	−14871
175	−302	−4906	−1725	−30115	−27432	−20421	−32134	−26534	−15040
200	−557	−5761	−2046	−30833	−28221	−21272	−31869	−26422	−15097
225	−870	−6626	−2375	−31571	−29030	−22146	−31493	−26197	−15042
250	−1242	−7499	−2711	−32326	−29858	−23042	−31005	−25860	−14873
275	−1672	−8380	−3056	−33099	−30706	−23961	−30405	−25411	−14592
300	−2161	−9270	−3407	−33888	−31572	−24901	−29693	−24850	−14198

Table IV. Standard potentials for the silver-silver halide electrodes (mV)

Temp. (°C)	AgCl/Ag				AgBr/Ag				AgI/Ag			
	LIHCA	(21)[1]	(21)[2]	(6)	LIHCA	(22)[1]	(22)[2]	(6)	LIHCA	(23)[1]	(23)[2]	(6)
25	222	222	222	222	73	72 ± 1	71	73	−151	−152	−152	−151
60	197	197	197	196	53	50 ± 1	50	53	−164	−166	−167	−165
90	170	170	170		31	25 ± 1	27		−181		−185	
100	160		160	160	22		18	22	−187	−193 ± 1	−192	−187
125	132	133	133		−1	−5 ± 1	−5		−205	−213 ± 1	−213	
150	102	103	103	103	−29	−31 ± 1	−32	−27	−227	−238 ± 1	−238	−226
175	69	71	71		−57	−61 ± 1	−62		−252	−270 ± 1	−271	
200	33	35	35	40	−90	−95 ± 1	−94	−84	−280	−309 ± 1	−307	−273
225	−6	−5	−4		−126		−130		−311		−346	
250	−48	−54 ± 2	−45	−34	−165		−169	−150	−345		−390	−331
275	−93	−90 ± 5	−90		−206		−210		−383		−437	
300	−141		−138	−124	−251		−255	−233	−424		−488	−406

[1] Experimental.
[2] Smoothed/extrapolated.

bromide standard potentials undoubtedly reflects the fact that these or similar experimental results were used to determine values for the parameters of the correspondence principle in the first place. This in no way detracts from the demonstrated general internal consistency of the approach, but suggests that the silver-silver iodide results may be a better indication of the accuracy to be expected. It should also be noted, however, that silver iodide undergoes a phase transition at 144.6°C (23), and it is possible that at least part of the discrepancy arises from the failure to account for this in the calculations.

The value of a_2 for simple anions used in these calculations was obtained from the parameters of the linear correspondence principle as they appeared in Criss and Cobble's original publication (1). The value of a_2 calculated after correcting for an apparent typographical error which was first noticed by Tremaine *et al.* (*a* for simple anions at 300°C should be −47.2 instead of −49.2) (28) is -1.72×10^{-1} calories mole^{-1} degree^{-2}. This "corrected" value actually causes a slight deterioration in the agreement between all calculated and observed values, with the original value fortuitously producing a fit which does not benefit significantly from optimization.

Even at 60°C, where the linear ionic heat capacity approximation should be least accurate, it compares well with experimental data from thermal electrode measurements. From [21] and [22], and the data in Table III,

$$E^{\circ *}_{H^+/H_2}(60°C, \text{LIHCA}) = 0.029\text{V} \qquad [27]$$

From the data of Fales and Mudge (24), deBethune *et al.* calculated an expression for the thermal potential of the hydrogen electrode (Pt/H_2 ($f = 1$), 0.1M HCl/sat'd KCl) which gives $E^*_{H^+(0.1m)/H_2}(60°C)$ as 0.022V (14). The standard thermal potential at 60°C can be calculated from [28], an equation obtained by generalizing Eq. [21] and [22] to include activities other than unity

$$E^{\circ *}_{H^+/H_2}(60°C) = E^*_{H^+(0.1m)/H_2}(60°C) + \left[\frac{RT}{\mathbf{F}} \ln a_{H^+}\right]_{;25°C} - \left[\frac{RT}{\mathbf{F}} \ln a_{H^+}\right]_{60°C} \qquad [28]$$

where $a_{H^+} = 0.1\ \gamma_\pm(\text{HCl})$. The values obtained by Greeley *et al.* (29) for $\gamma_\pm$(HCl, 0.1m), 0.7972 at 25°C and 0.776 at 60°C, yield

$$E^{\circ *}_{H^+/H_2}(60°C, \text{OBS.}) = 0.030\text{V} \qquad [29]$$

It is interesting to note that [22] predicts that the temperature coefficient of the thermal SHE potential, $\partial E^{\circ *}_{H^+/H_2}/\partial T$, decreases significantly as the temperature increases, contrary to the behavior first assumed by MacDonald (9). Using the values in Tables I and III, the temperature coefficient is 0.893 mV deg^{-1} at 25°C, passing through zero and changing sign at a temperature of about 265°C. This result differs slightly from MacDonald's later calculation (10) because of his "corrected" $\mu^\circ_{H^+}$ values.

Conclusions

1. The Criss-Cobble entropy correspondence principle makes possible surprisingly accurate predictions of thermodynamic properties in aqueous systems at temperatures up to *ca.* 300°C.

2. The linear ionic heat capacity approximation (LIHCA) reduces the number of parameters required, simplifies the calculations, and makes possible a one-step computation while improving over-all accuracy.

3. Extrapolation of the constant pressure approximation to temperatures above 300°C may involve considerable error.

4. It is important to state the $\mu_i^\circ(25°C)$ and $\bar{S}_i^\circ(25°C)$ values used in calculations on any system. Separate $\mu_i^\circ(T)$ values are the most useful parameters for subsequent applications of the data.

Manuscript submitted Sept. 23, 1977; revised manuscript received Jan. 3, 1978.

Any discussion of this paper will appear in a Discussion Section to be published in the December 1978 JOURNAL. All discussions for the December 1978 Discussion Section should be submitted by Aug. 1, 1978.

Publication costs of this article were assisted by the General Electric Company.

REFERENCES

1. C. M. Criss and J. W. Cobble, *J. Am. Chem. Soc.*, **86**, 5385 and 5391 (1964).
2. R. J. Biernat and R. G. Robins, *Electrochim. Acta*, **14**, 809 (1969); B. W. Edenborough and R. G. Robins, *ibid.*, **14**, 1285 (1969).
3. H. E. Townsend, Jr., *Corrosion Sci.*, **10**, 343 (1970).
4. R. L. Cowan and R. W. Staehle, *This Journal*, **118**, 557 (1971).
5. D. D. MacDonald, G. R. Shierman, and P. Butler, Atomic Energy of Canada Ltd., AECL-4136, 4137, 4138, 4139 (1972).
6. D. D. MacDonald and P. Butler, *Corrosion Sci.*, **13**, 259 (1973).
7. D. D. MacDonald, *ibid.*, **16**, 461 (1976).
8. J. W. Cobble and R. C. Murray, Jr., in the Annual Report for EPRI Contract No. RP 311-2, San Diego State University Foundation, March 1977.
9. D. D. MacDonald, in "Modern Aspects of Electrochemistry, Vol. 11, J. O'M. Bockris and B. E. Conway, Editors, pp. 141-197, Plenum Press, New York (1975).
10. D. D. MacDonald, Paper No. 146, NACE Corrosion/77, San Francisco, March 1977.
11. J. W. Cobble, *J. Am. Chem. Soc.*, **86**, 5394 (1964).
12. K. K. Kelley, Bulletin 584, Bureau of Mines, U.S. Government Printing Office, Washington (1960).
13. C. E. Wicks and F. E. Block, Bulletin 605, Bureau of Mines, U.S. Government Printing Office, Washington (1963).
14. A. J. deBethune, T. S. Licht, and N. Swendeman, *This Journal*, **106**, 616 (1959).
15. K. J. Laidler and C. Pegis, *Proc. Roy. Soc. (London)*, **A241**, 80 (1957).
16. H. S. Harned and R. A. Robinson, *Trans. Faraday Soc.*, **36**, 973 (1940).
17. R. A. Robinson and R. H. Stokes, "Electrolyte Solutions," Second Edition (Revised), p. 357, Butterworths, London (1965).
18. G. B. Naumov, B. N. Ryzhenko, and I. L. Khodakovsky," Handbook of Thermodynamic Data," Transl. from Russian by the U.S. Geological Survey, Report No. USGS-WRD-73-001 (1974).
19. P. VanRysselberghe, Introduction to "Atlas of Electrochemical Equilibria in Aqueous Solutions" by M. Pourbaix, Pergamon Press, Oxford (1966).
20. F. H. Sweeton, R. E. Mesmer, and C. F. Baes, Jr., *J. Solution Chem.*, **3**, 191 (1974).
21. R. S. Greeley, W. T. Smith, Jr., R. W. Stoughton, and M. H. Lietzke, *J. Phys. Chem.*, **64**, 652 (1960).
22. M. B. Towns, R. S. Greeley, and M. H. Lietzke, *ibid.*, **64**, 1861 (1960).
23. G. Kortüm and W. Häussermann, *Ber. Bunsenges. Physik. Chem.*, **69**, 594 (1965).
24. H. A. Fales and W. A. Mudge, *J. Am. Chem. Soc.*, **42**, 2434 (1920).
25. H. C. Helgeson and D. H. Kirkham, *Am. J. Sci.*, **274**, 1089 (1974).
26. N. B. S. Technical Note 270-3 (1968).
27. N. B. S. Technical Note 270-4 (1969).
28. P. R. Tremaine, R. VonMassow, and G. R. Shierman, *Thermochimica Acta*, **19**, 287 (1977).
29. R. S. Greeley, W. T. Smith, Jr., M. H. Lietzke, and R. W. Stoughton, *J. Phys. Chem.*, **64**, 1445 (1960).

Boron in Near-Intrinsic ⟨100⟩ and ⟨111⟩ Silicon under Inert and Oxidizing Ambients—Diffusion and Segregation

Dimitri A. Antoniadis,* Adalberto G. Gonzalez, and Robert W. Dutton

Stanford Electronics Laboratories, Stanford University, Stanford, California 94305

ABSTRACT

The diffusivity of boron in <100> and <111> silicon is experimentally determined under both inert and oxidizing (dry O_2) ambient conditions in the range of temperatures 850°-1200°C. The boron is implanted at moderate dose (1.3×10^{14} cm^{-2}) and energy (70 keV) and subsequently activated by a moderate temperature anneal. The resulting profile ensures near-intrinsic silicon at the processing temperatures and serves as initial condition for subsequent processing. Diffusivities and segregation coefficients are calculated as fitting parameters in numerical solution of the experiments. A systematic fitting procedure is used and the target experimental parameters are sheet resistances and junction depths. Inert ambient diffusivities agree well with previous measurements, thus demonstrating the integrity of newly published mobility data used in the simulations. Diffusivities in oxidizing ambient are enhanced, more so in <100> than in <111> silicon. The enhancement increases with decreasing temperature, being about 10 for <100> at 850°C. It is demonstrated that there is good agreement between the observed diffusivity enhancement and growth of oxidation stacking faults if an interstitialcy mechanism is invoked to explain both phenomena. Observed segregation coefficients are different for the two silicon orientations but they obey the same activation energy over the temperature range.

Boron is the dominant p-type dopant for silicon technology. For this reason a great amount of effort has been expended during the last two decades for the determination of physical properties of boron in silicon at fabrication conditions. Since the device electrical characteristics depend strongly on the final impurity distributions, a detailed understanding of boron impurity diffusivity in silicon and its partition (segregation) in the silicon-silicon oxide interface is essential.

It is presently established that boron diffuses at least partly by means of charged-defect interactions (1, 2). For this reason the diffusivity of boron is affected by substitutional impurities in silicon present at sufficient levels to cause the crystal to become extrinsic at the fabrication temperatures. The terms intrinsic and extrinsic in this paper refer to the condition of the silicon at the process temperature. Boron diffusivity in absence of oxidation is uniform, *i.e.*, independent of impurity concentration provided this concentration is lower than that of intrinsic carriers at the process temperature. We refer to this as "intrinsic boron diffusivity." Boron diffusivity under extrinsic conditions becomes a function of Fermi level position increasing as the Fermi level approaches the valence band and decreasing as the Fermi level approaches the conduction band. The results of this effect are to a large degree responsible for the abundance of conflicting values of boron diffusion coefficients. Reviews on this matter have been presented by Kendall and DeVries (4) and Fair (5).

It has also been established that the diffusivity of boron in silicon is enhanced by the growth of silicon dioxide at the surface (6-9). The degree of enhancement is greater in <100> crystal orientation than in <111>. Again a number of mostly conflicting diffusion coefficients have been reported mainly because of the coexistence, in most experiments, of high concentration effects, oxidation effects, and redistribution of boron at the moving silicon-silicon oxide boundary (10).

The redistribution of boron during oxidation is, to a large degree, controlled by the segregation (or partition) process at the moving silicon-oxide interface (3). This physical process gives rise to a nonunity segregation coefficient defined as $m = C_{si}/C_{ox}$, where C_{si} and C_{ox} are the impurity concentrations at the two sides of the interface. The only direct measurements of the ratio m for boron as a function of temperature and crystal orientation have been presented by Colby and Katz (11). Most of the other values appearing in the literature have been indirectly calculated from redistribution models under various degrees of approximations and thus do not present a consistent picture of the physical process (10).

In the present paper we report the results of a study of boron diffusivity in near intrinsic <100> and <111> silicon under inert (N_2) and oxidizing (dry O_2) ambients at various temperatures. For the oxidation cases we also calculate the effective segregation coefficients, which we define as the constant ratios, m_{eff}, that best fit the experimental data over the entire time of each experiment.

The initial distribution of boron for all experiments was established by means of an ion-implantation and annealing process that insures the complete boron electrical activation and the intrinsic silicon requirements at the temperatures of the experiments. Diffusivities and segregation coefficients have been calculated using a new IC process simulator (12) together with an automatic optimizer program that seeks the best-fit parameters compatible with the measured data. For the determination of diffusivities in inert atmosphere the only measured data were the initial and final sheet resistance for each experiment. For the simultaneous determination of diffusivity and segregation coefficients in the oxidation experiments, the additional information of junction depths was used. Recently reported hole mobilities were used (13, 14) for the calculation of sheet resistances resulting from the simulation. The reliability of the technique and the integrity of the mobility data is demonstrated by the excellent fit of the diffusivity in inert ambient by a single activation energy and the agreement with other reliable data (15).

In dry O_2, diffusivity enhancement has been observed, more so in <100> than in <111>. This is in

* Electrochemical Society Active Member.

Key words: boron, oxidation, diffusivity, enhancement, segregation.

qualitative agreement with previously reported data (9, 11). For both orientations the observed enhancement increases as the temperature is decreased and the results cannot be characterized by a single activation energy. We demonstrate that this behavior is predicted by the self-interstitial supersaturation model proposed by Hu (16) to explain the growth of stacking faults and the diffusivity enhancement during silicon oxidation. In this context we show that the diffusivity data obtained here are compatible with the stacking fault growth data obtained by Hu (17, 18).

The segregation coefficients determined here are generally higher than those measured by Colby and Katz.[1] Also in all cases the calculated segregation coefficient is higher in <100> than in <111> silicon, but their difference is not as large as that reported by the above workers.

Experiment

The substrate materials used were low dislocation density (≤100/cm²), Czochralski-grown, phosphorus-doped, <111> and <100> crystal orientation silicon wafers, with an initial resistivity of 5-10 Ω-cm. Clean wafers were oxidized at 1000°C for 60 min in dry oxygen, growing about 510Å of SiO_2 for <100> material and about 615Å of SiO_2 for <111> material. Subsequently the wafers were implanted with B^{11+} at a dose of 1.33×10^{14} atoms/cm², at an energy of 70 keV, and at 7° misalignment to minimize channeling. The oxide layer was used to minimize silicon damage at the surface during implantation and to prevent evaporation of impurities during subsequent nitrogen drive-ins. Such a static oxide film does not affect the diffusion of boron (6). Although it is possible to have oxygen knock-ons into the silicon during implantation (19), it was assumed that the amount of oxygen present in the lattice would not seriously affect the diffusion of boron (less than 10^{12} atoms/cm² get knocked on to a maximum depth of 1000Å in the worst case). After implantation, the wafers were annealed in an N_2 atmosphere at 900°C for 35 min. The implantation and the annealing conditions were chosen in order to give the initial distribution of substitutional boron that has been experimentally determined by Hofker *et al.* (20), using secondary ion mass spectroscopy (SIMS) and electrical profiling techniques. This distribution is shown in Fig. 1. The only difference between the present process and that of Hofker *et al.* was the presence of the thin capping oxide, in which a maximum of 6% of the implanted dose is retained. The importance of excluding the implant annealing phase from the diffusion experiments cannot be overemphasized. Transient diffusion phenomena (20, 21) occurring during the electrical activation of the implant can easily lead to overestimation of the normal (thermal) diffusivity, particularly at the lower temperatures (20). Also, since initial sheet resistances are needed with our method, the implant had to be fully electrically activated prior to subsequent processing. Each as-annealed wafer was cut into quarters and one quarter was retained as a reference, while the other three were used for experiments at the same temperature and ambient. Since the peak concentration of the as-annealed boron profile was below 4×10^{18} atoms/cm³ and the intrinsic carrier concentration even at the lowest temperature considered here (850°C) is about 5×10^{18} carriers/cm³ (22), the silicon substrate was near intrinsic under all conditions of our experiments and thus extrinsic diffusivity effects have been avoided.

For inert ambient experiments, <100> and <111> quarter wafers were subjected to nitrogen atmosphere drive-ins for different times and temperatures. For oxidizing ambient experiments, the quarter wafers were previously stripped of capping dioxide in 5:1 H_2O/HF solution until hydrophobic, and then subjected to 100% dry O_2 atmosphere drive-ins for different times and temperatures. In most cases diffusion of <100> and <111> wafers was performed simultaneously in the same furnace to guarantee the same processing conditions.

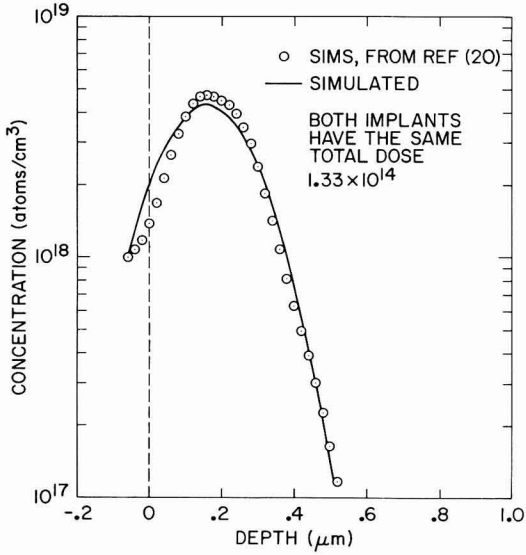

Fig. 1. Boron implant, 1.33×10^{14} ions/cm² dose, 70 keV, annealed at 900°C for 35 min.

After processing, junction depths were measured using angle lapping and electrical probing with a high precision spreading resistance two-point probe (23). The mechanical reliability of the probe yields junction depths with a resolution of ± 500Å for deep junctions (2-5 μm), and ± 250Å for shallow ones (0.5-2 μm). Some of the deeper junction depths were verified using groove and stain techniques and a sodium light dual-beam interferometer. Sheet resistances were measured using a light (45g) and a heavy pressure (180g) linear four-point probe array. Agreement between the measured values had a relative deviation no greater than 3%. Oxide thicknesses were measured with an ellipsometer at various points on the wafer, observing a fluctuation no greater than 2%. Good agreement was observed between the experimental thicknesses and those reported recently (24), except for the experiments at 900°C where thicknesses were consistently lower.

Analysis

The process simulator SUPREM (12) was used to model the impurity distribution of boron, on a computer, for every one of the different experimental processing schedules. In each case, the simulated profile characteristics were matched to the corresponding measured values. The diffusion and segregation coefficients were thus obtained as a result of the fitting process. In the simulation of oxidation, minor adjustments were made to the linear and parabolic oxide growth rates (25) in order to simulate the proper experimental oxide thicknesses.

The simulated junction depths and sheet resistances were compared with the corresponding measurements of these quantities. In each case, the initial estimates of diffusion and segregation coefficients were iteratively adjusted until agreement (within less than 1%) between measured and simulated values was established. The iterative adjustment was carried out by the built-in SUPREM optimizer (26). The optimizer

[1] The definition of the segregation coefficient here follows that of Grove *et al.* (19), and is the inverse of the one used by Colby and Katz. Since boron generally prefers the oxide, "higher" segregation coefficient, in this paper, means a smaller boron concentration in the oxide side of the interface for a given concentration in silicon.

is operated as a nonlinear equation solver in which the unknown diffusion coefficient in the case of inert ambient drive-ins is found by fitting the measured sheet resistance. In the case of oxidizing ambient drive-ins the diffusion and segregation coefficients are found by fitting both the measured sheet resistances and junction depths.

Optimized parameter extraction is a systematic way of obtaining model-dependent parameters from measured data, even under conditions where parameters interact strongly. This method proves most useful when two or more parameters are to be fitted simultaneously as in the case of oxidizing ambient diffusion, where the boron diffusivity tends to increase the junction depth and lower sheet resistance, whereas segregation and the moving boundary tend to raise sheet resistance and decrease junction depth. It is important to note that in this work both diffusion and segregation coefficients were extracted simultaneously.

The simulated sheet resistance computed by SUPREM is a strong function of the hole mobility. Recently available information (13, 14) has been used to achieve substantially better agreement with actual measured values than was possible using older references (27, 28). The new mobility data as well as a smooth function fitted to them are shown in Fig. 2. Details on the fitting function are given in the Appendix. In order to minimize the effect of small process variations and measuring equipment condition in the observed values of sheet resistance, a constant ratio technique was employed. Each time sheet resistance was measured on a processed wafer, the corresponding control wafer was also monitored. Thus the goal of the fitting process was to match the observed and simulated ratios of processed-to-unprocessed sheet resistances rather than exact absolute values. Since the control wafers reflect the state of the common initial impurity distributions, small variations in the process up to this step tend to cancel out. Also, by measuring process and control wafers at the same time, probe conditioning variations tend to cancel out.

Results and Discussion

Diffusion.—Figure 3 is an Arrhenius plot of boron diffusivity obtained in inert ambients. An activation energy of 3.42 eV with an intercept factor of 0.55 cm^2/sec (often called preexponential factor), is found to describe boron diffusivity in <111> and <100> crystal orientation silicon, in the range of 900°-1200°C. For comparison, the diffusivity obtained by Kurtz and Yee under near intrinsic conditions (15) is also plotted. The agreement of our results with those generally accepted data supports the reliability of our fitting approach, namely, using only sheet resistance data. As a further confirmation we also performed junction depth measurements in selected nonoxidized samples, and the agreement with simulation was found to be satisfactory.

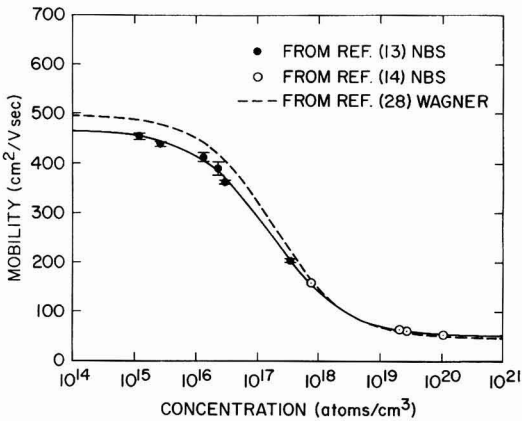

Fig. 2. Hole mobility in boron-doped silicon

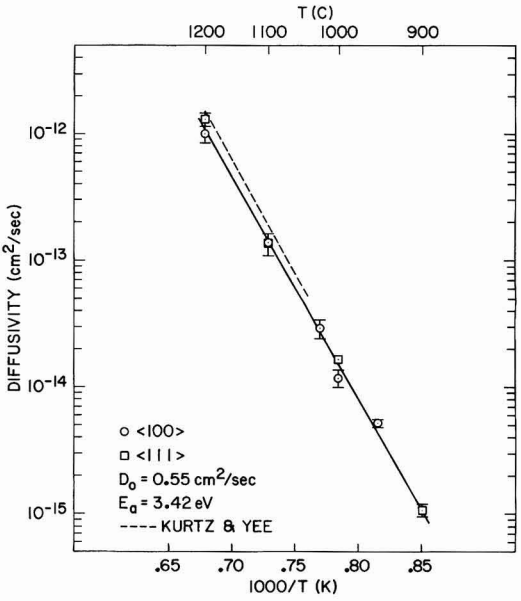

Fig. 3. Boron diffusivity in intrinsic silicon in nonoxidizing ambient

Having established the integrity of the sheet resistance approach we have been able to confidently use the additional information of junction depth for the simultaneous determination of diffusivity and effective segregation coefficient in the oxidation experiments. The results are shown in Fig. 4. As a reference, the inert ambient diffusivity is also plotted. Diffusivity enhancement has been obtained for the <100> orientations in practically all temperatures investigated. However, for the <111> orientation, enhancement was observed only at 900° and 850°C. Although other investigators have also reported absence of enhancement (6, 7) or reduced <111> enhancement (9) at the higher temperatures, we do recognize the fact that our data may be slightly underestimating the diffusivity because the spreading resistance method often tends to underestimate junction depth.

A remarkable feature of the data presented here is the multifold increase of boron diffusivity at the lower temperatures. For <100> silicon there exist enhancements of order 2, 5, and 10 at 1000°, 900°, and 850°C, respectively. For <111> silicon the enhancement order is 2 at 900°C and 5 at 850°C. It is clear that for both orientations the enhancement increases with decreasing temperature. An attempt to fit the data by a single activation energy over the entire range of the present experiments would be misleading.

An extensive set of boron diffusivities in <100>, <110>, and <111> silicon has recently been published by Masetti *et al.* (9). However, since they have used chemical predeposition the silicon was not intrinsic at least for part of the process duration. Furthermore, their numerical scheme cannot take concentration dependence into account. For dry O_2 in the range from 950° to 1200°C they have reported data fitted by single activation energies. Enhancement for <111> is small (about 1.2 over the whole range), but larger for <100>, increasing with decreasing temperature. Qualitatively these data are similar to ours but there is significant quantitative disagreement in the <100> case, particularly at 1000-1100°C. In general it

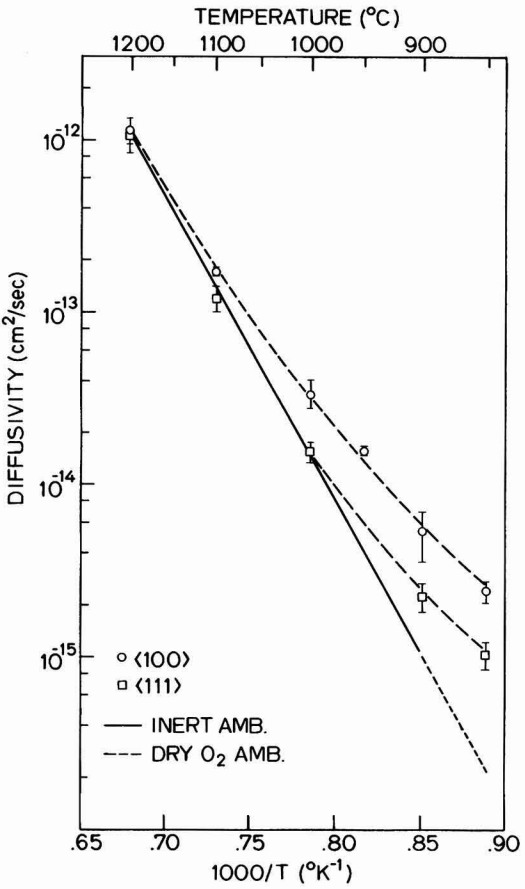

Fig. 4. Boron diffusivity in silicon in an oxidizing ambient

is difficult to compare our oxidation results to previously published data mainly because of differences in experimental conditions and in some instances, methods of data analysis. For this reason we will not pursue a comparative survey of the literature at this point.

Concentrating on the data presented in this paper, an explanation of the temperature-dependent behavior of the diffusivity enhancement will now be presented based on the model proposed by Hu (16) to explain the formation of stacking faults and enhanced diffusion during oxidation of silicon. Briefly, this model envisages a supersaturation of the silicon lattice by excess self-interstitials at concentrations dependent on the oxide growth rate and silicon orientation. These interstitials are thus responsible for the growth of stacking faults and, by invoking a dominant interstitialcy diffusion mechanism for boron, also responsible for diffusion enhancement. Assuming a fractional interstitialcy mechanism, f_A, it is straightforward to show that the effective diffusivity $\langle D \rangle$ of boron in an oxidation process of duration t, is given by

$$\langle D \rangle = \frac{1}{t}\int_0^t D\,dt$$

$$= D^* + \frac{D^*}{tC_i^*} f_A \int_0^t (C_i - C_i^*)\,dt \qquad [1]$$

where D^* is the intrinsic diffusivity of boron and C_i^* and C_i the intrinsic and the extrinsic concentrations of silicon self-interstitials, respectively. Using Hu's theory (16), the above equation allows one to relate the effective diffusivity to the size of oxidation stacking faults. Indeed, from Eq. [13] of Ref. (16) the length, r, of stacking faults as a function of the process duration, t, can be expressed as

$$r = \pi\alpha_0^2 D_i \int_0^t (C_i - C_i^*)\,dt \qquad [2]$$

where α_0 is the capture distance of interstitials by the faults and D_i the silicon interstitial diffusivity. Thus the ratio $\langle D \rangle / D^*$ can be expressed by

$$\frac{\langle D \rangle}{D^*} = 1 + f_A \frac{r}{\pi\alpha_0^2 D_i C_i^* t} \qquad [3]$$

Assuming further that the diffusivity of silicon is partly due to an interstitialcy mechanism (29, 30), we may write

$$D_i C_i^* = f_s D_s C_s \qquad [4]$$

where f_s is the fractional interstitialcy mechanism, and D_s and C_s the intrinsic diffusivity and lattice concentration of silicon. Thus Eq. [3] becomes

$$\frac{\langle D \rangle}{D^*} - 1 = \frac{f_A}{f_s} \frac{r}{\pi\alpha_0^2 D_s C_s t} \qquad [5]$$

Recently Hu (17, 18), published an empirical relationship for r based on his experiments

$$r = (Ae^{-Q_f/kT}) t^{0.8} \qquad [6]$$

where T is the absolute temperature, k is Boltzmann's constant, and for both wet and dry oxygen $Q_f = 2.3$ eV while the values of A for dry oxygen are $A = 326$ cm $\text{sec}^{-0.8}$ for ⟨100⟩, and $A = 156$ $\text{sec}^{-0.8}$ for ⟨111⟩ silicon. Finally, it is well known that at least within limited temperature ranges the self-diffusivity of silicon can be expressed in terms of a single activation energy, Q_s (4, 5, 31)

$$D_s = D_{os} \exp\left(-\frac{Q_s}{kT}\right) \qquad [7]$$

Hence using Eq. [6] and [7] in Eq. [5] we have

$$\left(\frac{\langle D \rangle}{D^*} - 1\right) t^{0.2} = \frac{f_A}{f_s} \frac{A}{\pi\alpha_0^2 D_{os} C_s} \exp\left(\frac{Q_s - Q_f}{kT}\right) \qquad [8]$$

In the above expression all factors are experimentally determinable with the exception of the ratio f_A/f_s.

Figure 5 is a plot of the quantity $(\langle D \rangle / D^* - 1) t^{0.2}$ obtained from our ⟨100⟩ experiments. It can be seen that this quantity exhibits a negative activation energy of −1.8 eV at the temperatures below 1000°C while over-all an activation energy of about −2 eV may be fitted. Assuming the experimentally determined values $Q_f = 2.3$ eV (17, 18) and $Q_s = 4.4$ eV (an average of values in literature for the low temperature end), the activation energy expected from Eq. [8] is −2.1 eV. Thus, there is at least good qualitative agreement between theory and experiments. This agreement is even better if the value $Q_s = 4.1$ eV recently obtained by Sanders and Dobson (31), near the lower temperatures of our experiments is used.

A quantitative comparison between theory and experiments is not directly feasible. The reason is mainly the presence of the term f_A/f_s. Accepting the Sanders and Dobson data (31), as representative of lower temperatures (5), and $\alpha_0 = 3.85 \times 10^{-8}$ cm, we obtain the following relationship from Eq. [8]

$$\frac{f_s}{f_A}\left(\frac{\langle D \rangle}{D^*} - 1\right) t^{0.2} = B \exp(1.8/kT) \qquad [9]$$

where $B = 2.4 \times 10^{-7}$ for boron in ⟨100⟩ silicon and $B = 1.1 \times 10^{-7}$ for boron in ⟨111⟩ silicon. Table I summarizes the observed $(\langle D \rangle / D^* - 1) t^{0.2}$ results

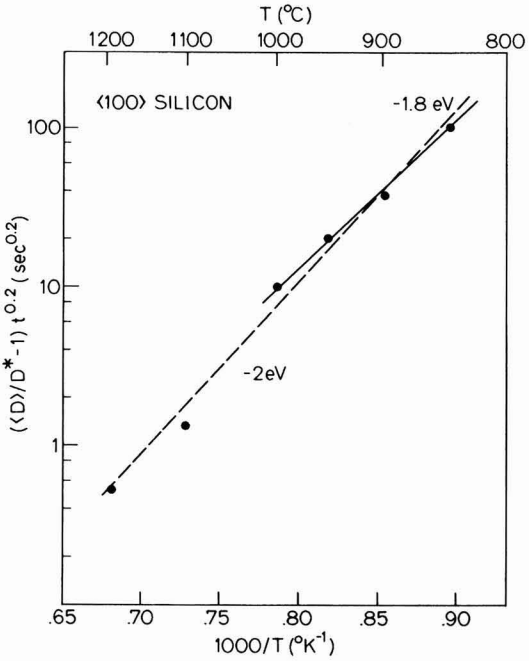

Fig. 5. The boron diffusivity enhancement factor in <100> silicon as a function of temperature.

and the calculated values of f_A/f_s from Eq. [9]. It is clear that a value of about 3 would be expected from the presented theory. The meaning of this is that the fractional interstitialcy mechanism for boron diffusion in silicon is about three times larger than that for silicon self-diffusion. Although this conclusion cannot be supported from independent data we do feel that it is quite plausible.

It is clear from Eq. [8] that the presented theory together with the experimentally determined growth of stacking faults predict a slight inverse time dependence ($\sim t^{-0.2}$) of the diffusivity enhancement. Due to the magnitude of experimental errors we have not attempted to accurately establish this time dependence. However, we have indeed observed a consistent time dependence suggesting at t^{-a} relation and although the exact value of "a" is not clear, there is conclusive evidence that it is smaller than 0.5.

In conclusion it should be mentioned that an inherent assumption in the present theory is that the concentration of excess silicon interstitials is not affected by the density of stacking faults. This assumption is quite valid since only a small fraction of the excess interstitials is expected to participate in the fault growth. Thus, although the density of oxidation stacking faults may vary significantly in accordance to the density of available nucleation sites that, in turn, depends on sample preparation, the length of the faults is only dependent on oxidation conditions and surface orientation (16, 7, 32). Thus, we do not expect that the introduction of boron by ion implantation (which increases strain sites) may have affected the diffusion enhancement mechanism. In addition, transient phenomena such as excess point defect concentration due to the ion implantation do not affect our results because, as already mentioned, all samples received annealing prior to the diffusion experiments.

Table I. f_A/f_s from data and theory

	From experiments $(\langle D\rangle/D^* - 1)\ t^{0.2}$ (sec.$^{0.2}$)		f_A/f_s	
T (°C)	<100>	<111>	<100>	<111>
850	104	42	3.6	3.2
900	38	14	2.9	2.3
950	21	—	3.3	—
1000	10	—	3.1	—

Segregation.—Under conditions of thermal equilibrium the chemical potential as seen by an impurity species such as B, As, or P must be continuous across the Si/SiO_2 boundary. Thus, generally the concentration of impurities across the boundary are not equal, giving rise to a nonunity equilibrium segregation coefficient, m_{eq}. Theoretical calculations only bracket the value of m_{eq} within several orders of magnitude. It is not clear whether during thermal oxidation of silicon the segregation process is actually in equilibrium. It thus follows that the actual impurity ratio may not be either equal to m_{eq} or even constant throughout an oxidation process step. In the present work we have assumed that at a given temperature, the segregation process can be characterized by a constant (effective) segregation coefficient. The segregation coefficients thus obtained are plotted as a function of temperature and silicon orientation in Fig. 6. For comparison, the data presented by Colby and Katz (11), Prince and Schwettmann (33), and Murarka (34) are also shown. As can be seen, our data can be fitted by a single activation energy over the entire range of temperature of the experiments. However, there is a disagreement with the other three sets of data. Although no explanation can be given at present, the difference in experimental methods between the various works needs to be outlined. (*i*) Colby and Katz have obtained their data by direct measurement of boron concentrations across the interface using SIMS. As in the present work they have used dry O_2 oxidation. However, unlike our case the silicon crystal was not intrinsic, but rather it was uniformly doped at relatively high concentration (2×10^{19} cm^{-3}). (*ii*) Prince and Schwettmann have obtained their data by a fitting technique similar to ours. However, their oxidation process was performed in steam ambient. (*iii*) Finally, Murarka (34) has also used a fitting technique similar to ours and in addition his experiments were at low dose and in dry O_2 ambient. Thus, the experimental and fitting procedures

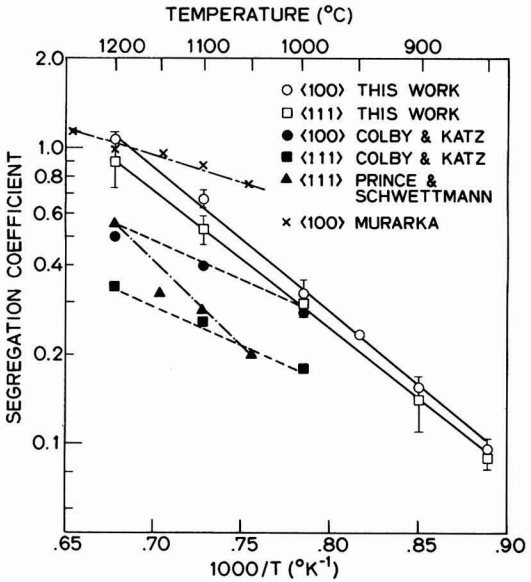

Fig. 6. Boron effective segregation coefficient in <100> and <111> silicon.

are similar with only two but possibly important differences. First, Murarka's samples were not annealed prior to the oxidation experiments, and second the mobility data he used was after Caughey and Thomas (27). If a fast-transient diffusivity exists at the beginning of the oxidation, the effect would be to preserve more boron in the silicon, thus appearing as a lower effective segregation coefficient. This effect would be more pronounced at lower temperatures (23), with a resulting decrease in the activation energy of the segregation coefficient.

Conclusions

The diffusivity of ion-implanted boron in <100> and <111> near-intrinsic silicon has been studied experimentally under inert (N_2) and oxidizing ambients (dry O_2). The method has consisted of fitting computer-simulated process results to observations by means of an automatic zero-in algorithm. As-annealed rather than as-implanted initial profiles were used to avoid the regime of transient diffusion during initial annealing and to ensure full implant activation. The initial profile was assumed similar to that experimentally determined (by SIMS) in another work (20) under almost identical conditions. For inert ambient experiments the only measured data were the initial and final sheet resistance. The determined intrinsic diffusivity agrees well with previously reported data (15) and thus it may be concluded that the recent mobility data used in the present simulation are quite realistic. Previously accepted mobility data (27, 28) would give different results.

In the oxidation experiments both sheet resistance and junction depth were measured. The fitting process has thus yielded the effective segregation and diffusion coefficients. Diffusivity enhancement has been observed in both orientations. In qualitative agreement with previous works more enhancement was observed in <100> than in <111>. Also this enhancement was found to increase with decreasing temperature. Quantitative differences do exist between this and the only comparable published work (9), which, however, was carried out using chemical deposition.

The determined effective segregation coefficients are in the general range of previously reported ones and obey a single activation energy. There is, however, a small difference between <100> and <111> orientations. Such an effect has been previously observed (11).

We have demonstrated that there is reasonable agreement between experimentally determined oxidation enhanced diffusion and growth of stacking faults, if one accepts the interstitialcy oversaturation model proposed by Hu (16). Within the context of this model it is necessary to assume at least a fractional interstitialcy diffusion mechanism for boron. Also, in order to bring the two sets of data to quantitative agreement, a fractional interstitial self-diffusion mechanism must be assumed for silicon, approximately three times smaller than for boron. The model readily predicts the observed increase of enhancement with decreasing temperature. It also predicts a slight time dependence of the diffusivity enhancement. At present the experimental errors of our method have not allowed verification of this dependence.

Acknowledgment

This research has been supported by ARO Contract DAAG-29-77-C-006.

Manuscript submitted Oct. 19, 1977; revised manuscript received Dec. 28, 1977.

Any discussion of this paper will appear in a Discussion Section to be published in the December 1978 JOURNAL. All discussions for the December 1978 Discussion Section should be submitted by Aug. 1, 1978.

Publication costs of this article were assisted by Stanford University.

APPENDIX

From the work of Caughey and Thomas (27), mobility can be expressed in the following functional form

$$\mu(C) = \mu_{min} + \frac{(\mu_{max} - \mu_{min})}{1 + (C/C_{ref})^{\beta}} \qquad [A\text{-}1]$$

where μ_{min} and μ_{max} are the minimum and maximum mobility values expected, C_{ref} a reference concentration value, and β an exponential factor that controls the slope around $C = C_{ref}$. From Ref. (13) and (14), the following values were obtained for this work

p-type	μ_{min}	μ_{max}	C_{ref}	β
Ref. (26)	47.7	495	6.3 E16	0.76
Ref. (27)	47.7	495	1.9 E17	0.76
This work	49.705	467.729	1.606 E17	0.700

n-type	μ_{min}	μ_{max}	C_{ref}	β
Ref. (26)	65	1330	8.5 E16	0.72
This work	55.24	1388.157	1.072 E17	0.733

The use of these new mobility function values resulted in excellent fit between measured and simulated sheet resistance values.

REFERENCES

1. B. L. Crowder, J. F. Ziegler, F. F. Morehead, and G. W. Cole, in "Ion Implantation in Semiconductors and Other Materials," B. L. Crowder, Editor, p. 267, Plenum Press, New York, (1973).
2. R. B. Fair, *This Journal*, **122**, 800 (1975).
3. A. S. Grove, D. Leistiko, Jr., and C. T. Sah, *J. Appl. Phys.*, **35**, 2695 (1964).
4. D. C. Kendall and D. B. DeVries, in "Semiconductor Silicon 1969," R. R. Haberecht and E. L. Kern, Editors, pp. 358-421, The Electrochemical Society Softbound Symposium Series, New York (1969).
5. R. B. Fair, in "Proceedings of the Third International Symposium on Silicon Materials Science and Technology," p. 968, The Electrochemical Society (1977).
6. W. G. Allen, *Solid-State Electron.*, **16**, 709 (1973).
7. W. G. Allen and K. V. Anand, *Solid-State Electron*, **14**, 397 (1971).
8. G. Masetti, P. Negrini, and S. Solmi, in "Redistribution and Anisotropic Diffusion of Boron in <100> and <111> Orientation Silicon," Alta Frequenza, Vol. 42, No. 11, pp. 626-630, (1973).
9. G. Masetti, S. Solmi, and G. Soncini, *Solid-State Electron.*, **19**, 545 (1976).
10. W. G. Allen and C. Atkinson, *ibid.*, **16**, 1283 (1973).
11. J. W. Colby and L. E. Katz, *This Journal*, **123**, 409 (1976).
12. D. A. Antoniadis, S. E. Hansen, R. W. Dutton, and A. G. Gonzales," Stanford Electronics Lab. Tech. Rep. No. 5019-1, May 1977.
13. NBS Special Pub. 400-29, W. M. Bullis, Editor, p. 16 (1977).
14. W. R. Thurber, Private communication.
15. A. D. Kurtz and R. Yee, *J. Appl. Phys.*, **31**, 303 (1960).
16. S. M. Hu, *ibid.*, **45**, 1567 (1974).
17. S. M. Hu, *ibid.*, **27**, 165 (1975).
18. S. M. Hu, *J. Vac. Sci. Technol.*, **14**, 17 (1977).
19. H. S. Rupprecht, in "NATO Advanced Study Institute on Process and Device Modeling for Integrated Circuit Design," Univ. Catholique de Louvain, France, July 19-29, 1977.
20. W. K. Hofker, H. W. Werner, D. P. Oosthoek, and H. A. M. deGrefte, *J. Appl. Phys.*, **2**, 265 (1973).
21. A. Chu and J. F. Gibbons, in "Proceedings of Fifth International Conference on Ion Implantation in Semiconductors and Other Materials," Plenum Press, New York (1976).
22. F. J. Morin and J. P. Maita, *Phys. Rev.*, **96**, (1954).
23. R. G. Mazur and D. H. Dickey, *This Journal*, **113**, 255 (1966).
24. R. W. Dutton, D. A. Antoniadis, J. D. Meindl, T. I. Kamins, K. C. Saraswat, B. E. Deal, and J. D. Plummer, Stanford Electronics Labs., Tech. Rep. No. 5021-1, Sect. 3.3 and Fig. 18 (1977).
25. B. E. Deal and A. S. Grove, *J. Appl. Phys.*, No. 36, (1965).
26. R. W. Dutton, A. G. Gonzalez, R. D. Rung, D. A.

Antoniadis, in "Semiconductor Silicon 1977," H. R. Huff and E. Sirtl., Editors, pp. 910-922, The Electrochemical Society Softbound Symposium Series, Princeton, N.J. (1977).
27. D. M. Caughey and R. E. Thomas, *Proc. IEEE*, **55**, 2192 (1967).
28. S. Wagner, *This Journal*, **119**, 1570 (1972).
29. A. Seeger and K. P. Chik, *Phys. Status Solidi*, **29**, 455 (1968).
30. S. M. Hu, "Atomic Diffusion in Semiconductors," D. Shaw, Editor, Chap. 5, Plenum Press, New York (1973).
31. I. R. Sanders and P. S. Dobson, *J. Mater Sci.*, **9**, 1987 (1974).
32. C. L. Clacys, E. E. Laes, G. J. Declerck, and R. J. van Overtraeten, in "Proceedings of Third International Symposium on Silicon Materials Science and Technology," p. 773, The Electrochemical Society, Princeton, N.J., May 1977.
33. J. L. Prince and F. N. Schwettmann, *This Journal*, **12**, 705 (1974).
34. S. P. Murarka, *Phys. Rev. B.*, **12**, 2502 (1975).

Preparation and Some Properties of Chemically Vapor-Deposited Si-Rich SiO_2 and Si_3N_4 Films

D. Dong,* E. A. Irene,* and D. R. Young

IBM Thomas J. Watson Research Center, Yorktown Heights, New York 10598

ABSTRACT

Films of SiO_2 and Si_3N_4 containing excess Si were prepared by chemical vapor deposition at 700°C by the reaction of gaseous SiH_4 and N_2O for the Si-rich SiO_2 and NH_3 for the Si-rich Si_3N_4. By adjusting the gas-phase ratio of the reactants it was possible to vary the amount of Si in the films. Transmission electron microscopy studies revealed that the films contain two amorphous phases. One phase is amorphous Si while the other is SiO_2 or Si_3N_4. The Si content of the films was measured by electron microprobe analysis. Ellipsometry measurements on the films were made at several angles of incidence in order to measure the film absorption coefficients which were found to increase with increasing Si content. The d-c conduction characteristic for the Si-rich films was found to be nonohmic. The resistivity at any given field was found to decrease with an increase of the Si content.

Films of silicon dioxide (SiO_2) and silicon nitride (Si_3N_4) prepared by chemical vapor deposition (CVD) have received considerable study. These films are used as gate dielectrics and for a variety of masking procedures within the MOS technology. Typically, the films are prepared in an open-tube CVD reactor at temperatures greater than 500°C by the reaction of a volatile silicon compound such as SiH_4 with a gaseous oxidant such as O_2, CO_2, H_2O, N_2O, etc. for SiO_2 films and SiH_4 with NH_3 for Si_3N_4 films. The films are usually amorphous and if the SiH_4 is maintained at about 10% or less of the reactive gas mixture, the film compositions are stoichiometric SiO_2 or Si_3N_4. It has been reported (1-4) that the Si content of Si_3N_4 films can be increased for CVD films. In these previous studies, the Si content of the films was inferred from refractive index changes, etch rate measurements, and electrical behavior. For Si-rich SiO_2 films, several articles (5-8) demonstrate the preparation of these films by sputtering, glow discharge, and evaporation techniques except for a recent paper (9), in which Si-rich SiO_2 was prepared by CVD using a SiH_4-N_2O-N_2 mixture. The Si-rich films exhibited higher conductivity (3, 4, 9) than the stoichiometric analogs, and the conductivity increased with Si content. Use was made of this variable conductivity property to controllably limit reverse current for a pn-junction diode (9).

The goals of the present study were to determine the CVD parameters which yield Si-rich SiO_2 and Si_3N_4 with a desired amount of Si; to identify the relationships between gas phase mixtures, solid phase composition, resistivity, and refractive index; and to determine whether the films are homogeneous or phase separated. Presently, there exists controversy (5, 7) whether Si-rich SiO_2 is composed of a mixture of Si-Si_4 and Si-SiO_4 tetrahedra or simply separate Si and SiO_2 phases. Therefore, transmission electron microscopy (TEM) was performed on the films prepared in this study to elucidate the morphology.

* Electrochemical Society Active Member.
Key words: dielectric films, variable conductivity, excess Si.

Experimental Procedures

CVD. —The CVD apparatus was the same resistance-heated system previously described (10). The Si-rich films were deposited on cleaned <100> oriented, chem-mechanically polished, 2 Ω-cm p-type Si wafers (3.2 cm diam). The cleaning procedure for the Si substrates was also previously reported (11). A temperature of 700°C was used for all depositions. This temperature was chosen to be low enough to preclude extensive decomposition of the SiH_4 prior to injection into the reaction zone of the furnace. Although higher temperatures can be used to prepare Si-rich films, the amount of SiH_4 used for the preparations becomes excessively large.

The Si-rich SiO_2 films were prepared by the reaction of gaseous N_2O and SiH_4; for Si-rich Si_3N_4, NH_3 and SiH_4 were the reactants. In both cases the reactants were diluted with a N_2 carrier. The total flow into the CVD reactor (at 20°C, 1 atm) was maintained at 15 liters/min (~13 cm/sec linear gas stream velocity) of which the reactant gases were always less than 0.5 liters/min. In order to alter the Si content of the films, the gas phase reactant ratios, R_O (N_2O/SiH_4), for Si-rich SiO_2 and R_N (NH_3/SiH_4) for Si-rich Si_3N_4 was varied.

The elemental composition of the films was obtained from electron microprobe analyses on films several thousands of angstroms thick. Film thickness, index of refraction, and optical adsorption were measured by ellipsometry. Electrodes for electrical measurements

were evaporated Al dots (0.8 mm diam) on the film side of the samples and gallium-indium paste was used for the Si side electrical contact.

Ellipsometry.—Excess Si in the films causes optical absorption. The absorption needs to be characterized in order to perform accurate ellipsometric measurements of the film thickness. For this purpose, a special procedure was used (12) in which ellipsometry was performed at multiple angles of incidence. The procedure is outlined as follows: (*i*) Two zone ellipsometric measurements were made on a particular sample at constant wavelength (5461Å) but at several angles of incidence, ϕ, ranging between 60° and 80° in 5° intervals. (*ii*) A range of values for adsorption, κ, was arbitrarily chosen. The film thickness, D, and the real part of the film refractive index, N, were calculated for each κ and at each ϕ. The relationship between κ, N in the complex refractive index, N is given by the equation

$$\overline{N} = N(1 - i\kappa)$$

(*iii*) For each value of ϕ a line in κ, N, and D space was obtained. The sets of lines for various ϕ were plotted together on a three coordinate axes graph. In principle, all the lines should intersect yielding one value for N, κ, and D. However, due to experimental uncertainties (12), a zone of convergence is realized. From the zone of convergence, an average value for N, κ, and D can be obtained. An example of the convergence is given in Fig. 1a. Figure 1b shows a cut of Fig. 1a showing the κ and N planes. Such projections were used to obtain the numerical values reported later.

Electrical measurements.—The resistivity, ρ, was measured with the 2 Ω-cm p-type silicon substrates in accumulation. Heavily doped substrates were not used in order to preclude possible dopant effects in the films. Capacitance-voltage measurements at 1 MHz were made to determine whether the films stored charge or whether they lost the injected charge as anticipated by considering the measured values of ρ.

In order to compare the results for films with different Si content, films of approximately the same thickness (700 ± 100Å) were measured. The applied voltage ramp speed and amplitude were kept constant and the films were ramped first from depletion to accumulation, and then in reverse. The hysteresis in the C-V curve measured on the voltage near flatband (called ΔV) is proportional to the amount of charge, assumed to be near the Si surface, stored by the films.

Transmission electron microscopy (TEM).—The samples for TEM studies were prepared as previously described (13). Starting with films ~500Å on an Si substrate, the substrate was etched with HF-HNO_3 mixtures. The etch mixtures vigorously attacked the Si-rich SiO_2 and stoichiometric SiO_2 films. The etchant moderately attacked Si-rich Si_3N_4 films and only slightly attacked stoichiometric Si_3N_4 films. The qualitative difference in the etch rates observed and the resultant morphologies lead to the results to be reported.

Results

Film composition.—The solid-phase compositions as a function of gas phase reactant ratios, R_O and R_N, are shown in Fig. 2a for Si-SiO_2 films and in Fig. 2b for Si-Si_3N_4 films. For the higher gas phase ratios, the films approach stoichiometric SiO_2 and Si_3N_4. For $R_O < 50$ and $R_N < 25$, there is Si enrichment of the oxide

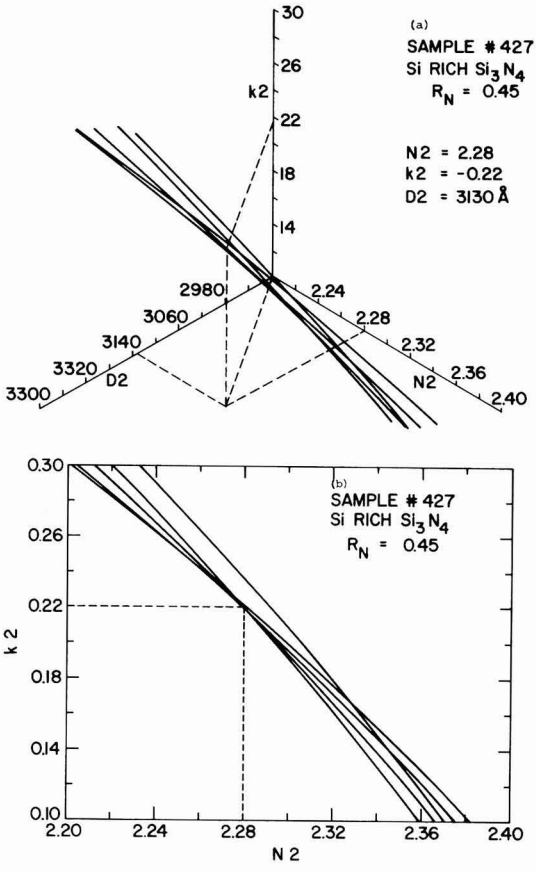

Fig. 1. a, A plot of the zone of intersection of the lines representing various angles of incidence, ϕ, on the axes of absorption coefficient, *K2*, real part of the refractive index, *N2*, and film thickness, *D2*; b, a cut of Fig. 1a showing the *K2*, *N2* plane.

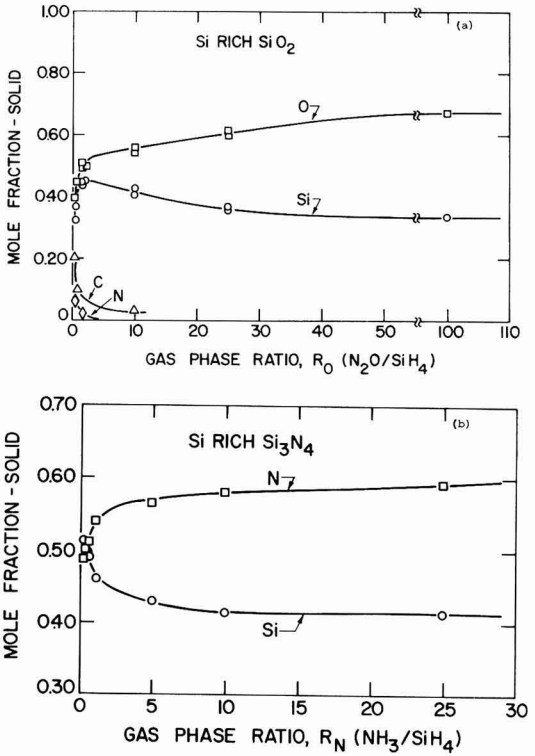

Fig. 2. a, Electron microprobe analyses of Si-rich SiO_2 *vs.* the gas-phase ratio; b, the same relationship for Si-rich Si_3N_4.

and nitride films. For the Si-rich Si_3N_4 films, the Si content increases smoothly with decreasing R_N for the entire range studied ($0.6 < R_N < 25$), and the Si content varies from 42 to 51% in this R_N range. Similarly, for R_O values between 100 and ~ 3, the Si content for the oxide films varies from 33 to 45%. However, for $R_O < 3$, both the Si and O content drop sharply while significant amounts of N and C appear. Later-reported resistivity values are also sensitive to this anomalous drop in Si content. Although not experimentally verified in this study, we believe that silicon oxynitride and/or oxycarbide type compounds were formed due to carbon impurities in the N_2O and the large amount of N_2 that was present.

Refractive index.—The optical absorption of these Si-rich films was characterized by the previously outlined ellipsometry procedures. The measured absorption coefficient values are shown in Fig. 3. The values of κ are seen to be small for the Si range studied, and if κ is assumed to be zero, less than 10% error in thickness is made for film thicknesses in the first ellipsometric period. Figure 3a shows that the absorption increases nearly linearly with Si content. Figure 3b shows that Si content for Si-rich SiO_2 films does not increase smoothly for low R_O values. In fact, as observed in Fig. 2a, the Si content drops for low R_O values while N and C levels increase. Therefore, κ is a sensitive measure of the Si content for these films.

Electrical measurements.—Figure 4 summarizes the resistivity measurements. The d-c behavior is seen to be nonohmic and ρ decreases as the Si content increases. Therefore, from Fig. 4a and 4b, films with desired values of ρ can be grown if the value for the operating field, E, across the film is specified. As mentioned previously for the Si-rich SiO_2 films at low values of R_O, the Si content drops anomalously. As seen in Fig. 4a, the curve for $R_O = 1$ shows larger values for ρ at any field studied than for the $R_O = 3$ curve. Therefore, the ρ value for a specified E is also

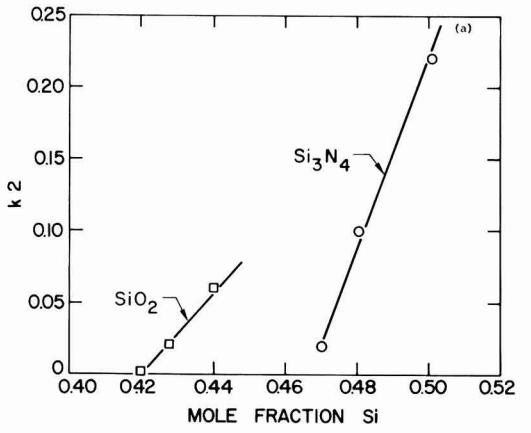

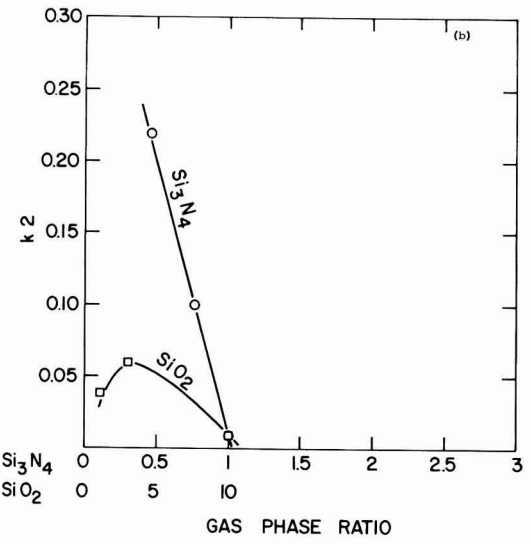

Fig. 3. a, The absorption coefficient, $K2$, vs. the Si content for both Si-rich SiO_2 and Si_3N_4 films; b, $K2$ vs. the gas-phase ratios R_O and R_N.

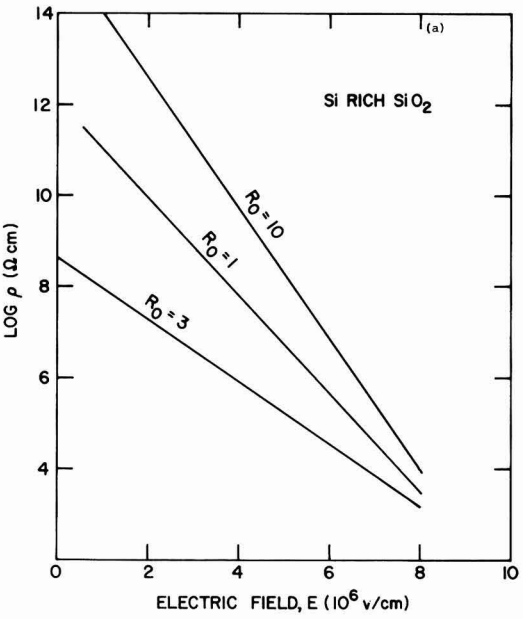

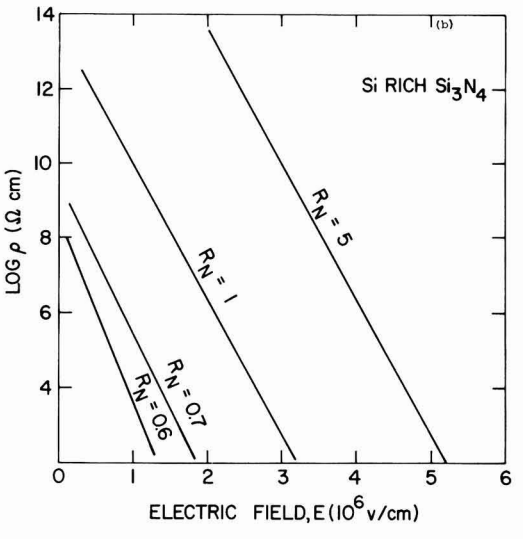

Fig. 4. a, The plot of $\log_{10} \rho$ vs. the applied electric field, E, for Si-SiO_2 with various gas phase ratios, R_O; b, the same as Fig. 4a for Si-Si_3N_4 for various R_N.

a sensitive indicator of the Si content of the film. For the Si-rich Si_3N_4 film, the Si content increased smoothly with decreasing R_N in the range studied, and the ρ values decreased for decreasing R_N.

The capacitance-voltage, C-V measurements are summarized in Fig. 5. Figure 5a shows that for Si-Si_3N_4 films the amount of stored charge, as measured by the hysteresis in the C-V curves, decreases with increasing Si content. This is to be expected inasmuch as with decreasing ρ the time constant for the storage of charge should also decrease. However, Fig. 5b for Si-SiO_2 shows an enhancement of charge storage with increasing Si content. This may be due to a thin thermal oxide being formed at the Si surface in the ambient containing N_2O. When the thin thermal oxide is coated with the Si-rich SiO_2, a metal, insulator, SiO_2, silicon (MIOS), charge storage structure is formed.

Transmission electron microscopy.—The TEM results are summarized by Fig. 6. The photographs are interpreted by remembering that the etchant used to prepare the samples attacks Si very vigorously, SiO_2 vigorously, and only very mildly attacks Si_3N_4. Figure 6a shows the TEM results for stoichiometric Si_3N_4. With the exception of some particulate in the films, the micrographs are featureless indicating uniform etching. Figure 6b, however, shows the result from the etchant attacking the Si-rich Si_3N_4. The bright areas are regions where Si has been preferentially attacked by etchant. Both photographs show only diffuse diffraction halos indicative of amorphous material. The Si-rich material shows randomly distributed Si areas having a rather connective appearance. Figure 6c and 6d show a comparison for stoichiometric and Si-rich SiO_2 films. Although the effect is not as definitive as for the Si_3N_4 films, it is clear that some regions of the

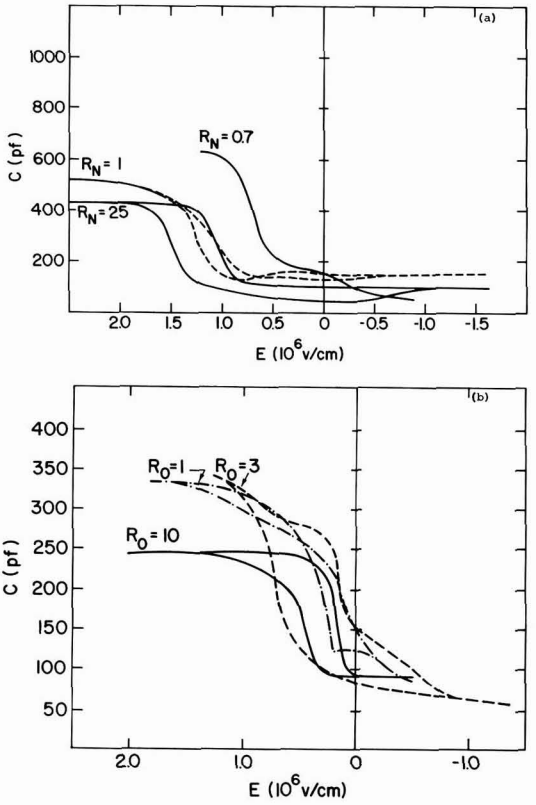

Fig. 5. a, C-V curves for Si-Si_3N_4 with various R_N; b, C-V curves for Si-SiO_2 with various R_O.

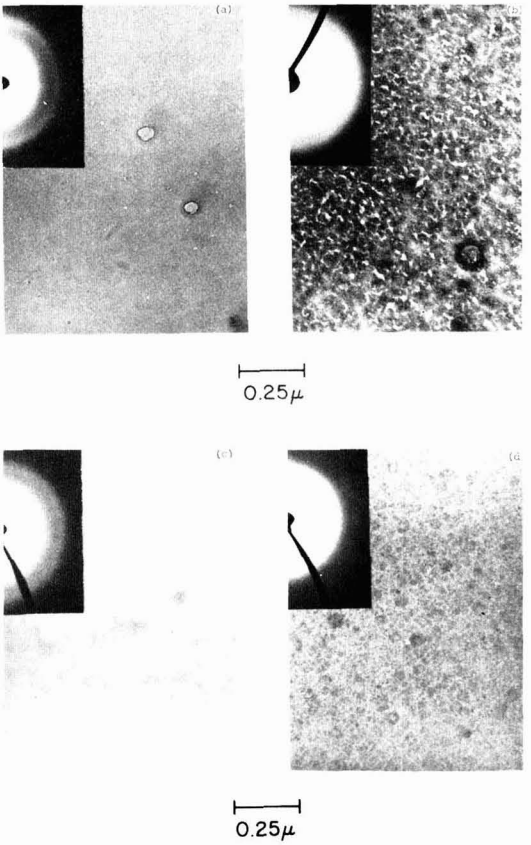

Fig. 6. TEM micrographs and diffraction patterns for stoichiometric and Si-rich Si_3N_4 and SiO_2. a, stoichiometric Si_3N_4, R_N = 25; b, Si-rich Si_3N_4, R_N = 0.5; c, stoichiometric SiO_2, R_O = 100; d, Si-rich SiO_2, R_O = 1.

Si-rich SiO_2 shown in Fig. 6d are attacked more vigorously than others while by comparison Fig. 6c shows uniform etching characteristics. Since SiO_2 and Si are attacked by the etchant, this result for Si-rich SiO_2 is expected. Both 6b and 6d reveal that the etched phase is connective rather than spherical.

Based on the morphologies discovered by TEM, it is concluded that these Si-rich materials are composed of two amorphous phases: a silicon phase and either a SiO_2 or Si_3N_4 phase.

Summary

It has been shown that films of SiO_2 and Si_3N_4 can be prepared with a controllable excess of Si by chemical vapor deposition by adjusting the gas phase reactant ratios. The excess Si forms a rather connective secondary phase under the conditions of the present study. The resistivity and optical absorption are both sensitive to the Si content of the films. The d-c conductive behavior for the Si-rich films is nonohmic but for any given field the resistivity decreases with increasing Si content.

Acknowledgment

The authors gratefully acknowledge the electron microprobe work by S. Ellmann and R. Schad and critical reviews of this manuscript by Drs. A. B. Fowler and J. A. VanVechten.

Manuscript submitted Nov. 3, 1977; revised manuscript received Dec. 20, 1977. This was Paper 268 pre-

sented at the Atlanta, Georgia, Meeting of the Society, Oct. 9-14, 1977.

Any discussion of this paper will appear in a Discussion Section to be published in the December 1978 JOURNAL. All discussions for the December 1978 Discussion Section should be submitted by Aug. 1, 1978.

Publication costs of this article were assisted by IBM Corporation.

REFERENCES

1. W. A. Kohler, *Metall. Trans.*, **1**, 735 (1970).
2. J. R. Yeargan and H. L. Taylor, *This Journal*, **115**, 273 (1968).
3. V. Y. Doo, D. R. Kerr, and D. R. Nichols, *ibid.*, **115**, 61 (1968).
4. K. Tanabashi and K. Kobayashi, *Jpn. J. Appl. Phys.*, **12**, 641 (1973).
5. H. R. Philipp, *J. Phys. Chem. Solids*, **32**, 1935 (1971).
6. M. V. Coleman and D. J. D. Thomas, *Phys. Status Solidi.*, **22**, 593 (1967).
7. B. J. Joyce, H. F. Sterling, and J. H. Alexander, *Thin Solid Films*, **1**, 481 (1967/1968).
8. J. S. Johannessen and W. E. Spicer, *J. Appl. Phys. Lett.*, **27** (1975).
9. T. Aoki, T. Matsushita, H. Yamoto, H. Hayashi, M. Okayama, and Y. Kawara, Paper 148 presented at the Toronto, Canada, Meeting of the Society, May 11-16, 1975.
10. V. J. Silvestri, E. A. Irene, S. Zirinsky, and J. D. Kuptsis, *J. Electron. Mater.*, **4**, 429 (1975).
11. E. A. Irene, *This Journal*, **121**, 1613 (1974).
12. S. S. So and K. Vedam, *J. Opt. Soc. Am.*, **62**, 16 (1971); S. S. So, IBM Tech. Rep. TR 55034 (1975); S. S. So, Private communication.
13. E. A. Irene, V. J. Silvestri, and G. R. Woolhouse, *J. Electron. Mater.*, **4**, 409 (1975).

Technical Notes

Protective Glassy Layers Passivating Copper at 500°C

B. J. Mulder

Philips Research Laboratories, Eindhoven, Netherlands

Copper objects of complicated shape have been coated with a protective glassy layer consisting mainly of SiO_2 with a thickness of a few tenths of a micron. The coating offers protection against oxidation in air at temperatures up to 500°C. The coating is applied by chemical vapor deposition in sealed ampuls using a technique worked out by Chu and Gruber (1) for coating semiconductor materials. The reactive gases (HF and H_2O) were not, however, introduced as such, but generated *in situ* from copper difluoridehydrate (2). Glass is transported from the walls of the ampul in a cooler zone onto the copper in a hotter zone.

The arrangement for the coating reaction is shown in Fig. 1. Ampuls were made of borosilicate glass. Larger ampuls were sprung open at A for loading. The ampuls contained: (*i*) Copper difluoridehydrate, preferably in a separate glass container with the powder not in direct sight of the copper substrate. The water content of the fluoride[1] was apparently not critical: the mono and the dihydrate served equally well. Normally a technical-grade monohydrate was used in amounts corresponding to 1-2 mg per milliliter of ampul volume; (*ii*) The carefully cleaned and degreased copper objects. The copper was normally pretreated with a polishing etch; (*iii*) A glass heat shield, protecting the copper against oxidation when the ampul was repaired (in a vertical position) at A. The ampul was pumped with a rotary pump and sealed at B. It was then heated without delay in a furnace with two temperature zones, one at 550°C (just below the softening point of the glass) where the copper was placed, and one at 500°C for the fluoride. Heating up took about 5-10 min; after another

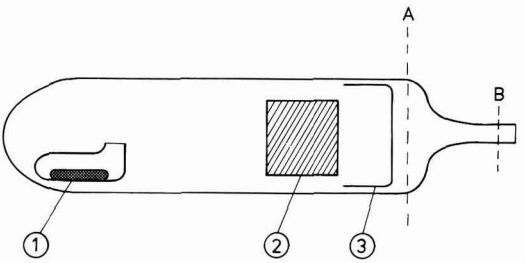

Fig. 1. Arrangement for chemical vapor deposition of glass onto copper in sealed borosilicate ampuls. Ampuls were used with diameters ranging from 10 to 60 mm and a length of about 250 mm.

30 min the ampul was taken out of the furnace and cooled. We froze the bottom end of the ampul in liquid nitrogen to prevent reverse transport reactions and also to avoid condensation of vapor on the copper.

The layers had a very uniform and smooth appearance, which was preserved when the copper was heated in air up to temperatures of 500°C. This suggests that the layers are essentially pinhole free.

The thickness of the layers was determined from measurements of their x-ray fluorescence.[2] with 500°C for the temperature of the source region and 550°C for the substrate the layers attained their final thickness of a few tenths of a micron in about 30 min. The thickness increased with the amount of copper di-

Key words: chemical vapor deposition, copper, passivation, SiO_2, glass.

[1] The water content of a hydrate was determined by slowly heating in air to 600°C and weighing the residue of CuO.

[2] The intensity of the characteristic fluorescence of silicon was referred to standard layers prepared by bias sputtering fused quartz on copper foil. The intensity was almost proportional to the thickness of the standards up to 0.4 μm. Since the sample layers consisted almost entirely of SiO_2, intensities were converted into thickness using data for fused quartz.

fluoride weighed into the ampul: for a tenfold increase in copper-difluoride (from 0.7 to 7 mg per ml volume of the ampul) the thickness approximately doubled from 0.15 to 0.3 μm SiO_2. The composition of the layer was studied qualitatively by secondary ion mass spectrometry (SIMS), revealing F, B, and OH as minor contaminants of the SiO_2. The F/Si ratio was determined quantitatively by electron-excited x-ray spectrometry[3] and was found to correspond to $x = 0.005$ in the composition formula $SiO_{2-x}F_{2x}$. Heating in air for 16 hr at 450°C approximately halved the fluorine content of the layers without affecting their integrity.

[3] Thin standard layers with a known Si/F ratio were prepared by mixing polyvinylidenefluoride, $[(—CH_2CF_2)_n]$ dissolved in hot cyclohexanone, and heavy silicone oil $[(-Si(CH_3)_2O)_n]$ dissolved in hot toluene, spraying the hot mixture onto warm copper foil and evaporating the solvents. The correction required for the difference between the mass absorption coefficients of standards and samples turned out to be quite small.

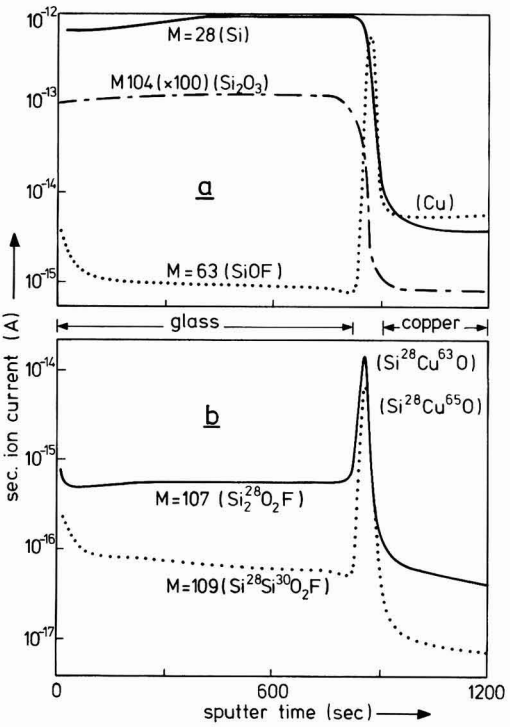

Fig. 2. Depth profiles obtained by SIMS for a 2000Å thick glass coating on copper.

An in-depth analysis with SIMS revealed the existence of an interlayer between glass and copper, characterized by the production of CuSiO clusters. Depth profiles of a typical coating are shown in Fig. 2. The curves were traced while scanning an area of 1 mm^2 with a primary beam of oxygen ions. Positive ions with a fixed mass and originating from the central 50 × 50 μm^2 region of the erosion crater were detected. The presence of an interlayer of ~ 200Å thick is evident from the peak in the curves traced for mass numbers 107 and 109 (Fig. 2b). In the peak the intensity ratio for the two mass numbers is equal to the abundance ratio of Cu^{63} and Cu^{65} (2.23), showing the peak to be associated with the production of CuSiO clusters. "Mixed" clusters (Cu and Si) are not observed in SIMS when scanning an abrupt junction (3) and are therefore indicative of the presence of an interlayer. To the left of the peak the intensity ratio in Fig. 2b is close to the ratio expected for Si^{28} and Si^{30} containing clusters (~14). Other noticeable features of the curves are the very efficient production of copper ions (see curve for M = 63) from the interlayer and the relatively high production of fluorine containing clusters from the surface region of the coating.

The interlayer may arise from the diffusion of copper into the defective SiO_2 at the temperature of the coating reaction. An in-depth inhomogeneity was also suggested by measurements of the electrically insulating properties of the layers, using a mercury drop as one of the electrodes. Layers thicker than about 0.1 μm behaved normally in that they withstood voltages corresponding to field strengths of several times 10^6 V/cm, whereas thinner layers usually broke down at voltages corresponding to only 10^4-10^5 V/cm.

Acknowledgments

The x-ray radiation of the layers was measured by E. W. J. M. van Meijl. SIMS was performed by H. A. M. de Grefte.

Manuscript submitted Sept. 23, 1977; revised manuscript received Jan. 5, 1978.

Any discussion of this paper will appear in a Discussion Section to be published in the December 1978 JOURNAL. All discussions for the December 1978 Discussion Section should be submitted by Aug. 1, 1978.

Publication costs of this article were assisted by Philips Research Laboratories.

REFERENCES

1. T. L. Chu and G. A. Gruber, *Trans. Metall. Soc. AIME*, **233**, 568 (1965).
2. Le Van My, G. Perinet, and P. Bianco, *J. Chim. Phys.*, **63**, 719 (1966).
3. H. A. M. de Grefte, Private communication.

Anodization of Layered Semiconductors: A Method to Count the Number of Layers

A. Moritani, H. Kubo, and J. Nakai

Department of Electronics, Faculty of Engineering, Osaka University, Suita, Osaka, 565, Japan

In the anodization process of metals and semiconductors, it has been known that there exist nonpassive (or active) states and passive states, depending on the surface potential of the anode materials. We define the nonpassive state as the state in which the anodic dissolution is in process or a nonpassive film is growing with little increase of the anode potential on the surface of the anode material when anodization is performed under constant current condition. In this paper we demonstrate that anodization provides a new and simple method to count the number of layers

Key words: semiconductor, anode, ellipsometry, passivity.

in some layered semiconductors by utilizing the property of the nonpassive-passive transition which has been widely observed in the fundamental anodic process in metals and semiconductors (1, 2).

The layered semiconductors have been a recent topic in both experimental and theoretical studies (3). The micalike layer structures are characterized by strong covalent bonds within each layer and by weak van der Waals forces between layers, so that there exist high and fairly wide potential barriers and the crystals are easily cleaved at the layer boundary which we may consider to be another surface. Therefore, it is reasonable to expect that if a layered semiconductor is anodized in the direction normal to the cleaved surface, the nonpassive-passive transition will repeat at the nth layer boundary (n = 1, 2, 3, . . .). Thus, a periodically varying structure reflecting the layered structure with the monolayer thickness of ~10Å is expected to be observed in the cell voltage *vs.* time (V_c-*vs.*-t) characteristic curve when anodization is performed under a proper constant current condition with the use of a proper electrolyte. These observations will enable us to count the number of layers in the layered semiconductors: we can count the number of layers by this method after some experiments with the layered semiconductor of interest are over.

The electrolytic cell-system used in this study consists of a platinum cathode, the semiconductor anode, a simple quartz beaker, a magnetic stirrer, and a solution of sodium borate in ethylene glycol as the electrolyte. The cell voltage is measured and recorded through a buffer amplifier with high input impedance. The second derivatives of the V_c-*vs.*-t characteristics are recorded simultaneously in order to clarify the periodic structure and make it easier to count the number. P-type Bi_2Te_3 and p-type GaTe with carrier concentrations of 1-5 × 10^{19} cm^{-3} and 0.5-2 × 10^{16} cm^{-3} at room temperature were used as the semiconductor samples. The samples were cleaved in laboratory air, and edges and ohmic contact of the samples were covered for insulation by an epoxy paint.

Periodically increasing cell voltages are observed in Fig. 1 and 2 for Bi_2Te_3 and GaTe, respectively, as expected. It is seen in these figures that these periodic structures are formed by repetition of the unit-lineshape shown in the insert of Fig. 1, where τ_n represents the duration time of the nonpassive state and V_{cn} represents the cell voltage increase in the passive state for the nth layer.

For the purpose of confirming that the unit lineshape really results from anodization of the monolayer, we have performed ellipsometric measurements on the anodic films grown by anodization of more than 20 layers and obtained the anodized film thickness of 16 ± 1Å for monolayer anodization. The ratio of this value to the monolayer thickness of Bi_2Te_3, *i.e.*, 10.16Å (4) is 1.57 which is in close agreement with the theoretically expected value.[1]

Another experiment was done as in what follows to confirm that the region indicated by τ_n in the unit lineshape is really in the nonpassive state. The experimental result of τ_n *vs.* current density J_d (τ_n-*vs.*-J_d) characteristics are shown in Fig. 3 where the solid and broken curves were obtained with the use of the electrolytes which were prepared by dissolving 100 and 200g of sodium borate in one liter of ethylene glycol, respectively. It is observed in Fig. 3 that τ_n increases as J_d decreases and is dependent upon the electrolyte: the slope of the τ_n-*vs.*-J_d characteristic lines in log-log plot is found in the range of −1-−2, depending upon the electrolyte. These observations may be sufficient for the verification that the region indicated by τ_n is in the nonpassive state.

[1] The theoretical ratio of the oxide thickness to the monolayer thickness of Bi_2Te_3 (so-called Pilling-Bedworth ratio) was evaluated to be 1.54 ± 0.02 under the assumption that the growth film consists of trioxides, i.e., Bi_2O_3 and TeO_3 which seem to be the most probable products of oxides from Bi_2Te_3; see Ref. (10).

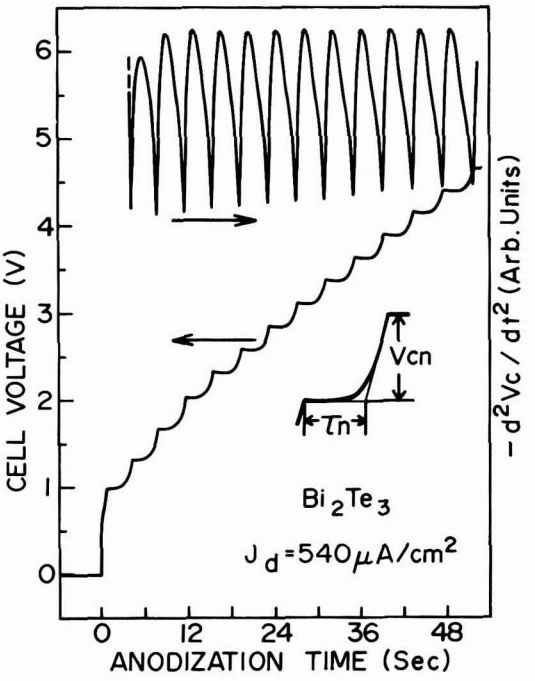

Fig. 1. The V_c-*vs.*-t characteristic and the second derivative of the V_c-*vs.*-t characteristic in Bi_2Te_3. Anodization was performed under constant current density J_d = 540 μA/cm². The initial voltage drop induces large transient output in the second derivative circuit, so that the initial part of the second derivative is not recorded in this figure. The inserted figure shows the unit lineshape from which the V_c-*vs.*-t characteristic curve is constructed.

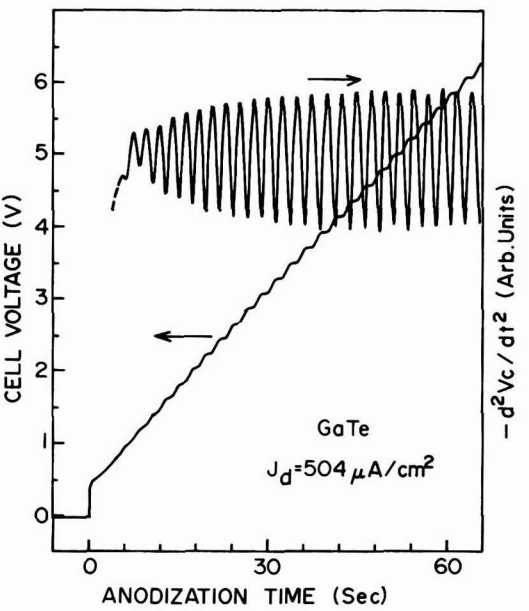

Fig. 2. The V_c-*vs.*-t characteristic and the second derivative of the V_c-*vs.*-t characteristic in GaTe. Anodization was performed with constant current density J_d = 504 μA/cm². The initial voltage drop induces large transient output in the second derivative circuit, so that the initial part of the second derivative is not recorded in this figure.

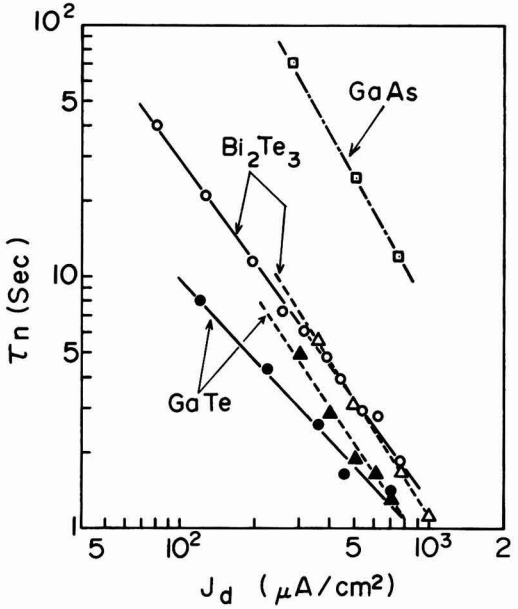

Fig. 3. The τ_n-vs.-J_d characteristics. The solid and broken lines were obtained with the use of electrolytes of sodium borate in ethylene glycol (100 g/liter) and (200 g/liter), respectively. The τ-vs.-t characteristic obtained in GaAs is shown for reference.

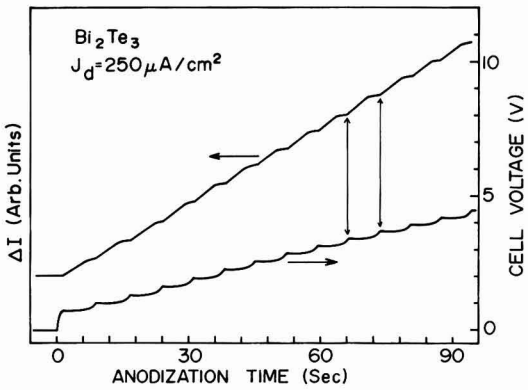

Fig. 4. The off-null signal of *in situ* ellipsometry (ΔI) and the corresponding V_c-vs.-t characteristic during constant current anodization with $J_d = 250\ \mu A/cm^2$ in Bi_2Te_3.

For reference, the τ-*vs.*-t characteristic observed in GaAs (5) is shown in Fig. 3, where τ is the duration time in the nonpassive region.

We have observed the periodic structure optically too in *in situ* ellipsometric measurements.[2] In Fig. 4, the *in situ* ellipsometry signal with initial null setting is shown together with V_c-*vs.*-t characteristic for Bi_2Te_3. ΔI is the increase of photomultiplier intensity due to the anodic film growth which causes the offset from the null setting. It is noted that ΔI shows rapid increase in the nonpassive region and little increase in the passive region. This observation strongly suggests that a conductive nonpassive film grows in the nonpassive state and transforms into a passive film in the passive state. These phenomena have been found in the anodic processes of iron and indium (6):[3] the initial film on iron in slightly alkaline solution at potentials $V < V_p$ is $Fe(OH)_2$, which transforms completely into Fe_2O_3 at higher potentials $V > V_p$, where V_p is a critical anode potential.

Thus, we have come to the stage that the unit lineshape represents anodization of the monolayer and it is possible to count the number of layers with extremely thin monolayer, *i.e.*, 7.45Å in GaTe (7) and 10.16Å in Bi_2Te_3 (4). In Fig. 1 and 2 are shown the second derivatives of the V_c-*vs.*-t characteristics which enable us to count more clearly the number, especially of the initial several layers in GaTe. We have counted the number up to 115 for Bi_2Te_3 and 95 ± 2 for GaTe in one anodization procedure.[4]

It should be noted that the nonpassive region for the first layer of Bi_2Te_3 was not observed in many cases, in other words, $\tau_1 \approx 0$. This experimental result for the first layer in Bi_2Te_3 may be corresponding to the observation in the anodization of GaAs by Harvey and Kruger (8). They have shown that, in the nonpassive region, no change in ellipsometric parameters attributable to a film forming on an initially clean anode was observed, but nonpassive anodic film was grown with virtually no change in potential when a vestige of a previously formed passive film presumably remained. In the present case, it is reasonable to consider that the passive film of the first layer can possibly be the nucleus for the nonpassive film growth of the second layer and this process repeats in the nth layer ($n \geq 2$).

It should be also noted that in Bi_2Te_3 the steady state in the anodization process is built up in the region $n \leq 5$ in many cases

$$V_{cn} \gtrsim V_{c(n+1)}; \quad (n = 1, 2, 3, 4),$$

$$V_{cn} = V_{c(n+1)}; \quad (n \geq 5)$$

On the other hand, a quite different feature from Bi_2Te_3 is observed before the steady state in anodization of GaTe: not little increase of cell voltage in the nonpassive (?) regions is observed in Fig. 2, which causes uncertainty in counting the number of initial few layers, and more layer numbers are required to realize the steady-state anodization than in Bi_2Te_3. The electrochemical mechanism which induces different values of V_{cn} or amplitude of the second derivative between, before, and under the steady state in both cases is not understood at present. However, it is a realistic idea that materials with different quality will be produced in different situations: one anodization proceeds adjacent to the electrolyte and the other at a distance from the electrolyte through the buffer layer of previously anodized film.

We have obtained very similar results in Bi_2Se_3 and GaSe to those in Bi_2Te_3 and GaTe. The anodized films of these semiconductors are easily removed by most acids and alkalis, so that successive anodization and removal of the films will enable us to count the number in thick semiconductor samples.

It is of great interest to investigate the structure and electrical property of the anodized films or to apply the present method to the intercalation study in the layered transition metal dichalcogenides (9).

Acknowledgments

The authors would like to thank Prof. C. Hamaguchi and Dr. T. Shirakawa for kindly providing the second derivative circuit and for useful discussions. They would also like to thank Professor H. Yoneyama for helpful and stimulating discussions. This work is partially supported by the Grant-in-Aid for Scientific Re-

[2] The details of the present experimental setup will be reported elsewhere. The readers should refer to Ref. (8) for details in the *in situ* ellipsometry.

[3] We have also obtained the experimental results which suggests the formation of the nonpassive film on GaAs which probably transforms into the passive film; see Ref. (5).

[4] The error limit is due to the uncertainty in counting the number of initial few anodized-layers of GaTe; it does not include miscount which would result if atomic layers of more than those contained within the monolayer are consumed in the anodic dissolution process before the onset of passivation in the initial stage of anodization.

search on "Surface Electronics" from the Ministry of Education of Japan.

Manuscript received June 1, 1977.

Any discussion of this paper will appear in a Discussion Section to be published in the December 1978 JOURNAL. All discussions for the December 1978 Discussion Section should be submitted by Aug. 1, 1978.

Publication costs of this article were assisted by Osaka University.

REFERENCES

1. T. P. Hoar, in "Modern Aspects of Electrochemistry," No. 2, J. O. M. Bockris, Editor, Butterworths Scientific Publications, London (1959).
2. H. Hasegawa and H. L. Hartnagel, *This Journal*, **123**, 713 (1976).
3. See, for instance, "Proceedings of International Conference on Layered Semiconductors and Metals," Bari, Italy, (1976); *Il Nuovo Ciment*, **38B**, (1977).
4. J. O. Jenkins, J. A. Rayne, and R. W. Ure, Jr., *Phys. Rev.*, **B5**, 3171 (1972).
5. A. Moritani, H. Kubo, and J. Nakai, *J. Appl. Phys.*, **48**, 2638 (1977).
6. V. Brusic "The Anodic Behavior of Metals and Semiconductors Series," J. W. Diggle, Editor, Marcel Dekker, Inc., New York (1972).
7. C. Tatsuyama, Ph.D. Thesis, Osaka University (1971).
8. W. W. Harvey and J. Kruger, *Electrochim. Acta*, **16**, 2017 (1971).
9. J. A. Wilson, F. J. Di Salvo, and S. Makajan, *Advances in Phys.*, **24**, 117 (1975).
10. "Handbook of Chemistry and Physics," R. C. Weast, Editor, Chemical Rubber Publishing Co., Cleveland, Ohio (1975).

Etching Characteristics of Phosphorus Containing Polycrystalline Silicon in a CF_4 Plasma

Kiyokatsu Jinno,[1] Hiroshi Kinoshita,[1] and Yasuo Matsumoto[1]

Tokyo Shibaura Electric Company, Limited, Toshiba Research and Development Center, Kawasaki 210, Japan

The use of a rf-generated plasma for the etching of dielectric and other films and for the removal of photoresists has become a viable alternative to the conventional wet chemical etching used in the fabrication of semiconductor devices since the plasma process is simpler and more economical (1-9). Using a CF_4 plasma for poly-Si etching eliminates the additional oxidation and associated process steps since photoresists can be used as a masking material in the plasma.

From a device fabrication viewpoint, it is important to investigate the plasma etching of phosphorus containing poly-Si which is widely used to reduce the resistivity of the interconnections and gate electrodes in MOS LSI's. In our experiments, phosphorus was introduced into the poly-Si films by two methods; doping with PH_3 during the chemical vapor deposition of the poly-Si films at 550°C in an Ar ambient (doped poly-Si method) and diffusion from a phosphosilicate glass (PSG) film after the deposition of an undoped poly-Si film by the decomposition of SiH_4 at 800°C in an N_2 ambient (diffused poly-Si method). The films were about 5000Å thick. Plasma etching was carried out in the IPC 2005-1813SC plasma etcher with an 8 in. diam quartz reactor with aluminum shield. The etching gas was a CF_4, the gas pressure was maintained at 0.6 Torr, and the rf power was kept at 150W. Film thicknesses were measured by using a Talystep.

The phosphorus concentration of the poly-Si films was varied by changing the flow rate ratio of PH_3 to SiH_4 and keeping the diffusion time at 1000°C. It was estimated by the Auger electron analysis.

In Fig. 1, the relative etch rates (defined as the etch rate of the doped poly-Si film to that of the undoped poly-Si film) of the poly-Si film formed by the two doping methods are shown as a function of phosphorus concentration. The two methods give almost the same results. It is apparent that the etch rate of phosphorus containing poly-Si films in a CF_4 plasma is independent of the doping methods and only depends on the phosphorus concentration in those films. This fact is clearly seen in Fig. 2 which shows the scanning electron micrographs of the cross section of a 4 μm wide line. The etch rate is high

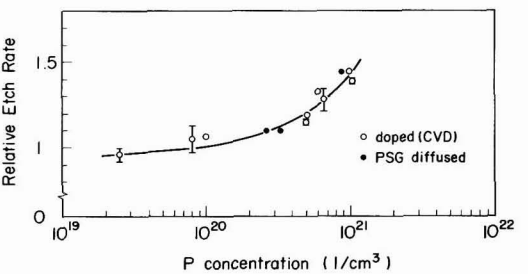

Fig. 1. Relative etch rate of the poly-Si films vs. phosphorus concentration.

at the surface of the diffused poly-Si film due to the high phosphorus concentration measured by the Auger electron analysis. From Auger electron analysis data, high phosphorus concentration regions exist to 800Å in depth from the diffused poly-Si film surface, whereas below the regions the phosphorus concentration takes a constant value and increases with increasing diffusion time. Meanwhile, the phosphorus-doped poly-Si film has an isotropical edge due to the uniform concentration of phosphorus measured by the Auger electron analysis. The etched profile of an undoped poly-Si film has also isotropical edge and is shown in Fig. 2 for a comparison.

In a CF_4 plasma etching, a gas plasma is generated in the reaction chamber by the rf power and silicon compound films begin to react with an activated fluorine species. A large plasma etch rate is obtained for elements which produce fluorides with high volatility. Therefore, phosphorus doping effect in a CF_4 plasma etching can be interpreted by high volatility of PH_3 (bp = 101.5°C at 760 mm Hg) compared to SiF_4 (bp = 94.8°C at 760 mm Hg) (10).

As a conclusion, the plasma etch rate of phosphorus containing poly-Si films is dependent on the phosphorus concentration, and the etched profile of those films depends on the phosphorus concentration distribution in depth direction.

Acknowledgment

The authors express their sincere thanks to Drs. Y. Nishi and S. Horiuchi for their useful discussions. They

[1] Present address: NEC-Toshiba Information Systems Incorporated, Kawasaki 210, Japan.
Key words: plasma etching, phosphorus effect, polycrystalline silicon.

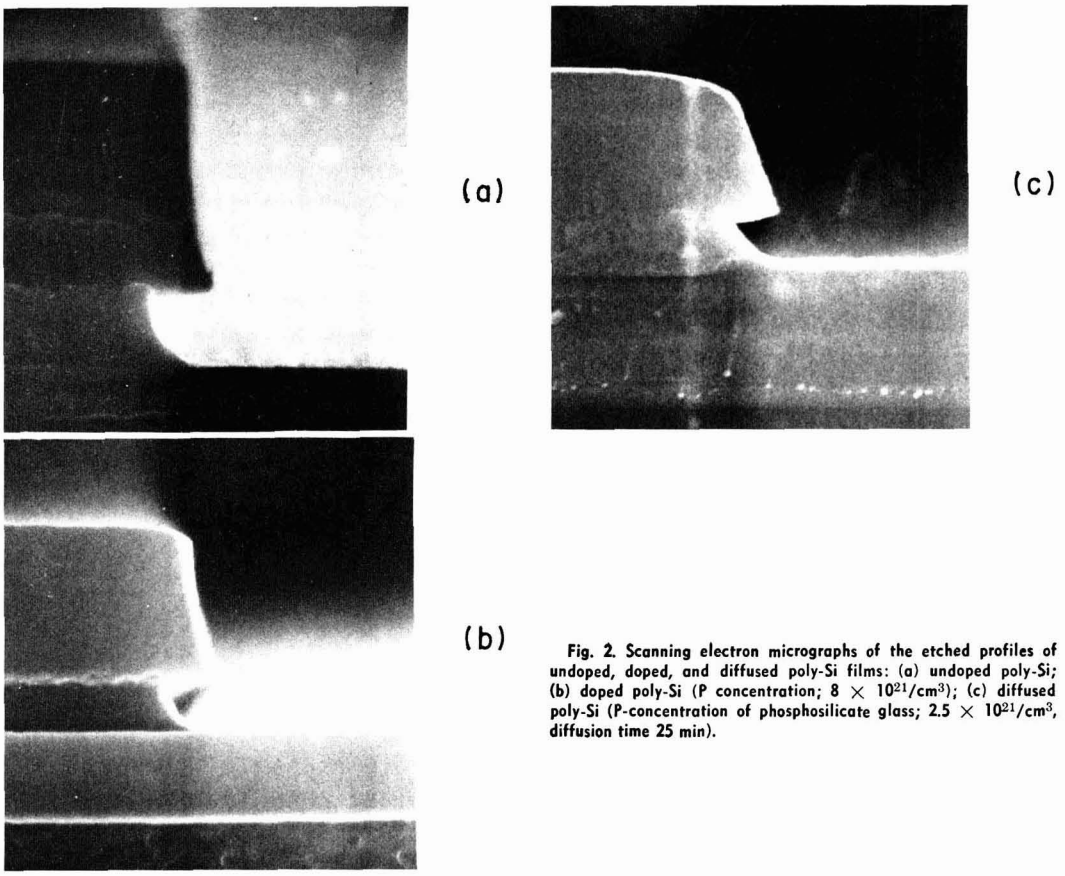

Fig. 2. Scanning electron micrographs of the etched profiles of undoped, doped, and diffused poly-Si films: (a) undoped poly-Si; (b) doped poly-Si (P concentration; 8 × 10^{21}/cm^3); (c) diffused poly-Si (P-concentration of phosphosilicate glass; 2.5 × 10^{21}/cm^3, diffusion time 25 min).

are also grateful to T. Matsuo, T. Moriya, and M. Yamanaka for their valuable support in the sample preparation and to T. Inoue for the Auger electron analysis.

Manuscript submitted May 11, 1977; revised manuscript received Nov. 10, 1977.

Any discussion of this paper will appear in a Discussion Section to be published in the December 1978 JOURNAL. All discussions for the December 1978 Discussion Section should be submitted by Aug. 1, 1978.

Publication costs of this article were assisted by Tokyo Shibaura Electric Company, Limited.

REFERENCES

1. H. Abe, in, "Proceedings of the 6th Conference on Solid State Devices," Tokyo (1974); O. Buturi, *J. Jpn. Soc. Appl. Phys.*, **44**, Suppl. 287 (1975).
2. R. A. H. Heinecke, *Solid-State Electron.*, **18**, 1146 (1975).
3. Y. Horiike and M. Shibagaki, in "Proceedings of the 7th Conference on Solid State Devices," Tokyo (1975); Suppl. to *J. Jpn. Appl. Phys.*, **15**, 13 (1976).
4. K. Jinno, Y. Matsumoto, and S. Inomata, *J. Electrochem. Soc. Jpn.*, **44**, 204 (1976).
5. L. Zielinski and G. C. Schwarz, Paper 53 presented at The Electrochemical Society Meeting, Toronto, Canada, May 11-16, 1975.
6. H. A. Clark, Paper 54 presented at The Electrochemical Society Meeting, Toronto, Canada, May 11-16, 1975.
7. A. R. Reinberg, Paper 50 presented at The Electrochemical Society Meeting, Washington, D.C., May 2-7, 1976.
8. M. Brochu and R. G. Poulson, Paper 51 presented at The Electrochemical Society Meeting, Washington, D.C., May 2-7, 1976.
9. A. Jacob, *Solid State Technol.*, Sept., p. 70 (1976).
10. "Handbook of Chemistry and Physics," WEAST 56th, CRC Press (1975-1976).

JOURNAL OF THE ELECTROCHEMICAL SOCIETY

ACCELERATED

—BRIEF COMMUNICATIONS—

MAY 1978

End Point Determination of Aluminum CCl_4 Plasma Etching by Optical Emission Spectroscopy

B. J. Curtis and H. J. Brunner

Laboratories RCA Limited, Zurich, Switzerland

The use of optical emission spectra for end point detection has been reported for the CF_4 plasma etching of Si (1, 2) and for the O_2 plasma stripping of photoresist (3, 5). This note reports the application of the method to the CCl_4 plasma etching of aluminium

Etching experiments were carried out in a parallel plate reactor consisting of a pyrex glass cylinder 30 cm in diameter and 35 cm high with ports to accommodate a silica window and a quadrupole mass-spectrometer; the end plates were made of stainless steel. The water-cooled electrodes, made of polished nickel-plated copper, were 20 cm in diameter and, for these experiments, were spaced 40 mm apart. CCl_4 was introduced through the centre of the upper electrode which was connected to a 13.56 MHz rf generator. The substrates were placed on the lower, grounded electrode. Optical emission spectra were taken on a Heathkit EUE-700 Monochromator using an RCA photomultiplier type IP28, a Keithley 601 electrometer as an amplifier and a chart recorder. The distance between the monochromator entrance slit and the plasma was 30 cm; the emission was viewed through the silica window without focussing.

Fig. 1 (upper) shows the spectrum of a CCl_4 plasma at a pressure of 7 Pa and 500 Watts power; the CCl_4 flowrate was 20 scc per minute. An unequivocal assignment (4) of all of the peaks has so far not been possible, even though the species present in the gas phase are known from mass-spectrometric measurements. However, bands due to CCl can be identified with maxima at 255.8 nm, 277.7 nm, 278.6 nm, 305.5 nm and 460 nm. Free chlorine is known to be present in the system and bands at 257.0 nm and 307.0 nm overlap with those due to CCl. The peaks at 199.1 nm, 297.2 nm and 312.7 nm are also probably due to reactive, chlorine containing species since during etching, their intensity is very much reduced (see Fig. 1 (lower)). The peaks at

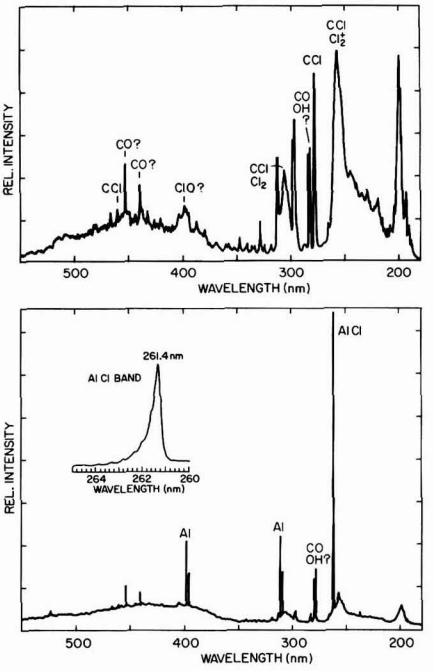

Fig. 1 (upper) Emission spectrum of CCl_4 plasma and 500 Watts, 7 Pa and 20 scc per minute flow rate. Scan rate 30 nm per minute. (Lower) Emission spectrum during CCl_4 plasma etching of aluminium under the same conditions as (upper). Spectrometer sensitivity one third of that used in (upper).

282.3 nm and 282.8 nm probably result from CO and OH; their intensity is unchanged during etching (Fig. 1 (lower)). The assignment of the peaks at 398.2 nm (possibly ClO) and at 438.7 nm and 452.8 nm (both possibly CO) is not certain.

Fig. 1 (lower) shows the spectrum obtained during the etching of an aluminium

plate of the same size as the grounded electrode. It should be noted that due to the high intensity of the peak at 261.4 nm, the sensitivity of the detection system was reduced by a factor of three compared to Fig. 1 (upper). The intensity of the CCl and Cl_2 lines is drastically reduced together with those at 199.1 nm, 297.2 nm and 312.7 nm which indicates that these too are probably due to a reactive chlorine containing species. A number of new peaks appear which can be identified as being due to AlCl (261.4 nm) and atomic Al (308.2 nm, 309.3 nm, 394.4 nm and 396.2 nm). In the inset, the AlCl band is shown at higher resolution.

For end point detection purposes, the AlCl band at 261.4 nm is more sensitive than the atomic Al lines which are not always detected from a small area substrate. Fig. 2 shows the course of etching a 3x3 cm substrate consisting of a 1300 nm thick Al layer evaporated onto a glass substrate. A photoresist grating with lines 200 um wide and a spacing of 200 um was defined on the Al layer. The CCl_4 plasma was ignited (500 Watts, 7 Pa, flow rate 20 scc per minute) and after an induction period of several minutes, etching began as indicated by the rapid build-up of the intensity of the 261.4 nm band. The decay of intensity at the end of etching was not so rapid but could possibly be influenced by geometrical factors. In this instance the etch rate was 185 nm per minute.

Etching can also be followed by the intensity of the lines resulting from CCl and/or Cl_2. For instance, the intensities of the peaks at 199.1 nm, 297.2 nm, 305.5 nm and 312.7 nm all decrease when etching begins and increase again at the end point.

In conclusion it can be said that the 261.4 nm emission band of AlCl is a sensitive indicator of aluminium etching in a CCl_4 plasma and should prove to be useful in further studies on this system and other halogen containing species. Furthermore, the CCl and/or Cl_2 peaks at 199.1 nm, 297.2 nm, 305.5 nm and 312.7 nm are also very effective end point indicators and merit further study.

Acknowledgement

The authors would like to thank H.W. Lehmann for useful discussions.

References

1. R.G. Poulsen and G.M. Smith, Semiconductor Silicon (1977), p. 1058-1070.
2. W.R. Harshbarger, R.A. Porter, T.A. Miller and P. Norton, Applied Spectroscopy 31 (3) p. 201-207 (1977)
3. J.E. Griffiths and E.O. Degenkolb, Applied Spectroscopy 31 (2), p. 134-137 (1977).
4. The spectra were identified with the aid of the book: "The Identification of Molecular Spectra", R.W.B. Pearse, A.G. Gaydon (Chapman & Hall 1976).
5. B.B. Stafford and G.J. Gorin, Solid State Technology 20 (9) 51-55 (1977).

Key words: Plasma etching, aluminium, emission spectroscopy

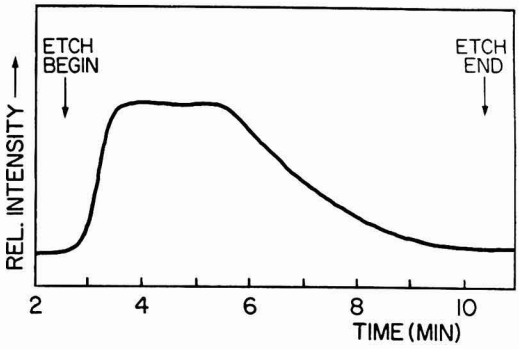

Fig. 2. CCl_4 plasma etching of a grating into an evaporated Al layer as followed by the intensity of the 261.4 AlCl band.

*Electrochemical Society Active Member.

Manuscript submitted Dec. 27, 1978; revised manuscript received March 23, 1978.

Publication costs of this article were assisted by Laboratories RCA Limited.

$CuInS_2$ Liquid Junction Solar Cells

M. Robbins, K. J. Bachmann,* V. G. Lambrecht, F. A. Thiel, J. Thomson, Jr., R. G. Vadimsky, S. Menezes, A. Heller,* and B. Miller*

Bell Laboratories, Murray Hill, New Jersey 07974

We report that single crystal and pressure sintered polycrystalline electrodes of n-$CuInS_2$ in the cells n-$CuInS_2$/1-2 F Na_2S, 1-3 F S°, 0-2 F NaOH/C exhibit good quantum efficiency under short circuit and respectable voltage at open circuit with irradiation at and above solar intensities. The output stability of the system at steady illumination appears particularly promising.

Samples of single crystal $CuInS_2$ were grown by the gradient freeze technique and were annealed in cadmium vapor at 700°C for 100 hours in sealed, evacuated silica tubes to convert the material into n-type of low resistivity. Polycrystalline $CuInS_2$ was prepared from ultrapure CuO and In_2O_3 (Alfa Research Chemicals). Appropriate mixtures of the oxides were heated in flowing H_2S at 800°C for 4 hours and cooled. The resulting $CuInS_2$ powder was pressure sintered at 700°C and 10,000 psi for 2 hrs. to yield pellets with 99.5 to 99.9% of single crystal density. The pellets were annealed in Cd vapor as above.

The experimental techniques for current-voltage curves, photospectra, and stability measurement have been earlier described (1,2). Studies of the temperature dependence of the current-voltage behavior were made with a jacketed cell equipped with a bottom optical flat and a semiconductor electrode of an approximately circular slice, indium back-contacted, and mounted on a steel shaft in a rotating disk configuration. A sequence of a 30 sec. immersion in 4:1 HCl-HNO_3, H_2O rinse, 30 sec 10% KCN immersion, and H_2O rinse was used to etch the semiconductor surface.

Current-voltage curves for n-$CuInS_2$ crystal electrodes in the jacketed cell exposed to constant tungsten-halogen illumination as a function of temperature are shown in Figure 1. The maximum power output vs. temperature is presented in the figure insert. At 60-75 mw/cm^2 insolation levels, cells with different n-$CuInS_2$ specimens delivered, at ambient temperatures, maximum power outputs corresponding to power conversion efficiencies of 3.5 - 4.3%. The temperature data at light intensities equivalent to up to three times AM2 show a 50% increase from 26 to 70°C. The corresponding fill factor improves from 0.23 to 0.31. Fill factors up to 0.45 have been measured at lower current density in 2F Na_2S - 3F S solution. The low fill factor reflects poor behavior at the foot of the voltammetric curve. Correcting the short circuit current to AM2 insolation (75 mw/cm^2) in the sunlight experiments, the quantum efficiency, calculated using the 21 ma/cm^2 theoretical value (3) for a 1.53 e.v. band gap (4), ranges from 50-60%.

Extended runs of $CuInS_2$ photoanodes (to 2 x 10^4 coul/cm^2 charge passage) produce no detectable weight loss or visible alteration in these cells, i.e. no evidence of photocorrosion. Additionally, the current output at short circuit or resistive load has been essentially constant for this same level of charge passage throughout test periods approximating 1.5 months of 8 hr./day sun.

*Electrochemical Society Active Member.

The n-$CuInS_2$ electrode is so far notable for its stability in operation in its anion-element redox couple. It resembles, in this respect, n-CdS which has a 2.4 e.v. band gap and thus a poorer overlap with the solar spectrum. Common anion cells avoid the ion exchange problem. Even for the weight-stable photoanode of n-CdSe in sulfide-polysulfide cells (2) such surface exchange processes appear implicated in output stability deterioration (5).

In view of the close to optimum band gap (6) for solar conversion of $CuInS_2$, these photoelectrochemical cells have considerable possibility for improvement in efficiency. If the fill factor can be increased to take advantage of the good limiting open circuit and short circuit parameters, the n-$CuInS_2$ based cell may be a useful entrant in the field of liquid junction solar cell systems.

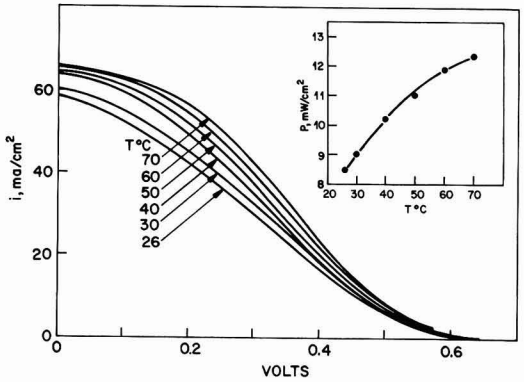

Fig. 1 Current-voltage curves for the cell n-$CuInS_2$/2F Na_2S, 3F S, 2F NaOH/C with constant tungsten-halogen illumination at different cell temperatures without stirring. The insert shows the maximum power plotted vs. temperature.

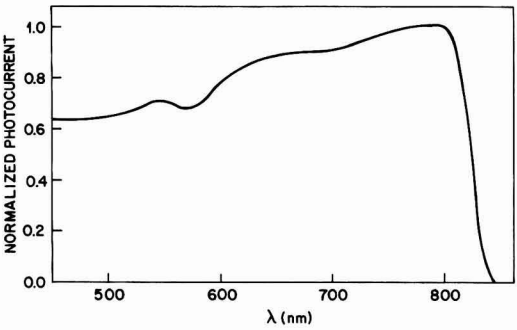

Fig. 2 Photocurrent spectrum at short circuit to a carbon electrode of a n-$CuInS_2$ electrode in 1F Na_2S-1F NaOH.

REFERENCES

1. A. Heller, K. C. Chang, and B. Miller, J. Electrochem. Soc. 124, 697 (1977).
2. B. Miller, A. Heller, M. Robbins, S. Menezes, K. C. Chang, and J. Thomson, Jr., J. Electrochem. Soc. 124, 1019 (1977).
3. H. J. Hovel, "Semiconductors and Semimentals, Vol. 11, Solar Cells", Academic Press, N. Y. (1975), p.38.
4. B. Tell, J. L. Shay, and H. M. Kasper, Phys. Rev. B 4, 2463, (1971).
5. A. Heller, G. P. Schwartz, R. G. Vadimsky, S. Menezes and B. Miller, to be published.
6. Ref. 3, p. 75.

Manuscript submitted Dec. 21, 1977; revised manuscript received Feb. 24, 1978.

Publication costs of this article were assisted by Bell Laboratories.

JOURNAL OF THE ELECTROCHEMICAL SOCIETY

REVIEWS AND NEWS

MAY 1978

Heinz Gerischer—Palladium Medalist

Charles W. Tobias[1]

The Palladium Medal of the Society, established in 1951, is given for distinguished contributions to the field of electrochemical science and corrosion. What this award is designed to recognize was clearly demonstrated already in 1951 by the selection of Carl Wagner as the first medalist. The 13th recipient of this award, Professor Heinz Gerischer, follows a list of eminent scientists: Wagner, Furman, Evans, Bonhoeffer, Frumkin, Uhlig, Hackerman, Delahaye, Hoar, Brewer, Levich, and Pourbaix. A commendable lack of chauvinism has been evident in the selection of the medalists: eight of the 13 recipients were foreign nationals.

Heinz Gerischer's career started out under what one could call less than auspicious circumstances. A series of nearly miraculous turn of events are responsible for his having been admitted at all, in 1938, to any university in Germany. No sooner did he complete his first year as a student in chemistry in Leipzig, then in 1939 he had to join the German army, only to be ejected as a half-aryan in 1941. Allowed to return to continue his studies in Leipzig, obviously a serious mistake on the part of Nazi authorities, he obtained his chemistry diploma in 1943. Then, with another forced interruption during war time in "Arbeitsdienst," he stayed on as a researcher in Karl-Friedrich Bonhoeffer's laboratory.

In 1946, after obtaining his doctorate, he followed Bonhoeffer to the University of Berlin. According to Gerischer, Bonhoeffer, a great scientist and an exceptional human being, was perhaps the greatest single influence in his life. At a time when all intellectual and human values crumbled Bonhoeffer saved not only human lives, he was among the few who succeeded in maintaining a thin thread of continuity in the great tradition of science in Germany.

In 1949, during the blockade of Berlin, Gerischer again followed his mentor, this time to Gottingen, where Bonhoeffer was named the director of the newly created Max Planck Institute für Physikalische Chemie.

During the five years Gerischer spent in Gottingen he developed a definite interest in an academic career. As a consequence of the somewhat rigid structure of the German academic scene, he had to move on to work toward his habilitation to achieve the status of a dozent. In 1954 he joined the Max Planck Institute für Metallforschung in Stuttgart, heading a small department of corrosion science. In Stuttgart Gerischer enjoyed a considerable degree of freedom in the selection of research topics and in accepting students working on their doctoral dissertations. In 1955 he became a dozent at the University of Stuttgart and began to lecture there, and in 1960 he was advanced to full membership of the Max Planck Gesellschaft. Soon thereafter, in 1962, he accepted an invitation to the Technische Hochschule in Munich as a Professor Extraordinarius.

Seven years later, in 1969, after he had advanced in academic rank, and following service in various important academic administrative positions, he accepted an invitation to become the director of the Fritz Haber Institute of the Max Planck Gesellschaft in Berlin. Since 1970 he resides in the director's villa on Faradayweg and heads an institution of great renown, one that was directed earlier by Fritz Haber, under whose guidance Bonhoeffer obtained his doctorate. The series of events that led to Gerischer's directorship of this famed institution involved many improbable turns, many near miracles. It is indeed fortunate for Germany and for science that today a man of Gerischer's intellectual caliber and integrity occupies this very influential post.

Gerischer's early work addressed various problems in the area of kinetics and mechanisms of electrode processes. Numerous papers originating from the 1950's and early 1960's concern the elucidation of mechanisms of anodic and cathodic reactions involving simple and complex ions, others pertain to corrosion and electrocatalysis. His papers on electrode reactions of complex ions and on electrocrystallization processes are examples of the best work published on these subjects in the fifties and sixties.

Gerischer made important contributions to the development of new experimental techniques for the investigation of fast electrode reactions. Among these the potential-step and current-step methods, and the invention of the double-pulse method deserves particular mention. He designed and employed a special flow cell for the study of fast homogeneous reactions and also developed a temperature step method for similar purposes.

These earlier investigations were based on classical concepts, macroscopic treatments of electrode phenomena, in which Gerischer's contributions were particularly significant through the introduction of new experimental techniques, resulting in important improvements in the accuracy with which kinetic parameters could be obtained.

Already during his student days in Leipzig, Gerischer, after reading Gurney's book, "Ions in Solutions," thought of the desirability of employing electronic energy levels to the description of electrode reactions. However it was only in the mid-fifties, after he came across Brattain and Garrett's work involving the first electrochemical experiments with germanium, that he realized the opportunity offered by semiconductors for the application of electronic states in the interpretation of electrode reactions. His first paper on the anodic dissolution of n- and p-type germanium, coauthored with his student Fritz Beck, was published in 1957, and some 70 papers concerning semiconductor electrodes have followed since. When Gerischer moved to Munich, his nascent interest in photoelectrochemistry received a strong boost by the long tradition in spectroscopy and photochemistry in the institute he joined. Here he

[1] Introductory remarks by C. W. Tobias, Department of Chemical Engineering, University of California, Berkeley, on the occasion of the presentation of the Palladium Medal Award to Heinz Gerischer on October 11, 1977, at the Atlanta Meeting of the Society.

began to use semiconductor and insulator electrodes to study the reactions of excited molecules, especially of dyes. Finally, in Berlin he extended his work to include photoreactions at metal electrodes, specifically photoelectron emission into electrolytes and photooxidation of electrolyte components.

Thus, Gerischer is realizing the dream he had as a student in Leipzig; the analysis of electrode reaction mechanisms from an atomistic point of view, using atomic and electronic energy schemes. Many of you already know that his work established the foundations on which some of the present, very exciting developments in the area of photogalvanic cells are based.

It is evident that the recipient of the Palladium Medal of 1977 has covered in his research activities a large part of electrochemical science, and that he has made significant contributions to a number of disciplines represented in the various Divisions of this Society. To the surprise of no one his nomination to the Palladium award was cosponsored by an unprecedented large number of Divisions of the Society.

In concluding my introduction of the Palladium Medalist I only want to add a brief personal note. I studied Professor Gerischer's papers far before I met him in the early sixties. In subsequent years I have seen him on many occasions, and had the opportunity for close interaction with him during his stay as a visiting scientist in the Lawrence Radiation Laboratory in 1967-1968. This personal knowledge of the man allows me to say that Professor Gerischer's great talent and fine contributions to science are matched by his qualities as a human being.

For this reason it is with the greatest of pleasure that I present to you Professor Heinz Gerischer, the Palladium Medalist of 1977.

Electrochemistry of the Excited Electronic State

Heinz Gerischer[2]

Since the Palladium Medal of The Electrochemical Society is one of the greatest honors an electrochemist can be awarded with, I feel very pleased and honored to be the thirteenth recipient of this medal. I want to express my sincere thanks to you, Mr. President, as the representative of the society and particularly to you, Charles, for your so very kind and friendly introduction. You have mentioned therein how decisive my personal contact with K. F. Bonhoeffer was for my life, scientifically and otherwise. It was 20 years ago that this medal was awarded to him, but he tragically passed away before he received the message. Now, I am standing here in his succession being strongly reminded of his unforgettable personality. This is a very personal reason for me to acknowledge this medal particularly highly and to be so especially touched at this occasion.

I would not be standing in this place if I should not have found, over the years, the cooperation of a number of highly talented co-workers. Most of my contributions to various fields of electrochemistry have been made possible by their enthusiasm and their devotion to research. Without mentioning individual names, I wish to express my gratitude to all of them for their personal contributions.

The subject of my lecture has little to do with the problems which I have studied 10-20 years ago. Although it was apparently my contributions to these areas—according to the published appreciation—which should be acknowledged by this award, I have deliberately chosen a different subject for my presentation. This not only corresponds to my more recent interests, it also demonstrates that electrochemistry is still widening its objectives and far from being exhausted although it has a very long history.

Most of the electrochemistry work is still done in the dark and the electrochemists hope to enlighten themselves to understand the complicated systems with which they have to deal. However, more than a century ago, Becquerel had already illuminated the electrodes of Galvanic cells and detected photovoltaic effects (1). This created great excitement among the then very small and exclusive scientific community, but it certainly did not promote the understanding of electrochemistry. On the contrary, the speculations about such photoelectrochemical phenomena contributed to the fact that some parts of electrochemistry, especially the nonthermodynamic ones, appeared to the scientists of neighboring fields for a long period of time as quite obscure.

This situation has changed since the time when electrochemists could profit from the development of solid-state physics and photochemistry and have learned to combine these experiences with their classical electrochemical knowledge. This has demonstrated once more that electrochemistry is an interdisciplinary science and that a competent electrochemist must be alert to developments in various fields. We know today that all these photoelectrochemical effects are caused by the generation of excited electronic states, and my intention is to explain in this lecture the basic phenomena which are due to the presence of excited electronic states. I am especially pleased that I can address this lecture to a society which has combined in its development so closely the interests of electrochemists and solid-state physicists. The topic I will discuss today demonstrates forcibly how necessary it is to connect these two fields.

Reactivity in the Excited State

Electron transfer between a donor and an acceptor is one of the most common of electrochemical reactions. In Galvanic cells the donor or the acceptor is the electrode. It is obvious that this type of electrochemical reaction must be affected by electronic excitation. Figure 1 shows in a very simple picture how electronic excitation influences electron transfer processes.

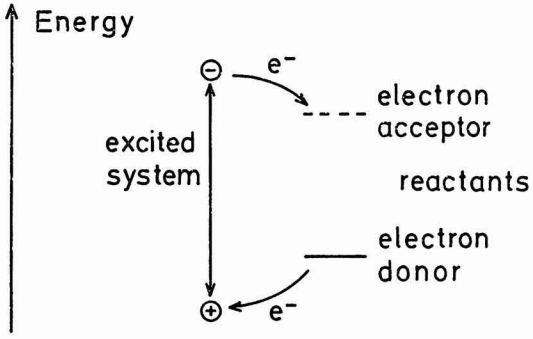

Fig. 1. Energy scheme for electron transfer between excited system and electron donor or acceptor.

[2] Palladium Medal Address delivered October 11, 1977, at the Atlanta, Georgia, Meeting of The Electrochemical Society. The medal was struck from palladium supplied by the International Nickel Company, 67 Wall Street, New York, New York 10005.

Electron transfer occurs between an occupied and a vacant electronic quantum state. Light absorption changes the distribution of electrons over the available electronic energy levels. As a consequence, electrons at higher energy levels are created simultaneously with vacant electronic states at low energies. The electrons of the high energy levels can be transferred to electron acceptors in this energy range. The vacant electronic states at low energy levels can be filled by electron donors with electronic energies in this region as is indicated in Fig. 1. We see immediately that, in electrochemical language, cathodic redox processes will be accelerated by light absorption and also anodic redox reactions will be enhanced. If the excitation energy is large enough, redox processes will become possible which cannot occur in the dark.

There are other possibilities of generating excited electronic states, for example, the application of very high electric fields to solids. We shall, however, limit our discussion with one exception to the generation of excited states by light absorption only.

What happens in an electrochemical system after light absorption depends both on the light absorber, which can be the electrode or one component of a redox couple, and on the reaction partner, which can be a redox couple or an electrode. In Fig. 2 three typical cases are shown which we shall later discuss in more detail. The excited molecule corresponds to the excitation of a redox system, and a possible consequence is, as we see, electron transfer in two opposite directions in contact with an electrode. In case of an electronic excitation in the electrode we shall distinguish between a metal and a semiconductor electrode. At both types of electrodes, cathodic and anodic electron-transfer processes can be induced by light absorption as is indicated in this figure. We shall discuss this in more detail later.

The other type of electrochemical reaction which occurs at interfaces is ion transfer. How electronic excitation affects an ion transfer process is much less obvious than for electron transfer. One can, however, expect that ion-transfer reactions also can be accelerated by electronic excitation. The reasons are given in Fig. 3. Ion transfer at the interface between an electrode and electrolyte must involve an energy barrier. If the initial state of this process is electronically excited, the energy of this state will be increased. How much depends on the localization of the excitation energy. The influence on the transition state will be much smaller, and there is no influence on the final state. Figure 3 shows schematically that the activation energy for the ion-transfer process will be reduced by electronic excitation, and in some cases, as we shall later discuss, this effect even controls the possibility of ion transfer.

We will make a brief estimation of how large these effects might be. It must be taken into consideration that excited electronic states have a limited lifetime.

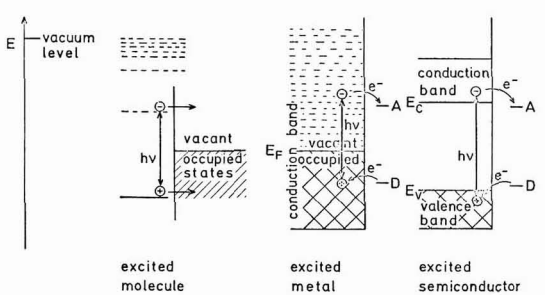

Fig. 2. Energy scheme for electron transfer between excited molecule and metal, excited metal, or excited semiconductor and redox couples.

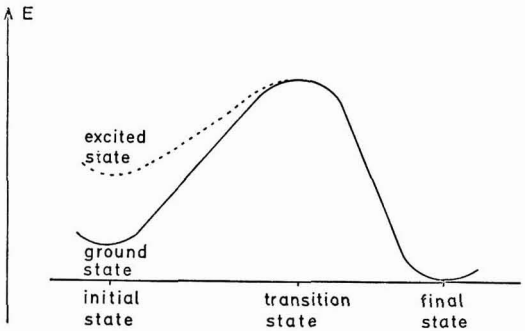

Fig. 3. Influence of electronic excitation on ion transfer reaction

The efficiency will therefore depend on the relation between the lifetime of the excited state and the time needed for completing the electrochemical reaction. Table I gives some characteristic time constants for electron transfer, ion transfer, and the lifetimes of excited states.

It is obvious that the chance to see the effect of electronic excitation is much larger for an electron-transfer process than for ion transfer, because electron transfer is so much faster. On the other hand, the efficiency of electronic excitation in metal electrodes will be very low because of the extremely short lifetime of excited states in metals. This is quite different for semiconductors and insulators where we therefore can expect to find very pronounced effects. In the following we shall discuss a typical case for every kind of excitation.

Excited Molecules as Redox Reactants

To understand the action of an excited molecule as an electron donor or electron acceptor we must get some idea of the redox potential of an excited redox system (2). This depends clearly on whether the reduced or the oxidized component of the redox system is excited. For this discussion we shall use the so-called absolute scale of redox potentials which is closely related to the electronic energy level system of solid-state physics (3, 4). The relation between the electrochemical redox scale and this absolute scale is given in the definitions and the energy scheme shown in Fig. 4. A comparison of the two scales is shown in Fig. 5.[3]

What happens with the redox potentials of a molecule in the excited state is shown in the following two figures. Figure 6 describes this in a very simplified molecular orbital picture. We consider a molecule in its singlet state and assume that the lowest vacant molecular orbital is the acceptor orbital for the reduction of this molecule while the highest occupied orbital is the donor orbital. By electronic excitation to the lowest excited singlet state an electron will be promoted from the donor orbital to the acceptor orbital. We see that the situation is just inverted now. The previous donor orbital becomes an acceptor orbital while the previous acceptor orbital has become the donor orbital. This means that the redox potential

[3] It should be mentioned that the position of the NHE, located in this picture at $E_{NHE} = -4.5$ eV, is still open to discussion (31, 32).

Table I. Comparison between reaction time and lifetime

Electron transfer			10^{-12}-10^{-14} sec
Ion transfer			10^{-10}-10^{-12} sec
Molecules	}	Excited singlets	10^{-8} 10^{-12} sec
	}	Excited triplets	10^{-3}-10^{-10} sec
Metals		Excited electrons	10^{-14}-10^{-16} sec
Semiconductors and insulators	}	Excited electrons or holes	10^{2}-10^{-13} sec

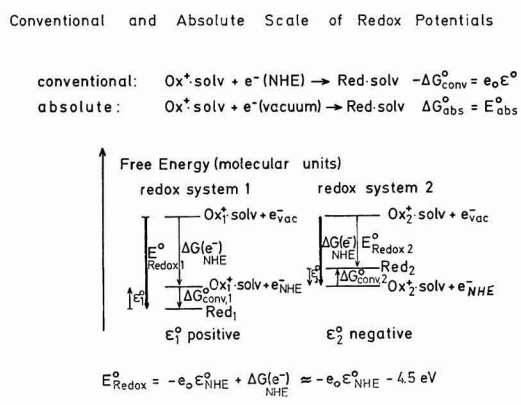

Fig. 4. Conventional and absolute scale of redox potentials derived from the free-energy changes in the corresponding redox reactions.

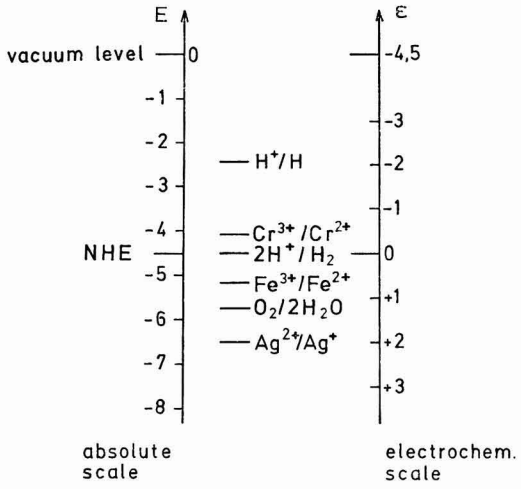

Fig. 5. Comparison of conventional and absolute scale of redox potentials.

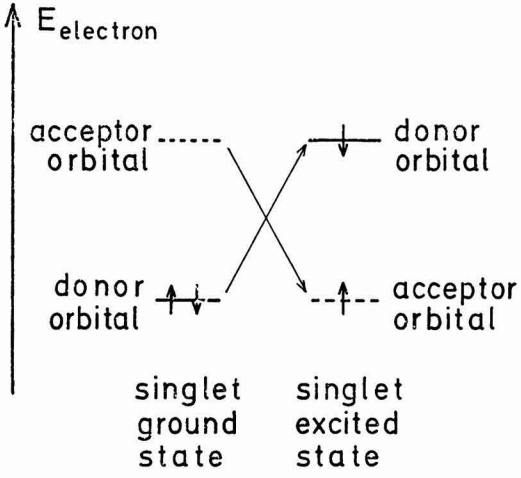

Fig. 6. Energy position of redox orbitals of a molecule in the ground state and the excited state according to simplest M O-picture.

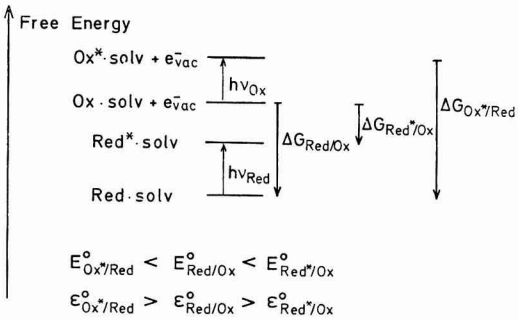

Fig. 7. Shift of redox potentials by electronic excitation of the reduced or the oxidized species of a redox couple derived from the free-energy changes.

of an excited molecule is shifted in two directions. Its reductive power has been increased simultaneously with its oxidative power. Figure 7 shows this more concretely in a free energy scale for a redox system with two components where either the reduced species is excited or the oxidized species. This picture demonstrates that the shift of the redox potential between the reaction in the ground state and in the excited state is just given by the stored excitation energy in the molecule. If the reduced component is excited, the free energy for electron abstraction is reduced by this amount and the redox potential is shifted in the negative direction in the conventional electrochemical scale while excitation of the oxidized component increases the energy gained by electron addition, this meaning that the redox potential of the system is shifted in the positive direction of the conventional electrochemical scale.

What happens when such an electronic excitation occurs exactly at the interface between the electrolyte and an electrode? The various possibilities are shown in Fig. 8 where metals, semiconductors, or insulators are assumed as the electrode material (5, 6). The positions of the electronic energy levels in the excited molecule are represented again in the simplified molecular orbital picture. The figure shows that in contact with a metal in a situation where no dark reaction is possible, electron transfer in both directions will be opened after excitation of the molecule. This means that no external current can be observed in such cases since both processes will compensate each other. This is a mechanism of energy quenching by mutual electron exchange. Even if one of these processes should be faster than the other, the reverse process will occur in the dark as a consecutive reaction. The chance that such photocurrents can be found at metal electrodes is, therefore, very dim. Only in cases where a very fast chemical reaction follows one of the electron-transfer steps which prevents the reverse process can photocurrents be observed in such systems. If photoeffects are found, they are usually caused either by the existence of nonmetallic surface layers on the electrode or by photochemical reactions in the electrolyte which generate species with a different redox potential which can either be oxidized or reduced at the electrode during their lifetime.

The attractive cases involve contact between an excited molecule and a semiconductor as shown in (b) and (c) of Fig. 8. What happens in such a case depends on the relative position between the energy bands and the redox orbitals of the excited molecules. In case (b) electron injection into the conduction band is possible and can be observed as an anodic photocurrent. In case (c) electron extraction from the valence band equivalent to hole injection will occur, and a cathodic photocurrent is found. Case (d) shows a system

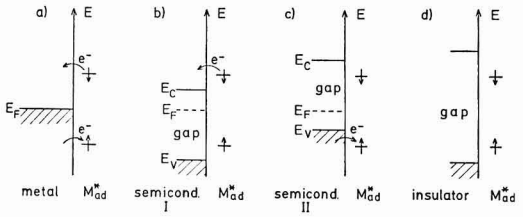

Fig. 8. Typical situations for electron transfer between an excited molecule and various solids.

where the bandgap is too wide to permit any kind of electron transfer.

In this picture we have not yet discussed another possibility of energy quenching which is very efficient at a contact with metals, that is, energy transfer. This is found whenever the absorption spectrum of the electrode overlaps the fluorescence spectrum of the excited molecule (7, 8). To avoid this, the bandgap of the semiconductor must exceed the energy stored in the molecule after excitation. This is another reason why photocurrents at metal electrodes are usually not caused by direct electron transfer in the excited state.

Figures 9 and 10 give examples of cases (b) and (c) of Fig. 8. Figure 9 shows a comparison between the absorption spectrum of a dye molecule in solution and the action spectrum of the photocurrents if this dye is brought into contact with a ZnO electrode which is suitably polarized to collect all injected charge carriers (9). This requires an anodic bias in case of electron injection, as found at the ZnO electrode. Figure 10 shows hole injection by the same excited dye molecule at a p-type GaP-electrode (10) where we have the situation of Fig. 9(c). Since the bandgap

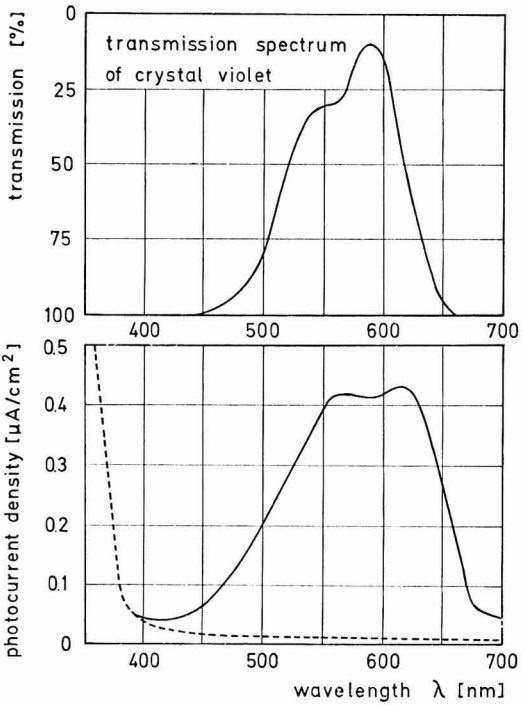

Fig. 9. Photocurrent spectrum for electron injection from crystal-violet into a ZnO electrode in comparison with absorption spectrum of the dye in solution.

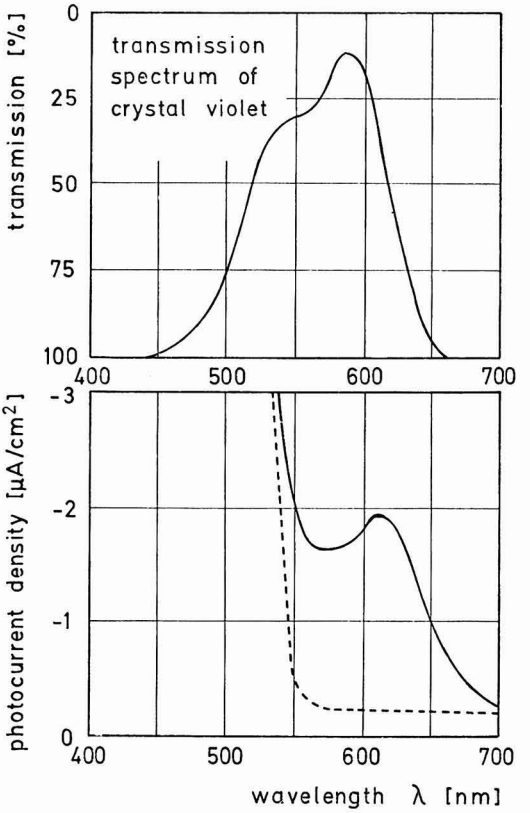

Fig. 10. Photocurrent spectrum for hole injection from crystal-violet into a GaP electrode in comparison with absorption spectrum of the dye in solution.

of GaP is not wide enough, only the long range part of the dye absorption spectrum can be used for this kind of sensitization.

Such experiments provide sensitive tests of models for the spectral sensitization of solid materials (11), which has long found wide technical application in photography. This demonstrates again the close relationship of electrochemistry and solid-state physics.

Electronically Excited Metals

Now we consider electronic excitation in metals. Although we have stated earlier in the paper that we should not expect large effects due to the short lifetime of excited states in a metal, we are all aware that photoemission from metals into vacuum is a process well known for a long time. The reason that there is any chance to observe an effect of electronic excitation despite the short lifetime is the fact that electrons have an enormous velocity and therefore a chance to reach the surface in a very short time after excitation. Photoemission from a solid into vacuum is limited by the height of the energy barrier for leaving the solid material. For a metal in contact with the electrolyte the situation is not different. Only the shape of the energy barrier and its height are modified. In case of an aqueous electrolyte there is some interaction between the free electrons and the solvent which reduces the energy barrier. In addition to this, the electric potential drop in the electrical double layer at the interface influences the barrier height drastically and gives the means to alter it systematically.

Photoelectron emission into electrolytes has been studied in recent years quite intensively by the Russian School (12, 13), centered in the Institute of the Academy of Sciences which was headed by the late Professor Frumkin, after it had been started by the pioneering work of Barker (14). Some recent investigations in our institute, mainly done by J. K. Sass, have demonstrated that this technique is especially useful for studying the excitation and emission mechanism of electrons from solids in energy ranges which are not accessible to experiments *in vacuo* (15, 16).

Figure 11 shows the modification of the threshold for photoelectron emission by the presence of a condensed medium like an aqueous solution. The magnitude of the photocurrent depends on the quantum energy of the light, on the electrode material, and on the electrode potential. Two typical results are shown in Fig. 12 for a gold electrode. One sees, however, that not only cathodic photocurrents can be observed but also anodic ones (17). It can be concluded that the anodic photocurrents mean the oxidation of water by vacant electronic states at deep energy levels. These are excited holes in the metal.

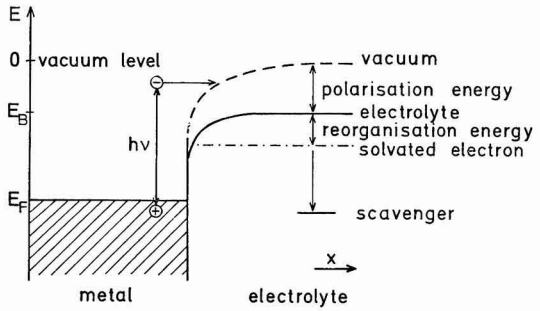

Fig. 11. Energy barrier for photoelectron emission from a metal into an electrolyte in comparison to the barrier against vacuum.

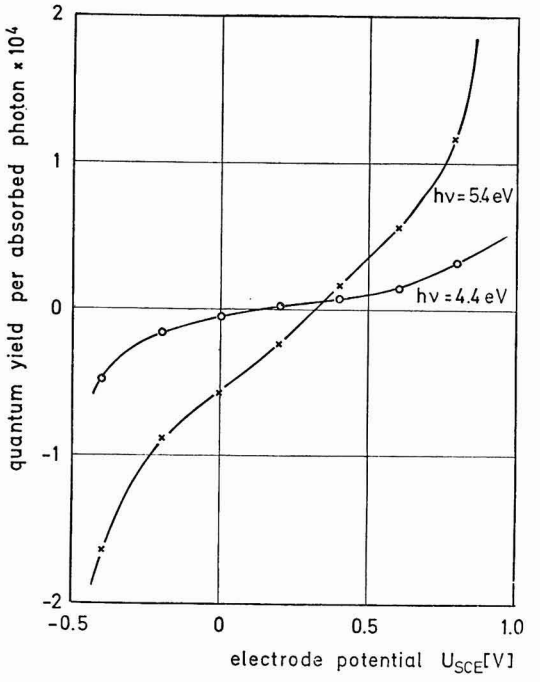

Fig. 12. Photocurrent-potential curves for a gold electrode in 1M H_2SO_4 for two different light energies.

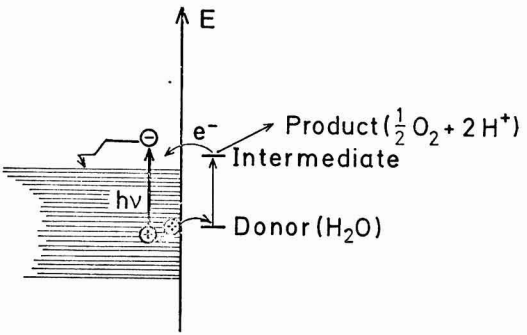

Fig. 13. Water oxidation by excited holes at the metal-electrolyte contact in terms of energy levels.

Figure 13 shows the mechanism of this reaction which ends in molecular oxygen. The potential dependence of the cathodic and anodic photocurrents clearly indicates that there is an energy threshold for both processes, photoelectron emission and water oxidation, which varies with the applied potential. If we assume that the potential drop between the electrode and the electrolyte is located exclusively in the Helmholtz double layer, a variation of the electrode potential means that the Fermi level, relative to the energy levels in solution, is shifted up or down by the applied voltage, and both thresholds are shifted in parallel, but in opposite direction. This is shown in Fig. 14.

Photoelectron emission studies at single crystal faces demonstrate that the crystal orientation plays an important role for the quantum yield. One knows from thermodynamics that the energy threshold between the bulk of a metal and the electrolyte is the same for any face at a given electrode potential. Nevertheless, photoemission quantum yield varies drastically with orientation as shown in Fig. 15 (18). This effect is most pronounced if polarized light is used (19). One

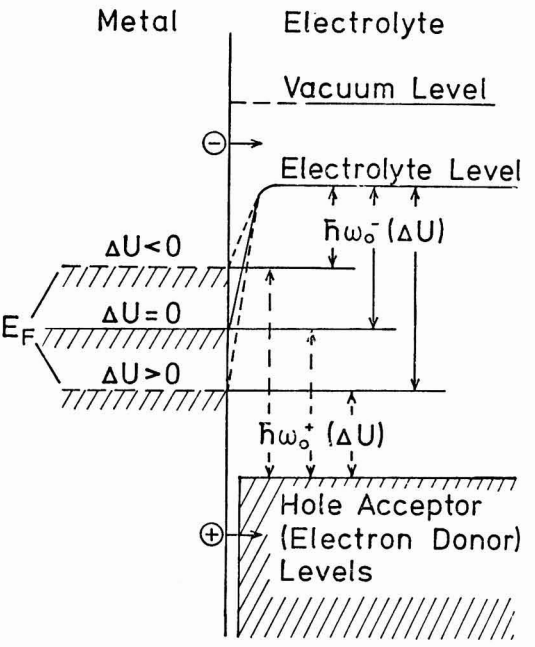

Fig. 14. Variation of the energy thresholds for photoelectron emission and photohole oxidation by the electrode potential.

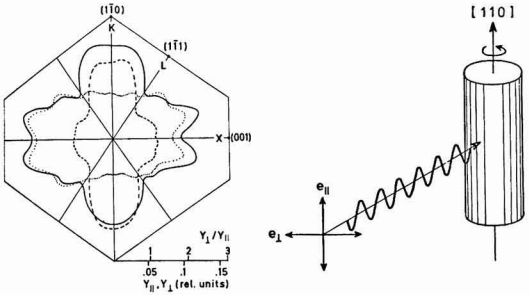

Fig. 15. Variation of the photoemission yields ($Y_\perp$ (———), $Y_\parallel$ (· · ·), and the ratio $Y_\perp/Y_\parallel$ (– – –) with crystallographic orientation on the single crystal cylinder surface for $h\nu = 3.45$ eV. A schematic illustration of the experimental geometry is shown on the right-hand side of the figure.

sees in Fig. 15 considerable differences in the efficiency for the two modes of polarization. This can be understood by correlating the different excitation conditions with the band structure of a metal. The momenta of the excited electrons and the chance to pass the barrier depend on crystalline direction.

As mentioned at the beginning of the paper, one should expect also that ion transfer should be accelerated by electronic excitation. There is, however, to my knowledge only one case where this effect has been observed at a metal electrode in the absence of a surface coverage with an oxide layer or other surface compound (20). This case is shown in Fig. 16. The gold electrode tends to dissolve in the presence of halide ions in a narrow range of electrode potentials just before an oxide layer is formed on the surface. The figure shows that in this range the dissolution rate is somewhat enhanced by illumination. The mechanism of this phenomenon, however, is still somewhat obscure and needs further studies.

Electronic Excitation in Semiconductors

As we expect from our estimation earlier in the paper, semiconductors show much more pronounced photoeffects than metals if light is absorbed beneath the surface. Quantum yields close to 1 can be obtained if the light is absorbed exclusively in a space-charge layer underneath the surface where a high enough electric field provides full separation of the electron hole pairs generated by light absorption. Such a situation can be reached at n- or p-type semiconductors by applying a suitable voltage which creates a depletion layer of large enough depth (21, 22), as is shown in Fig. 17. If electron donors or acceptors are present, the minority carriers reaching the surface will undergo redox reactions with these components of a redox couple. This will create a photovoltage of opposite sign to the initially present voltage across the space charge layer as is indicated in Fig. 17. Such photovoltages are the driving force for any kind of photoelectrolysis as in photoelectrochemical solar cells based on light absorption in semiconductors.

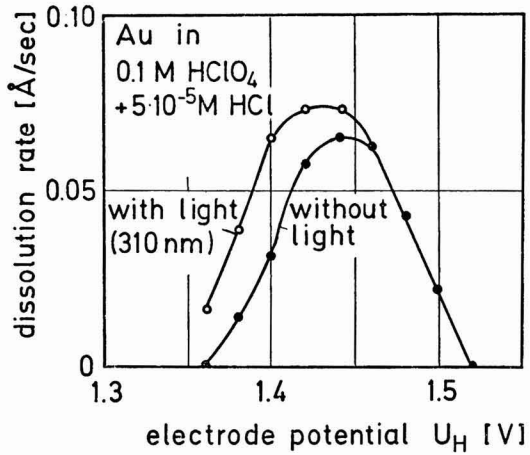

Fig. 16. Influence of illumination on the dissolution rate of gold in chloride-containing electrolyte.

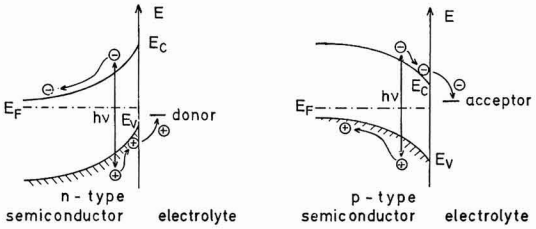

Fig. 17. Electron hole pair separation in illuminated depletion layer of a semiconductor.

If no suitable components of a redox couple are present the minority carriers will accumulate in the surface and the chance for ion-transfer reactions is enhanced (23). In most semiconductors the accumulation of holes means the weakening of bonding states and the preformation of a cationic state in the surface (24). Such cationic states react easily with nucleophilic reagents from the electrolyte and form reaction products which can be soluble in the form of ions or may be deposited as another compound on the surface.

The accumulation of electrons in the surface also usually results in the weakening of the surface bonds by the occupation of antibonding or nonbonding states. The consequence is a preformation of an anionic state in the surface which easily can react with electrophilic components of the electrolyte. Decomposition of the semiconductor is the result. Table II summarizes a number of such reactions.

The quantum yield of all these photoreactions by excitation of the semiconductor depends on the penetration depth of the light and the extension of the space charge layer. The penetration depth of the light decreases drastically as the photon energy approaches the bandgap energy. The extension of the space-charge layer increases with applied voltage. These two effects are clearly shown in Fig. 18 for an n-type ZnO-electrode, where the photocurrents are compared at equal light intensities for different wave lengths and at different voltages. If one measures the photocurrent at a given voltage, the action spectrum of the semiconductor is revealed in the photocurrents. Some examples are given in Fig. 19 for two n-type and one p-type material.

These large effects of photoexcitation in semiconductors have in recent years found great interest for the purpose of solar light to energy conversion (25-27). In such systems the sensitivity of semiconductors to decomposition reactions in contact with electro-

Table II

Anodic oxidation

$$CdS + 2\,h^+ + aq \rightarrow Cd^{2+} \cdot aq + S$$
$$ZnO + 2\,h^+ + aq \rightarrow Zn^{2+} \cdot aq + \tfrac{1}{2}\,O_2$$
$$GaAs + 6\,h^+ + aq \rightarrow Ga^{3+} \cdot aq + AsO_3^{-} \cdot aq + 4\,H^+ \cdot aq$$

Cathodic reduction

$$CdS + 2e^- + aq \rightarrow Cd + S^{2-} \cdot aq$$
$$ZnO + 2e^- + aq \rightarrow Zn + 2\,OH^- \cdot aq$$
$$Cu_2O + 2e^- + aq \rightarrow 2Cu + 2\,OH^- \cdot aq$$

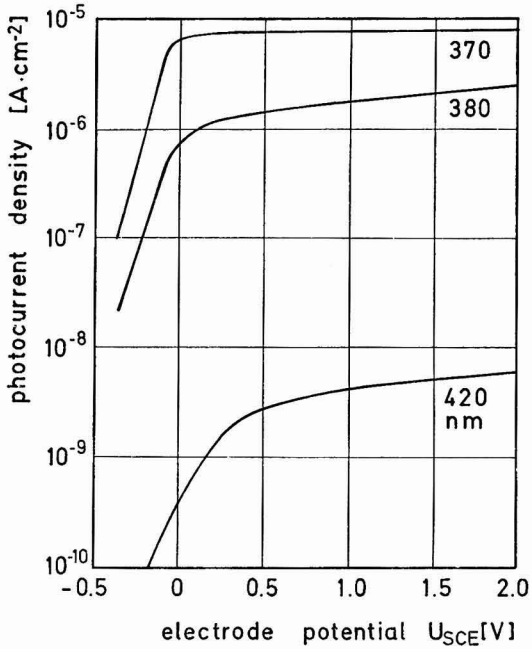

Fig. 18. Photocurrent-potential curves for ZnO electrodes at illumination with light of different penetration depth.

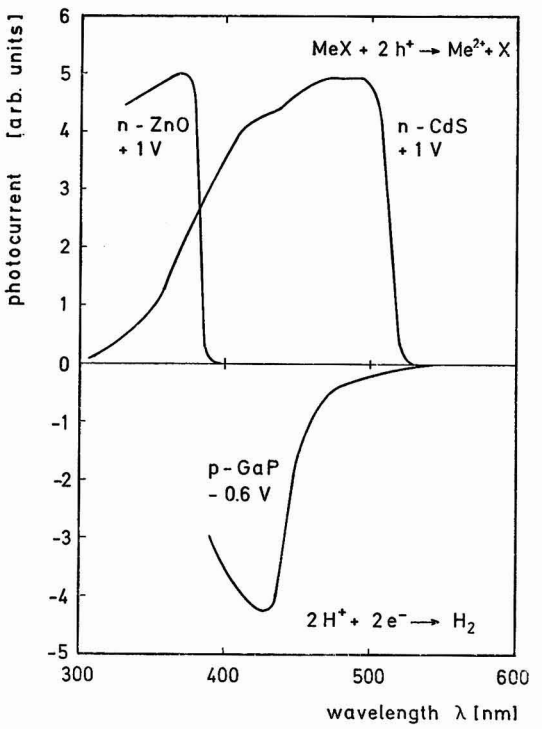

Fig. 19. Photocurrent spectra for n- and p-type semiconductors in saturation range.

lytes is the largest obstacle (28) Many research groups are working hard to overcome these difficulties and to develop devices by which either hydrogen or electric power can be generated in a photoelectrochemical cell.

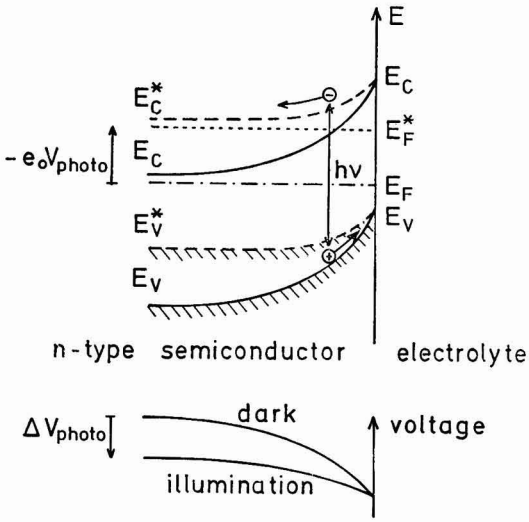

Fig. 20. Generation of a photovoltage in illuminated Schottky barrier.

The common bases of all these devices is the fact that semiconductor/electrolyte contacts form a Schottky barrier if the electrolyte contains a suitable redox system. Illumination of this Schottky barrier generates a photovoltage which acts as the driving force for electrolysis. As shown in Fig. 20, the source of the power and the mechanism of light to electrical energy conversion is the same as in photovoltaic solid-state devices. Therefore, semiconductor/electrolyte systems are subject to the same limitations in energy conversion efficiency as are the usual solid-state devices. The advantage of the electrochemical systems is the fact that this type of Schottky barrier can be formed very easily and without any problems with regard to the epitaxial conditions to avoid lattice misfit at the contact between two solids. The price one pays, however, is a susceptibility of the material to decomposition. The future will show whether technically reliable and efficient devices can be built on this principle.

Generation of Excited States by Electrolysis

Finally, we discuss somewhat the inverse of the processes discussed earlier, *i.e.*, the electrolytic generation of excited states. I shall not include the generation of excited states in homogeneous electrolytes which leads to luminescence and where the reaction partner can be generated by electrolysis. The discussion shall be restricted to the direct generation of excited states by electrode reactions.

Again, this can only be observed at semiconductors since the signal which indicates the generation of an excited electron state is light emission. How this is accomplished at the semiconductor electrode is shown in Fig. 21. If conditions can be found where the redox system injects minority carriers into the surface, they will recombine with the majority carriers. This is often a radiative process. Figure 21 shows this schematically for electron injection into a p-type semiconductor and hole injection into an n-type. In Fig. 22 are given the spectra of the emitted light from various electrodes where the conditions of Fig. 21 were met (29). These spectra for various n-type semiconductors show that the emitted light not only stems from band-to-band recombination, but sometimes contains light with smaller energy. It can be assumed that this light comes from recombination via surface states according to a mechanism which is shown in Fig. 23. Similar results have been obtained by electron injection into

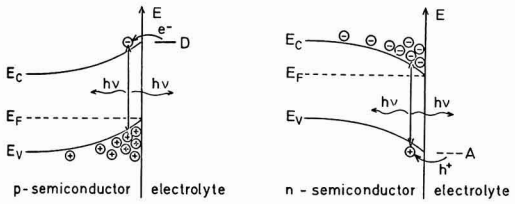

Fig. 21. Generation of luminescence by injection of minority carriers from redox systems into accumulation layer at the semiconductor/electrolyte contact.

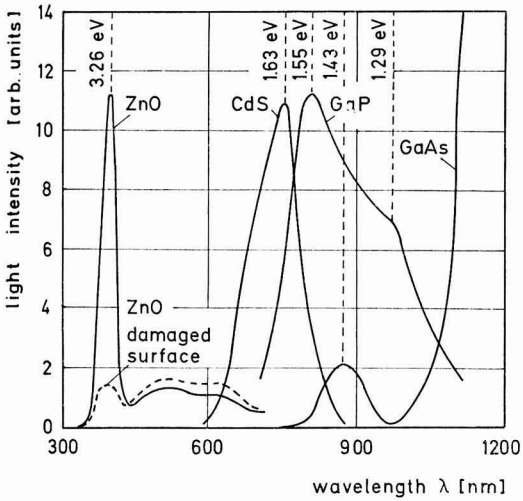

Fig. 22. Luminescence spectra of n-type semiconductors with hole injection by the radical SO_4^- with high oxidation potential.

p-type GaP (30). Such experiments can be very useful for elucidating the mechanism of electrochemical reactions at semiconductors and also for characterizing the electronic situation at a semiconductor electrolyte contact.

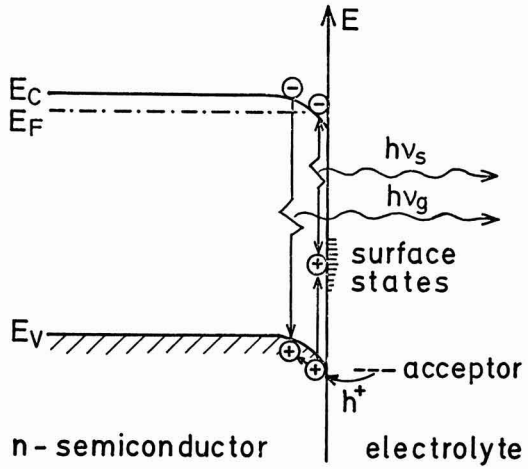

Fig. 23. Energy terms for luminescence by recombination from band-to-band or via surface states.

Summary

I have treated in my brief review only the simplest cases. As usual, the problems are in reality much more complicated and many questions are still open to discussion. There are many more applications of electronic excitation as a sensitive tool for studying the mechanism of electrode reactions or the properties of surface layers formed in an electrochemical process. I hope that the few examples given have demonstrated that the study of excited electronic states in electrochemistry is an exciting subject and I am convinced that many more electrochemists will be fascinated by this field in years to come. I am sure that this subject will contribute further to improving the understanding between electrochemists and solid-state physicists.

Acknowledgments

Those of my former and present co-workers who have made possible the contributions from my laboratory to the field which I have discussed in this lecture are portrayed in my last picture. I wish to express my appreciation.

Fig. 24. Co-workers of Heinz Gerischer.

REFERENCES

1. E. Becquerel, *C.R. hebd. Séances Acad. Sci.*, **9**, 58, 145, 561, 711 (1839).
2. H. Gerischer, *Faraday Discuss.*, **58**, 219 (1974).
3. F. Lohmann, *Z. Naturforschung*, **22a**, 813 (1967).
4. S. Trasatti, in "Advances in Electrochemistry and Electrochemical Engineering," H. Gerischer and C. W. Tobias, Editors, **10**, 213 John Wiley & Sons, New York (1977).
5. H. Gerischer, *Photochem. Photobiol.*, **16**, 243 (1972).
6. H. Gerischer, *Isr. J. Chem.*, **14**, 138 (1975).
7. Th. Förster, *Ann. Physik*, **2**, 55 (1948).
8. H. Kuhn, *J. Chem. Phys.*, **53**, 101 (1970).
9. H. Tributsch and H. Gerischer, *Ber. Bunsenges. Phys. Chem.*, **73**, 251, 850 (1969).
10. R. Memming and H. Tributsch, *J. Phys. Chem.*, **75**, 562 (1971).
11. H. Gerischer and F. Willig, "Topics in Current Chemistry," **61**, p. 31, Springer Verlag, Berlin-Heidelberg New York (1976).
12. Yu. V. Pleskov and Z. A. Rotenberg, *J. Electroanal. Chem.*, **20**, 1 (1969).
13. A. M. Brodsky and Yu. V. Pleskov, "Progress in Surface Science," Vol. 2, part 1, Pergamon Press, Oxford (1972).
14. G. C. Barker, A. W. Gardner, and D. S. Sammon, *This Journal*, **113**, 1182 (1966).
15. J. K. Sass, *Surf. Sci.*, **51**, 199 (1975).
16. J. K. Sass, E. Meyer, and H. Gerischer, *Ber. Bunsenges. Phys. Chem.*, **79**, 1077 (1975).
17. H. Gerischer, E. Meyer, and J. K. Sass, *ibid.*, **76**, 1191 (1972).
18. J. K. Sass and H. J. Lewerenz, Submitted to *J. Phys.*
19. J. K. Sass, H. Laucht, and S. Stucki, in "Proceedings of the International Symposium on Photoemission," Noordwijk, The Netherlands, R. F. Willis *et al.*, Editors, p. 83, European Space Agency, Paris (1976).
20. H. Gerischer, E. Meyer, and J. K. Sass, *Werkst. Korros.*, **25**, 235 (1974).
21. V. A. Myamlin and Yu. V. Pleskov, "Electrochemistry of Semiconductors," Plenum Press, New York (1962).
22. H. Gerischer, in "Physical Chemistry," Vol. IX A, H. Eyring, D. Henderson, and W. Jost, Editors, Academic Press, New York (1970).
23. H. Gerischer and F. Beck, *Z. Phys. Chem.*, **23**, 113 (1960).
24. H. Gerischer and W. Mindt, *Electrochim. Acta*, **13**, 1329 (1968).
25. A. Fujishima and K. Honda, *Nature (London)*, **238**, 37 (1972).
26. H. Gerischer, *J. Electroanal. Chem.*, **58**, 263 (1975).
27. "Proceedings of the Conference on Semiconductor-Liquid Junction Solar Cells," The Electrochemical Society, Princeton, N.J. (1977).
28. H. Gerischer, *J. Electroanal. Chem.*, In press.
29. B. Pettinger, H.-R. Schöppel, and H. Gerischer, *Ber. Bunsenges. Phys. Chem.*, **80**, 845 (1976).
30. R. Memming, *This Journal*, **116**, 785 (1969).
31. S. Trasatti, "Advances in Electrochemistry and Electrochemical Engineering," Vol. 10 H. Gerischer and Ch. W. Tobias, Editors, p. 213, J. Wiley & Sons, New York (1977).
32. R. Gomer and G. Tryson, *J. Chem. Phys.*, **66**, 4413 (1977).

CARL WAGNER, 1901-1977

Mankind is blessed, on very rare occasions, with an individual whose professional talents, achievements, and personal qualities are so outstanding and unique that he stands alone. Such a man was Carl Wagner, who died on 10 December 1977 in Göttingen, Germany, following several months of illness.

Carl Wagner, known throughout the world as the "father of solid-state chemistry," gave to colleagues, to students and to those that corresponded with him an unparalleled insight into the analysis and often the solution of problems which covered a wide range of the sciences. He was completely unselfish in sharing his ideas and thoughts with the world's scientific community through his technical papers, his memos, his letters, and his personal discussions.

He was born in Leipzig, Germany, on May 25, 1901 and obtained his doctorate in physical chemistry in 1924 from the University of Leipzig after attending both the University of Munich and the University of Leipzig. His very first paper "Die Oberflächenspannung verdünnter Elektrolytlösungen," "Physik. Z.," **25,** 474 (1925) was an indication of the greatness that this man was to attain. The elegant mathematical relations developed by Wagner to describe the deficiency of solute and, subsequently, the surface tension increase of the interfacial region of dilute electrolytic solutions were later further analyzed and simplified by L. Onsager and N. N. T. Samaras, "J. Chem. Phys.," **2,** 528 (1934).

Following his doctorate work, Wagner went to the University of Munich (1924-1927) where he served as an Assistant and obtained his "habilitation"—a German academic procedure which permits one to teach at the university level. His acquaintanceship with W. Jost took him to the Bodenstein Institut at the University of Berlin (1927-1928) where, at a colloquium, at Dahlem, he first met W. Schottky who introduced him to the problems of point defects in solid-state chemistry. Prior to this meeting, Wagner's publications were primarily concerned with analytical chemistry, photochemistry, and kinetics of reactions in electrolytic solutions, but following this meeting his thoughts turned to problems concerned with the solid state.

After a year at the Bodenstein Institut, Wagner spent five years (1928-1933) at the University of Jena as a privatdozent (≅Assistant Professor). A number of classic publications originated during this period among which were his papers on irreversible thermodynamics ["Annal. Phys.," **3,** No. 5, 629 (1929); **6,** No. 5, 370 (1930)], on the theory of point defects in solids [(i) "Z. Physik. Chem.," **B11,** 163 (1930) with W. Schottky; and (ii) "Z. Physik. Chem.," Bodenstein-Festband, 177 (1931)], and on high temperature oxidation processes [(i) "Z. Physik. Chem.," **B21,** 25 (1933); (ii) **B32,** 447 (1936); and (iii) **B40,** 197 (1938)]. In addition, at the age of 28, Carl Wagner served, with H. Ulich, as co-author of the book "Thermodynamik" (Springer-Verlag, 1929) with W. Schottky as the main author.

Dr. Wagner then went to the University of Hamburg for a year (1933-1934) as a visiting professor after which he accepted a professorship in physical chemistry at the Technische Hochschule in Darmstadt. He taught there for eleven years (1934-1945) including the World War II years. Wagner's productivity of outstanding publications during this period of time continued at an amazing rate. Among the papers that stand out were those concerned with the mechanisms of formation of ternary compounds ["Z. Physik. Chem.," **B34,** 309 (1936); **B34,** 317 (1936) with E. Koch], a theoretical analysis of the "doping" effect upon point defect concentrations ["Z. Physik. Chem.," **B38,** 295 (1938) with E. Koch], the classic mixed-potential, corrosion-related paper with Traud ["Z. Elektrochem.," **44,** 391 (1938)] and his second book contribution which appeared in Vol. 1, part 2 "Handbuch der Metallphysik," edited by Masing with Wagner's contributions appearing on pp. 1-206. This work was later to appear as "Thermodynamics of Alloys," Addison-Wesley Press, 1952.

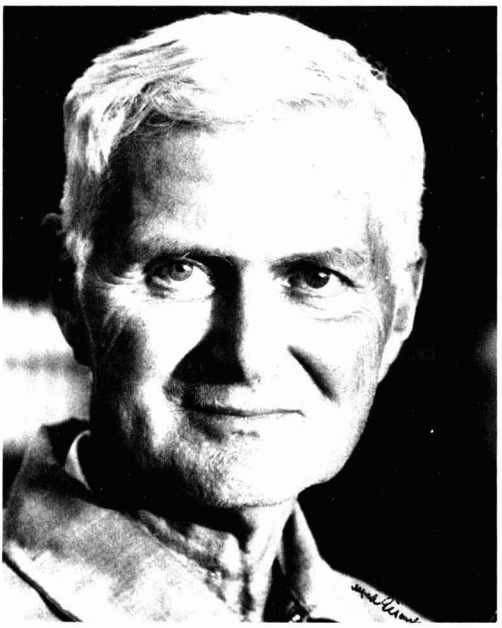

Carl Wagner

Following World War II, Carl Wagner came to the U.S.A. as one of von Braun's scientific advisors at Fort Bliss, Texas. He continued to publish during his four-year stay at Fort Bliss (1945-1949) covering again a rather wide range of subjects including dopant effects during parabolic oxidation processes, ["Acta Chem. Scand.," **1,** 547 (1947) with K. E. Zimens] and dissolution processes controlled by diffusion and natural convection ["J. Phys. Colloid. Chem.," **53,** 1030 (1949)].

Dr. Wagner, in 1949, joined the Metallurgy Department at MIT where he remained until 1958. His contributions were vast—on diffusion ["J. Metals," **4,** 91 (1952)], on interaction coefficients ["Thermodynamics of Alloys," Addison-Wesley Press, 1952], on point defects [**This Journal, 99,** 346C (1952); "J. Phys. Chem.," **57,** 738 (1953)], on solid electrolytes [**This Journal, 104,** 379 (1957) with K. Kiukkola], on minority electronic point defects ["J. Chem. Phys.," **26,** 1597 (1957) with J. B. Wagner, Jr.], and on high temperature oxidation processes [in "Atom Movements," ASM, 153 (1951); **This Journal, 99,** 369 (1952); "ibid.," **103,** 571 1956); "ibid.," **103,** 627 (1956)].

In 1958, Carl Wagner returned to Germany as Director of the Max-Planck-Institut für Phys. Chemie in Göttingen; and he had a particularly difficult position to fill since the former director, Karl F. Bonhoeffer, who had died suddenly, had been deservedly admired and respected by his colleagues and students. Nevertheless, Wagner through his direct, honest, well-organized administration soon gained the confidence of the Institut's personnel and, regardless of personality differences within the Institut they always stood united and proud of their kind "Chief" and their Institut's scientific endeavors. From 1958 to 1968, at which time Prof. Wagner retired as director of the Institut, the Institut served as a base for visiting scientists from many lands. Wagner in his quiet, pleasant manner instilled and inspired many who worked at his Institut. He cared for those who were in contact with him with sincere, honest affection, and although he always remained adamant about correctness in scientific works he, somehow, had the great capacity to overlook any errors in personal endeavors.

Carl Wagner, 1901-1977 Con't

During this period and virtually until the last few months of his life Wagner continued to publish. Some of these works were concerned with the theory of Ostwald ripening ["Z. Elektrochem.," **65,** 581 (1961)], disorder in ternary ionic crystals ["Z. Physik. Chem. N.F.," **31,** 198 (1962) with H. Schmalzried], the limitations of galvanic cells because of displacement reactions [**This Journal, 110,** 326 (1963) with A. Werner], transition between linear and parabolic oxidation kinetics ["Ber. Bunsenges. Physik. Chem.," **70,** 775 (1966)], catalytic processes ["Advances in Catalysis," **21,** 323 (1970)], surface chemistry ["Nachricht. Akad. Wissenschaften Göttingen," 37-63 (1973)]; and his third book "Methods of Natural Sciences and Technical Research" (Bibliographisches Institut AG, Zurich, 1974).

Carl Wagner was the first recipient (1951) of the Palladium Metal of The Electrochemical Society and also received, in 1973, the Gold Medal of the American Society for Metals. Other awards are unknown to the author at this time.

He did not marry nor did he have any close relatives at the time of his death.

Although this memorial to Carl Wagner has aimed primarily at outlining his professional positions and publications, I would be totally remiss in this work if I failed to mention the great respect, admiration, and trust that Wagner engendered in his associates. He was a kind and considerate gentleman who gave unselfishly to all. We shall miss him in our personal lives and in the sciences; however, we shall always remember him in accord with Schiller ". . . Wer den Besten seiner Zeit genug getan, der hat gelebt für alle Zeiten."

George Simkovich
The Pennsylvania State University

DIVISION NEWS

Dielectrics and Insulation Division

Report of the Nominating Committee

The Nominating Committee is pleased to report the following slate of candidates for divisional officers to be elected at the annual business meeting of the Dielectrics and Insulation Division at the Society Meeting in Seattle, Washington, May 21-26, 1978:

Chairman—R. G. Frieser
Vice-Chairman—R. N. Tauber
Secretary—A. Bell
Treasurer—J. A. Amick

Laurence D. Locker
Chairman

SECTION NEWS

Chicago

The Chicago Local Section held its fifth meeting of the program year on February 9, 1978. The speaker was Dr. T. Janson of Argonne National Laboratory who presented a review on a biomimetic approach to solar energy conversion. Dr. Janson briefly discussed the various types of chlorophylls and their role in photosynthesis. Chlorophyll "a" which contains a magnesium atom in the center of the porphyrin-type structure and three carbonyl groups, is involved in the collection and conversion of solar energy in plants. The structure and composition of chlorophyll "a" was investigated by visible, infrared, and NMR spectroscopy. These results led to an interpretation for the photoactive behavior of chlorophyll "a" in the "synthetic leaf" experiment. The chlorophyll "a" was deposited on various metal supports (Ag, Pt, An) and the emf generated by exposure to light was monitored between two Pt electrodes. Typically, currents of 1 μA and emf's of 10-180 mV were generated in the synthetic leaf experiment. Dr. Janson pointed out that this experimental arrangement is not practical for solar energy conversion; however, the information obtained by these studies could lead to the understanding necessary for the design of solar energy devices.

K. Kinoshita
Secretary

Cleveland

On February 20, 1978, the Cleveland Local Section held an afternoon seminar and laboratory open house and an evening general meeting at Case Laboratories for Electrochemical Studies. Both the afternoon and evening sessions were covered by Professor Uziel Landau, Chemical Engineering Department, Case Western Reserve University. The "Electrochemical Aspects of High Speed Electrodeposition" was the subject discussed in both sessions. A more basic approach was given in the afternoon session, in which the various factors affecting the current distribution were critically analyzed. Professor Landau's talk in the evening session was centered more on the practical aspects of high speed electroplating, in which a practical method of achieving selective metal deposition by controlled current distribution was given in detail.

Chin-Ho Lee
Secretary

Metropolitan New York

On March 1, 1978, fifty members and guests of the Metropolitan New York Local Section heard a talk by David Linden, recently retired Chief of Power Sources Technical Area, U.S. Army Electronics Command, entitled "New Lithium Primary Batteries." Dr. Linden outlined some of the advantages and disadvantages of lithium batteries, in which interest started in the early 1960's. Lithium offers a higher voltage than other batteries such as zinc or magnesium, and it is light weight, gives a high energy density, and can be stored for long periods. He pointed out, however, that it requires a nonaqueous electrolyte and that some of the lithium batteries can pose safety hazards. He gave performance characteristics of some types of lithium batteries and compared these to other types of batteries. He mentioned in particular the lithium/sulfur dioxide and lithium/thionyl chloride systems. Dr. Linden outlined various solutions to the safety hazards and touched briefly on solid-conducting electrolyte systems, such as lithium/iodide, and solid-cathode systems, such as lithium/vanadium, pentoxide/manganese dioxide, pentoxide/carbon fluoride, and pentoxide/copper sulfide. He concluded his talk with a listing of some of the lithium primary battery manufacturers and the types of lithium batteries they produce.

Shelie M. Granstaff, Jr.
Executive Committee Member

OBITUARY

Donald Wood, Founder of the Hill Cross Company, Incorporated, West New York, New Jersey, died on February 5, 1978.

Dr. Wood had been active in the plating industry since the 1920's. In 1942 he coauthored a chapter on "Silver Plating" in the first printing of "Modern Electroplating." He published a well-known paper in 1938 ("Metal Ind.," **36,** 330) describing an activation process for stainless steel, which is known throughout the industry as "Woods Nickel Strike." He worked on the Manhattan ("A Bomb") project during World War II, after which he founded Hill Cross Company in 1945.

Dr. Wood was an Active Member of The Electrochemical Society. He regularly participated in the Metropolitan New York Local Section activities. He served on the Host Committee for the 135th meeting held in New York in May 1969. Dr. Wood was an Active Member of the American Chemical Society and a Life Member of the American Society for Metals. He was also an Active Member of several section branches of the American Electroplater's Society, serving in the capacities of President and Secretary. In 1969, Dr. Wood served on the AES Research Board and received the Frank Lane Award.

NEWS ITEMS

1978 International Symposium on Gallium Arsenide and Related Compounds

The next conference of the biennial International Symposium on Gallium Arsenide and Related Compounds will be held September 24-27, 1978, at the Colony Hotel, St. Louis, Missouri. Authors are invited to submit abstracts in the areas of materials preparation, materials characterization, opto-electronics, microwave devices, solar cells, and other device technology, by June 1, 1978. For additional information, please contact: D. W. Shaw, Secretary, 1978 International GaAs Symposium, Mail Station 118, Texas Instruments Inc., P.O. Box 5936, Dallas, Texas 75222.

Read Conference on Electrodeposition

On August 7-11, 1978, the Read Conference on Electrodeposition (formerly Penn State Conference on Electrodeposition) will be held at The Pennsylvania State University. The conference is being organized with the intent of examining in detail certain topic areas of current interest in electroplating. This will be an off-the-record, informal meeting, which will be open to all participants for the expression of their views. For further information, please contact: Dr. H. W. Pickering, Chairman, Read Conference in Electrodeposition, 209 Mineral Industries Bldg., The Pennsylvania State University, University Park, Pa. 16802.

American Vacuum Society Symposium

The greater New York chapter of the American Vacuum Society is planning a one-day symposium on June 14, 1978, entitled "Ion Implantation—New Prospects for Material Modifications." The Symposium will be held at the IBM Thomas J. Watson Research Center in Yorktown Heights, New York, and will consist of two sessions on (i) new materials, and (ii) altered material properties. For further information, please contact: Walter Brown, Chairman, Bell Laboratories, Murray Hill, N.J. 07974.

Gordon Research Conferences

The Gordon Research Conferences for the summer of 1978 are to be held at various locations in New Hampshire and California from June 12 to August 25, 1978. Applications for each conference must be made on the standard application form. These and complete program details may be obtained by writing to the office of the Director: Dr. Alexander M. Cruickshank, Director, Gordon Research Conferences, Pastore Chemical Laboratory, University of Rhode Island, Kingston, Rhode Island 02881.

Discussion on Corrosion Control by Coatings

A discussion entitled "Corrosion Control by Coatings" will be held on November 3-15, 1978, at Lehigh University under the sponsorship of the Office of Naval Research. Further information may be obtained from Prof. Henry Leidheiser, Jr., Sinclair Laboratory #7, Lehigh University. Bethlehem, Pa. 18015.

Conference on Special Melting and Metallurgical Coatings

The American Vacuum Society is sponsoring an International Vacuum Metallurgy Conference on Special Melting and Metallurgical Coatings to be held April 2-6, 1979 in San Diego, California. The conference was established for the dissemination of information of films and coatings in all aspects of materials technology.

Technical papers are requested reporting significant advances in the theoretical, practical, industrial application, novel, and academic aspects of special melting and metallurgical coatings. For further information, please contact: Dr. G. K. Bhat, Carnegie-Mellon Institute of Research, 4400 Fifth Ave., Pittsburgh, Pa. 15213; telephone 412-578-2000 for special melting; or Dr. R. F. Bunshah, 6532 Boelter Hall, University of California, Los Angeles, Calif. 90024; telephone 213-825-2210 for metallurgical coatings.

Book Reviewers Needed

The Electrochemical Society needs competent individuals to review books for the Journal.

Any Society member who wishes to volunteer his services should send his name, address, and field of competence to the attention of the Book Review Editor, Dr. Julius Klerer, c/o The Electrochemical Society, P.O. Box 2071, Princeton, N.J. 08540

Nominations Solicited for the 1979 Olin Palladium Medal Award

Nominations are solicited by the Honors and Awards Committee for the 1979 Olin Palladium Medal Award. The next award will be presented at the Fall 1979 Meeting of the Society in Los Angeles, California.

The recipient shall be distinguished for contributions to the field of electrochemical science and corrosion. The recipient need not be a member of the Society, nor shall there be any restrictions or reservations regarding age, sex, race, citizenship, or place of origin or residence.

The award consists of a palladium medal and a nickel replica, both bearing the recipient's name, and the sum of one thousand five hundred dollars.

The recipient will deliver a general address to the Society on a subject related to the contributions for which the award is being presented.

Previous medalists have been:

Carl Wagner—1951
Nathaniel H. Furman—1953
Ulick R. Evans—1955
Karl F. Bonhoeffer—1957
Aleksandr N. Frumkin—1959
Herbert H. Uhlig—1961
Norman Hackerman—1965
Paul Delahay—1967
Thomas P. Hoar—1969
Leo Brewer—1971
V. G. Levich—1973
M. J. N. Pourbaix—1975
H. Gerischer—1977

Documents supporting the nominations need not be lengthy. They typically are made up of a description of the contributions made, a biography, and a list of publications. The publication list should include the paper titles, and it is helpful if the most significant publications are identified.

Nominations will close at the opening of the Fall 1978 Meeting. In order to facilitate distribution of the documents to Selection Committee members, please submit the nominations not later than September 15, 1978, to the Chairman of the Selection Committee, Dr. Fritz G. Will, General Electric Company, Research and Development Center, P.O. Box 8, Schenectady, New York 12301.

NEW MEMBERS

It is a pleasure to announce the following new members of The Electrochemical Society as recommended by the Admissions Committee and approved by the Board of Directors in March 1978.

Life Member

Moore, T. A., Corpus Christi, Tx.

Active Members

Bernard, C., St. Martin d'Heres, France
English, A. T., Summit, N.J.
Frankel, I., Springfield, Va.
Grabner, E. W., Frankfurt, Germany
Hale, J. M., Geneva, Switzerland
Jacob, K. T., Toronto, Ont., Canada
Lindsey, P. C., Jr., Richmond, Ca.
Mar, H. Y. B., Minneapolis, Mn.
Metzgar, T. D., Dallas, Tx.
Misra, S. S., Hoffman Estates, Il.
Packwood, D. L., Palo Alto, Ca.
Pavlov, D., Sofia, Bulgaria
Polcari, M. R., West Hurley, N.Y.
Preusch, C. D., Pittsburgh, Pa.
Redzinski, G. E., Cassopolis, Mi.
Sorenson, D. D., Bloomington, Mn.
Spangenberg, S. F., Midland, Mi.
Staley, R. H., Cambridge, Ma.
Vaidyanathan, K. V., Urbana, Il.
Wang, J. T., Sunnyvale, Ca.

Student Members

Davis, D. G., Berkeley, Ca.
Johnson, W. B., Philadelphia, Pa.
Kapusta, S., Houston, Tx.
Mlynko, W. E., Berkeley, Ca.
Ng, H. K., London, England
Ponce, F. A., Stanford, Ca.
Wilson, D. F., Storrs, Ct.

Reinstatement

Haas, R. M., Detroit, Mi.

BOOK REVIEW

"Annual Review of Materials Science," edited by R. A. Huggins, R. H. Bube, and R. W. Roberts. Published by Annual Reviews Co., Inc., Palo Alto, California (1977). 537 pages; $17.00.

In this, its 7th volume, the Materials Science review series seems to have reached full maturity. With three articles on structure, three on processing and related subjects, seven on properties and phenomena, and two on special materials, a very good balance has been achieved in this volume while serving the editors' main objective of providing useful reviews of recent progress and trends in materials science emphasizing the fundamentally similar phenomena, structural aspects, and tools and techniques applicable to a wide variety of materials. Among the materials discussed are alkali and alkaline earth halides, semiconductors, ceramics, steels, dental amalgam, high temperature alloys, and films and coatings of various types. More than a third of the articles were prepared by foreign authors.

The following articles, comprising about half the volume, are thought to be of particular interest to readers of **This Journal:** Kröger on defect chemistry in crystalline solids, Grimmeiss on deep level impurities in semiconductors, Bendow on fundamental optical phenomena in infrared window materials, Haacke on transparent conducting coatings, Thornton on high rate thick film growth, Grabke and Hörz on kinetics and mechanisms of gas metal interactions, and Stringer on hot corrosion of high temperature alloys. It is especially appropriate that the customary prefatory chapter chosen for this volume, "Point Defects and Their Interaction" was written by Carl Wagner, a veritable giant in the field, who passed from our midst just two months ago. It is likely his final publication.

The articles average about 30 pages and more than 100 references each. They are, without exception, competently written, and provide a current view of their subjects and lead-in to the pertinent literature. Many reveal new insights into the subject field and suggest new lines of research or development. The editors' decision to include chapters on topics which have recently been the subject of entire monographs may well be questioned, however. If this action was thought necessary for the sake of completeness, then it would seem that the readers' interests would have been better served by restricting the scope of such articles in some fashion rather than to expect the authors to accomplish in 30 pages what they themselves or their colleagues have elsewhere found necessary to expound in several hundred pages or more.

Full author and subject indexes are provided to the present volume as well as cumulative indexes to the authors and chapter titles of articles appearing in the prior volumes 3-7 of "Annual Review of Materials Science." A flyleaf lists selected titles of materials related chapters from other current members of the "Annual Reviews" family. Examples of possible interest to ECS members include "Waste Materials" and "Energy Storage" from "Annual Review of Energy" (1976) and "Pico-Second Spectroscopy" and "Laser Induced Fluorescence" from "Annual Review of Physical Chemistry" (1977).

J. H. Westbrook
General Electric Company
Schenectady, New York

ADVERTISERS' INDEX

NEW BOOKS

Progress in Solid State Chemistry, Vol. 10, edited by J. O. McCaldin and G. Somorjai.

1976, Pergamon Press, Inc., Maxwell House, Fairview Park, Elmsford, NY 10523. 284 pages, bound. $37.50.

The present volume includes two papers on oxides and sulfides of transition metals, one of which continues from previous volumes the exposition of ideas by one of the pioneers of solid-state chemistry. Subjects being reviewed a second time, but by a different author with a different viewpoint, are catalysis, phase diagrams, liquid crystals, and silver halides. Epitaxial growth processes used in semiconductor fabrication are again treated in the very timely article on molecular beam epitaxy. Of further interest to the semiconductor field is the article on photovoltaic cells used in the conversion of solar energy.

Electrodeposition of Chromium from Chromic Acid Solutions, by G. Dubpernell.

1977, Pergamon Press, Inc., Maxwell House, Fairview Park, Elmsford, NY 10523. 95 pages, bound. $12.50.

The book contains introductory chapters on the history, economic importance, and the two common forms of deposited chromium. The catalyst balance or its ratio to chromic acid concentration is discussed to show the importance of this controlling factor. The review of empirical tests for catalyst concentration and bath balance serves to emphasize the control exerted by the catalyst concentration. The final chapter discusses the complex subject of fluoride catalysts.

Aluminium Electrolysis: The Chemistry of the Hall-Heroult Process, by K. Grjotheim et al.

1977, Aluminium-Verlag GmbH, P.O. Box 1207, D-4000, Dusseldorf, Germany, 350 pages, bound.

This text presents a comprehensive treatise on the theory of aluminum electrolysis prepared by a team of eminent researchers in the field. In the volume, emphasis has been placed on the presentation of not only experimental data obtained but also the theoretical and experimental difficulties and uncertainties that still exist. The book deals with phase equilibria, thermodynamic data, structural species of cryolite-alumina melts, physicochemical properties, electrochemical properties, the electrode processes, interaction between aluminum and the electrolyte, current efficiency, and some technological aspects.

Metallic Coatings for Corrosion Control, by V. E. Carter.

1977, Butterworths, 19 Cummings Park, Woburn, MA 01801. 183 pages, bound.

This monograph outlines the chemical processes by which metallic coatings can control corrosion, and describes the various methods of applying coatings and testing their quality and performance. The book will help designers, engineers, and architects to select from the wide range of coatings the one best suited to a corrosion problem. Without involving the reader too deeply in the techniques of the coating processes, it will enable him/her to understand the preparation and application of coatings and how the limitations of individual steps of a process can affect the performance of the finished article.

International Congress on Marine Corrosion and Fouling; 4th: Proceedings.

1977, Centre de Recherches et d'Etudes, Oceanographiques 73, rue de Sèvres, 92100 Boulogne, France. 543 pages, bound.

This proceedings contains about 70 papers and discussions. Among the subjects covered are: Effect of rosin on high toxin antifouling paints; performance of platinum anodes in impressed current cathodic protection; observations of secondary attachment mechanisms in marine fouling algae; economical high performance zinc coating for marine use; fatigue of notched 1018 steel in sea water; studies on the reaction mechanism

of the adhesive of barnacles; cathodic protection of pipeline intervals; an apparatus for the study of marine corrosion of metals in the presence and absence of macrofouling; replaceable deep groundbed evaluation; and stress corrosion crack growth in aluminium alloys.

Electrochemical Reactor Design, by D. Pickett.

1977, Elsevier, P.O. Box 211, Amsterdam, The Netherlands; and 52 Vanderbilt Ave., New York, NY 10017. 434 pages, bound. $50.75.

This book has been written predominantly to show chemical engineers that the design of electrochemical systems is an area entirely within their scope, and for electrochemists who are interested in finding out how their data can be used to design processes. The first four chapters contain basic material. Chapters 5 and 6 present the design methods and these are primarily based on the classification of electrochemical reactors according to their operational mode. This classification is analogous to that used for conventional chemical reactors and permits comparison to be made with the design of non-electrochemical processes. Chapter 7 discusses miscellaneous design factors including methods of electrical connection and optimization.

Traité D'électricité, edited by G. Goudet.

1975, Masson & Cie Paris. Available in the U.S. from Scientific & Medical Publications of France, Corp., 14 E. 60th St., New York, NY 10022. 3 vol., bound. Vol. 1, $17.68; Vol. 2, $19.24; Vol. 3, $19.76.

The three volumes are: "Non-Time Dependent Electric and Magnetic Phenomena," "Time-Dependent Electric and Magnetic Phenomena," and "Electricity and Matter." Areas covered are: preliminary mathematics; electrostatics; direct current; magnetostatics; approximation of quasistationary states; electrical measurement; alternating currents in the approximation of quasistationary states; general laws of electromagnetism; conversion of electrical energy; electrochemical phenomena; gas and plasmas; electric and magnetic properties of solids; and quantum mechanics.

Biological and Artificial Membranes and Desalination of Water, edited by R. Passino.

1976, Elsevier, P.O. Box 211, Amsterdam, The Netherlands; and 52 Vanderbilt Ave., New York, NY 10017. 901 pages, bound. $99.75.

The thirty papers are grouped under the following headings: Water needs and the importance of desalination; structure of biological membranes and methods of study; ionic permeability and transport in biological and artificial membranes; artificial membranes-thermodynamics and transport; and general aspects of membranes phenomena. Some specific topics discussed: nuclear energy and water desalination; electrical methods in the study of biological membranes; electrical behavior of "excitable" artificial membranes; inorganic ion exchange membranes; chemical engineering problems regarding reverse osmosis process operation; and function and structure of membranes.

The Structure of Non-Crystalline Materials, edited by P. H. Gaskell.

1977, Taylor & Francis Ltd., 10-14 Macklin St., London WC2b 5NF, England. 262 pages, bound.

This volume provides a description of the present state of understanding of amorphous solids, covering silicate and chalcogenide glasses, semiconductors, polymers, and the recently discovered metal glasses. It provides a panorama of glass-structure determination and describes almost every method available.

The Rotating Disc Electrode, by Yu. V. Pleskov and V. Yu. Filinovskii.

1976, Plenum Publishing Corp., 227 W. 17th St., New York, NY 10011. 402 pages bound. $42.50.

This volume offers a complete survey of the many applications of the rotating-disk electrode, one of the principal techniques used in contemporary experimental electrochemistry. The authors review the properties of this unique method, notably its high accuracy in the measurement of diffusional fluxes and its uniform accessibility to surface and stationary conditions, providing the first full, systematic presentation of the theory and methodology of the rotating-disk electrode as well as the most important experimental results obtained through its use. The book reviews the experimental studies carried out with the help of this device, involving: the mechanism and kinetics of electrochemical reactions; the measurement of kinetic and catalytic currents; determination of the corrosion rates of metals; mass transfer; and analytical applications of the electrode.

Imaging Systems, by K. I. Jacobson and R. E. Jacobson.

1976, Halsted Press, 605 Third Ave., New York, NY 10016. 319 pages, bound. $27.50.

With the subtitle "Mechanisms and Applications of Established and New Photosensitive Processes," this book brings to the scientist and technologist information about the imaging systems with which they are becoming increasingly more involved. The early sections cover the normal color and monochrome silver halide systems including the preparation and constituents of the emulsion, the mechanism and chemistry of development, nonconventional methods such as solarization, Herschel effect, thermostabilization, and printing out papers, as well as the color negative, positive and reversal systems, dye destruction, imbibition, dye-gelatin transfer, and so on. There is a separate section on unconventional processing, and alternative systems are discussed.

Industrial Crystallization, edited by J. W. Mullin.

1976, Plenum Press, 227 W. 17th St., New York, NY 10011. 473 pages, bound. $45.00.

This volume presents fundamental and applied research on the use of crystallization in industry. The work reported covers a broad, multidisciplinary spectrum, ranging from solid-state physics to phase equilibria, from diffusional mass transfer to fluid mechanics, and from strength of materials to solution structure. Among the important topics discussed are: secondary nucleation; crystal growth kinetics; crystal habit modification; crystallizer design; industrial crystallizer operation; and case studies.

Electronic Processes in Unipolar Solid-State Devices, by D. Dascalu.

1977, Abacus Press, England. Distributed in the U.S. by International Scholarly Book Services, Inc., P.O. Box 555, Forest Grove, OR 97116.

London International Conference on Carbon and Graphite; 4th.

1976, Society of Chemical Industry, 14 Belgrave Sq., London, S.W.1, England. 808 pages, bound.

Oxides and Oxide Films, Vol. 5, edited by A. K. Vijh.

1977, Marcel Dekker Inc., 270 Madison Ave., New York, NY 10016. 184 pages, bound.

Union Internationale d'Electrothermie; 8th Congress.

Comite Organisateur: CBEE, Galerie Ravenstein 4/8, B 1000 Brussels, Belgium. 143 pages, paper.

Energy Futures: Industry and the New Technologies, by S. W. Herman et al.

1977, Inform, Inc. Available from Ballinger Publishing Co., 17 Dunster St., Cambridge, MA 02138. 661 pages, bound.

Symposium Commemorating 50 Years of Electron Diffraction, Proceedings, edited by L. 0. Boackway.

1977, Polycrystal Book Service, P.O. Box 11567, Pittsburgh, PA 15238. 126 pages, paper. $7.50.

Extractive Metallurgy of Copper, by A. K. Biswas and W. G. Davenport.

1976, Pergamon Press, Inc., Maxwell House, Fairview Park, Elmsford, NY 10523. 438 pages, bound. $15.00.

Stabilization of Photographic Silver Halide Emulsions, by E. J. Birr.

1974, Focal Press London & Hastings House, Publishers, 10 E. 40th St., New York, NY 10016. 275 pages, bound. $49.00.

Except where noted, these books have been prepared by the staff of The Engineering Societies Library, and were selected for inclusion in the **Journal** by Dr. Daniel Cubicciotti of Stanford Research Institute. The Electrochemical Society does not have copies available for sale or loan. Orders for the books should be forwarded directly to the publishers.

POSITIONS AVAILABLE

Please address replies to the box number shown, c/o The Electrochemical Society, Inc., P. O. Box 2071, Princeton, N. J. 08540.

Solid-State Electrochemist — research associate position. Work on fast ionic conductors, alkali metal solid electrolytes, mixed ionic-electronic conductors, and related materials for battery systems. Do experimental and theoretical research on transport properties of solids, involving use of controlled-atmosphere glove boxes, alkali metals at high temperatures, instrumentation, use of on-line computer control, and analysis of experiments. Must also be able to supervise graduate students, technicians, equipment design, and minicomputer programming. Technical background in materials science, physics, or chemistry and at least two years of postdoctoral experience required. Salary is $19,000-$21,000, depending upon qualifications. Send resume and copies of publications to Mary C. Clark, Bechtel International Center, P.O. Box 5816, Stanford, Calif. 94305.

Electrochemical Engineering—Postdoctoral research associate. Position available immediately in the engineering aspects of a large fuel cell program for energy storage applications. Chemistry and chemical engineering Ph.D.'s with experience in computer programming and applied mathematics are invited to apply. Enjoy the small town atmosphere in rural upstate New York between the beautiful St. Lawrence Seaway and the majestic Adirondack Mountains. For application, send resume and two letters of recommendation to: Dr. D-T. Chin, Department of Chemical Engineering, Clarkson College of Technology, Potsdam, New York 13676. Clarkson is an equal employment/affirmative action employer.

Electrochemist — for lithium battery research. World's largest manufacturer of batteries for the cardiac pacemaker industry seeks a researcher (M.S. or Ph.D.) to investigate new battery systems and to characterize and improve existing systems. A good theoretical background and several years experience in nonaqueous electrochemistry is required. Send resume and salary requirements to: Alan A. Schneider, Ph.D., Director of Research, Catalyst Research Corp., 1421 Clarkview Rd., Baltimore, Md. 21209; 301-296-7000.

POSITIONS WANTED

Metallurgical/Corrosion Engineer—Ph.D. expected in June 1978. Thesis on high temperature electrochemical study of aqueous corrosion in Fe-Ni-Cr alloy systems. Strong background in electrochemistry, physical metallurgy, thermodynamics, and fracture mechanics. Seeking position in R&D or consulting. Location and salary open. Reply Box C-207.

Engineer/Materials Scientist—Ph.D. Six years experience in research and development in metal oxides and thin film technology. Works involve preparation by RF sputtering, characterization and fabrication of vanadium oxide and thin film thermistor devices. Studies include electrical properties, metallization, and passivation techniques. Strong background in electron optics and x-ray diffraction. Publications and patent. Reply Box C-208.

Physical Metallurgist/Materials Scientist—Ph.D., May 1978. Desires challenging R&D or product development position. Strong background and summer training in: silicon-integrated circuit processing; physics of solid-state devices; structure-property correlations with TEM, SEM, and x-ray diffraction; crystal imperfections; mechanical testing; nondestructive testing; fracture mechanics; coatings and composites. Please contact: K. S. Rao, 1609 East 7th St., Tucson, Ariz. 85719; telephone 602-884-1361.

Chemist, Metallurgist—Heavy experience in staff engineering, lab work, R&D, production/management, skills in printed and integrated circuitry plating, electroforming, job shop management, and all aspects of plating and finishing. Desires challenging position, solid five-figure salary. Prefer Florida or West/Southwest, but no restrictions. A real pro who can deliver and troubleshoot (advanced technology) in either a large or small business. Reply Box C-209.

Positions Wanted

Society members of any class may, at no cost and for the purposes of professional employment, place not more than three identical insertions per calendar year, not to exceed 8 lines each. Count 43 characters per line, including box number, which the Society will assign.

Inco Limited, Inco United States, Inc. and ESB Incorporated will grant or cause to be granted to any person making written application therefor licenses of certain patents, patent applications and know-how related to the controlled microgeometry ("CMG") process of forming, perforating, and activating metallic foil and constructing battery electrodes therefrom. Licensees will also be granted certain immunities from suit with respect to other patents. CMG know-how will be furnished to know-how licensees in a written manual available at a cost of $1,000.

Such patent and know-how licenses, immunities and manual are available on the terms set forth in paragraphs IV(A) and (B) of the final judgment entered on January 30, 1978, in Civil Action No. 76-152 by the United States District Court for the Eastern District of Pennsylvania. Requests for the foregoing licenses, immunities or written manual should be addressed in writing to one of the following:

Ewan C. MacQueen, Esq.
Inco Limited
One New York Plaza
New York, N.Y. 10004

Ewan C. MacQueen, Esq.
Inco United States, Inc.
One New York Plaza
New York, N.Y. 10004

A. J. Rossi, Esq.
ESB Incorporated
5 Penn Center Plaza
Philadelphia, Pa. 19103

THE ELECTROCHEMICAL SOCIETY BOOKS IN PRINT

Monograph Series

The following hardbound volumes are sponsored by The Electrochemical Society, Inc. and published by John Wiley & Sons, Inc., 605 Third Avenue, New York, N.Y. 10016. Members of the Society can receive a 33% discount by ordering from Society Headquarters. Books and invoice are mailed by publisher. Nonmembers (including subscribers) must order direct from the publisher. All prices subject to change without notice.

Corrosion Handbook, edited by Herbert H. Uhlig (1948). 1188 pages, **$37.25.**

Arcs in Inert Atmospheres and Vacuum, edited by W. E. Kuhn. A 1956 Spring Symposium (1956). 188 pages, **$13.00.**

The Stress Corrosion of Metals, by Hugh I. Logan (1966). 306 pages, **$25.75.**

The Corrosion of Light Metals, by H. P. Godard, W. B. Jepson, M. R. Bothwell, and R. L. Kane (1967). 360 pages, **$23.25.**

High-Temperature Materials and Technology, edited by I. E. Campbell and E. M. Sherwood (1967). 1022 pages, **$45.50.**

Alkaline Storage Batteries, by S. Uno Falk and Alvin J. Salkind (1969). 656 pages, **$48.00.**

The Primary Battery, Volume I, edited by George W. Heise and N. Corey Cahoon (1971). 500 pages, **$37.25.**

Zinc-Silver Oxide Batteries, edited by Arthur Fleischer and John J. Lander (1971). 544 pages, **$41.00.**

The Corrosion of Copper, Tin, and Their Alloys, by Henry Leidheiser, Jr. (1971). 411 pages, **$47.50.**

Corrosion in Nuclear Applications, by W. E. Berry (1971). 572 pages, **$36.25.**

Handbook on Corrosion Testing and Evaluation, edited by W. H. Ailor (1971). 873 pages, **$54.50.**

Modern Electroplating, edited by Frederick A. Lowenheim. Third Edition (1974). 801 pages, **$35.50.**

Marine Corrosion, by Francis L. LaQue (1975). 332 pages, **$25.25.**

The Primary Battery, Volume II. edited by George W. Heise and N. Corey Cahoon (1975). 528 pages, **$42.25.**

Lead-Acid Batteries, by Hans Bode (1977). 387 pages, **$29.00.**

Society Symposium Series

The following softbound symposium volumes are sponsored and published by The Electrochemical Society, Inc., P.O. Box 2071, Princeton, N.J. 08540. Orders filled at the list price given, subject to availability. Enclose payment with order.

High-Temperature Metallic Corrosion of Sulfur and Its Compounds. Z. A. Foroulis, Editor. A 1969 symposium. 276 pages, **$4.50.**

Electron and Ion Beam Science and Technology, Fourth International Conference. R. Bakish, Editor. A 1970 symposium. 680 pages, **$7.50.**

Fundamentals of Electrochemical Machining. C. L. Faust, Editor. A 1970 symposium. 365 pages, **$4.50.**

Electron and Ion Beam Science and Technology, Fifth International Conference. R. Bakish, Editor. A 1972 symposium. 420 pages, **$5.50.**

Electrochemical Contributions to Environmental Protection. T. R. Beck, O. B. Cecil, C. G. Enke, J. McCallum, and S. T. Wlodek, Editors. A 1972 symposium. 173 pages, **$4.00.**

Oxide-Electrolyte Interfaces. R. S. Alwitt, Editor. A 1972 symposium. 312 pages, **$9.00.**

Marine Electrochemistry. J. B. Berkowitz, M. Banus, M. J. Pryor, R. Horne, P. L. Howard, G. C. Whitnack, and H. V. Weiss, Editors. A 1972 symposium. 416 pages, **$15.00.**

Semiconductor Silicon 1973. H. R. Huff and R. R. Burgess, Editors. A 1973 symposium. 936 pages, **$15.00.**

Electrochemical Bioscience and Bioengineering. H. T. Silverman, I. F. Miller, and A. J. Salkind, Editors. A 1973 symposium. 268 pages, **$8.00.**

Chlorine Bicentennial Symposium. T. C. Jeffery, P. A. Danna, and H. S. Holden, Editors. A 1974 symposium. 404 pages, **$11.00.**

Electrocatalysis. M. W. Breiter, Editor. A 1974 symposium. 378 pages, **$12.00.**

Electron and Ion Beam Science and Technology, Sixth International Conference. R. Bakish, Editor. A 1974 symposium. 594 pages, **$16.00.**

Properties of Electrodeposits—Their Measurement and Significance. R. Sard, H. Leidheiser, Jr., and F. Ogburn, Editors. A 1974 symposium. 430 pages, **$13.00.**

Metal-Slag-Gas Reactions and Processes. Z. A. Foroulis and W. W. Smeltzer, Editors. A 1975 symposium. 1032 pages, **$20.00.**

Chemistry and Physics of Aqueous Gas Solutions. W. A. Adams, G. Greer, J. E. Desnoyers, G. Atkinson, G. S. Kell, K. B. Oldham, and J. Walkley, Editors. A 1975 symposium. 522 pages, **$11.00.**

Chemical Vapor Deposition, Fifth International Conference. J. M. Blocher, Jr., H. E. Hintermann, and L. H. Hall, Editors. A 1975 symposium. 848 pages, **$18.00.**

Thermal and Photostimulated Currents in Insulators. D. M. Smyth, Editor. A 1975 symposium. 215 pages, **$7.00.**

Energy Storage. H. P. Silverman and J. B. Berkowitz, Editors. A 1975 symposium. 258 pages, **$8.00.**

Etching. H. G. Hughes and M. J. Rand, Editors. A 1976 symposium. 203 pages, **$7.00.**

Electron and Ion Beam Science and Technology, Seventh International Conference. R. Bakish, Editor. A 1976 symposium. 632 pages, **$18.00.**

International Symposium on Solar Energy. J. B. Berkowitz and I. A. Lesk, Editors. A 1976 symposium. 372 pages, **$10.00.**

International Symposium on Molten Salts. J. P. Pemsler, J. Braunstein, K. Nobe, D. R. Morris, and N. E. Richards, Editors. A 1976 symposium. 632 pages, **$16.00.**

Properties of High Temperature Alloys. Z. A. Foroulis and F. S. Pettit, Editors. 851 pages, **$12.00.**

Semiconductor Silicon 1977. H. R. Huff and E. Sirtl, Editors. A 1977 symposium. 1100 pages, **$15.00.**

A History of The Electrochemical Society. R. M. Burns with E. G. Enck. 160 pages, **$5.00.**

Semiconductor-Liquid Junction Solar Cells. A. Heller, Editor. A 1977 symposium. 340 pages, **$7.00.**

Load-Leveling. N. P. Yao and J. R. Selman, Editors. A 1977 symposium. 412 pages, **$13.00.**

Chemical Vapor Deposition, Sixth International Conference. L. F. Donaghey, P. Rai-Choudhury, and R. N. Tauber, Editors. A 1977 symposium. 596 pages, **$14.00.**

Electrode Materials and Processes for Energy Conversion and Storage. J. D. E. McIntyre, S. Srinivasan, and F. G. Will, Editors. A 1977 symposium. 1048 pages, **$20.00.**

High Temperature Metal Halide Chemistry. D. L. Hildenbrand and D. D. Cubicciotti, Editors. A 1977 symposium. 678 pages, **$17.00.**

APPLICATION FOR ADMISSION

TO

The Electrochemical Society, Inc.

Return completed application to:

Secretary
The Electrochemical Society, Inc.
Post Office Box 2071, Princeton, New Jersey 08540

For office use only

Info. Req. _____ Rec'd _____ Checked: _____

Notice of Ackn. _____ Accep. _____ Approved: _____

_____ $ _____ Elected:
recap

To the Board of Directors of The Electrochemical Society, Inc:

Name _____
(please print)

hereby makes application for admission to The Electrochemical Society, Inc., as a _____ member, and encloses the amount of $ _____ covering the first year's dues. (Please see reverse side for proper class of membership and dues applying thereto, noting the options with regard to the date of election and active life membership and the credit available for nonmember meeting registration.)

1. Date of Birth: _____

2. Education:

Institution	Dates Attended	Major Subject	Degree Earned

3. Work Experience:

Name of Employer (current, followed by previous)	Dates	Position

4. Please indicate your DiVISIONAL and GROUP interests in numerical order, starting with the number 1 for your primary interest(s).

—— Battery
—— Corrosion
—— Dielectrics and Insulation
—— Electrodeposition
—— Electronics—check interest(s) below
☐ General Materials and Processes
☐ Luminescence
☐ Semiconductors
—— Electrothermics and Metallurgy
—— Energy Technology Group
—— Industrial Electrolytic
—— Organic and Biological Electrochemistry
—— Physical Electrochemistry

5. Please check LOCAL SECTION with which you wish to affiliate:

—— Boston
—— Chicago
—— Cleveland
—— Columbus
—— Detroit
—— Indianapolis
—— Metropolitan N.Y.
—— Midland (Mich.)
—— Natl. Capital Area
—— Niagara Falls
—— North Texas
—— Ontario-Quebec
—— Pacific Northwest
—— Philadelphia
—— Pittsburgh
—— Rocky Mountain
—— San Francisco
—— So. Calif.-Nevada
—— None

6. Our Constitution provides that two Active Members of the Society (who can substantiate the above record) must recommend you for admission to membership. It will facilitate the handling of your application if you are able to have your references sign this application form; if this is not convenient, please list their names and addresses. On a student application, only a single faculty member recommendation with signature (including title and institution) is required.

Name (please print)	Signature	Address
Name (please print)	Signature	Address

The undersigned certifies that the above statements are correct and agrees, if elected to the Society, to be governed by its Constitution and Bylaws and to promote the objects of the Society as stated in its Constitution.

_____
(Signature)

Please print complete address as it should appear on mailings.

_____
_____
_____
_____

Date _____ 19__

EXTRACTS FROM THE CONSTITUTION AND BYLAWS

CONSTITUTION—Article II

Membership

Section 1. The individual membership shall consist of Active, Honorary and Emeritus Members. The Board of Directors may from time to time authorize other classifications of membership as defined in the Bylaws of the Society.

(*Active Member—Annual Dues $30.00*)

Active Member

Section 2. An Active Member shall be interested in electrochemistry or allied subjects and possess a Bachelor's degree, or its equivalent, in engineering or natural science. In lieu of a Bachelor's degree, or its equivalent, any combination of years of undergraduate study and years of relevant work experience in electrochemistry or allied subjects adding to at least seven years shall be required. Election to Active Membership shall require the recommendation of two Active Members in good standing.

BYLAWS—Article II

Non-Voting Membership
(*Student Member—Annual Dues $3.00*)

Student Member

Section 1. Student Member. A Student Member shall be a full-time undergraduate or graduate student registered for a degree in natural science or engineering. The applicant for Student Membership shall be recommended by a member of the faculty of the school. Upon graduation with a Bachelor's degree or equivalent in natural science or engineering, the Student Member may apply for Active Membership. The application shall be approved by two Active Members of the Society in good standing. If the Student Member enters graduate school as a full-time student, the person may choose to apply for Active Membership or remain a Student Member.

BYLAWS—Article XXI

Dues and Fees

Dues

Section 1. The annual dues for Active Members shall be thirty dollars. The annual dues for Student Members shall be three dollars. Each member shall receive the JOURNAL OF THE ELECTROCHEMICAL SOCIETY.

Date of Election

Section 2. When individuals are elected to membership, they must elect to initiate their membership as of January 1 or July 1 of the year of election; or, if elected during the last quarter, January 1 of the year following election. In the case of a July 1 election for starting membership, dues will be prorated.

Active Life Membership

Section 3. Any Active Member who shall pay in one lump sum the amount equivalent to two-thirds of the remaining dues to age sixty-five at the time of payment, but not less than an amount of 5 years of full dues, shall be exempt from payment of any further dues and shall be considered an Active Member during the remainder of his or her life.

BOARD OF DIRECTORS ACTION OF OCTOBER 9, 1960

Nonmember Meeting Registration Credit

If application for new membership is received within four months of the payment of nonmember registration at a Society Meeting by the applicant, the difference between the nonmember and member registration fees shall be credited toward the first year's dues.

CONSTITUTION—Article III

Admission and Dismissal of Members

Section 1. Application for individual membership shall be in writing on a form adopted by the Board of Directors.

Section 2. The Admissions Committee shall be a rotating committee consisting of three members. One member shall be appointed each year by the President with the approval of the Board of Directors for a term of three years to replace the outgoing member. This Committee shall receive from the Secretary all properly executed and properly recommended applications for admission which he has received from persons desirous of becoming members of the Society. It shall be the duty of this Committee, after examining the credentials of applicants, to make appropriate recommendation to the Board as to approval or rejection of the applications. Unanimous approval of an applicant by this Committee shall be required before the candidate's name may be submitted to the Board of Directors for election. The election to membership shall be by a mail vote of the Board of Directors. The candidate shall be considered elected two weeks after the date the proposed membership list is mailed to the Board if no negative votes have been received by the Secretary. If a candidate receives one negative vote, his application shall then be considered and voted upon at the next meeting of the Board of Directors. Two negative votes cast at this meeting shall exclude a candidate. The Board of Directors may refuse to elect a candidate who, in its opinion, is not qualified for membership. The names of those elected shall be announced to the Society. Duly elected candidates shall have all the rights and privileges of membership as soon as their entrance fee, if any, and dues for the current year have been paid.

Section 3. A member desiring to resign shall send a written resignation to the Office of the Society.

Section 4. Upon the written request of ten or more Active Members that, for cause stated therein, a member be dismissed, the Board of Directors shall consider the matter and, if there appears to be sufficient reason, shall advise the accused of the charges against him. He shall then have the right to present a written defense, and to appear in person before a meeting of the Board of Directors, of which meeting he shall receive notice at least twenty days in advance. Not less than two months after such meeting the Board of Directors shall finally consider the case and, if in the opinion of the majority of the Board of Directors a satisfactory defense has not been made and the accused member has not in the meantime tendered his resignation he shall be dismissed from the Society.

Section 7. The entrance fee, if any, annual dues and any other payments to be made by the members of the Society shall be paid in accordance with regulations set forth in the Bylaws.

Section 8. Any member delinquent in dues after April 1 shall not receive the Society's publications and will not be allowed to vote in any Society election until such dues are paid. All members in arrears for one year after April 1 shall lose their membership status and can be reinstated only by action of the Board of Directors.

THE ELECTROCHEMICAL SOCIETY PATRON MEMBERS

Bell Telephone Laboratories, Inc.
Murray Hill, N.J.

Dow Chemical Co.
Inorganic Chemicals Dept., Midland, Mich.

E. I. du Pont de Nemours and Co.
Plastic Products and Resins Department
Wilmington, Del.

General Electric Co.
Battery Business Department, Gainesville, Fla.
Chemical Laboratory, Knolls Atomic Power Laboratory, Schenectady, N.Y.
Electronic Capacitor Products Section, Irmo, S.C.
Lamp Div., Cleveland, Ohio
Materials & Process Laboratory, Large Steam Turbine-Generator Dept., Schenectady, N.Y.
Research and Development Center,
Physical Chemistry Laboratory & Power Systems Laboratory,
Signal Processing & Communication Laboratory,
Schenectady, N.Y.
Semiconductor Products Dept.,
Syracuse, N.Y.

International Business Machines Corp.
New York, N.Y.

The International Nickel Co., Inc.
New York, N.Y.

Olin Corporation
Chemicals Div., Research Dept., New Haven, Conn.

Philips Research Laboratories
Eindhoven, Holland

Union Carbide Corp.
Battery Products Div., Corporate Research Dept.,
New York, N.Y.

Westinghouse Electric Corp.
Electronic Tube Div., Elmira, N.Y.
Lamp Div., Bloomfield, N.J.
Semiconductor Div., Youngwood, Pa.
Research Laboratories, Pittsburgh, Pa.
K. W. Battery Co., Westinghouse Subsidiary,
Skokie, Ill.

THE ELECTROCHEMICAL SOCIETY SUSTAINING MEMBERS

The Aerospace Corporation
Los Angeles, Calif.

Airco Industrial Gases
Murray Hill, N.J.

Airco Speer Carbon-Graphite
St. Marys, Pa.

Allied Chemical Corp.
Industrial Chemicals Division
Solvay, N.Y.

Aluminum Co. of America
New Kensington, Pa.

Aluminum Co. of Canada, Ltd.
Montreal, P.Q., Canada

AMAX Inc.
New York, N.Y.

AMP Incorporated
Harrisburg, Pa.

Analog Devices, Inc.
Norwood, Mass.

Applied Materials, Inc.
Santa Clara, Calif.

Asahi Chemical Industry Canada, Ltd.
Toronto, Ontario, Canada

ASARCO Incorporated
South Plainfield, N.J.

BASF Wyandotte Corporation
Wyandotte, Mich.

Battelle Memorial Institute
Columbus, Ohio

Beckman Instruments, Inc.
Fullerton, Calif.

Bell-Northern Research
Ottawa, Ont., Canada

Bethlehem Steel Corp.
Bethlehem, Pa.

Boeing Co.
Seattle, Wash.

The Borg-Warner Corp.
Roy C. Ingersoll Research Center
Des Plaines, Ill.

Brown, Boveri & Co., Ltd.
Research Center
Baden, Switzerland

Canadian Industries Ltd.
Montreal, P.Q., Canada

Carborundum Co.
Niagara Falls, N.Y.

Chrysler Corporation
Detroit, Michigan

Cominco Ltd.
Trail, B.C., Canada

The Continental Group, Inc.
Technical Office at LMSC
Palo Alto, Calif.

Corning Glass Works
Corning, N.Y.

Crawford & Russell Inc.
Stamford, Conn.

Diamond Shamrock Corp.
Painesville, Ohio

Dow Corning Corporation
Hemlock, Mich.

Duro-Test Corp.
North Bergen, N.J.

Eastman Kodak Co.
Rochester, N. Y.

Electrochemical Technology Corp.
Seattle, Wash.

Electrode Corporation
Chardon, Ohio

Eltra Corp.
Prestolite Div., Toledo, Ohio
C&D Batteries, Conshohocken, Pa.

ESB Incorporated
Ray-O-Vac Div., Madison, Wisc.
Technology Center, Yardley, Pa.

SUSTAINING MEMBERS (CONTINUED)

Ever Ready Co. (Holdings) Ltd.
Whetstone, London, England

Exmet Corporation
Bridgeport, Conn.

Exxon Research and Engineering Co.
Corporate Research Battery Unit
Linden, N.J.
Engineering Technology Div.
Florham Park, N.J.

Fairchild Camera & Instrument Corp.
Research and Development Laboratory
Palo Alto, Calif.

FMC Corp.
Inorganic Chemicals Div.
Buffalo, N.Y.

Foote Mineral Co.
Exton, Pa.

Ford Motor Co.
Dearborn, Mich.

General Motors Corporation
Delco Electronics Div., Kokomo, Ind.
Delco-Remy Div., Anderson, Ind.
Research Laboratories Div., Warren, Mich.

Globe-Union, Inc.
Milwaukee, Wisc.

B. F. Goodrich Chemical Co.
Cleveland, Ohio

Gould Inc.
Gould Laboratories—
Electrical & Electronics Research
Energy Research
Rolling Meadows, Ill.
Gould Laboratories
Cleveland, Ohio

Great Lakes Carbon Corp.
New York, N.Y.

GTE Laboratories
Waltham, Mass.

GTE Sylvania Incorporated
Chemical & Metallurgical Division
Towanda, Pa.

The Harshaw Chemical Co.
Cleveland, Ohio

Hewlett Packard Company
Loveland, Colo.

Hill Cross Co., Inc.
West New York, N.J.

Honeywell, Inc.
Power Sources Center
Horsham, Pa.

Hooker Chemical Corp.
Niagara Falls, N.Y. (2 memberships)

HP Associates
Palo Alto, Calif.

Hughes Research Laboratories
Div. of Hughes Aircraft Co.
Malibu, Calif.

Industrial Innovation Center
Tehran, Iran

Kaiser Aluminum & Chemical Corp.
Pleasanton, Ca.

Kawecki Berylco Industries, Inc.
Boyertown, Pa.

Kennecott Copper Corp.
New York, N.Y.

Kerr-McGee Corporation
Technical Center
Oklahoma City, Okla.

Arthur D. Little, Inc.
Cambridge, Mass.

Lockheed Missiles & Space Co., Inc.
Research Laboratory
Palo Alto, Calif.

Mallory Battery Company
Tarrytown, N.Y. (2 memberships)

Marathon Battery Co.
Waco, Texas

Marston Bermuda
Hamilton, Bermuda

Matsushita Electric Industrial Co., Ltd.
Osaka, Japan

Microwave Associates, Inc.
Burlington, Mass.

Molycorp, Inc.
New York, N.Y.

Monsanto Company
St. Louis, Mo.

Motorola Inc.
Phoenix, Ariz.

M&T Chemicals Inc.
Detroit, Mich.

NL Industries, Inc.
New York, N.Y.

Occidental Research Corporation
La Verne, California

Olin Corporation
Metals Research Laboratories
New Haven, Conn.

Owens-Illinois Inc.
Toledo, Ohio

Oxy Metal Industries Corp.
Warren, Mich.

Perkin-Elmer Corp.
Norwalk, Conn.

Phelps Dodge Refining Corp.
Maspeth, N.Y.

Philips Laboratories. Inc.
Briarcliff Manor, N.Y.

PPG Industries, Inc.
Chemical Div.
Pittsburgh, Pa.

RCA Corporation
Color Picture Tube Division
Lancaster, Pa.

Reynolds Metals Co.
Reduction Research Div.
Sheffield, Ala.

Rockwell International
El Segundo, Calif.

SAFT America, Inc.
Valdosta, Ga.

Sandia Laboratories
Albuquerque, N. M.

J. C. Schumacher Co.
Oceanside, Calif.

Siemens Aktiengesellschaft
Munich, Germany

Signetics Corp.
Sunnyvale, Ca.

Sobin Chemical Co.
Orrington, Maine

Sperry Research Center
Sudbury, Mass.

Sprague Electric Co.
North Adams, Mass.

Stackpole Carbon Co.
St. Marys, Pa.

Standard Telecommunication Laboratories Ltd.
Essex, England

Stauffer Chemical Co.
Dobbs Ferry, N.Y.

St. Joe Minerals Corp.
Monaca, Pa.

Teletype Corp.
Skokie, Ill.

Texas Instruments Inc.
Attleboro, Mass.
Dallas, Texas

Tokyo Shibaura Electric Co., Ltd.
Toshiba Research and
Development Center
Kawasaki, Japan

United States Steel Corp.
Research Laboratory
Monroeville, Pa.

Varian Associates
Palo Alto, Calif.

Wacker Chemitronic
Burghausen, Germany

Western Electric
Princeton, N.J.

Xerox Corporation
Rochester, N.Y.

Yardney Electric Corporation
Pawcatuck, Conn.

Zenith Radio Corp.
Chicago, Ill.